Mechanistic Studies of Oxygen Activation and Atom Transfer Reactions with Mononuclear Vanadium(III), Iron(II), and Palladium(0) Complexes

A dissertation submitted by

Taryn D. Palluccio

In partial fulfillment of the requirements

for the degree of

Doctor of Philosophy

in

Chemistry

Tufts University

February 2015

Advisor:

Professor Elena V. Rybak-Akimova

ABSTRACT

This thesis comprises the area of oxygen binding, activation, and related oxygen atom transfer processes promoted by mononuclear transition metal complexes of vanadium(III), iron(II), and palladium(0).

The first part of this thesis details the mechanistic studies of ligand binding and oxygen atom transfer (OAT) reactions to the three-coordinate complex $V^{III}(N[^tBu]Ar)_3$ (Ar = 3,5-$Me_2C_6H_3$). The kinetics of OAT to $V(N[^tBu]Ar)_3$ from N_2O and other *N*-oxides is presented in Chapter 1, which revealed a wide range of kinetic behavior influenced by the mode and strength of coordination of the *N*-oxide and its ease of atom transfer. The importance of ligand binding, the initial step in the OAT reaction, is highlighted. Chapter 2 presents the kinetics of nitrile (RCN) binding to $V(N[^tBu]Ar)_3$, which serves as a comparative study with $Mo(N[^tBu]Ar)_3$. Studies revealed much faster binding of nitriles to $V(N[^tBu]Ar)_3$, which coordinate exclusively in an η^1-fashion. The differences in binding rates and affinities due to metal substitution are emphasized. The kinetic study of dioxygen binding to $V(N[^tBu]Ar)_3$ is presented in Chapter 3. Formation of the novel (η^2-O_2)$V(N[^tBu]Ar)_3$ adduct proceeds through a biphasic process involving rapid formation of (η^1-O_2)$V(N[^tBu]Ar)_3$ which subsequently isomerizes to the η^2-O_2 product. The rates of formation and interconversion of (η^1-O_2)$V(N[^tBu]Ar)_3$ and (η^2-O_2)$V(N[^tBu]Ar)_3$ were quantified.

Chapter 4 details the mechanistic study of dioxygen binding to $Pd^0(IPr)_2$ (IPr = 1,3-bis(2,6-diisopropyl)phenylimidazol-2-ylidene), which forms an unprecedented *trans*-(η^1-O_2)$_2$Pd(IPr)$_2$ adduct. The unstable (η^2-O_2)Pd(IPr)$_2$ intermediate forms at low

temperatures and reacts further with O_2 at higher temperatures to produce *trans*-(η^1-O_2)$_2$Pd(IPr)$_2$. The reaction is proposed to proceed through a steady state (η^1-O_2)Pd(IPr)$_2$ intermediate that can trap a second molecule of O_2 to form the unique final product. This work highlights how subtle changes in ligand sterics dramatically affect the relative stabilities of (η^2-O_2)Pd(NHC)$_2$ (NHC = *N*-heterocyclic carbene) adducts.

The comparative study of biomimetic non-heme iron complexes supported by aminopyridine macrocyclic ligands (PyMACs) is presented in Chapter 5, including the preparation of two novel complexes that are potent oxygenation catalysts. This work highlights the effect of the axial donor on the structure and reactivity towards olefin epoxidation and provides preliminary insight into the nature of reactive intermediates.

ACKNOWLEDGEMENTS

I would first like to sincerely thank my research advisor, Dr. Elena Rybak-Akimova, for being a constant source of insight and encouragement over the past six years. I am so grateful for the many great scientific opportunities she has provided for me and I feel lucky to have worked for such a warm and easygoing leader. I also want to thank my committee members Dr. Terry Haas and Dr. Robert Stolow for their insight, support, and advice throughout the years I've spent at Tufts.

I am honored to have had the opportunity for extensive collaborations with research groups outside of Tufts, and I wish to acknowledge our collaborators Dr. Carl Hoff (University of Miami), Dr. Kit Cummins (MIT), and Dr. Manuel Temprado (Universidad de Alcalá), as well as the members of their research groups for their help and assistance with our projects. It was truly a pleasure working with you all and learning from you. A majority of this thesis exists because of these collaborative efforts. And especially to Dr. Hoff, who has gone out of his way to help me both professionally and personally: I can't thank you enough for all the valuable discussions on kinetics, and your kind words of encouragement.

I thank all of my lab mates in the Rybak-Akimova lab, especially Drs. Celeo Guifarro, Wanhua Ye, Meaghan Germain, and Xianru Sun for being so helpful and supportive in (and out of) the lab. Also to everyone else I've had the pleasure of working with over the years at Tufts: Anna Dukovich, Guang Yang, Reza Latifi, Olga Makhylnets, Evan Haas, Voltaire Organo, Jeffrey Wikstrom, Yurii Moroz, Garvey MacKenzie, Marc Piquette, and Tim Han. Much thanks for putting up with me! Also

thanks to David Wilbur and Larry Aulenback for their assistance with instruments and every little issue they were of help with during my time at Tufts.

I wish to thank Dr. Peter Mueller not only for taking the time to serve on my committee, but for sharing his love of crystallography with me and taking me under his wing. Because of him, I was able to develop my crystallographic skills more than I ever thought I would during graduate school and connect with many wonderful crystallographers from all over the world. I am forever grateful for his advice and friendship.

I am also eternally grateful to my undergraduate research advisor Dr. Stephen Waratuke and many of the professors and staff from Bridgewater State University's Chemistry and Biology departments: Steven Haefner, Tammy King, Patricia Mancini, Ed Brush, Jeffrey Bowen, and Jane Doherty, just to name a few. You are my inspiration and just knowing that you've been rooting for me over these years has truly given me the motivation to get through graduate school. *An understanding heart is everything in a teacher, and cannot be esteemed highly enough. One looks back with appreciation to the brilliant teachers, but with gratitude to those who touched our human feeling. The curriculum is so much necessary raw material, but warmth is the vital element for the growing plant and for the soul of the child*.

To my brothers Erik and Kurt, my cousin Jill, and my dear friends Nick Wilton, Celeo Guifarro, Lynwood Walker, Christina Zaino, Chuck Kokoros, Jamie Ash, and Trey Lawrence: *There is no happiness like that of being loved by your fellow creatures, and feeling that your presence is an addition to their comfort*. I am grateful for the countless times you have cleaned me up when I was a mess (figuratively speaking for the most

part), and for still wanting to stick around after the fact. ☺ You have helped me learn a lot about myself over these past few years. You have opened my mind to the idea of actually paying some attention to what the hell is going on in the world around me. You have all contributed to the person I have become today. And even though time has and will probably continue to take us apart, *our roots will always be tangled and I'm glad for that.*

While on the subject of companions, I must mention my feline ones. I am glad that domestication exists because when you don't want to be alone and yet don't want to be around people, as has happened often over the course of this work, pets come in handy. My beloved kitty Peanuts was my best buddy for twenty-one years. We grew up side by side and she almost made it long enough to see me through this Ph.D. And to Dudley, my new buddy, for making it impossible to do any work from home!

And lastly, to my parents: I could never have done this without you by my side. You've managed to keep me grounded yet help me to dream big at the same time and I am so very grateful for that. I love you so much and can't thank you enough for all of your encouragement and support throughout my life. This one's for you.

Taryn

TABLE OF CONTENTS

Mechanistic Studies of Oxygen Activation and Atom Transfer Reactions with Mononuclear Vanadium(III), Iron(II), and Palladium(0) Complexes

Chapter 6. Unpublished X-Ray Structural Data

LIST OF TABLES

CHAPTER 1.

APPENDIX 1.

CHAPTER 2.

APPENDIX 2.

CHAPTER 3.

APPENDIX 3.

CHAPTER 4.

APPENDIX 4.

CHAPTER 5.

APPENDIX 5.

CHAPTER 6.

LIST OF FIGURES

CHAPTER 1.

APPENDIX 1.

CHAPTER 2.

APPENDIX 2.

CHAPTER 3.

APPENDIX 3.

CHAPTER 4.

APPENDIX 4.

CHAPTER 5.

APPENDIX 5.

CHAPTER 6.

PREFACE

This thesis primarily comprises the area of oxygen binding, activation, and related atom transfer processes promoted by mononuclear transition metal complexes of iron(II), vanadium(III), and palladium(0). Oxygen atom transfer reactions to and from transition metal centers represent important steps in many transition metal catalyzed oxidation reactions and this work primarily involved the understanding of how these processes unfold at the molecular level. We rely on the stopped-flow technique in conjunction with UV/visible spectroscopic measurements to gain insight into the mechanisms of these rapid reactions. Insight from such studies is useful in that it may ultimately lead to novel complexes capable of carrying out environmentally friendly and selective aerobic oxidations. These systems reveal a wide array of kinetic behavior with sometimes surprising results, and the information gained from this work is essential for the advancement of small molecule activation by synthetic transition metal complexes.

The detailed stopped-flow kinetic studies that are presented herein began during my second year of graduate school when I took over a project concerning the study of nitrile binding to the very air and moisture sensitive $V(N[^tBu]Ar)_3$ (Ar = 3,5-$Me_2C_6H_3$) complex. This initial work subsequently evolved into several additional projects that spanned over several years, including studies of oxygen atom transfer kinetics with $V(N[^tBu]Ar)_3$ and O_2 binding reactions with $V(N[^tBu]Ar)_3$ and $Pd(IPr)_2$ (IPr = 1,3-bis(2,6-diisopropyl)phenyl- imidazol-2-ylidene). In addition to the work devoted to understanding how small molecules like O_2, RO (R = organic groups), and nitriles interact with the metal center (i.e., ligand binding and activation), investigation of how

such activated intermediates interact with substrates have also been undertaken for biomimetic non-heme model systems which promote catalytic olefin epoxidation in reactions with H_2O_2 or organic oxygen atom transfer donors.

The kinetic studies presented in the first four chapters of the thesis is part of a collaborative effort with several research groups outside of Tufts, including those of Professors Carl Hoff (University of Miami, Coral Gables, FL), Kit Cummins (MIT, Cambridge, MA), and Manuel Temprado (Universidad de Alcalá, Madrid, Spain). I am grateful to have been a part of this talented team and the fact that these scientific investigations involved worldwide collaborations attests to the significance of the work and the results that we have published. I take this time to again acknowledge Drs. Carl Hoff, Kit Cummins, and Manuel Temprado, as well as their respective research groups, for their numerous contributions to this work. The detailed studies presented in Chapters 1 through 4 were only made possible by their generosity in supplying compounds and their expertise in thermochemical, computational, and crystallographic analyses. Although working together and combining our areas has led to several significant publications, this thesis highlights these scientific stories from a mechanistic perspective and draws from the data collected by others in order to provide a greater understanding of the context of this work.

Chapters 1 through 3 deal with the study of the kinetic studies of ligand binding and oxygen atom transfer (OAT) reactions to the sterically shielded, three-coordinate vanadium(III) complex, $V(N[^tBu]Ar)_3$. The rates and mechanisms of oxygen atom transfer (OAT) to $V(N[^tBu]Ar)_3$ from a variety of *N*-oxides, including N_2O, with varying BDEs and steric environments is presented in Chapter 1. A wide range of kinetic

behavior was observed and it was ultimately shown that there is no clear correlation of OAT rates with the N−O bond dissociation energies of the oxygen atom donors. OAT from N_2O proceeds through an overall third order reaction that requires two equivalents of $V(N[^tBu]Ar)_3$ for cleavage of the N−O bond. The organic adducts of mesityl nitrile oxide (SIPr/MesCNO, SIPr = 1,3-bis(2,6-diisopropyl)phenylimidazolin-2-ylidene) or nitrous oxide (IPr/N_2O [IPr = 1,3-bis(2,6-diisopropyl)phenylimidazol-2-ylidene] and dbabhNO [7-nitroso-2,3:5,6-dibenzo-7-azabicyclo-[2.2.1]hepta-2,5-diene]) were found to react much faster than free MesCNO or N_2O, respectively, despite increased steric hindrance. It was ultimately determined that the initial ligand binding step has a strong influence on the rate of the oxygen atom transfer reaction.

The kinetics of nitrile binding is presented in Chapter 2, which was performed in an effort to quantify the binding rates and compare these results with the analogous molybdenum *tris*-anilide complex, $Mo(N[^tBu]Ar)_3$. The significance of this study stems from our knowledge of the differences in substrate binding rates and efficiencies in molybdenum and vanadium containing nitrogenases. The comparative study of the binding rates of nitriles, which serve as substrate analogs to dinitrogen, has provided useful information regarding the differences in the coordination modes, reactivity, and formation rates of these metal-nitrile adducts. Stopped-flow UV/visible spectroscopic data ultimately revealed much faster binding of nitriles to the vanadium complex, which coordinate to the vanadium center exclusively in an η^1-fashion.

The study of dioxygen binding to $V(N[^tBu]Ar)_3$ is presented in Chapter 3, which led to the structural characterization of the first non-vanadyl V(V) peroxide complex. A two-step binding mechanism was deduced from stopped-flow studies and we were able to

observe and quantify the rates of formation and conversion of the η^1-O_2 intermediate to the η^2-O_2 product, which is a pathway that has been proposed in the literature as well as met with some controversy.

Chapter 4 presents the kinetic study of dioxygen binding to the two-coordinate late transition metal Pd(0) complex, $Pd(IPr)_2$ (IPr = 1,3-bis(2,6-diisopropyl)phenyl-imidazol-2-ylidene), which results in formation of a completely novel O_2 binding mode for Pd(II). The unprecedented *trans*-$(\eta^1\text{-}O_2)_2Pd(IPr)_2$ adduct binds two molecules of dioxygen in an end-on fashion, and appears to also form the typical $(\eta^2\text{-}O_2)Pd(IPr)_2$ adduct only at low temperatures. The reaction is proposed to proceed through a steady state $(\eta^1\text{-}O_2)Pd(IPr)_2$ intermediate that can trap a second molecule of O_2 to form the unique final product, or dissociate back to free $Pd(IPr)_2$ and O_2. Interestingly, *trans*-$(\eta^1\text{-}O_2)_2Pd(IMes)_2$ is not formed from reactions between the structurally related $Pd(IMes)_2$ complex (IMes = *N*,*N*-bis(2,4,6-trimethyl)phenylimidazol-2-ylidene) and O_2; the stable $(\eta^2\text{-}O_2)Pd(IMes)_2$ adduct is the sole product in this case. This work ultimately highlights how subtle changes in ligand sterics dramatically affect the relative stabilities of $(\eta^2\text{-}O_2)Pd(NHC)_2$ (NHC = *N*-heterocyclic carbene) adducts and lead to different reactivity channels.

In Chapter 5, we focus more in depth on the study of the reactions of activated oxygenated metal complexes towards substrates of interest, where the results of research regarding catalytic olefin epoxidation by novel biomimetic non-heme iron(II) complexes supported by aminopyridine macrocycles bearing a functionalized pendant arm are presented. These simple systems serve as rigid scaffolds that are suitable for coordination of an iron center while incorporation of a functionalized pendant arm can provide an

additional donor atom and/or an intramolecular proton delivery pathway in reactions with H_2O_2. Several ferrous complexes supported by derivatives of the ligands of interest have been shown to be catalytically active in "green" alkene epoxidations with hydrogen peroxide. Our new systems show enhanced reactivity towards olefin substrates and have allowed for decreased catalyst loadings relative to earlier derivatives. The preparation and characterization of two new complexes is reported along with the studies of their catalytic activity and insight into the identity of reaction intermediates. The primary goal of this study was to determine how the functionalized pendant arm alters the reactivity of the complex towards olefin epoxidation and related oxygen atom transfer processes and this work is still in progress.

Lastly, Chapter 6 presents the crystal structures of new metal complexes supported by several PyMAC ligands.

If you would be a real seeker after truth, it is necessary that at least once in your life you doubt, as far as possible, all things.

Rene Descartes

Mechanistic Studies of Oxygen Activation and Atom Transfer Reactions with Mononuclear Vanadium(III), Iron(II), and Palladium(0) Complexes

CHAPTER 1

Kinetic, Computational, and Thermodynamic Study of the Cleavage of the N−O Bond of *N*-Oxides by a Vanadium(III) Tris-Anilide Complex[1]

1.1. Introduction

Understanding the factors that govern oxygen atom transfer reactions (OAT) from nitrogen oxides (XNO) to metal complexes is of essential importance in the development of catalytic oxidation chemistry, with emphasis on devising methods to incorporate nitrous oxide as a terminal oxidant. N_2O is a potent greenhouse gas and has recently been classified as the major contributor to stratospheric ozone depletion.[2] Utilization of N_2O in oxidation reactions would be of high environmental and economic significance, however, a barrier to this is its relatively inert nature as an oxidant.[3] Since the discovery by Armor and Taube that oxidation of Cr^{2+} by N_2O was accelerated by a factor of 10^8 when N_2O was complexed by $[Ru(NH_3)_5]^{2+}$,[4] a number of studies have focused on whether metal mediated oxidation by N_2O proceeds by initial coordination through the terminal N or O atom of the molecule. Recent computational studies by Lin et al.[5] reveal that OAT reactions of N_2O to early and middle transition metal complexes proceed faster by initial coordination through nitrogen to form an *N*-nitrosoimide complex ($L_nM{=}N{-}N{=}O$) which can then undergo an essentially barrierless OAT to a second equivalent of metal complex, resulting in overall third order reactivity. Caulton and coworkers[6] had earlier performed computational studies in which novel binding modes for N_2O were proposed, one of

which includes a two electron reduction of N_2O to yield an *N*-nitrosoimido resembling that formulated by Lin et al.[5] Despite the logical assumption that coordination is a prerequisite for activation, metal adducts of N_2O remain exceedingly rare and the only structurally characterized example was reported recently in 2011. In that case, $(tpa^{Mes})V(N_2O)$ (tpa = tris(pyrrolylmethylamine)) was found to contain a linear, N-bound nitrous oxide ligand that was not consistent with the nitrosoimido binding motif.[7] There are also relatively few experimental kinetic studies of OAT from N_2O to metal complexes in solution,[8] and to the best of our knowledge, no examples of third order kinetics implying a ternary transition state exist. Detailed kinetic, thermodynamic, and computational studies of the reaction of $Mo(N[^tBu]Ar)_3$ (Ar = 3,5-$Me_2C_6H_3$) with N_2O, which results in cleavage of the N−N rather than the N−O bond to yield $N{\equiv}Mo(N[^tBu]Ar)_3$ and $ON{-}Mo(N[^tBu]Ar)_3$, have been reported earlier.[9]

While nitrous oxide represents an important substrate, other nitrogen oxides are also of significance and generally require catalytic activation in OAT, the first step of which is transfer to an active metal complex.[10] A general two step mechanism involving initial oxidant binding followed by OAT is illustrated for XNO in Eq. 1.1 below.

$$ML_n + XNO \underset{k_{-1}}{\overset{k_1}{\rightleftharpoons}} XNO{-}ML_n \xrightarrow{k_2} OML_n + XN \qquad (1.1)$$

Although the reaction sequence appears simple, depiction of a generic $XNO{-}ML_n$ adduct neglects to illustrate its important features, including spin state, geometry, bond strength, and charge transfer, which can undergo significant change depending on the exact nature

of the X group. All of these factors will affect the magnitudes of the rate constants involved with the OAT reaction. Comprehensive kinetic studies by Schultz and Holm[11] regarding OAT cycling between $Mo^{VI}(O)_2(^tBuL{-}NS)_2$ and $Mo^{IV}O(^tBuL{-}NS)_2$ ($(L\text{-}NS)_2$ = 2,6-bis(2,2-diphenyl-2-sulfidoethyl)pyridine(2−)) showed that the rates of OAT to the reduced complex from a range of substrates with varying steric constraints, basicities, and X−O BDEs, spanned more than four orders of magnitude (Figure 1.1). In some cases, there was good correlation between the rates of OAT and the BDE of the substrate bond being broken, but the substrate with the largest BDE studied, Ph_3AsO (103 kcal mol^{-1}), had an activation energy the same as that for the one with the smallest BDE, Ph_2SeO (43 kcal mol^{-1}).

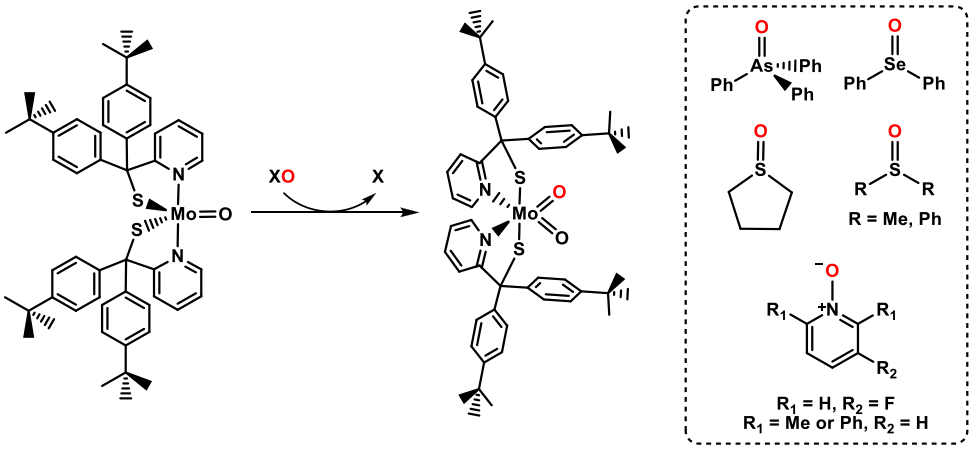

Figure 1.1. OAT reaction scheme involving $[Mo^{IV}(O)(^tBuL{-}NS)_2]$ with structures of XO substrates reported in the study. Figure adapted from ref 11.

Studies of OAT to rhenium complexes by Abu-Omar and coworkers[12] revealed the importance of ligand binding, the first step in the OAT reaction scheme, and actual atom transfer in the following step. The importance of electronic factors, symmetry, and

geometry in OAT reactions involving tris-silox (silox = $[(CH_3)_3C)_3SiO]^-$) complexes of Group 5 metals have been reported, where emphasis on achieving a bent M-O-X transition state for successful OAT was highlighted.[13] The effects of spin-state changes on gas phase OAT to Cr(III) porphyrin complexes were recently investigated by Mayer and coworkers, who found that OAT reactions did not occur above a certain threshold bond strength.[14] "Ultrafast" and "ultraslow" rates of OAT involving low-coordinate late transition metal complexes have been studied by Brown et al.[15] Interestingly, they found that the rates of degenerate intermetal OAT between the $(Mes)_3Ir^{III}$/ $(Mes)_3Ir^{V}O$ and $(ArN)_3Os^{VI}$/$(ArN)_3Os^{VIII}O$ (Mes = 2,4,6-trimethylphenyl; Ar = 2,6-diisopropylphenyl) couples differ by twelve orders of magnitude, despite similar metal-oxo BDEs and reactivities toward PPh_3 oxidation. Although much work has allowed us to understand transition metal mediated OAT reactions in detail for specific systems, it is clear that no single attribute governs the relative rates of OAT and comparisons from one system to another can only be made with considerable risk. Furthermore, discrepancies between the thermodynamics and kinetics of metal mediated OAT reactions is a well-documented theme in the literature[12,16] and the range of factors controlling these reactions, particularly for paramagnetic complexes, is complex and a number of questions remain unanswered.

We have recently reported studies of OAT from mesityl nitrile oxide (MesCNO) to main group PR_3 (R = Me, Cy, Ph) acceptors.[17] During that work the blue nitrile oxide/carbene adduct SIPr/MesCNO (SIPr = 1,3-bis(2,6-diisopropyl)phenylimidazolin-2-ylidene), in which the C atom of the *N*-heterocyclic carbene (NHC) is bound to the $C_{nitrile}$ atom of MesCNO, was isolated and structurally characterized by our collaborators. It was also found that formation of NHC adducts with MesCNO suppressed oxygen atom

transfer to main group elements. While reaction with Lewis bases was stopped by blocking attack at the $C_{nitrile}$ atom, this was not observed to happen in reactions with the Lewis acid metal complex V(N[^{t}Bu]Ar)$_3$, presumably since attack in this case occurred directly at the terminal O atom of MesCNO rather than at the interior $C_{nitrile}$ atom.

The initial goal of the current work was to quantitatively compare the rates of OAT to V(N[^{t}Bu]Ar)$_3$ from MesCNO and its NHC adduct SIPr/MesCNO simply to see which was faster. During this time, Severin and coworkers[18] reported characterization of stable covalent adducts of NHCs with N_2O and also showed that these adducts readily react with V(Mes)$_3$.[19] This prompted us to extend our work to compare N_2O and IPr/N_2O (IPr = 1,3-bis(2,6-diisopropyl)phenylimidazol-2-ylidene) and to study a series *N*-oxides with N−O bond dissociation enthalpies (BDEs) spanning a range of nearly 100 kcal mol^{-1}.

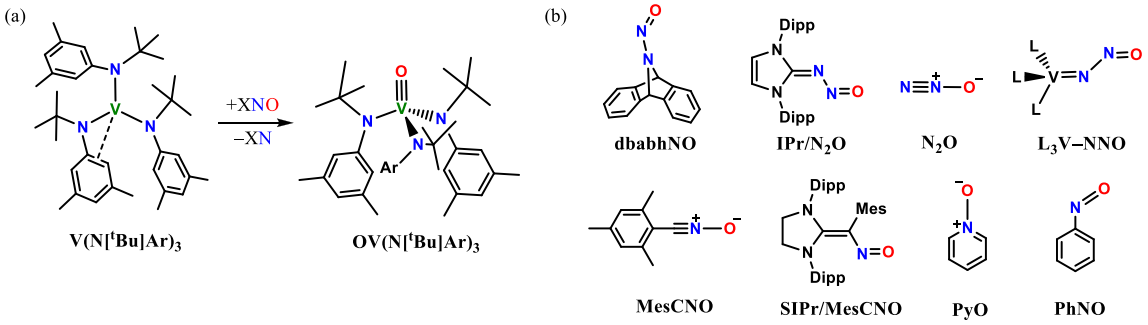

Figure 1.2. (a) General reaction scheme of OAT to V(N[^{t}Bu]Ar)$_3$. (b) Structure of all XNO reagents studied. Ar = (3,5-Me$_2$C$_6$H$_3$); Dipp = 2,6-diisopropylphenyl; Mes = 2,4,6-trimethylphenyl; L = (N[^{t}Bu]Ar). Note that the L$_3$V=N–N=O species is proposed, based on computational results, to be the precursor complex for dinuclear OAT from N_2O.

This chapter presents the detailed kinetic studies of OAT to V(N[^{t}Bu]Ar)$_3$ from the series of *N*-oxides shown in Figure 1.2. Stopped-flow experiments showed a range of

kinetic behavior that is influenced by both the mode and strength of coordination of the *N*-oxide and its ease of atom transfer. While all bond cleavage reactions studied involve $V(N[^tBu]Ar)_3$ and a N−O bond, a wide range of kinetic behavior was observed, allowing us to characterize individual reaction steps in detail.

1.2. Experimental Methods

General Considerations. Samples of $V(N[^tBu]Ar)_3$ (Ar = 3,5-$Me_2C_6H_3$)[20] were graciously provided by members of the Cummins group (MIT, Cambridge, MA). Mesityl nitrile oxide (MesCNO),[21] pyridine-*N*-oxide (PyO), nitrosobenzene (PhNO), IPr/N_2O[18] (IPr = 1,3-bis(2,6-diisopropyl)phenylimidazol-2-ylidene), SIPr/MesCNO[17] (SIPr = 1,3-bis(2,6-diisopropyl)phenylimidazolin-2-ylidene), and 7-nitroso-2,3:5,6-dibenzo-7-azabicyclo-[2.2.1]hepta-2,5-diene (dbabhNO)[22] were graciously supplied by members of the Hoff group (University of Miami, Coral Gables, FL). All acquired samples were stored in a glove box freezer (−35 °C) and used without further purification. Anhydrous toluene (HPLC grade, ≥ 99.9%) was purchased from Sigma Aldrich and dried on an Innovative Technologies PureSolv 400 solvent purification system. Electronic grade N_2O (99.999%, Airgas) was passed through a column of potassium hydroxide pellets prior to use to remove any residual higher nitrogen oxides. Additional characterizations, crystallographic data, and calorimetric measurements were performed by collaborators at MIT (Cummins group) and University of Miami (Hoff group). The reader is referred to ref 1 for further details regarding these procedures.

Crystallographic Details. Diffraction quality red-orange crystals of $OV(N[^tBu]Ar)_3$ were grown via slow evaporation of a C_6D_6 solution and were glued onto the end of a thin glass fiber. X-ray intensity data were measured by using a Bruker SMART APEX2 CCD-based diffractometer using Mo Kα radiation (λ = 0.71073 Å). The raw data frames were integrated with the SAINT+ program by using a narrow-frame integration algorithm.[23] Corrections for Lorentz and polarization effects were also applied with SAINT+. An empirical absorption correction based on the multiple measurement of equivalent reflections was applied using the program SADABS.[24] All structures were solved by a combination of direct methods and difference Fourier syntheses, and refined by full-matrix least-squares on F^2, by using the SHELXTL software package.[25] Crystal data, data collection parameters, and results of the analyses are provided in Appendix 1, Table 1A.2. All non-hydrogen atoms were refined anisotropically. All hydrogen atoms were included at geometrically idealized positions and refined using a riding model.[26] $OV(N[^tBu]Ar)_3$ crystallized in the cubic crystal system and the systematic absences in the intensity data were consistent with the unique space group $I\bar{4}3d$. Crystallographically, this molecule lies on a C_3 symmetry site and thus contains only one-third of a molecule in the asymmetric unit.

Stopped-flow Kinetics. Due to the high O_2 and moisture sensitivity of $V(N[^tBu]Ar)_3$, particular care was taken in solution preparation. At the millimolar concentration level it is difficult to avoid all contamination and some indications of this were observed at either the beginning or end of some kinetic runs. All reported data was replicated to ensure that the major reaction channel was observed in all cases.

Toluene solutions of $V(N[^tBu]Ar)_3$ and XNO reagents were prepared in an MBraun glove box filled with ultra high purity argon (Airgas) and loaded into gastight Hamilton syringes. Saturated solutions of N_2O were prepared by bubbling gas into gastight syringes containing dry toluene for 20 minutes; dilutions of the N_2O saturated solvent were performed anaerobically to obtain the desired [N_2O] before mixing in the stopped flow cell. The solubility of N_2O in toluene was taken as 133 mM at 25 °C.[9b] Time resolved UV-visible spectra were acquired over a range of temperatures (–80 °C to +25 °C) using a Hi-Tech Scientific KinetAsyst SF-61DX2 CryoStopped-Flow system (TgK Scientific Ltd.) equipped with a quartz tungsten halogen light source, a J&M TIDAS diode array detector and a Brandenburg 4479 Series PMT monochromator. The instrument was equipped with stainless steel plumbing lined with PEEK tubing and a 1.00 cm^3 quartz mixing cell submerged in an ethanol cooling bath. The temperature in the mixing cell was maintained to ± 0.1°C using a CAL 3200 automatic temperature controller. Data acquisition was performed using TIDAS-DAQ and/or Kinetic Studio software programs and mixing times were 2-3 ms. All flow lines were washed extensively with argon-saturated anhydrous toluene prior to charging the drive syringes with reactant solutions and the driving syringe compartment was continuously flushed with argon during the experiments to preserve anaerobicity. All experiments were performed in a single-mixing mode of the instrument with a 1:1 (v/v) mixing ratio. Reactions were studied under pseudo-first order conditions using excess XNO whenever possible. All concentrations are reported after mixing in the stopped-flow cell. Data analysis was performed using Kinetic Studio, IGOR Pro 5.0 (Wavemetrics, Inc.), and ReactLab Kinetics Global Analysis software (JPlus Consulting Pty. Ltd.). All observed

rate constants are reported in Appendix 1 and represent an average of three to seven measurements which gave an acceptable standard deviation (≤ 10 %). All remaining parameters derived from the kinetic data are reported with their standard deviations.

Computational Details. All computational studies were performed by Manuel Temprado, Universidad de Alcalá Department of Physical Chemistry, Madrid, Spain. Electronic structure calculations were carried out using the BP86[27] density functional with the 6-311G(d,p) basis sets as implemented in the Gaussian 09 suite of programs.[28] Minimum energy structures were optimized by computing analytical energy gradients. The obtained stationary points were characterized by performing energy second derivatives, confirming them as minima by the number of negative eigenvalues of the hessian matrix of the energy. Computed electronic energies were corrected for zero-point energy, and thermal energy to obtain H^0. To derive binding energies, the basis set superposition error (BSSE) was computed using counterpoise calculations.[29] The X–O bond dissociation enthalpies were derived by determining the enthalpy of reaction with molecular oxygen for a certain X/XO couple as previously described.[17] For the metal-containing species, optimizations were performed using the Stuttgart-Dresden MDF10[30] fully relativistic effective core potential and basis for V including a set of additional *f* functions and the triple-zeta quality basis set (6-311G(d,p)) for all other elements. TD BP86/6-311G(d,p) calculations were additionally performed for selected species.

1.3. Results

The main point of this work is experimental mapping of the range of behavior of the OAT reactivity of nitrogen oxides (XNO) with $V(N[^tBu]Ar)_3$. All XNO compounds studied (Figure 1.2) were found to react rapidly and cleanly with paramagnetic $V(N[^tBu]Ar)_3$ at room temperature in toluene to produce the diamagnetic $OV(N[^tBu]Ar)_3$ complex as confirmed by NMR spectroscopy.[1] The experimental work has also been supported by thermochemical analyses and theoretical calculations which will be discussed as needed.

In an effort to give insight into structural factors that can influence OAT reactivity in this particular system, the structural parameters for $V(N[^tBu]Ar)_3$ and $OV(N[^tBu]Ar)_3$ are briefly discussed. In the absence of crystallographic characterization of $V(N[^tBu]Ar)_3$, DFT calculations yielded the minimum energy structure as shown in Figure 1.3. The most stable configuration is a high spin d^2 species that exhibits one close contact with two carbons atoms in one of the aryl rings, a structural feature that has been observed previously in the X-ray structure of the related $V(N[Ad]Ar)_3$ complex (Ad = adamantyl).[31] Ligand binding to $V(N[^tBu]Ar)_3$ will involve displacement of this η^3-allylic-like interaction, which will influence both the thermodynamics (enthalpy of reaction) and kinetics (enthalpy of activation) of the OAT reaction. This process can in theory proceed through either associative displacement of this interaction by the incoming ligand, or by an intramolecular dissociative mechanism in which a vacant site is generated prior to ligand association. DFT calculations confirm, however, that the corresponding conformer without this interaction is not a minimum in the potential energy surface, indicating that the ligand most likely associatively attacks the metal

complex to displace the allylic interaction. Removal of this interaction in V(N[^{t}Bu]Ar)$_3$ by constrained optimizations accounts for about 4 kcal mol^{-1} in the thermochemistry of ligand binding, and likely in the enthalpy of activation as well.[1]

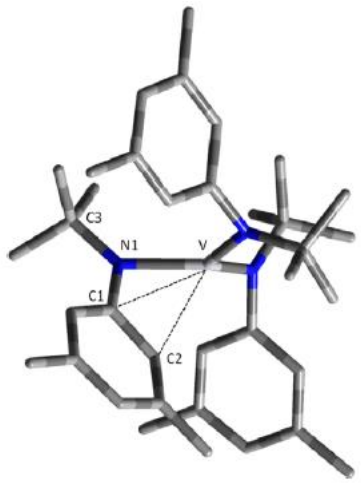

Figure 1.3. Optimized structure of V(N[^{t}Bu]Ar)$_3$ at the bp86/6-311G(d,p) (MDF10 for V with an additional set of f functions) level. Selected interatomic distances (Å) and angles (°): V−C1 = 2.45; V−C2 = 2.42; V−N1−C1 = 92.1; V−N1−C3 = 138.3; C1−N1−C3 = 124.6; Σ(N−V−N) = 356.1.

The crystal structure of the diamagnetic tetrahedral OV(N[^{t}Bu]Ar)$_3$ complex resembles related chalcogenide structures of V(N[Ad]Ar)$_3$ and V(N[^{t}Bu]Ar)$_3$ reported previously.[31,32] As shown in Figure 1.4, the *tert*-butyl groups of all three amido ligands point upwards and the three aryl rings point away from the oxo ligand. The short V−O distance of 1.590(3) Å is consistent with it being a triple bond.[33] Space-filling representation of the structure shown in Figure 1.4 illustrates the lack of free space available for access to the O atom of OV(N[^{t}Bu]Ar)$_3$, and by inference that an intermediate XNO–V(N[^{t}Bu]Ar)$_3$ complex leading to OV(N[^{t}Bu]Ar)$_3$ would have considerable steric constraint in the placement of the XN group.

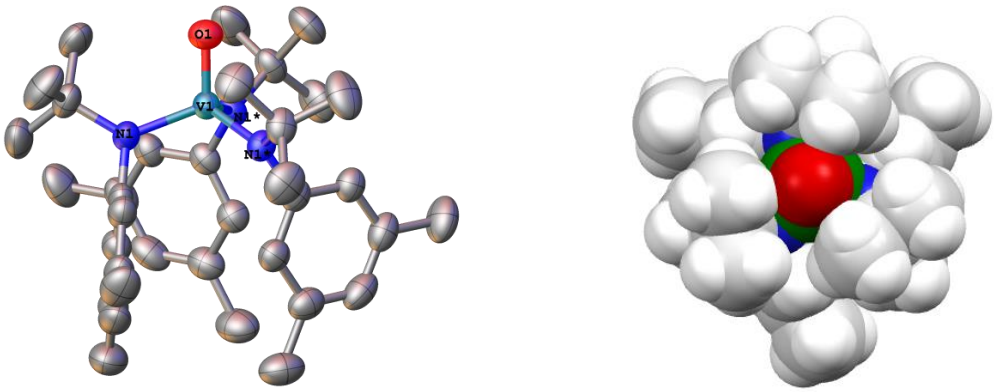

Figure 1.4. *Left*: Thermal ellipsoid plot of OV(N[^{t}Bu]Ar)$_3$ drawn at the 50 % probability level. Hydrogen atoms omitted for clarity. Selected interatomic distances (Å) and angles (°): V1−O1 = 1.590(3); V1−N1 = 1.883(2); O1−V1−N1 = 107.87(5); N1−V1−N1* = 111.03(5). *Right*: Space filling model highlighting restricted access to the bound oxo group (red). Also shown: V (green); N (blue); C (gray); H (white).

Thermochemical analysis of the V−O BDE in OV(N[^{t}Bu]Ar)$_3$ (experimental value of 154 ± 3 kcal mol^{-1}; DFT calculated value of 151.3 kcal mol^{-1}) reveal it to be one of the strongest metal oxo bonds to be determined experimentally.[34] The N−O BDEs in the *N*-oxides studied (Table 1.1) are all significantly weaker than the V−O BDE in OV(N[^{t}Bu]Ar)$_3$, making N−O bond cleavage exothermic by 46 to 144 kcal mol^{-1}.[1]

Table 1.1. Experimental and computational bond dissociation energies (BDE) for OV(N[^{t}Bu]Ar)$_3$ and the *N*-oxide series.

Bond	Compound	BDE$_{calc}$ (kcal mol^{-1})	BDE$_{expt}$ (kcal mol^{-1})	Ref
V≡O	OV(N[^{t}Bu]Ar)$_3$	151.3[a]	154 ± 3	1
N−O	N_2O	40	-----	35
N−O	PyO	63	-----	36
N−O	PhNO	108.2[a]	-----	1
N−O	IPr/N_2O	62.0[a]	-----	1
N−O	SIPr/MesCNO	74.6[a]	-----	1
N−O	dbabhNO	10.4[a,b]	9.7 ± 3.0[b]	1
N−O	MesCNO	53	-----	36

[a] Calculated at the bp86/6-311G(d,p) level (MDF10 with an additional set of f functions for V). [b] The BDE value includes rearrangement of the dbabhN fragment to anthracene and N_2.

The kinetics of the OAT reactions were studied by the stopped-flow method and in all cases time-resolved visible spectra showed conversion of $V(N[^tBu]Ar)_3$ to $OV(N[^tBu]Ar)_3$ (λ_{max} = 453 nm) in toluene. For PhNO, variable temperature NMR experiments were necessary to study the kinetics of $OV(N[^tBu]Ar)_3$ formation. Four categories of kinetic behavior were observed and are discussed individually in the following sections: (I) Dinuclear OAT following an overall third order rate law (N_2O); (II) Formation of stable oxidant-bound complexes followed by OAT in a separate step (PyO and PhNO); (III) Transient formation and decay of metastable oxidant-bound intermediates on the timescale of OAT (SIPr/MesCNO and IPr/N_2O); (IV) Steady state kinetics in which no detectable intermediates are observed (dbabhNO and MesCNO).

1.3.1. Category I: Dinuclear OAT Following an Overall Third Order Rate Law

Oxygen atom transfer from N_2O to $V(N[^tBu]Ar)_3$ occurs within minutes at room temperature in toluene as evidenced by the characteristic color change from dark green to golden orange. Time-resolved spectra acquired over a broad temperature range (−62 to +25 °C) showed clean conversion to $OV(N[^tBu]Ar)_3$ with no detectable intermediates (Figure 1.5a). Kinetic traces (λ = 453 nm) obtained at the three highest temperatures (+7, +16 and +25 °C) under pseudo-first order conditions (excess N_2O) did not fit to a rate law that is first order in $[V(N[^tBu]Ar)_3]$; instead, as shown in Figure 1.5b, excellent fits were obtained from a rate law that is second order in $[V(N[^tBu]Ar)_3]$. The observed second order rate constants (with respect to metal complex, k_{eff}) obtained from these fits varied linearly with $[N_2O]$ which confirmed first order behavior in $[N_2O]$ and yielded third order rate constants for the high temperature OAT reaction.

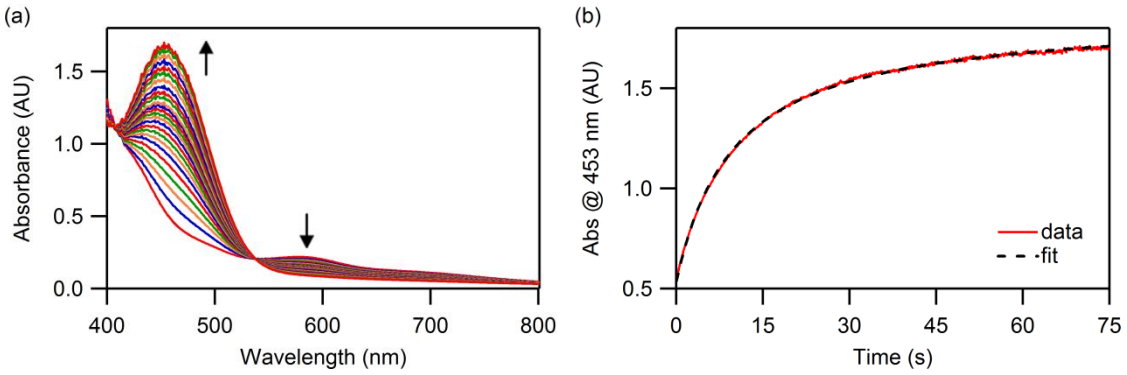

Figure 1.5. (a) Time-resolved spectra obtained from the reaction between V(N[^{t}Bu]Ar)$_3$ (0.3 mM) and N_2O (66 mM) in toluene over 75 s at 25 °C. (b) Kinetic trace at λ = 453 nm (red) with second order fit (black dashed line).

Derived third order rate constants (k_3) of 4,670 ± 285 M^{-2} s^{-1} (25 °C), 5,380 ± 512 M^{-2} s^{-1} (16 °C) and 6,870 ± 136 M^{-2} s^{-1} (7 °C) were obtained from the slopes of the linear plots of the observed second order rate constant (k_{eff}) versus [N_2O] as shown in Figure 1.6a. An Eyring plot yielded activation parameters for the high temperature third order reaction: $\Delta H^{\ddagger}_{\text{3rd order}} = -4.1 \pm 0.5$ kcal mol^{-1} and $\Delta S^{\ddagger}_{\text{3rd order}} = -56 \pm 2$ cal mol^{-1} K^{-1}. The large negative activation entropy is in keeping with a ternary transition state while the negative composite activation enthalpy suggests an exothermic binding of N_2O to V(N[^{t}Bu]Ar)$_3$ followed by formation of a dinuclear transition state L_3V–NNO–VL_3 (L = N[^{t}Bu]Ar) with a low barrier to oxidative addition.

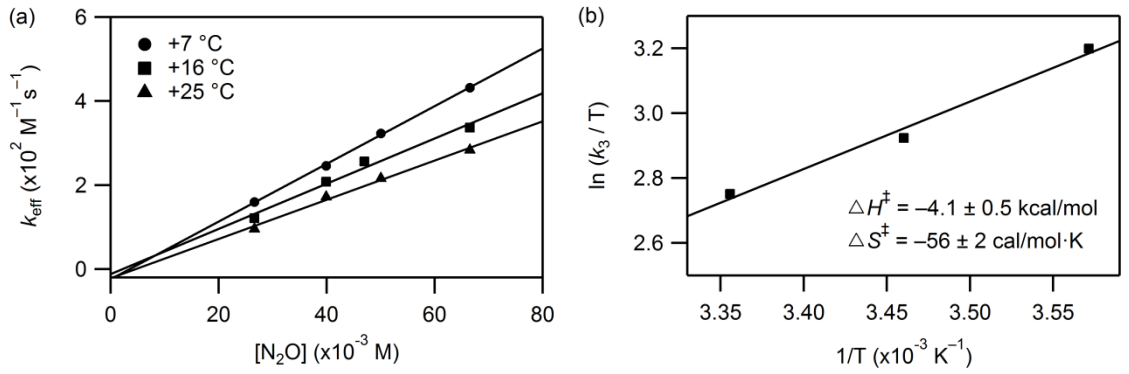

Figure 1.6. (a) Plots of k_{eff} versus $[N_2O]$ at various concentrations (27 - 66 mM) over a temperature range of 7 to 25 °C with $[V(N[^tBu]Ar)_3]_0$ = 0.3 mM. (b) Eyring plot for the high temperature third order (overall) reaction with derived activation parameters.

At an intermediate temperature of −14 °C, kinetic traces did not fit well to either first or second order rate laws with respect to $[V(N[^tBu]Ar)_3]$ (see Appendix 1, Figures 1A.1 and 1A.2). As discussed later, the behavior at intermediate temperature could be successfully modeled in terms of an overall mechanism of mixed reaction order, but temperature resolution into two limiting regimes, overall third order kinetics (second order in metal complex, first order in N_2O) at high T and overall second order kinetics (first order in both metal complex and N_2O) at low T, provided the initial convincing evidence for the mechanism. At low temperatures (−62, −53, −35 °C) the reaction was found to obey pseudo-first order kinetics. Traces at λ = 453 nm fit well to as single exponential equation (Appendix 1, Figure 1A.3b) and observed rate constants depended linearly on $[N_2O]$ as shown in Figure 1.7a. Derived overall second order rate constants (k_1) were 0.055 ± 0.005 M^{-1} s^{-1} (−62 °C), 0.119 ± 0.006 M^{-1} s^{-1} (−53 °C) and 0.386 ± 0.007 M^{-1} s^{-1} (−35 °C). Activation parameters for the low temperature second order reaction were $\Delta H^{\ddagger}$ = 6.7 ± 0.3 kcal mol^{-1} and $\Delta S^{\ddagger}$ = −32 ± 1 cal mol^{-1} K^{-1} (Figure 1.7b).

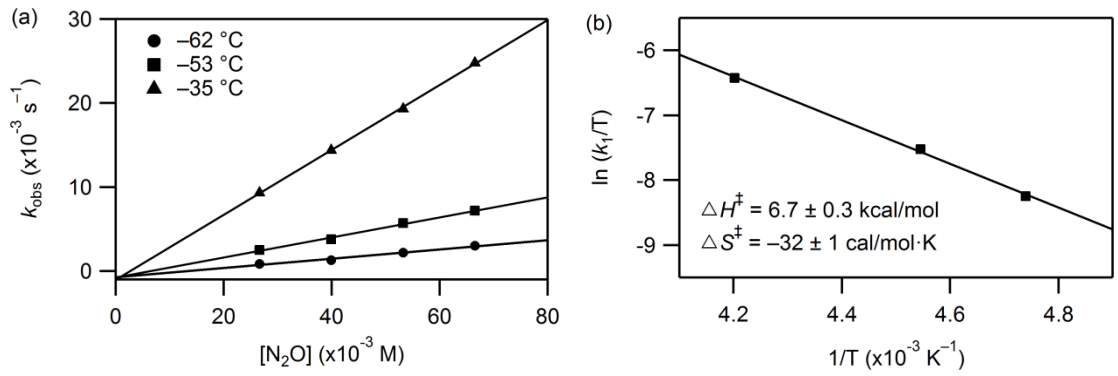

Figure 1.7. (a) Plot of k_{obs} versus [N_2O] at various concentrations (27 - 66 mM) over the temperature range of −62 to −35 °C with [V(N[^{t}Bu]Ar)$_3$]$_0$ = 0.3 mM. (b) Eyring plot with derived activation parameters for the low temperature second order (overall) reaction.

The change in reaction order and in the sign of effective activation enthalpy as a function of temperature also suggests stepwise bimetallic activation of N_2O in which the rate determining step changes with temperature. Dinuclear activation of N_2O by the mechanism shown in Eq. 1.2 and assuming a steady state in [(N[^{t}Bu]Ar)$_3$V–NNO] (in keeping with the clean isosbestic points and failure to detect a spectroscopically observable intermediate) yields the rate law shown in Eq. 1.3.

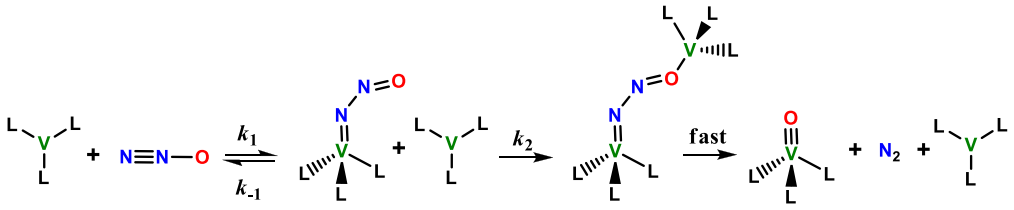

(1.2)

$$\text{Rate} = \frac{k_1 k_2 [\text{V(N[}^t\text{Bu]Ar)}_3]^2 [\text{N}_2\text{O}]}{k_{-1} + k_2 [\text{V(N[}^t\text{Bu]Ar)}_3]} \qquad (1.3)$$

This will yield two limiting rate laws: if $k_{-1} >> k_2[V(N[^tBu]Ar)_3]$, overall third order kinetics will be observed with $k_{obs} = (k_1k_2/k_{-1})$. On the other hand, if $k_2[V(N[^tBu]Ar)_3] >> k_{-1}$, second order kinetics will be followed with $k_{obs} = k_1$. The observed kinetic behavior over the entire temperature range is consistent with this type of mechanism. The method described above was useful to delineate behavior. This was followed by full computer simulation of the kinetic data over all temperatures to the three-step mechanism in Eq. 1.4 using the ReactLab Kinetics program.

$$\begin{aligned}
&(1)\ V(N[^tBu]Ar)_3 + N_2O \xrightarrow{k_1} ONN{-}V(N[^tBu]Ar)_3 \\
&(2)\ ONN{-}V(N[^tBu]Ar)_3 \xrightarrow{k_{-1}} V(N[^tBu]Ar)_3 + N_2O \\
&(3)\ ONN{-}V(N[^tBu]Ar)_3 + V(N[^tBu]Ar)_3 \xrightarrow{k_2} OV(N[^tBu]Ar)_3 + N_2 + V(N[^tBu]Ar)_3
\end{aligned} \qquad (1.4)$$

Although individual rate constants k_1, k_{-1}, and k_2 could be determined by the program, a range of values for k_{-1} and k_2 were found to be acceptable provided the proper k_{-1}/k_2 ratio was fulfilled. Steady-state analysis described earlier supports this observation, and identifies k_{-1}/k_2 as the kinetic parameter that, along with k_1, describes the system. As a result, the k_{-1}/k_2 ratio is reported and used in kinetic discussions, since it is known to a higher accuracy than poorly-defined individual rate constants k_{-1} and k_2. Calculated values for k_1 were consistent and are in excellent agreement with k_1 values derived from the experimental low temperature data. Singular value decomposition (SVD) analysis suggested three colored components in the reaction system and the spectra for these components ($V(N[^tBu]Ar)_3$, $ONN{-}V(N[^tBu]Ar)_3$, and $OV(N[^tBu]Ar)_3$) were calculated

during the fitting procedure. The calculated spectra for V(N[^{t}Bu]Ar)$_3$ and OV(N[^{t}Bu]Ar)$_3$ are in excellent agreement with the experimental data and remained consistent across all modeled datasets. The calculated spectrum of ONN−V(N[^{t}Bu]Ar)$_3$, however, was variable due to the fact that this steady-state intermediate never builds up to an appreciable extent. Calculated spectra and concentration profiles obtained from the model at the intermediate temperature of −14 °C are shown in Figure 1.8. Calculated rate constants are provided in Table 1.2.

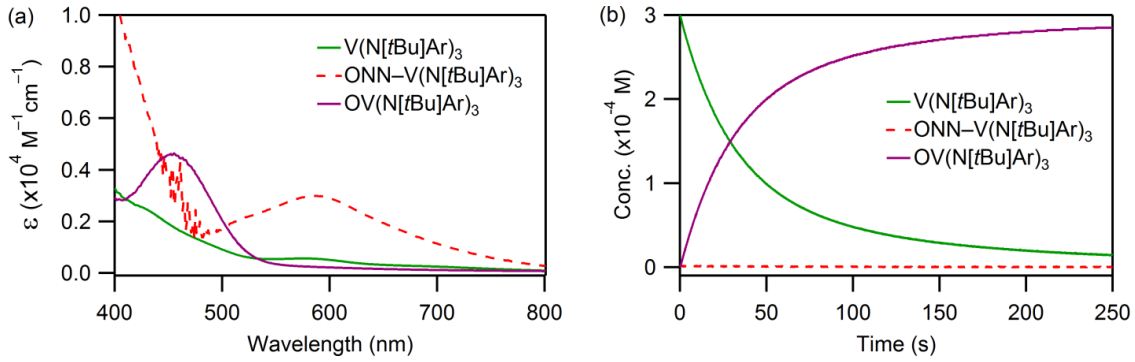

Figure 1.8. (a) Representative calculated spectra of colored components obtained from modeling at −14 °C (intermediate temperature) with [V(N[^{t}Bu]Ar)$_3$]$_0$ = 0.3 mM and [N_2O]$_0$ = 27 mM. Although the calculated spectrum for ONN–V(N[^{t}Bu]Ar)$_3$ is shown, it could not be accurately determined since its concentration remains close to zero throughout the reaction. (b) Concentration profiles for colored components.

The activation parameters derived from the kinetic model are as follows: $\Delta H_1^{\ddagger}$ = 6.3 ± 0.3 kcal mol^{-1} and $\Delta S_1^{\ddagger}$ = −34 ± 1 cal mol^{-1} K^{-1} for k_1; $\Delta H_{-1}^{\ddagger}$ = 13 ± 1 kcal mol^{-1} and $\Delta S_{-1}^{\ddagger}$ = −6 ± 2 cal mol^{-1} K^{-1} for k_{-1}; and $\Delta H_2^{\ddagger}$ = 3.0 ± 0.1 kcal mol^{-1} and $\Delta S_2^{\ddagger}$ = −27 ± 1 cal mol^{-1} K^{-1} for k_2. The predicted third order activation parameters of $\Delta H^{\ddagger}_{\text{3rd order}}$ = $\Delta H^{\ddagger}_{(k_1 + k_2 - k_{-1})}$ = (6.3 + 3.0 − 13) = −3.7 kcal mol^{-1} and $\Delta S^{\ddagger}_{\text{3rd order}}$ = $\Delta S^{\ddagger}_{(k_1 + k_2 - k_{-1})}$ = (−34

+ (−27) – (−6)) = −55 cal mol^{-1} K^{-1} are in excellent agreement with the direct experimental estimates from the high temperature data discussed above. The crossover in reaction mechanism is due to the high activation energy for the dissociation step (k_{-1}) causing it to overtake k_2 at higher T. The enthalpy of binding of N_2O, $\Delta H^0 = (\Delta H^{\ddagger}_{k_1} - \Delta H^{\ddagger}_{k_{-1}}) = (6.3 - 13) = -6.7$ kcal mol^{-1}, is in agreement with the DFT calculated enthalpy of binding of N_2O (N-bound, singlet) of −7.1 kcal mol^{-1} (see Table 1A.1). The high temperature third order reaction has an apparent negative enthalpy of activation and appears to speed up with decreasing temperature. If this reaction were an elementary third order step rather than a composite one, the change to second order kinetics and concomitant slowing down with temperature would not be observed. Provided k_{-1} has a higher enthalpy of activation than does k_2, the rate will decrease more rapidly with decreasing temperature and cause the observed change in the rate-limiting step. This observed behavior is predicted from the analysis of time-resolved spectral data, supporting the proposed stepwise bimetallic mechanism depicted in Eq. 1.2.

Table 1.2. Rate constants and activation parameters obtained from modeling the $V(N[^tBu]Ar)_3/N_2O$ system over a range of temperatures (−62 to +25 °C) to the three-step model in Eq. 1.4. Average values of rate constants from two separate datasets are reported along with standard deviations. Initial concentrations of reactants were fixed at 0.3 mM for $V(N[^tBu]Ar)_3$ and either 27 mM or 66 mM for N_2O. Activation parameters associated with each process were derived from Eyring plots (see Appendix 1, Figure 1A.6) and are discussed in the main text.

T (°C)	k_1 (M^{-1} s^{-1})	k_{-1} (s^{-1})	k_2 ($\times 10^3$ M^{-1} s^{-1})	k_{-1}/k_2 (M)
−62	$(3.8 \pm 1.2)\cdot 10^{-2}$	$(2.5 \pm 0.5)\cdot 10^{-3}$	3.56 ± 0.04	$(7.0 \pm 1.2)\cdot 10^{-7}$
−53	$(1.1 \pm 0.1)\cdot 10^{-1}$	$(1.4 \pm 0.8)\cdot 10^{-2}$	5.93 ± 0.01	$(2.3 \pm 1.3)\cdot 10^{-6}$
−35	$(3.8 \pm 0.2)\cdot 10^{-1}$	$(8.7 \pm 1.9)\cdot 10^{-2}$	10 ± 1	$(8.6 \pm 2.5)\cdot 10^{-6}$
−14	1.4 ± 0.1	1.93 ± 0.01	21 ± 1	$(9.2 \pm 0.6)\cdot 10^{-5}$
+7	2.9 ± 0.2	7.2 ± 0.4	28 ± 3	$(2.6 \pm 0.4)\cdot 10^{-4}$
+16	3.7 ± 0.2	22 ± 0.5	38 ± 1	$(5.8 \pm 0.1)\cdot 10^{-4}$
+25	4.9 ± 0.7	42 ± 2.9	43 ± 1	$(9.8 \pm 0.5)\cdot 10^{-4}$
$\Delta H^{\ddagger}$	6.3 ± 0.3	13 ± 1	3.0 ± 0.1	kcal mol^{-1}
$\Delta S^{\ddagger}$	-34 ± 1	-6 ± 2	-27 ± 1	cal mol^{-1} K^{-1}

1.3.2. Category II: Formation of Stable Oxidant-Bound Complexes Followed by OAT in a Separate Step

1.3.2.1. PyO. The reaction between excess PyO and $V(N[^tBu]Ar)_3$ could be readily separated into ligand binding at low temperatures (−80 to −53 °C) and OAT from the PyO–$V(N[^tBu]Ar)_3$ adduct at higher temperatures (0 to 20 °C). Low temperature time-resolved spectral changes assigned to PyO binding at −80 °C are shown in Figure 1.9a. A rapid rise in lower energy absorption bands was detected within the first second of reaction, with concomitant decay occurring under ≈ 550 nm and an isosbestic point near 570 nm. This was followed by slow conversion to the expected $OV(N[^tBu]Ar)_3$ complex, which was too slow to monitor conveniently via stopped-flow at low temperature. Pseudo-first order kinetics were obeyed and absorbance versus time traces (λ = 650 nm, formation) fit well to a single exponential function with $k_{obs} = k_1[PyO] + k_{-1}$. Resolution of k_{obs} into its k_1 and k_{-1} components was carried out graphically via plots

of k_{obs} versus [PyO] which have slopes of k_1 and intercepts of k_{-1}. Data for the slope (k_1) is generally known to higher accuracy than data for the intercept (k_{-1}) as is typical in this type of analysis. Second-order rate constants (k_1) representing formation of a PyO–V(N[^{t}Bu]Ar)$_3$ adduct were obtained as shown in Appendix 1, Figure 1A.7. The near zero intercepts suggest that this process can be regarded as irreversible over the temperature range studied. An Eyring plot was used to obtain activation parameters of $\Delta H_1^{\ddagger} = 6.8 \pm 0.4$ kcal mol^{-1} and $\Delta S_1^{\ddagger} = -7 \pm 2$ cal mol^{-1} K^{-1}. Notable is the low entropy of activation for ligand binding in this system, which is expected to involve cleavage of the aryl contact in V(N[^{t}Bu]Ar)$_3$ to yield a less restricted structure. Temperature dependent second order rate constants for PyO binding are provided in Table 1.3.

Near room temperature, formation of the PyO adduct is too fast for measurement by the standard stopped-flow method and it is rapidly produced upon mixing of reactants. This allowed for convenient following of the second step in the OAT reaction sequence as the PyO–V(N[^{t}Bu]Ar)$_3$ complex converts to OV(N[^{t}Bu]Ar)$_3$ and pyridine. Time-resolved spectral data corresponding to this process are shown in Figure 1.9b.

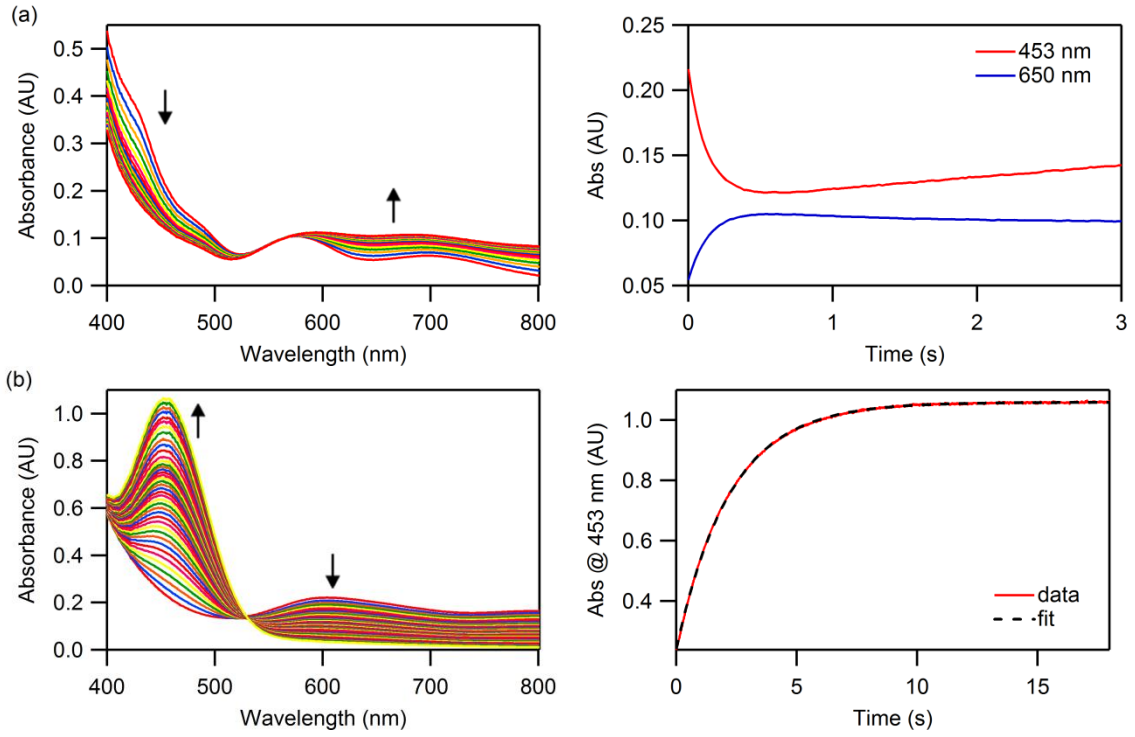

Figure 1.9. (a) Time-resolved spectral changes accompanying the reaction between V(N[^{t}Bu]Ar)$_3$ (0.3 mM) and PyO (2 mM) at −80 °C acquired over 580 ms, showing growth of PyO–V(N[^{t}Bu]Ar)$_3$ (longer wavelengths) with decay of V(N[^{t}Bu]Ar)$_3$ at shorter wavelengths and an isosbestic point near 570 nm. *Top right*: 3 s kinetic traces at λ = 453 and 650 nm. Longer reaction times show slow conversion to OV(N[^{t}Bu]Ar)$_3$ (see Figure 1A.8 for an example). (b) Time-resolved spectral changes accompanying the reaction between V(N[^{t}Bu]Ar)$_3$ (0.2 mM) and PyO (10 mM) at 0 °C acquired over 18 seconds, showing formation of OV(N[^{t}Bu]Ar)$_3$ (λ = 453 nm) with concomitant decay of rapidly formed PyO–V(N[^{t}Bu]Ar)$_3$ occurring at longer wavelengths. *Bottom right*: Kinetic trace at λ = 453 nm with fit to a single exponential function.

The broad, lower energy absorbance band assigned to PyO–V(N[^{t}Bu]Ar)$_3$ (λ = 600 − 800 nm) decays steadily as OV(N[^{t}Bu]Ar)$_3$ (λ_{max} = 453 nm) grows in, with a sharp isosbestic point located near λ = 525 nm. The observed rate constants measured at high temperatures showed no dependence on [PyO] (Figure 1.10a). Since ligand binding occurs much faster than OAT (k_1[PyO] >> k_2), the PyO-bound complex rapidly builds up and k_{obs} values corresponding to the OAT step measured at high T are in the limits of saturation with respect to [PyO]. The reaction was thus treated as zero order in PyO and

average values of k_{obs} were taken as the true first order rate constant (k_2) for product formation from PyO–V(N[^{t}Bu]Ar)$_3$. Temperature dependent rate constants obtained for the OAT step were 0.430 ± 0.056 s^{-1} (0 °C), 1.11 ± 0.06 s^{-1} (10 °C), 1.84 ± 0.08 s^{-1} (15 °C), and 3.19 ± 0.26 s^{-1} (20 °C). Activation parameters associated with k_2 were derived from an Eyring plot (Figure 1.10b): $\Delta H_2^{\ddagger}$ = 15 ± 1 kcal mol^{-1} and $\Delta S_2^{\ddagger}$ = −4 ± 2 cal mol^{-1} K^{-1}. The OAT reaction shows a high value of $\Delta H^{\ddagger}$ and a negative $\Delta S^{\ddagger}$ that is small in absolute value.

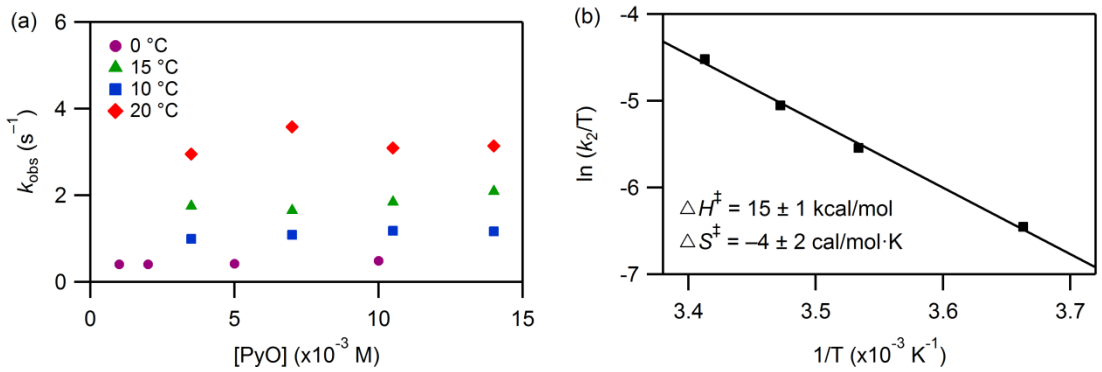

Figure 1.10. (a) Second order rate plots for OV(N[^{t}Bu]Ar)$_3$ formation with V(N[^{t}Bu]Ar)$_3$ (0.2 or 0.3 mM) and PyO (1 - 14 mM) over a temperature range of 0 °C to 20 °C. (b) Eyring plot with derived activation parameters.

1.3.2.2. PhNO. The kinetics of PhNO binding was also studied by the stopped-flow method at low temperatures (−80 to −53 °C). The corresponding time-resolved spectral changes revealed rapid formation of intense absorbance bands at λ_{max} = 477 and 740 nm that are assigned to the PhNO–V(N[^{t}Bu]Ar)$_3$ adduct (Figure 1.11a). The rates of formation of PhNO–V(N[^{t}Bu]Ar)$_3$ were quantified by following the growth in absorbance at λ = 740 nm under pseudo-first order conditions. As was the case for PyO binding, observed rate constants depended linearly on [PhNO] and intercepts were very

close to zero (Figure 1.12a). Activation parameters for PhNO binding were derived from an Eyring plot as shown in Figure 1.12b: $\Delta H_1^{\ddagger} = 5.7 \pm 0.5$ kcal mol^{-1} and $\Delta S_1^{\ddagger} = -14 \pm 3$ cal mol^{-1} K^{-1}. Temperature dependent rate constants for PhNO binding are collected in Table 1.3.

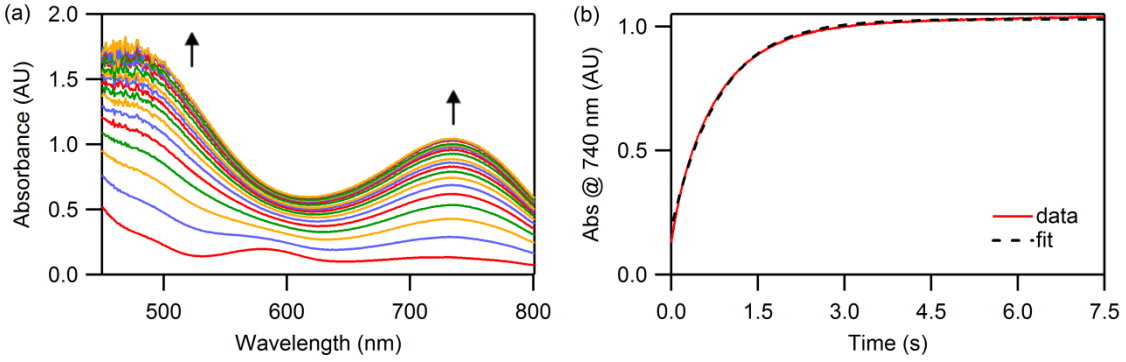

Figure 1.11. (a) Time-resolved spectral changes upon reaction of V(N[^{t}Bu]Ar)$_3$ (0.3 mM) with excess PhNO (1 mM) at −80 °C over 7.5 s. (b) Kinetic trace at λ = 740 nm (red) with fit to a single exponential function (black dashed line).

The rather dramatic changes in the time-resolved spectra that are observed upon binding of PhNO to V(N[^{t}Bu]Ar)$_3$ are in contrast to those described earlier for PyO binding. Low temperature (−70 °C) ^{1}H NMR spectra were acquired for these adducts in an effort to yield insight into the observed spectral differences noted from stopped-flow studies.[1] The PhNO−V(N[^{t}Bu]Ar)$_3$ adduct contained narrow peaks in its NMR spectrum consistent with it being a diamagnetic complex while PyO−V(N[^{t}Bu]Ar)$_3$ was confirmed to be a paramagnetic complex that very slowly converted to OV(N[^{t}Bu]Ar)$_3$ and pyridine at −70 °C. The differences in the UV-visible spectra for these two adducts can therefore be explained by the differences in their spin states (high spin PyO adduct versus low spin PhNO adduct). The experimental findings are supported by DFT calculations, which

predict a triplet ground state for the PyO−V(N[^{t}Bu]Ar)$_3$ adduct. Minima were found for both the singlet and triplet η^1-PhNO−V(N[^{t}Bu]Ar)$_3$ adducts, with the singlet species being lower in energy by 7.2 kcal mol^{-1} (Appendix 1, Table 1A.1). The experimental findings are also in agreement with TD DFT calculated UV-visible spectra for the two adducts (Appendix 1, Figure 1A.9).

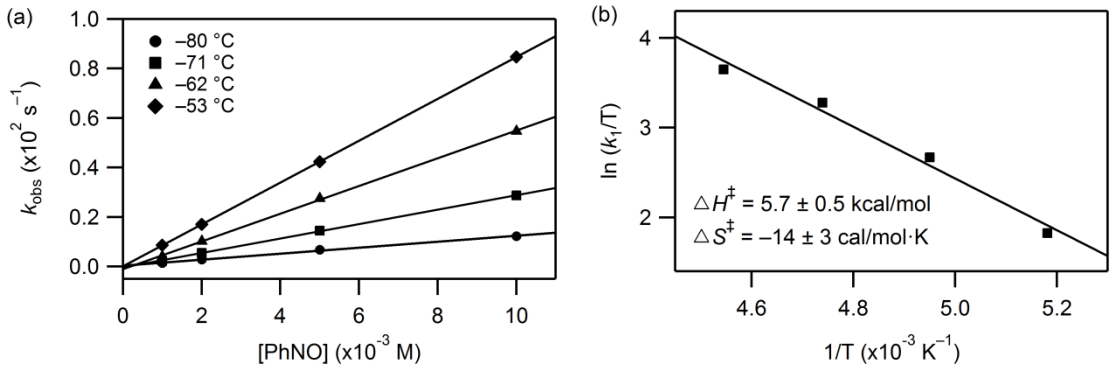

Figure 1.12. (a) Plots of k_{obs} versus [PhNO] (1 - 10 mM) over a temperature range of −80 °C to −53 °C with [V(N[^{t}Bu]Ar)$_3$]$_0$ = 0.3 mM. (b) Eyring plot for PhNO binding with derived activation parameters.

Conversion from the PhNO-bound species to OV(N[^{t}Bu]Ar)$_3$ did not occur to an appreciable extent at −70 °C but could be followed readily by ^{1}H NMR at elevated temperatures (22 to 45 °C) using the signals corresponding to PhNO−V(N[^{t}Bu]Ar)$_3$ and OV(N[^{t}Bu]Ar)$_3$. Temperature dependent rate constants obtained for the OAT step (decay of PhNO−V(N[^{t}Bu]Ar)$_3$) were 0.00031 ± 0.00006 s^{-1} (22 °C), 0.0015 ± 0.0003 s^{-1} (35 °C), and 0.0034 ± 0.0007 s^{-1} (45 °C). Derived activation parameters were $\Delta H_2^{\ddagger}$ = 19 ± 2 kcal mol^{-1} and $\Delta S_2^{\ddagger}$ = −9 ± 5 cal mol^{-1} K^{-1}.

Decomposition of *in situ* PhNO−V(N[^{t}Bu]Ar)$_3$ to OV(N[^{t}Bu]Ar)$_3$ is nearly quantitative in terms of vanadium containing products as determined from ^{51}V NMR analysis.[1] The organic side products (some identified, some not) suggest that extrusion of free nitrenes is involved in the mechanism. In 1:1 reactions of complex and PhNO, azobenzene is formed, and in the presence of excess PhNO, which is well known as a trapping agent for triplet nitrenes,[37] azoxybenzene is also produced. (PhN)V(N[^{t}Bu]Ar)$_3$ is also detected in reactions containing excess metal complex. Further insight into the mechanism is beyond the scope of this investigation.

Table 1.3. Temperature dependent second order rate constants and activation parameters measured for ligand binding (k_1) with the category II *N*-oxides. Rate constants for the OAT reaction step (k_2) are given in the main text.

T (°C)	k_1 ($\times 10^3$ M^{-1} s^{-1})	
	PyO	PhNO
−80	2.36 ± 0.09	1.20 ± 0.05
−71	6.03 ± 0.19	2.92 ± 0.04
−62	13.2 ± 0.54	5.60 ± 0.08
−53	23.0 ± 1.2	8.46 ± 0.01
$\Delta H_1^{\ddagger}$ (kcal mol^{-1})	6.8 ± 0.4	5.7 ± 0.5
$\Delta S_1^{\ddagger}$ (cal mol^{-1} K^{-1})	−7 ± 2	−14 ± 3

1.3.3. Category III: Transient Formation and Decay of Metastable Oxidant-Bound Intermediates on the Timescale of OAT

1.3.3.1. SIPr/MesCNO. Stopped-flow kinetic measurements of the reaction between excess SIPr/MesCNO (2 - 12.5 equivalents) and V(N[^{t}Bu]Ar)$_3$ (0.3 mM) were performed over a broad temperature range (−80 °C to −12 °C). The low temperature (−80 to −62 °C) reactions could be divided into two parts as shown in Figure 1.13. The first stage of the reaction is characterized by a rapid, intense growth in absorbance over the

entire spectral region. In the second stage, there is a leveling off in the absorbance near that seen for OV(N[^{t}Bu]Ar)$_3$ at λ = 453 nm, but at wavelengths above 500 nm there is steady decrease in absorption (Figure 1.13b, inset). At temperatures above −62 °C, however, this intensely absorbing species was not detected and only clean, rapid conversion of V(N[^{t}Bu]Ar)$_3$ to OV(N[^{t}Bu]Ar)$_3$ was observed with isosbestic points near λ = 415 and 525 nm (Figure 1A.10).

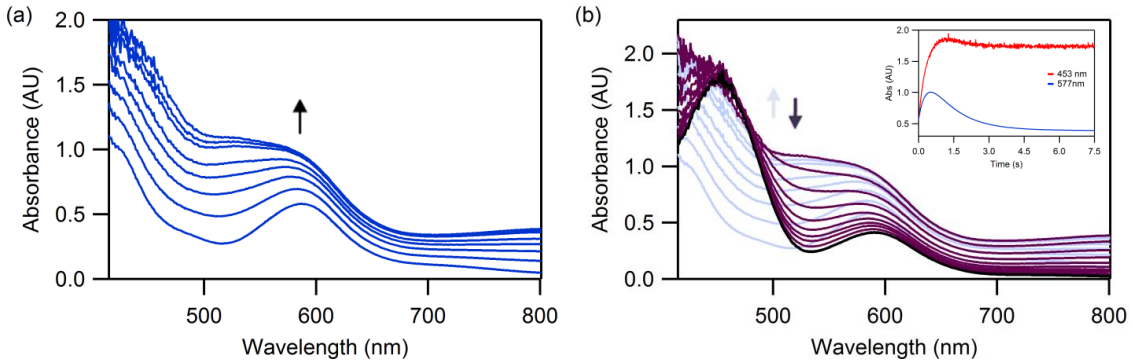

Figure 1.13. Time-resolved spectra obtained from the reaction of V(N[^{t}Bu]Ar)$_3$ (0.3 mM) with SIPr/MesCNO (3 mM) at −80 °C acquired over 7.5 seconds. (a) Initial stage of the reaction (0 - 0.6 s) where rapid adduct formation is observed. (b) Spectral changes during the second phase of the reaction (0.6 - 7.5 s) showing decay of the broad lower energy bands (purple traces) superimposed on its prior accumulation. *Inset*: Kinetic traces at λ = 453 nm and 577 nm.

Two possible sources of the colored intermediate species were considered as shown in Eqs. 1.5 and 1.6.[a] The accepted mechanism that best fits the kinetic data and calculated spectroscopic data is one in which the colored intermediate is in fact due to formation of an SIPr/MesCNO−V(N[^{t}Bu]Ar)$_3$ adduct as outlined in Eq. 1.5. An alternate mechanism is given in Eq. 1.6, which involves formation of the deoxygenated SIPr/MesCN fragment. A stable azirine formed by reaction of an NHC with a nitrile has

[a] The organic side products depicted alongside OV(N[^{t}Bu]Ar)$_3$, MesCN and SIPr, were detected in the OAT reactions by ^{1}H NMR analysis (see ref 1, Supporting Information).

been reported recently though it was found to be pale yellow.[38] TD DFT calculations predict a low intensity band at λ = 473 nm for the SIPr/MesCN fragment (Figure 1A.15), but the absorption observed at longer wavelengths in stopped-flow experiments cannot be attributed to this fragment.

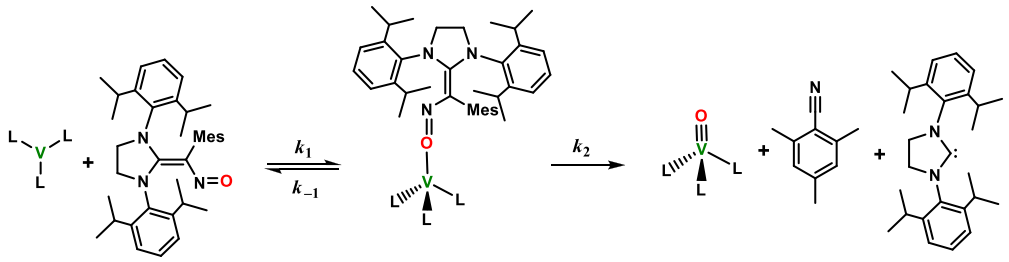

(1.5)

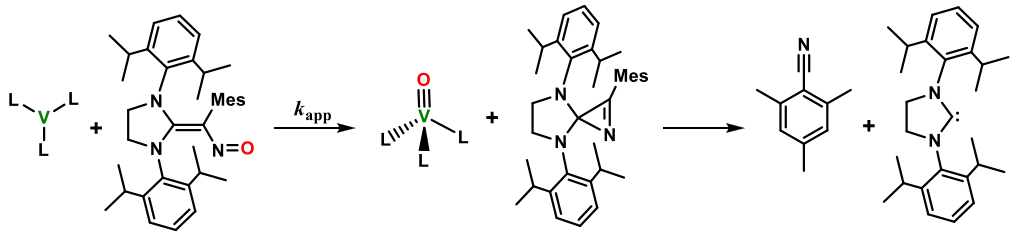

(1.6)

DFT calculations were performed for a truncated model of the SIPr/MesCNO−V(N[^{t}Bu]Ar)$_3$ adduct where the 2,6-diisopropylphenyl substituents on the nitrogen atoms of the NHC in the real system were replaced by methyl groups and the mesityl group replaced by a phenyl group. Both singlet and triplet potential energy minima were found, with the triplet species being more stable by about 4 kcal mol^{-1}. This can be explained in terms of the alleviation of steric strain imposed by this bulky ligand in the triplet versus singlet state, since the V−O bond length is longer in the high-spin structure (1.874 Å versus 1.796 Å). In the real system, the energetic difference favoring

the high-spin over the low-spin structure is expected to be even greater owing to the presence of the larger isopropyl substituents. Furthermore, the TD DFT computed UV-visible spectrum of the triplet SIMe/PhCNO−V(N[^{t}Bu]Ar)$_3$ truncated model (Figure 1A.15) is in keeping with kinetic modeling studies in which the spectral changes in Figure 1.13 are in fact due to adduct formation and decay in a manner similar to that described for IPr/N_2O (*vide infra*).

Analysis of the kinetic data at λ = 453 nm was possible over the entire temperature range studied and kinetic traces fit well to a single exponential equation. Observed rate constants showed a linear dependence on [SIPr/MesCNO] and composite second order rate constants (k_{app}) corresponding to formation of OV(N[^{t}Bu]Ar)$_3$ from V(N[^{t}Bu]Ar)$_3$ and SIPr/MesCNO were obtained (see Appendix 1). Analysis of low temperature (−80 to −62 °C) data at λ = 577 nm was also performed since the rise and decay in absorbance were clearly defined. Fitting traces to a double exponential equation yielded observed rate constants for each process (k_{1obs} and k_{2obs}). Values of k_{1obs} showed a linear dependence on [SIPr/MesCNO] with non-zero intercepts as shown in Figure 1.14.

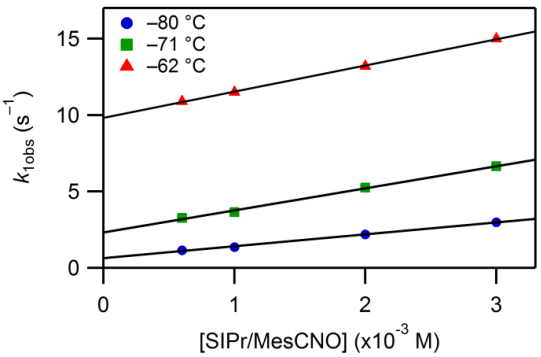

Figure 1.14. Plots of k_{1obs} versus [SIPr/MesCNO] (0.6 - 3 mM) with linear fits, obtained from analysis of kinetic traces at λ = 577 nm. Data was acquired over a temperature range of −80 to −62 °C with [V(N[^{t}Bu]Ar)$_3$]$_0$ = 0.3 mM.

Second-order rate constants (k_1) were derived from the slopes of the linear plots and intercepts were taken as estimates for k_{-1}, allowing for K_{eq} values to be estimated from the kinetic data (Tables 1A.9 and 1A.10). Eyring plots were used to derive activation parameters for both the forward and reverse reactions, which are provided in Appendix 1, Figure 1A.13. In contrast, plots of the second observed rate constant (k_{2obs}) did not show a linear dependence on [SIPr/MesCNO] and instead appeared to saturate (Figure 1.15a). Plots of inverse k_{2obs} versus inverse [SIPr/MesCNO] were linear, which is consistent with a pre-association step prior to oxidative addition as outlined in Eq. 1.5. The rate law is given in Eq. 1.7, and nonlinear least-squares fitting of the data to Eq. 1.7 yielded values for k_2 and K_{eq} (Table 1A.11). The values obtained for K_{eq} are in good agreement with those determined previously from analysis of the k_{1obs} versus [SIPr/MesCNO] plots.

$$\frac{d[OV(N[^tBu]Ar)_3]}{dt} = k_{obs}[V(N[^tBu]Ar)_3] = \frac{k_2 k_{eq}[XNO]}{1 + K_{eq}[XNO]}[V(N[^tBu]Ar)_3] \qquad (1.7)$$

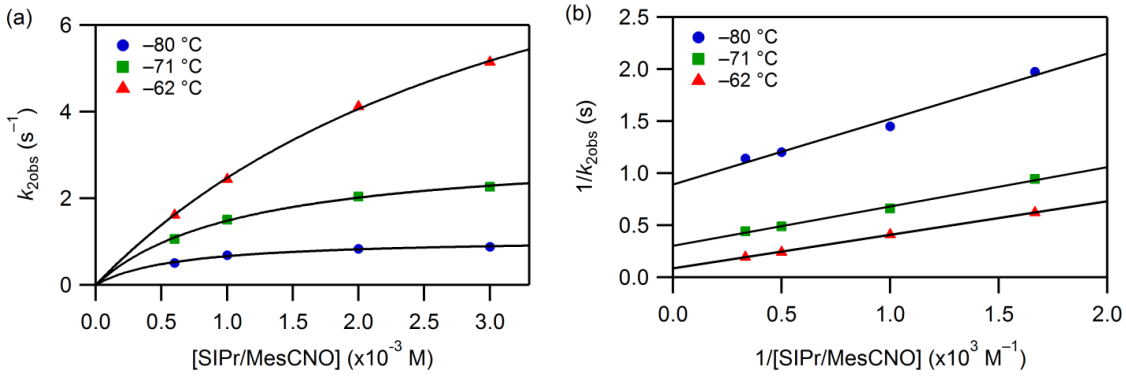

Figure 1.15. (a) Plots of k_{2obs} versus [SIPr/MesCNO] with fits to Eq. 1.7 for the decay of SIPr/MesCNO−V(N[^{t}Bu]Ar)$_3$ measured at λ= 577 nm with 0.3 mM V(N[^{t}Bu]Ar)$_3$ and SIPr/MesCNO (0.6 - 3 mM) over the temperature range of −80 to −62 °C. (b) Plots of $1/k_{2obs}$ versus 1/[SIPr/MesCNO] with linear fits.

The kinetic data were also supported by global modeling to the mechanism shown in Eq. 1.5, which corresponds to reversible XNO binding followed by OAT from the pre-formed adduct. Calculated values for k_1 (XNO binding) and k_2 (OAT) were in reasonable agreement with those obtained from analysis of the experimental data and are provided in Table 1.4. Values for k_{-1} are less precise and treated only as estimates (see Appendix 1). Activation parameters derived from the model are $\Delta H_1^{\ddagger} = 4.9 \pm 0.4$ kcal mol^{-1} and $\Delta S_1^{\ddagger} = -19 \pm 2$ cal mol^{-1} K^{-1} for ligand binding (k_1) and $\Delta H_2^{\ddagger} = 9.3 \pm 0.3$ kcal mol^{-1} and $\Delta S_2^{\ddagger} = -9 \pm 1$ cal mol^{-1} K^{-1} for OAT (k_2). Spectra calculated by the fitting program for all colored components are shown in Figure 1.16.

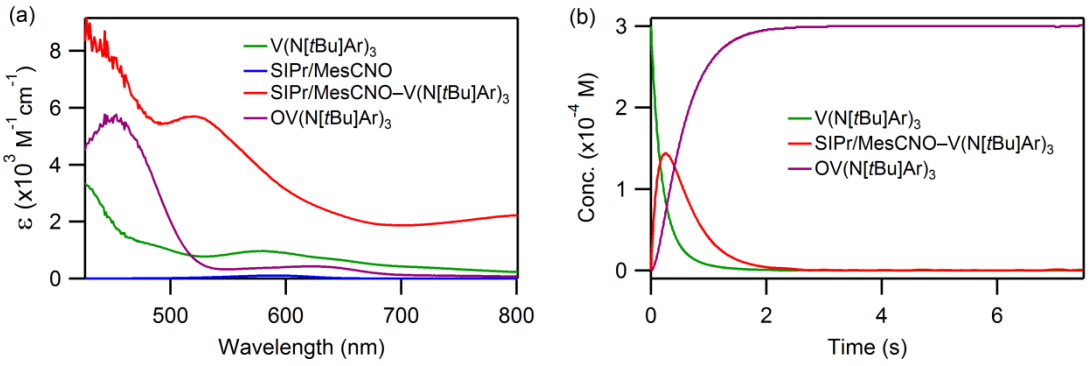

Figure 1.16. (a) Representative calculated spectra of colored components obtained from the kinetic model at −71 °C with $[V(N[^tBu]Ar)_3]_0 = 0.3$ mM and $[SIPr/MesCNO]_0 = 3$ mM. A known spectrum for SIPr/MesCNO was incorporated in all cases while the remaining colored components were calculated by the fitting program. (b) Concentration profiles for colored components. The concentration profile for SIPr/MesCNO is not shown since it is present in pseudo-first order excess.

1.3.3.2. IPr/N_2O. Analogous to the reactions with SIPr/MesCNO, the time-resolved UV-visible spectral changes accompanying the reaction between excess IPr/N_2O (2 - 12 equivalents) and $V(N[^tBu]Ar)_3$ (0.25 mM) at low temperatures (−62 °C to −35 °C)

could also be divided into two parts as shown in Figure 1.17. The first stage of the reaction is characterized by a rapid, intense growth in absorbance over the entire spectral region with a band centered near λ = 475 nm. A slower decay process follows where the intense band at 475 nm is found to blue-shift to the expected maximum for OV(N[^{t}Bu]Ar)$_3$ (λ = 453 nm).

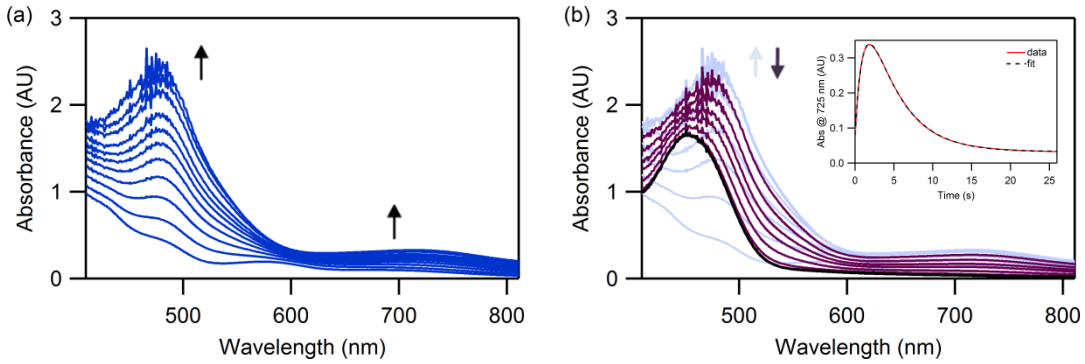

Figure 1.17. Time resolved spectra obtained from the reaction of V(N[^{t}Bu]Ar)$_3$ (0.25 mM) with IPr/N_2O (1 mM) at −62 °C acquired over 26 seconds. (a) Rapid formation is observed initially across the entire spectral window which maximizes within ca. 2 s. (b) Decay of the intensely absorbing intermediate (purple traces) superimposed on its prior accumulation, ultimately ending with the expected spectrum of OV(N[^{t}Bu]Ar)$_3$ (black trace). *Inset*: Kinetic trace at λ = 725 nm with fit to a double exponential function.

For technical reasons, the kinetic data were analyzed at λ = 725 nm and traces were fit to the general two term rate law, rate = A_1 exp(−k_{1obs}t) + A_2 exp(−k_{2obs}t).[b] Plots of k_{1obs} versus [IPr/N_2O] were linear with non-zero intercepts while plots of k_{2obs} versus [IPr/N_2O] appeared to saturate (Figures 1A.18a and 1A.20a, respectively). Analysis of the experimental data was performed as described for SIPr/MesCNO previously and

[b] In most systems, the change in absorbance at λ = 453 nm (λ_{max} for OV(N[^{t}Bu]Ar)$_3$) was followed. For reactions with IPr/N_2O, however, the absorbance was too intense in that region of the spectrum. Analysis of data at 453 nm, when possible (i.e., at lowest concentration of IPr/N_2O), was in agreement with analysis at λ = 725 nm.

these results are provided in Appendix 1. Global modeling of the kinetic data yielded rate constants that were in excellent agreement with experimentally derived values and are provided in Table 1.4. Spectra calculated by the modeling program for the colored species involved in the reaction were consistent across the temperature and concentration ranges studied and are shown in Figure 1.18.

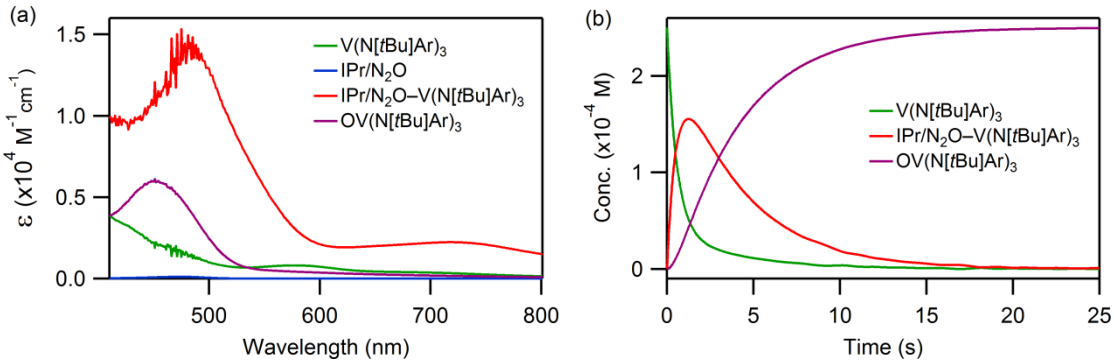

Figure 1.18. (a) Representative calculated spectra of colored components obtained from modeling at −62 °C with $[V(N[^tBu]Ar)_3]_0$ = 0.25 mM and $[IPr/N_2O]_0$ = 2 mM. A known spectrum for IPr/N_2O was incorporated while the remaining colored components were calculated. (b) Concentration profiles for colored components. The concentration profile for IPr/N_2O is not shown since it is present in pseudo-first order excess.

Interestingly, DFT calculations predict a very small energetic difference between the singlet and triplet $IMe/N_2O–V(N[^tBu]Ar)_3$ adducts which suggests that both may coexist in equilibrium upon adduct formation (see Table 1A.1). The spectrum of $IPr/N_2O–V(N[^tBu]Ar)_3$ obtained from the kinetic model, however, is in good agreement with that obtained computationally by TD DFT calculations for the singlet adduct of the truncated model IMe/N_2O (Figure 1A.21). Derived activation parameters from the kinetic model were in good agreement with experimentally determined values and are $\Delta H_1^{\ddagger}$ = 5.6

± 0.4 kcal mol^{-1} and $\Delta S_1^{\ddagger}$ = −18 ± 2 cal mol^{-1} K^{-1} (for ligand binding, k_1) and $\Delta H_2^{\ddagger}$ = 13 ± 1 kcal mol^{-1} and $\Delta S_2^{\ddagger}$ = 1 ± 2 cal mol^{-1} K^{-1} (for OAT, k_2).

Table 1.4. Calculated rate constants and activation parameters obtained from global modeling of SIPr/MesCNO and IPr/N_2O kinetic data using the ReactLab Kinetics program. Spectra for the three colored components (V(N[^{t}Bu]Ar)$_3$, XNO−V(N[^{t}Bu]Ar)$_3$, and OV(N[^{t}Bu]Ar)$_3$) were calculated during the fitting procedure.

T (°C)	k_1 (M^{-1} s^{-1})		k_2 (s^{-1})	
	SIPr/MesCNO[a,b]	IPr/N_2O[a,c]	SIPr/MesCNO[a,b]	IPr/N_2O[a,c]
−80	1,010 ± 28	282 ± 83	0.901 ± 0.012	0.012 ± 0
−71	1,710 ± 185	-----	2.94 ± 0.38	-----
−62	3,270 ± 133	785 ± 54	7.87 ± 0.34	0.308 ± 0.014
−53	-----	1,520 ± 26	-----	1.05 ± 0.03
−44	-----	3,000 ± 11	-----	2.93 ± 0.04
−35	-----	5,550 ± 123	-----	8.84 ± 0.17
$\Delta H^{\ddagger}$ (kcal mol^{-1})	4.9 ± 0.4	5.6 ± 0.4	9.3 ± 0.3	13 ± 1
$\Delta S^{\ddagger}$ (cal mol^{-1} K^{-1})	−19 ± 2	−18 ± 2	−9 ± 1	1 ± 2

[a] The average values of rate constants obtained from modeling two separate datasets are reported with standard deviations. [b] Initial reactant concentrations were fixed at 0.3 mM and 3 mM for V(N[^{t}Bu]Ar)$_3$ and SIPr/MesCNO, respectively. A known spectrum for SIPr/MesCNO was incorporated while spectra for the remaining colored components were calculated during the fitting procedure. [c] Initial reactant concentrations were fixed at 0.25 mM and 2 mM for V(N[^{t}Bu]Ar)$_3$ and IPr/N_2O, respectively. A known spectrum for IPr/N_2O was incorporated while spectra for the remaining colored components were calculated during the fitting procedure.

1.3.4. Category IV: Steady State Kinetics Without Observable Intermediates

1.3.4.1. dbabhNO. The kinetics of the OAT reaction between V(N[^{t}Bu]Ar)$_3$ and dbabhNO were measured at low temperatures (−71 to −44 °C) using excess dbabhNO (3.3 to 33-fold excess). The intense absorbance band at λ = 453 nm corresponding to OV(N[^{t}Bu]Ar)$_3$ grew in within seconds as shown in Figure 1.19. Absorbance bands assignable to an intermediate dbabhNO−V(N[^{t}Bu]Ar)$_3$ were not detected in the time-resolved spectra; only clean conversion to OV(N[^{t}Bu]Ar)$_3$ from V(N[^{t}Bu]Ar)$_3$ with isosbestic points near λ = 417 and 526 nm was observed.

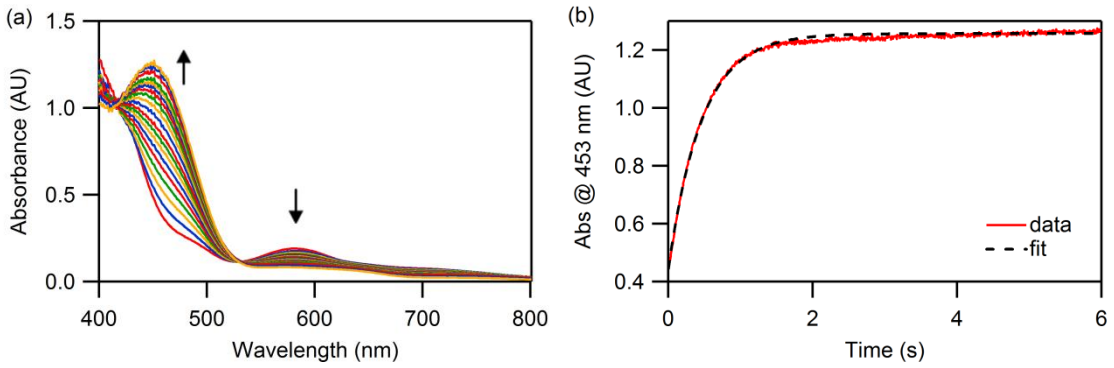

Figure 1.19. (a) Time-resolved spectral changes accompanying the reaction between V(N[^{t}Bu]Ar)$_3$ (0.3 mM) and dbabhNO (2 mM) at −71 °C acquired over 7.5 seconds showing growth of OV(N[^{t}Bu]Ar)$_3$ (λ_{max} = 453 nm) with concomitant decay occurring at longer wavelengths. (b) Kinetic trace at 453 nm (red line) with fit to a single exponential function (black dashed line).

Kinetic traces fit well to a single exponential rate law and linear plots of the observed rate constant (k_{obs}) versus [dbabhNO] yielded second order rate constants (k_{app}), where, assuming a steady-state in [dbabhNO−V(N[^{t}Bu]Ar)$_3$], $k_{app} = k_1k_2/(k_{-1}+k_2) = k_1/(1+k_{-1}/k_2)$ for product formation. Since the intermediate was not detected in the time-resolved spectra, the composite rate constant cannot be broken down further. Activation parameters for the composite reaction were derived from the Eyring plot shown in Figure 1.20b: $\Delta H_{app}^{\ddagger} = 6.3 \pm 0.3$ kcal mol^{-1} and $\Delta S_{app}^{\ddagger} = -13 \pm 1$ cal mol^{-1} K^{-1}. Temperature dependent composite second order rate constants are compiled in Table 1.5.

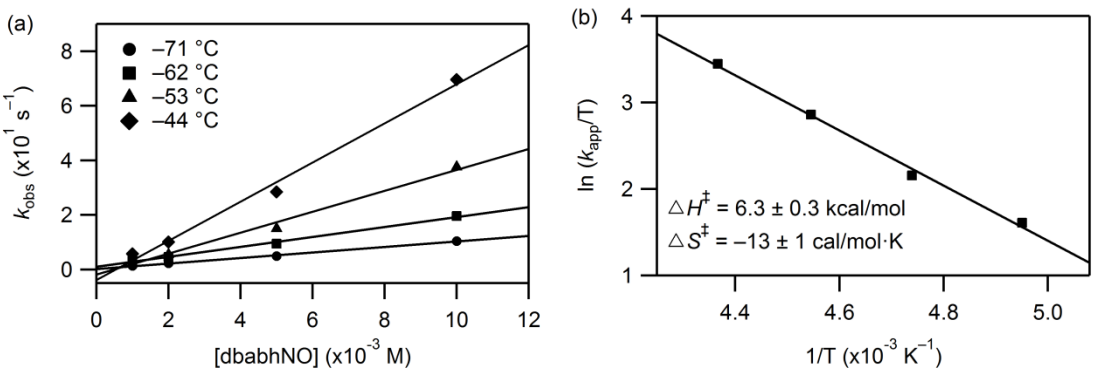

Figure 1.20. (a) Plots of k_{obs} versus dbabhNO at various concentrations (1 - 10 mM) over a temperature range of −71 to −44 °C with $[V(N[^tBu]Ar)_3]_0$ = 0.3 mM. (b) Eyring plot with derived activation parameters.

1.3.4.2. MesCNO. Reactions of excess MesCNO (12 to 93-fold excess) with $V(N[^tBu]Ar)_3$ showed similar spectroscopic behavior to that of dbabhNO as shown in Appendix 1, Figure 1A.24. Unlike dbabhNO, the linear plots of k_{obs} versus MesCNO concentration appeared to give nonzero intercepts, which suggest that k_{-1} plays a role in the kinetic scheme (Figure 1.21a). Derived activation parameters from the Eyring plot shown in Figure 1.21b are $\Delta H_{app}^{\ddagger}$ = 5.3 ± 0.8 kcal mol^{-1} and $\Delta S_{app}^{\ddagger}$ = −24 ± 3 cal mol^{-1} K^{-1}. Despite a slightly lower value of $\Delta H^{\ddagger}$ (~1 kcal mol^{-1}), the rate constant for the reaction of MesCNO at −62 °C (81 M^{-1} s^{-1}) is over 20 times slower than that for dbabhNO at the same temperature (1,820 M^{-1} s^{-1}). This is due to the more unfavorable entropy of activation for OAT. Temperature dependent second order rate constants for the category IV OAT reactions are collected in Table 1.5.

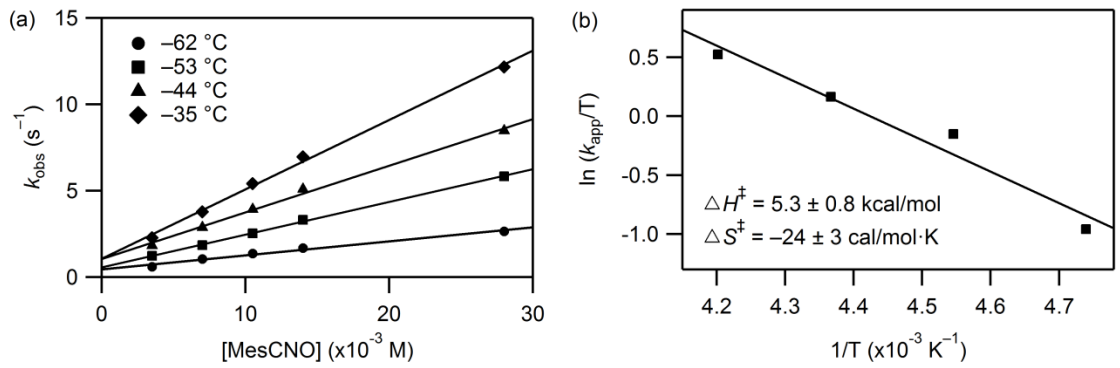

Figure 1.21. (a) Plots of k_{obs} versus MesCNO at various concentrations (3.5 - 28 mM) over a temperature range of −62 to −35 °C with $[V(N[^tBu]Ar)_3]_0$ = 0.3 mM. (b) Eyring plot with derived activation parameters.

Table 1.5. Temperature dependent composite second order rate constants and activation parameters for $OV(N[^tBu]Ar)_3$ formation from reactions of $V(N[^tBu]Ar)_3$ with dbabhNO and MesCNO.

T (°C)	k_{app} (× 10^3 M^{-1} s^{-1})	
	dbabhNO	MesCNO
−71	1.01 ± 0.03	-----
−62	1.82 ± 0.09	0.081 ± 0.006
−53	3.84 ± 0.30	0.189 ± 0.004
−44	7.18 ± 0.46	0.270 ± 0.010
−35	-----	0.402 ± 0.012
$\Delta H_{app}^{\ddagger}$ (kcal mol^{-1})	6.3 ± 0.3	5.3 ± 0.8
$\Delta S_{app}^{\ddagger}$ (cal mol^{-1} K^{-1})	−13 ± 1	−24 ± 3

1.4. Discussion

The factors involved in the OAT reactions of $V(N[^tBu]Ar)_3$ with the range of *N*-oxides shown in Figure 1.2 have been delineated. Since measured rate constants vary in these systems, it is useful to view the overall efficacy of the OAT reactions under a common set of conditions as shown in Figure 1.22. As can been deduced from this plot, the net rate of OAT without regard to the detailed mechanism is in the following order,

from slowest to fastest: PhNO << N_2O < PyO < IPr/N_2O < MesCNO < dbabhNO ≈ SIPr/MesCNO. Derived rate constants and their assignments, along with activation parameters and N−O BDEs, are collected in Table 1.6.

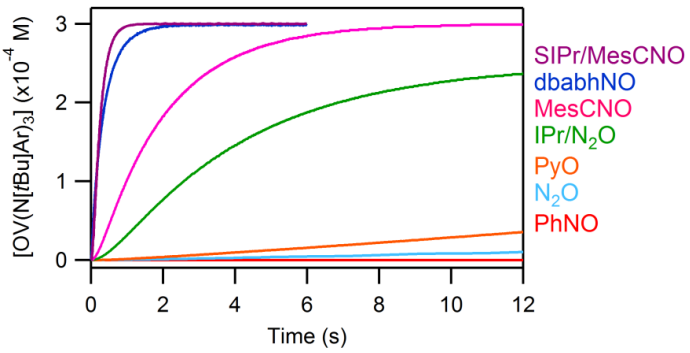

Figure 1.22. Rate of formation of OV(N[^{t}Bu]Ar)$_3$ as a function of time at −62 °C under a similar set of conditions. [XNO]$_o$ = 3 mM (SIPr/MesCNO, MesCNO); 2 mM (PyO, PhNO, dbabhNO, IPr/N_2O); 66 mM (N_2O). [V(N[^{t}Bu]Ar)$_3$]$_o$ = 0.3 mM (for reactions with PhNO, MesCNO, dbabhNO, SIPr/MesCNO, and N_2O); 0.25 mM (for reaction with IPr/N_2O); 0.2 mM (for reaction with PyO).

All of the *N*-oxides studied, except for N_2O, which undergoes dinuclear OAT, follow the general mechanism outlined in Eq. 1.1. The reaction between N_2O and V(N[^{t}Bu]Ar)$_3$ can also be viewed as following the same mechanism if it is instead considered as a reaction between V(N[^{t}Bu]Ar)$_3$ and ONN−V(N[^{t}Bu]Ar)$_3$. From a kinetic standpoint, an ideal OAT reagent would display rapid binding (large k_1), slow dissociation (small k_{-1}), and very rapid OAT (large k_2). The k_1/k_{-1} ratio represents the equilibrium constant (K_{eq}) for substrate binding, which will necessarily be large for a good OAT reagent, as will the k_2/k_{-1} ratio.

For PyO and PhNO, it was possible to measure both the rates of substrate binding and OAT and to characterize the intermediates by low *T* NMR spectroscopy. For

SIPr/MesCNO and IPr/N_2O, the intermediate adducts were observed to rapidly form and decay in stopped-flow experiments and kinetic modeling allowed for individual rate constants to be resolved. For MesCNO and dbabhNO, however, intermediate adducts were not detectable and only composite rate constants could be determined. For N_2O, the rate of binding was obtained from analysis of the kinetic data but this is proposed to involve binding through N as opposed to O. For systems where individual rate constants could be resolved, the rate of binding is in the order of PyO > PhNO > SIPr/MesCNO > IPr/N_2O >> N_2O and spans almost six orders of magnitude. The rates of OAT, where they could be determined, show an even wider range of values that span ten orders of magnitude: SIPr/MesCNO > IPr/N_2O >> PyO >> PhNO. In reactions with N_2O, the proposed *N*-nitrosoimido intermediate cannot be detected but kinetic analysis suggests it to be a rapid OAT reagent to free V(N[^{t}Bu]Ar)$_3$.

The rate constants for XNO binding to V(N[^{t}Bu]Ar)$_3$ at −62 °C in Table 1.6 can be compared with the published value of 2.6×10^4 M^{-1} s^{-1} for O_2 binding to form a low-spin η^1-O_2−V(N[^{t}Bu]Ar)$_3$ adduct.[39] The very fast rate of dioxygen binding, faster even than PyO, may be attributed to its small size as well as the fact that it may approach and bind from either end of the molecule, giving it a larger open steric window for binding. Of special note is the ultra slow rate for N_2O binding, which, according to DFT calculations, involves formation of a low-spin η^1-N-bound adduct. It is postulated that the rearrangements involved upon N_2O binding, which is in effect an oxidative addition reaction, lead to the slow association of this substrate with V(N[^{t}Bu]Ar)$_3$. This is discussed further in Section 1.4.1.

Table 1.6. Kinetic data for reactions of XNO and V(N[^{t}Bu]Ar)$_3$ (BDE in kcal mol^{-1}, $\Delta H^{\ddagger}$ in kcal mol^{-1}, $\Delta S^{\ddagger}$ in cal^{-1} mol K^{-1}).

Category	Substrate	BDE	$k_{assigned}$[a]	k (−62 °C)	$\Delta H^{\ddagger}$	$\Delta S^{\ddagger}$
I	N_2O	40[b]	k_1 (M^{-1} s^{-1})[c]	0.038 ± 0.012	6.3 ± 0.3	−34 ± 1
			k_2 (M^{-1} s^{-1})[c]	very fast[h]	3.0 ± 0.1	−27 ± 1
II	PyO	63[d]	k_1 (M^{-1} s^{-1})	13,250 ± 540	6.8 ± 0.4	−7 ± 2
			k_2 (s^{-1})	$8.5\cdot10^{-5}$[e]	15 ± 1	−4 ± 2
	PhNO	108[f]	k_1 (M^{-1} s^{-1})	5,600 ± 79	5.7 ± 0.5	−14 ± 3
			k_2 (s^{-1})	$4.7\cdot10^{-10}$[e]	19 ± 2	−9 ± 5
III	SIPr/MesCNO	75[f]	k_1 (M^{-1} s^{-1})[c]	3,270 ± 133	4.9 ± 0.4	−19 ± 2
			k_2 (s^{-1})[c]	7.87 ± 0.34	9.3 ± 0.3	−9 ± 1
	IPr/N_2O	62[f]	k_1 (M^{-1} s^{-1})[c]	785 ± 54	5.6 ± 0.4	−18 ± 2
			k_2 (s^{-1})[c]	0.308 ± 0.014	13 ± 1	+1 ± 2
IV	MesCNO	53[d]	k_{app} (M^{-1} s^{-1})[i]	81 ± 6	5.3 ± 0.8	−24 ± 3
	dbabhNO	10[g]	k_{app} (M^{-1} s^{-1})[i]	1,820 ± 90	6.3 ± 0.3	−13 ± 1

[a] k_1 refers to bimolecular rate constants for XNO binding; k_2 refers to rate constants for OAT; k_{app} refers to composite bimolecular rate constants for reactions where individual rate constants could not be resolved. [b] Calculated from gas phase data in ref 35. [c] Values taken from kinetic model. [d] Value taken from ref 36. [e] Value extrapolated from Eyring plot for OAT at high T. [f] Calculated at the BP86/6-311G(d,p) level; this value includes dissociation of the deoxygenated adduct to its components in solution. [g] Derived from thermochemical data reported in this work (see ref 1). [h] As discussed earlier, a value of 3,560 M^{-1} s^{-1} was determined from the kinetic model, however, in reality it is the k_2/k_{-1} ratio that is known accurately rather than the individual values for k_{-1} and k_2. It can be concluded only that k_2 is very fast, even at low T. [i] $k_{app} = k_1k_2/(k_{-1}+k_2)$.

Data for PyO reactivity, since it allowed for separate determination of k_1 and k_2, provides some insight for other substrates where that was not possible. The value of k_1 for PyO (13,250 M^{-1} s^{-1} at −62 °C) provides a useful approximation for the maximum possible rate of OAT. For the category IV reactions following a steady state model where detectable intermediate does not buildup, $k_{app} = k_1k_2/(k_{-1}+k_2)$, which can also be expressed as $k_{app} = k_1(1/[1+k_{-1}/k_2])$. Thus the k_{app} values will be smaller than k_1 dependent upon the k_{-1}/k_2 ratio. At −62 °C, k_{app} for MesCNO (81 M^{-1} s^{-1}), dbabhNO (1,820 M^{-1} s^{-1}), and SIPr/MesCNO (4,930 M^{-1} s^{-1}; see Appendix 1) are less than k_1 for PyO and imply greatly differing values of k_{-1}/k_2.

It is important to recognize that substrate binding is quite different for individual substrates and this blurs the distinction between the binding and OAT reaction steps. Examples of both high-spin (PyO−V(N[^{t}Bu]Ar)$_3$) and low-spin (PhNO−V(N[^{t}Bu]Ar)$_3$) adducts were detected from experiments, which reveals that the spin crossover event, which is required at some point along the reaction path, could be considered part of the initial binding process or part of the oxidative addition step. Despite these complexities, the activation enthalpies for binding in all systems where ligand coordination rates were obtained is on the order of 6 ± 1 kcal mol^{-1} regardless of adduct spin state. This is not much higher than the estimated value of 4 kcal mol^{-1} that is required to displace the η^3-arene interaction present in V(N[^{t}Bu]Ar)$_3$ (Figure 1.3). This implies that ligand binding to the complex lacking this interaction would be around 2 kcal mol^{-1}, which is consistent with the generally low activation enthalpy for ligand binding to a metal center with a vacant site. Since the enthalpies of activation for XNO binding remain relatively constant, the entropy of activation plays an important role in determining the rate constant values.

The following sections discuss individual XNO substrates in more detail.

1.4.1. Category I (N_2O). Due to importance as a ligand and the fact that it undergoes dinuclear activation, N_2O is discussed in more detail. The pioneering work of Taube's group[4] had shown that the preformed $[(NH_3)_5Ru(N_2O)]^{2+}$ complex underwent rapid OAT with Cr^{2+} while reactions between Cr^{2+} and N_2O required months under similar conditions. This earlier work sets the precedence for dinuclear OAT involving nitrous oxide between two different metal fragments. Chang et al. have reported the first crystal

structure of an N_2O complex, (tpa^{Mes})V−NNO,[7] which may be similar in nature to any intermediate complex formed between N_2O and V(N[^{t}Bu]Ar)$_3$. The presence of the axially coordinated base in the (Mes)$_3$V system results in formation of a high-spin, linear N_2O complex. In contrast, DFT calculations regarding (N[^{t}Bu]Ar)$_3$V−NNO suggest that it is a low-spin complex that can be viewed as having undergone spin pairing and oxidative addition to form a V(V) complex with a doubly bent N_2O ligand (Figure 1.23), which is in keeping with earlier computational studies performed by Caulton and coworkers[6] and analogous structurally characterized products.[40] DFT calculations have also revealed that binding of N_2O to V(N[^{t}Bu]Ar)$_3$ through its oxygen atom is thermodynamically unfavorable (triplet ground state, ΔH_{bind} = 12.1 kcal mol^{-1}) as is formation of the high-spin N-bound adduct (ΔH_{bind} = 3.1 kcal mol^{-1}). The only computed stable binding mode is through formal oxidation of the vanadium center resulting in the diamagnetic V(V) nitrosoimdo complex (ΔH_{bind} =−7.1 kcal mol^{-1}), however, this is also expected to be of marginal stability since an unfavorable entropy of binding will cancel the favorable enthalpic term.

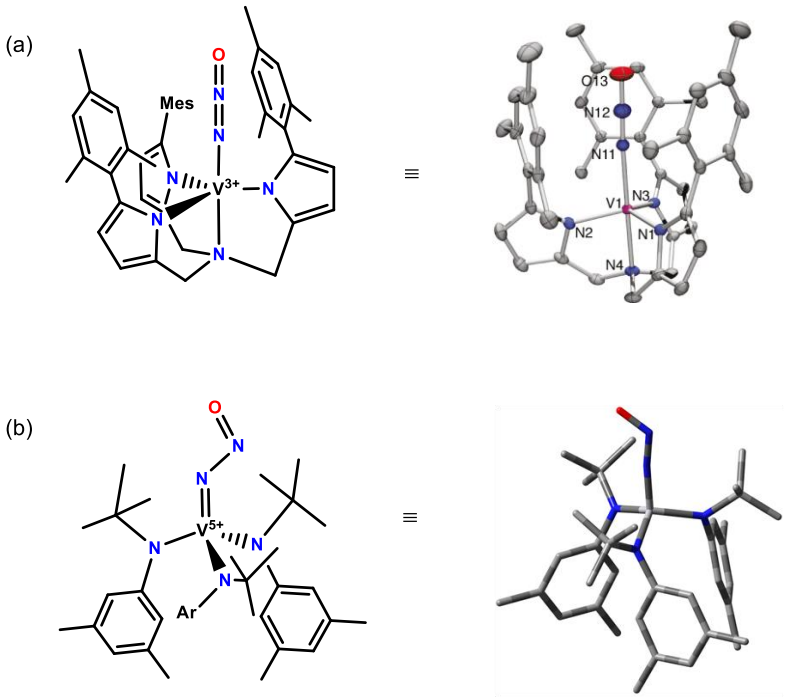

Figure 1.23. (a) Structure of the crystallographically characterized $(tpa^{Mes})_3V{-}NNO$ complex reported by Chang et al. (thermal ellipsoid plot taken from ref 7). (b) Proposed structure of $(N[^tBu]Ar)_3V{-}NNO$ based on computational studies performed in this work. Optimized structure of $(N[^tBu]Ar)_3V{-}NNO$ (singlet) was calculated at the bp86/6-311G(d,p) (MDF10 for V with an additional set of f functions) level. Selected interatomic distances (Å) and angles are provided in Table 1A.1.

The slow rate of binding observed in kinetics experiments at high temperatures is in keeping with the fact that binding is a highly reversible process. The major factor that determines the fate of $(N[^tBu]Ar)_3V{=}N{-}N{=}O$ once it is formed is the k_{-1}/k_2 ratio, which describes the rate of its dissociation back to reactants versus the rate of its trapping by free $V(N[^tBu]Ar)_3$ to yield a bridging $L_3V{=}N{-}N{=}O{-}VL_3$ intermediate species that readily decomposes into OVL_3, N_2, and free VL_3 (L = $(N[^tBu]Ar)_3$). The proposed termolecular reaction for N_2O is consistent with recently published calculations by Lin et al.[5] who have concluded that OAT in the VCp_2 system occurs by initial binding of N_2O

through its terminal N atom to one V center, followed by essentially barrierless OAT to a second V center.

The derived reaction profile for OAT between N_2O and two moles of $V(N[^tBu]Ar)_3$ is shown in Figure 1.24. The profile is computed based on the experimental enthalpies of activation for k_1 ($\Delta H_1^{\ddagger}$ = 6.3 kcal mol^{-1}), k_{-1} ($\Delta H_{-1}^{\ddagger}$ = 13 kcal mol^{-1}) and k_2 ($\Delta H_2^{\ddagger}$ = 3.0 kcal mol^{-1}). The equilibrium binding enthalpy of −6.7 kcal mol^{-1} was also calculated from this data ($\Delta H_{bind} = \Delta H_1^{\ddagger} - \Delta H_{-1}^{\ddagger}$). The data shows that there is a much greater activation enthalpy for k_{-1} relative to k_2. However, the entropy change for dissociation (k_{-1}, $\Delta S^{\ddagger}$ = −6 cal mol K^{-1}) is much less negative than that associated with the OAT step (k_2, $\Delta S^{\ddagger}$ = −27 cal mol K^{-1}). Therefore as the temperature is raised, k_{-1} will increase much faster than k_2. This has the consequence of moving the transition state from TS1 to TS2 in Figure 1.24 with the result that third order kinetics is followed at high temperature and second order kinetics at low temperature. The slowness of the reaction as compared with other binding reactions is reflected primarily in the unfavorable activation entropy.

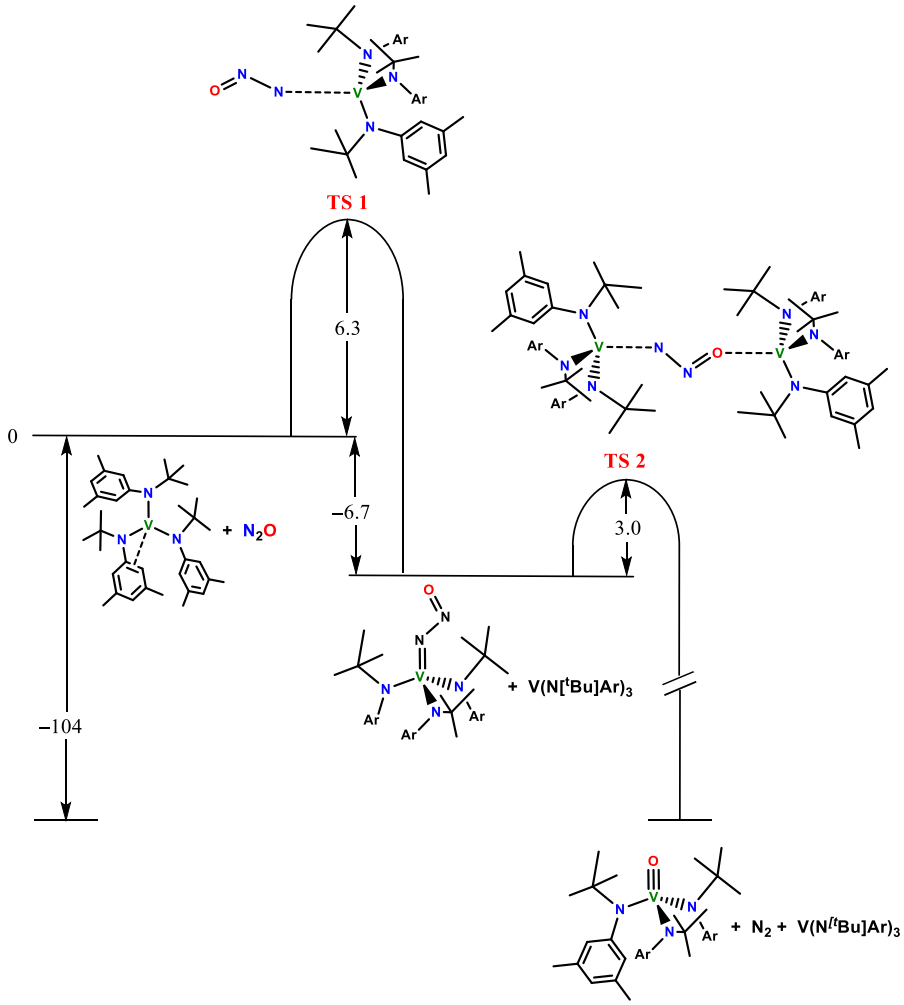

Figure 1.24. Potential energy diagram for the reaction $2VL_3 + N_2O \rightarrow OVL_3 + N_2 + VL_3$ via dinuclear activation of substrate. At low *T*, the rate-determining step occurs at the point of ligand binding (TS 1) and the reaction obeys the rate law $dP/dt = k_1[VL_3][N_2O]$. At high *T*, the rate-determining step occurs at formation of the dinuclear complex (TS 2) and the reaction obeys the rate law $dP/dt = (k_1k_2/k_{-1})[VL_3]^2[N_2O]$. See Section 1.4.1 for additional discussion.

It is of interest to compare this reaction with that of $Mo(N[^tBu]Ar)_3$, in which dinuclear activation of N_2O results in cleavage of the N−N bond as opposed to the N−O bond according to (Eq. 1.8).[9b] The rate-determining step in that case was initial binding of N_2O to form the highly potent nitrosylating agent $(N[^tBu]Ar)_3Mo{-}NNO$. Activation

parameters for the binding process were $\Delta H^{\ddagger}$ = 9.7 kcal mol^{-1} and $\Delta S^{\ddagger}$ = −24 cal mol K^{-1}. Generation of free NO[41] was excluded based on competition and trapping experiments.

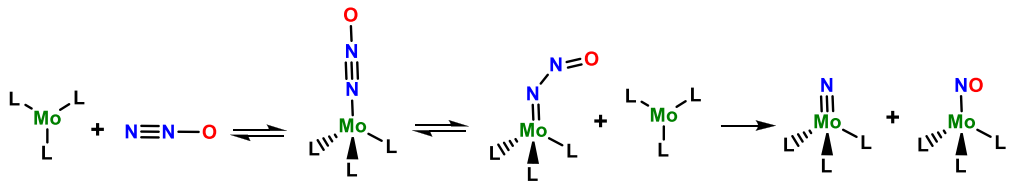

(1.8)

1.4.2. Category II (PyO and PhNO). PyO has the fastest rate of binding of all the substrates studied in this work. Formation of the high-spin (S = 1) PyO−V(N[^{t}Bu]Ar)$_3$ adduct was essentially irreversible at low temperatures. The electron density residing on the donor O atom of PyO is expected to be greater than that for the other linear XNO substrates studied here and the stability of high-spin O-bound donors is expected to be in the order: PyO > MesCNO > N_2O; DFT calculated values for binding enthalpies in these systems support this assumption (Table 1A.1). The NHC-bound substrates SIPr/MesCNO and IPr/N_2O are also expected to have increased electron density on the donor O atoms as compared with MesCNO and N_2O, respectively (*vide infra*). Despite rapid and irreversible adduct formation and an N−O BDE that is similar to or lower than that for IPr/N_2O and SIPr/MesCNO, respectively, PyO underwent relatively slow OAT. The high enthalpy of activation of 15 ± 1 kcal mol^{-1} associated with the OAT step (k_2) led to readily separable substrate binding and oxidative addition processes. It is postulated that OAT is slow due to the lack of ligand π^* orbitals available to accept electron density as the OAT reaction progresses, which may force a higher energy transition state involving

a larger geometric rearrangement that requires use of σ^* orbitals. Further computational studies are in progress to test this hypothesis.

The rate of PhNO binding occurs reasonably fast at low temperatures, yet OAT does not occur to an appreciable extent until near 0 °C. This is partially due to its high N−O BDE (108.2 kcal mol^{-1}, Table 1.1). The nitroso moiety of PhNO is isoelectronic with O_2, but unlike O_2 it has a singlet ground state. NMR studies confirmed that the PhNO−V(N[^{t}Bu]Ar)$_3$ species is diamagnetic, as are both the η^1 and η^2-O_2 complexes of V(N[^{t}Bu]Ar)$_3$.[39] The η^2 binding mode was shown to be considerably more stable in the case of O_2. This is in contrast to PhNO, which was shown computationally to be most stable in the η^1 binding mode, presumably for steric reasons. OAT from PhNO most likely occurs through unimolecular decomposition of the stable PhNO−V(N[^{t}Bu]Ar)$_3$ complex to generate OV(N[^{t}Bu]Ar)$_3$ and free ^{3}NPh. The ultra slow nature of OAT in this particular system, in addition to its high BDE, seems to be a consequence of the high stability of the PhNO−V(N[^{t}Bu]Ar)$_3$ adduct (ΔH_{bind} = −54 ± 2 kcal mol^{-1}) and possible generation of the unstable triplet nitrene.[1]

It is worth noting the differences between the DFT computed structures of the high-spin PyO and low-spin PhNO adducts of V(N[^{t}Bu]Ar)$_3$, the structures of which are depicted in Figure 1.25. In addition to differing in spin state, there are significant differences in the V−O bond lengths (2.007 Å for PyO vs. 1.751 Å for PhNO) and the degree of pyramidalization of the metal center. The degree of pyramidalization about the metal center can be quantified by the sum of the three N_{eq}−V−N_{eq} bond angles [Σ(N−V−N)] between V and the equatorial amide nitrogen donor atoms of the anilide ligands. For example, the planarity of V(N[^{t}Bu]Ar)$_3$ (Σ(N−V−N) = 356.1°) is clearly

altered upon formation of OV(N[^{t}Bu]Ar)$_3$ (Σ(N−V−N) = 336.7°). The PyO adduct resembles the structure of free V(N[^{t}Bu]Ar)$_3$ in the sense that the three N_{eq} atoms remain nearly planar (Σ(N−V−N) = 353.7°), whereas the PhNO adduct looks more like the product oxo complex as judged from the decrease in Σ(N−V−N) and the positions of the three ligand *tert*-butyl groups, which point towards the oxo unit.

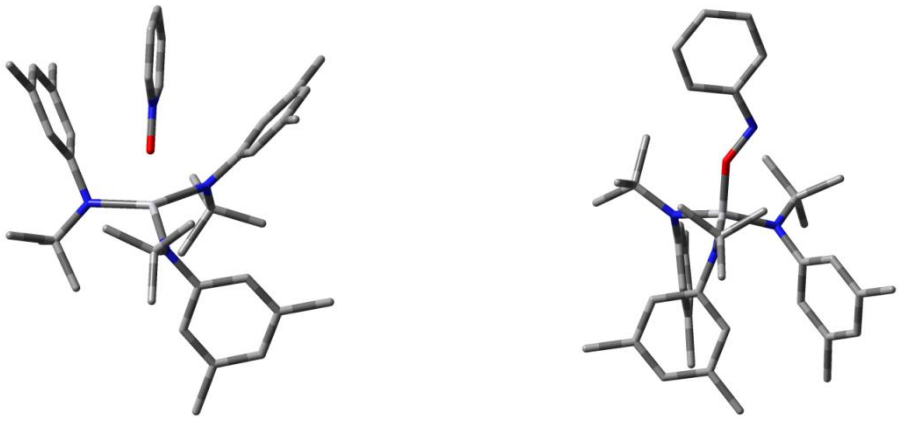

Figure 1.25. Optimized structures at the bp86/6-311G(d,p) (MDF10 for V with an additional set of f functions) level for the η^1-PyO–V(N[^{t}Bu]Ar)$_3$ triplet (left) and η^1-PhNO–V(N[^{t}Bu]Ar)$_3$ singlet (right). For selected interatomic distances and angles see Table 1A.1.

1.4.3. Category III (SIPr/MesCNO and IPr/N_2O). As shown in Table 1A.1, DFT calculations predict more favorable binding enthalpies for both SIPr/MesCNO and IPr/N_2O relative to free MesCNO and N_2O. This is likely due to increased electron density on the terminal O atoms of the NHC-bound *N*-oxides which results from inductive effects of the highly basic NHCs.[1] DFT calculations also predict that both the triplet and singlet truncated model adducts for IPr/N_2O−V(N[^{t}Bu]Ar)$_3$ (where IMe was used in place of IPr) are energetically similar. The DFT computed UV-visible spectrum for the singlet IMe/N_2O−V(N[^{t}Bu]Ar)$_3$ species is in good agreement with the

experimental spectral data for the intermediate detected in stopped-flow experiments. In contrast, the truncated model for the SIPr/MesCNO−V(N[^{t}Bu]Ar)$_3$ adduct (IMe and Ph in place of IPr and Mes, respectively) is more stable in the triplet state and the DFT computed UV-visible spectrum for this intermediate is consistent with experimental observations. As mentioned earlier, the longer V−O bond predicted for the triplet structure helps to ease the steric strain imposed by this bulky ligand.

The acceleration of the overall rate of OAT with SIPr/MesCNO and IPr/N_2O (relative to free MesCNO and N_2O) was an unexpected finding, since they have stronger N−O bonds (see BDEs in Table 1.1) and increased steric hindrance. This result is attributed to an increased favorability of ligand binding as mentioned previously as well as the possibility that "bent" XNO structures may facilitate the reaction by pre-forming a geometry more suitable for OAT. Furthermore, the accessibility of low lying ligand π^* orbitals to participate in OAT may contribute to the observed rate enhancement. Also worth noting is that MesCNO reacts faster than N_2O and this order is retained in the NHC-bound substrates as well.

An unanswered question in these specific systems is at which point they fragment to smaller pieces. This is illustrated for SIPr/MesCNO in Eqs. 1.9 and 1.10, where two possible OAT pathways are shown.

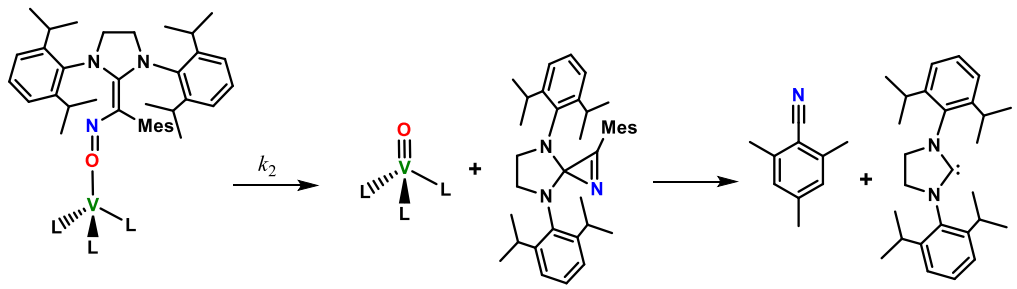

(1.9)

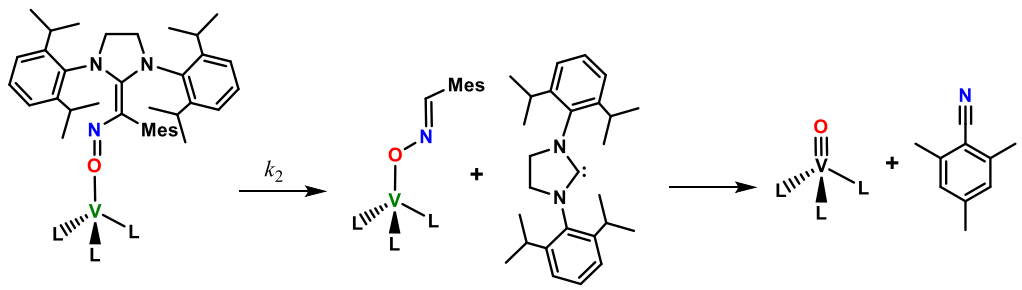

(1.10)

Eq. 1.9 implies that OAT could occur with dissociation of an intact SIPr/MesCN fragment that subsequently dissociates to SIPr and MesCN.[42] An alternative possibility is shown in Eq. 1.10, which involves dissociation of the NHC from the SIPr/MesCNO−VL_3 adduct. In this case, the NHC can be viewed as a catalyst that delivers MesCNO in a configuration more suitable for OAT. The enhanced rates of OAT from the NHC-bound oxidants suggest their possible utility as catalysts for substrate activation.[43] Additional studies are required, however, to decipher substrate fragmentation in more detail.

1.4.4. Category IV (dbabhNO and MesCNO). Reactions of $V(N[^tBu]Ar)_3$ with these substrates cleanly generate the oxo complex in a single observable step; the apparent kinetic parameters for these formally bimolecular processes are listed in Table 1.6. The rate of reaction of MesCNO is intermediate between that of the two NHC containing *N*-oxides studied (SIPr/MesCNO and IPr/N_2O) with the important exception that an intermediate adduct is not detected. This implies that the steady-state assumption is valid, where intermediate forms and decays at similar rates. It is postulated that dissociation of MesCNO−$V(N[^tBu]Ar)_3$ (governed by k_{-1}) plays a role in slowing down the reaction. Provided $k_{-1} >> k_2$, the net rate of OAT via a steady-state mechanism becomes $k_{obs} = k_1k_2/k_{-1} = K_{eq}k_2$. Experimental plots of k_{obs} versus [MesCNO] appear to give non-zero

intercepts upon increasing temperature, suggesting that substrate dissociation plays a role in the kinetic scheme. Resolution of whether the slow rate of OAT is due to poorer ligand binding (larger k_{-1}) or slower OAT (smaller k_2) will require additional investigation.

MesCNO most closely resembles N_2O in terms of structure and bonding, in that both contain linear X−N−O moieties consisting of a sp hybridized N atom with delocalized π-bonding. However, it reacts much faster than does N_2O. This can be attributed to the differences involved with initial binding (binding through O versus N) and the fact that N_2O requires dinuclear activation. MesCNO is computed to bind to $V(N[^tBu]Ar)_3$ in an endothermic fashion (+4.1 kcal mol^{-1}, Table 1A.1) with a minimum energy structure found only in the triplet potential energy surface. Unlike the high-spin minimum energy adducts calculated for PyO and N_2O (O-bound), which have relatively long V−O bonds (ca. 2 Å) and show only minor deviations in the planarity of the vanadium center (see Σ(N−V−N) values in Table 1A.1), the MesCNO−VL_3 adduct displays a contracted V−O bond (1.849 Å) and a very different Σ(N−V−N) value of 339.3° that compares with $OV(N[^tBu]Ar)_3$ (Σ(N−V−N) = 336.7°). Furthermore, the DFT-calculated Mulliken spin density of the vanadium center is attenuated, supporting substantial electron transfer from the metal to the ligand.[1]

The net rate of reaction of dbabhNO is also intermediate between that of the NHC-containing *N*-oxides. The reaction is relatively fast as compared with MesCNO and has k_{app} values approaching the range expected for ligand binding. This implies a more efficient atom transfer than that for MesCNO. It can be postulated that $k_1 > 1.8 \times 10^3$ M^{-1} s^{-1} at −62 °C for the dbabhNO reaction. For IPr/N_2O, which reacts more slowly than dbabhNO, $k_1 = 785 \pm 54$ M^{-1} s^{-1} and $k_2 = 0.308 \pm 0.014$ s^{-1} at −62 °C. It is clear that k_1 is

larger for dbabhNO and also that the overall rate of reaction is faster. Since an intermediate adduct does not build up, it can be concluded that k_2 must also be larger for dbabhNO than for IPr/N_2O.

The very low N−O BDE of ≈10 kcal mol^{-1} suggests that dbabhNO would be a potent OAT reagent to V(N[^{t}Bu]Ar)$_3$ based on thermodynamics alone.[1] The measurement of the N−O BDE involves complete fragmentation of dbabhNO to O, anthracene, and N_2. In the initial stages of the OAT reaction to V(N[^{t}Bu]Ar)$_3$, however, complete fragmentation of dbabhNO is not necessarily required and may occur subsequent to formation of OV(N[^{t}Bu]Ar)$_3$, which could be the reason why it is not the most rapid OAT reagent in the series studied here. It is also possible that it is not the fastest simply due to a slower rate of binding (relative to SIPr/MesCNO), with OAT occurring instantaneously once the molecule is bound to the metal center.

1.5. Conclusion

The initial goal of this work was to determine whether the NHC-bound *N*-oxides SIPr/MesCNO and IPr/N_2O reacted faster, slower, or at the same rate as free MesCNO and N_2O. The unanticipated kinetic results allowed us to take a more complete view of OAT in the XNO series. While the facts lie in the rate and activation parameters themselves, the mechanistic picture that evolves is not as simple as was initially expected. It seems clear, as pointed out by other workers in this area, that a detailed mechanistic understanding must necessarily involve a complete picture involving ligand binding, spin transitions, electron transfer, bond cleavage, and fragment elimination.

These need not occur in that order and may appear in different steps for different substrates. For example, PhNO binding involves electron transfer and spin pairing in a single step; PyO binding, in contrast, remains in a high-spin state that later undergoes electron transfer and spin pairing before going onward to complete OAT. It is tempting to state that initial binding is the key factor in the OAT process in most cases, but such a statement neglects the fact that binding occurs differently for different substrates. The main difference in the rate of binding of PyO and N_2O is the entropy of activation to form the oxidant-bound complex. Surprisingly, the activation enthalpies overlap within experimental error. This may relate to the transition state for binding being relatively distant from the vanadium center for the high-spin PyO adduct, which remains paramagnetic, as compared with N_2O, which is computed to yield a low-spin complex in which oxidation of the metal center has already occurred and which is formulated as a bent diamagnetic $(N[^tBu]Ar)_3V{=}N{-}N{=}O$ complex. This may require a much more constricted reaction pathway despite the fact that both are ligand binding events. The current work presents the experimental backdrop for additional computational and experimental studies, but has also generated several notable results:

(a) No simple correlation between N−O BDE and rates of OAT was found. Despite formally stronger BDEs and increased steric hindrance for SIPr/MesCNO and IPr/N_2O, they undergo more rapid OAT to the sterically hindered $V(N[^tBu]Ar)_3$ complex than free MesCNO and N_2O. This is attributed primarily to electronic factors making available an NO π^* orbital.

(b) Rates of ligand binding play an important role in the overall OAT process, however, it is a complex role since both low- and high-spin $XNO{-}V(N[^tBu]Ar)_3$ adducts

can result. In some cases, ligand binding is the rate-determining step; in other cases, it is OAT from the adduct that is rate-determining.

(c) OAT from N_2O occurs in a termolecular process involving reversible formation of the N-bound ONN−V(N[^{t}Bu]Ar)$_3$, which then forms L_3V−ONN−VL_3 prior to OAT. The rate determining step changes as a function of temperature due to the activation parameters involved for reversible binding relative to that for OAT as discussed earlier.

(d) The relatively slow rate of OAT from PyO is attributed to slow conversion of the high-spin PyO−V(N[^{t}Bu]Ar)$_3$ to a low-spin form. The lack of an available NO π^* orbital may force a more bent transition state than for other adducts.

(e) The slow rate of OAT from PhNO, despite detection of a stable low-spin PhNO−V(N[^{t}Bu]Ar)$_3$ adduct, is due to the stability of this adduct combined with a relatively large activation enthalpy for expulsion of the unstable ^{3}NPh fragment.

(f) The unique reagent dbabhNO undergoes rapid OAT to V(N[^{t}Bu]Ar)$_3$. Its N−O BDE of 10 kcal mol^{-1} implies that generation of ^{3}O is thermodynamically favored at room temperature.

(g) Bent XNO structures, as in SIPr/MesCNO, IPr/N_2O, dbabhNO, and ONN−V(N[^{t}Bu]Ar)$_3$, appear to undergo more rapid OAT than the linear N_2O and MesCNO counterparts.

(h) The enhanced OAT rates for the NHC-bound oxidants may lead to their utilization as accelerants in additional OAT reactions.

In summary, the kinetic results, in conjunction with thermodynamic analyses and DFT calculations, provide a complete yet complex picture of OAT in the $V(N[^tBu]Ar)_3$ system.

1.6. References

(1) *This chapter is reproduced in part with permission from:* Palluccio, T. D.; Rybak-Akimova, E. V.; Majumdar, S.; Cai, X.; Chui, M.; Temprado, M.; Silvia, J. S.; Cozzolino, A. F.; Tofan, D.; Velian, A.; Cummins, C. C.; Captain, B.; Hoff, C. D. Thermodynamic and Kinetic Study of Cleavage of the N−O Bond of *N*-Oxides by a Vanadium(III) Complex: Enhanced Oxygen Atom Transfer Reaction Rates for Adducts of Nitrous Oxide and Mesityl Nitrile Oxide. *J. Am. Chem. Soc.*, **2013,** *135*, 11357. Copyright 2013 American Chemical Society.

(2) Ravishankara, A. R.; Daniel, J. S.; Portmann, R. W. *Science*, **2009**, *326*, 123.

(3) Tolman, W. B. *Angew. Chem. Int. Ed.*, **2010**, *49*, 1018.

(4) Armor, J. N.; Taube, H. *J. Am. Chem. Soc.*, **1971**, *93*, 6476.

(5) (a) Yu, H.; Jia, G.; Lin, Z. *Organometallics*, **2009**, *28*, 1158−1164. (b) Yu, H.; Jia, G.; Lin, Z. *Organometallics*, **2008**, *27*, 3825−3833. (c) Yu, H.; Jia, G.; Lin, Z. *Organometallics*, **2007**, *26*, 6769.

(6) Fan, H.; Caulton, K. G. *Polyhedron*, **2007**, *26*, 4731.

(7) Piro, N. A.; Lichterman, M. F.; Harman, W. H.; Chang, C. J. *J. Am. Chem. Soc.*, **2011**, *133*, 2108.

(8) (a) Jana, A.; Roesky, H. W.; Schulzke, C. *Dalton Trans.*, **2010**, *39*, 132−138. (b) Demir, S.; Montalvo, E.; Ziller, J. W.; Meyer, G.; Evans, W. J. *Organometallics*, **2010**, *29*, 6608. (c) Harrold, N. D.; Waterman, R.; Hillhouse, G. L.; Cundari, T. R. *J. Am. Chem. Soc.*, **2009**, *131*, 12872. (d) Harman, W. H.; Chang, C. J. *J. Am. Chem. Soc.*, **2007**, *129*, 15128. (e) Kaplan, A. W.; Bergman, R. G. *Organometallics*, **1997**, *16*, 1106.

(9) (a) Laplaza, C. E.; Odom, A. L.; Davis, W. M.; Cummins, C. C.; Protasiewicz, J. D. *J. Am. Chem. Soc.*, **1995**, *117*, 4999. (b) Cherry, J. P. F.; Johnson, A. R.; Baraldo, L. M.; Tsai, Y. C.; Cummins, C. C.; Kryatov, S. V.; Rybak-Akimova, E. V.; Capps, K. B.; Hoff, C. D.; Haar, C. M.; Nolan, S. P. *J. Am. Chem. Soc.*, **2001**, *123*, 7271.

(10) Enemark, J. H.; Cooney, J. J. A.; Wang, J.; Holm, R. H. *Chem. Rev.*, **2004**, *104*, 1175.

(11) Schultz, B. E.; Holm, R. H. *Inorg. Chem.*, **1993**, *32*, 4244.

(12) McPherson, L. D.; Drees, M.; Khan, S. I.; Strassner, T.; Abu-Omar, M. M. *Inorg. Chem.*, **2004**, *43*, 4036.

(13) (a) Veige, A. S.; Slaughter, L. M.; Wolczanski, P. T.; Matsunaga, N.; Decker, S. A.; Cundari, T. R. *J. Am. Chem. Soc.*, **2001**, *123*, 6419. (b) Veige, A. S.; Slaughter, L. M.; Lobkovsky, E. B.; Wolczanski, P. T.; Matsunaga, N.; Decker, S. A.; Cundari, T. R. *Inorg. Chem.*, **2003**, *42*, 6204.

(14) Crestoni, M. E.; Fornarini, S.; Lanucara, F.; Warren, J. J.; Mayer, J. M. *J. Am. Chem. Soc.*, **2010**, *132*, 4336.

(15) Fortner, K. C.; Laitar, D. S.; Muldoon, J.; Pu, L.; Braun-Sand, S. B.; Wiest, O.; Brown, S. N. *J. Am. Chem. Soc.*, **2007**, *129*, 588.

(16) Abu-Omar, M. M.; Appelman, E. H.; Espenson, J. H. *Inorg. Chem.*, **1996**, *35*, 7751.

(17) Cai, X.; Majumdar, S.; Fortman, G. C.; Frutos, L. M.; Temprado, M.; Clough, C. R.; Cummins, C. C.; Germain, M. E.; Palluccio, T.; Rybak-Akimova, E. V.; Captain, B.; Hoff, C. D. *Inorg. Chem.*, **2011**, *50*, 9620.

(18) Tskhovrebov, A. G.; Solari, E.; Wodrich, M. D.; Scopelliti, R.; Severin, K. *Angew. Chem. Int. Ed.*, **2012**, *51*, 232.

(19) Tskhovrebov, A. G.; Solari, E.; Wodrich, M. D.; Scopelliti, R.; Severin, K. *J. Am. Chem. Soc.*, **2012**, *134*, 1471.

(20) Fickes, M. G. Synthesis and Reactivity of Vanadium and Niobium Complexes Containing Sterically Demanding Amido Ligands, Ph.D Thesis, Massachusetts Institute of Technology, 1998.

(21) For a description see supporting information files in: Barybin, M. V.; Diaconescu, P. L.; Cummins C. C. *Inorg. Chem.* **2001**, *40*, 2892 which presents a modified preparation from the original: Grundmann, C.; Dean, J. M. *J. Org. Chem*. **1965**, *30*, 2809.

(22) Carpino, L. A.; Padykula, R. E.; Barr, D. E.; Hall, F. H.; Krause, J. G.; Dufresne, R. F.; Thoman, C. J. *J. Org. Chem*. **1988**, *53*, 2565.

(23) Apex2 Version 2.2-0 and SAINT+ Version 7.46A; Bruker Analytical X-ray System, Inc., Madison, Wisconsin, USA, 2007

(24) Sheldrick, G. M. SADABS: Program for Empirical Absorption Correction of Area Detectors **1996**.

(25) (a) Sheldrick, G. M. SHELXTL Version 6.1; Bruker Analytical X-ray Systems, Inc., Madison, Wisconsin, USA, 2000. (b) Sheldrick, G. M. *Acta Cryst*., **2008,** *A64*, 112.

(26) Müller, P.; Herbst-Irmer, R.; Spek, A. L.; Schneider, T. R.; Sawaya, M. R. *Crystal Structure Refinement: A Crystallographer's Guide to SHELXL*. IUCr Texts on Crystallography; Oxford University Press: Oxford, 2006.

(27) (a) Becke, A. D. *J. Chem. Phys.*, **1993**, *98*, 5648. (b) Perdew, J. P. *Phys. Rev. B*, **1986**, *33*, 8822.

(28) Frisch, M.J. *et al*. Gaussian 09, revision B.01; Gaussian, Inc.: Wallingford, CT, 2010.

(29) (a) Simon, S.; Duran, M.; Dannenberg, J. J. *J. Chem. Phys.*, **1996**, *105*, 11024. (b) Boys, S. F.; Bernardi, F. *Mol. Phys.*, **1970**, *19*, 553.

(30) (a) Martin, J. M. L.; Sundermann, A. *J. Chem. Phys*., **2001**, *114*, 3408. (b) Dolg, M.; Wedig, U.; Stoll, H.; Preuss, H. *J. Chem. Phys*., **1987**, *86*, 866.

(31) Ruppa, K. B. P.; Desmangles, N.; Gambarotta, S.; Yap, G.; Rheingold, A. L. *Inorg. Chem.*, **1997**, *36*, 1194.

(32) Brask, J. K.; Dura-Vila, V.; Diaconescu, P. L.; Cummins, C. C. *Chem. Commun.*, **2002**, 902.

(33) Pyykkö, P.; Atsumi, M. *Chem. Eur. J.*, **2009**, *15*, 12770.

(34) The most commonly cited O=M bond strength measured for a complex in solution is that of Watt, G. D.; McDonald, J. W.; Newton, W. E. *J. Less-Common Met.*, **1977**, *54*, 415.

(35) Calculated from gas phase data obtained from http://webbook.nist.gov

(36) Luo, Y. R. *Handbook of Bond Dissociation Energies in Organic Compounds*; CRC Press: Boca Raton, FL, 2003.

(37) (a) Liang, T. Y.; Schuster, G. B. *J. Am. Chem. Soc.*, **1987**, *109*, 7803. (b) Takaoka, A.; Moret, M. E.; Peters, J. C. *J. Am. Chem. Soc.*, **2012**, *134*, 6695.

(38) Moerdyk, J. P.; Bielawski, C. W. *J. Am. Chem. Soc.*, **2012**, *134*, 6116.

(39) Cozzolino, A. F.; Tofan, D.; Cummins, C. C.; Temprado, M.; Pallucio, T. D.; Rybak Akimova, E. V.; Majumdar, S.; Cai, X.; Captain, B.; Hoff, C. D. *J. Am. Chem. Soc.*, **2012**, *134*, 18249.

(40) (a) Fickes, M. G.; Davis, W. M.; Cummins, C. C. *J. Am. Chem. Soc.*, **1995**, *117*, 6384. (b) Proulx, G.; Bergman, R. G. *J. Am. Chem. Soc.*, **1995**, *117*, 6382.

(41) Khoroshun, D. V.; Musaev, D. G.; Morokuma, K. *Organometallics*, **1999**, *18*, 5653.

(42) We are aware that some NHC/nitrile adducts are reported to be stable, however, no adduct between SIPr and MesCN exists to the best of our knowledge.

(43) Enders, D.; Niemeier, O.; Henseler, A. *Chem. Rev.*, **2007**, *107*, 5606.

APPENDIX 1

Kinetic, Computational, and Thermodynamic Study of the Cleavage of the N−O Bond of *N*-Oxides by a Vanadium(III) Tris-Anilide Complex

Table 1A.1. Computational Summary of XNO binding to $V(N[^tBu]Ar)_3$.[a]

Ligand	Multiplicity	V−O (Å)	V−O−N (°)	Σ(N−V−N)[c] (°)	ΔH_{bind}[a] (kcal mol^{-1})
N_2O (O-bound)[b]	triplet	2.164	140.6	352.7	+12.1
N_2O (N-bound)	triplet	1.856[d]	168.1[e]	343.3	+3.1
N_2O (N-bound)	singlet	1.710[d]	170.5[e]	335.9	−7.1
PyO[b]	triplet	2.007	134.0	353.7	−2.3
PhNO	triplet	1.888	123.9	338.7	−24.1
PhNO	singlet	1.751	142.3	336.9	−31.3
SIMe/PhCNO[f,g]	triplet	1.874	126.8	338.9	−11.8
SIMe/PhCNO[f,g]	singlet	1.796	137.8	336.3	−7.7
IMe/N_2O[f]	triplet	1.869	131.4	342.6	−18.6
IMe/N_2O[f]	singlet	1.756	156.9	340.1	−18.3
MesCNO[b]	triplet	1.849	122.6	339.3	+4.1

[a] Calculated at the bp86/6-311G(d,p) level (MDF10 with an additional set of f functions for V). [b] Minima were found only in the triplet potential energy surface. [c] Sum of the three $(N-V-N)_{anilides}$ bond angles. [d] V−N bond length. [e] V−N−N angle. [f] Calculations corresponding to the adduct with a truncated model where the 2,6-diisopropylphenyl substituents on the N atoms of the *N*-heterocyclic carbene in the real system have been replaced by methyl groups. [g] Calculations corresponding to the adduct with a truncated model where the mesityl group has been replaced by an unsubstituted phenyl ring. For more information, refer to ref 1.

Table 1A.2. Crystallographic and refinement parameters for OV(N[^{t}Bu]Ar)$_3$.

Empirical formula	$C_{36}H_{54}N_3OV$
Formula weight	595.76
Temperature (K)	296(2)
Wavelength (Å)	0.71073
Crystal system	Cubic
Space group	I−43d (no. 220)
a (Å)	24.0912(9)
b (Å)	24.0912(9)
c (Å)	24.0912(9)
α (°)	90
β (°)	90
γ (°)	90
V (Å^3)	13982.2(9)
Z	16
ρ_{calc} (g cm^{-1})	1.132
μ (mm^{-1})	0.313
F(000)	5152
Crystal size (mm^3)	0.42 × 0.32 × 0.06
$2\theta_{max}$ (°)	56.10
Index ranges	$-31 \le h \le 28$
	$-24 \le k \le 31$
	$-31 \le l \le 13$
Reflections collected	29806
Independent reflections	2775 [R_{int} = 0.0421]
Completeness to θ_{max} (%)	100.0
Absorption correction	Semi-empirical from equivalents
Max. and min. transmission	0.7461 and 0.6359
Refinement method	Full-matrix least squares on F^2
Data / restraints / parameters	2775 / 0 / 129
Goodness-of-fit on F^2	1.047
Final R indices [I > 2σ(I)][a]	R_1 = 0.0360, wR_2 = 0.0911
R indices (all data)[a]	R_1 = 0.0495, wR_2 = 0.1007
Largest diff. peak and hole (e Å^{-3})	0.198 and −0.147

[a] $R_1 = \sum||F_o| - |F_c|| / \sum|F_o|$; $wR_2 = \{\sum w(F_o^2 - F_c^2)^2 / \sum w(F_o^2)^2\}^{1/2}$

1.3.1. Category I: Dinuclear OAT following an overall third order rate law

Table 1A.3. Pseudo-second order (k_{eff}) and third order (k_3) rate constants obtained from fitting high temperature (+7 to +25 °C) kinetic traces (λ = 453 nm, formation) to a second order equation, $y = \{-\Delta Abs/(1 + [V(N[^tBu]Ar)_3]_0 k_{eff} t)\} + Abs_\infty$, with $[V(N[^tBu]Ar)_3]_0$ = 0.3 mM.

+7 °C	$[N_2O]$ (M)	k_{eff} (M^{-1} s^{-1})	k_3 (M^{-2} s^{-1})
	0.027	160	6,870 ± 136
	0.040	246	
	0.050	323	
	0.066	432	
+16 °C	$[N_2O]$ (M)	k_{eff} (M^{-1} s^{-1})	k_3 (M^{-2} s^{-1})
	0.027	121	5,380 ± 512
	0.040	208	
	0.047	256	
	0.066	337	
+25 °C	$[N_2O]$ (M)	k_{eff} (M^{-1} s^{-1})	k_3 (M^{-2} s^{-1})
	0.027	96	4,670 ± 285
	0.040	172	
	0.050	216	
	0.066	284	

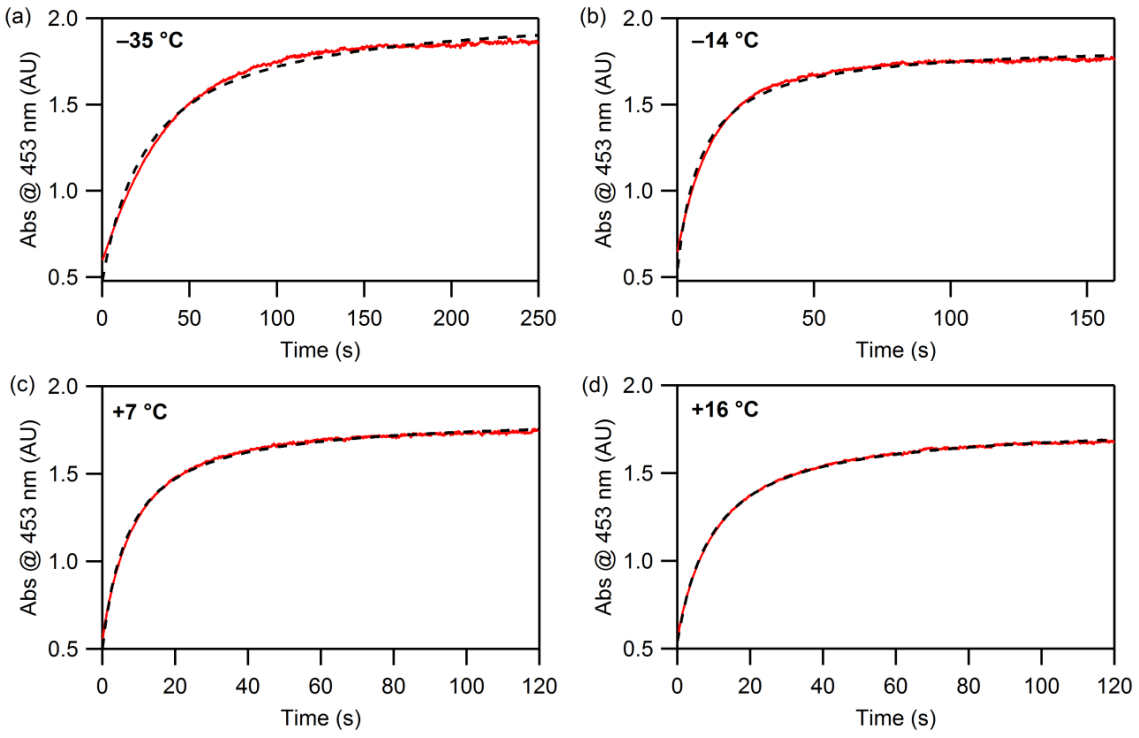

Figure 1A.1. Kinetic traces at λ = 453 nm (solid red lines) from reactions of 0.3 mM V(N[^{t}Bu]Ar)$_3$ with 66 mM N_2O with fits to the second order equation (black dashed lines) as a function of temperature, highlighting unacceptable fits at temperatures of −14 °C and below (a, b) and acceptable fits at temperatures ≥ +7 °C (c, d).

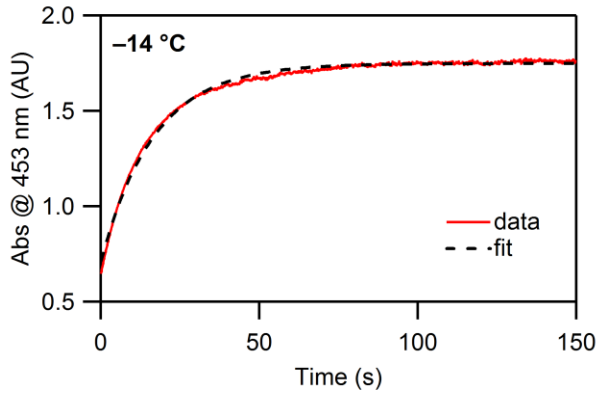

Figure 1A.2. Kinetic trace at λ = 453 nm (solid red line) from reaction of 0.3 mM V(N[^{t}Bu]Ar)$_3$ with 66 mM N_2O at the intermediate *T* of −14 °C with unacceptable fit to a single exponential equation, y = −A**exp*(−k_{obs}t) + C.

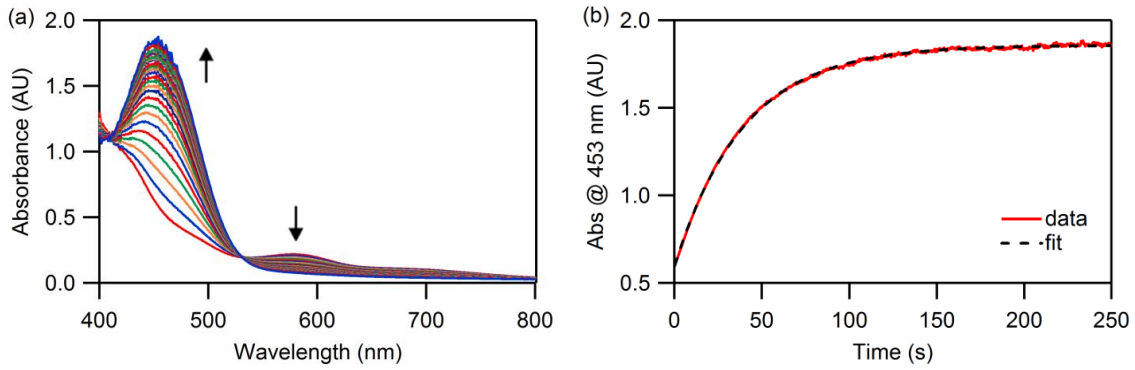

Figure 1A.3. (a) Time-resolved spectral changes accompanying the low temperature reaction between $V(N[^tBu]Ar)_3$ (0.3 mM) and N_2O (66 mM) at −35 °C acquired over 250 seconds showing formation of $OV(N[^tBu]Ar)_3$ (λ_{max} = 453 nm) with concomitant decay occurring at longer wavelengths. (b) Kinetic trace at 453 nm (red line) with single exponential fit (black dashed line).

Table 1A.4. Pseudo-first order (k_{obs}) and second order (k_1) rate constants obtained from fitting low temperature (−62 to −35 °C) kinetic traces (λ = 453 nm, formation) to a single exponential equation, y = −A**exp*(−k_{obs}t) + C. In all cases, the intercept was close to zero. $[V(N[^tBu]Ar)_3]_0$ = 0.3 mM.

−62 °C	$[N_2O]$ (M)	k_{obs} (× 10^{-3} s^{-1})	k_1 (× 10^{-3} M^{-1} s^{-1})
	0.027	0.850	
	0.040	1.32	55.4 ± 4.8
	0.053	2.20	
	0.066	3.02	
−53 °C	$[N_2O]$ (M)	k_{obs} (× 10^{-3} s^{-1})	k_1 (× 10^{-3} M^{-1} s^{-1})
	0.027	2.53	
	0.040	3.80	119 ± 6
	0.053	5.70	
	0.066	7.18	
−35 °C	$[N_2O]$ (M)	k_{obs} (× 10^{-3} s^{-1})	k_1 (× 10^{-3} M^{-1} s^{-1})
	0.027	9.30	
	0.040	14.4	386 ± 7
	0.053	19.3	
	0.066	24.8	

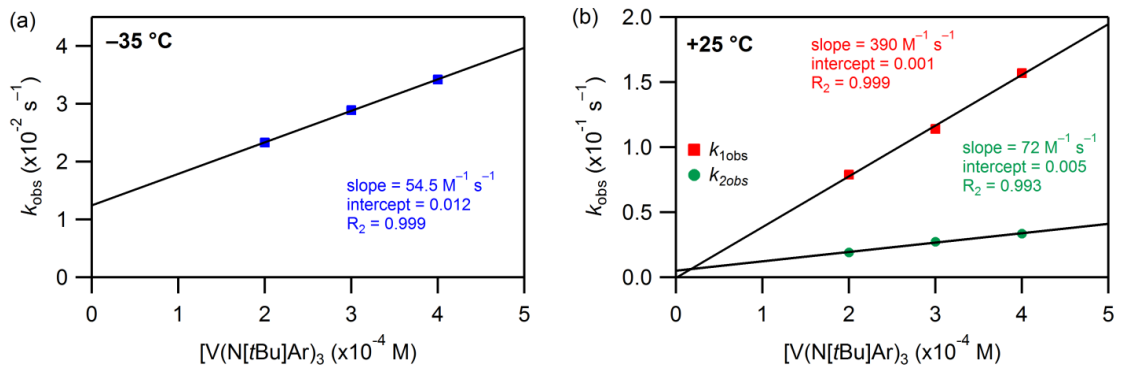

Figure 1A.4. Plots of k_{obs} as a function of [V(N[^{t}Bu]Ar)$_3$] (0.2, 0.3, 0.4 mM) in the presence of a fixed [N_2O] (66 mM) at (a) −35 °C and (b) +25 °C with linear fits. At −35 °C, kinetic traces at λ = 453 nm were fit to a single exponential equation to yield values of k_{obs}. At +25 °C, traces were fit to a double exponential equation, where both k_{1obs} and k_{2obs} showed a linear dependence on the initial concentration of metal complex. Ultimately, these plots reveal a more complicated reaction order with respect to [V(N[^{t}Bu]Ar)$_3$] and kinetic modeling was necessary to decipher the mechanism.

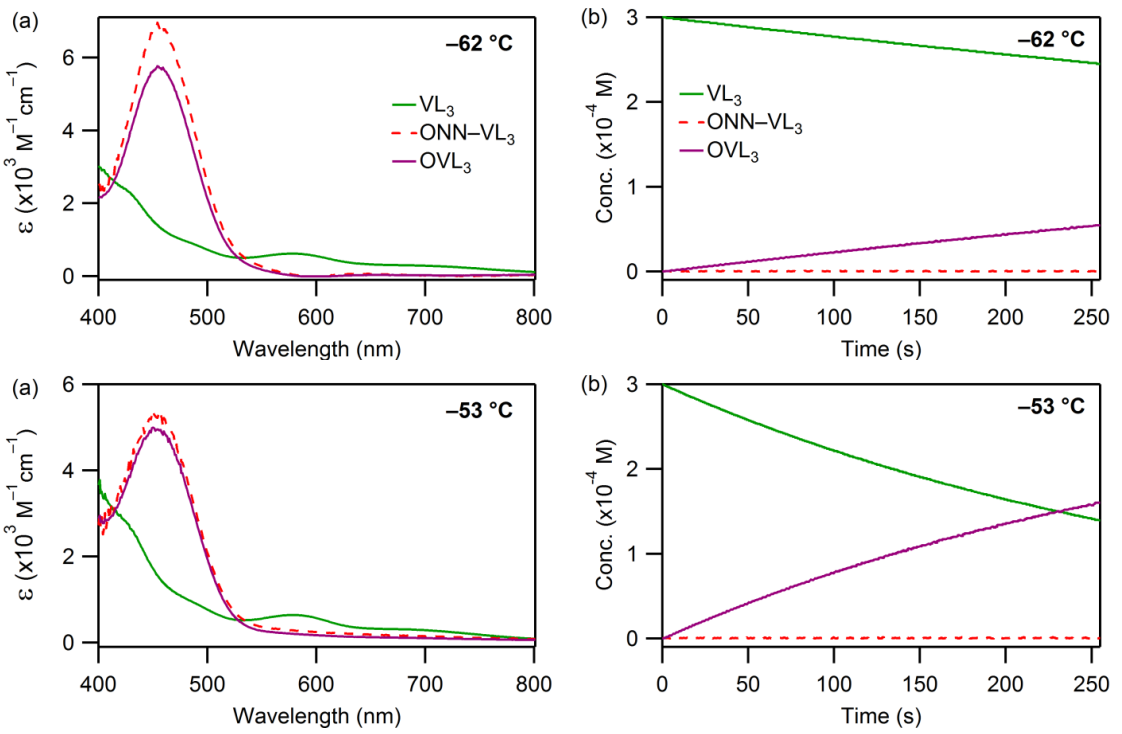

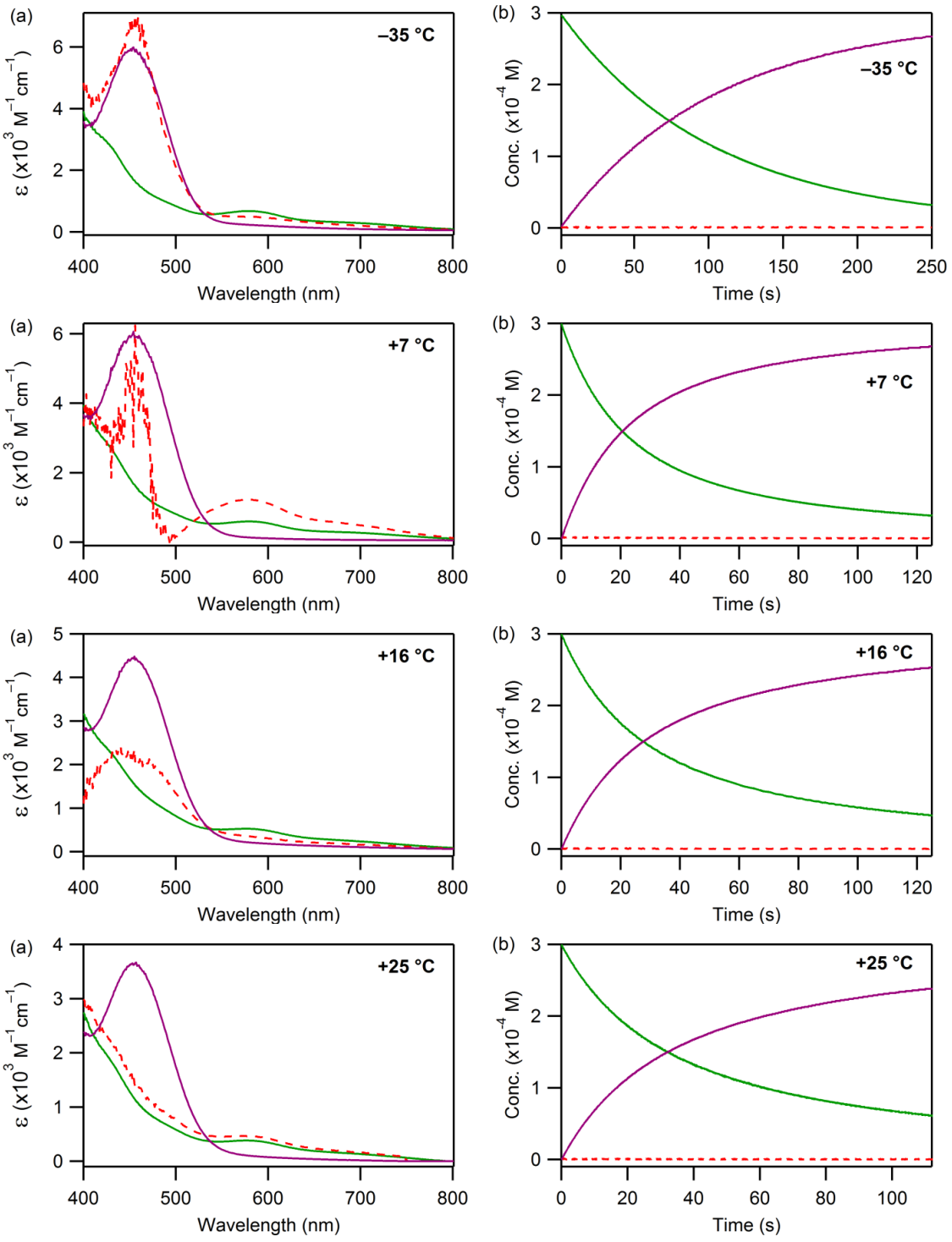

Figure 1A.5. (a) Calculated spectra of colored components obtained from modeling the $V(N[^tBu]Ar)_3$-N_2O system at various temperatures. Although the spectrum for the intermediate $ONN{-}V(N[^tBu]Ar)_3$ adduct was calculated, it is not known to any degree of accuracy since its concentration remains close to zero throughout the reaction. (b) Concentration profiles for colored components. $[V(N[^tBu]Ar)_3]_0$ = 0.3 mM and $[N_2O]_0$ = 27 mM.

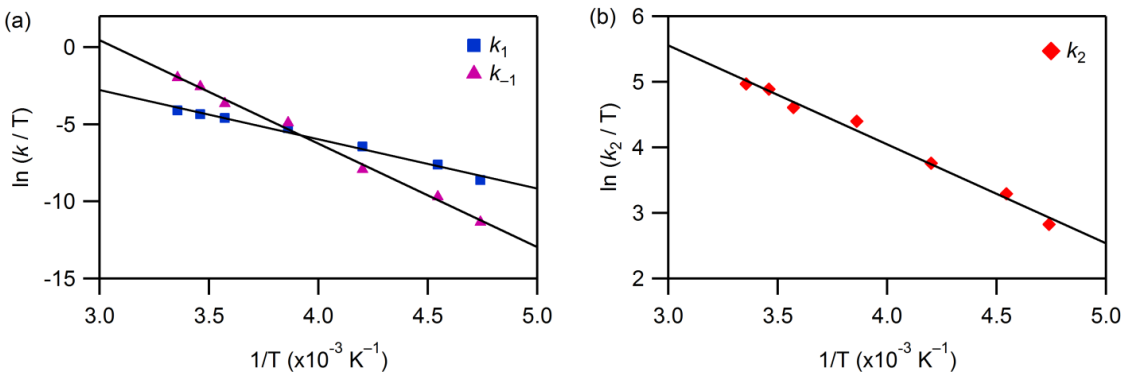

Figure 1A.6. Eyring plots for k_1, k_{-1} (a) and k_2 (b) obtained from kinetic modeling from which the following activation parameters were derived. k_1: $\Delta H_1^{\ddagger} = 6.3 \pm 0.3$ kcal mol^{-1}, $\Delta S_1^{\ddagger} = -34 \pm 1$ cal mol^{-1}·K^{-1}; k_{-1}: $\Delta H_{-1}^{\ddagger} = 13 \pm 1$ kcal mol^{-1}, $\Delta S_{-1}^{\ddagger} = -6 \pm 2$ cal mol^{-1} K^{-1}; k_2: $\Delta H_2^{\ddagger} = 3.0 \pm 0.1$ kcal mol^{-1}, $\Delta S_2^{\ddagger} = -27 \pm 1$ cal mol^{-1} K^{-1}.

1.3.2. Category II: Formation of stable oxidant-bound complexes followed by OAT in a separate step

1.3.2.1. PyO

Table 1A.5. Temperature dependent pseudo-first order and second order rate constants for PyO−V(N[^{t}Bu]Ar)$_3$ adduct formation measured at λ = 650 nm with 0.2 mM V(N[^{t}Bu]Ar)$_3$ and PyO (1 - 10 mM). Observed rate constants were obtained from fitting kinetic traces to a single exponential equation, rate = −A**exp*(−k_{obs}t) + C.

−80 °C	[PyO] (M)	k_{obs} (s^{-1})	k_1 (M^{-1} s^{-1})
	0.001	3.51	
	0.002	6.59	2,360 ± 89
	0.005	14.1	
	0.010	25.0	
−71 °C	[PyO] (M)	k_{obs} (s^{-1})	k_1 (M^{-1} s^{-1})
	0.001	6.47	
	0.002	13.1	6,030 ± 185
	0.005	32.8	
	0.010	60.8	
−62 °C	[PyO] (M)	k_{obs} (s^{-1})	k_1 (M^{-1} s^{-1})
	0.001	13.8	
	0.002	28.7	13,250 ± 540
	0.005	73.4	
	0.010	133	
−53 °C	[PyO] (M)	k_{obs} (s^{-1})	k_1 (M^{-1} s^{-1})
	0.001	27.5	
	0.002	53.7	23,040 ± 1,220
	0.005	134	
	0.010	235	

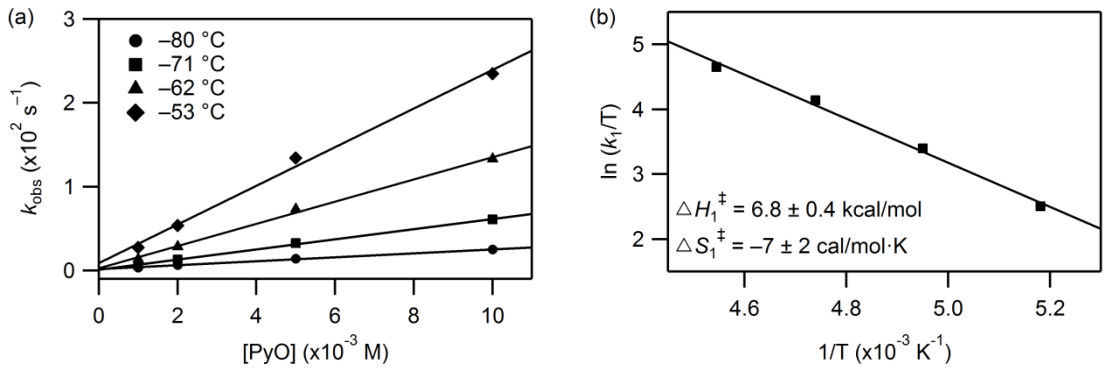

Figure 1A.7. (a) Plots of k_{obs} versus [PyO] (1 - 10 mM) over a temperature range of −80 to −53 °C with $[V(N[^tBu]Ar)_3]_o$ = 0.2 mM. (b) Eyring plot for PyO binding with derived activation parameters.

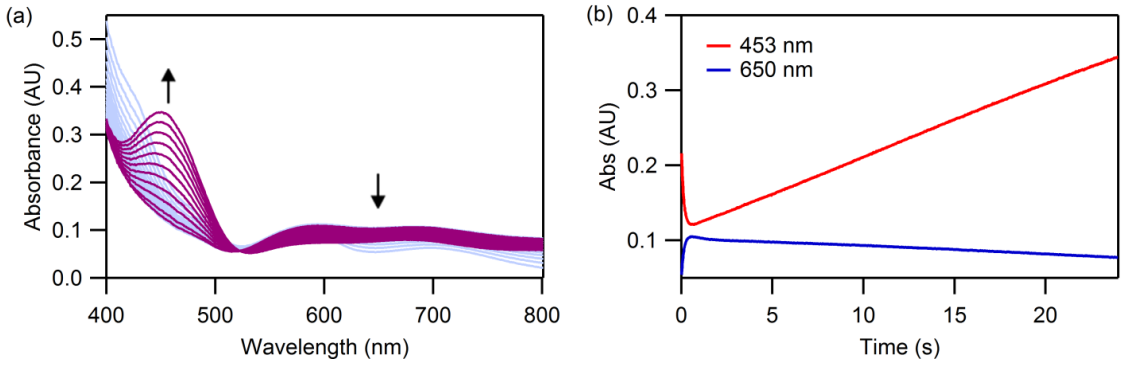

Figure 1A.8. (a) Time-resolved spectral changes accompanying the reaction of $V(N[^tBu]Ar)_3$ (0.2 mM) and PyO (2 mM) acquired over 24 s at −80 °C, highlighting slow conversion of PyO−$V(N[^tBu]Ar)_3$ (blue traces show its accumulation; see also Figure 1.9 in Chapter 1) to $OV(N[^tBu]Ar)_3$ (purple traces) at low temperature. (b) Kinetic traces at λ = 453 nm and 650 nm over 24 s. Growth in absorbance at λ = 453 nm represents formation of $OV(N[^tBu]Ar)_3$.

Table 1A.6. Temperature dependent pseudo-first order (k_{obs}) and true first order rate constants (k_2) for $OV(N[^tBu]Ar)_3$ formation measured at λ = 453 nm with 0.3 mM (10 to 20 °C) or 0.2 mM (0 °C) $V(N[^tBu]Ar)_3$ and PyO (1 - 14 mM). Observed rate constants were obtained from fitting kinetic traces to a single exponential equation, rate = $-A*exp(-k_{obs}t) + C$.

0 °C	[PyO] (M)	k_{obs} (s^{-1})	k_2 (s^{-1})
	0.001	0.406	0.430 ± 0.056
	0.002	0.405	
	0.005	0.420	
	0.010	0.489	
10 °C	[PyO] (M)	k_{obs} (s^{-1})	k_2 (s^{-1})
	0.0035	0.995	1.11 ± 0.06
	0.007	1.09	
	0.0105	1.18	
	0.014	1.17	
15 °C	[PyO] (M)	k_{obs} (s^{-1})	k_2 (s^{-1})
	0.0035	1.76	1.84 ± 0.08
	0.007	1.66	
	0.0105	1.85	
	0.014	2.09	
20 °C	[PyO] (M)	k_{obs} (s^{-1})	k_2 (s^{-1})
	0.0035	2.95	3.19 ± 0.26
	0.007	3.58	
	0.0105	3.10	
	0.014	3.14	

1.3.2.2. PhNO

Table 1A.7. Temperature dependent pseudo-first order and second order rate constants for PhNO−V(N[^{t}Bu]Ar)$_3$ adduct formation measured at λ = 740 nm with 0.3 mM V(N[^{t}Bu]Ar)$_3$ and PhNO (1 - 10 mM). Observed rate constants were obtained from fitting kinetic traces to a single exponential equation, rate = −A**exp*(−k_{obs}t) + C.

−80 °C	[PhNO] (M)	k_{obs} (s^{-1})	k_1 (M^{-1} s^{-1})
	0.001	1.42	
	0.002	2.78	1,200 ± 49
	0.005	6.82	
	0.010	12.2	
−71 °C	[PhNO] (M)	k_{obs} (s^{-1})	k_1 (M^{-1} s^{-1})
	0.001	2.37	
	0.002	5.53	2,920 ± 36
	0.005	14.5	
	0.010	28.7	
−62 °C	[PhNO] (M)	k_{obs} (s^{-1})	k_1 (M^{-1} s^{-1})
	0.001	4.14	
	0.002	10.3	5,600 ± 79
	0.005	27.5	
	0.010	54.7	
−53 °C	[PhNO] (M)	k_{obs} (s^{-1})	k_1 (M^{-1} s^{-1})
	0.001	8.60	
	0.002	17.1	8,460 ± 8
	0.005	42.3	
	0.010	84.7	

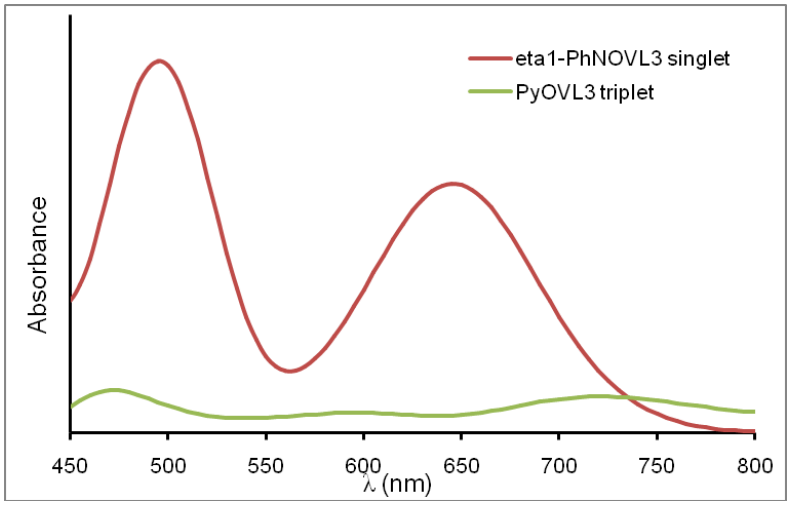

Figure 1A.9. TD DFT (BP86/6-311G(d,p)) calculated electronic spectra for the singlet PhNO−V(N[^{t}Bu]Ar)$_3$ (red spectrum) and triplet PyO−V(N[^{t}Bu]Ar)$_3$ (green spectrum) adducts.

1.3.3. Category III: Transient formation and decay of metastable oxidant-bound intermediates on the timescale of OAT

1.3.3.1. SIPr/MesCNO

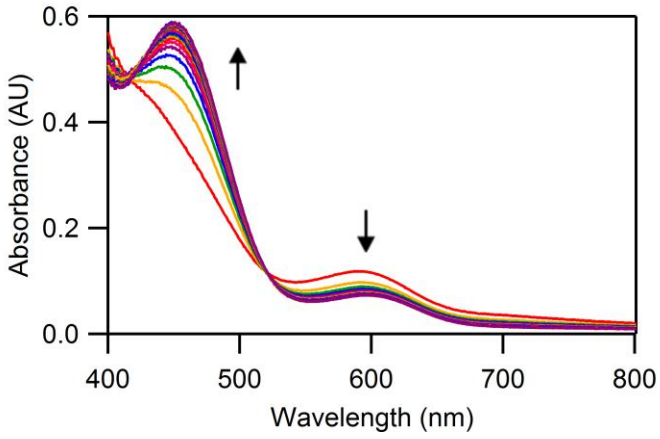

Figure 1A.10. Time-resolved spectral changes observed for the reaction between V(N[^{t}Bu]Ar)$_3$ (0.2 mM) and SIPr/MesCNO (0.6 mM) at −12 °C acquired over 13 s. Selected traces shown for clarity. Buildup of the intensely absorbing intermediate adduct was not observed at temperatures above −62 °C.

Table 1A.8. Temperature dependent pseudo-first order (k_{obs}) and second order (k_{app}) rate constants for product formation at λ= 453 nm with 0.3 mM V(N[^{t}Bu]Ar)$_3$ and SIPr/MesCNO (0.6 - 3.8 mM). Observed rate constants were obtained from fitting kinetic traces to a single exponential equation, rate = −A**exp*(−k_{obs}t) + C.

−80 °C	[SIPr/MesCNO] (M)	k_{obs} (s^{-1})	k_{app} (M^{-1} s^{-1})
	0.0006	0.786	
	0.001	1.28	1,330 ± 29
	0.002	2.70	
	0.003	3.94	
−71 °C	[SIPr/MesCNO] (M)	k_{obs} (s^{-1})	k_{app} (M^{-1} s^{-1})
	0.0006	1.39	
	0.001	2.27	3,300 ± 129
	0.002	5.69	
	0.003	9.19	
−62 °C	[SIPr/MesCNO] (M)	k_{obs} (s^{-1})	k_{app} (M^{-1} s^{-1})
	0.0006	1.72	
	0.001	3.10	4,930 ± 190
	0.002	8.09	
	0.003	13.4	
−53 °C	[SIPr/MesCNO] (M)	k_{obs} (s^{-1})	k_{app} (M^{-1} s^{-1})
	0.0006	3.10	
	0.001	5.52	8,350 ± 383
	0.002	13.6	
	0.003	23.0	
−44 °C	[SIPr/MesCNO] (M)	k_{obs} (s^{-1})	k_{app} (M^{-1} s^{-1})
	0.0006	5.52	
	0.001	9.70	14,040± 820
	0.002	22.6	
	0.003	39.2	
−35 °C	[SIPr/MesCNO] (M)	k_{obs} (s^{-1})	k_{app} (M^{-1} s^{-1})
	0.0006	9.00	
	0.001	16.0	21,800 ± 806
	0.002	37.0	
	0.003	61.2	
−30 °C	[SIPr/MesCNO] (M)	k_{obs} (s^{-1})	k_{app} (M^{-1} s^{-1})
	0.0006	15.8	
	0.0015	48.4	37,900 ± 899
	0.0025	90.1	
	0.0038	134	

−21 °C	[SIPr/MesCNO] (M)	k_{obs} (s^{-1})	k_{app} (M^{-1} s^{-1})
	0.0006	24.4	
	0.0015	68.1	48,700 ± 594
	0.0025	119	
	0.0038	177	
−12 °C	[SIPr/MesCNO] (M)	k_{obs} (s^{-1})	k_{app} (M^{-1} s^{-1})
	0.0006	37.4	
	0.0015	98.3	64,600 ± 2,350
	0.0025	169	
	0.0038	240	

Plots of k_{obs} versus [SIPr/MesCNO] were linear and the slope of each line represents the second order rate constant (k_{app}) for $OV(N[^tBu]Ar)_3$ formation over the stated temperature range. As discussed in Chapter 1, the mechanism of OAT involves the buildup and decay of a metastable SIPr/MesCNO–$V(N[^tBu]Ar)_3$ adduct that occurs on the timescale of OAT. Since the individual processes are not resolved in this region of the spectrum, the measured rate constants and activation parameters include contributions from all reaction steps.

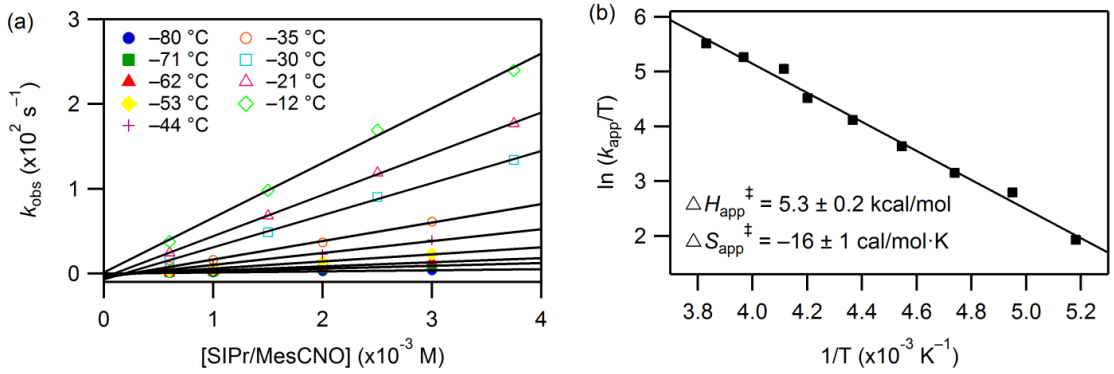

Figure 1A.11. (a) Plots of k_{obs} versus SIPr/MesCNO at various concentrations (0.6 - 3.8 mM) over a temperature range of −80 to −12 °C with $[V(N[^tBu]Ar)_3]_0$ = 0.3 mM. (b) Eyring plot with derived activation parameters.

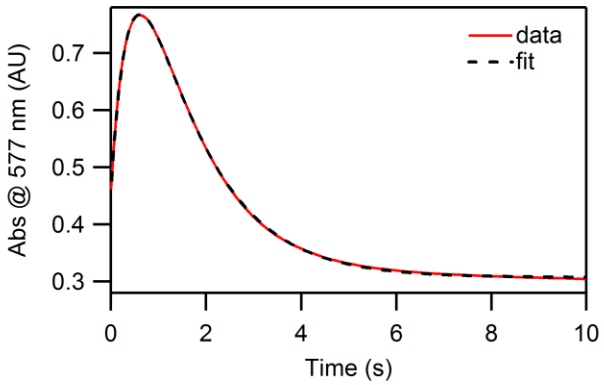

Figure 1A.12. Kinetic trace at λ = 577 nm (red line) at −80 °C highlighting a two-step process with double exponential fit (black dashed line). $[V(N[^tBu]Ar)_3]_0$ = 0.3 mM and $[SIPr/MesCNO]_0$ = 2 mM.

Table 1A.9. Temperature dependent pseudo-first order and second order rate constants corresponding to the first process measured at λ = 577 nm (formation) with 0.3 mM $V(N[^tBu]Ar)_3$ and SIPr/MesCNO (0.6 - 3 mM). Observed rate constants were obtained from fitting kinetic traces to a double exponential equation, rate = $-A_1*exp(-k_{1obs}t)-A_2*exp(-k_{2obs}t)+C$.

−80 °C	[SIPr/MesCNO] (M)	k_{1obs} (s^{-1})	k_1 (M^{-1} s^{-1})
	0.0006	1.15	
	0.001	1.36	776 ± 29
	0.002	2.20	
	0.003	2.98	
−71 °C	[SIPr/MesCNO] (M)	k_{1obs} (s^{-1})	k_1 (M^{-1} s^{-1})
	0.0006	3.26	
	0.001	3.64	1,440 ± 57
	0.002	5.25	
	0.003	6.64	
−62 °C	[SIPr/MesCNO] (M)	k_{1obs} (s^{-1})	k_1 (M^{-1} s^{-1})
	0.0006	10.9	
	0.001	11.5	1,720 ± 33
	0.002	13.2	
	0.003	15.0	

Table 1A.10. Estimation of k_{-1} and equilibrium constants from the experimental data at various temperatures for the first process occurring at λ= 577 nm with 0.3 mM V(N[^{t}Bu]Ar)$_3$ and SIPr/MesCNO (0.6 - 3 mM).

T (°C)	k_{-1}(s^{-1})	K_{eq} (M^{-1})
−80	0.64 ± 0.05	1,200 ± 110
−71	2.3 ± 0.1	620 ± 40
−62	9.8 ± 0.1	180 ± 4

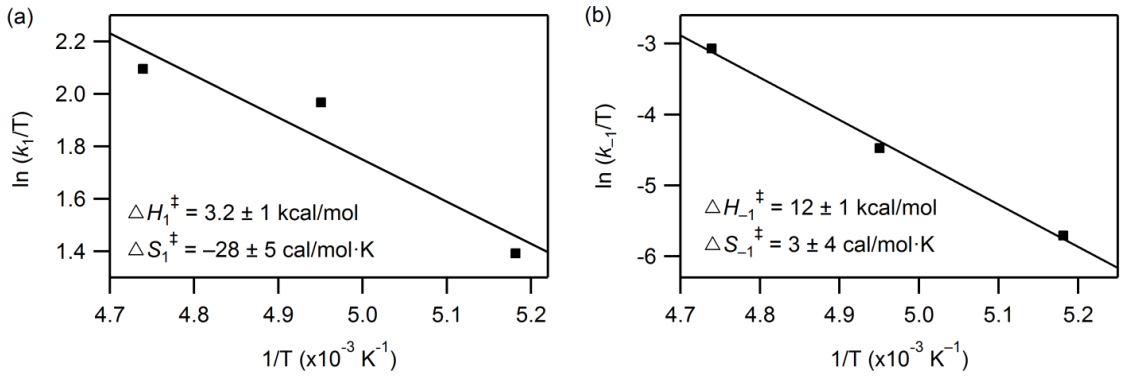

Figure 1A.13. Eyring plots for the first process obtained from analysis of the experimental data at λ = 577 nm over the temperature range of −80 to −62 °C with derived activation parameters. (a) Eyring plot for ligand binding (k_1) and (b) Eyring plot for ligand dissociation (k_{-1}).

Table 1A.11. First order rate (k_2) and equilibrium (K_{eq}) constants obtained from nonlinear least-squares fitting of the experimental data corresponding to the second process (decay) occurring at λ = 577 nm to Eq. 1.7.

T (°C)	k_2 (s^{-1})	K_{eq} (M^{-1})
−80	1.08 ± 0.05	1,610 ± 256
−71	3.15 ± 0.11	889 ± 78
−62	11.4 ± 0.5	276 ± 19

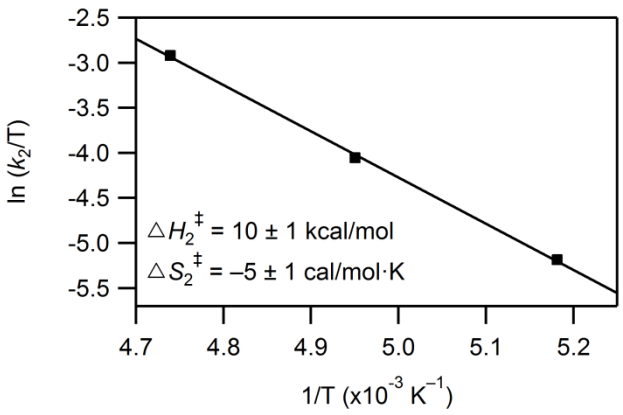

Figure 1A.14. Eyring plot obtained from analysis of the experimental data for the second process corresponding to OAT (k_2) with derived activation parameters.

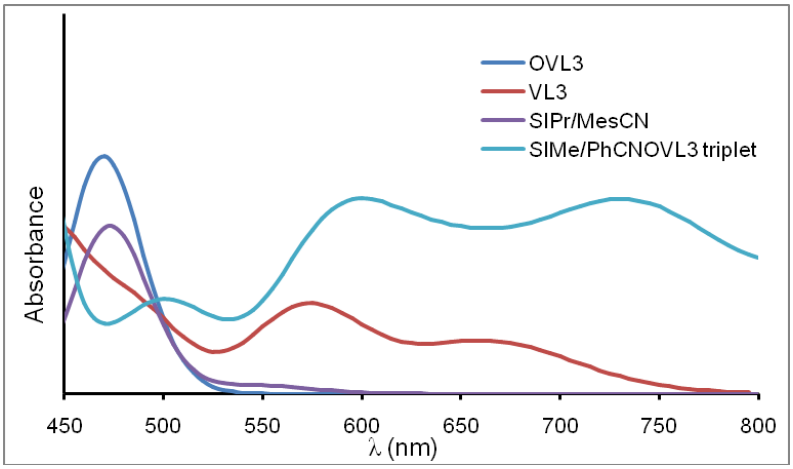

Figure 1A.15. TD BP86/6-311G(d,p) calculated electronic spectra for selected species involved in the reaction of V(N[^{t}Bu]Ar)$_3$ with SIMe/PhCNO.

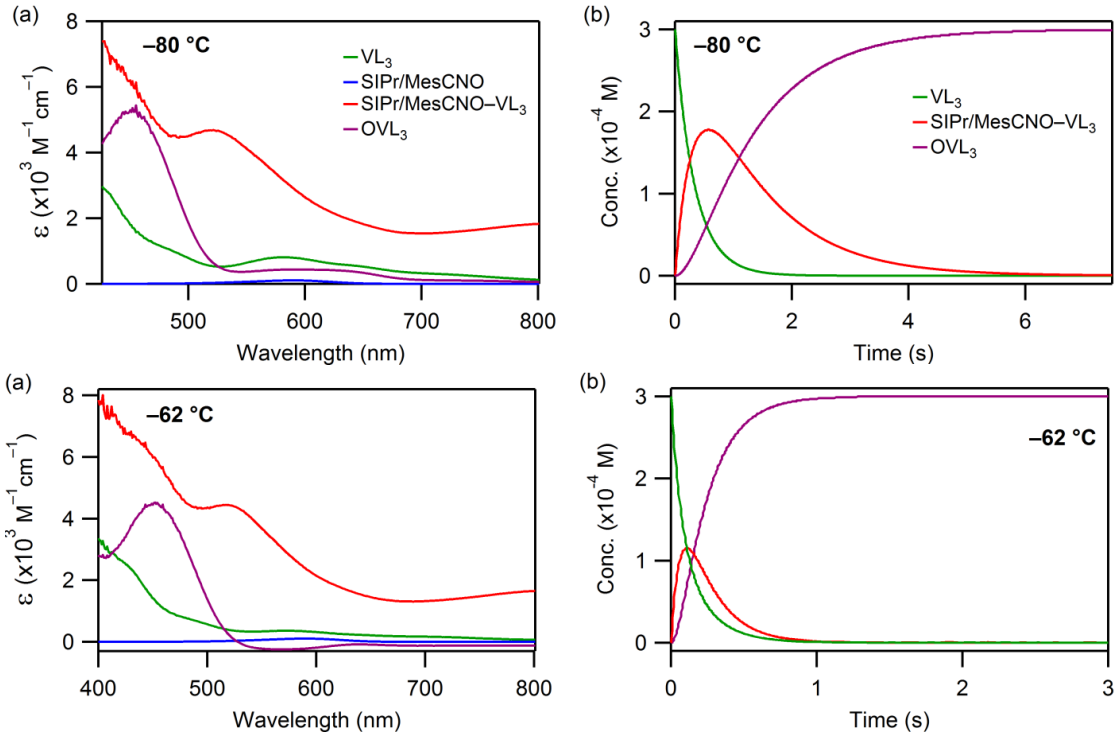

Figure 1A.16. (a) Calculated spectra of colored components obtained from the kinetic model at the remaining temperatures of −80 °C (top row) and −62 °C (bottom row) with $[V(N[^tBu]Ar)_3]_0$ = 0.3 mM and $[SIPr/MesCNO]_0$ = 3 mM. A known spectrum for SIPr/MesCNO was incorporated in all cases while the remaining colored components were calculated by the fitting program. (b) Concentration profiles for colored components. The concentration profile for SIPr/MesCNO is not shown since it is present in pseudo-first order excess.

Table 1A.12. Calculated rate constants for ligand dissociation (k_{-1}) and K_{eq} estimates (K_{eq} = k_1/k_{-1}) obtained from global modeling of the SIPr/MesCNO kinetic data using the ReactLab Kinetics program. Average values of rate constants obtained from two separate datasets are reported with standard deviations.

T (°C)	k_{-1} (s^{-1})	K_{eq} (M^{-1})
−80	-----	-----
−71	0.627 ± 0.33	2,730 ± 1,460
−62	2.09 ± 0.32	1,560 ± 248

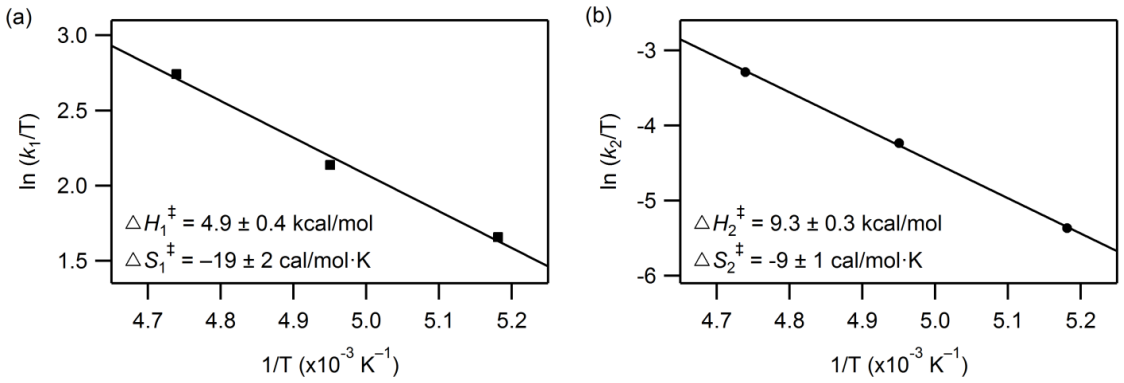

Figure 1A.17. Eyring plots with activation parameters for ligand binding (k_1) and OAT (k_2) in the SIPr/MesCNO system derived from the results of the kinetic model over the temperature range of −80 to −62 °C.

1.3.3.2. IPr/N_2O

Table 1A.13. Temperature dependent pseudo-first order rate constants obtained from fits at λ = 725 nm with 0.25 mM V(N[^{t}Bu]Ar)$_3$ and IPr/N_2O (0.5 - 3 mM). Observed rate constants were obtained from fitting kinetic traces to a double exponential equation, rate = $-A_1*exp(-k_{1obs}t)-A_2*exp(-k_{2obs}t) + C$.

−62 °C	[IPr/N_2O] (M)	k_{1obs} (s^{-1})	k_{2obs} (s^{-1})
	0.0005	0.548	0.200
	0.001	0.908	0.245
	0.002	1.67	0.260
	0.003	2.48	0.259
−53 °C	[IPr/N_2O] (M)	k_{1obs} (s^{-1})	k_{2obs} (s^{-1})
	0.0005	1.46	0.584
	0.001	1.88	0.796
	0.002	3.52	0.851
	0.003	5.25	0.850
−44 °C	[IPr/N_2O] (M)	k_{1obs} (s^{-1})	k_{2obs} (s^{-1})
	0.0005	3.43	1.39
	0.001	4.17	2.09
	0.002	7.12	2.35
	0.003	10.6	2.39
−35 °C	[IPr/N_2O] (M)	k_{1obs} (s^{-1})	k_{2obs} (s^{-1})
	0.0005	10.2	2.72
	0.001	10.8	4.24
	0.002	15.8	6.02
	0.003	21.1	6.75

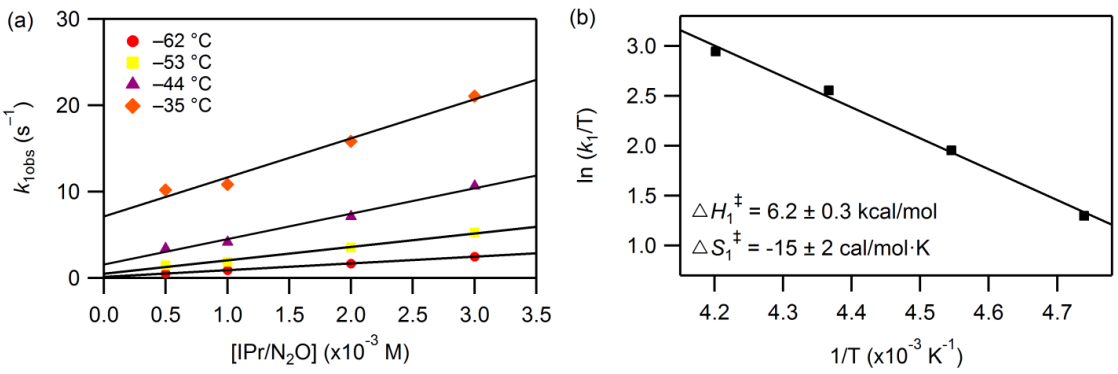

Figure 1A.18. (a) Plots of k_{1obs} versus [IPr/N_2O] with linear fits acquired over a temperature range of −62 to −35 °C with [V(N[^{t}Bu]Ar)$_3$]$_0$ = 0.25 mM and [IPr/N_2O]$_0$ = 0.5 - 3 mM. (b) Eyring plot with derived activation parameters.

The intercepts from k_{1obs} versus [IPr/N_2O] plots were taken as estimates for k_{-1}, allowing for K_{eq} values to be estimated from the kinetic data (Table 1A.14).

Table 1A.14. Temperature dependent second order rate constants (k_1) obtained from the slopes of the linear plots of k_{1obs} vs. [IPr/N_2O], first-order rate constants (k_{-1}) for the reverse reaction obtained from the intercepts, and estimates for K_{eq} (k_1/k_{-1}).

T (°C)	k_1 ($M^{-1}s^{-1}$)	k_{-1} (s^{-1})	K_{eq} (M^{-1})
−62	774 ± 12	0.145 ± 0.022	5,340 ± 814
−53	1,550 ± 104	0.500 ± 0.196	3,110 ± 1,240
−44	2,950 ± 246	1.56 ± 0.46	1,890 ± 588
−35	4,520 ± 460	7.14 ± 0.87	633 ± 100

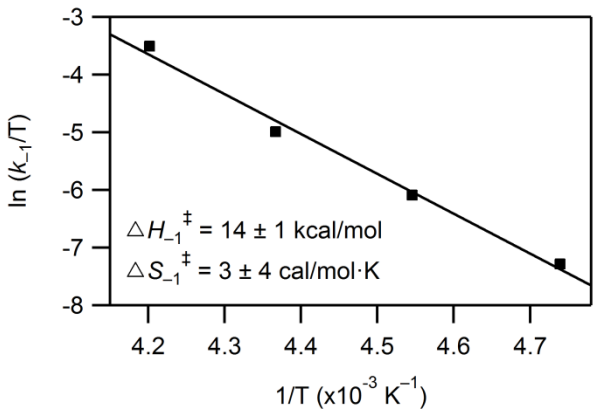

Figure 1A.19. Eyring plot for the reverse reaction (k_{-1}) with derived activation parameters.

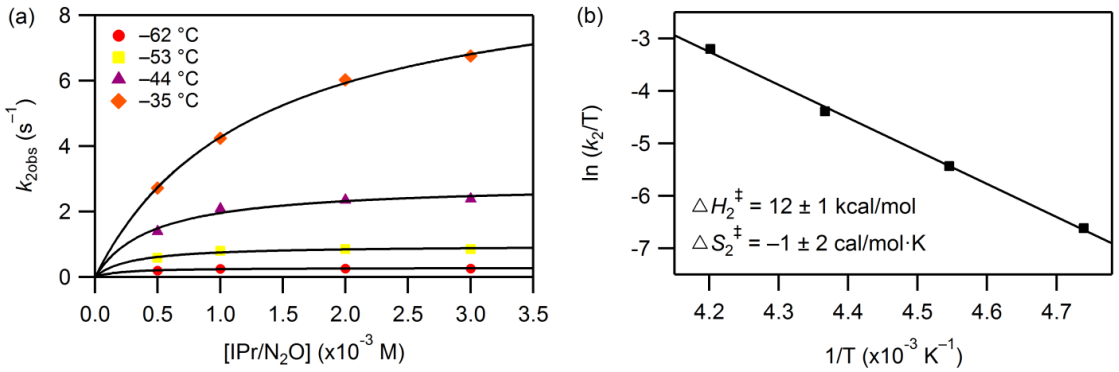

Figure 1A.20. (a) Plots of k_{2obs} versus [IPr/N_2O] with fits to Eq. 1.7 over a temperature range of −62 to −35 °C with $[V(N[^tBu]Ar)_3]_0$ = 0.25 mM and $[IPr/N_2O]_0$ = 0.5 - 3 mM. (b) Eyring plot for OAT (k_2) with derived activation parameters.

Table 1A.15. Temperature dependent first order rate constants (k_2) corresponding to the second process (decay) measured at λ = 725 nm obtained from fitting the k_{2obs} saturation plots to Eq. 1.7. Equilibrium constants (K_{eq}) associated with the initial binding step were also obtained from these fits and are in excellent agreement with the previous estimates given in Table 1A.14.

T (°C)	k_2 (s^{-1})	K_{eq} (M^{-1})
−62	0.282 ± 0.009	5,270 ± 1,100
−53	0.961 ± 0.056	3,530 ± 1,050
−44	2.85 ± 0.20	2,200 ± 595
−35	9.69 ± 0.25	788 ± 49

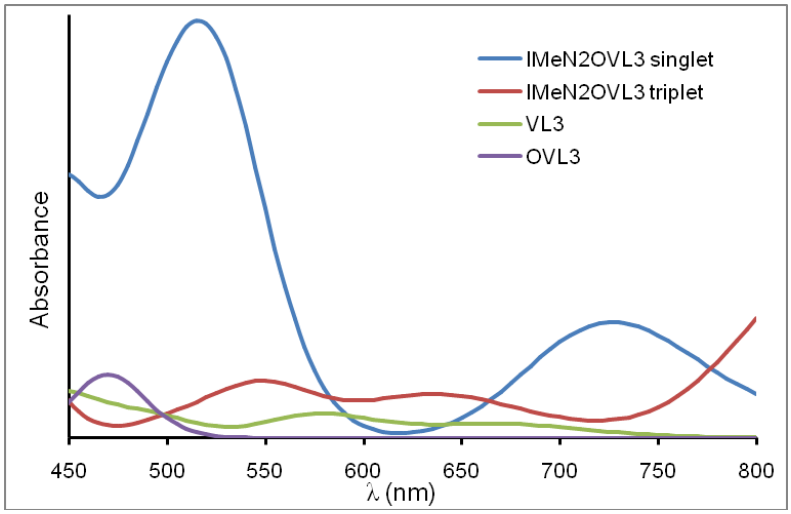

Figure 1A.21. TD BP86/6-311G(d,p) calculated electronic spectra for selected species involved in the reaction of $V(N[^tBu]Ar)_3$ with IMe/N_2O.

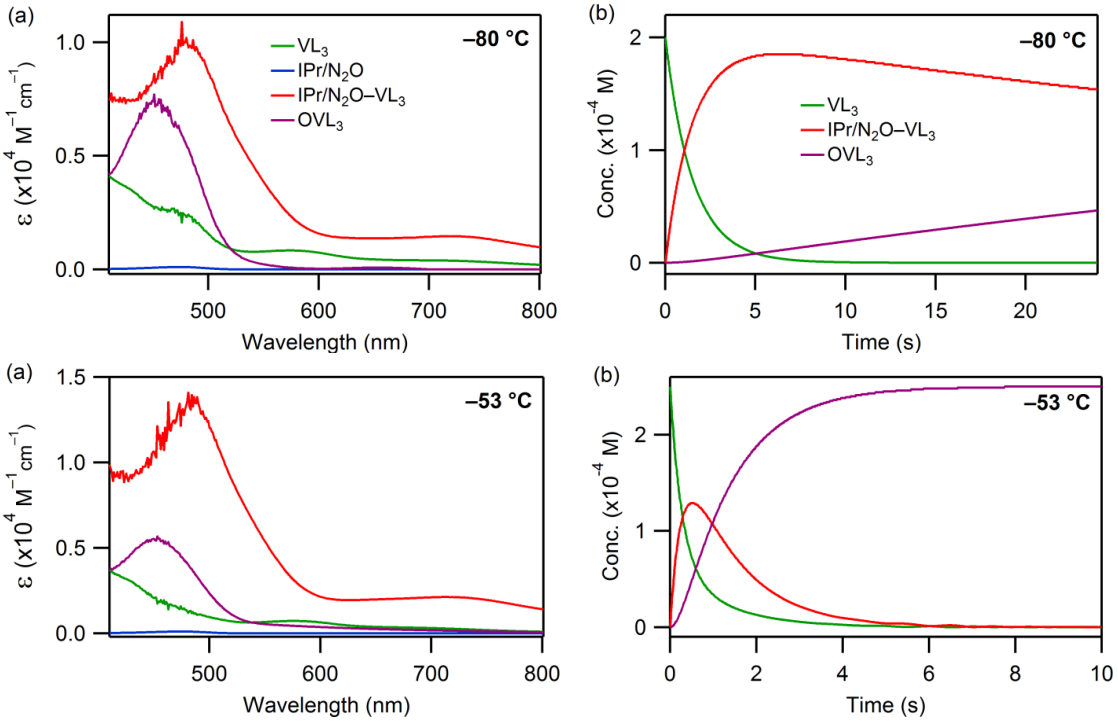

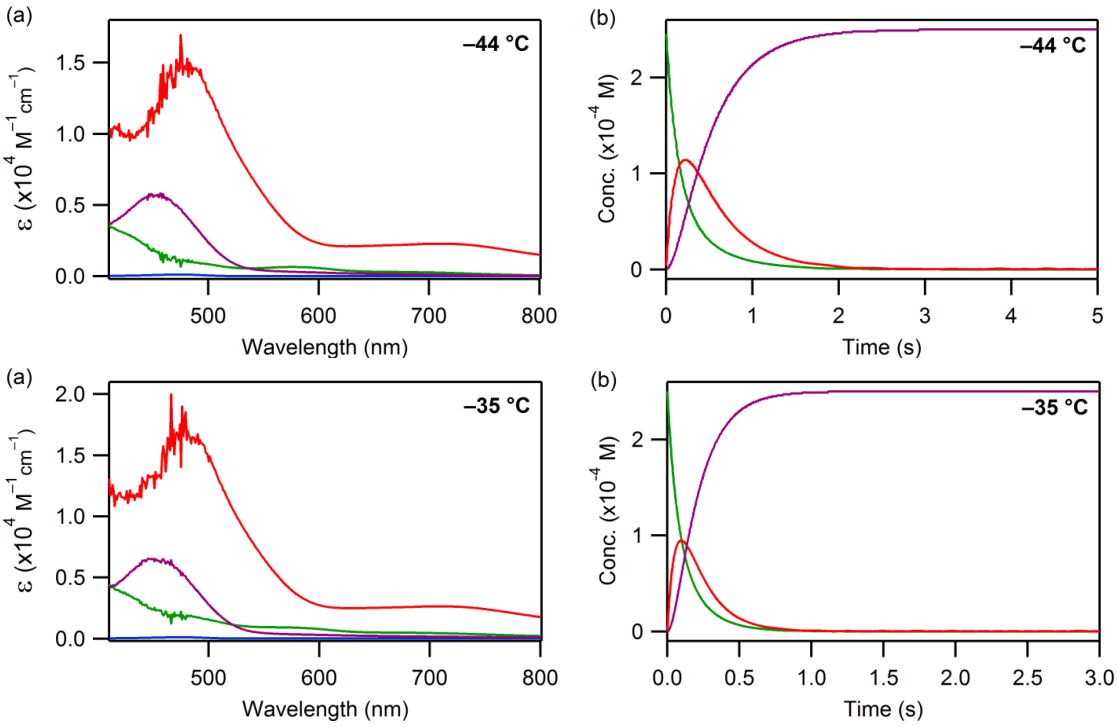

Figure 1A.22. (a) Calculated spectra of colored components obtained from the kinetic model at the remaining temperatures of −80 °C, −53 °C, −44 °C, and −35 °C with $[V(N[^tBu]Ar)_3]_0$ = 0.25 mM and $[IPr/N_2O]_0$ = 2 mM. A known spectrum for IPr/N_2O was incorporated in all cases while the remaining colored components were calculated by the fitting program. (b) Concentration profiles for colored components. The concentration profile for IPr/N_2O is not shown since it is present in pseudo-first order excess.

Table 1A.16. Calculated rate constants for ligand dissociation (k_{-1}) and K_{eq} estimates (K_{eq} = k_1/k_{-1}) obtained from global modeling of the IPr/N_2O kinetic data using the ReactLab Kinetics program. Average values of rate constants obtained from two separate datasets are reported with standard deviations.

T (°C)	k_{-1} (s^{-1})	K_{eq} (M^{-1})
−80	-----	-----
−62	0.225 ± 0.045	3490 ± 738
−53	0.487 ± 0.006	3120 ± 66
−44	0.836 ± 0.078	3590 ± 335
−35	1.88 ± 0.032	2950 ± 82

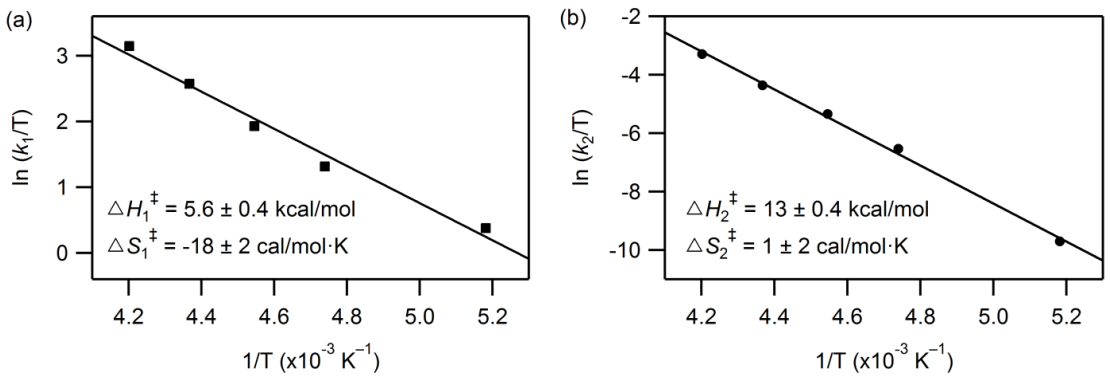

Figure 1A.23. Eyring plots with activation parameters for ligand binding (k_1) and OAT (k_2) in the IPr/N_2O system, derived from the results of the kinetic model over the temperature range of −80 to −35 °C.

1.3.4. Category IV: Steady state kinetics without observable intermediates

1.3.4.1. dbabhNO

Table 1A.17. Temperature dependent pseudo-first order and second order rate constants for product formation at λ = 453 nm with 0.3 mM V(N[^{t}Bu]Ar)$_3$ and dbabhNO (1 - 10 mM). Observed rate constants were obtained from fitting kinetic traces to a single exponential equation, rate = −A**exp*(−k_{obs}t) + C.

−71 °C	[dbabhNO] (M)	k_{obs} (s^{-1})	k_{app} (M^{-1} s^{-1})
	0.001	1.31	
	0.002	2.27	1,010 ± 33
	0.005	4.96	
	0.010	10.4	
−62 °C	[dbabhNO] (M)	k_{obs} (s^{-1})	k_{app} (M^{-1} s^{-1})
	0.001	3.34	
	0.002	4.60	1,820 ± 94
	0.005	9.43	
	0.010	19.6	
−53 °C	[dbabhNO] (M)	k_{obs} (s^{-1})	k_{app} (M^{-1} s^{-1})
	0.001	3.53	
	0.002	5.55	3,840 ± 296
	0.005	15.1	
	0.010	37.6	

−44 °C	[dbabhNO] (M)	k_{obs} (s^{-1})	k_{app} (M^{-1} s^{-1})
	0.001	5.72	
	0.002	10.1	7,180 ± 465
	0.005	28.5	
	0.010	69.6	

1.3.4.2. MesCNO

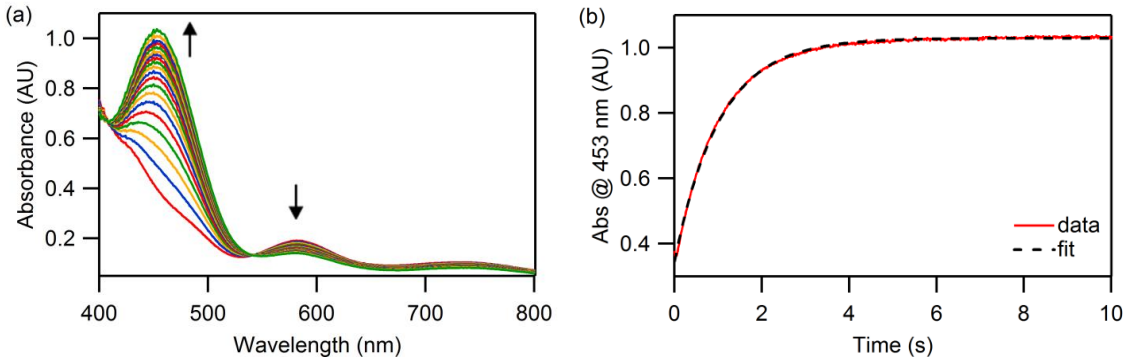

Figure 1A.24. (a) Time-resolved spectral changes accompanying the reaction between V(N[^{t}Bu]Ar)$_3$ (0.3 mM) and MesCNO (7 mM) at −62 °C acquired over 10 seconds showing formation of OV(N[^{t}Bu]Ar)$_3$ (λ_{max} = 453 nm) with concomitant decay occurring at longer wavelengths. (b) Kinetic trace at 453 nm (red line) with single exponential fit (black dashed line).

Table 1A.18. Temperature dependent pseudo-first order and second order rate constants for product formation measured at λ = 453 nm with 0.3 mM V(N[^{t}Bu]Ar)$_3$ and MesCNO (3.5 - 28 mM). Observed rate constants were obtained from fitting kinetic traces to a single exponential equation, rate = −A**exp*(−k_{obs}t) + C.

−62 °C	[MesCNO] (M)	k_{obs} (s^{-1})	k_{app} (M^{-1} s^{-1})
	0.0035	0.597	
	0.007	1.05	
	0.0105	1.37	81.1 ± 6.2
	0.014	1.69	
	0.028	2.65	
−53 °C	[MesCNO] (M)	k_{obs} (s^{-1})	k_{app} (M^{-1} s^{-1})
	0.0035	1.23	
	0.007	1.84	
	0.0105	2.53	189 ± 4
	0.014	3.32	
	0.028	5.84	
−44 °C	[MesCNO] (M)	k_{obs} (s^{-1})	k_{app} (M^{-1} s^{-1})
	0.0035	1.84	
	0.007	2.88	
	0.0105	3.94	270 ± 10
	0.014	5.10	
	0.028	8.48	
−35 °C	[MesCNO] (M)	k_{obs} (s^{-1})	k_{app} (M^{-1} s^{-1})
	0.0035	2.28	
	0.007	3.79	
	0.0105	5.42	402 ± 12
	0.014	6.96	
	0.028	12.2	

CHAPTER 2

Diagonal Relationships in Ligand Binding: Nitrile Coordination to Vanadium and Molybdenum Tris-Anilide Complexes[1]

2.1. Introduction

The diagonal relationship between vanadium and molybdenum has long been invoked for observed similarities in the reactivity of these two metals.[2] However, there are also noticeable differences between vanadium and molybdenum with respect to electronic properties and reactivity: fewer d-electrons for V^{n+} compared to Mo^{n+} result in a more pronounced electrophilic character of vanadium, while smaller ionic radius may increase electrostatic metal-ligand interactions and potentially hinder access to the metal center supported by bulky multidentate ligands. Surprisingly, quantitative thermodynamic and kinetic data on comparative ligand binding to low-valent vanadium and molybdenum complexes are limited[3] and include primarily ligand binding or substitution in carbonyl complexes.[4] Fundamental questions on the factors that determine relative rates and strength of ligand binding to molybdenum and vanadium remain to be addressed.

Recent interest in characterizing ligand binding to these metals is inspired, in part, by the nitrogenase family of metalloenzymes, key enzymes in the nitrogen fixation cycle that reduce atmospheric N_2 to NH_3. A key cofactor in nitrogenase contains an iron-sulfur cluster that may also include molybdenum (Mo N_2ase, the most common and best-characterized nitrogenase), or vanadium (V N_2ase).[5,6] It is believed that these enzymes

are mechanistically similar: when the VFe protein is substituted into the complementary protein in Mo N_2ase, the enzyme remains functional.[7] The reactivities of nitrogenase enzymes vary with the metal cofactor in efficiency, turnover rates, substrate binding and affinity for coordinated species.[5] For example, V N_2ase reacts approximately 1.6 times more slowly with N_2 at room temperature than Mo N_2ase, but at low temperatures, the efficiency of V N_2ase surpasses Mo N_2ase.[8] Furthermore, coordinating substrates that inhibit catalysis of Mo N_2ase are much less effective in the inhibition of V N_2ase. CO, for example, inhibits Mo N_2ases in the reduction of both azide and cyanide, whereas significant substrate reduction with V N_2ase still occurs in the presence of CO. These examples illustrate the significance of ligand binding rates and binding affinity in the overall reactivity of the enzyme.[5,6,9]

Complementing the studies of nitrogenase, the development of homogeneous transition metal complexes that are capable of binding and cleaving dinitrogen has been an active area of research. Many of the systems involve binding of dinitrogen to sterically shielded transition metal centers prior to the cleavage event. Examples include Cummins's molybdenum tris-anilide complexes,[10,11] Floriani's low valent niobium complexes,[12] and the work of Mindiola,[13] Gambarotta,[14] and Cloke[15,16] on N_2 splitting with vanadium complexes. The initial dinitrogen complex, which generally forms in a left-lying equilibrium with free N_2, is difficult to observe in these systems. In order to gain some insight into ligand binding process, nitriles (RCN) or isonitriles (RNC), which are electronically similar to N_2, provide a suitable model system. Coupled with similar work on iron complexes,[17] the thermodynamic and kinetic differences of nitrile binding between molybdenum and vanadium will provide powerful benchmarks for

understanding how substrates, substrate analogs, intermediates, and inhibitors may interact with the nitrogenase active site.

The thermodynamics and kinetics of ligand binding to the N_2-cleaving molybdenum(III) tris-anilide complex, Mo(N[^{t}Bu]Ar)$_3$ (Ar = 3,5-$Me_2C_6H_3$), was recently probed using various nitriles that afford end-on (η^1) or side-on (η^2) adducts.[18] For example, benzonitrile (PhCN) binds rapidly and reversibly to Mo(N[^{t}Bu]Ar)$_3$; spectroscopic and computational data indicate an η^1-coordination mode for benzonitrile and related aryl nitriles. In contrast, dimethylcyanamide (Me_2NCN) initially binds end-on but then isomerizes rapidly to a side-on adduct that is stable and relatively unreactive. At temperatures between −80 to −40 °C, the η^1 intermediate Me_2NCN−Mo(N[^{t}Bu]Ar)$_3$ complex can be trapped via radical coupling with PhSSPh to yield the ketimide complex $Me_2NC(SPh)N$−Mo(N[^{t}Bu]Ar)$_3$ as shown in Figure 2.1. At higher temperatures, the η^1- to η^2-isomerization is faster than reaction with the disulfide.

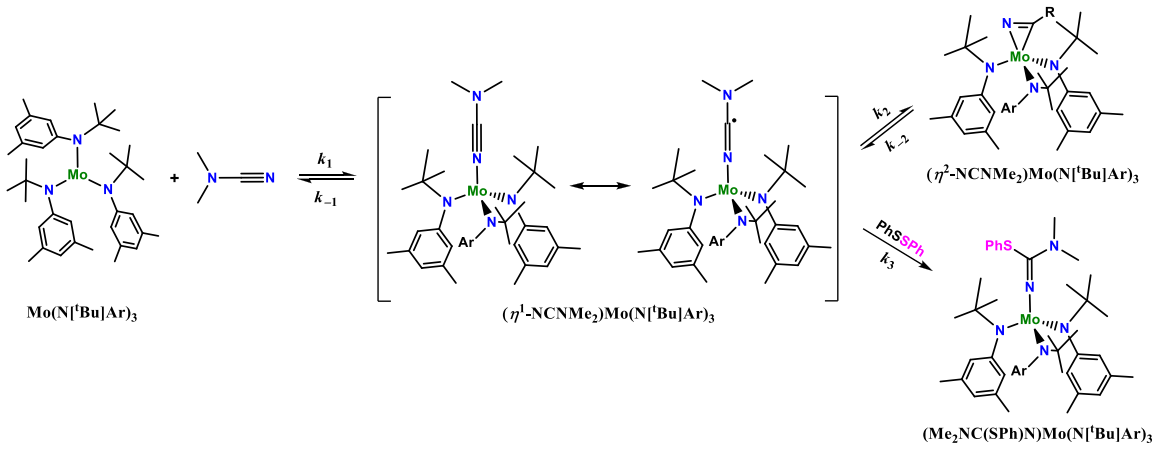

Figure 2.1. Reaction scheme for Mo(N[^{t}Bu]Ar)$_3$ (Ar = 3,5-$Me_2C_6H_3$) with dimethylcyanamide (Me_2NCN). The η^1-Me_2NCN adduct can be trapped at low temperatures with diphenyl disulfide (PhSSPh) to produce the ketimide complex ($Me_2NC(SPh)N$)Mo(N[^{t}Bu]Ar)$_3$. Image adapted from ref 18.

The high propensity of η^1-arylnitrile adducts of Mo(III) anilides to undergo radical couplings at the nitrile carbon atom led to limited stability of these species and precluded their structural characterization.[19] We are currently interested in nitrile binding to V(N[^{t}Bu]Ar)$_3$, for comparison to the related Mo(N[^{t}Bu]Ar)$_3$ complex, in order to gain insight into the differences in ligand binding affinities and rates due to metal substitution. The reaction of nitriles with V(N[^{t}Bu]Ar)$_3$ presents an excellent opportunity to explore the vanadium(III)-molybdenum(III) diagonal relationships in thermodynamics and kinetics of ligand binding. Several end-on nitrile adducts of V(N[^{t}Bu]Ar)$_3$ have been synthesized and characterized or spectroscopically analyzed as part of this work (Figure 2.2), and with Me_2NCN in particular, it was of interest to see if the vanadium complex would also display the same preferential η^2-coordination geometry as observed in the molybdenum system. Interestingly, the structurally characterized Me_2NCN−V(N[^{t}Bu]Ar)$_3$ product confirmed that the nitrile coordinates to the vanadium center in an η^1-fashion (Figure 2.3).

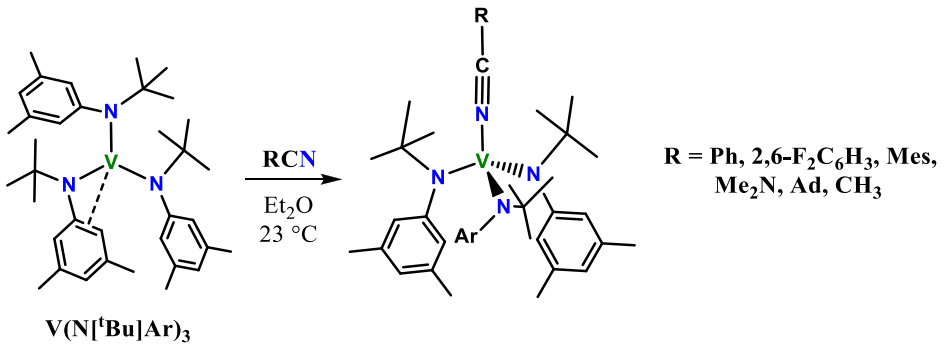

Figure 2.2. General synthetic scheme for preparation of η^1-RCN adducts of V(N[^{t}Bu]Ar)$_3$. Ar = 3,5-$Me_2C_6H_3$; Mes = mesityl; Ad = adamantyl.

The kinetics and thermodynamics of binding of various nitriles that differ in electronic and steric properties is presented herein, along with theoretical calculations that provide additional insight into the experimental data. Greater stability of the nitrile adducts with a d^2-metal (V^{3+}) with respect to radical couplings at the carbon atom of the C≡N bond allowed for isolation and structural characterization of the end-on (η^1) complexes and for measurements of the energetics of the end-on coordination of small molecules with an element-nitrogen triple bond (RC≡N and RN≡C). Understanding the similarities and differences in the electronic and steric factors that govern small molecule binding to sterically shielded, coordinatively unsaturated V(III) and Mo(III) centers may ultimately provide insight into initial steps of activation of N_2 and other molecules with strong element-element multiple bonds.

2.2. Experimental Methods

General Considerations. Samples of $V(N[^tBu]Ar)_3$ (Ar = 3,5-$Me_2C_6H_3$)[20] were graciously provided by members of the Cummins group (MIT, Cambridge, MA), stored in a glove box freezer (−35 °C), and used without further purification. All syntheses, characterizations, crystallographic data, calorimetric measurements, and FT-IR experiments were performed by collaborators at MIT (Cummins group) and University of Miami (Hoff group). The reader is referred to refs 1 and 21 for further details regarding these procedures. Anhydrous toluene and acetonitrile (HPLC grade, ≥ 99.9%) were purchased from Sigma Aldrich and dried on an Innovative Technologies PureSolv 400 solvent purification system. Solid nitriles and adamantyl isonitrile (AdNC) were

purchased from commercial vendors and used without further purification. Liquid nitriles (dimethylcyanamide (Me_2NCN) and benzonitrile (PhCN)) were distilled under reduced pressure and subject to several freeze-pump-thaw cycles before being stored in a glove box.

Stopped-Flow Kinetics. Toluene solutions of $V(N[^tBu]Ar)_3$ and substrates were prepared in an MBraun glove box filled with ultra high purity argon (Airgas) and loaded in Hamilton gastight syringes. Time-resolved UV-visible spectra (λ = 400–800 nm) were acquired over a range of temperatures (–62 to –35 °C) using a Hi-Tech Scientific SF-61DX2 Multi-mixing CryoStopped-Flow system (TgK Scientific Ltd.) equipped with a Hi-Tech Scientific LHT50 tungsten light source, a J&M TIDAS diode array detector, and a Brandenburg 4479 Series PMT monochromator. The instrument was equipped with stainless steel plumbing lined with PEEK tubing and a 1.00 cm^3 quartz mixing cell submerged in an ethanol cooling bath. The temperature in the mixing cell was maintained to ± 0.1°C using a CAL 3200 automatic temperature controller. Data acquisition was performed using TIDAS-DAQ and/or Kinetic Studio software programs and mixing times were 2-3 ms. All flow lines were washed extensively with argon-saturated anhydrous toluene prior to charging the drive syringes with reactant solutions and the driving syringe compartment was continuously flushed with argon during the experiments to preserve anaerobicity. Experiments were performed in a single-mixing mode of the instrument with a 1:1 (v/v) mixing ratio. Reactions were studied under pseudo-first order conditions using excess substrates. Data analysis was performed using Kinetic Studio (TgK Scientific) and IGOR Pro 5.0 (Wavemetrics, Inc.) software

programs. All observed rate constants are provided in Appendix 2 and represent an average of at least three measurements which gave an acceptable standard deviation (within 10 %). All remaining quantities derived from the kinetic data are reported with their standard deviations. All concentrations are reported after mixing in the stopped-flow cell.

Computational Details. All computational studies were performed by Manuel Temprado, Universidad de Alcalá Department of Physical Chemistry, Madrid, Spain. Electronic structure calculations using the BP86[22] pure density functional method as implemented in the Gaussian 03 suite of programs[23] were carried out. Structures were optimized using the LANL2DZ[24] basis (LANL2DZ ECP and basis for Mo; the Dunning-Huzinaga D95V[25] basis for all other atoms). Optimizations of several conformers using several anilide environments and different conformations of the nitrile ligands were carried out to determine the geometry of the global minimum in each case. In order to obtain more reliable molecular structures, the lowest energy minima derived from these calculations were further optimized by including f functions and Stuttgart-Dresden MWB28[26] quasi-relativistic or MDF10[27] fully relativistic effective core potential and basis[28] for Mo and V respectively, and the triple-zeta quality basis set, 6-311G(d,p), for all other elements. Hessians were calculated at the same level of theory as the optimizations to confirm the nature of the stationary points. Since the computed Hessians of a couple of optimized structures were found to possess small negative eigenvalues, the zero-point vibrational effects were not included in the final energies.

2.3. Results

2.3.1. Structural Analysis of Nitrile and Isonitrile Adducts

Addition of nitriles to dark green-brown solutions of V(N[^{t}Bu]Ar)$_3$ (in diethyl ether or toluene) results in an immediate color change to deep purple, indicative of nitrile binding. The purple 2,6-$F_2C_6H_3CN$−V(N[^{t}Bu]Ar)$_3$ and Me_2NCN−V(N[^{t}Bu]Ar)$_3$ adducts were structurally characterized and revealed an end-on coordination mode for the bound nitriles (Figure 2.3). In addition, the purple η^1-isonitrile adduct AdNC−V(N[^{t}Bu]Ar)$_3$ was structurally characterized, which was prepared in an analogous fashion (Figure 2.4).

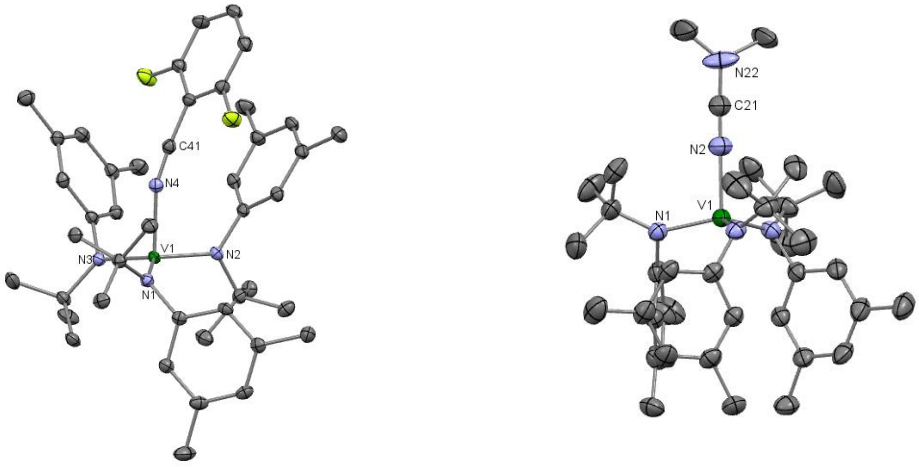

Figure 2.3. Thermal ellipsoid plots of 2,6-$F_2C_6H_3CN$−V(N[^{t}Bu]Ar)$_3$ (left) and Me_2NCN−V(N[^{t}Bu]Ar)$_3$ (right) shown at the 50 % probability level. Hydrogen atoms and disordered C21−N22−Me_2 group (right) have been omitted for clarity. Selected distances (Å) and angles (°) for 2,6-$F_2C_6H_3CN$−V(N[^{t}Bu]Ar)$_3$: V1–N1 = 1.947(2), V1–N2 = 1.943(2), V1–N3 = 1.942(2), V1–N4 = 2.044(2), N4–C41 = 1.151(3), N1–V1–N4 = 99.83(7), N2–V1–N4 = 89.70(7), N3–V1–N4 = 98.76(7), V1–N4–C41 = 161.7(2). Selected distances (Å) and angles (°) for Me_2NCN−V(N[^{t}Bu]Ar)$_3$: V1–N1 = 1.936(2), V1–N2 = 2.037(3), N2–C21 = 1.151(5), N1–V1–N1 = 116.47(3), N1–V1–N2 = 100.96(5), V1–N2–C21 = 180.0(4).

The crystal structure of 2,6-$F_2C_6H_3CN$−V(N[^{t}Bu]Ar)$_3$ contains a vanadium center in a distorted trigonal monopyramidal coordination geometry (avg. $N_{anilide}$–V–$N_{nitrile}$ =

96.10(12)°; avg. $N_{anilide}$–V–$N_{anilide}$ = 118.89(12)°). The V–$N_{nitrile}$ interatomic distance of 2.044(2) Å is longer than the V–$N_{anilide}$ distances (avg. = 1.944(3) Å). The anilide ligands adopt what we term a one-down, two-up arrangement, where one of the three aryl rings points downward away from the nitrile and two point upward towards it. This conformation likely arises from steric effects between the coordinated nitrile and the ligand *tert*-butyl groups. Furthermore, there is a deviation from linearity in the V–N–C angle (161.7(2)°) which may result from a π-stacking interaction between the phenyl ring of the nitrile and the phenyl substituent on one of the anilides. This structural feature was also noted for (Ph(H)C=N)Mo(N[^{t}Bu]Ar)$_3$.[29]

The crystal structure of Me_2NCN−V(N[^{t}Bu]Ar)$_3$ unambiguously reveals an η^1 binding mode for the cyanamide ligand. The anilide ligands adopt a crystallographically imposed three-fold symmetrical arrangement which is markedly different than that observed in the structures of 2,6-$F_2C_6H_3CN$−V(N[^{t}Bu]Ar)$_3$ and AdNC−V(N[^{t}Bu]Ar)$_3$. The V–$N_{nitrile}$ interatomic distance of 2.037(3) Å is comparable with the V–$N_{nitrile}$ distance of 2.044(2) Å observed in 2,6-$F_2C_6H_3CN$−V(N[^{t}Bu]Ar)$_3$. Compared with other known vanadium (III) η^1-nitrile complexes,[30,31] both of the adducts reported here show typical structural features. Interestingly, V(III) has been shown to be competent at binding nitriles in an η^2-fashion.[32] Hypothesizing that Me_2NCN might be in a rapid-equilibrium process between the η^1- and η^2-forms, we experimentally tested for the formation of the η^2-complex of V(N[^{t}Bu]Ar)$_3$ (which is expected to be diamagnetic) at low temperatures via ^{1}H NMR spectroscopy. At –80 °C, no diamagnetic species were observed. In fact, all complexes gave rise to paramagnetically shifted and broadened

resonances, and we hypothesize that the steric hindrance of the anilide ligands precludes nitriles from binding in a side-on fashion in this system.[1]

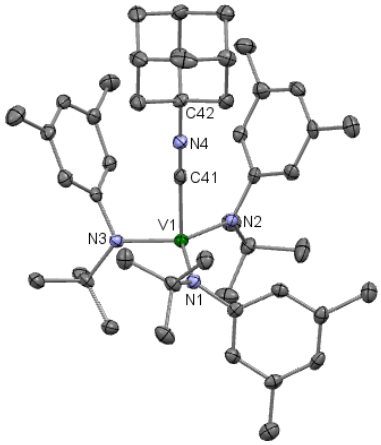

Figure 2.4. Thermal ellipsoid plot of AdNC−V(N[^{t}Bu]Ar)$_3$ shown at the 50 % probability level. Hydrogen atoms and disordered toluene have been omitted for clarity. Selected distances (Å) and angles (°):V1−N1 = 1.933(4), V1−N2 = 1.944(3), V1−N3 = 1.928(3), V1–C41 = 2.068(5), C41–N4= 1.159(5),V1–C41–N4 = 177.0(4), C41–N4–C42 = 175.7(4), N1−V1−N2 = 121.90(14), N1−V1−N3= 113.94(15), N2−V1−N3 = 120.21(14), N1−V1−C41 = 98.82(16), N2−V1−C41 = 92.96(16), N3−V1−C41 = 98.33(16). See ref 21 for further details.

The solid state structure of AdNC−V(N[^{t}Bu]Ar)$_3$ displays a similar coordination geometry to that observed for the 2,6-$F_2C_6H_3CN$−V(N[^{t}Bu]Ar)$_3$ adduct (avg. $N_{anilide}$–V–$C_{isonitrile}$ = 96.7(3)°; avg. $N_{anilide}$–V–$N_{anilide}$ = 118.7(3)°). The anilide ligands exhibit the same one-down, two-up arrangement, with typical V–$N_{anilide}$ bond lengths (avg. = 1.935(6) Å). The coordinated AdNC moiety is linear (V–C–N = 177.0(4)°) and the V−$C_{isonitrile}$ distance (2.068(5) Å) is slightly longer than the V−$N_{nitrile}$ bond lengths found for the structurally characterized nitrile adducts.

The C≡N distance in free AdNC has not been reported, but that of MeNC has (1.167 Å)[33] and is slightly longer than that found in the structure of AdNC−V(N[^{t}Bu]Ar)$_3$

(1.159 Å). The slightly shorter C≡N distance in the adduct, coupled with the FT-IR data (*vide infra*), suggests a lack of donation of electron density from the d_{xz} and d_{yz} orbitals on V to vacant π* orbitals on AdNC.[21]

2.3.2. Reactivity of η^1-nitrile adducts

With regard to reactivity, there is a stark difference between the (η^1-RCN)V(N[^{t}Bu]Ar)$_3$ complexes and the analogous adducts in the Mo(N[^{t}Bu]Ar)$_3$ system. The nitrile adducts of Mo(N[^{t}Bu]Ar)$_3$ have been found to possess significant unpaired electron density on the carbon atom of the nitrile ligand. As a result, the complexes were shown to undergo bimolecular coupling reactions and could be efficiently trapped by common radical sources (Figure 2.5).[18,34] In contrast, inner sphere one-electron oxidants react at the vanadium metal center to give vanadium(IV) products, [(η^1-RCN)V(N[^{t}Bu]Ar)$_3$]$^+$.[1,35] Similarly, inner sphere two-electron oxidants, such as O_2, react with V(N[^{t}Bu]Ar)$_3$ (in the presence of nitriles) at the metal center to give vanadium(V) products.[36]

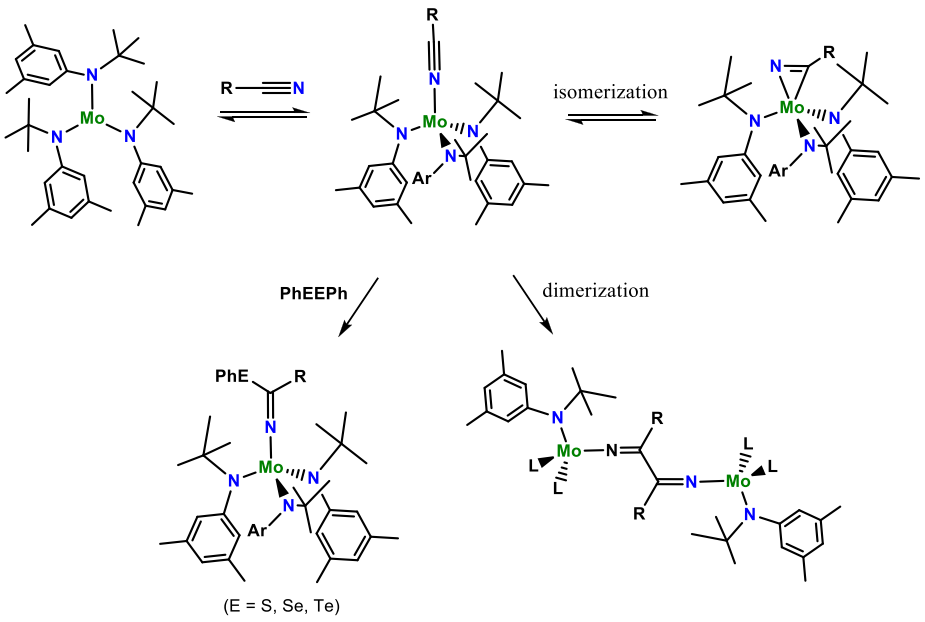

Figure 2.5. Reaction pathways observed for reactions of nitriles with Mo(N[^{t}Bu]Ar)$_3$.

It appears that the on-off equilibrium associated with nitrile binding allows for free V(N[^{t}Bu]Ar)$_3$ to be the dominant reactant in solution under the conditions tested. Attempts to shift the equilibrium in favor of the nitrile complexes (e.g., using excess nitrile or cooling the reaction mixtures), while successful from the thermodynamic and kinetic standpoint, gave similar results with respect to dominant reactivity (metal-centered rather than nitrile-centered). Furthermore, room temperature reaction of V(N[^{t}Bu]Ar)$_3$ with O_2 in the presence of excess ^{t}BuCN afforded the crystallographically characterized dioxygen adduct, (η^2-O_2)V(N[^{t}Bu]Ar)$_3$, and it is postulated that tempering of the O_2 reaction via weak nitrile coordination prevented undesirable side reactions, including oxygen atom transfer to a second molecule of V(N[^{t}Bu]Ar)$_3$ to form the vanadium(V) oxo species.[36]

2.3.3. Spectroscopic and Thermochemical Studies of Nitrile Binding

The IR spectra of both solid and toluene solution samples of selected RCN−V(N[^{t}Bu]Ar)$_3$ complexes contain the expected absorbance band around 2200 cm^{-1} assigned to the $\nu_{C\equiv N}$ stretching mode characteristic of η^1-bound nitriles[37] (Table 2.1), with only slight shifts between free and bound RCN that suggests little to no activation of the C≡N bonds. One electron oxidation of PhCN−V(N[^{t}Bu]Ar)$_3$ affords the V(IV) [PhCN−V(N[^{t}Bu]Ar)$_3$]$^+$ cation (*vide supra*),[1] which shifts $\nu_{C\equiv N}$ to higher frequency (2249 cm^{-1}) relative to the analogous V(III) adduct (2218 cm^{-1}) and is consistent with a decrease in π-back donation upon oxidation of the V center.

In contrast to V(III) nitrile adducts, Mo(III) nitrile complexes show significant shifts in $\nu_{C\equiv N}$, consistent with pronounced π-backbonding. The extent of backbonding also appears to depend on the nature of RCN. Particularly significant is the change in direction of $\nu_{C\equiv N}$ shifts due to nitrile coordination to V(N[^{t}Bu]Ar)$_3$; for the majority aromatic nitriles, the C≡N stretching frequency decreases, albeit minimally, as expected for π-backbonding, while the opposite trend is observed for aliphatic substrates (Me_2NCN and AdNC). Furthermore, aromatic nitriles bearing electron-withdrawing substituents favor backbonding while electron-donating substituents have the opposite effect. This trend is well illustrated by a pair of para-substituted benzonitriles: electron-rich 4-$Me_2N(C_6H_4)CN$ binds weakly to V(N[^{t}Bu]Ar)$_3$ and shifts $\nu_{C\equiv N}$ to higher frequency ($\Delta\nu_{C\equiv N}$ = 8 cm^{-1}) while electron-poor 4-$F_3C(C_6H_4)CN$ binds more strongly and displays a 10 cm^{-1} $\nu_{C\equiv N}$ shift to lower frequency. The effect is even more pronounced with strongly electron-withdrawing fluorine substituents: $\nu_{C\equiv N}$ for 2,6-$F_2C_6H_3CN$ shifts by −24 cm^{-1}, while F_5C_6CN results in a shift of −37 cm^{-1} upon binding to V(N[^{t}Bu]Ar)$_3$.

A large shift in $\nu_{C\equiv N}$ was noted for AdNC binding in the case of Mo(N[^{t}Bu]Ar)$_3$ ($\Delta\nu_{C\equiv N}$ = −367 cm^{-1}), consistent with the known tendency of this ligand to act as a π-acceptor. On the other hand, isonitrile coordination to V(N[^{t}Bu]Ar)$_3$ results in a shift to higher frequency ($\Delta\nu_{C\equiv N}$ = 22 cm^{-1}) that again suggests minimal contributions from π-backbonding in the case of vanadium.

Table 2.1. FT-IR spectroscopic data for binding of selected nitriles to M^{III}(N[^{t}Bu]Ar)$_3$ (M = V, Mo). Values reflect the η^1-binding mode unless otherwise specified.

	ν_{CN} (cm^{-1})			$\Delta\nu_{CN}$ (cm^{-1})[a]	
RCN or RNC	Free RCN or RNC	M = V	M = Mo	M = V	M = Mo
2,6-$F_2C_6H_3CN$	2242	2218	1962[b]	−24	−280
F_5C_6CN	2244	2207	2000 (br)	−37	−244
4-$F_3CC_6H_4CN$	2234	2224	2014	−10	−220
4-$Me_2NC_6H_4CN$	2216	2224	2019	8	−197
MesCN	2220[c]	-----	2023[c]	-----	−197
PhCN	2230	2218	2035[c]	−12	−195
Me_2NCN	2218	2256	1570[c]	38	−648
η^2-Me_2NCN	2218	-----	1650[c]	-----	−568
AdCN	2234	-----	2079[c]	-----	−155
AdNC	2129[d]	2151[d]	1762[e]	22	−367

[a] ν_{CN}(bound) − ν_{CN}(free). [b] Measured in C_6D_6. [c] Values taken from ref 18. [d] Value taken from ref 21. [e] Value taken from ref 40.

Thermodynamic data for reversible binding of 2,6-$F_2C_6H_3CN$ was also measured in toluene solution by variable temperature FT-IR. Representative spectral data are shown in Figure 2A.1 and a van't Hoff plot of these data in Figure 2A.2. Data were analyzed utilizing bands of both the complex and the free nitrile and a K_{eq} value of ≈ 72 M^{-1} was obtained at 20 °C. We also investigated the reversible nature of AdCN binding via spectrophotometric titration at elevated temperatures (10 to 40 °C). By monitoring the changes in absorbance of the AdCN−V(N[^{t}Bu]Ar)$_3$ product at λ = 688 nm (in toluene

solution) as a function of varying [AdCN], we estimated that $K_{eq} \approx 2{,}600$ at 20 °C (Figures 2.6 and 2A.3). The molar fraction of nitrile adduct also increases at lower temperatures (Figure 2A.4), which is in qualitative agreement with a moderately exothermic equilibrium binding. A binding enthalpy of −17 kcal mol^{-1} was estimated from this data (Figure 2A.5), however, the relatively narrow temperature range (10 to 40 °C) and potential decomposition of V(N[^{t}Bu]Ar)$_3$ in dilute solution outside of an inert atmosphere limit the accuracy of this value. Therefore, solution calorimetry measurements were undertaken where a large excess of AdCN was used to shift the equilibrium towards product; a value of $\Delta H = -12.6(5)$ kcal mol^{-1} was obtained and is accepted as the accurate value for this substrate. The experimental value is in reasonable agreement with the computed value of −10.5 kcal mol^{-1} (*vide infra*).

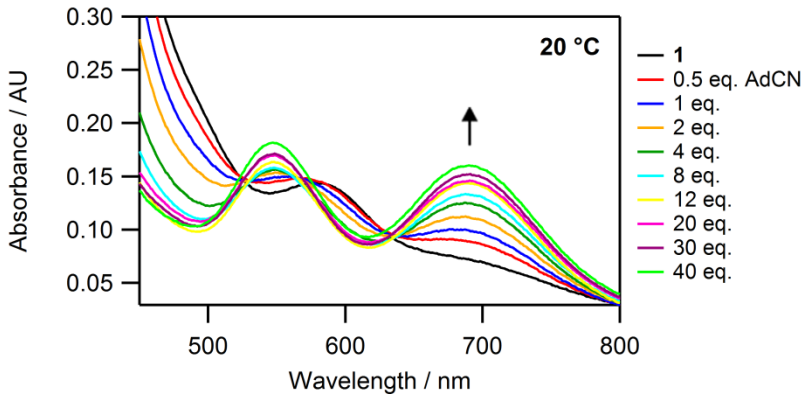

Figure 2.6. Spectrophotometric titration of AdCN (0.5 to 40 eq.) with V(N[^{t}Bu]Ar)$_3$ (0.2 mM) at 20 °C. A Benesi-Hildebrand plot for the spectrophotometric titration of AdCN at 20 °C yielded a derived value of $K_{eq} = 2{,}600$ M^{-1} for AdCN binding as shown in Figure 2A.3.

Relatively weak IR spectroscopic features for the adducts of PhCN, MesCN, and Me_2NCN prevented accurate determination of K_{eq} by vibrational spectroscopy, so direct

solution calorimetric measurements were performed. The thermodynamic data is collected in Table 2.2.

Table 2.2. Thermodynamic data (ΔH in kcal mol^{-1} and ΔS in cal mol^{-1} K^{-1}) for nitrile and AdNC binding in toluene solution to V(N[^{t}Bu]Ar)$_3$ collected via calorimetric measurements (PhCN, MesCN, Me_2NCN) or variable *T* FT-IR spectroscopic methods (2,6-$F_2C_6H_3CN$). The previously published data for Mo(N[^{t}Bu]Ar)$_3$ is provided for comparison.

	V(N[^{t}Bu]Ar)$_3$		Mo(N[^{t}Bu]Ar)$_3$[a]	
RCN/RNC	ΔH	ΔS	ΔH	ΔS
2,6-$F_2C_6H_3CN$	−9.5 ± 0.5	−22 ± 5	-----	-----
PhCN	−14.4 ± 1.5	-----	−14.5 ± 1.5	−40 ± 5
MesCN	−7.0 ± 1.8	-----	−15.4 ± 1.5	−52 ± 5
Me_2NCN	−16.4 ± 0.8[b]	-----	−22.0 ± 1.0[c]	-----
AdCN	−12.6 ± 0.5	−10 ± 7	−6 ± 2	−20 ± 7
AdNC	−17.1 ± 0.7	-----	−29.1 ± 0.5[d]	-----

[a] Values taken from ref 18 unless stated otherwise. [b] η^1-binding mode. [c] η^2-binding mode. [d] Value taken from ref 40.

In contrast to the apparent equilibrium binding of AdCN, the isomeric isonitrile AdNC binds to V(N[^{t}Bu]Ar)$_3$ quantitatively at room temperature in dilute solutions; maximum optical absorbance of the adduct is reached upon addition of 1 eq. of AdNC to V(N[^{t}Bu]Ar)$_3$ and no further changes in the spectra are observed with increasing concentrations of AdNC (Figure 2A.6). In this case, solution calorimetry measurements were feasible, and a value of −17.1(7) kcal mol^{-1} was obtained for the enthalpy of AdNC binding. The experimental value agrees well with the computed value of −18.3 kcal mol^{-1} (*vide infra*).

2.3.4. Kinetic Studies of Nitrile Binding

Reactions of $V(N[^tBu]Ar)_3$ with various nitriles were found to be surprisingly rapid even at low temperatures. The rapid binding kinetics of several nitriles (aromatic nitriles 2,6-$F_2C_6H_3CN$, PhCN, and MesCN, as well as aliphatic nitriles Me_2NCN, AdCN, and MeCN) to $V(N[^tBu]Ar)_3$ were investigated using stopped-flow methodology with spectrophotometric registration. The growth of absorption bands assigned to the η^1-nitrile adducts was observed in all reactions and nitrile binding was very clean and well-behaved. For example, the time-resolved spectra for 2,6-$F_2C_6H_3CN$ binding (Figure 2.7a) reveals significant build up at λ = 525 nm and λ = 687 nm. Similar spectral changes were observed for other aromatic nitriles; time-resolved spectra of PhCN binding revealed the formation of two peaks at λ = 490 nm and λ = 687 nm, and MesCN binding is characterized by the formation of two peaks at λ = 502 nm and λ = 705 nm (Appendix 2, Figures 2A.9 and 2A.11, respectively). Aliphatic nitriles, such as acetonitrile (MeCN) and adamantyl nitrile (AdCN), also bind rapidly to $V(N[^tBu]Ar)_3$, yielding purple adducts with distinct visible spectra. The time-resolved spectra for the reaction with Me_2NCN at −62 °C showed the decay of the absorption peak of $V(N[^tBu]Ar)_3$ at λ =580 nm concomitant with growth at λ = 560 nm and a lower energy transition at λ = 705 nm (Figure 2.7b). Very similar spectral changes were noted upon reactions of $V(N[^tBu]Ar)_3$ with the remaining aliphatic nitriles (MeCN and AdCN) as shown in Appendix 2 (Figures 2A.14 and 2A.16, respectively).

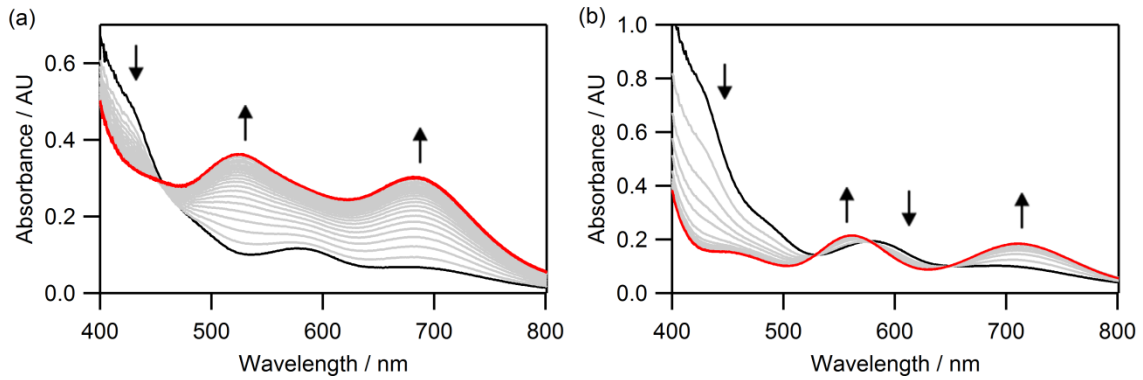

Figure 2.7. (a) Time-resolved spectral changes accompanying the reaction between V(N[^{t}Bu]Ar)$_3$ and 2,6-$F_2C_6H_3CN$ at −44 °C, acquired over 2 s. (b) Time-resolved spectral changes accompanying the reaction between V(N[^{t}Bu]Ar)$_3$ and Me_2NCN at −62 °C, acquired over 12 s. Selected traces are shown for clarity. The initially recorded spectrum is shown in black and the final spectrum in red.

Single wavelength measurements were necessary to quantify rapid nitrile binding to V(N[^{t}Bu]Ar)$_3$ at variable concentrations and temperatures (typically, −62 to −35 °C). The reactions became too fast to measure at higher temperatures and the low solubility of the nitrile adducts interfered with the stopped-flow experiments at lower temperatures; see Figure 2.8 for an example of kinetic traces recorded for aromatic nitrile binding via single wavelength mode. The kinetic traces were fit to either a single or double exponential function to yield observed rate constants, k_{obs}. In cases where double exponential fits were used, only k_{1obs} was found to depend on [nitrile] and thus was the only step analyzed. The randomness/irreproducibility in k_{2obs} appeared to be associated with decomposition of the highly air- and moisture-sensitive complex over time during stopped-flow experiments.

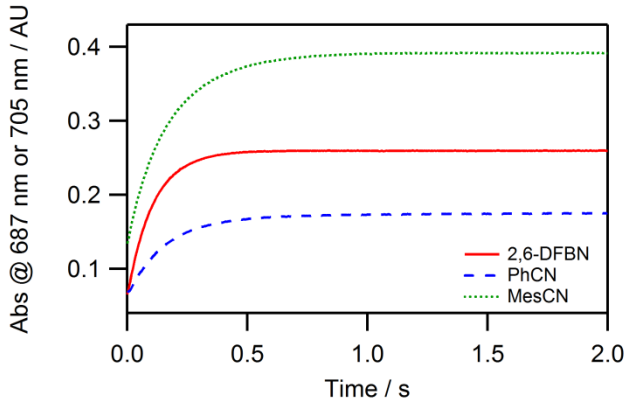

Figure 2.8. Single wavelength kinetic traces of aromatic RCN (1 mM) binding to V(N[^{t}Bu]Ar)$_3$ (0.3 mM) at −44 °C (2,6-$F_2C_6H_3CN$ and PhCN at λ = 687 nm; MesCN at λ = 705 nm).

Varying the concentration of the nitriles resulted in a systematic linear increase in k_{obs}. This behavior corresponds to the reaction of reversible nitrile binding to V(N[^{t}Bu]Ar)$_3$ as described by Eq. 2.1. For example, graphical analysis of k_{obs} vs. [2,6-$F_2C_6H_3CN$] reveals a linear relationship with the slope equal to k_{on} and an intercept corresponding to k_{off} as shown in Figure 2.9a. At lower temperatures, essentially zero intercept indicated that the equilibrium was completely shifted toward product formation. At higher temperatures (e.g., −44 and −35 °C for 2,6-$F_2C_6H_3CN$ in Figure 2.9a), the reverse reaction, nitrile dissociation, became noticeable.

$$V(N[^tBu]Ar)_3 + RCN \underset{k_{off}}{\overset{k_{on}}{\rightleftharpoons}} RCN{-}V(N[^tBu]Ar)_3 \qquad (2.1)$$

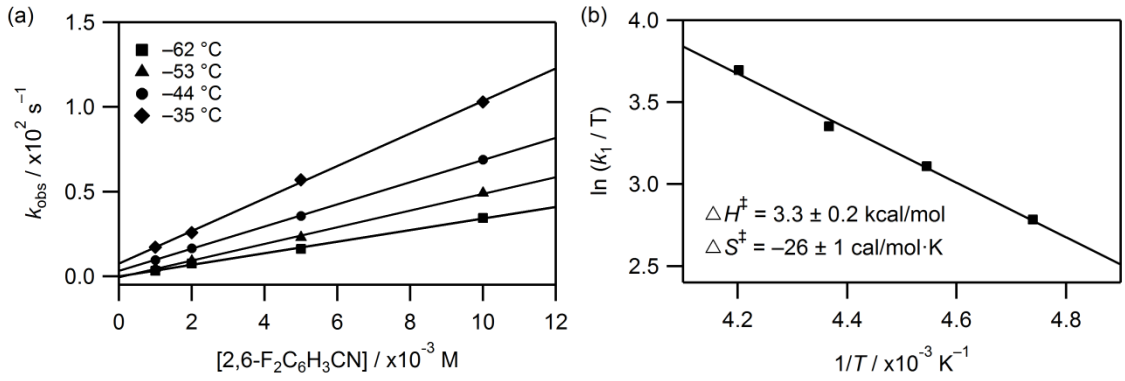

Figure 2.9. (a) Plot of k_{obs} versus [2,6-$F_2C_6H_3CN$] at various concentrations (1-10 mM) over a temperature range of −62 to −35 °C with [V(N[^{t}Bu]Ar)$_3$]$_0$ = 0.3 mM. (b) Eyring plot for 2,6-$F_2C_6H_3CN$ binding to V(N[^{t}Bu]Ar)$_3$ with derived activation parameters.

Rate constants derived from the data in Figure 2.9a, and analogous measurements for the series of nitriles studied are reported in Table 2.3 (additional data at other temperatures are available in Appendix 2). The accuracy in k_{off} values is relatively low, as these values are determined from the intercepts of the dependencies of k_{obs} on the concentrations of nitrile. Kinetic estimates of K_{eq} were thus not warranted from these data.

Table 2.3. Rate constants (k_{on} and k_{off}) for RCN and RNC binding to V(N[^{t}Bu]Ar)$_3$ at selected temperatures.

RCN or RNC	T (°C)	k_{on} (×10^3 M^{-1} s^{-1})	k_{off} (s^{-1})^a
2,6-$F_2C_6H_3CN$	−62	3.41 ± 0.12	-----
	−35	9.59 ± 0.18	7.6 ± 1.1
PhCN	−62	3.85 ± 0.06	---
	−35	10.1 ± 0.2	1.9 ± 1.3
MesCN	−62	1.39 ± 0.03	---
	−35	9.02 ± 0.21	3.3 ± 1.2
Me_2NCN	−62	3.72 ± 0.24	---
	−44	11.7 ± 0.7	1.1 ± 4.2

RCN or RNC	T (°C)	k_{on} ($\times 10^3$ M^{-1} s^{-1})	k_{off} (s^{-1})[a]
MeCN	−62	1.79 ± 0.06	---
	−35	13.7 ± 0.7	5 ± 4
AdCN	−62	0.919 ± 0.150	---
	−35	6.71 ± 0.02	1.5 ± 0.1
AdNC	−62	3.08 ± 0.09	---
	−35	11.8 ± 0.7	8.6 ± 3.8

[a] k_{off} values were estimated from the intercepts of the plots of k_{obs} vs. [RCN] or [RNC] at higher temperatures only; the intercepts were negligible at temperatures below −35 °C.

Activation parameters for nitrile binding were calculated from Eyring plots (see Figure 2.9b and Appendix 2 for remaining substrates). Activation enthalpies and entropies (Table 2.4) reflect a similar energy profile for all nitriles, with low activation barriers and fairly large negative values of activation entropies, which are expected for bimolecular binding. Similar values of activation parameters are typical for nitrile binding reactions to structurally related coordinatively unsaturated complexes.[17,18,38]

For direct comparison of electron-deficient aromatic nitrile binding to vanadium and molybdenum tris-anilide complexes, the kinetics of 2,6-$F_2C_6H_3CN$ coordination to $Mo(N[^tBu]Ar)_3$ was also studied (see Appendix 2), and revealed spectral changes and reaction rates very similar to the overall behavior of other aromatic nitriles (PhCN and MesCN) reported previously.[18,29,39]

Table 2.4. Comparison of bimolecular rate constants (k_1) and activation parameters measured for coordination of various nitriles and one isonitrile to M(N[^{t}Bu]Ar)$_3$ (M = V or Mo).

RCN or RNC		V(N[^{t}Bu]Ar)$_3$[a]	Mo(N[^{t}Bu]Ar)$_3$
PhCN[b]	k_1 (−40 °C) (M^{-1} s^{-1})	8,060	468 ± 22
	$\Delta H^{\ddagger}$ (kcal mol^{-1})	2.9 ± 0.6	5.2 ± 0.2
	$\Delta S^{\ddagger}$ (cal mol^{-1} K^{-1})	−28 ± 3	−24 ± 1
	$\Delta G^{\ddagger}$ (−40 °C) (kcal mol^{-1})	9.4	10.8
2,6-$F_2C_6H_3CN$	k_1 (−40 °C) (M^{-1} s^{-1})	7,470	316 ± 3
	$\Delta H^{\ddagger}$ (kcal mol^{-1})	3.3 ± 0.2	4.7 ± 0.4
	$\Delta S^{\ddagger}$ (cal mol^{-1} K^{-1})	−26 ± 1	−26 ± 2
	$\Delta G^{\ddagger}$ (−40 °C) (kcal mol^{-1})	9.4	10.8
MesCN[b]	k_1 (−40 °C) (M^{-1} s^{-1})	6,610	193 ± 14
	$\Delta H^{\ddagger}$ (kcal mol^{-1})	6.4 ± 0.3	5.0 ± 0.3
	$\Delta S^{\ddagger}$ (cal mol^{-1} K^{-1})	−13 ± 2	−26 ± 1
	$\Delta G^{\ddagger}$ (−40 °C) (kcal mol^{-1})	9.4	11.1
Me_2NCN[b]	k_1 (−40 °C) (M^{-1} s^{-1})	15,500	708[a,d]
	$\Delta H^{\ddagger}$ (kcal mol^{-1})	5.6 ± 0.3	6.4 ± 0.4[d]
	$\Delta S^{\ddagger}$ (cal mol^{-1} K^{-1})	−15 ± 1	−18 ± 2[d]
	$\Delta G^{\ddagger}$ (−40 °C) (kcal mol^{-1})	9.0	10.6
MeCN	k_1 (−40 °C) (M^{-1} s^{-1})	10,100	---
	$\Delta H^{\ddagger}$ (kcal mol^{-1})	7.2 ± 0.3	---
	$\Delta S^{\ddagger}$ (cal mol^{-1} K^{-1})	−9 ± 2	---
	$\Delta G^{\ddagger}$ (−40 °C) (kcal mol^{-1})	9.2	---
AdCN[b]	k_1 (−40 °C) (M^{-1} s^{-1})	5,090	97[a]
	$\Delta H^{\ddagger}$ (kcal mol^{-1})	6.7 ± 0.8	5 ± 1
	$\Delta S^{\ddagger}$ (cal mol^{-1} K^{-1})	−12 ± 4	−28 ±5
	$\Delta G^{\ddagger}$ (−40 °C) (kcal mol^{-1})	9.6	11.5
AdNC[e]	k_1 (−40 °C) (M^{-1} s^{-1})	10,100	16,000[a,d]
	$\Delta H^{\ddagger}$ (kcal mol^{-1})	4.6 ± 0.3	5.5 ± 0.5
	$\Delta S^{\ddagger}$ (cal mol^{-1} K^{-1})	−20 ± 1	−15 ± 4
	$\Delta G^{\ddagger}$ (−40 °C) (kcal mol^{-1})	9.2	9.0

[a] Rate constants at −40 °C were extrapolated or interpolated from Eyring plots. [b] Data for Mo(N[^{t}Bu]Ar)$_3$ taken from ref 18. [c] 2,6-DFBN = 2,6-$F_2C_6H_3CN$. [d] k_1 and activation parameters represent formation of the end-on (η^1) adduct. [e] Data for Mo(N[^{t}Bu]Ar)$_3$ taken from ref 40.

Interestingly, sterically hindered nitriles such as AdCN and MesCN still bind rapidly to V(N[^{t}Bu]Ar)$_3$ at low temperatures, but this is now due to a less unfavorable activation entropy. Binding of these bulky nitriles appears to be governed solely by steric effects, which can play a major role for the smaller vanadium(III) ion as discussed further in Section 2.4.

In order to compare the rates of nitrile versus isonitrile binding to V(N[^{t}Bu]Ar)$_3$, stopped-flow kinetic experiments were also performed with AdNC. Time-resolved spectral changes and overall kinetics were remarkably similar to those observed for aliphatic nitrile binding (Figure 2.10) and revealed a rapid second order process which is somewhat faster for AdNC than for AdCN. In contrast to nitrile binding, coordination of AdNC to V(N[^{t}Bu]Ar)$_3$ proved to be essentially irreversible over a broad temperature range (*vide supra*). Reaction of the molybdenum tris-anilide complex with AdNC was reported previously,[40] and the kinetic parameters associated with AdNC binding to M(N[^{t}Bu]Ar)$_3$ (M = Mo, V) are also provided in Table 2.4.

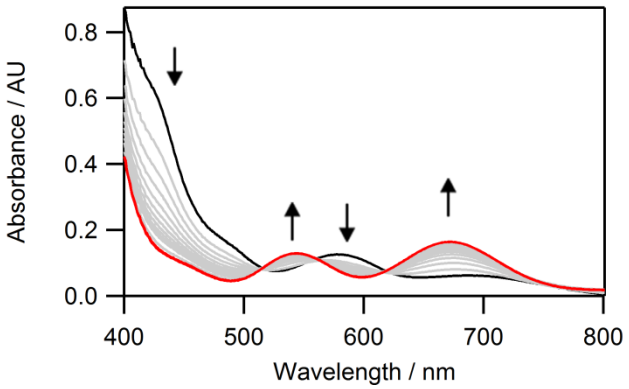

Figure 2.10. Time-resolved spectral changes accompanying the reaction between V(N[^{t}Bu]Ar)$_3$ (0.3 mM) and AdNC (1 mM) at −62 °C, acquired over 9 s. Selected traces shown for clarity. Initial spectrum is shown in black and final spectrum in red.

2.3.5. Computational Studies

DFT calculations were performed for a series of RCN−M(N[^{t}Bu]Ar)$_3$ complexes (M= V, Mo) in an effort to gather more knowledge about the structure of the adducts and nature of the M–$N_{nitrile}$ bond. A summary of selected calculated bond lengths and angles is collected in Appendix 2, Tables 2A.9 and 2A.10. The most stable configuration for V(N[^{t}Bu]Ar)$_3$ is formulated as a high spin d^2 species. As discussed in Chapter 1, calculations predict that the conformation exhibits one close aryl contact that is lower in energy by 4.1 kcal mol^{-1} than the corresponding conformation without this sort of η^3-allylic interaction.[41] The same structural feature has been observed previously in the crystal structure of the related V(N[Ad]Ar)$_3$ complex.[42]

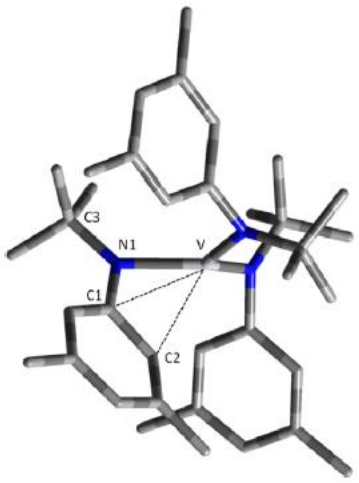

Figure 2.11. Optimized structure of V(N[^{t}Bu]Ar)$_3$ at the bp86/6-311G(d,p) (MDF10 for V with an additional set of f functions) level. Selected interatomic distances (Å) and angles (°): V−C1 = 2.45, V−C2 = 2.42, V−N1−C1 = 92.1, V−N1−C3 = 138.3, C1−N1−C3 = 124.6, Σ(N−V−N) = 356.1.

For the 2,6-$F_2C_6H_3$CN−V(N[^{t}Bu]Ar)$_3$ and Me_2NCN−V(N[^{t}Bu]Ar)$_3$ adducts, the computed and experimental geometries obtained from X-ray crystallographic studies are

in good agreement. DFT calculations predict that the most stable conformers in the η^1-RCN−V(N[^{t}Bu]Ar)$_3$ adducts exhibit the one-down, two-up arrangement mentioned previously, where two of the anilide phenyl rings are positioned in proximity to the bound nitrile to alleviate steric crowding. In contrast, the most stable conformers present normally in the η^1-RCN−Mo(N[^{t}Bu]Ar)$_3$ cases exhibit just one "up" oriented anilide. Interestingly, the structure of Me_2NCN−V(N[^{t}Bu]Ar)$_3$ calculated with the one-down, two-up arrangement is enthalpically more stable than the one obtained by X-ray crystallography. Packing forces could be responsible for this phenomenon.

Although the V(III) ion is smaller than Mo(III),the M–$N_{nitrile}$ bond is shorter for all η^1-nitrile complexes in the Mo system, indicating a more favorable metal-nitrile interaction. Furthermore, the N≡C nitrile bond is elongated when M = Mo, suggesting a more effective backbonding from the metal in this case.

The M–N–C fragments as well as the N–C–R moieties in the nitrile adducts of vanadium are essentially linear for all the η^1-RCN–V(N[^{t}Bu]Ar)$_3$ complexes studied. In contrast, for M = Mo and RCN = MeCN (142.0°), Me_2NCN (127.7°), AdCN (154.9°) and to a lesser extent 4-$Me_2NC_6H_4CN$ (168.9°), calculations predict a considerable deviation from linearity in the N–C–R arrangement. In fact, 4-$Me_2NC_6H_4CN$−Mo(N[^{t}Bu]Ar)$_3$ is more reactive towards dimerization than 4-$F_3CC_6H_4CN$−Mo(N[^{t}Bu]Ar)$_3$[18] in spite of having similar Mulliken spin densities at the $C_{nitrile}$ atom (see Appendix 2, Table 2A.12). This seems to indicate that the deviation from linearity in the N–C–R angle enhances the reactivity toward dimerization (or the reactivity of coordinated nitrile with other coupling partners) as was suggested in our previous work.[18]

DFT predictions of the binding enthalpy for all adducts studied are collected in Table 2.5 and there is reasonable agreement between the experimental and calculated values. The binding enthalpies for the Mo(III) complexes are in general higher than the corresponding values for the V(III) adducts. Moreover, binding of aryl nitriles containing electron-withdrawing groups appears more thermodynamically favorable, a phenomenon that is much more apparent in the case of M = Mo. For example, the difference in energy of binding between 4-$F_3CC_6H_4CN$ and 4-$Me_2NC_6H_4CN$ is 6.4 kcal mol^{-1} when M = Mo, whereas the same difference is just 1.8 kcal mol^{-1} when M = V.

Table 2.5. Comparison of calculated and experimental binding enthalpies (ΔH in kcal mol^{-1}) for nitrile and AdNC binding to M(N[^{t}Bu]Ar)$_3$ (M = V, Mo). Values reflect the η^1 binding mode unless stated otherwise.

	V(N[^{t}Bu]Ar)$_3$		Mo(N[^{t}Bu]Ar)$_3$	
RCN	calc	exp	calc	exp
2,6-$F_2C_6H_3CN$	−14.3	−9.5 ± 0.5	−20.8	-----
F_5PhCN	−15.3	-----	−22.8	-----
4-$F_3CC_6H_4CN$	−15.2	-----	−20.8	-----
PhCN	−13.7	−14.4 ± 1.5	−16.3	−14.5±1.5[a]
4-$Me_2NC_6H_4CN$	−13.4	-----	−14.4	-----
η^2-Me_2NCN	−14.8	-----	−23.2	−22.0±1.0[a]
Me_2NCN	−12.7	−16.4 ± 0.8	−20.1	-----
η^2-MeCN	−2.6	-----	−11.2	-----
MeCN	−11.1	-----	−11.9	-----
AdCN	−10.5	−12.6 ± 0.5	−8.7	−6 ± 2[a]
AdNC	−18.3	−17.1 ± 0.7	−32.9	−29.1 ± 0.5[b]

[a] Experimental values taken from ref 18. [b] Experimental value taken from ref 40.

Regarding the η^1- versus η^2-Me_2NCN−M(N[^{t}Bu]Ar)$_3$ structures, the η^2-conformers were found to be enthalpically more stable (by 2.1 kcal mol^{-1} for V and 3.1 kcal mol^{-1} for Mo). However, the solid-state structure of Me_2NCN−V(N[^{t}Bu]Ar)$_3$ as

determined by X-ray crystallography unequivocally shows an η^1-coordination mode for the cyanamide ligand. In spite of the η^2-conformer having a more favorable enthalpy according to calculations, a less favorable entropy should be expected for formation of the side-on complex, and the entropic effect could be responsible for this discrepancy.

Mulliken spin densities calculated at the BP86/6-311G(d,p) (MWB28 for Mo and MDF10 for V with an additional set of f functions) level of theory (Table 2A.12) reveal that the spin densities are mainly located at the metal for all vanadium-nitrile complexes. However, a large contribution in the nitrile C atom (> 0.20) was generally obtained. This spin localization in the carbon accounts for the observed C radical character and therefore the reactivity previously observed for the RCN−Mo(N[^{t}Bu]Ar)$_3$ complexes.[29,39] The Mulliken spin density located on the C of the nitrile is similar in the Mo and V complexes, although somewhat higher in the V derivatives. In spite of this, the radical reactivity is more pronounced in the Mo complexes; they dimerize or react with coupling partners easily and this kind of reactivity was not observed for the V analogues. In addition, there is not a large delocalization of the spin density in the arene ring of the adducts of the aromatic nitriles. However, the C_{para} exhibits a higher radical character in the V compounds, and it increases as the electron-accepting power of the nitrile increases.

2.4. Discussion

V(N[^{t}Bu]Ar)$_3$ provided an excellent opportunity to explore the thermodynamics and kinetics of nitrile and isonitrile binding to a low-valent, coordinatively unsaturated 3*d*

metal center, and to compare these data with the analogous Mo(N[^{t}Bu]Ar)$_3$ complex. A range of aromatic and aliphatic nitriles displayed simple 1:1 coordination to V(N[^{t}Bu]Ar)$_3$, affording end-on (η^1) adducts, some of which were crystallographically characterized. Furthermore, nitrile adducts of V(N[^{t}Bu]Ar)$_3$ are rather stable and do not undergo radical couplings at the nitrile carbon. This behavior is different from that observed in reactions of nitriles with Mo(N[^{t}Bu]Ar)$_3$, where initial end-on binding was often followed by subsequent isomerization to a more thermodynamically stable side-on (η^2) adduct and/or by radical couplings of the coordinated nitriles.[18,34,39] Relatively simple reactivity modes observed for nitrile coordination to V(N[^{t}Bu]Ar)$_3$ allowed us to gain insights into the initial nitrile binding events and to characterize them quantitatively using stopped-flow methodology. A direct comparison of nitriles of varying size (MeCN vs. AdCN) became possible, as well as the coordination of nitriles of similar size with different electronic structures and propensities to bind side-on (MeCN vs. Me$_2$NCN). Trends established for aliphatic nitriles could be extended to aromatic nitriles: electronic effects were unraveled by studying the coordination of unsubstituted benzonitrile, PhCN, in comparison with electron-poor difluorobenzonitrile (2,6-F$_2$C$_6$H$_3$CN) or electron-rich mesitylnitrile (MesCN). Incorporating flourine, or especially, methyl substituents in the 2,6-positions of the aromatic ring was also expected to enhance the steric bulk of the incoming ligand.

2.4.1. Electronic Factors in Substrate Binding

Electronic differences between molybdenum and vanadium resulted in somewhat different structures of the starting tris-anilide complexes. The availability of an empty

orbital in the triplet vanadium(III) system allows for an additional allylic interaction with one of the anilide aryl rings. This interaction must be removed prior to coordination of additional ligands (such as nitriles); the computed energy difference between the structure with a vacant site at vanadium and the structure with a "masked" site in the aryl-bound form is 4.1 kcal mol^{-1}. This enthalpic penalty would be partially offset by a favorable entropic contribution due to increased flexibility of anilide substituents. Ligand binding to a vanadium(III) vacant site is expected to occur with very low barrier, although rearrangement of the anilide framework may be needed to accommodate sterically bulky substituents.

The case of $Mo(N[^tBu]Ar)_3$ is different since the ground state is a quartet, and thus contains an unpaired electron in each of the metal orbitals. Therefore, in order for binding of an additional ligand, two of the electrons must pair up. Despite the availability of the unmasked coordination site, the required change in spin state would result in an energetic penalty. The nearly constant enthalpic barrier found for ligand binding in the Mo case is due to the fact that the quartet potential energy surface is repulsive and a minimum energy crossing point (MECP) between both potential energy surfaces (quartet and doublet) has to be reached. After that point, apart from steric constraints, essentially no energetic barrier should be expected for ligand binding.

Electronic differences between molybdenum and vanadium also influence the structures of nitrile adducts and the nature of metal-nitrile interactions. Despite the larger atomic size of molybdenum, computed $Mo–N_{nitrile}$ bond lengths are shorter than the corresponding distances in the vanadium structures (Appendix 2, Tables 2A.9 and 2A.10), indicating stronger $Mo–N_{nitrile}$ bonds due to more favorable π-backbonding. This

is in agreement with calculated C≡N bond distances as well, which are considerably lengthened in molybdenum complexes (e.g., from 1.169 to 1.200 Å in free vs. coordinated PhCN, respectively). This effect is less pronounced in vanadium complexes, where coordinated nitrile C≡N bond lengths (≈ 1.18 Å computed; ≈ 1.15 Å for experimentally determined structures) are much closer to the free C≡N lengths.

The different degrees of π-backbonding in Mo(III) versus V(III) nitrile adducts is also supported by the experimentally observed shifts in IR frequencies upon nitrile coordination to M(N[^{t}Bu]Ar)$_3$ complexes, which are significantly smaller for V than for Mo (Table 2.1). In addition, the experimental $\nu_{C\equiv N}$ for PhCN−Mo(N[^{t}Bu]Ar)$_3$ (2035 cm^{-1}) is similar to that reported for the radical anion of *p*-dimethylaminobenzonitrile in the gas phase (2040 cm^{-1} for the triplet state; 2096 cm^{-1} for the singlet),[43] which is in keeping with formulation of PhCN−Mo(N[^{t}Bu]Ar)$_3$ as a bound nitrile radical anion. Despite the observed preference of V(N[^{t}Bu]Ar)$_3$ to engage in σ-donor interactions with incoming nitriles, the complex reacts readily with 1-adamantyl isonitrile (AdNC), a ligand that tends to preferentially engage in π-acceptor interactions with metal centers. Interestingly, $\nu_{C\equiv N}$ for AdNC−V(N[^{t}Bu]Ar)$_3$ is shifted to higher frequency as compared to free AdNC, and the solid state structure displays a linear geometry for the bound substrate with a shortened N≡C bond. Collectively, these observations suggest that little to no electron transfer occurs from vanadium to the isonitrile ligand.[21]

2.4.2. Thermodynamics of Substrate Binding

Nitrile binding to V(N[^{t}Bu]Ar)$_3$ is generally less exothermic than nitrile binding to its Mo(III) counterpart (Table 2.5). Calculations also predict similar binding energies

for electron-rich or electron-poor aromatic nitriles with V(N[^{t}Bu]Ar)$_3$, whereas nitrile binding to Mo(N[^{t}Bu]Ar)$_3$ is more sensitive to electronic effects (e.g., binding of electron-withdrawing 2,6-$F_2C_6H_3CN$ is more exothermic than PhCN binding). Experimentally, steric effects appear to dominate in aromatic nitrile binding to V(N[^{t}Bu]Ar)$_3$. Incorporating either electron-withdrawing or electron-donating substituents on the phenyl ring of the nitrile decreases the enthalpy of binding of aromatic nitriles to V(N[^{t}Bu]Ar)$_3$ from −14.4 ± 1.5 kcal mol^{-1} for PhCN to −9.5 ± 0.5 kcal mol^{-1} for 2,6-$F_2C_6H_3CN$, and to −7.0 ± 1.8 kcal mol^{-1} for MesCN. Aliphatic nitriles also bind to V(N[^{t}Bu]Ar)$_3$ readily, and their binding affinities appear comparable to that of aromatic nitriles. Sterically hindered AdCN displayed equilibrium binding at room temperature, which is indicative of weaker complexation, however, calorimetric measurements afforded a moderately exothermic binding enthalpy of −12.6 kcal mol^{-1}. It appears that less favorable binding entropy for this bulky ligand is responsible for the lower free energy changes. Interestingly, the bulky aliphatic isonitrile, AdNC, binds to V(N[^{t}Bu]Ar)$_3$ with a fairly large enthalpy of −17.1 kcal mol^{-1}.[21] Still, coordination of AdNC to Mo(N[^{t}Bu]Ar)$_3$ is significantly more exothermic (−29.1 kcal mol^{-1})[40] as expected for the molybdenum complex with preference for π-backbonding with incoming ligands. In this case, the $\nu_{C\equiv N}$ is shifted over 400 cm^{-1} to lower frequency and the isonitrile ligand adopts a bent rather than linear geometry, a behavior clearly different from the one observed in the vanadium analogue.

The allylic interaction between one of the aryl rings of the anilide ligands and the metal center in V(N[^{t}Bu]Ar)$_3$ should be taken into account when the strength of ligand binding to V(N[^{t}Bu]Ar)$_3$ is compared to the strength of ligand binding to Mo(N[^{t}Bu]Ar)$_3$,

which lacks this interaction.[10,11] Correcting for the enthalpy of the allylic interaction in V(N[^{t}Bu]Ar)$_3$ (−4.1 kcal mol^{-1}) results in M−N$_{nitrile}$ bond energies that are slightly greater for V(N[^{t}Bu]Ar)$_3$ than Mo(N[^{t}Bu]Ar)$_3$ for all but electron-poor nitriles, a trend that seems to contradict the shorter (calculated) Mo−N$_{nitrile}$ bond distances. However, the loss of M−N$_{anilide}$ π-donation in the nitrile-bound complexes relative to the starting complexes is expected to be greater for Mo(N[^{t}Bu]Ar)$_3$ since the distortion from the trigonal planar structures of M(N[^{t}Bu]Ar)$_3$ upon nitrile binding is less pronounced in the case of the vanadium derivatives.

Breaking of the vanadium-aryl interaction upon nitrile binding to V(N[^{t}Bu]Ar)$_3$ also affects the entropy of ligand binding. The smaller than expected unfavorable entropy of binding of nitriles to V(N[^{t}Bu]Ar)$_3$ as compared to Mo(N[^{t}Bu]Ar)$_3$ likely results from increasing the flexibility of the anilide substituents of V(N[^{t}Bu]Ar)$_3$ when the vanadium-aryl interaction is broken in the course of nitrile coordination. Steric bulk of the incoming nitrile affects primarily the enthalpy of nitrile binding to the vanadium complex (e.g., the difference in Δ*H* for PhCN and MesCN binding is large). In contrast, steric effects on the thermodynamics of nitrile binding to Mo(N[^{t}Bu]Ar)$_3$ are primarily entropic in nature; the adduct of MesCN is less stable than the adduct of PhCN due to unfavorable entropic contributions from anilide ligand rearrangements that are necessary to accommodate incoming bulky nitrile.[40]

2.4.3. Kinetics of Substrate Binding

Although nitrile binding to V(N[^{t}Bu]Ar)$_3$ is thermodynamically less favorable, it occurs nearly two orders of magnitude faster than nitrile binding to Mo(N[^{t}Bu]Ar)$_3$ in

spite of the necessity to break the interaction of the pendant arene to the vanadium center. No spin state changes occur in the case of vanadium; in contrast, the quartet ground state of Mo(N[^{t}Bu]Ar)$_3$ changes to a doublet in the process of nitrile coordination, which may contribute to slowing down the reaction. Nitrile binding to V(N[^{t}Bu]Ar)$_3$ was found to proceed rapidly even at low temperatures and detailed kinetic studies revealed a second order process with similarly large values of rate constants for coordination of several different nitriles (Table 2.3). For example, the second order rate constants range from 5,090 M^{-1} s^{-1} to 15,500 M^{-1} s^{-1} at −40 °C, with aliphatic nitriles reacting slightly faster than aromatic nitriles (with the exception of AdCN, which reacted the slowest). The slightly slower rates of binding of aromatic nitriles appear to arise primarily from steric effects created by the nitrile phenyl rings. Placing substituents on the aromatic rings slows down nitrile coordination regardless of their electron-donating- or withdrawing properties; both electron-poor 2,6-$F_2C_6H_4CN$ and electron-rich MesCN bind to V(N[^{t}Bu]Ar)$_3$ somewhat slower than unsubstituted PhCN. The dominant role of steric effects in controlling the rates of nitrile binding to V(N[^{t}Bu]Ar)$_3$ is even more apparent in the series of aliphatic nitriles, where the bulky AdCN substrate cuts the reaction rate in half as compared to the reaction with MeCN.

Differences in the electronic structures of MeCN and Me_2NCN that were sufficient to change the preferential coordination mode of the latter nitrile in reactions with Mo(N[^{t}Bu]Ar)$_3$ had very small effects on the rates and outcome of nitrile reactions with V(N[^{t}Bu]Ar)$_3$.

Isonitriles, which are electronically different from nitriles, also bind to V(N[^{t}Bu]Ar)$_3$ rapidly. Interestingly, coordination of AdNC is irreversible and occurs ca.

two times faster than coordination of AdCN. In general, ligand binding rates at the vacant sites in transition metal complexes are primarily governed by steric rather than electronic factors; in contrast, ligand dissociation rates are much more sensitive to the electronic structure of the coordinated monodentate ligand, and dissociation rates tend to increase as the metal-ligand bond strength decreases.[3,44] However, electronic effects in ligand binding rates become apparent when AdNC coordination to V(N[^{t}Bu]Ar)$_3$ is compared with Mo(N[^{t}Bu]Ar)$_3$. Despite the faster binding rates of nitriles to the vanadium tris-anilide complex, isonitrile binding is somewhat faster for molybdenum tris-anilide (Table 2.4). This trend originates from the much larger change in relative rates of RCN and RNC binding for molybdenum(III) and is attributable to the tendency of Mo(N[^{t}Bu]Ar)$_3$ to participate in π-bonding with the incoming isonitrile. Doublet PES is more attractive in the case of AdNC addition than in the case of RCN addition and thus MECP is located at lower energy.

Additional insights into the mechanisms of ligand binding to M(N[^{t}Bu]Ar)$_3$ can be obtained by analyzing the activation parameters for these reactions (Table 2.4). While large differences in the rate constants for nitrile binding to V(N[^{t}Bu]Ar)$_3$ and Mo(N[^{t}Bu]Ar)$_3$ were observed, the corresponding differences in activation enthalpies are small. Indeed, a 10-fold increase in the rate constant can be achieved with a decrease in reaction barrier of only 1-2 kcal mol^{-1}. The values of $\Delta G^{\ddagger}$ (−40 ºC) provided in Table 2.4 (calculated from experimental values of $\Delta H^{\ddagger}$ and $\Delta S^{\ddagger}$) are nearly constant for nitrile addition to V(N[^{t}Bu]Ar)$_3$ (9.0 - 9.6 kcal mol^{-1}) and are ca. 1-2 kcal mol^{-1} lower than Mo(N[^{t}Bu]Ar)$_3$ (10.6 - 11.5 kcal mol^{-1}), in line with the observed 10- to 100-fold difference in measured second order rate constants. Tracing these energetic differences to

enthalpic versus entropic contributions is difficult, in view of relatively low accuracy in determining activation entropies and widespread enthalpy-entropy correlations. Nevertheless, it is useful to point out some trends in activation parameters. The higher activation enthalpies found for the coordination of bulky aromatic nitriles is likely related to the rearrangement of the tris-anilide framework required for accommodating the incoming substrate. For example, the crystal structure of 2,6-$F_2C_6H_3CN{-}V(N[^tBu]Ar)_3$ (Figure 2.3) demonstrates how the anilides can rotate away from their original positions (see Figure 2.11). Coordination of aliphatic nitriles to $V(N[^tBu]Ar)_3$ appears to be characterized by somewhat higher activation enthalpies (ca. 7 kcal mol^{-1} for MeCN and AdCN) that are generally compensated by less negative activation entropies. In general, faster nitrile binding to $V(N[^tBu]Ar)_3$ as compared to $Mo(N[^tBu]Ar)_3$ can be attributed, in most cases, to differences in the activation enthalpy, which tends to be smaller for vanadium.

Available kinetic data for low-valent vanadium are limited to early studies on ligand substitution in vanadium carbonyls,[45] qualitative NMR evidence of kinetic lability of vanadium(III) isonitriles provided by Lippard et al.,[46] and relatively rapid associative ligand substitution of carboxylates and aminocarboxylates at V(III) in aqueous solutions.[47]

Faster nitrile ligand binding to vanadium(III) as compared to molybdenum(III) may also be explained by the different population of *d*-orbitals in these metal ions; an additional orbital vacancy exists with V(III) (d^2) but not with Mo(III) (d^3) centers. A similar trend can be illustrated with the solvent exchange rates and activation parameters of the aqua complexes. Water exchange rates for aqua complexes of Mo(III) and V(III), *k*

= 5 × 10^{-3} s^{-1} and 500 s^{-1}, respectively, shows that the process is several orders of magnitude slower for $Mo(III)_{aq}$ than for $V(III)_{aq}$.[3] Direct comparison between ligand exchange in molybdenum and vanadium complexes is only possible for low valent carbonyl complexes; activation parameters associated with ligand exchange rates for $M(CO)_6$ (M = Mo, V) with PBu_3 were $\Delta H^{\ddagger}$ = 21.6 kcal mol^{-1} and $\Delta S^{\ddagger}$= −7 cal mol^{-1} K^{-1} for Mo, and $\Delta H^{\ddagger}$ = 7.7 kcal mol^{-1} and $\Delta S^{\ddagger}$ = −25.2 cal mol^{-1} K^{-1} for V.[48,49] The enthalpic barrier for ligand exchange with $V(CO)_6$ is smaller by more than 10 kcal mol^{-1} and both activation entropies are negative, suggestive of an associative mechanism. These data indicate significantly faster ligand binding as well as more favorable energetics for coordination of monodentate ligands to V over Mo. While these general trends hold for the addition of a nitrile to the bulky tris-anilide complexes studied in this work, the differences in the reaction rates in vanadium vs. molybdenum tris-anilide systems is much smaller. It appears that ligand binding to sterically hindered metal centers is regulated primarily by the accessibility of the metal center, while the electronic effects due to the differences in the *d*-orbital population in molybdenum(III) and vanadium(III) complexes becomes somewhat less important. An additional factor that may slow down ligand binding to $V(N[^tBu]Ar)_3$ is the need to break the V-aryl allylic interaction in order to accommodate the incoming nitrile. In the absence of the ground state stabilization of $V(N[^tBu]Ar)_3$, an even greater rate enhancement for ligand coordination to vanadium(III) compared to molybdenum(III) can be expected.

The indirect consequence of weaker, but faster nitrile coordination to V(III) is much faster nitrile dissociation from vanadium complexes. Short residence time of coordinated nitriles could account for metal-based rather than nitrile-based reactivity with

externally added oxidants or radical coupling partners. End-on nitrile adducts with Mo(III) anilides displayed sufficient thermodynamic and kinetic stability, which allowed us to take advantage of radical-like character of the $C_{nitrile}$ atom and to prepare a series of ketimidate products of Mo(III)-assisted radical couplings.[18,34,39] A better understanding of the thermodynamics and kinetics of nitrile binding to vanadium(III) complexes will allow for rational selection of synthetic systems amenable to controlled coordination of small molecules to a single vanadium center (similar to room temperature nitrile-assisted isolation of the side-on dioxygen adduct of $V(N[^tBu]Ar)_3$).[36] Alternatively, selective two-electron functionalization of coordinated ligands may also become possible (similar to the low temperature oxygenation of the bound nitrile in the $^tBuCN{-}V(N[^tBu]Ar)_3$ complex by O_2).[36] Additional studies in this area remain in progress.

2.5. Conclusion

In summary, nitrile binding to $V(N[^tBu]Ar)_3$ is dominated by σ-donor interactions while π-backbonding plays an important role in the case of $Mo(N[^tBu]Ar)_3$. Nevertheless, very rapid and exothermic binding of AdNC, a well-known π-accepting ligand, to $V(N[^tBu]Ar)_3$ was still observed. The more pronounced electrophilic character of the d^2 V(III) ion accounts for the tendency of vanadium to undergo very rapid ligand exchange reactions. The observed ca. 100-fold faster nitrile coordination to $V(N[^tBu]Ar)_3$ as compared to $Mo(N[^tBu]Ar)_3$ follows this expected trend, but is nevertheless remarkable, because second order rate constants exceeding 10^4 $M^{-1}s^{-1}$ were observed at low temperatures (from −60 to −40 °C), and reactions were often complete in less than a

second. Unexpectedly, bulky substituents on anilide ligands did not suppress rapid access of incoming nitrile molecules to $V(N[^tBu]Ar)_3$. Similar reaction rates and activation parameters were found for a series of aromatic and aliphatic nitriles and relatively small differences in nitrile reactivity with $V(N[^tBu]Ar)_3$ are attributed to steric rather than electronic effects. Crystal structures of selected RCN−$V(N[^tBu]Ar)_3$ complexes illustrate that rotation of one of the anilide ligands help accommodate the incoming nitrile molecule. While AdNC binds rapidly to $V(N[^tBu]Ar)_3$, binding to $Mo(N[^tBu]Ar)_3$ is even faster for this substrate, reversing the typical V > Mo trend for relative rates of ligand binding to these two metal centers. The availability of d-orbitals for π-backbonding at Mo(III) is likely responsible for unusually fast coordination of isonitriles to $Mo(N[^tBu]Ar)_3$.

Intrinsic differences in ligand binding rates at molybdenum versus vanadium centers uncovered in this work may have implications for ligand binding to other classes of molybdenum and vanadium complexes, as well as molybdenum- and vanadium-containing nitrogenases. Specifically, lower activity of vanadium nitrogenase cannot be explained by slower ligand binding rates, since low-valent vanadium centers show facile reactivity with molecules containing element-nitrogen triple bonds, and outperform their molybdenum counterparts in terms of rates and activation parameters of ligand binding. It is clear from this work that steric protection of vanadium centers does not shut down or significantly retard ligand binding events. Further detailed studies of vanadium-promoted reactivity of nitriles and isonitriles are underway.

2.6. References

(1) *This chapter is reproduced in part with permission from:* Palluccio, T. D.; Germain, M. E.; Silvia, J. S.; Cummins, C. C.; Temprado, M.; Rybak-Akimova, E. V.; Hoff, C. D. Diagonal Relationships in Ligand Binding: Nitrile and Isonitrile Coordination to Vanadium and Molybdenum Tris-Anilide Complexes. *Manuscript in preparation*.

(2) (a) Rehder, D. *Coord. Chem. Rev.*, **1999**, *182*, 297. (b) Rayner-Canham, G. *Found. Chem.*, **2011**, *13*, 121.

(3) Tobe, M. L.; Burgess, J. *Inorganic Reaction Mechanisms*; Addison Wesley Longman Inc.: New York, 1999.

(4) Atwood, J. D. *J. Organometallic Chem.*, **1990**, *383*, 59.

(5) Eady, R. R. *Chem. Rev.*, **1996**, *96*, 3013.

(6) Lee, C. C.; Wiig, J. A.; Ribbe, M. W.; Hu, Y. *Nitrogenase Assembly and catalysis*. In: *Encyclopedia of Inorg. Bioinorg. Chem. Online*, **2011-2012**, Wiley. DOI: 10.1002/9781119951438.eibc0149.pub2.

(7) Fisher, K.; Dilworth, M. J.; Newton, W. E. *Biochemistry*, **2006**, *45*, 4190.

(8) Miller, R. W.; Eady, R. R. *Biochem. J.*, **1988**, *256*, 429.

(9) Crans, D. C.; Smee, J. J.; Gaidamauskas, E.; Yang, L. *Chem. Rev.*, **2004**, *104*, 849.

(10) Laplaza, C. E.; Cummins, C. C. *Science*, **1995**, *268*, 861.

(11) Laplaza, C. E.; Johnson, M. J. A.; Peters, J. C.; Odom, A. L.; Kim, E.; Cummins, C. C.; George, G. N.; Pickering, I. J. *J. Am. Chem. Soc.*, **1996**, *118*, 8623.

(12) Zanotti-Gerosa, A.; Solari, E.; Giannini, L.; Floriani, C.; Chiesi-Villa, A.; Rizzoli, C. *J. Am. Chem. Soc.*, **1998**, *120*, 437.

(13) Tran, B. L.; Pinter, B.; Nichols, A. J.; Chen, C. H.; Krzystek, J.; Ozarowski, A.; Telser, J.; Baik, M. H.; Meyer, K.; Mindiola, D. J. *J. Am. Chem. Soc.*, **2012**, *134*, 13035.

(14) Vidyaratne, I.; Crewdson, P.; Lefebvre, E.; Gambarotta, S. *Inorg. Chem.*, **2007**, *46*, 8836.

(15) Clentsmith, G. K. B.; Bates, V. M. E.; Hitchcock, P. B.; Cloke, F. G. N. *J. Am. Chem. Soc.*, **1999**, *121*, 10444.

(16) Studt, F.; Lamarche, V. M.; Clentsmith, G. K.; Cloke, F. G.; Tuczek, F. *Dalton Trans.*, **2005**, *6*, 1052.

(17) Shearer, J.; Jackson, H. L.; Schweitzer, D.; Rittenberg, D. K.; Leavy, T. M.; Kaminsky, W.; Scarrow, R. C.; Kovacs, J. A. *J. Am. Chem. Soc.*, **2002**, *124*, 11417.

(18) Germain, M. E.; Temprado, M.; Castonguay, A.; Kryatova, O. P.; Rybak-Akimova, E. V.; Curley, J. J.; Mendiratta, A.; Tsai, Y. C.; Cummins, C. C.; Prabhakar, R.; McDonough, J. E.; Hoff, C. D. *J. Am. Chem. Soc.*, **2009**, *131*, 15412.

(19) Tsai, Y. C.; Stephens, F. H.; Meyer, K.; Mendiratta, A.; Gheorghiu, M. D.; Cummins, C. C. *Organometallics*, **2003**, *22*, 2902.

(20) Fickes, M. G. Synthesis and Reactivity of Vanadium and Niobium Complexes Containing Sterically Demanding Amido Ligands, Ph.D Thesis, Massachusetts Institute of Technology, 1998.

(21) Majumdar, S.; Stauber, J. M.; Palluccio, T. D.; Cai, X.;Velian, A.;Rybak-Akimova, E.V.;Temprado, M.; Captain, B.; Cummins, C. C.;Hoff, C. D. Role of Axial Base Coordination in Isonitrile Binding and Chalcogen Atom Transfer to Vanadium(III) Complexes. *Inorg. Chem., Article ASAP*.

(22) (a) Becke, A. D. *J. Chem. Phys.*, **1993**, *98*, 5648. (b) Perdew, J. P. *Phys. Rev. B*, **1986**, *33*, 8822.

(23) Frisch, M. J. et al. Gaussian 03, revision D.01; Gaussian, Inc.: Wallingford, CT 2004.

(24) (a) Hay, P. J.; Wadt, W. R. *J. Chem. Phys.*, **1985**, *82*, 270. (b) Wadt W. R.; Hay, P. J. *J. Chem. Phys.*, **1985**, *82*, 284. (c) Hay, P. J.; Wadt, W. R. *J. Chem. Phys.*, **1985**, *82*, 299.

(25) Dunning T. H. Jr.; Hay, P. J. in *Modern Theoretical Chemistry*, Ed. Schaefer H. F. III, Vol. 3, Plenum, New York, 1976, 1-28.

(26) Andrae, D.; Haeussermann, U.; Dolg, M.; Stoll, H.; Preuss, H. *Theor. Chim. Acta*, **1990**, *77*, 123.

(27) Dolg, M.; Wedig, U.; Stoll, H.; Preuss, H. *J. Chem. Phys.*, **1987**, *86*, 866.

(28) Martin, J. M. L.; Sundermann, A. *J. Chem. Phys.*, **2001**, *114*, 3408.

(29) Temprado, M.; McDonough, J. E.; Mendiratta, A.; Tsai, Y. C.; Fortman, G. C.; Cummins, C. C.; Rybak-Akimova, E. V.; Hoff, C. D. *Inorg. Chem.*, **2008**, *47*, 9380.

(30) Gerlach, C. P.; Arnold, J. *J. Chem. Soc., Dalton Trans.*, **1997**, 4795.

(31) Brussee, E. A. C.; Meetsma, A.; Hessen, B.; Teuben, J. H. *Chem. Commun.*, **2000**, 497.

(32) Billen, M.; Hornung, G.; Preuss, F. *Z. Naturforsch. B*, **2003**, *58*, 975.

(33) Kessler, M.; Ring, H.; Trambarudo, R.; Gordy, W. *Phys. Rev.*, **1950**, *79*, 54.

(34) Mendiratta, A.; Cummins, C. C. *Inorg. Chem.*, **2005**, *44*, 7319.

(35) Silvia, J. S.; Cummins, C. C. *J. Am. Chem. Soc.*, **2009**, *131*, 446.

(36) Cozzolino, A. F.; Tofan, D.; Cummins, C. C.; Temprado, M.; Palluccio, T. D.; Rybak-Akimova, E.V.; Majumdar, S.; Cai, X.; Captain, B.; Hoff, C. D. *J. Am. Chem. Soc.*, **2012**, *134*, 18249.

(37) Nakamoto, K. *Infrared and Raman Spectra of Inorganic and Coordination Compounds*, 5th ed.; Wiley: New York, 1997.

(38) McDonough, J. E.; Weir, J. J.; Sukcharoenphon, K.; Hoff, C. D.; Kryatova, O. P.; Rybak-Akimova, E. V.; Scott, B. L.; Kubas, G. J.; Mendiratta, A.; Cummins, C. C. *J. Am. Chem. Soc.*, **2006**, *128*, 10295.

(39) Mendiratta, A.; Cummins, C. C.; Kryatova, O. P.; Rybak-Akimova, E. V.; McDonough, J. E.; Hoff, C. D. *J. Am. Chem. Soc.*, **2006**, *128*, 4881.

(40) Stevens, F. H; Figueroa, J. S.; Cummins, C. C.; Kryatova, O. P.; Kryatov, S. V.; Rybak-Akimova, E.V.; McDonough, J.E.; Hoff, C.D. *Organometallics*, **2004**, *23*, 3126.

(41) Palluccio, T.D.; Rybak-Akimova, E.V.; Majumdar, S.; Cai, X.; Chui, M.; Temprado, M.; Silvia, J.S.; Cozzolino, A.F.; Tofan, D.; Velian, A.; Cummins, C.C.; Captain, B.; Hoff, C.D. *J. Am. Chem. Soc.*, **2013**, *135*, 11357.

(42) Ruppa, K. B. P.; Desmangles, N.; Gambarotta, S.; Yap, G.; Rheingold, A. L. *Inorg. Chem.*, **1997**, *36*, 1194.

(43) Hamaguchi, H. *Acta Phys. Pol. A*, **1999**, *95*, 37.

(44) Rybak-Akimova, E. V. In *Physical Inorganic Chemistry: Reactions, Processes, and Applications*; Bakac, A., Ed.; Wiley: Hoboken, NJ, 2010; pp 109−188.

(45) (a) Kowalewski, R. M.; Basolo, F.; Trogler, W. C.; Gedridge, R. W.; Newbound, T. D.; Ernst, R. D. *J. Am. Chem. Soc.*, **1987**, *109*, 4860. (b) Hallinan, N. C.; Morelli, G. Basolo, F. *J. Am. Chem. Soc.*, **1988**, *110*, 6585.(c) Trogler W.C. *Int. J. Chem. Kinetics*, **1987**, *19*, 1025.

(46) Silverman, L. D.; Dewan, J. C.; Giandomenico, C. M.; Lippard, S. J. *Inorg. Chem.*, **1980**, *19*, 3379.

(47) Ikeda, Y.; Soya, S.; Tomiyasu, H.; Fukutomi, H. *Bull.Chem. Soc. Jpn.*, **1981**, *54*, 3768.

(48) Douglas, B. E.; McDaniel, D. H.; Alexander, J. J. *Concepts and Models of Inorganic Chemistry*, 3rd Ed.; John Wiley & Sons, Inc.: New York, 1994.

(49) Shi, Q.; Richmond, T. G.; Trogler, W. C.; Basolo, F. *J. Am. Chem. Soc.*, **1984**, *106*, 71.

APPENDIX 2

Diagonal Relationships in Ligand Binding: Nitrile Coordination to Vanadium and Molybdenum Tris-Anilide Complexes

2.3.3. Spectroscopic and Thermochemical Studies of Nitrile Binding

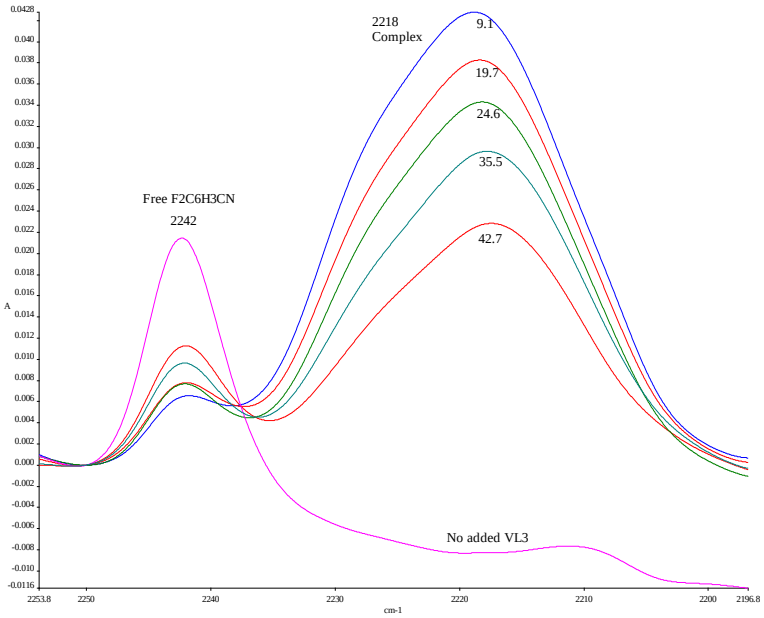

Figure 2A.1. Variable temperature FT-IR spectra for 2,6-$F_2C_6H_3CN$ binding to V(N[^{t}Bu]Ar)$_3$ in toluene (0.043 M V(N[^{t}Bu]Ar)$_3$ and nitrile) over a temperature range of 9.1 to 42.7 °C.

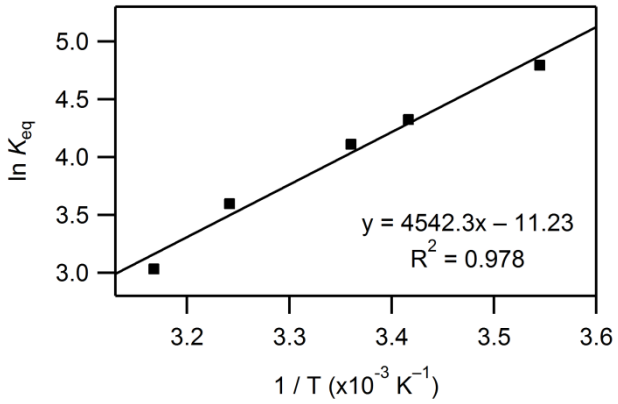

Figure 2A.2. van't Hoff plot for 2,6-$F_2C_6H_3CN$ binding to V(N[^{t}Bu]Ar)$_3$ from which the derived value of $K_{eq} \approx 72$ M^{-1} (20 °C) was obtained. [V(N[^{t}Bu]Ar)$_3$]$_0$ = 43 mM.

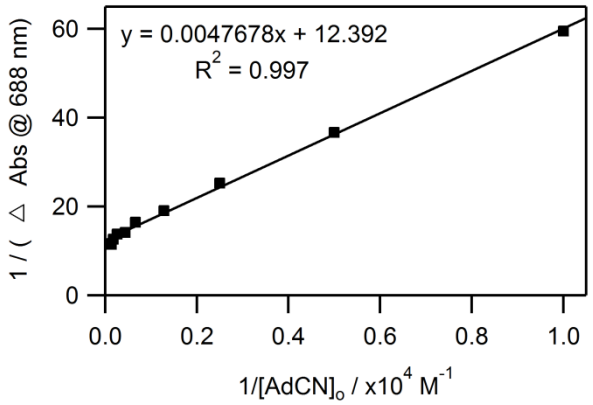

Figure 2A.3. Benesi-Hildebrand plot for the spectrophotometric titration of AdCN at 20 °C from which a derived value of $K_{eq} \approx 2{,}600$ M^{-1} was obtained for AdCN binding to V(N[^{t}Bu]Ar)$_3$. [V(N[^{t}Bu]Ar)$_3$]$_0$ = 0.2 mM.

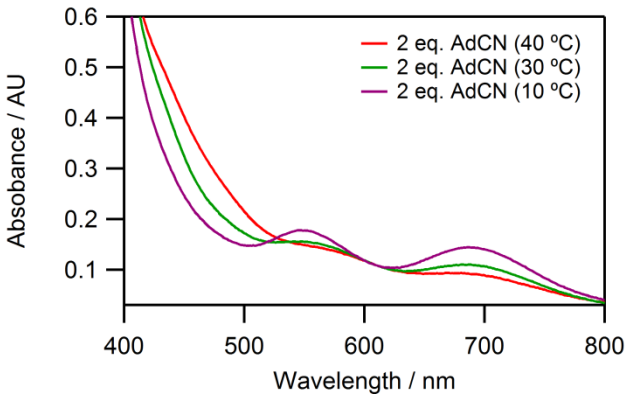

Figure 2A.4. Variable temperature UV/visible spectra of V(N[^{t}Bu]Ar)$_3$ (0.2 mM) + 2 eq. AdCN (0.4 mM) highlighting the change in intensity of the absorbance bands attributed to the AdCN−V(N[^{t}Bu]Ar)$_3$ adduct.

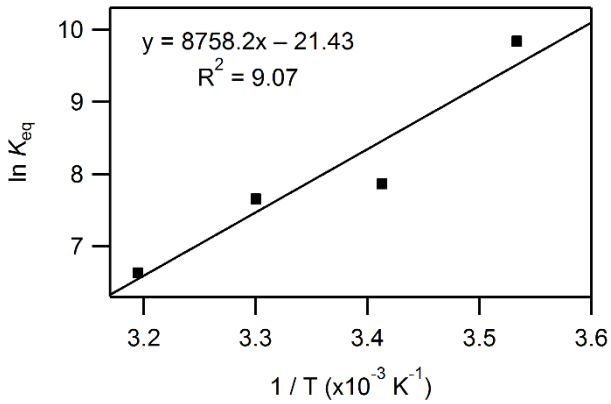

Figure 2A.5. van't Hoff plot for AdCN binding to V(N[^{t}Bu]Ar)$_3$ obtained from spectrophotometric titration over the temperature range of 10 to 40 °C with [V(N[^{t}Bu]Ar)$_3$]$_0$ = 0.2 mM. A binding enthalpy of −17 kcal mol^{-1} and entropy of −43 cal mol^{-1} K^{-1} were obtained and are treated only as estimates.

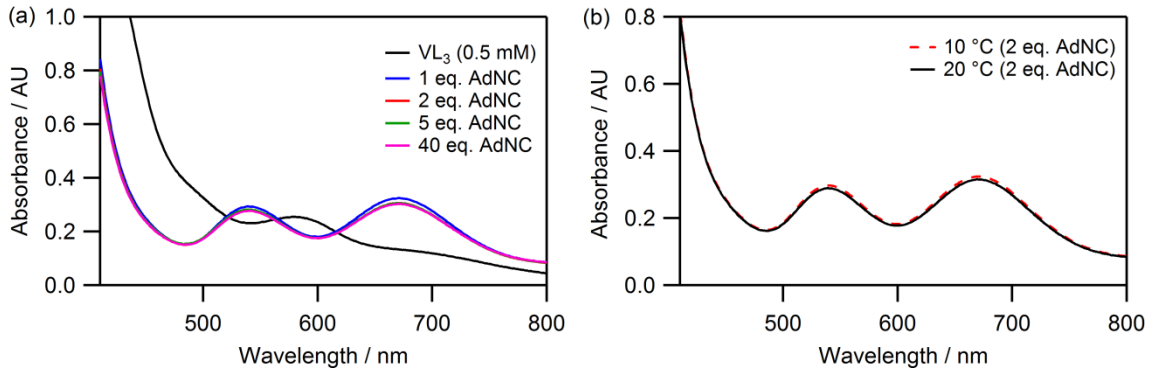

Figure 2A.6. (a) Spectrophotometric titration of AdNC (1 to 40 eq.) with V(N[^{t}Bu]Ar)$_3$ (0.5 mM) at 20 °C. The intensity of the absorbance bands attributed to the AdNC−V(N[^{t}Bu]Ar)$_3$ adduct are unaffected by the amount of AdNC. (b) Spectra of the AdNC−V(N[^{t}Bu]Ar)$_3$ adduct at two different temperatures, also confirming that binding is essentially irreversible at elevated *T*.

2.3.4. Kinetic Studies of Nitrile Binding

Table 2A.1. Temperature dependent pseudo-first order (k_{obs}) and second order (k_1) rate constants for adduct formation measured at λ = 687 nm with 0.3 mM V(N[^{t}Bu]Ar)$_3$ and varying [2,6-$F_2C_6H_3CN$]. Kinetic traces at the two lowest temperatures (−62 and −53 °C) were fit using a biexponential function; only k_{1obs} was analyzed as k_{2obs} showed no dependence on [2,6-$F_2C_6H_3CN$] and could arise from decomposition of the highly air- and moisture-sensitive complex. All remaining kinetic traces were fit using a single exponential function.

−62 °C	[2,6-$F_2C_6H_3CN$] (M)	k_{obs} (s^{-1})	k_1 ($\times 10^3$ M^{-1} s^{-1})
	0.001	3.21	3.41 ± 0.12
	0.002	7.54	
	0.005	16.2	
	0.010	34.4	
−53 °C	[2,6-$F_2C_6H_3CN$] (M)	k_{obs} (s^{-1})	k_1 ($\times 10^3$ M^{-1} s^{-1})
	0.001	5.05	4.93 ± 0.14
	0.002	9.17	
	0.005	23.0	
	0.010	49.2	
−44 °C	[2,6-$F_2C_6H_3CN$] (M)	k_{obs} (s^{-1})	k_1 ($\times 10^3$ M^{-1} s^{-1})
	0.001	9.65	6.55 ± 0.05
	0.002	16.6	
	0.005	35.6	
	0.010	68.8	

−35 °C	[2,6-$F_2C_6H_3CN$] (M)	k_{obs} (s^{-1})	k_1 ($\times 10^3$ M^{-1} s^{-1})
	0.001	17.3	
	0.002	25.8	9.59 ± 0.18
	0.005	57.0	
	0.010	103	

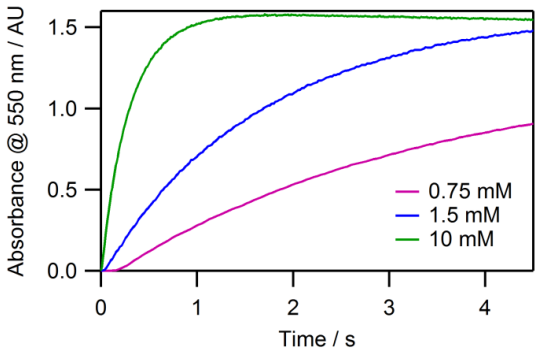

Figure 2A.7. Overlay of selected kinetic traces at λ = 550 nm highlighting formation of the 2,6-$F_2C_6H_3CN$−$Mo(N[^tBu]Ar)_3$ adduct at −40 °C as a function of [2,6-$F_2C_6H_3CN$]. Reactions acquired in single wavelength mode with $[Mo(N[^tBu]Ar)_3]_0$ = 0.15 mM.

Table 2A.2. Temperature dependent pseudo-first order (k_{obs}) and second order (k_1) rate constants for adduct formation measured at λ = 550 nm with 0.15 mM $Mo(N[^tBu]Ar)_3$ and varying [2,6-$F_2C_6H_3CN$].

−40 °C	[2,6-$F_2C_6H_3CN$] (M)	k_{obs} (s^{-1})	k_1 ($\times 10^3$ M^{-1} s^{-1})
	0.00075	0.30	
	0.0015	0.58	
	0.006	1.99	0.316 ± 0.003
	0.01	3.30	
	0.015	4.80	
−20 °C	[2,6-$F_2C_6H_3CN$] (M)	k_{obs} (s^{-1})	k_1 ($\times 10^3$ M^{-1} s^{-1})
	0.00075	0.66	
	0.0015	1.22	
	0.006	4.54	0.750 ± 0.007
	0.01	7.45	
	0.015	11.4	

0 °C	[2,6-$F_2C_6H_3CN$] (M)	k_{obs} (s^{-1})	k_1 ($\times 10^3$ M^{-1} s^{-1})
	0.00075	1.48	
	0.0015	2.84	
	0.006	9.29	1.93 ± 0.13
	0.01	20.6	
	0.015	28.2	
+20 °C	[2,6-$F_2C_6H_3CN$] (M)	k_{obs} (s^{-1})	k_1 ($\times 10^3$ M^{-1} s^{-1})
	0.00075	3.32	
	0.0015	5.49	2.95 ± 0.24
	0.006	16.2	
	0.01	31.3	

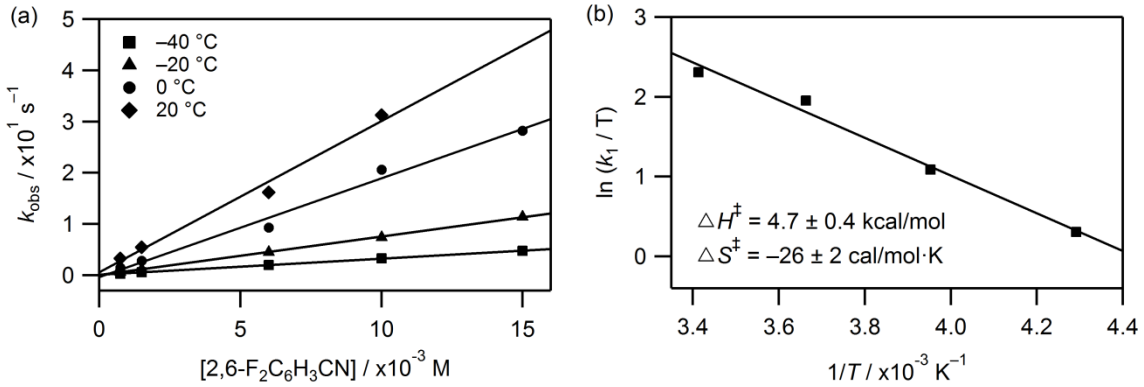

Figure 2A.8. (a) Temperature dependent plots of k_{obs} versus [2,6-$F_2C_6H_3CN$] for Mo(N[^{t}Bu]Ar)$_3$. (b) Eyring plot for 2,6-$F_2C_6H_3CN$ binding to Mo(N[^{t}Bu]Ar)$_3$ (0.15 mM) over a temperature range of −40 °C to +20 °C with derived activation parameters.

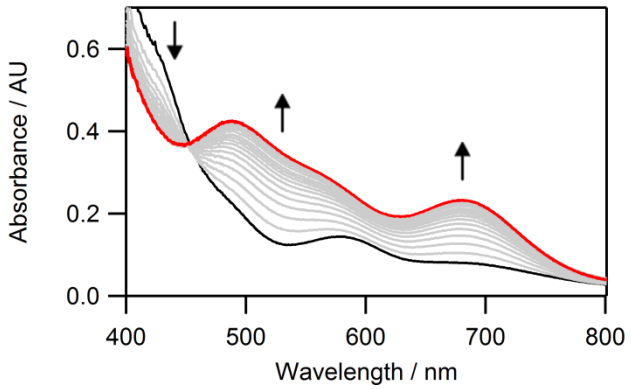

Figure 2A.9. Time-resolved spectra of PhCN (1 mM) binding to V(N[^{t}Bu]Ar)$_3$ (0.3 mM) at −44 °C, acquired over 2 s. Selected traces shown for clarity. The initially recorded spectrum is shown in black and the final spectrum in red.

Table 2A.3. Temperature dependent pseudo-first order (k_{obs}) and second order (k_1) rate constants for product formation at λ = 687 nm with 0.3 mM V(N[^{t}Bu]Ar)$_3$ and varying [PhCN]. Kinetic traces at −62 °C were fit using a biexponential function; only k_{1obs} was analyzed as k_{2obs} showed no dependence on [PhCN] and could arise from decomposition of the highly air- and moisture-sensitive complex. All remaining kinetic traces were fit using a single exponential function.

−62 °C	[PhCN] (M)	k_{obs} (s^{-1})	k_1 ($\times 10^3$ M^{-1} s^{-1})
	0.001	2.09	
	0.002	5.96	3.85 ± 0.06
	0.005	16.8	
	0.010	36.9	
−53 °C	[PhCN] (M)	k_{obs} (s^{-1})	k_1 ($\times 10^3$ M^{-1} s^{-1})
	0.001	4.9	
	0.002	9.04	5.16 ± 0.20
	0.005	22.3	
	0.012	61.2	
−44 °C	[PhCN] (M)	k_{obs} (s^{-1})	k_1 ($\times 10^3$ M^{-1} s^{-1})
	0.001	6.4	
	0.002	12.2	6.14 ± 0.07
	0.005	30.1	
	0.010	61.6	
−35 °C	[PhCN] (M)	k_{obs} (s^{-1})	k_1 ($\times 10^3$ M^{-1} s^{-1})
	0.001	12.4	
	0.002	22.9	10.1 ± 0.2
	0.005	50.6	
	0.010	104	

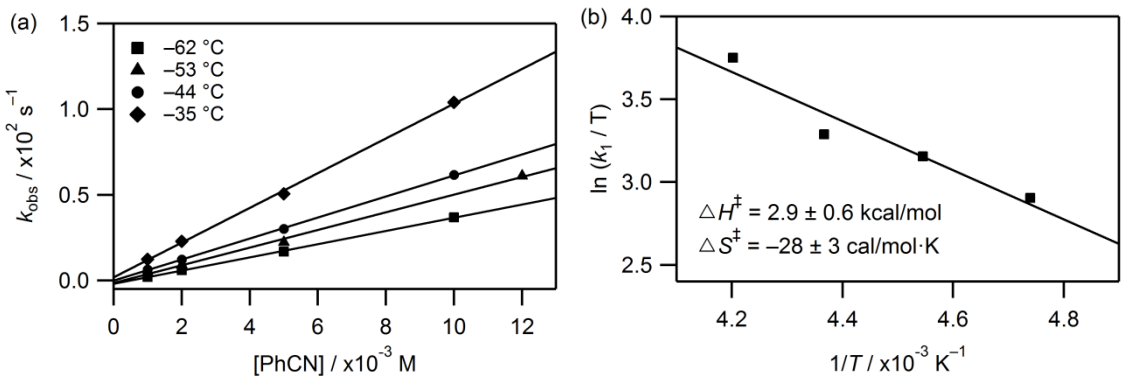

Figure 2A.10. (a) Temperature dependent plots of k_{obs} versus [PhCN]. (b) Eyring plot for PhCN binding to V(N[^{t}Bu]Ar)$_3$ (0.3 mM) over a temperature range of −62 °C to −35 °C with derived activation parameters.

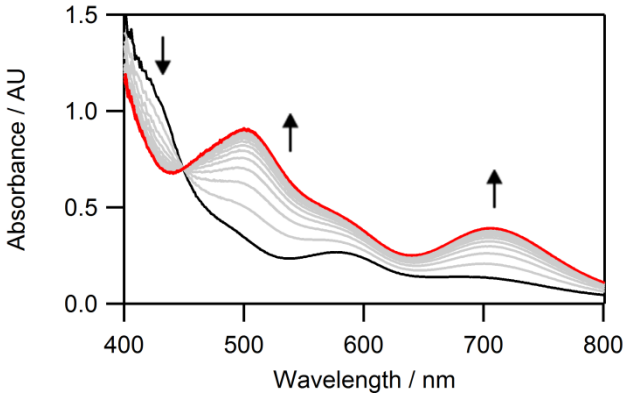

Figure 2A.11. Time-resolved spectra of MesCN (1 mM) binding to V(N[^{t}Bu]Ar)$_3$ (0.3 mM) at −44 °C, acquired over 4 s. Selected traces shown for clarity. The initially recorded spectrum is shown in black and the final spectrum in red.

Table 2A.4. Temperature dependent pseudo-first order (k_{obs}) and second order (k_1) rate constants for adduct formation measured at λ = 705 nm with 0.3 mM V(N[^{t}Bu]Ar)$_3$ and varying [MesCN]. Kinetic traces were fit using either a single or biexponential function; when biexponential fits were employed, only k_{1obs} was analyzed as k_{2obs} showed no dependence on [MesCN] and was not reproducible.

−62 °C	[MesCN] (M)	k_{obs} (s^{-1})	k_1 ($\times 10^3$ M^{-1} s^{-1})
	0.001	1.93	
	0.002	3.76	1.39 ± 0.03
	0.005	7.78	
	0.010	14.6	

−53 °C	[MesCN] (M)	k_{obs} (s^{-1})	k_1 ($\times 10^3$ M^{-1} s^{-1})
	0.001	3.90	
	0.002	5.73	3.08 ± 0.10
	0.005	16.2	
	0.010	31.1	
−44 °C	[MesCN] (M)	k_{obs} (s^{-1})	k_1 ($\times 10^3$ M^{-1} s^{-1})
	0.001	5.54	
	0.002	10.6	5.92 ± 0.08
	0.005	28.2	
	0.010	58.5	
−35 °C	[MesCN] (M)	k_{obs} (s^{-1})	k_1 ($\times 10^3$ M^{-1} s^{-1})
	0.001	11.3	
	0.002	21.5	9.02 ± 0.21
	0.005	50.1	
	0.010	92.8	
−26 °C	[MesCN] (M)	k_{obs} (s^{-1})	k_1 ($\times 10^3$ M^{-1} s^{-1})
	0.001	18.8	
	0.002	34.6	15.5 ± 0.2
	0.005	79.4	
	0.010	159	

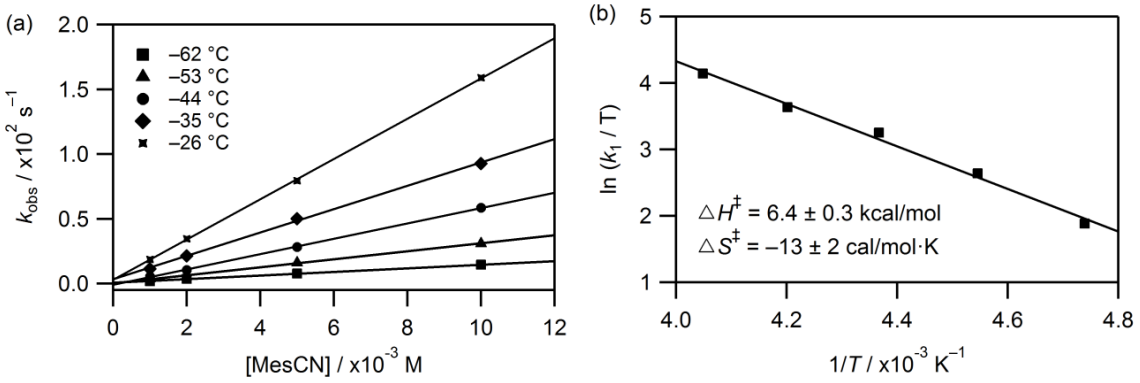

Figure 2A.12. (a) Temperature dependent plots of k_{obs} versus [MesCN]. (b) Eyring plot for MesCN binding to V(N[^{t}Bu]Ar)$_3$ (0.3 mM) over a temperature range of −62 °C to −26 °C with derived activation parameters.

Table 2A.5. Temperature dependent pseudo-first order (k_{obs}) and second order (k_1) rate constants for product formation measured at λ = 705 nm with 0.3 mM V(N[^{t}Bu]Ar)$_3$ and varying [Me_2NCN]. Formation traces were fit to either a single or biexponential equation.

−62 °C	[Me_2NCN] (M)	k_{obs} (s^{-1})	k_1 ($\times 10^3$ M^{-1} s^{-1})
	0.001	3.24	
	0.002	5.04	3.72 ± 0.24
	0.005	15.1	
	0.010	36.1	
−54 °C	[Me_2NCN] (M)	k_{obs} (s^{-1})	k_1 ($\times 10^3$ M^{-1} s^{-1})
	0.001	5.21	
	0.002	8.26	6.76 ± 0.56
	0.005	25.1	
	0.010	65	
−49 °C	[Me_2NCN] (M)	k_{obs} (s^{-1})	k_1 ($\times 10^3$ M^{-1} s^{-1})
	0.001	7.72	
	0.002	13.3	8.71 ± 0.42
	0.005	45	
	0.010	84	
−44 °C	[Me_2NCN] (M)	k_{obs} (s^{-1})	k_1 ($\times 10^3$ M^{-1} s^{-1})
	0.001	11.5	
	0.002	22.2	11.7 ± 0.7
	0.005	66	
	0.010	116	

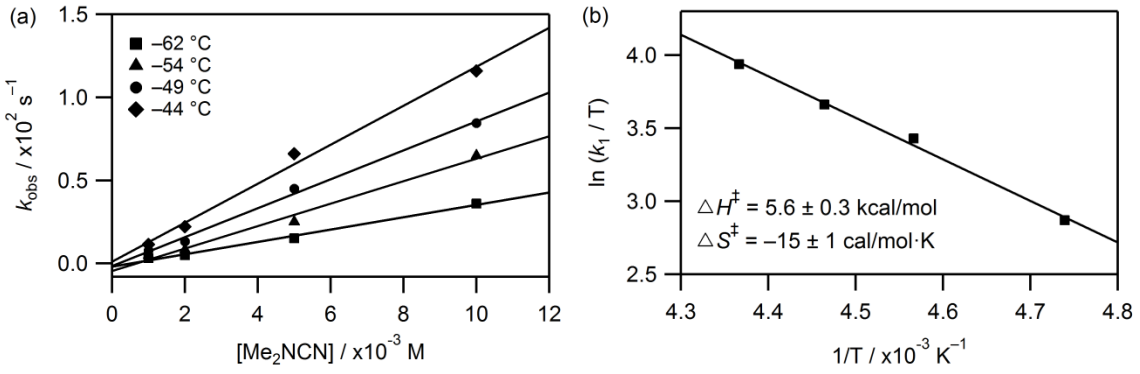

Figure 2A.13. (a) Temperature dependent plots of k_{obs} versus [Me_2NCN]. (b) Eyring plot for Me_2NCN binding to V(N[^{t}Bu]Ar)$_3$ (0.3 mM) over a temperature range of −62 °C to −44 °C with derived activation parameters.

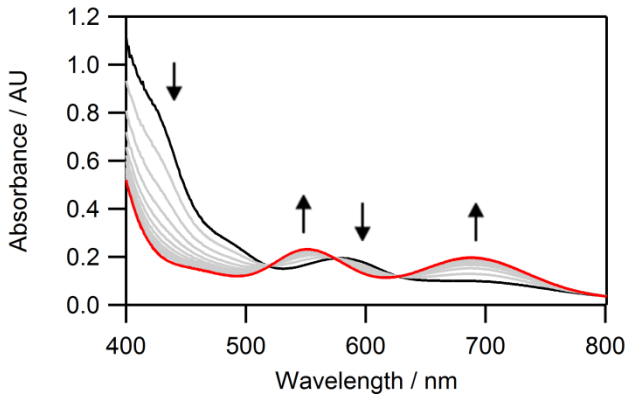

Figure 2A.14. Time-resolved spectral changes accompanying the reaction between V(N[^{t}Bu]Ar)$_3$ (0.3 mM) and MeCN (1 mM) at −53 °C, acquired over 9 s. Selected traces shown for clarity. Initial spectrum is shown in black and final spectrum in red.

Table 2A.6. Temperature dependent pseudo-first order (k_{obs}) and second order (k_1) rate constants for product formation measured at λ = 687 nm with 0.3 mM V(N[^{t}Bu]Ar)$_3$ and varying [MeCN]. Formation traces were fit to a biexponential equation at −62 °C with only k_{1obs} showing a dependence on [MeCN]. Formation traces at all remaining temperatures fit well to a single exponential equation.

−62 °C	[MeCN] (M)	k_{obs} (s^{-1})	k_1 ($\times 10^3$ M^{-1} s^{-1})
	0.001	2.08	
	0.002	4.28	1.79 ± 0.06
	0.005	8.86	
	0.010	18.4	
−53 °C	[MeCN] (M)	k_{obs} (s^{-1})	k_1 ($\times 10^3$ M^{-1} s^{-1})
	0.001	4.37	
	0.002	9.00	3.58 ± 0.08
	0.005	19.4	
	0.010	37.0	
−44 °C	[MeCN] (M)	k_{obs} (s^{-1})	k_1 ($\times 10^3$ M^{-1} s^{-1})
	0.001	7.47	
	0.002	19.9	8.05 ± 0.46
	0.005	45.4	
	0.010	81.4	
−35 °C	[MeCN] (M)	k_{obs} (s^{-1})	k_1 ($\times 10^3$ M^{-1} s^{-1})
	0.001	13.9	
	0.002	36.9	13.7 ± 0.7
	0.005	74.8	
	0.010	141	

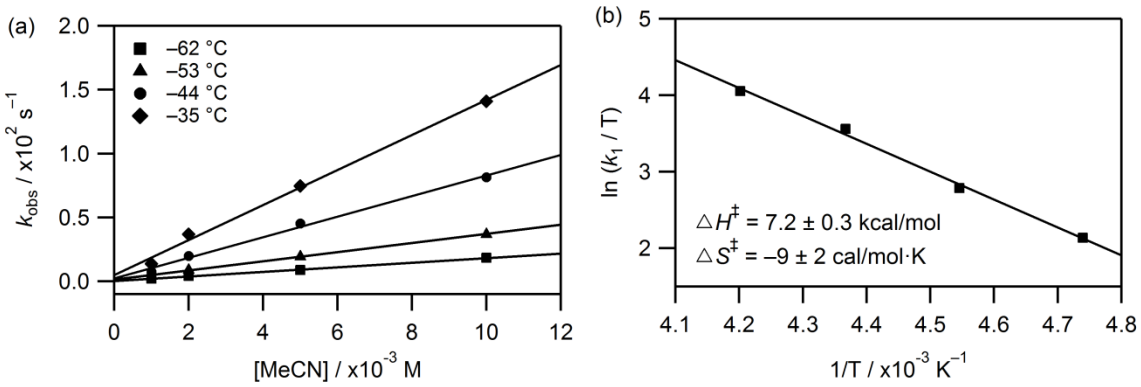

Figure 2A.15. (a) Temperature dependent plots of k_{obs} versus [MeCN]. (b) Eyring plot for MeCN binding to V(N[^{t}Bu]Ar)$_3$ (0.3 mM) over a temperature range of −62 °C to −35 °C with derived activation parameters.

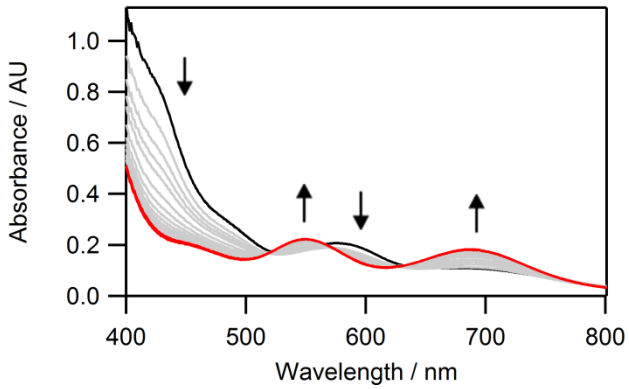

Figure 2A.16. Time-resolved spectral changes accompanying the reaction between V(N[^{t}Bu]Ar)$_3$ (0.3 mM) and AdCN (1 mM) at −62 °C, acquired over 9 s. Selected traces shown for clarity. Initial spectrum is shown in black and final spectrum in red.

Table 2A.7. Temperature dependent pseudo-first order (k_{obs}) and second order (k_1) rate constants for product formation measured at λ = 687 nm with 0.3 mM V(N[^{t}Bu]Ar)$_3$ and varying [AdCN]. Formation traces were fit to a single exponential equation in all cases.

−62 °C	[AdCN] (M)	k_{obs} (s^{-1})	k_1 ($\times 10^3$ M^{-1} s^{-1})
	0.001	1.57	
	0.002	2.52	0.919 ± 0.015
	0.005	5.42	
	0.010	9.84	
−53 °C	[AdCN] (M)	k_{obs} (s^{-1})	k_1 ($\times 10^3$ M^{-1} s^{-1})
	0.001	2.68	
	0.002	4.92	2.52 ± 0.06
	0.005	12.0	
	0.010	25.3	
−44 °C	[AdCN] (M)	k_{obs} (s^{-1})	k_1 ($\times 10^3$ M^{-1} s^{-1})
	0.001	5.17	
	0.002	9.59	3.86 ± 0.11
	0.005	22.0	
	0.010	40.0	
−35 °C	[AdCN] (M)	k_{obs} (s^{-1})	k_1 ($\times 10^3$ M^{-1} s^{-1})
	0.001	8.09	
	0.002	14.9	6.71 ± 0.02
	0.005	35.2	
	0.010	68.5	

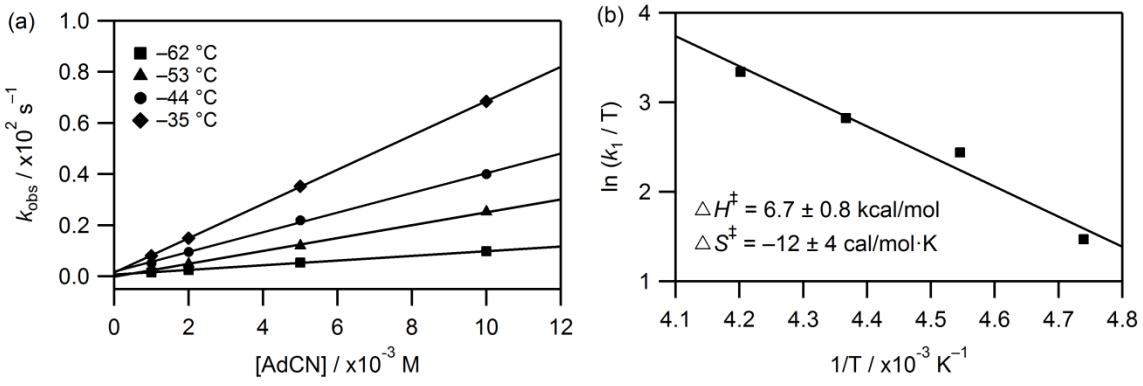

Figure 2A.17. (a) Temperature dependent plots of k_{obs} versus [AdCN]. (b) Eyring plot for AdCN binding to V(N[^{t}Bu]Ar)$_3$ (0.3 mM) over a temperature range of −62 °C to −35 °C with derived activation parameters.

Table 2A.8. Temperature dependent pseudo-first order (k_{obs}) and second order (k_1) rate constants for product formation measured at λ = 673 nm with 0.3 mM V(N[^{t}Bu]Ar)$_3$ and varying [AdNC]. Formation traces were fit to a biexponential equation at −62 °C with only k_{1obs} showing a dependence on [AdNC]. Formation traces at all remaining temperatures fit well to a single exponential equation.

−62 °C	[AdNC] (M)	k_{obs} (s^{-1})	k_1 ($\times 10^3$ M^{-1} s^{-1})
	0.001	3.60	
	0.002	5.93	3.08 ± 0.09
	0.005	14.8	
	0.010	31.1	
−53 °C	[AdNC] (M)	k_{obs} (s^{-1})	k_1 ($\times 10^3$ M^{-1} s^{-1})
	0.001	5.38	
	0.002	9.97	5.12 ± 0.05
	0.005	25.2	
	0.010	51.3	
−44 °C	[AdNC] (M)	k_{obs} (s^{-1})	k_1 ($\times 10^3$ M^{-1} s^{-1})
	0.001	9.61	
	0.002	18.8	8.58 ± 0.19
	0.005	46.3	
	0.010	86.9	
−35 °C	[AdNC] (M)	k_{obs} (s^{-1})	k_1 ($\times 10^3$ M^{-1} s^{-1})
	0.001	16.7	
	0.002	33.2	11.8 ± 0.7
	0.005	72.4	
	0.010	124	

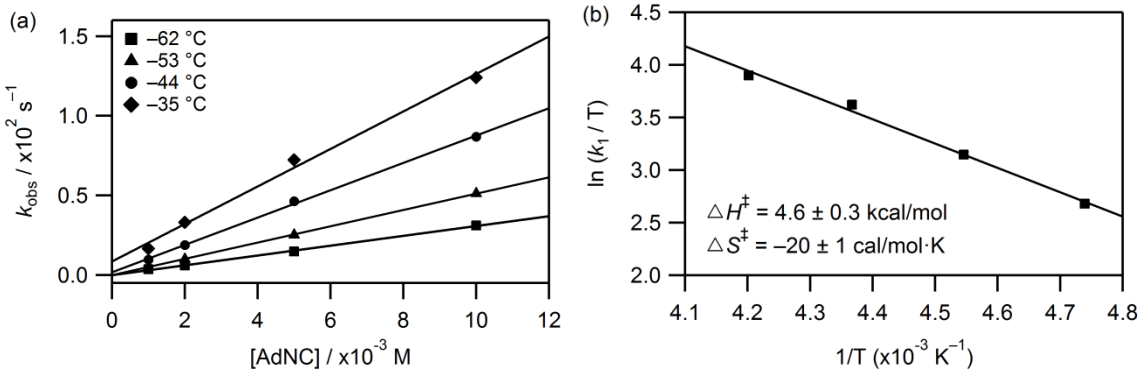

Figure 2A.18. (a) Temperature dependent plots of k_{obs} versus [AdNC]. (b) Eyring plot for AdNC binding to V(N[^{t}Bu]Ar)$_3$ (0.3 mM) over a temperature range of −62 °C to −35 °C with derived activation parameters.

2.3.5. Computational Studies

Table 2A.9. Calculated bond lengths (Å) and angles (°) for aromatic nitriles and RCN−M(N[^{t}Bu]Ar)$_3$ adducts (M = V, Mo). η^1 binding mode unless stated otherwise.

RCN	2,6-DFBN	F_5PhCN	4-$F_3CC_6H_4CN$	PhCN	4-$Me_2NC_6H_4CN$
N−C (free nitrile)	1.168	1.168	1.169	1.169	1.171
			RCN−VL_3		
$V-N_{nitrile}$	1.935	1.926	1.936	1.945	1.959
N−C	1.184	1.185	1.183	1.181	1.181
$V-N_{avg}$	1.93	1.93	1.93	1.94	1.95
V−N−C	173.5	174.2	178.6	178.6	177.8
N−C−R	176.4	175.5	179.2	178.4	178.9
$\Sigma(N_{eq}-V-N_{eq})$	350.3	350.5	351.2	352.4	352.6
			RCN−MoL_3		
$Mo-N_{nitrile}$	1.909	1.903	1.912	1.917	1.913
N−C	1.202	1.204	1.202	1.200	1.205
$Mo-N_{avg}$	2.00	2.00	2.00	2.00	2.01
Mo−N−C	177.1	177.0	176.1	176.4	177.0
N−C−R	179.5	176.8	179.2	178.7	168.9
$\Sigma(N_{eq}-Mo-N_{eq})$	353.0	353.0	353.3	353.4	353.7

Table 2A.10. Calculated bond lengths (Å) and angles (°) for aliphatic nitriles and RCN−M(N[^{t}Bu]Ar)$_3$ adducts (M = V, Mo). η^1 binding mode unless stated otherwise.

RCN	MeCN	AdCN	Me_2NCN	η^2-Me_2NCN	η^2-MeCN
N−C (free nitrile)	1.165	1.167	1.175	1.175	1.165
			RCN−VL_3		
$V-N_{nitrile}$	1.981	nd[a]	1.985	1.890	1.959
N−C	1.171	nd	1.181	1.292	1.257
$V-N_{avg}$	1.95	nd	1.95	1.93	1.93
V−N−C	175.6	nd	179.4	74.2	72.4
N−C−R	177.3	nd	177.5	129.5	133.3
$\Sigma(N_{eq}-V-N_{eq})$	354.5	nd	353.7	333.5	335.0
			RCN−MoL_3		
$Mo-N_{nitrile}$	1.895	1.920	1.847	2.017	2.092
N−C	1.215	1.207	1.270	1.290	1.261
$Mo-N_{avg}$	2.01	2.01	1.99	2.02	2.02
Mo−N−C	175.7	172.7	167.4	72.6	71.2
N−C−R	142.0	154.9	127.7	129.8	131.7
$\Sigma(N_{eq}-Mo-N_{eq})$	354.2	352.8	347.0	334.0	341.8

[a] Not determined.

Table 2A.11. Comparison of calculated and experimental IR Frequencies for free RCN and $M(N[^tBu]Ar)_3$ (M = V, Mo) adducts (η^1 binding mode unless stated otherwise). All values in cm^{-1}. L = N[ᵗBu]Ar.

	Free RCN			RCN−VL_3		RCN−MoL_3	
RCN	ν_{calc}	ν_{exp}	$\Delta\nu_{calc-exp}$	ν_{calc}	ν_{exp}	ν_{calc}	ν_{exp}[a]
2,6-$F_2C_6H_3CN$	2189	2242	−53	2061	2218	2021	-----
F_5PhCN	2193	2245	−52	2057	2207	2008	-----
4-$F_3CC_6H_4CN$	2175	2234	−59	2057	2224	2005	-----
PhCN	2169	2231	−62	2066	2218	2009	2035
4-$Me_2NC_6H_4CN$	2153	2217	−64	2070	2224	1846	-----
η^2-Me_2NCN	2168	2218	−50	1586	-----	1585	1650
Me_2NCN	2168	2218	−50	2153	2256	1618	1570
η^2-MeCN	2202	2253	−51	1625	-----	1615	-----
MeCN	2202	2253	−51	2138	-----	1832	-----
AdCN	2168	2234	−66	-----	-----	1852	2079

[a] ν_{exp} values taken from ref 18.

Table 2A.12. Calculated Mulliken spin densities (L = N[ᵗBu]Ar) (η^1 binding mode unless stated otherwise).

	RCN−VL_3			RCN−MoL_3		
RCN	$C_{nitrile}$	V	C_{para}	$C_{nitrile}$	Mo	C_{para}
2,6-$F_2C_6H_3CN$	0.30	1.72	0.11	0.25	0.82	−0.02
F_5PhCN	0.32	1.68	0.10	0.27	0.79	−0.02
4-$F_3CC_6H_4CN$	0.29	1.17	0.10	0.23	0.83	−0.01
PhCN	0.28	1.81	0.08	0.23	0.81	0.00
4-$Me_2NC_6H_4CN$	0.26	1.89	0.04	0.21	0.70	0.05
η^2-Me_2NCN	-----	-----	-----	−0.06	0.88	-----
Me_2NCN	0.20	1.98	-----	0.08	0.83	-----
η^2-MeCN	-----	-----	-----	−0.06	0.88	-----
MeCN	0.25	1.97	-----	0.22	0.84	-----
AdCN	nd[a]	nd	-----	0.22	0.82	-----

[a] Not determined.

CHAPTER 3

Two-Step Binding of Dioxygen to a Vanadium(III) Tris-Anilide Complex to Form a Non-Vanadyl Vanadium(V) Peroxo Complex[1]

3.1. Introduction

Activation of dioxygen at mononuclear transition-metal centers can yield either end-on (η^1) or side-on (η^2) O_2 complexes.[2] It is generally held that the η^1 binding motif is more reactive than the η^2 motif.[3] The formation of side-on O_2 complexes can proceed by initial end-on binding followed by isomerization or possibly by concerted binding of O_2 to form the side-on η^2-O_2 complex in a single step. In spite of the fact that the two-step activation of O_2 to form a side-bound adduct is logical, limited evidence for this pathway exists. Cases where both forms of binding can be observed are rare, and there are few quantitative kinetic studies in which the rates of binding and isomerization have been directly measured. Kinetic data obtained for the treatment of four- and five-coordinate iridium(I) complexes with oxygen are in keeping with initial end-on binding followed by rapid rearrangement upon dissociation of a ligand,[4] but since ligand dissociation is a prerequisite for η^2 coordination in this particular system, that result is not reflective of systems having a vacant coordination site where η^2 binding could in principle occur directly. Treatment of a copper(I) complex with O_2 leads to a side-on O_2 complex that density functional theory (DFT) calculations indicate is formed by initial end-on binding followed by a low-barrier isomerization to give the final side-bound product.[5] It has

recently been shown that increasing steric constraints with bulky ligands yields a bis-superoxo complex (η^1-O_2)$_2$Pd(IPr)$_2$ (IPr = 1,3-bis(2,6-diisopropylphenyl)imidazol-2-ylidene)[6] as opposed to the side-on peroxo complex in (η^2-O_2)Pd(IMes)$_2$ (IMes = *N*,*N*′-bis(2,4,6-trimethylphenyl)-imidazol-2-ylidene).[7] The kinetics of O_2 binding to form the (η^1-O_2)$_2$Pd(IPr)$_2$ is presented in Chapter 4.

Vanadium peroxo complexes are important as both natural[8] and industrial[9] oxidation catalysts. Vanadium peroxides are typically formed from V^{IV} or V^{V} precursors by reaction with hydrogen peroxide or alkyl hydroperoxides.[10] There are limited examples where O_2 is used as the oxidant[11] and there are only a handful of cases in which structurally characterized early transition metal peroxo complexes have been prepared directly by reaction with O_2.[12] In the case of V^{III} complexes, oxidation by O_2 typically produces a V^{V} oxo species resulting from a bimetallic, four-electron reduction of O_2.[13] In this chapter, the kinetics of O_2 binding to the sterically crowded early transition metal complex V(N[^{t}Bu]Ar)$_3$ (Ar = 3,5-$Me_2C_6H_3$) is presented, which proceeds through an intermediate η^1-peroxo complex en route to the η^2-peroxo complex. The η^2-peroxo adduct, (η^2-O_2)V(N[^{t}Bu]Ar)$_3$, represents the first structurally characterized example of a non-vanadyl monoperoxo complex.

3.2. Experimental Methods

General Considerations. Anhydrous toluene (HPLC grade, ≥ 99.9%) was purchased from Sigma Aldrich and dried on an Innovative Technologies PureSolv 400 solvent purification system. Samples of V(N[^{t}Bu]Ar)$_3$ (Ar = 3,5-$Me_2C_6H_3$)[14] were graciously

provided by members of the Cummins group (MIT, Cambridge, MA), stored in a glove box freezer (−35 °C), and used without further purification. Pure O_2 (ultra dry grade) was obtained from Airgas and used as received. All syntheses, characterizations, crystallographic data, calorimetric measurements, and high temperature ^{1}H NMR kinetic studies were performed by collaborators at MIT (Cummins group) and University of Miami (Hoff group). The reader is referred to Appendix 3 as well as reference 1 for further details regarding these procedures.

Crystallographic Details. Diffraction quality dark green blocks of (η^2-O_2)V(N[^{t}Bu]Ar)$_3$ were grown from pentane at –35 °C, and diffraction quality dark red blocks of ^{t}BuC(=O)N≡V(N[^{t}Bu]Ar)$_3$ were isolated from a pentane solution of ^{t}BuCN-V(N[^{t}Bu]Ar)$_3$ following treatment with O_2 at –45 °C. The crystals were mounted in Paraton-N oil (Hampton Research) on a MiTeGen MicroMount (Ithaca, NY). Low temperature data were collected on a Siemens Platform three-circle diffractometer coupled to a Bruker-AXS Smart Apex CCD detector with graphite-monochromated Mo Kα radiation (λ = 0.71073 Å), performing ω- and φ-scans. Two domains with minimal overlap were identified for (η^2-O_2)V(N[^{t}Bu]Ar)$_3$. The structure solved and refined satisfactorily by integrating only the major domain. The two domains in the crystal of ^{t}BuC(=O)N≡V(N[^{t}Bu]Ar)$_3$ were identified using CELL_NOW.[15] Both structures were solved by direct methods using SHELXS and refined against F^2 on all data by full-matrix least squares with SHELXL-97.[16] A semi-empirical absorption correction (SADABS or TWINABS) were applied to the diffraction data.[17] All non-hydrogen atoms were refined anisotropically. All hydrogen atoms were included at geometrically calculated positions

and refined using a riding model.[18] The isotropic displacement parameters of all hydrogen atoms were fixed at 1.2 times the U_{eq} value of the atoms which they are linked to (1.5 for methyl groups).

(η^2-O_2)V(N[^{t}Bu]Ar)$_3$ crystallized in the cubic *I*−43*d* space group with one-third of a molecule in the asymmetric unit, which enforces disorder of the peroxo moiety over three positions. The occupancy of the O atoms was allowed to refine freely to account for the possibility of co-crystallization of the oxo complex OV(N[^{t}Bu]Ar)$_3$. The anilide *tert*-butyl group was modeled as a disorder over two positions (71.9 %).

^{t}BuC(=O)N≡V(N[^{t}Bu]Ar)$_3$ crystallized in the orthorhombic space group $P2_12_12_1$ with one molecule in the asymmetric unit. Two domains were identified using CELL_NOW and the data was reduced using TWINABS. The final data was refined against the HKLF4 data, giving a minor component of 43.3 %. Additional crystallographic details are available in Appendix 3, Table 3A.4.

Stopped-Flow Kinetics. Toluene solutions of V(N[^{t}Bu]Ar)$_3$ were prepared in an MBraun glove box filled with ultra high purity argon (Airgas) and loaded in Hamilton gastight syringes equipped with three-way valves. Saturated solutions of O_2 were prepared by bubbling gas into gastight syringes containing dry toluene for at least 20 minutes; dilutions of the O_2 saturated solvent were performed anaerobically to obtain the desired [O_2] before mixing. The solubility of O_2 in toluene was taken as 8.3 mM at 20 °C.[19] Time resolved spectra (λ = 400 - 800 nm) were acquired over a range of temperatures (−80 to −53 °C) using a Hi-Tech Scientific KinetAsyst SF-61DX2 CryoStopped-Flow system (TgK Scientific Ltd.) equipped with a quartz tungsten halogen light source, a J&M

TIDAS diode array detector and a Brandenburg 4479 Series PMT monochromator. The instrument was equipped with stainless steel plumbing lined with PEEK tubing and a 1.00 cm^3 quartz mixing cell submerged in an ethanol cooling bath. The temperature in the mixing cell was maintained to ± 0.1 °C. Data acquisition was performed using TIDAS-DAQ and/or Kinetic Studio software programs and mixing times were 2 to 3 ms. All flow lines were washed extensively with argon saturated dry toluene prior to loading reactant solutions and the driving syringe compartment was continuously flushed with argon during the experiments to preserve anaerobicity. All experiments were performed in a single-mixing mode of the instrument with a 1:1 (v/v) mixing ratio. Reactions were studied under pseudo-first order conditions using excess O_2. Data analysis was performed using Kinetic Studio (TgK Scientific) and IGOR Pro 5.0 (Wavemetrics, Inc.) software programs. All observed rate constants are reported in Appendix 3 and represent an average of three to seven measurements which gave an acceptable standard deviation (within 5 - 10 %) and all remaining quantities derived from the kinetic data (k, k_2, K_{eq} and activation parameters) are reported with their standard deviations.

Computational Details. All computational studies were performed by Manuel Temprado, Universidad de Alcalá Department of Physical Chemistry, Madrid, Spain. Electronic structure calculations used to obtain thermodynamic values were carried out using the BP86[20] pure density functional method as implemented in the Gaussian 09 suite of programs.[21] Structures were optimized using the LANL2DZ[22] basis (LANL2DZ ECP and basis for V; the Dunning-Huzinaga D95V[23] basis for all other atoms). Optimizations of several conformers using several anilide environments were carried out to determine the

geometry of the global minimum in each case. In order to obtain more reliable molecular structures, the lowest energy minima derived from these calculations were further optimized by including f functions[24] and Stuttgart-Dresden MDF10[25] fully relativistic effective core potential and basis for V, and the triple-zeta quality basis set, 6-311G(d,p), for all other elements. To derive binding energies, the basis set superposition error (BSSE) was computed using counterpoise calculations.[26]

Additional calculations, including frequency calculations and those pertaining to reactivity, were performed using ORCA 2.8 quantum chemistry program package from the development team at the University of Bonn.[27] In all cases, the LDA and GGA functional employed were those of Perdew and Wang.[28] In addition, all calculations were carried out using the Zero-Order Regular Approximation (ZORA)[29] in conjunction with the SARC-TZV(2pf) basis set for vanadium, the SARC-TZV basis set hydrogen, and SARC-TZV(p) set for all other elements.[30] Spin-restricted Kohn-Sham determinants have been chosen to describe the closed-shell wavefunctions, employing the RI approximation and the tight SCF convergence criteria provided by ORCA. Numerical frequency calculations were performed on the optimized structures. NBO calculations were performed using NBO 5.0.[31]

3.3. Results and Discussion

The reactions of $V(N[^tBu]Ar)_3$ with a variety of oxygen atom transfer (OAT) reagents to form cleanly the vanadium oxo complex $OV(N[^tBu]Ar)_3$ were recently investigated.[32] The O≡V bond $OV(N[^tBu]Ar)_3$ (154 ± 3 kcal mol^{-1}) is strong enough that

the reaction of V(N[^{t}Bu]Ar)$_3$ with O_2 to generate an O atom is thermodynamically favorable, as shown in Eq. 3.1:

$$V(N[^tBu]Ar)_3 + O_2 \rightarrow OV(N[^tBu]Ar)_3 + O \qquad \Delta H = -35 \text{ kcal mol}^{-1} \qquad (3.1)$$

The reaction of V(N[^{t}Bu]Ar)$_3$ with excess O_2 in toluene at −78 °C irreversibly produced a forest-green colored solution, in contrast to the red-orange color of OV(N[^{t}Bu]Ar)$_3$. NMR studies showed the green complex to be a diamagnetic species that slowly decomposed upon warming with minimal production of OV(N[^{t}Bu]Ar)$_3$. Addition of excess V(N[^{t}Bu]Ar)$_3$ followed by warming to room temperature did lead to production of the oxo complex. These observations suggested the sequence of reactions shown in Figure 3.1.

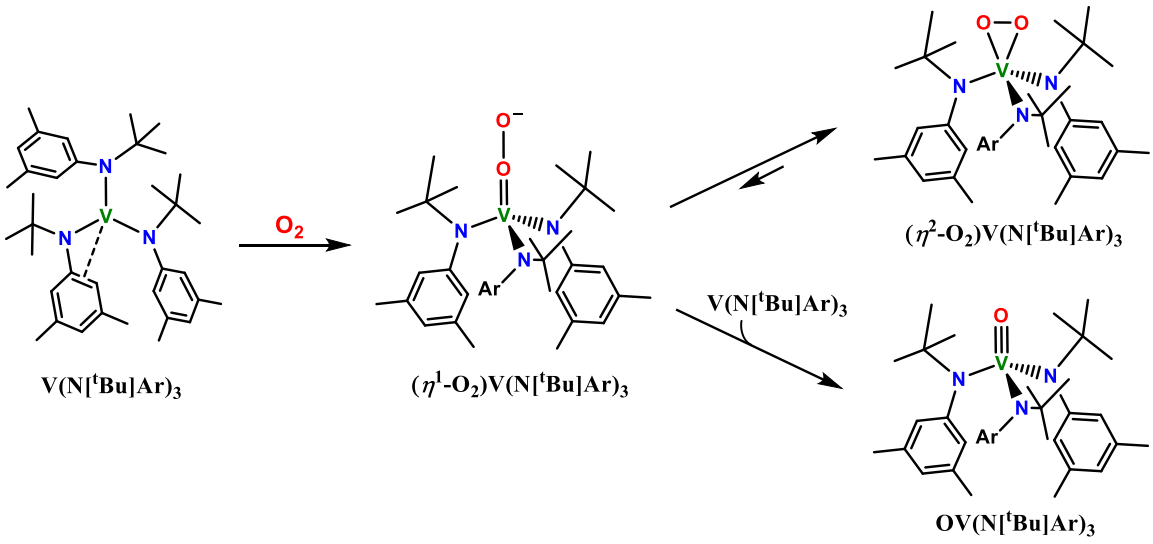

Figure 3.1. Reaction sequence for V(N[^{t}Bu]Ar)$_3$ with O_2.

Initial attempts to isolate pure crystals of (η^2-O_2)V(N[^{t}Bu]Ar)$_3$ were frustrated by contamination with OV(N[^{t}Bu]Ar)$_3$ since both have the same unit cell parameters and readily co-crystallize. Since the reaction of (η^2-O_2)V(N[^{t}Bu]Ar)$_3$ with V(N[^{t}Bu]Ar)$_3$ produces the oxo complex, it was hypothesized that reaction of a weakly bound nitrile adduct of V(N[^{t}Bu]Ar)$_3$ would minimize the concentration of free starting complex and result in cleaner formation of (η^2-O_2)V(N[^{t}Bu]Ar)$_3$ when O_2 was delivered to a concentrated solution of V(N[^{t}Bu]Ar)$_3$. Stopped-flow kinetic and NMR studies later revealed that at temperatures below −30 °C, the reaction of (η^2-O_2)V(N[^{t}Bu]Ar)$_3$ with V(N[^{t}Bu]Ar)$_3$ is sufficiently slow that tempering the reactivity of V(N[^{t}Bu]Ar)$_3$ by this weak ligand binding is not required when O_2 is present in excess. A fortuitous byproduct of the "nitrile method" was the accidental discovery of the pivaloylimido complex ^{t}BuC(=O)N≡V(N[^{t}Bu]Ar)$_3$, as discussed later.

The "nitrile method" ultimately proved to be a facile way to prepare and isolate gram quantities of (η^2-O_2)V(N[^{t}Bu]Ar)$_3$ at room temperature. ^{51}V NMR spectroscopy showed no contamination by OV(N[^{t}Bu]Ar)$_3$ (−171 ppm) and only one peak at 198 ppm due to (η^2-O_2)V(N[^{t}Bu]Ar)$_3$ (Appendix 3, Figures 3A.1 and 3A.2). This is a very high frequency relative to those for known V^V peroxides (−520 to −650 ppm)[33] and is reflective of the unique ligand environment used to support the vanadium peroxide moiety in (η^2-O_2)V(N[^{t}Bu]Ar)$_3$, including the lack of a vanadyl moiety. Diffraction-quality crystals of (η^2-O_2)V(N[^{t}Bu]Ar)$_3$ were obtained by recrystallization from pentane at −35 °C. The asymmetric unit consists of one-third of a molecule, the remainder being generated by a crystallographic threefold axis (Figure 3.2). This necessitates the disorder

of the peroxo moiety over three positions, as clearly seen in the density map (Figure 3A.3).

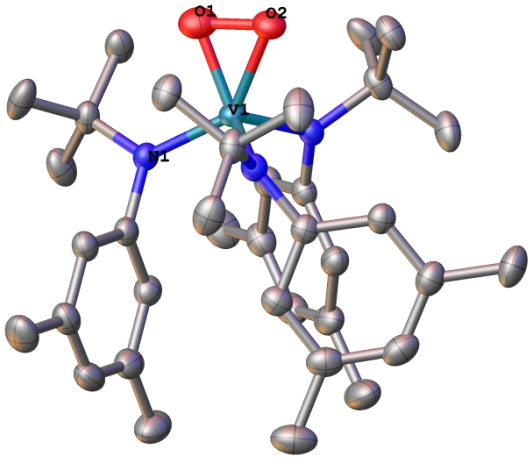

Figure 3.2. X-ray structure of (η^2-O_2)V(N[^{t}Bu]Ar)$_3$ with thermal ellipsoids shown at 50% probability. Hydrogen atoms, symmetry-related oxygen atoms, and disordered ^{t}Bu groups have been omitted for clarity. Selected distances (Å) and angles (°): V1−N1 = 1.887(1); V1−O1 = 1.777(4); V1−O2 = 1.908(4); O1−O2 = 1.416(5); O1−V1−O2 = 45.1(2).

The full molecule has a five-coordinate V^V center with two of the coordination sites occupied by the two oxygen atoms of the peroxo ligand. This is the first structurally characterized example of a non-vanadyl peroxo species,[34] with the exception of per(peroxo)vanadium structures reported previously.[35] The structure exhibits unequal V−O bond distances (1.777(4) and 1.908(4) Å), the average of which (1.843 Å) is significantly shorter than the average V−O_{peroxo} distance of structurally characterized vanadium peroxo systems (1.878 Å).[36] The oxygen atom that is farther away from the vanadium center (O2) appears to engage in a weak hydrogen bond with a neighboring $CH_{aryl\text{-}Me}$ (O···H = 2.68 Å, C(H)···O = 3.36 Å; see Figure 3A.4)[37] and is located trans to a V−N bond (N−V−O2 = 141.5(1)°). Thus, the V−O2 bond is likely lengthened because of

the synergistic influences of the hydrogen bond and the *trans* anilide ligand. The O−O peroxide bond length (1.416(5) Å) is also short compared with the average O−O bond in known V^V peroxo complexes (average 1.430 Å, median 1.436 Å).[36]

Time-resolved UV-visible spectra obtained from low temperature stopped-flow experiments gave clear evidence for a two-step binding process as shown in Figure 3.3. Upon mixing of reactant solutions at −80 °C, a rapid growth in absorbance was observed across most of the spectrum (λ = 400 - 682 nm, with a tight isosbestic point located at 682 nm and decay at longer wavelengths), which was followed by a slower formation phase and loss of the isosbestic point. Over longer reaction time periods (up to 18 s), negligible decay in absorbance was noticeable at higher energy wavelengths and has been attributed to decomposition of the highly air- and moisture-sensitive complex over time and was thus omitted from data analysis.

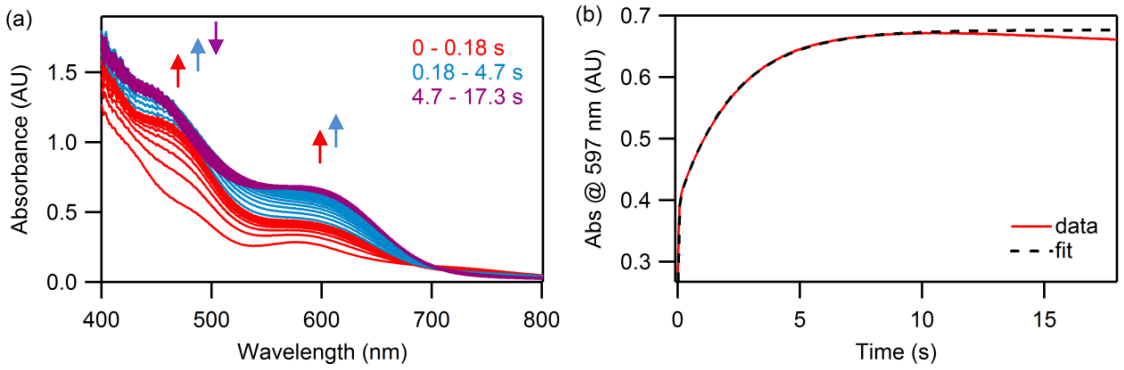

Figure 3.3. (a) Time-resolved spectral changes accompanying the reaction between $V(N[^tBu]Ar)_3$ (0.3 mM) and O_2 (2.5 mM) at −80 °C over 17.2 s. Selected traces are shown for clarity and have been color-coded according to time frames listed in the plot. (b) Kinetic trace at λ = 597 nm with fit to a biexponential function. Fits were typically terminated prior to the late stage decay observed at this wavelength. See Appendix 3 for additional comments on fitting procedures.

Formation traces fit very well to a biexponential function, *rate = –A1* exp(–k_{1obs}t) + –A2* exp(–k_{2obs}t) + C*, which yielded observed rate constants k_{1obs} and k_{2obs} for η^1-peroxo and η^2-peroxo complex formation, respectively. For quantitative analysis, traces at λ = 597 nm were used since they displayed the largest change in absorbance for each process and did not contain interferences from decomposition that occurred over longer time periods in stopped-flow experiments (see Figures 3A.6 and 3A.7 in Appendix 3 for additional comments on fitting procedures). Plots of the first observed rate constant (k_{1obs}) versus [O_2] (Figure 3.4a) were linear and the slopes of the lines represent the second order rate constants (k_1) for formation of the intermediate (η^1-O_2)V(N[^{t}Bu]Ar)$_3$ complex. Temperature dependent values of k_1 are provided in Table 3.1 and reveal that the initial binding to form the (η^1-O_2)V(N[^{t}Bu]Ar)$_3$ intermediate is extremely rapid even at −80 °C. The relative magnitudes of k_1 versus k_{-1} (noted from the intercepts in the plots of k_{1obs} versus [O_2]) suggest that the reaction is essentially irreversible over the temperature range studied.

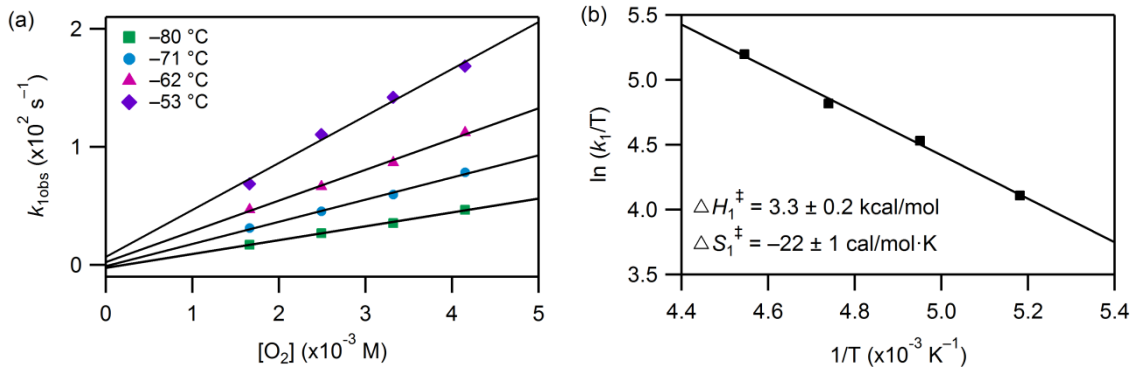

Figure 3.4. (a) Temperature dependent bimolecular rate plots corresponding to formation of (η^1-O_2)V(N[^{t}Bu]Ar)$_3$ from −80 °C to −53 °C with [V(N[^{t}Bu]Ar)$_3$]$_0$ = 0.3 mM and [O_2]$_0$ = 1.7 to 4.15 mM. (b) Eyring plot with derived activation parameters.

Activation parameters for this process were derived from the Eyring plot shown in Figure 3.4b and the low enthalpy of activation found for this reaction step ($\Delta H_1^{\ddagger}$ = 3.3 ± 0.2 kcal mol^{-1}) is typical of O_2 binding at a vacant metal site.[6,38] The entropy of activation ($\Delta S_1^{\ddagger}$ = −22 ± 1 cal mol^{-1} K^{-1}) is consistent with an associative process.

Table 3.1. Temperature dependent second order rate constants (k_1) for formation of (η^1-O_2)V(N[^{t}Bu]Ar)$_3$ and estimation of k_{-1} and K_{eq} for O_2 binding. Values of k_{1obs} are provided in Appendix 3, Table 3A.1.

T (°C)	k_1 (×10^3 M^{-1}s^{-1})	k_{-1} (s^{-1})	K_{eq} (×10^3 M^{-1})
−80	11.8 ± 0.4	−2.5 ± 1.3	-----
−71	18.8 ± 1.0	−0.9 ± 2.9	-----
−62	26.1 ± 1.2	2.4 ± 3.5	11 ± 16
−53	39.8 ± 3.0	6.8 ± 9.0	5.8 ± 7.7

The second, slower process governed by k_{2obs} showed no dependence on [O_2] as shown in Figure 3.5a; an average value of k_{2obs} at each temperature was taken as the true first order rate constant (k_2) for isomerization of (η^1-O_2)V(N[^{t}Bu]Ar)$_3$ to (η^2-O_2)V(N[^{t}Bu]Ar)$_3$ (Table 3.2). The derived activation parameters for this process reveal a much higher activation enthalpy ($\Delta H_2^{\ddagger}$ = 10 ± 1 kcal mol^{-1}) than that of the previous step and an entropy of activation that is close to zero (Figure 3.5b), which further supports the assignment of this step as rearrangement of the intermediate end-on peroxo to the side-on peroxo adduct. Solution calorimetric studies of the reaction of V(N[^{t}Bu]Ar)$_3$ with O_2 to form (η^2-O_2)V(N[^{t}Bu]Ar)$_3$ (10 °C in heptane) yielded ΔH = −75.0 ± 2.0 kcal mol^{-1}.

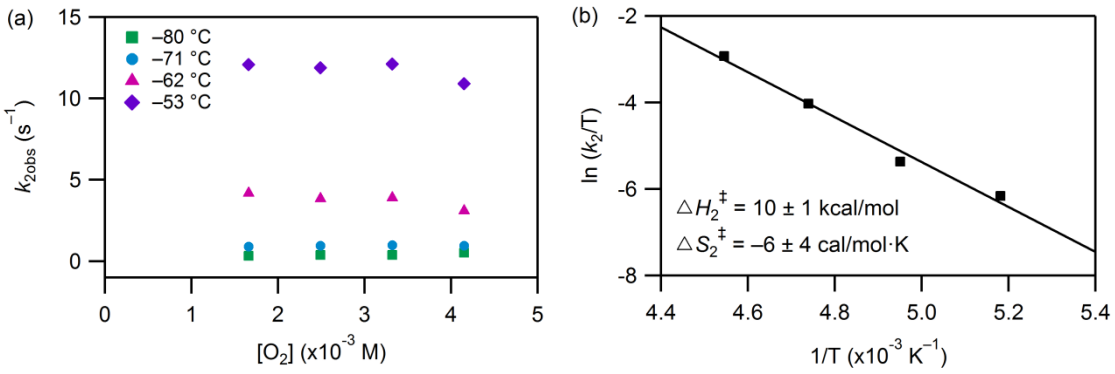

Figure 3.5. (a) Temperature dependent bimolecular rate plots corresponding to formation of (η^2-O_2)V(N[^{t}Bu]Ar)$_3$ from −80 °C to −53 °C with [V(N[^{t}Bu]Ar)$_3$]$_0$ = 0.3 mM and [O_2]$_0$ = 1.7 to 4.15 mM. (b) Eyring plot with derived activation parameters.

Table 3.2. Temperature dependent first order rate constants for η^2-peroxo formation (k_2) measured at λ= 597 nm with [V(N[^{t}Bu]Ar)$_3$]$_0$ = 0.3 mM. Observed rate constants (k_{2obs}) were obtained from biexponential fits over a 3 s (at two lower temperatures) or 2 s (at two higher temperatures) time range (see Figure 3A.7). The average value of k_{2obs} was obtained across the [O_2] range at each temperature and these values were taken as the true first order rate constant (k_2) for η^2-peroxo formation. Values of k_{2obs} are provided in Appendix 3, Table 3A.2.

T (°C)	k_2 (s^{-1})
−80	0.408 ± 0.086
−71	0.944 ± 0.039
−62	3.77 ± 0.46
−53	11.8 ± 0.6

Binding of O_2 to V(N[^{t}Bu]Ar)$_3$ was also investigated computationally, and DFT geometry optimizations of the η^1-O_2 and η^2-O_2 adducts were carried out for both the singlet and triplet spin states. The minimal-energy triplet geometry was found to be 26.2 kcal mol^{-1} higher than the minimal-energy singlet geometry. For the singlet manifold, two stable structures were computed, corresponding to the η^1-O_2 complex and the η^2-O_2 complex. A small energy difference of only 4.2 kcal mol^{-1} was found for the two isomers, favoring η^2 binding. The DFT-minimized structure of (η^2-O_2)V(N[^{t}Bu]Ar)$_3$

contains a more symmetrical peroxo ligand than found experimentally. The computed V−O distances are 1.830 and 1.851 Å, and the O−O distance is 1.471 Å. Minimization of (η^2-O_2)V(N[^{t}Bu]Ar)$_3$ while constraining it to have the crystallographic V−O and O−O metrics yields an energy that is only 2.4 kcal mol^{-1} higher, an increase for which the formation of the weak hydrogen bond (< 4 kcal mol^{-1}) compensates.[37a]

The computed metrical parameters and electronic structure of the intermediate (η^1-O_2)V(N[^{t}Bu]Ar)$_3$ species are consistent with its formulation as a V^V peroxo as opposed to a V^{IV} superoxo species. The DFT-calculated η^1-O_2 complex has a V−O distance of 1.676 Å, an O−O distance of 1.307 Å, and a V−O−O bond angle of 179.3°. The Mayer bond order[39] of the O−O bond decreases upon isomerization, going from 0.98 in (η^1-O_2)V(N[^{t}Bu]Ar)$_3$ to 0.82 in (η^2-O_2)V(N[^{t}Bu]Ar)$_3$, consistent with a more activated, albeit less accessible, O_2 in the side-bound adduct. The end-bound complex has a Mayer bond order of 1.13 for the V−O bond, which is an increase in multiple-bond character with respect to the V−O bonds in (η^2-O_2)V(N[^{t}Bu]Ar)$_3$ (average = 0.93 Å), consistent with the short V−O bond length. In fact, the main contributing resonance structure according to natural resonance theory analysis[40] contains a V−O double bond and an O−O single bond; the main contributing resonance structure for (η^2-O_2)V(N[^{t}Bu]Ar)$_3$ contains two V−O single bonds and an O−O single bond. The potential energy surface for the isomerization of (η^1-O_2)V(N[^{t}Bu]Ar)$_3$ to (η^2-O_2)V(N[^{t}Bu]Ar)$_3$ was mapped by varying the V−O−O bond angle from 180 to 67° as shown in Figure 3.6.

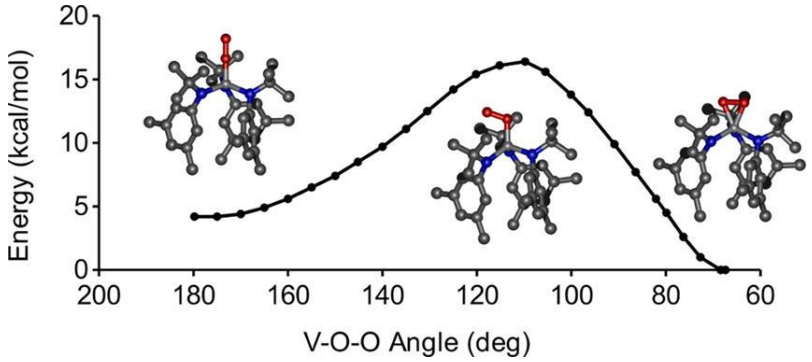

Figure 3.6. DFT-calculated potential energy surface for isomerization of (η^1-O_2)V(N[^{t}Bu]Ar)$_3$ to (η^2-O_2)V(N[^{t}Bu]Ar)$_3$ with computed values of $\Delta H_{isomerization}$ = 4.2 kcal mol^{-1} and $\Delta H^{\ddagger}_{isomerization}$ = 16.4 kcal mol^{-1}.

A transition state ([(η^1-O_2)V(N[^{t}Bu]Ar)$_3$]‡) was located at a V−O−O angle of 109.8°, providing an activation energy (E_a) of 12.2 kcal mol^{-1} for the η^1 to η^2 isomerization process, which is in good agreement with experiment. The isoelectronic chromium nitrosyl complexes, which are known to be N-bound, have been previously isolated and were readily deoxygenated by (THF)V(Mes)$_3$ to give the terminal Cr^{VI} nitrido species.[41] If the analogous (η^1-O_2)V(N[^{t}Bu]Ar)$_3$ species exists in equilibrium with (η^2-O_2)V(N[^{t}Bu]Ar)$_3$, then addition of V(N[^{t}Bu]Ar)$_3$ could be used to deoxygenate the η^1-O_2 peroxo complex to give two equivalents of the oxo complex, OV(N[^{t}Bu]Ar)$_3$ (Figure 3.1). Indeed, ^{1}H NMR spectroscopic kinetic studies of the reaction of (η^2-O_2)V(N[^{t}Bu]Ar)$_3$ with V(N[^{t}Bu]Ar)$_3$ confirmed this, and an activation energy of 14 ± 3 kcal mol^{-1} was determined for this process (Appendix 3, Figures 3A.8 - 3A.10). The computed enthalpy of activation for conversion of (η^2-O_2)V(N[^{t}Bu]Ar)$_3$ to (η^1-O_2)V(N[^{t}Bu]Ar)$_3$ ($\Delta H^{\ddagger}$ = 16.4 kcal mol^{-1}) is in good agreement with the experimentally derived value. Despite the fact that it is thermodynamically comparable to N_2O as an OAT reagent, the deoxygenation of (η^2-O_2)V(N[^{t}Bu]Ar)$_3$ by V(N[^{t}Bu]Ar)$_3$ is relatively

slow. This is interpreted to be a result of the requisite formation of (η^1-O_2)V(N[^{t}Bu]Ar)$_3$, which is sterically more accessible for OAT with V(N[^{t}Bu]Ar)$_3$ than is the η^2-O_2 isomer, as illustrated by the Fukui functions when plotted on the electron density (Figures 3A.12 - 3A.14).[42]

Figure 3.7 shows a combined potential energy diagram for this system in which the experimental energy of O_2 binding has been combined with the computed relative energies for (η^1-O_2)V(N[^{t}Bu]Ar)$_3$ and (η^2-O_2)V(N[^{t}Bu]Ar)$_3$ binding and interconversion; also incorporated in the diagram are the activation energies from the stopped-flow and ^{1}H NMR kinetic experiments. For reasons that are not yet understood, the overall computed ΔH of binding of O_2 to V(N[^{t}Bu]Ar)$_3$ to yield (η^2-O_2)V(N[^{t}Bu]Ar)$_3$ is −51.2 kcal mol^{-1}, which is in nontrivial disagreement with the experimental value of −75 kcal mol^{-1}. In contrast, good agreement between theory and experiment was found for the computed O≡V bond strength in OV(N[^{t}Bu]Ar)$_3$.[32]

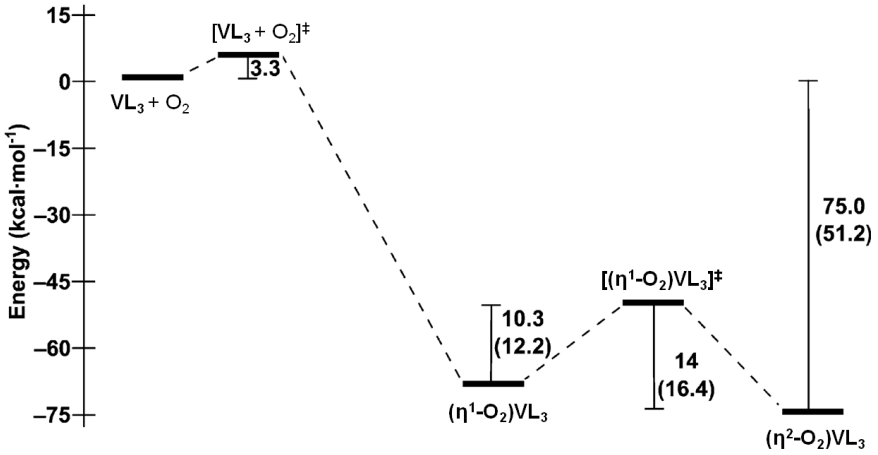

Figure 3.7. Experimental and DFT-calculated (in parentheses) potential energy diagram (in kcal mol^{-1}) for the reaction between O_2 and V(N[^{t}Bu]Ar)$_3$ to form (η^2-O_2)V(N[^{t}Bu]Ar)$_3$. L = N[^{t}Bu]Ar.

Lastly, during attempts to obtain pure (η^2-O_2)V(N[^{t}Bu]Ar)$_3$ by addition of ^{t}BuCN to solutions of V(N[^{t}Bu]Ar)$_3$ followed by addition of O_2, it was observed that at −45 °C a change in color from royal purple to dark green occurred over the course of one hour. The reaction mixture was assayed by ^{51}V NMR spectroscopy and was found to contain a mixture of (η^2-O_2)V(N[^{t}Bu]Ar)$_3$ and a new product whose ^{51}V NMR signal was split into a 1:1:1 triplet (Figure 3.8 inset).

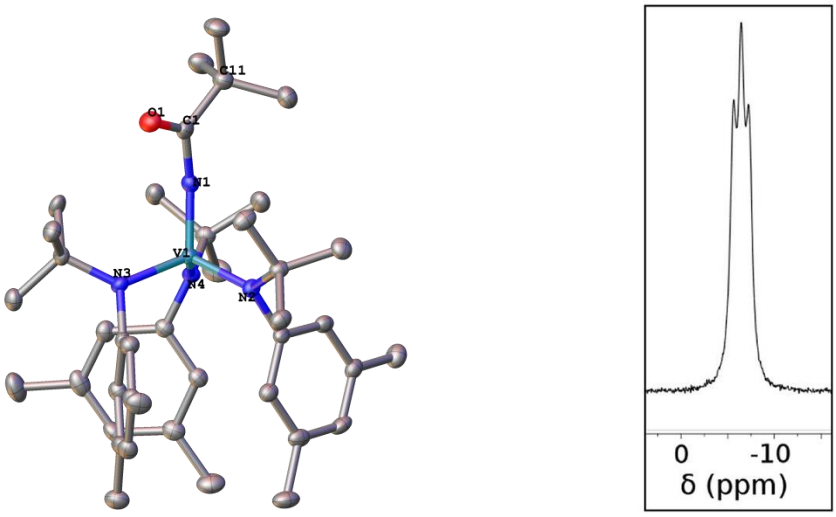

Figure 3.8. Thermal ellipsoid plot of (^{t}BuC(=O)N)V(N[^{t}Bu]Ar)$_3$ drawn at the 50% probability level; hydrogen atoms have been omitted for clarity. Selected atomic distances (Å) and angles (deg): V1−N1 = 1.695(3); V1−N2 = 1.875(2); V1−N3 = 1.888(2); V1−N4 = 1.894(3); N1−C1 = 1.390(4); C1−O1 = 1.218(4); V1−N1−C1 = 151.9(2); N1−C1−O1 = 120.8(3); N1−C1−C11 = 118.0(3). Inset: ^{51}V NMR spectrum of (^{t}BuC(=O)N)V(N[^{t}Bu]Ar)$_3$ in THF.

Manually isolated crystals of the new product were determined to be the result of aerobic oxygen atom transfer to the bound nitrile to form the acylimido species, (^{t}BuC(=O)N)V(N[^{t}Bu]Ar)$_3$, as shown in Figure 3.8. Acylimido moieties are typically prepared by the treatment of terminal metal nitrides with acylating agents;[43] rarer is the direct oxidation of a metal-bound nitrile to form the acylimido.[44] The spin-spin coupling

is assigned to $^{1}J_{^{14}N-^{51}V}$ coupling (83 Hz). The identity of (^{t}BuC(=O)N)V(N[^{t}Bu]Ar)$_3$ was further confirmed via its independent synthesis from Na[N≡V(N[^{t}Bu]Ar)$_3$][45] and pivaloyl chloride.

3.4. Conclusion

This work reports the structure, physical studies, and mechanism of formation of a novel side-on vanadium peroxo complex and represents the first structurally characterized example of a non-vanadyl V^{V} peroxide obtained from the controlled reaction of an unsaturated V^{III} complex with O_2. Despite the industrial and biological importance of oxidation reactions mediated by metal centers,[8,9] the formation of early metal peroxides by the direct reaction of a low-valent and unsaturated transition-metal complex with O_2 is still remarkably rare. Moreover, we were able to observe and quantify the rates of η^1 to η^2 conversion in O_2 binding via stopped-flow methodology, a pathway that has been proposed as a general step in η^2-peroxide formation from O_2.[2] The energy difference between the two binding modes is small and implies that it could be influenced in either direction by tailoring of the ligand environment.

Solution calorimetric studies of the binding of O_2 to V(N[^{t}Bu]Ar)$_3$ suggest that η^2-O_2V(N[^{t}Bu]Ar)$_3$ should be a potent oxidant. It is encouraging that careful tailoring of the reaction conditions led to the clean generation of (η^2-O_2)V(N[^{t}Bu]Ar)$_3$ from O_2, suggesting that similar control may be applied more generally to other low valent and unsaturated early transition-metal complexes, leading to a class of thermodynamically

potent OAT reagents. Additional studies of O_2 binding and activation in this and related systems are still in progress.

3.5. References

(1) *This chapter is reproduced in part with permission from:* Cozzolino, A. F.; Tofan, D.; Cummins, C. C.; Temprado, M.; Palluccio, T. D.; Rybak-Akimova, E. V.; Majumdar, S.; Cai, X.; Captain, B.; Hoff, C. D. Two-Step Binding of O_2 to a Vanadium(III) Trisanilide Complex to Form a Non-Vanadyl Vanadium(V) Peroxo Complex. *J. Am. Chem. Soc.*, **2012**, *134*, 18249−18252. Copyright 2012 American Chemical Society.

(2) Rybak-Akimova, E. V. In *Physical Inorganic Chemistry: Reactions, Processes, and Applications*; Bakac, A., Ed.; Wiley: Hoboken, NJ, 2010; pp 109-188.

(3) Unno, M.; Chen, H.; Kusama, S.; Shaik, S.; Ikeda-Saito, M. *J. Am. Chem. Soc.*, **2007**, *129*, 13394.

(4) De Waal, D. J. A.; Gerber, T. I. A.; Louw, W. J.; Van Eldik, R. *Inorg. Chem.*, **1982**, *21*, 2002.

(5) Aboelella, N. W.; Kryatov, S. V.; Gherman, B. F.; Brennessel, W. W.; Young, V. G.; Sarangi, R.; Rybak-Akimova, E. V.; Hodgson, K. O.; Hedman, B.; Solomon, E. I.; Cramer, C. J.; Tolman, W. B. *J. Am. Chem. Soc.*, **2004**, *126*, 16896.

(6) Cai, X.; Majumdar, S.; Fortman, G. C.; Cazin, C. S. J.; Slawin, A. M. Z.; Lhermitte, C.; Prabhakar, R.; Germain, M. E.; Palluccio, T.; Nolan, S. P.; Rybak-Akimova, E. V.; Temprado, M.; Captain, B.; Hoff, C. D. *J. Am. Chem. Soc.*, **2011**, *133*, 1290.

(7) Popp, B. V.; Wendlandt, J. E.; Landis, C. R.; Stahl, S. S. *Angew. Chem., Int. Ed.*, **2007**, *46*, 601.

(8) Wever, R. In *Vanadium: Biochemical and Molecular Biological Approaches*; Michibata, H., Ed.; Springer: New York, 2012; pp 95-125.

(9) Conte, V.; Coletti, A.; Floris, B.; Licini, G.; Zonta, C. *Coord. Chem. Rev.*, **2011**, *255*, 2165.

(10) Butler, A.; Clague, M. J.; Meister, G. E. *Chem. Rev.*, **1994**, *94*, 625.

(11) (a) Egdal, R. K.; Bond, A. D.; McKenzie, C. J. *Dalton Trans.*, **2009**, 3833. (b) Waidmann, C. R.; DiPasquale, A. G.; Mayer, J. M. *Inorg. Chem.*, **2010**, *49*, 2383.

(12) (a) Arzoumanian, H.; Petrignani, J. F.; Pierrot, M.; Ridouane, F.; Sanchez, J. *Inorg. Chem.*, **1988**, *27*, 3377. (b) Hagadorn, J. R.; Arnold, J. *Inorg. Chem.*, **1997**, *36*, 2928. (c) Hanna, T. E.; Lobkovsky, E.; Chirik, P. J. *Inorg. Chem.*, **2007**, *46*, 2359. (d) Jeske, P.; Haselhorst, G.; Weyhermüller, T.; Wieghardt, K.; Nuber, B. *Inorg. Chem.*, **1994**, *33*, 2462. (e) Lyashenko, G.; Saischek, G.; Pal, A.; Herbst-Irmer, R.; Mösch-Zanetti, N. C. *Chem. Commun.*, **2007**, 701. (f) Matoga, D.; Szklarzewicz, J.; Mikuriya, M. *Inorg. Chem.*, **2006**, *45*, 7100. (g) Matoga, D.; Szklarzewicz, J.; Samotus, A.; Burgess, J.; Fawcett, J.; Russell, D. R. *Polyhedron*, **2000**, *19*, 1503. (h) Qin, K.; Incarvito, C. D.; Rheingold, A. L.; Theopold, K. H. *Angew. Chem., Int. Ed.*, **2002**, *41*, 2333. (i) Sofetis, A.; Fotopoulou, F.; Raptopoulou, C. P.; Zafiropoulos, T. F.; Perlepes, S. P.; Klouras, N. *Polyhedron*, **2009**, *28*, 3356. (j) Stanciu, C.; Jones,

M. E.; Fanwick, P. E.; Abu-Omar, M. M. *J. Am. Chem. Soc.*, **2007**, *129*, 12400. (k) Van Asselt, A.; Trimmer, M. S.; Henling, L. M.; Bercaw, J. E. *J. Am. Chem. Soc.*, **1988**, *110*, 8254. (l) Yokoyama, A.; Han, J. E.; Cho, J.; Kubo, M.; Ogura, T.; Siegler, M. A.; Karlin, K. D.; Nam, W. *J. Am. Chem. Soc.*, **2012**, *134*, 15269.

(13) (a) Groysman, S.; Goldberg, I.; Goldschmidt, Z.; Kol, M. *Inorg. Chem.*, **2005**, *44*, 5073. (b) Liu, Z.; Anson, F. C. *Inorg. Chem.*, **2001**, *40*, 1329. (c) Tsuchida, E. *Coord. Chem. Rev.*, **2003**, *237*, 213.

(14) Fickes, M. G. Synthesis and Reactivity of Vanadium and Niobium Complexes Containing Sterically Demanding Amido Ligands, Ph.D Thesis, Massachusetts Institute of Technology, 1998.

(15) Sheldrick, G. M. CELL_NOW **2003**.

(16) Sheldrick, G. M. SHELX97 (Includes SHELXS97, SHELXL97, CIFTAB) - Programs for Crystal Structure Analysis, release 97-2 **1998**.

(17) (a) Sheldrick, G. M. SADABS: Program for Empirical Absorption Correction of Area Detectors **1996**. (b) Sheldrick, G. M. TWINABS: Program for Performing Absorption Corrections to X-ray Diffraction Patterns Collected from Non-Merohedrally Twinned and Multiple Crystals **2002**.

(18) Müller, P.; Herbst-Irmer, R.; Spek, A. L.; Schneider, T. R.; Sawaya, M. R. *Crystal Structure Refinement: A Crystallographer's Guide to SHELXL*. IUCr Texts on Crystallography; Oxford University Press: Oxford, 2006.

(19) Battino, R.; Rettich, T. R.; Tominaga, T. *J. Phys. Chem. Ref. Data*, **1983**, *12*, 163.

(20) (a) Becke, A. D. *J. Chem. Phys.*, **1993**, *98*, 5648. (b) Perdew, J. P. *Phys. Rev. B*, **1986**, *33*, 8822.

(21) Frisch, M. J. et al. Gaussian 09, revision B.01 **2010**.

(22) (a) Wadt, W. R.; Hay, P. J. *J. Chem. Phys.*, **1985**, *82*, 284. (b) Hay, P. J.; Wadt, W. R. *J. Chem. Phys.*, **1985**, *82*, 279. (c) Hay, P. J.; Wadt, W. R. *J. Chem. Phys.*, **1985**, *82*, 299.

(23) Dunning Jr., T. H.; Hay, P. J. *Modern Theoretical Chemistry, Vol. 3*; Schaefer III, H. F., Ed.; Plenum: New York, 1976; pp. 1-28.

(24) Martin, J. M. L.; Sundermann, A. *J. Chem. Phys.*, **2001**, 114.

(25) Dolg, M.; Wedig, U.; Stoll, H.; Preuss, H. *J. Chem. Phys.*, **1987**, *86*, 866.

(26) (a) Boys, S. F.; Bernardi, F. *Mol. Phys.*, **1970**, 19. (b) Simon, S.; Duran, M.; Dannenberg, J. J. *J. Chem. Phys.*, **1996**, 105.

(27) Neese, F. ORCA, Version 2.8 **2010**.

(28) Perdew, J. P.; Wang, Y. *Phys. Rev. B*, **1992**, *45*, 13244.

(29) (a) van Lenthe, E.; Baerends Evert, J.; Snijders, J. G. *J. Chem. Phys.*, **1993**, *99*, 4597. (b) Heully, J. L.; Lindgren, I.; Lindroth, E.; Lundqvist, S.; Maartensson-Pendrill, A. M. *J. Phys. B: At. Mol. Phys.*, **1986**, *19*, 2799.

(30) (a) Pantazis, D. A.; Chen, X.-Y.; Landis, C. R.; Neese, F. *J. Chem. Theory Comput.*, **2008**, *4*, 908. (b) Schaefer, A.; Horn, H.; Ahlrichs, R. *J. Chem. Phys.*, **1992**, *97*, 2571.

(31) (a) Glendening, E. D.; Badenhoop, J. K.; Reed, A. E.; Carpenter, J. E.; Bohmann, J. A.; Morales, C. M.; Weinhold, F. NBO 5.0 **2001**. (b) Glendening, E. D.; Badenhoop, J. K.; Weinhold, F. *J. Comp. Chem.*, **1998**, *19*, 628. (c) Glendening, E. D.; Weinhold, F. *J. Comp. Chem.*, **1998**, *19*, 593. (d) Glendening, E. D.; Weinhold, F. *J. Comp. Chem.*, **1998**, *19*, 610.

(32) Palluccio, T. D.; Rybak-Akimova, E. V.; Majumdar, S.; Cai, X.; Chui, M.; Temprado, M.; Silvia, J. S.; Cozzolino, A. F.; Tofan, D.; Velian, A.; Cummins, C. C.; Captain, B.; Hoff, C. D. *J. Am. Chem. Soc.*, **2013,** *135*, 11357.

(33) Tatiersky, J.; Pacigová, S.; Sivák, M.; Schwendt, P. *J. Argent. Chem. Soc.*, **2009**, *97*, 181.

(34) Sergienko, V. S. *Crystallogr. Rep.*, **2004**, *49*, 907.

(35) (a) Grzywa, M.; Łasocha, W. *Z. Kristallogr.*, **2007**, *222*, 95. (b) Won, T. J.; Barnes, C. L.; Schlemper, E. O.; Thompson, R. C. *Inorg. Chem.*, **1995**, *34*, 4499.

(36) (a) Cambridge Structural Database, version 5. 3, Nov 2011 with 586977 entries. (b) Allen, F. H. *Acta Crystallogr.*, **2002**, *B58*, 380.

(37) (a) Desiraju, G.; Steiner, T. *The Weak Hydrogen Bond*; Oxford University Press: Oxford, U.K., 1999. (b) Weinhold, F.; Klein, R. A. *Mol. Phys.*, **2012**, *110*, 565.

(38) (a) Rybak-Akimova, E. V.; Marek, K.; Masarwa, M.; Busch, D. H. *Inorg. Chim. Acta*, **1998**, *270*, 151. (b) Fry, H. C.; Scaltrito, D. V.; Karlin, K. D.; Meyer, G. J. *J. Am. Chem. Soc.*, **2003**, *125*, 11866.

(39) Mayer, I. Int. *J. Quantum Chem.*, **1984**, *26*, 151.

(40) Glendening, E. D.; Badenhoop, J. K.; Weinhold, F. *J. Comput. Chem.*, **1998**, *19*, 628.

(41) Odom, A. L.; Cummins, C. C.; Protasiewicz, J. D. *J. Am. Chem. Soc.*, **1995**, *117*, 6613.

(42) Yang, W.; Parr, R. G.; Pucci, R. *J. Chem. Phys.*, **1984**, *81*, 2862.

(43) (a) Leung, W. H.; Chim, J. L. C.; Williams, I. D.; Wong, W. T. *Inorg. Chem.*, **1999**, *38*, 3000. (b) Clough, C. R.; Greco, J. B.; Figueroa, J. S.; Diaconescu, P. L.; Davis, W. M.; Cummins, C. C. *J. Am. Chem. Soc.*, **2004**, *126*, 7742. (c) Figueroa, J. S.; Piro, N. A.; Clough, C. R.; Cummins, C. C. *J. Am. Chem. Soc.*, **2006**, *128*, 940.

(44) (a) Thomas, S.; Lim, P. J.; Gable, R. W.; Young, C. G. *Inorg. Chem.*, **1998**, *37*, 590. (b) Nielson, A. J.; Hunt, P. A.; Rickard, C. E. F.; Schwerdtfeger, P. *J. Chem. Soc., Dalton Trans.*, **1997**, 3311.

(45) Brask, J. K.; Fickes, M. G.; Sangtrirutnugul, P.; Durà-Vilà, V.; Odom, A. L.; Cummins, C. C. *Chem. Commun.*, **2001**, 1676.

APPENDIX 3

Two-Step Binding of Dioxygen to a Vanadium(III) Tris-Anilide Complex to Form a Non-Vanadyl Vanadium(V) Peroxo Complex

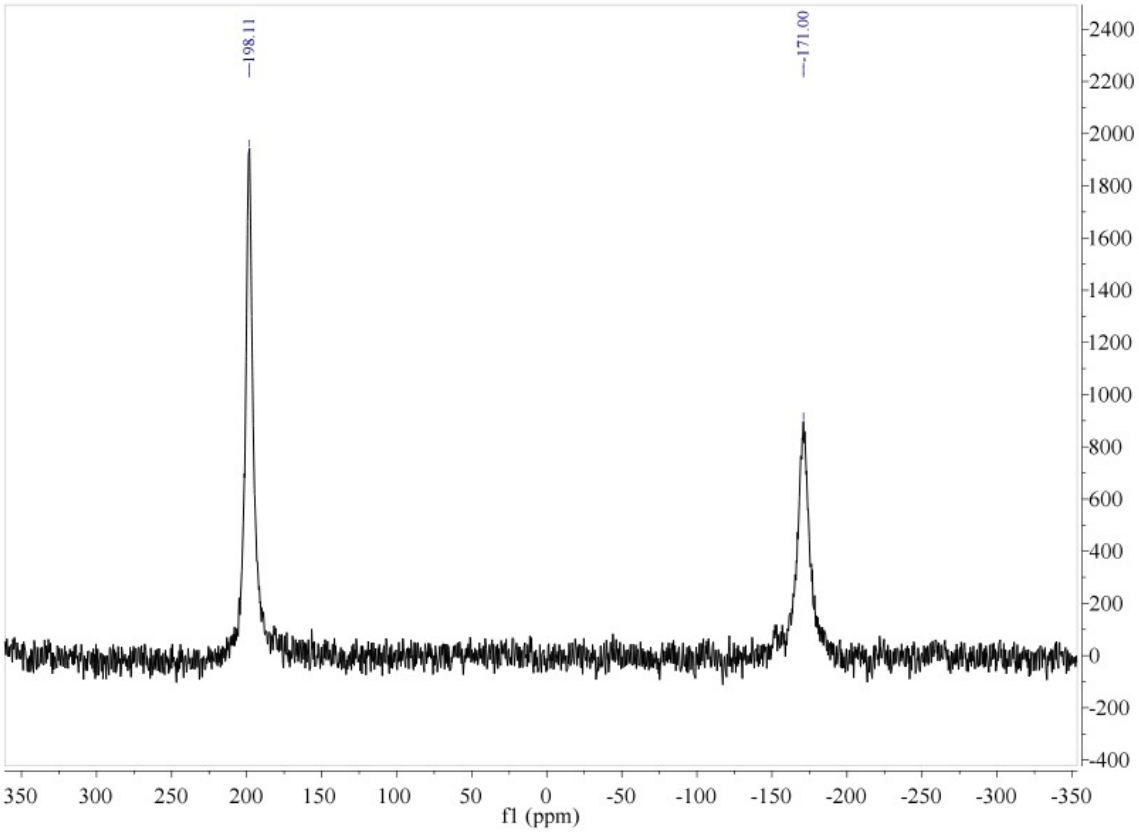

Figure 3A.1. ^{51}V NMR spectrum of (η^2-O_2)V(N[^{t}Bu]Ar)$_3$ in toluene revealing a mixture of OV(N[^{t}Bu]Ar)$_3$ (–171 ppm) and (η^2-O_2)V(N[^{t}Bu]Ar)$_3$ (198 ppm) (referenced externally to $OVCl_3$). Sample was prepared at –78 °C via reaction of V(N[^{t}Bu]Ar)$_3$ with 1 atm O_2 in the absence of ^{t}BuCN.

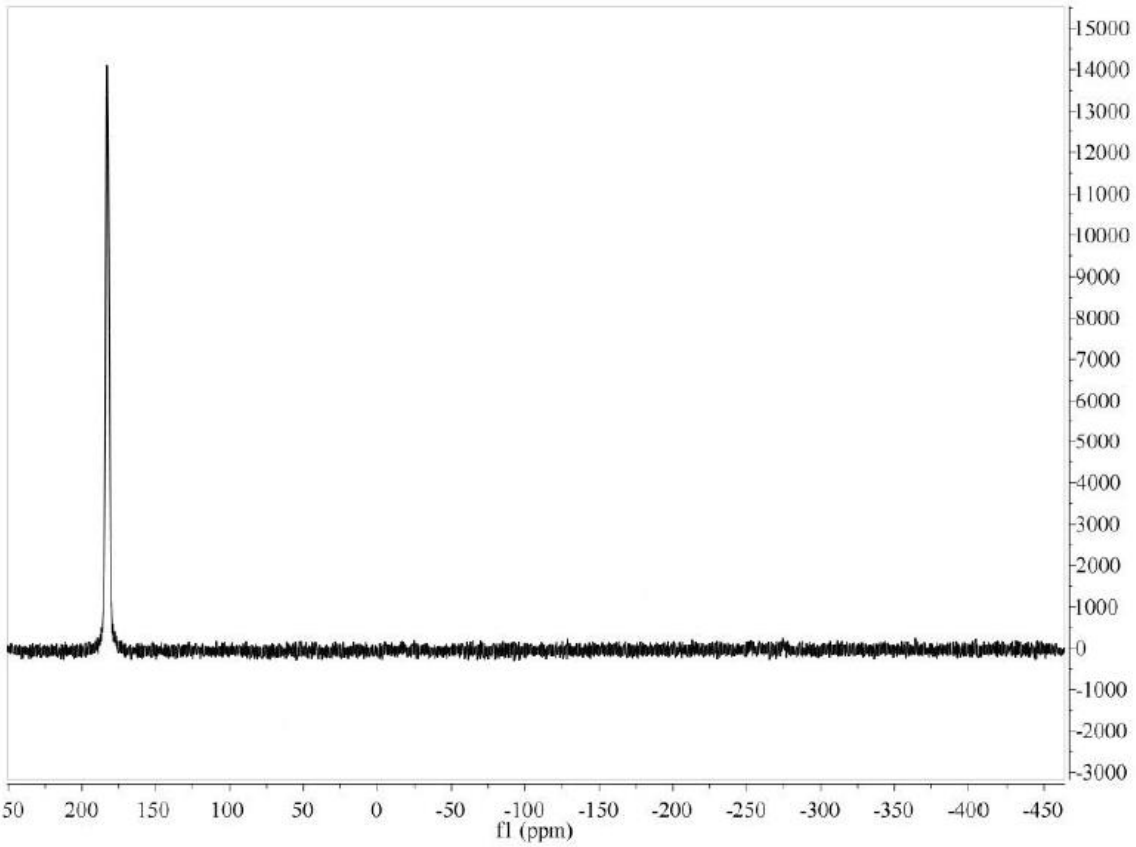

Figure 3A.2. ^{51}V NMR spectrum of (η^2-O_2)V(N[^{t}Bu]Ar)$_3$ in pentane prepared at ambient temperature via the "nitrile method". Signal appears at 183.1 ppm and shows no contamination from OV(N[^{t}Bu]Ar)$_3$ (referenced externally to $OVCl_3$).

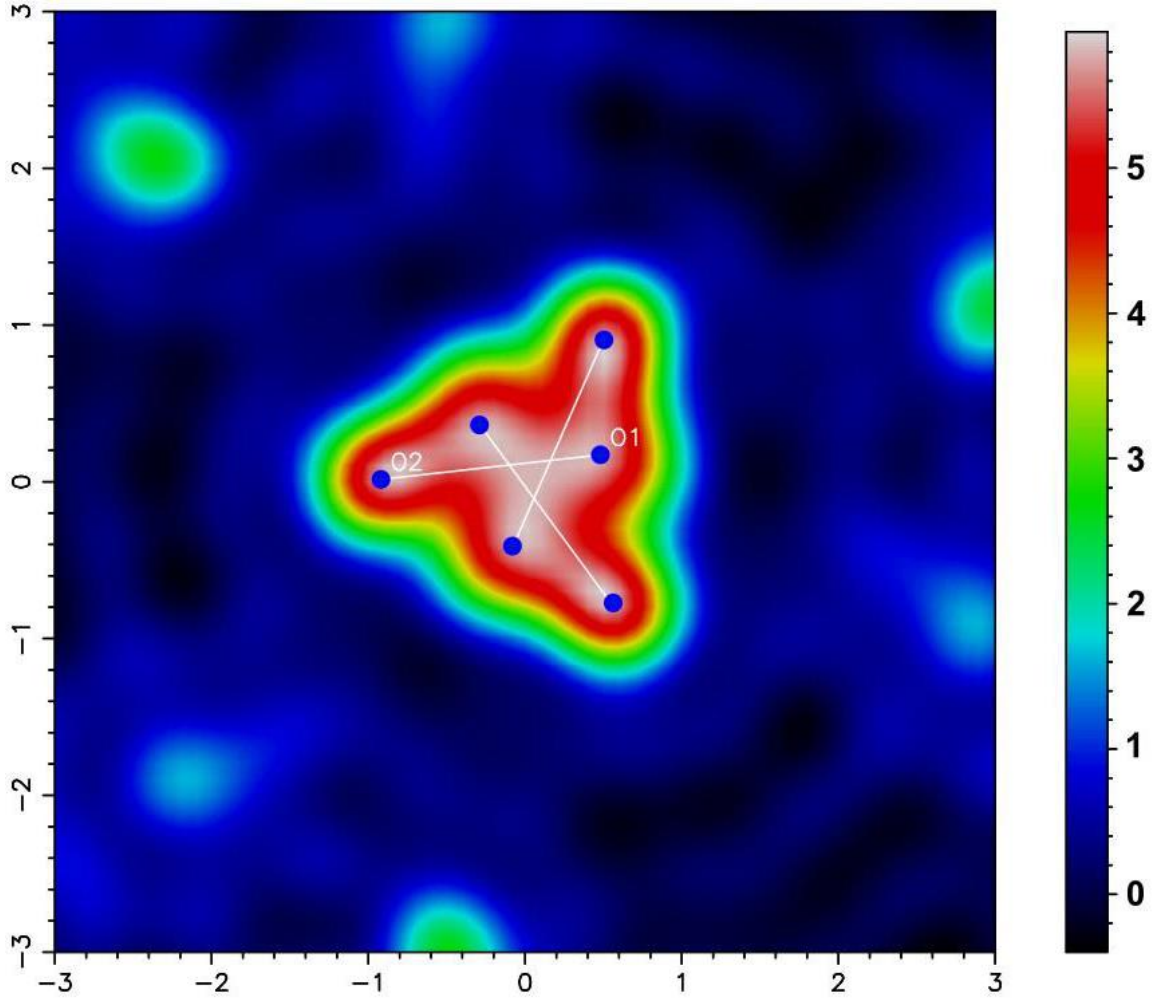

Figure 3A.3. Electron density map (e/Å^3) from the crystal structure of (η^2-O_2)V(N[^{t}Bu]Ar)$_3$ cut through the O_2 plane. Atom positions are indicated with blue spots and bonds are indicated with white lines.

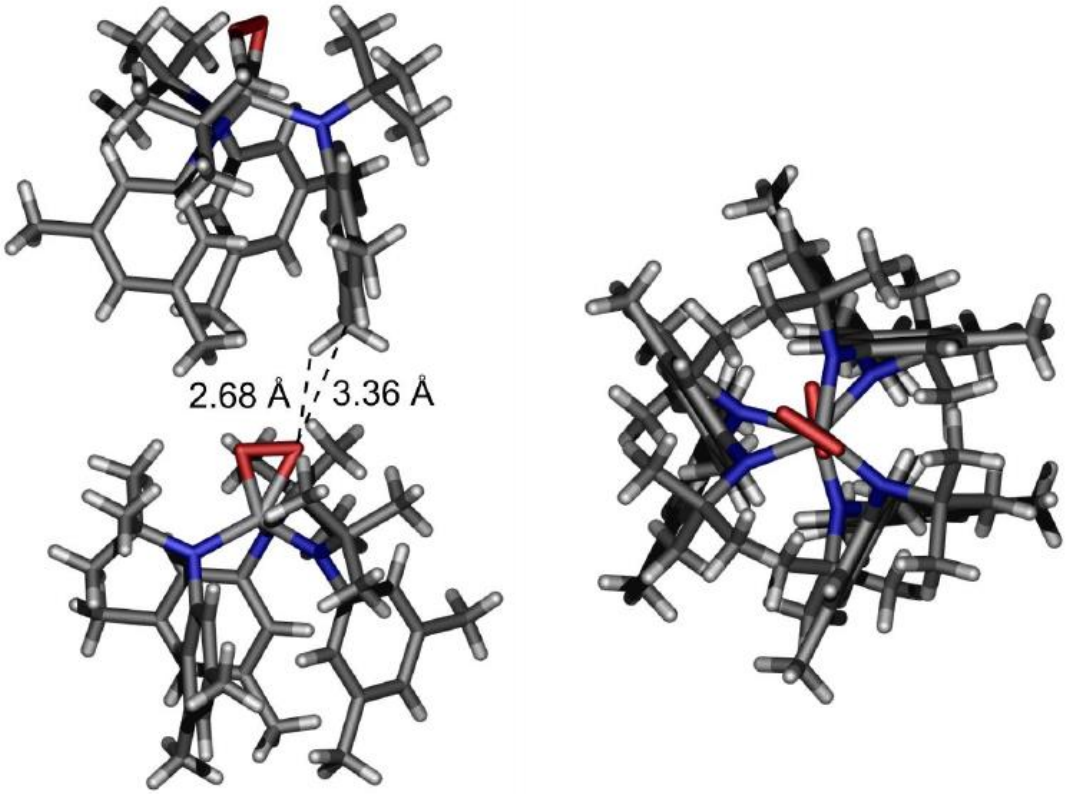

Figure 3A.4. The side and top view of a neighboring pair of molecules of (η^2-O_2)V(N[^{t}Bu]Ar)$_3$ from the crystal structure illustrating the C(H)-O hydrogen bonding pattern.

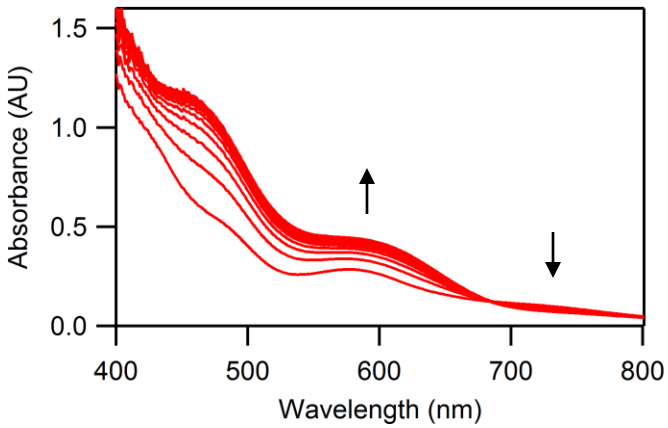

Figure 3A.5. Initial time-resolved spectral changes for the reaction between V(N[^{t}Bu]Ar)$_3$ (0.3 mM) and O_2 (2.5 mM) at −80 °C captured over the first 0.25 s of reaction, highlighting the presence of an isosbestic point at λ = 682 nm.

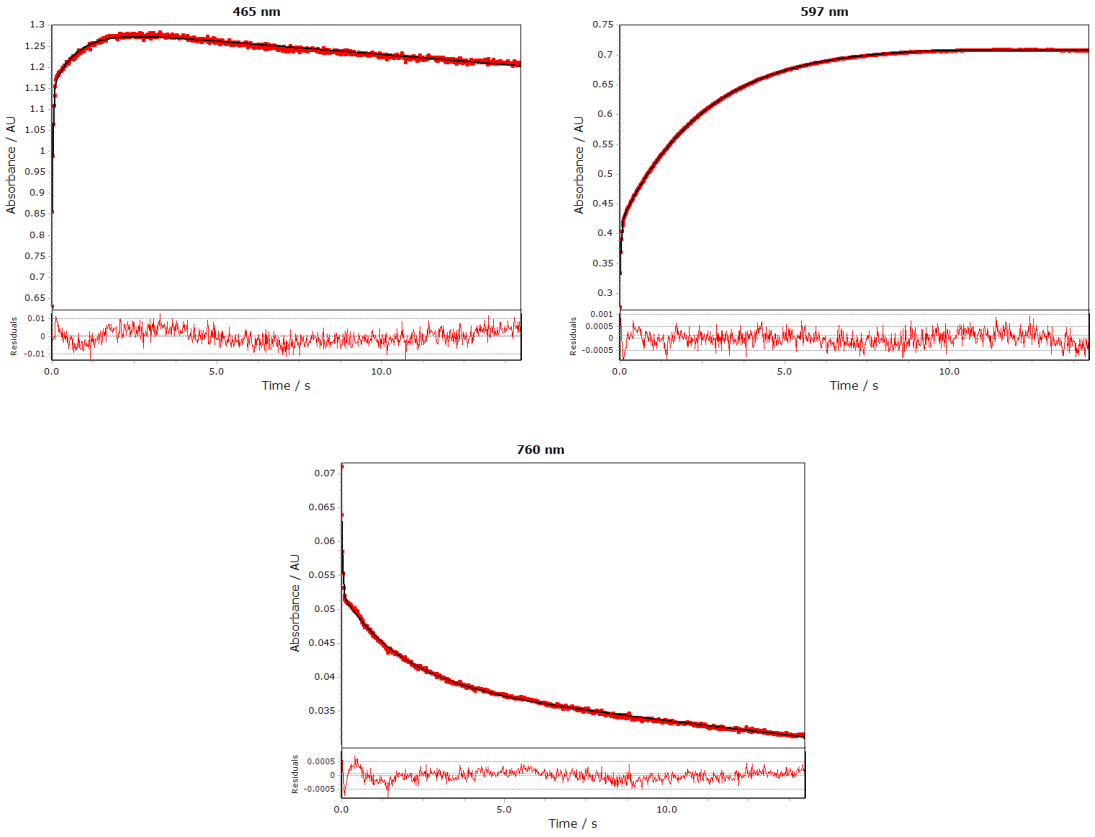

Figure 3A.6. Cross sections of the reaction between V(N[^{t}Bu]Ar)$_3$ (0.3 mM) and O_2 (2.5 mM) acquired over 14 s at –80 °C (red markers) with biexponential fits (black lines) and residuals; λ = 465 nm (top left); 597 nm (top right); 760 nm (bottom center). Values of k_{1obs} were essentially identical at all selected wavelengths and showed a linear dependence on [O_2]. Values of k_{2obs} were found to be independent of [O_2]. For quantitative analysis, kinetic traces at λ= 597 nm were used since it displayed the largest change in absorbance for each process and did not contain interferences from decomposition that occurred over longer time periods in stopped-flow experiments.

Since the measured pseudo-first order rate constants for the first step are very large relative to the second step, and the timescale of the reaction chosen such that the second slower process would be essentially complete (and as a result contain the majority of the data points), the precision in k_{1obs} was tested by fitting kinetic traces in different manners as outlined in the caption of Figure 3A.7 below.

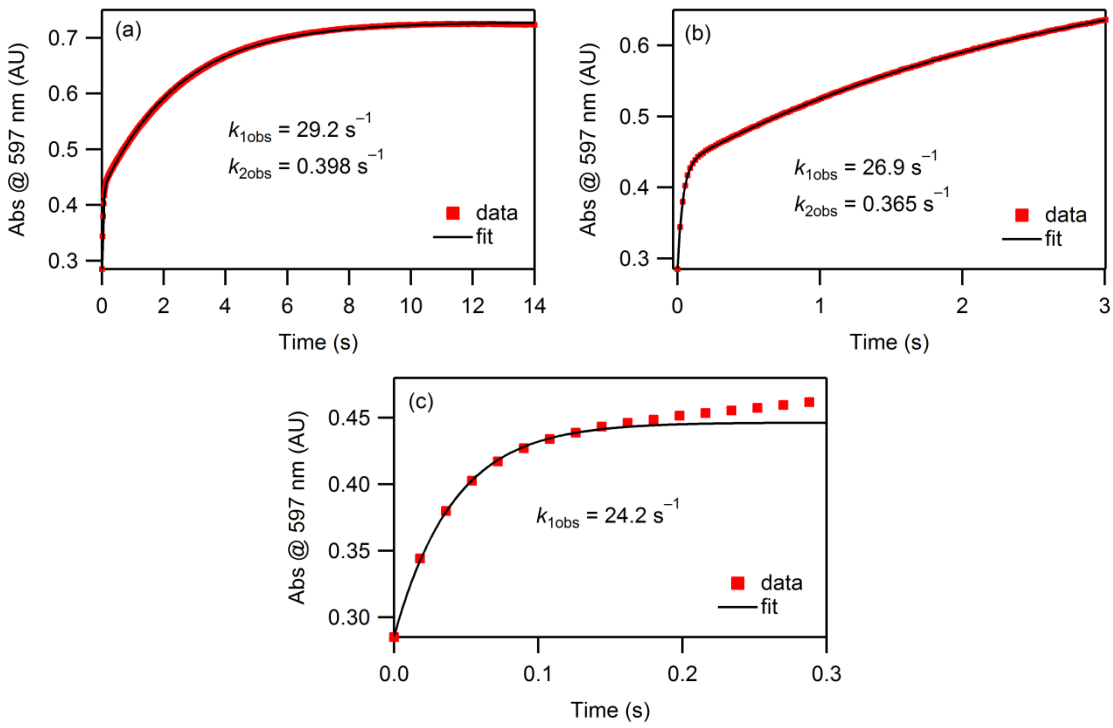

Figure 3A.7. Representative examples of fitting a kinetic trace at λ = 597 nm in different manners at −80 °C with $[O_2]_0$ = 2.5 mM (red markers = experimental data; black lines = fits). (a) Biexponential fitting of entire kinetic trace. (b) Biexponential fitting of kinetic trace to 3 s. (c) Single exponential fitting focused on first rapid process only (to 150 ms). Values for k_{1obs} were relatively unaffected by the method of fitting employed. The pseudo-first order rate constants for the second process (k_{2obs}) obtained from biexponential fits remained essentially unchanged when fits terminated at 3 s and longer.

Table 3A.1. Temperature dependent pseudo-first order rate constants (k_{1obs}) corresponding to formation of (η^1-O_2)V(N[^{t}Bu]Ar)$_3$ at λ = 597 nm with $[V(N[^tBu]Ar)_3]_0$ = 0.3 mM. Observed rate constants were obtained from biexponential fits over a 3 s (−80 °C, −71 °C) or 2 s (−62 °C, −53 °C) time range.

	k_{1obs} (s^{-1})			
$[O_2]$ (M)	−80 °C	−71 °C	−62 °C	−53 °C
0.0017	17.1	31.2	46.9	68.8
0.0025	27.0	45.4	66.6	110
0.0033	35.6	59.6	86.9	142
0.0042	46.8	78.4	112	168

Table 3A.2. Temperature dependent pseudo-first order rate constants corresponding to formation of (η^2-O_2)V(N[^{t}Bu]Ar)$_3$ at λ = 597 nm with [V(N[^{t}Bu]Ar)$_3$]$_0$ = 0.3 mM. Observed rate constants were obtained from biexponential fits over a 3 s (−80 °C, −71 °C) or 2 s (−62 °C, −53 °C) time range. The average value of k_{2obs} was obtained across the [O_2] range at each temperature and these values were taken as the true first order rate constant (k_2) for (η^2-O_2)V(N[^{t}Bu]Ar)$_3$ formation as reported in Table 3.2 in Chapter 3.

	k_{2obs} (s^{-1})			
[O_2] (M)	−80 °C	−71 °C	−62 °C	−53 °C
0.0017	0.339	0.894	4.19	12.1
0.0025	0.378	0.949	3.86	11.9
0.0033	0.382	0.983	3.91	12.1
0.0042	0.533	0.951	3.11	10.9

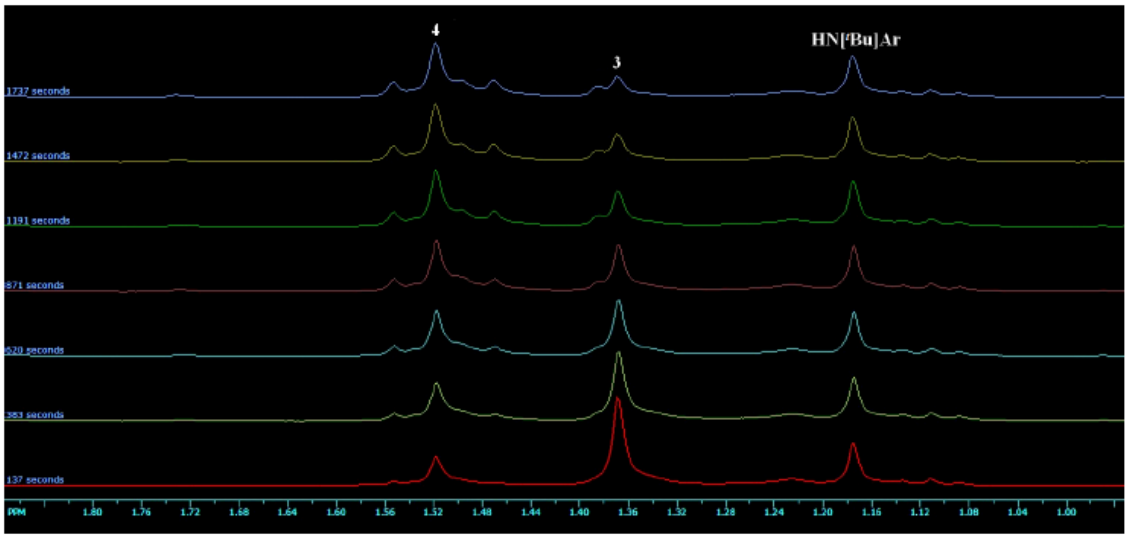

Figure 3A.8. Time dependent ^{1}H NMR spectra obtained at 22 °C from reaction of excess V(N[^{t}Bu]Ar)$_3$ (30.5 mM in toluene-d_8) with O_2 (0.1 mL, 0.0045 mmol O_2 assuming ideal gas behavior; 0.13 eq. per starting complex) illustrating the decrease in (η^2-O_2)V(N[^{t}Bu]Ar)$_3$ (**3**) that is coupled with the increase of OV(N[^{t}Bu]Ar)$_3$ (**4**) in the presence of V(N[^{t}Bu]Ar)$_3$. The calculated initial concentration of (η^2-O_2)V(N[^{t}Bu]Ar)$_3$ under these conditions is 4.5 mM. The majority of the sample contains the paramagnetic starting V(N[^{t}Bu]Ar)$_3$ complex, which has no resonances in the region between δ = 1 and 2 ppm. A small amount of free ligand, HN[^{t}Bu]Ar, is always present in solution but does not interfere with kinetic measurements.

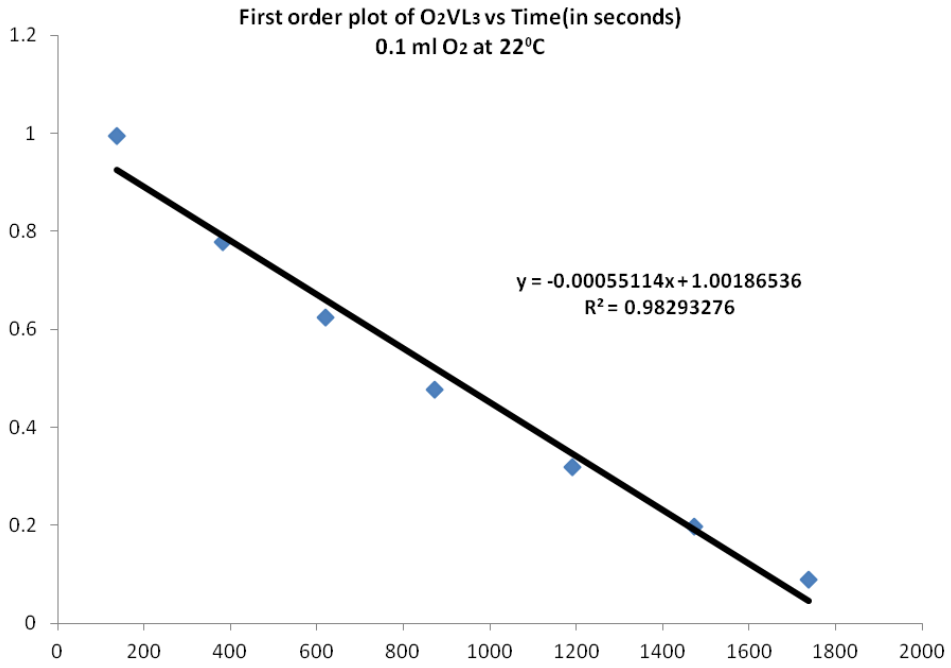

Figure 3A.9. Plot of ln[(η^2-O_2)V(N[^{t}Bu]Ar)$_3$] versus time (s) for the time dependent ^{1}H NMR reaction of V(N[^{t}Bu]Ar)$_3$ + O_2 (0.13 eq.) → (η^1-O_2)V(N[^{t}Bu]Ar)$_3$ + V(N[^{t}Bu]Ar)$_3$ → 2 OV(N[^{t}Bu]Ar)$_3$ + V(N[^{t}Bu]Ar)$_3$ shown in Figure 3A.8. Doubling or halving the concentration of V(N[^{t}Bu]Ar)$_3$ did not result in changes outside of the experimental error in the observed rate which indicated that the rate determining step under conditions of 3- to 7-fold excess of V(N[^{t}Bu]Ar)$_3$ was conversion of (η^2-O_2)V(N[^{t}Bu]Ar)$_3$ to (η^1-O_2)V(N[^{t}Bu]Ar)$_3$.

Due to difficulties in integration of the paramagnetic solutions, the reactions could only be followed for slightly more than one half life and the rate constants quoted from the time dependent ^{1}H NMR data are considered accurate to 20 %. Average values of first order rate constants for the high temperature rate limiting conversion of (η^2-O_2)V(N[^{t}Bu]Ar)$_3$ to (η^1-O_2)V(N[^{t}Bu]Ar)$_3$ are given in Table 3A.3. The data were not considered accurate enough to warrant an Eyring plot, so an Arrhenius plot was instead constructed to obtain the activation energy (E_a) of 14 ± 3 kcal mol^{-1} as shown in Figure 3A.10.

Table 3A.3. Temperature dependent first order rate constants (k_3) for conversion of (η^2-O_2)V(N[^{t}Bu]Ar)$_3$ to (η^1-O_2)V(N[^{t}Bu]Ar)$_3$ in reactions with excess V(N[^{t}Bu]Ar)$_3$ to produce the oxo complex OV(N[^{t}Bu]Ar)$_3$.

T (°C)	k_3 ($\times 10^{-4}$ s^{-1})
0	0.81
+10	1.65
+22	5.6

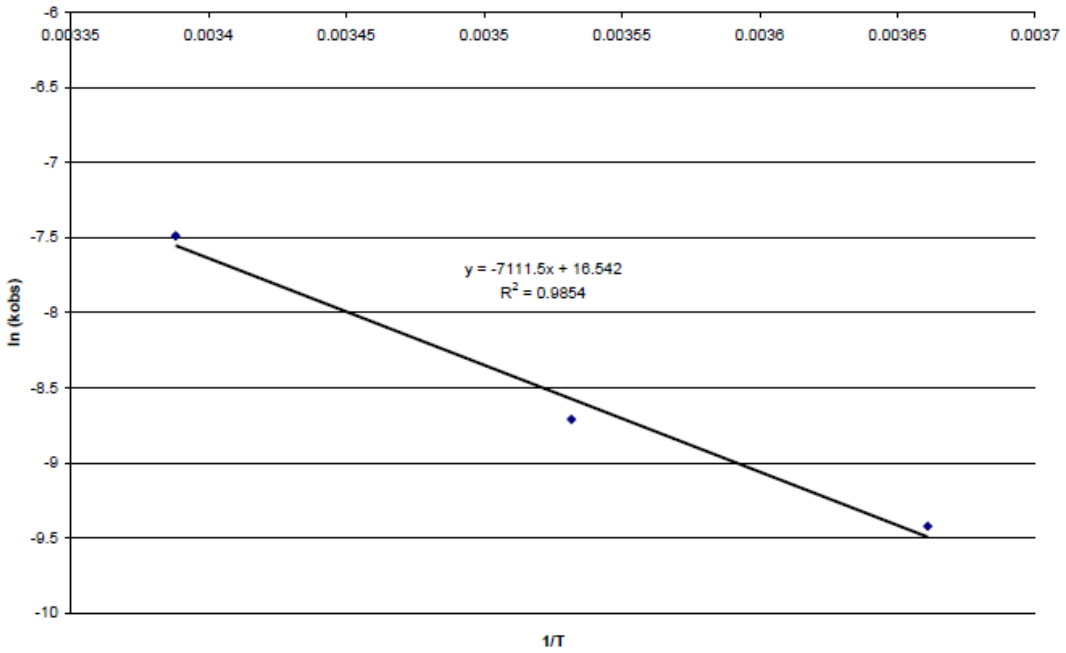

Figure 3A.10. Arrhenius plot for the high temperature ^{1}H NMR reaction of excess V(N[^{t}Bu]Ar)$_3$ with O_2, from which the derived activation energy (E_a) of 14 ± 3 kcal mol^{-1} was derived.

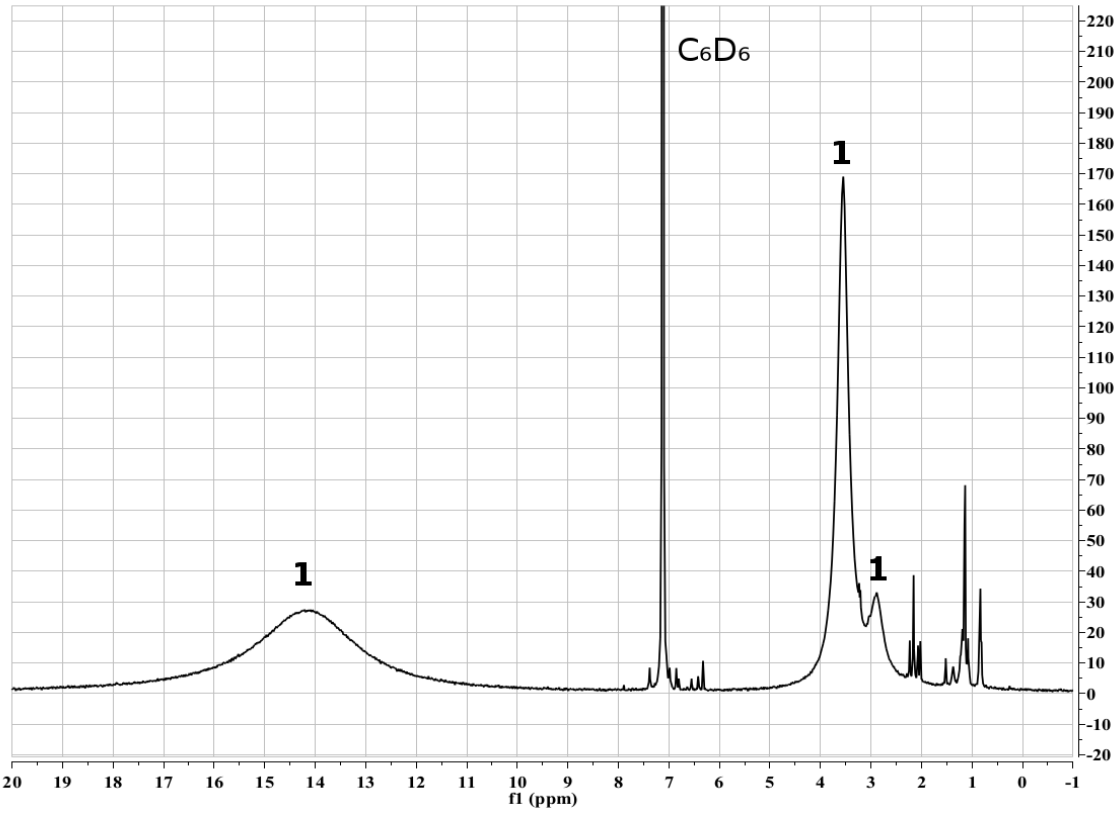

Figure 3A.11. ^{1}H NMR spectrum of V(N[^{t}Bu]Ar)$_3$ (**1**) in benzene-d_6.

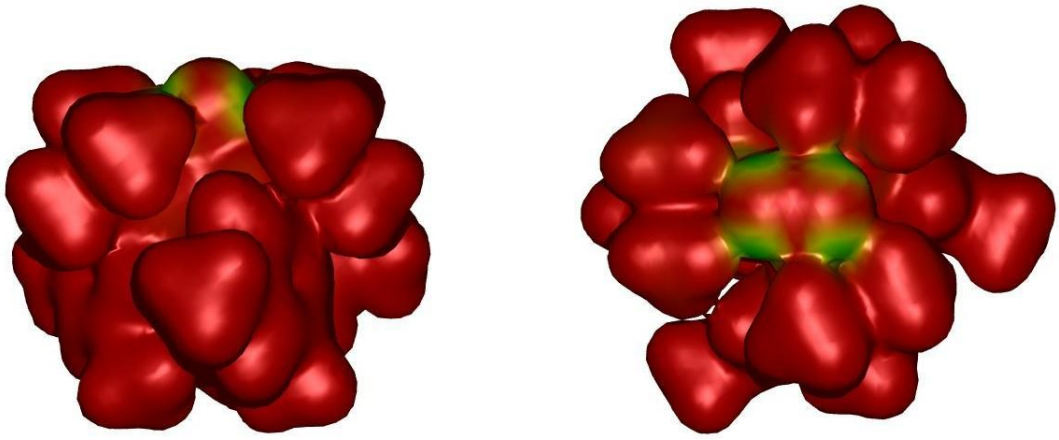

Figure 3A.12. Map of electrophilic susceptibility (ψ_{HOMO}^2) of (η^2-O$_2$)V(N[^{t}Bu]Ar)$_3$ plotted on the electron density isosurface (0.01 e/Å^3). Red = 0, blue = 0.003.

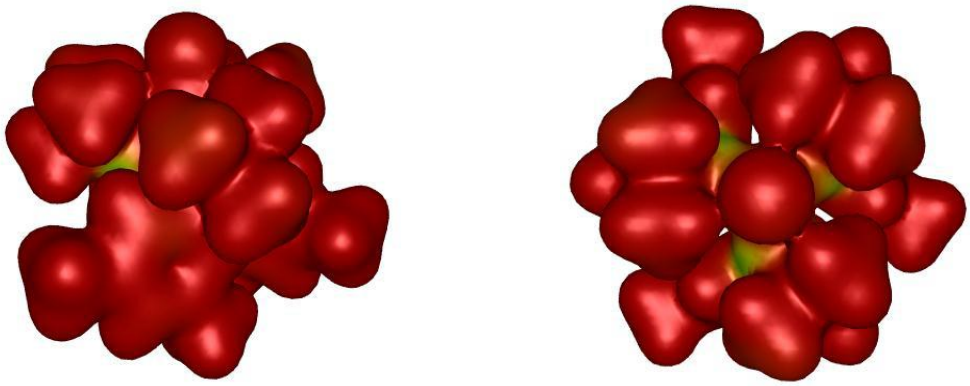

Figure 3A.13. Map of electrophilic susceptibility (ψ_{HOMO}^2) of (η^1-O_2)V(N[^{t}Bu]Ar)$_3$ plotted on the electron density isosurface (0.01 e/Å^3). Red = 0, blue = 0.003.

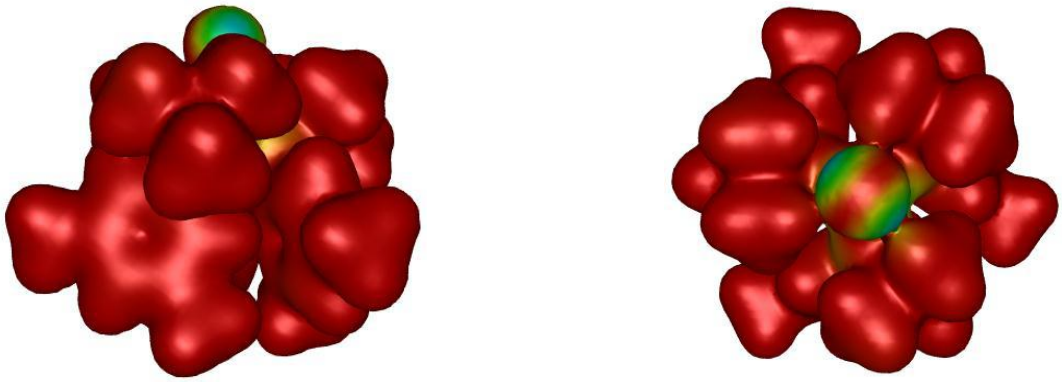

Figure 3A.14. Map of electrophilic susceptibility (ψ_{HOMO-1}^2 − one of a degenerate pair) of (η^1-O_2)V(N[^{t}Bu]Ar)$_3$ plotted on the electron density isosurface (0.01 e/Å^3). Red = 0, blue = 0.003.

Table 3A.4. Crystallographic and refinement parameters for (η^2-O_2)V(N[^{t}Bu]Ar)$_3$ and (^{t}BuC(=O)N)V(N[^{t}Bu]Ar)$_3$.

	(η^2-O_2)V(N[^{t}Bu]Ar)$_3$	(^{t}BuC(=O)N)V(N[^{t}Bu]Ar)$_3$
Empirical formula	$C_{36}H_{54}N_3O_2V$	$C_{41}H_{63}N_4OV$
Formula weight	611.76	678.89
Temperature (K)	100(2)	100(2)
Wavelength (Å)	0.71073	0.71073
Crystal system	Cubic	Orthorhombic
Space group	$I\bar{4}3d$	$P2_12_12_1$
a (Å)	23.919(2)	9.872(2)
b (Å)	23.919(2)	19.708(4)
c (Å)	23.919(2)	19.941(4)
α (deg)	90	90
β (deg)	90	90
γ (deg)	90	90
V (Å^3)	13685(2)	3880(1)
Z	16	4
ρ_{calc} (g cm^{-1})	1.188	1.162
μ (mm^{-1})	0.324	0.291
F(000)	5280	1436
Crystal size (mm^3)	0.20 × 0.20 × 0.10	0.20 × 0.20 × 0.20
θ range (deg)	2.09 to 30.02	1.45 to 30.03
Index ranges	$-33 \le h \le 33$	$0 \le h \le 13$
	$-33 \le k \le 33$	$0 \le h \le 27$
	$-33 \le l \le 33$	$0 \le h \le 28$
Reflections collected	151622	6268
Independent reflections	3356 [R_{int} = 0.0690]	6268 [R_{int} = 0.0000][a]
Completeness to θ_{max} (%)	100.0	100.0
Absorption correction	Semi-empirical from equivalents	Semi-empirical from equivalents
Max. and min. transmission	0.9683 and 0.9380	0.9441 and 0.9441
Refinement method	Full-matrix least squares on F^2	Full-matrix least squares on F^2
Data / restraints / parameters	3356 / 118 / 183	6268 / 0 / 443
Goodness-of-fit on F^2	1.091	1.078
Final R indices [I > 2σ(I)][b]	R_1 = 0.0319, wR_2 = 0.0772	R_1 = 0.0622, wR_2 = 0.1143
R indices (all data)[b]	R_1 = 0.0386, wR_2 = 0.0826	R_1 = 0.0799, wR_2 = 0.1211
Absolute structure parameter	−0.01(2)	0.53(3)
Largest diff. peak and hole (e Å^{-3})	0.200 and −0.269	0.349 and −0.380

[a] Statistics reflect the fact that the values are merged in TWINABS. An approximate R(int) from merging in TWINABS is 0.0622. [b] $R_1 = \sum||F_o| - |F_c|| / \sum|F_o|$; $wR_2 = \{\sum w(F_o^2 - F_c^2)^2 / \sum w(F_o^2)^2\}^{1/2}$.

Supplementary Data for O_2 Binding Kinetics with $V[(Me_3SiNCH_2CH_2)_3N]$

Qualitative experiments showed that addition of excess O_2 to toluene solutions of $V[(Me_3SiNCH_2CH_2)_3N]$ (see Figure 3A.15 for structure) at low temperatures lead to production of a dark green species, similar to the observations noted for O_2 binding to $V(N[^tBu]Ar)_3$.[1] Gradually warming cold solutions of $V[(Me_3SiNCH_2CH_2)_3N]$ exposed to O_2 resulted in conversion of the dark green solution to an orange solution. Addition of O_2 to $V[(Me_3SiNCH_2CH_2)_3N]$ at ambient temperatures also led to production of the green color, which formed only transiently prior to turning orange (Figure 3A.16).

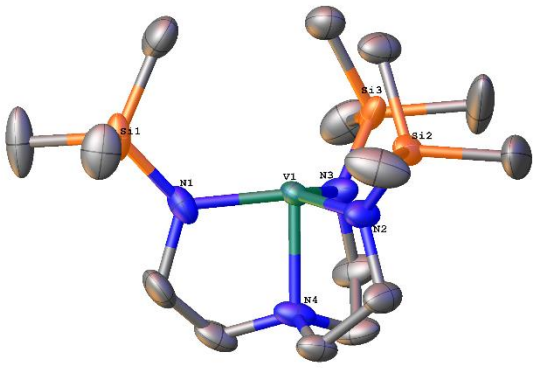

Figure 3A.15. Crystal structure of $V[(Me_3SiNCH_2CH_2)_3N]$ with ellipsoids drawn at the 50 % probability level. Hydrogen atoms are omitted for clarity. Selected interatomic distances (Å) and angles (°): V1−N1 = 1.927(2); V1−N2 = 1.931(2); V1−N3 = 1.931(2); V1−N4 = 2.070(2); N2−V1−N3 = 119.28(8); N3−V1−N1 = 119.58(8); N2−V1−N1 = 118.85(8); N4−V1−N1 = 85.31(7). See Chapter 2, ref 21 for additional information.

Figure 3A.16. *Left*: Toluene solution of V[(Me$_3$SiNCH$_2$CH$_2$)$_3$N] (1 mM) after addition of pure O_2 at ambient temperature. *Right*: Toluene solution of V[(Me$_3$SiNCH$_2$CH$_2$)$_3$N] (1 mM) after addition of pure O_2 at low temperature (≈ −78 °C). 100% O_2 (extra dry grade) was sparged directly into each vial for approximately 15 s.

A UV-visible spectrum of the orange solution was taken and is shown below in Figure 3A.17. Based on the qualitative observations, it is likely that an O_2 adduct is generated at low temperatures, and thus initial kinetic studies were performed over a temperature range of −80 to −53 °C in an effort to determine the rate of formation of this green adduct as described in the following paragraphs.

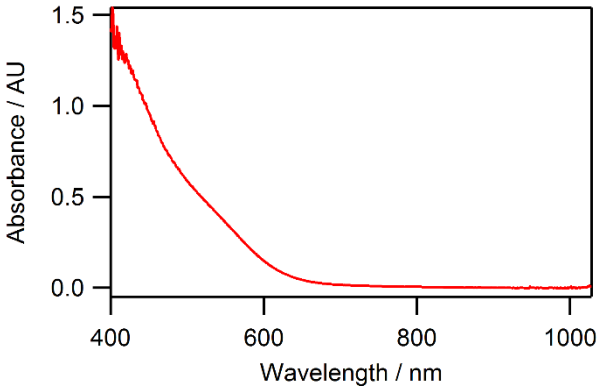

Figure 3A.17. UV/visible spectrum of the orange species (0.5 mM after mixing) in toluene taken at −35 °C. It was pre-generated in a gastight syringe by sparging 100 % O_2 into a 1 mM solution of V[(Me$_3$SiNCH$_2$CH$_2$)$_3$N] at ambient *T* until the orange color developed.

Initial stopped-flow experiments were conducted at low temperatures (−80, −71, −62, −53 °C) under pseudo-first order conditions using 0.5 mM $V[(Me_3SiNCH_2CH_2)_3N]$ and excess O_2 concentrations (1.7 mM to 4.15 mM). An example of the time-resolved spectral changes observed upon the reaction of $V[(Me_3SiNCH_2CH_2)_3N]$ with 1.7 mM O_2 at −80 °C is shown in Figure 3A.18. As can be seen from the data, formation of the presumed dark green O_2 adduct led to noticeable spectral changes that included formation of an intense absorbance band at λ = 458 nm as well as formation of a broad band centered near λ = 705 nm and decay at longer wavelengths. An isosbestic point was noted at λ ≈ 825 nm.

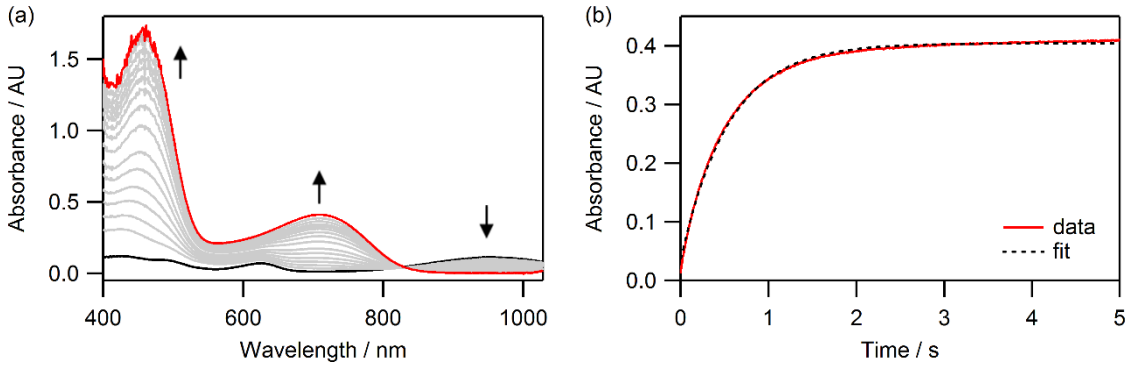

Figure 3A.18. (a) Time-resolved spectral changes (400 nm - 1027 nm) accompanying the reaction between $V[(Me_3SiNCH_2CH_2)_3N]$ (0.5 mM) and O_2 (1.7 mM) acquired over 5 s at −80 °C. Selected traces shown for clarity. (b) Formation trace at λ = 705 nm with single exponential fit.

Analysis of kinetic traces at multiple wavelengths (λ = 459 nm, 705 nm, 950 nm) resulted in consistent values of k_{obs}, so λ = 705 nm was chosen in an effort to quantify the rates of formation of the green species from low temperature data. Subsequent measurements were performed in single wavelength mode due to the rapidity of the

reaction (see Figure 3A.19); in all cases, the kinetic traces fit well to a single exponential function. Observed rate constants (k_{obs}) derived from the exponential fits of kinetic traces are provided in Table 3A.5. A linear dependence of k_{obs} on [O_2] was observed at all temperatures, revealing a first order dependence on O_2. The slopes of the linear k_{obs} vs. [O_2] plots represent the second order rate constant (k_1) for formation of the green O_2 adduct as shown in Figure 3A.20a. Second order rate constants for product formation are given in Table 3A.5. The reaction at low temperature is considered to be essentially irreversible; the intercepts in the k_{obs} vs. [O_2] plots are slightly negative (but very close to zero) and changes in the final absorbance values noted in kinetic traces were not always reproducible due to the highly air- and moisture-sensitive V[($Me_3SiNCH_2CH_2$)$_3$N].

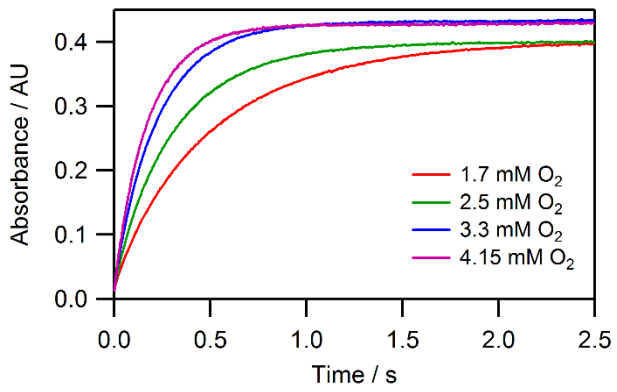

Figure 3A.19. Formation traces (λ = 705 nm) at −80 °C as a function of [O_2]$_0$.

Table 3A.5. Temperature dependent pseudo-first order (k_{obs}) and second order (k_1) rate constants obtained from analysis of formation traces at λ = 705 nm for the low temperature reaction of V[(Me$_3$SiNCH$_2$CH$_2$)$_3$N] (0.5 mM) with excess O$_2$.

	k_{obs} (s^{-1})			
[O$_2$] (M)	−80 °C	−71 °C	−62 °C	−53 °C
0.0017	2.01	2.96	4.55	6.50
0.0025	3.23	4.60	7.09	10.6
0.0033	4.36	6.38	9.98	14.7
0.00415	5.54	8.41	12.8	18.7
k_1 (M^{-1} s^{-1})	1,440 ± 22	2,230 ± 54	3,390 ± 56	4,990 ± 64

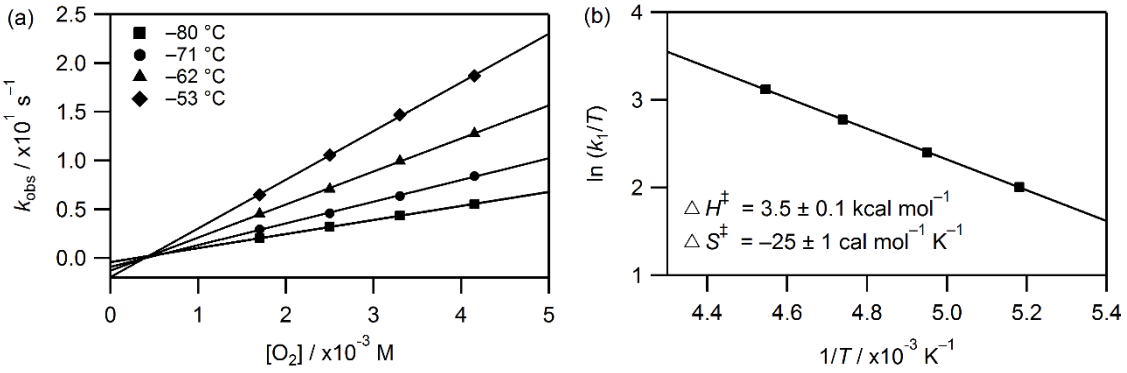

Figure 3A.20. (a) Plots of k_{obs} versus [O$_2$] for the reaction between V[(Me$_3$SiNCH$_2$CH$_2$)$_3$N] (0.5 mM) and excess O$_2$ (1.7 - 4.15 mM) over the temperature range of −80 °C to −53 °C with linear fits. (b) Eyring plot with derived activation parameters for the low temperature reaction.

Variable temperature measurements allowed for determination of the activation parameters associated with this process via an Eyring plot: $\Delta H^‡$ = 3.5 kcal mol^{-1} and $\Delta S^‡$ = −25 cal mol^{-1} K^{-1} (Figure 3A.20b). The activation enthalpy reveals a low barrier for O$_2$ addition and the relatively large negative activation entropy is consistent with an associative process. Interestingly, the activation parameters for the reaction between V[(Me$_3$SiNCH$_2$CH$_2$)$_3$N] and O$_2$ at low *T* are essentially identical to those found for formation of the (η^1-O$_2$)V(N[^{t}Bu]Ar)$_3$ adduct ($\Delta H_1^‡$ = 3.3 ± 0.2 kcal mol^{-1} and $\Delta S^‡$ = −22

± 1 cal mol^{-1} K^{-1}), despite a rather large difference in the reaction rates (O_2 binding to $V(N[^tBu]Ar)_3$ is approximately 8 times faster).

Additional work is in progress to fully characterize the mode of O_2 binding $V[(Me_3SiNCH_2CH_2)_3N]$ at low temperatures.

In an effort to probe the conversion of the green species to the orange species, additional stopped-flow reactions were performed at 20 °C. Formation of the green complex appears too fast to measure accurately at this temperature; however, its conversion to the orange species could be followed conveniently by monitoring relatively slow decay (≈ 100 s) of the broad absorbance band located at λ = 705 nm. An example of the time-resolved spectra obtained from the room temperature reaction is provided in Figure 3A.21 below.

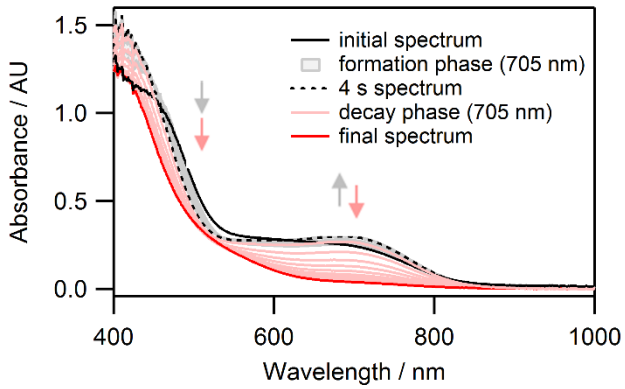

Figure 3A.21. Time-resolved spectral changes accompanying the reaction between $V[(Me_3SiNCH_2CH_2)_3N]$ (0.5 mM) and O_2 (1.7 mM) at 20 °C acquired over 80 s. The first 4 s of reaction is characterized by a growth phase at 705 nm (gray traces); this is followed by a slower decay phase (pink traces) that ultimately ends with the expected spectrum of the orange species (red trace). The initial time = 0 s trace is shown as a solid black line. The reaction was monitored for a total of 80 s.

Although the prominent feature of the reaction results in decay of the absorbance band assigned to the green species, the initial few seconds of reaction revealed a reproducible formation phase at λ = 705 nm that completed within approximately 4 s, regardless of $[O_2]_0$ (see Figure 3A.22). Initial fitting attempts focusing solely on the decay phase occurring at λ = 705 nm fit very well to a single exponential equation. Interestingly, the observed rate constant for the decay of the green species (k_{obs}) shows no dependence on $[O_2]$ (Table 3A.6).

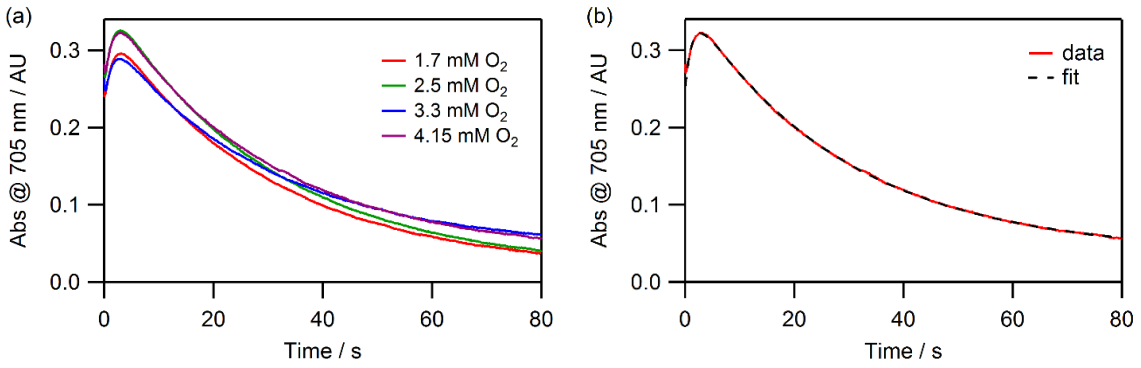

Figure 3A.22. (a) Kinetic traces at λ = 705 nm as a function of $[O_2]$ at 20 °C with $[V[(Me_3SiNCH_2CH_2)_3N]]_0$ = 0.5 mM. (b) Representative kinetic trace fit to a biexponential function.

The kinetic traces were also fit using a biexponential function to include the initial growth phase noted in most of the traces. In that case, k_{2obs} values, which correspond to the decay in absorbance, agree very well with k_{obs} obtained from the single exponential fits. k_{1obs} values, which correspond to the formation phase, show no dependence on $[O_2]$. Observed rate constants obtained from all methods of fitting are provided in Table 3A.6 below.

Table 3A.6. Observed rate constants (average value of at least two datasets) obtained from fitting kinetic traces (λ = 705 nm) at 20 °C to a single or double exponential function. With single exponential fits, only the decay was analyzed by omitting the first 4.2 s of reaction. V[$(Me_3SiNCH_2CH_2)_3N$] = 0.5 mM.

		Single exponential	Double exponential	
20 °C	$[O_2]$ (M)	k_{obs} (s^{-1}), decay	k_{1obs} (s^{-1}), formation	k_{2obs} (s^{-1}), decay
	0.0017	0.0338	0.725	0.0341
	0.0025	0.0335	0.685	0.0338
	0.0033	0.0344	0.648	0.0346
	0.00415	0.0338	0.677	0.0340

Reactions were also performed with varying V[$(Me_3SiNCH_2CH_2)_3N$] in an effort to determine if the decay rate was second order in metal complex, but decreasing the concentration of metal complex had no noticeable effect on the value of the observed rate constant (Table 3A.7), which suggests that the reaction occurring at 20 °C is first order in V[$(Me_3SiNCH_2CH_2)_3N$]. It would be useful to run additional experiments over an intermediate *T* range (−30 to +10 °C) in order to better understand the initial spectral changes that have been observed at elevated temperature. Additional work is also necessary to better understand the nature of this reaction.

Table 3A.7. Observed rate constants (average value of at least two datasets) obtained from fitting decay traces (λ = 705 nm) at 20 °C to a single exponential equation. The first 4.2 s of reaction was omitted from fits. V[$(Me_3SiNCH_2CH_2)_3N$] = 0.3 mM or 0.5 mM and $[O_2]$ was fixed at 4.15 mM.

20 °C	[V($(Me_3SiNCH_2CH_2)_3N$)] (M)	$[O_2]$ (M)	k_{obs} (s^{-1})
	0.0003	0.00415	0.0346
	0.0005	0.00415	0.0338

CHAPTER 4

The Mechanism of Reaction of O_2 with $Pd(IPr)_2$: Low Temperature Formation of (η^2-O_2)$Pd(IPr)_2$ and Trapping of (η^1-O_2)$Pd(IPr)_2$ with O_2 to Form *trans*-(η^1-O_2)$_2Pd(IPr)_2$[1,2]

4.1. Introduction

Coordination chemists often think of ligand binding in terms of donation of a lone pair of electrons from the ligand (Lewis base) to a vacant orbital on the metal center (Lewis acid). However, the situation is more complex with $^3O_2$ in particular, since the net transfer of electrons is not from the ligand to the metal, but instead from the metal to the ligand.[3] The initial step in O_2 binding may indeed involve donation of a lone pair of electrons from O_2 to the metal, as in conventional ligand binding, but the overall process involves subsequent transfer of electron density from the metal to O_2; as a result, bound O_2 is partially of fully reduced.[4] To further complicate matters, changes in the metal's spin-state and changes in O_2 hapticity (from end-on (η^1) to side-on (η^2)) may also occur. Examples of typical dioxygen binding modes to a single metal center are provided in Figure 4.1. It is important to note that the simplified scheme shown in Figure 4.1 neglects to show the ambiguity that can often result in the assignment of a dioxygen ligand as either a superoxo or peroxo moiety; the limiting cases are merely shown.

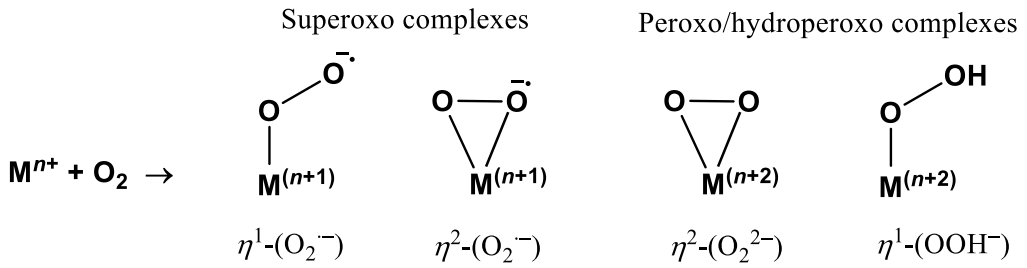

Figure 4.1. Typical dioxygen binding modes in mononuclear transition metal-O_2 complexes. Figure adapted from ref 4. For superoxo and peroxo complexes, the metal's oxidation state increases by +1 and +2, respectively.

In reality, a range of electronic distributions between $M^{n+1}(O_2^{\cdot-})$ and $M^{n+2}(O_2^{2-})$ are possible, and the exact nature of the electronic structure for a given dioxygen complex will depend on the metal center and the type(s) of ancillary ligand(s) used.[4] Information regarding the O−O bond order, typically obtained from structural and/or spectroscopic data (e.g., O−O bond lengths and vibrational frequencies), often allows for an assignment to be made.

The majority of mononuclear dioxygen complexes that have been structurally characterized are formulated as η^2-peroxide adducts. The first notable example is that of Vaska's complex,[5] which binds O_2 reversibly to form the coordinatively saturated $[Ir(CO)(PPh_3)_2(Cl)(\eta^2\text{-}O_2)]$ adduct (Figure 4.2). The exact nature of this and related dioxygen adducts[6] was under debate for some time. The dioxygen ligand in Vaska's complex was initially formulated as a side-on superoxide (bound to a formal Ir(II) metal center) based on the measured O−O bond length of 1.30(3) Å obtained from the original room temperature X-ray structure, but subsequent studies led to its reassignment as an Ir(III) side-on peroxo complex; the corrected O−O bond length of 1.47(1) Å, obtained from low temperature X-ray data, was reported in 2006.[7]

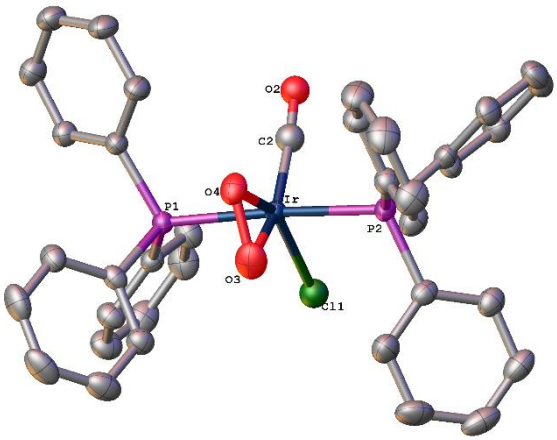

Figure 4.2. X-ray structure of Vaska's complex, $[Ir(CO)(PPh_3)_2(Cl)(\eta^2\text{-}O_2)]$, obtained from ref 7. Hydrogen atoms and several disordered groups are omitted for clarity. The crystallographic information file is also available from the Cambridge Crystallographic Data Center (CCDC no. 702740).

Since Vaska's discovery, a large number of η^2-O_2 peroxo complexes have emerged, especially for late transition metal complexes of Ir, Pt, Pd, and Co.[8] η^1-O_2 complexes, which are generally thought to be more reactive than their η^2-O_2 counterparts,[9] are well characterized intermediates in hemoglobin, myoglobin, and related metalloenzymatic chemistry;[10] far less common, however, are reports on the isolation of synthetic end-on O_2 adducts. Schindler and co-workers[11] recently isolated and structurally characterized the first η^1-O_2 adduct of Cu, $[Cu(TMG_3tren)O_2](SbF_6)$, by employing the sterically demanding TMG_3tren (TMG_3 = tris(tetramethylguanidino); tren = (tris(2-aminoethyl)amine)) ligand (Figure 4.3). Remarkably, the adduct was stable at low temperatures and could bind dioxygen reversibly. The η^1-O_2 ligand was assigned as a superoxide based on the experimentally determined O−O bond length of 1.280(3) Å, which is longer than the O=O bond length in O_2 (1.21 Å) and much shorter than the O−O bond length in the peroxide anion (O_2^{2-}) (1.49 Å).[7] Furthermore, this complex was shown

to oxidize phenols via H-atom abstraction and promotes intramolecular ligand hydroxylation.[12] In contrast, the (η^2-O_2) adducts of copper supported by β-diketiminate and anilide-imine ligands remain inert towards easily oxidizable substrates.[13]

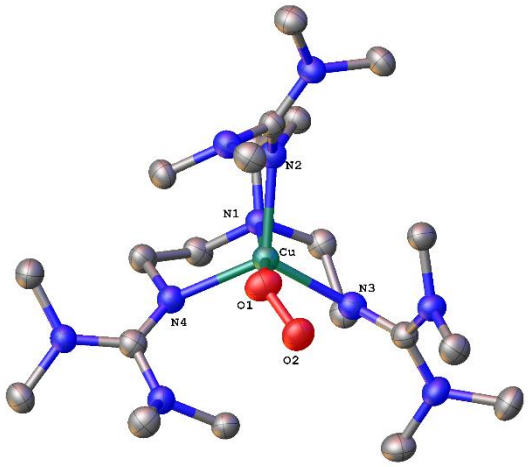

Figure 4.3. X-ray structure of $[Cu(TMG_3tren)O_2]^+$ drawn at the 50 % probability level. Hydrogen atoms, solvent molecules, and disordered O2 atom are omitted for clarity. TMG_3 = tris(tetramethylguanidino); tren = (tris(2-aminoethyl)amine). The crystallographic information file is available from the Cambridge Crystallographic Data Center (CCDC no. 287898). Relevant bond lengths are provided in the main text.

In many cases, the final product of O_2 association is, in fact, an η^2-O_2 adduct, but it may proceed through an initial η^1 bonding form which subsequently isomerizes. This is a matter of some controversy in recent literature. Roth[14] has published detailed kinetic isotope binding studies of $^{18}O_2$ and concluded that a two-step mechanism for forming η^2-peroxides is difficult to argue in the absence of spectrophotometrically detectable intermediates. In contrast, Stahl[15] has performed calculations in which both η^1 and η^2 binding modes are stable minima and the conversion of η^1 to η^2 occurs as a separate step in O_2 binding. Stahl's calculations are in agreement with our recent report[16] on O_2

binding to the early transition metal complex V(N[^{t}Bu]Ar)$_3$, where we were able to observe and quantify the conversion of an intermediate η^1-O_2 adduct en route to the (η^2-O_2)V(N[^{t}Bu]Ar)$_3$ peroxo complex from low temperature kinetic data.

The significance of this work revolves around the fundamental goal of developing new homogenous oxidation catalysts that affect selective aerobic oxidation of organic molecules.[17] In this regard, catalytic oxidations utilizing two-coordinate, 14-electron Pd(0) complexes bearing *N*-heterocyclic carbene (NHC) and/or tertiary phoshine (PR_3) ligands has been an active area of research.[18] Nolan et al.[19] have reported the preparation and isolation of several mixed two-coordinate [Pd(L)(L')] (L = NHC, L' = NHC or PR_3) complexes and found that they readily react with O_2 to form stable η^2-O_2 peroxo complexes as shown in Figure 4.4. In spite of the recent interest in this chemistry, relatively few studies have dealt with the kinetics and thermodynamics of oxygen binding to [Pd(L)(L')] systems.[20]

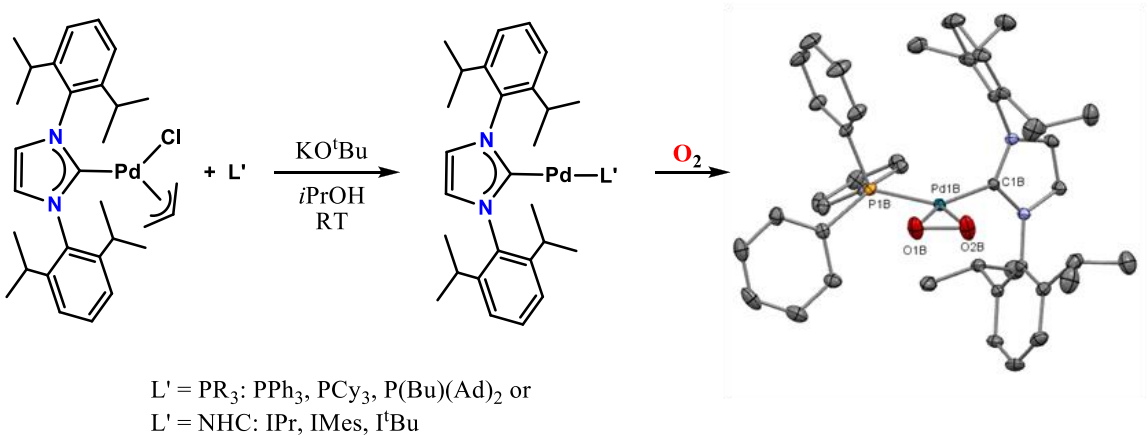

Figure 4.4. Synthetic route to [Pd^0(L)(L')] complexes reported by the Nolan group (taken from ref 19) with solid state structure of (η^2-O_2)Pd(IPr)(PPh_3) shown. Hydrogen atoms and second molecule in the asymmetric unit have been omitted for clarity. The crystallographic information file is available from the Cambridge Crystallographic Data Center (CCDC no. 682048).

Our work in this area began with the physical studies of [Pd(L)(L')] complexes, with emphasis on deciphering how changes in ligand environment influence the rate and energetics of O_2 binding.[2] During the course of this study, the novel *bis*-superoxo complex *trans*-(η^1-O_2)$_2$Pd(IPr)$_2$ (IPr = 1,3-bis(2,6-diisopropyl)phenylimidazol-2-ylidene) was isolated and structurally characterized by our collaborators and revealed an unprecedented O_2 binding mode for palladium(II) (Figure 4.5). This result was quite surprising since binding of O_2 to [Pd(L)(L')] complexes studied to date had exclusively yielded *cis*-[Pd(L)(L')(η^2-O_2)] peroxo structures.[19,21]

This chapter reports the mechanistic study of formation of the novel *trans*-[(η^1-O_2)$_2$Pd(IPr)$_2$] complex and provides evidence for low temperature (< −40 °C) formation of an unstable intermediate that has been formulated as *cis*-(η^2-O_2)Pd(IPr)$_2$ based on its NMR spectral data and computational studies.[1,22] At higher temperatures (> −40 °C), this complex reacts further with O_2 to form *trans*-(η^1-O_2)$_2$Pd(IPr)$_2$ in a reaction which has been kinetically analyzed and is proposed to proceed through formation of (η^1-O_2)Pd(IPr)$_2$, which is maintained at steady state concentrations and can be trapped by O_2 to form *trans*-Pd(IPr)$_2$(η^1-O_2)$_2$ or dissociate to regenerate Pd(IPr)$_2$.

4.2. Experimental Methods

General Considerations. Samples of Pd(IPr)$_2$ and Pd(IMes)$_2$ (IMes = *N*,*N*-bis(2,4,6-trimethyl)phenylimidazol-2-ylidene) were synthesized according to previously published procedures[19,23] and graciously supplied by members of the Hoff group (University of Miami, Coral Gables, FL), stored in a glove box freezer, and used without

further purification. The reader is referred to refs 2 and 22 for additional details regarding syntheses and characterization of the O_2 adducts. Anhydrous toluene (HPLC grade, ≥ 99.9%) was purchased from Sigma Aldrich and dried on an Innovative Technologies PureSolv 400 solvent purification system. Pure O_2 (ultra dry grade) was obtained from Airgas and used as received.

Stopped-Flow Kinetics. Toluene solutions of $Pd(IPr)_2$ or $Pd(IMes)_2$ were prepared in an MBraun glove box filled with ultra high purity argon (Airgas) and loaded in Hamilton gastight syringes equipped with three-way valves. Saturated solutions of O_2 were prepared by bubbling gas into gastight syringes containing dry toluene for at least 20 minutes; dilutions of the O_2 saturated solvent were performed anaerobically to obtain the desired [O_2] before mixing. The solubility of O_2 in toluene was taken as 8.3 mM at 20 °C.[24] Time resolved spectra (λ = 400−700 nm) were acquired over a range of temperatures (−85 to +25 °C) using a Hi-Tech Scientific KinetAsyst SF-61DX2 CryoStopped-Flow system (TgK Scientific Ltd.) equipped with a quartz tungsten halogen light source, a J&M TIDAS diode array detector and a Brandenburg 4479 Series PMT monochromator. The instrument was equipped with stainless steel plumbing lined with PEEK tubing and a 1.00 cm^3 quartz mixing cell submerged in an ethanol cooling bath. The temperature in the mixing cell was maintained to ± 0.1 °C using a CAL 3200 automatic temperature controller. Data acquisition was performed using TIDAS-DAQ and/or Kinetic Studio software programs and mixing times were 2 - 3 ms. All flow lines were washed extensively with argon saturated dry toluene prior to loading reactant solutions. All experiments were performed in a single-mixing mode of the instrument

with a 1:1 (v/v) mixing ratio. Reactions were studied under pseudo-first order conditions using excess O_2. All concentrations are reported after mixing in the stopped-flow cell. Data analysis was performed using Kinetic Studio, IGOR Pro 5.0 (Wavemetrics, Inc.), and ReactLab Kinetics Global Analysis software (JPlus Consulting Pty. Ltd.). All observed rate constants are reported in Appendix 4 and represent an average of three to seven measurements which gave an acceptable standard deviation (within 5 - 10 %) and all remaining quantities derived from the kinetic data are reported with their standard deviations.

4.3. Results and Discussion

The crystal structure of the novel complex unambiguously shows oxygen binding consistent with a *trans*-[(η^1-O_2)$_2$Pd(IPr)$_2$] composition as shown in Figure 4.5. There are only a limited number of reports concerning η^1-O_2 palladium complexes which include structural data for [(^{F}PNP)Pd(η^1-O_2)] that was reported shortly after us[25] and *in situ* spectroscopic characterization of Pd(II) superoxides generated from reactions with KO_2 or H_2O_2.[26] The square planar Pd(II) complex contains *trans*-O_2 ligands that have been formulated as superoxides based on the average O−O bond length of 1.327(18) Å, which is close in value to the O−O bond lengths reported for the structurally characterized end-on superoxo complex [Cu^{III}(TMG$_3$tren)(O_2)]$^+$ and the [(^{F}PNP)Pd^{II}(O_2)] adduct (1.293(2) Å). The C31−Pd−C1 and O1−Pd−O3 angles of 178.2(4)° and 178.8(3)°, respectively, reveal the nearly linear nature of ligand binding in this system. For comparison, Stahl's

cis-[(η^2-O_2)$_2$Pd(IMes)$_2$] peroxo complex is also shown in Figure 4.5, which has an O−O bond length of 1.443(2) Å[21a] consistent with a two electron reduced dioxygen ligand.

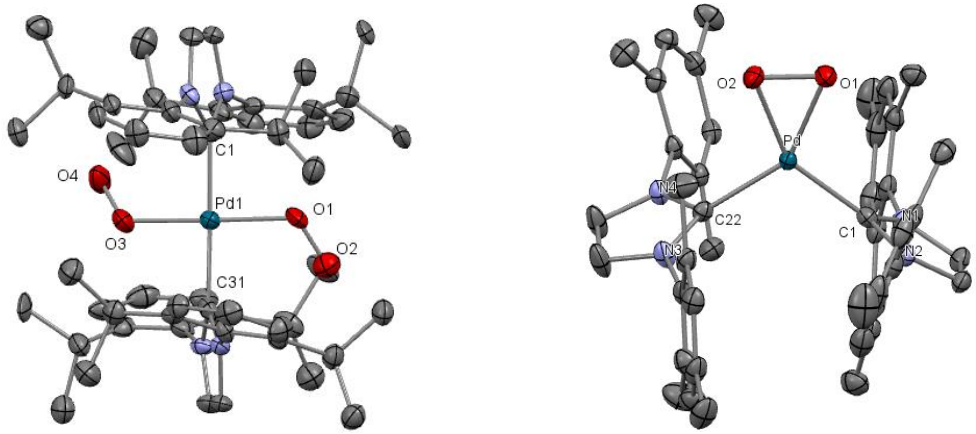

Figure 4.5. *Left*: X-ray structure of *trans*-(η^1-O_2)$_2$Pd(IPr)$_2$ (CCDC no. 800883) with thermal ellipsoids shown at the 50 % probability level. Hydrogen atoms and hexane molecule are omitted for clarity. Selected interatomic distances (Å) and angles (°): Pd−O1 = 2.010(8), Pd−O3 = 2.012(8), Pd−C1 = 2.059(11), Pd−C31 = 2.065(11), O1−O2 = 1.314(11), O3−O4 = 1.340(11), O3−Pd−O1 = 178.8(3), O3−Pd−C31 = 88.7(4), O1−Pd−C31 = 92.3(4), O3−Pd−C1 = 90.1(4), O1−Pd−C1 = 88.9(4), C31−Pd−C1 = 178.2(4). *Right*: X-ray structure of *cis*-(η^2-O_2)Pd(IMes)$_2$ reported by Stahl and co-workers (ref 21a) with ellipsoids shown at the 50 % probability level.

The sensitivity of bonding geometry has recently been demonstrated[27] for *cis*-[Pt(NHC)$_2$(CH$_3$)$_2$], where adjusting the steric parameters[28] of the NHC ligand was shown to lead to differing reactivity channels. The sensitivity of reaction product to the sterics of the NHC is also highlighted in the present work, where the change from IMes to IPr results in quite different reactivities with respect to O_2 binding.

Thermochemical analysis of O_2 binding to selected [Pd(L)(L')] systems was undertaken by our collaborators[22] (Table 4.1) and surprisingly, binding of two moles of O_2 to Pd(IPr)$_2$ yielded the lowest binding enthalpy of all the [Pd(L)(L')] complexes studied. The binding entropy for two moles of O_2 is expected to be highly unfavorable,

however, based on the structure of the *trans*-(η^1-O_2)$_2$Pd(IPr)$_2$ complex, it is possible that there would be less entropy loss for the *trans*-NHC ligand arrangement. The *cis*-NHC geometry is expected to cause a large unfavorable entropic interaction.

Table 4.1. Enthalpies of O_2 binding to [Pd(L)(L')] (L = NHC, L' = NHC or PR_3) complexes in toluene solution. For comparison, the enthalpy and entropy of O_2 binding to Vaska's complex[29] are provided (ΔH in kcal mol^{-1} and ΔS in cal mol^{-1} K^{-1}).

Complex	Product	ΔH	ΔS
Pd(IPr)(P(*p*-tolyl)$_3$)[a]	*cis*-(η^2-O_2)Pd(IPr)(P(*p*-tolyl)$_3$)	−26.2 ± 1.9	-----
Pd(SIPr)(PCy$_3$)[a]	*cis*-(η^2-O_2)Pd(SIPr)(PCy$_3$)	−25.6 ± 0.6	-----
Pd(IPr)$_2$	*trans*-(η^1-O_2)$_2$Pd(IPr)$_2$	−24.0 ± 0.4	-----
	cis-(η^2-O_2)Pd(IPr)$_2$	−15 ± 1[b]	−45 ± 2[b]
Pd(IMes)$_2$	*cis*-(η^2-O_2)Pd(IMes)$_2$	−27.9 ± 1.5	-----
Ir(Cl)(CO)(PPh$_3$)$_2$	*cis*-(η^2-O_2)Ir(Cl)(CO)(PPh$_3$)$_2$	−17.1	−37

[a] Tolyl = $CH_3C_6H_4$, Cy = cyclohexyl. [b] Values obtained from variable temperature kinetic experiments as discussed in the following sections.

The following sections detail the study of the mechanism of formation of the *trans*-[(η^1-O_2)$_2$Pd(IPr)$_2$] complex, which led to some notable surprises.

4.3.1. Low Temperature Formation of (η^2-O_2)Pd(IPr)$_2$

Initial stopped-flow kinetic studies were performed at low temperatures (−85 to −70 °C) and interestingly, time-resolved spectra acquired at −85 °C did not show conversion to the expected orange-red *bis*-superoxo complex; instead, rapid decay of the absorbance bands corresponding to yellow-orange Pd(IPr)$_2$ were observed upon reaction with excess O_2 as shown below in Figure 4.6. The resulting solution was pale yellow in color.

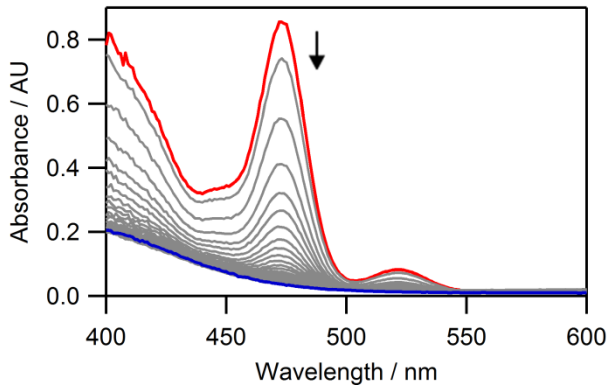

Figure 4.6. Time-resolved spectral changes observed upon reaction of $Pd(IPr)_2$ (0.25 mM) and O_2 (1.7 mM) in toluene at −85 °C over 3 s. Selected traces are shown for clarity. The initial time = 0 s trace corresponding to absorbance of the starting $Pd(IPr)_2$ complex (λ_{max} = 473 nm) is shown in red and the final spectrum in blue.

This observation was somewhat puzzling since it is reminiscent of O_2 binding to related [Pd(L)(L')] systems (L = NHC; L' = NHC or PR_3) studied by us,[2] which bind O_2 rapidly and irreversibly to produce the colorless diamagnetic (η^2-O_2)Pd(L)(L') adducts. For example, time-resolved spectra obtained from reactions of $Pd(IMes)_2$ (0.1 mM) with O_2 reveals complete loss of spectral features upon reaction (Figure 4.7). The rate of formation of the colorless (η^2-O_2)$Pd(IMes)_2$ adduct proved too fast to measure accurately by the conventional stopped-flow method, even at −80 °C (see Appendix 4).

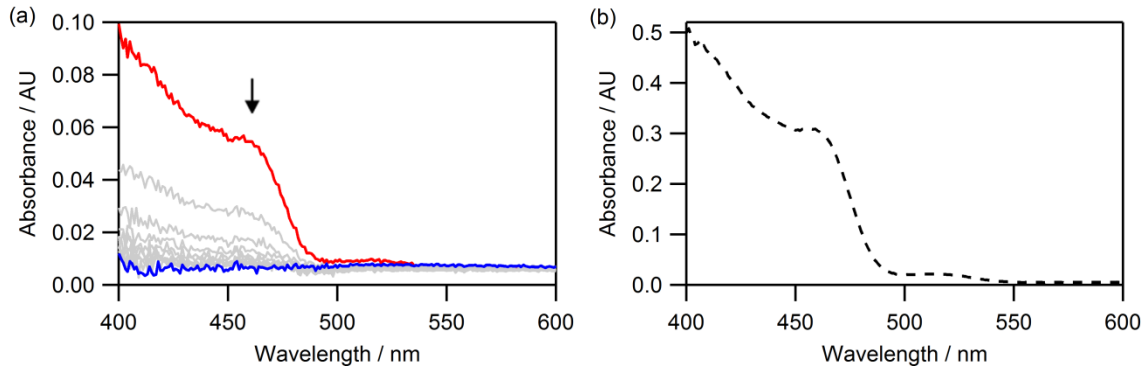

Figure 4.7. (a) Time-resolved spectral changes accompanying the reaction between $Pd(IMes)_2$ (0.1 mM) and O_2 (0.1 mM) at −80 °C acquired over 3 s. Selected traces are shown for clarity. The initial time = 0 s trace is shown in red; gray traces were acquired at 0.003 s intervals and the final spectrum after 3 s reaction is shown in blue. (b) Absorbance spectrum of 0.1 mM $Pd(IMes)_2$ in toluene highlighting its shoulder peak at $\lambda \approx 458$ nm with $\varepsilon \approx 3{,}090$ M^{-1} cm^{-1}. Most of the spectral decay that occurs upon O_2 binding happens within the instrument dead time of 2-3 ms and is therefore not resolvable with diode array detection.

Accurate measurements of the rate constants for these processes are better performed using single wavelength detection, and once the overall spectral features were examined, single wavelength measurements were utilized to study the rapid bleaching event at variable concentrations and temperatures. For the $Pd(IPr)_2$-O_2 system, analysis of decay traces at $\lambda = 473$ nm as a function of varying $[O_2]$ at −85 °C revealed a systematic linear increase in the value of the observed rate constant (k_{obs}) (Figure 4.8b), confirming a simple first order dependency on $[O_2]$ in the overall second order forward reaction (k_1) shown in Eq. 4.1.

$$Pd(IPr)_2 + O_2 \underset{k_{-1}}{\overset{k_1}{\rightleftharpoons}} (\eta^2\text{-}O_2)Pd(IPr)_2 \qquad (4.1)$$

For the reaction in Eq. 4.1, linear plots of k_{obs} versus $[O_2]$ have slopes equal to k_1 and intercepts equal to k_{-1}. The plots in Figure 4.8b reveal an increase in the intercept the as temperature increases, suggesting that the rapid binding event may be reversible. It is important to note that the accuracy in k_{-1} values (and derived values of K_{eq}) is typically low, and because the reaction is already extremely fast and nearing the limits of measurement, we regard these values as loose estimates. Furthermore, due to the large difference in the relative magnitudes of k_1 versus k_{-1}, the dissociation reaction can be neglected, from the kinetic standpoint, at these low temperatures (−85 °C to −70 °C). Rate constants (k_1) for the low temperature second order reaction are provided in Table 4.2. Activation parameters for this O_2 binding step were calculated from the Eyring plot shown in Figure 4.9.

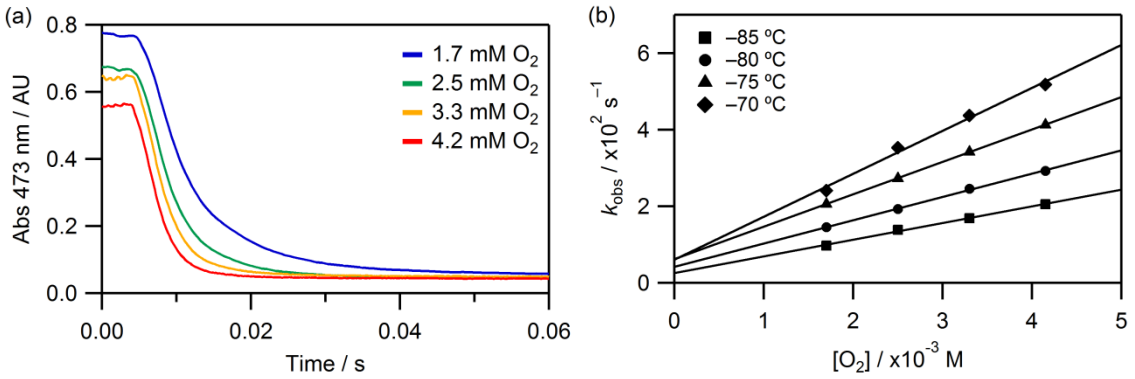

Figure 4.8. (a) Decay traces at λ = 473 nm acquired in single-wavelength mode at −80 °C as a function of $[O_2]_0$. (b) Temperature dependent plots of k_{obs} versus $[O_2]$ (markers) with linear fits (lines). Intercepts are non-zero and increase with increasing *T*.

Table 4.2. Temperature dependent second order rate constants (k_1), estimates of dissociation rates (k_{-1}), and activation parameters for the first O_2 binding step measured by stopped-flow at low temperatures.

T (°C)	k_1 ($\times 10^4$ M^{-1} s^{-1})	k_{-1} (s^{-1})
−85	4.36 ± 0.18	25 ± 5
−80	6.08 ± 0.14	42 ± 4
−75	8.46 ± 0.05	62 ± 2
−70	11.2 ± 0.7	61 ± 22
$\Delta H_1^{\ddagger}$ (kcal mol^{-1} K^{-1})	4.4 ± 0.7	-----
$\Delta S_1^{\ddagger}$ (cal mol^{-1} K^{-1})	−13 ± 1	-----

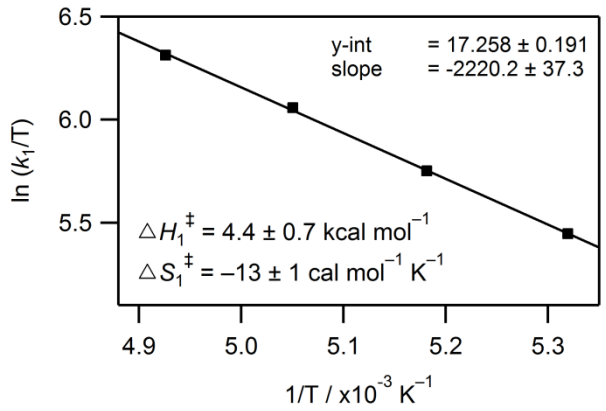

Figure 4.9. Eyring plot for the low temperature (−85 to −70 °C) reaction of $Pd(IPr)_2$ with O_2 with derived activation parameters.

The relatively low enthalpy of activation is typical of O_2 binding to a vacant site[30] and the negative activation entropy is consistent with an associative process.

The observations noted from low temperature stopped-flow experiments prompted additional studies concerning the identity of the essentially colorless adduct that forms at ultra low temperatures. ^{1}H NMR experiments at −70 °C gave sharp signals consistent with a diamagnetic species. (Figure 4.10). The diamagnetic NMR spectrum and the pale yellow color of the low T O_2 adduct indicate that the initial O_2 binding step may in fact lead to formation of the square planar, side-on peroxo (η^2-O_2)$Pd(IPr)_2$

complex, in keeping with the reported NMR data for (η^2-O_2)Pd(IMes)$_2$.[21a] Upon elevating the temperature, the diamagnetic features of the peaks gradually disappear and the emergence of paramagnetic peaks indicate formation of (η^1-O_2)$_2$Pd(IPr)$_2$. No spectroscopic evidence for an intermediate (η^1-O_2)Pd(IPr)$_2$ was detected; it is expected to be a paramagnetic superoxide complex based on computational studies of O_2 binding to the truncated Pd(IMe)$_2$ model complex reported earlier.[15] Attempts to grow crystals of (η^2-O_2)Pd(IPr)$_2$ at low temperatures have so far been unsuccessful.

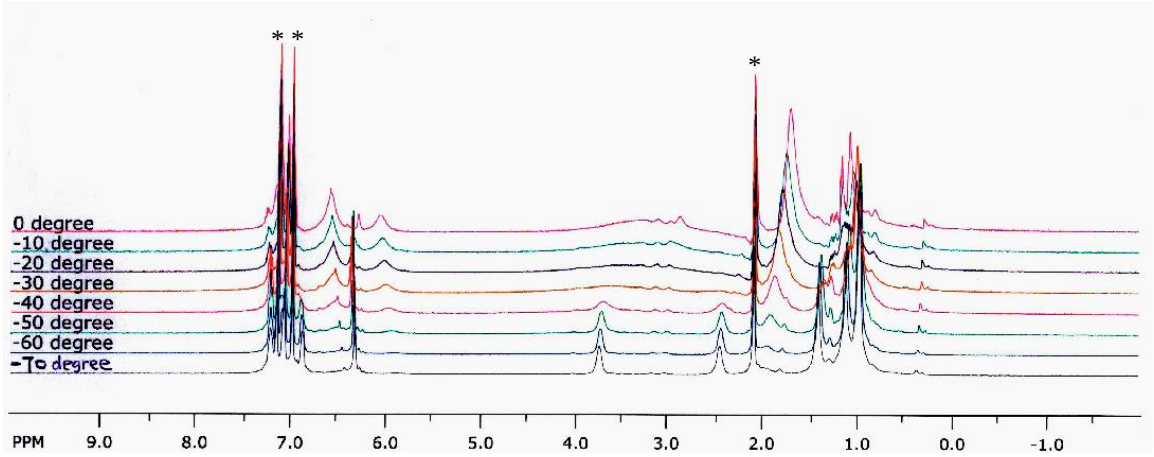

Figure 4.10. ^{1}H NMR spectra of Pd(IPr)$_2$ in toluene-d_8 after addition of O_2 at variable temperatures (−70 to 0 °C). Asterisk denotes solvent peak. Data taken from ref 1 or see also ref 22.

These findings reveal that one molecule of O_2 binds very rapidly to the metal center in the temperature range of −85 to −60 °C, forming a diamagnetic, pale yellow complex with a weakly bound O_2 ligand. In contrast to Pd(IMes)$_2$, which binds O_2 irreversibly,[15,21a] O_2 can be removed by evacuation from Pd(IPr)$_2$ at temperatures as low as −70 °C.[1] The complex also gradually loses O_2 and converts back cleanly and quantitatively to Pd(IPr)$_2$ in the process of warming to ≈ −30 °C under continuous

vacuum without any spectroscopic degradation.[1,22] Cooling the solution back to −70 °C and re-adding O_2 again results in bleaching of the orange solution with formation of (η^2-O_2)Pd(IPr)$_2$. This cycle can be performed several times without sample decomposition at low temperature.[22] However, if samples of (η^2-O_2)Pd(IPr)$_2$ are warmed under an O_2 atmosphere, a second mole of O_2 binds to form *trans*-(η^1-O_2)$_2$Pd(IPr)$_2$. Once the *bis*-superoxo complex is formed, applying vacuum does not regenerate the starting material.[2]

Formed samples of (η^2-O_2)Pd(IPr)$_2$, if evacuated to remove all dissolved O_2 when warmed up to room temperature in the absence of excess O_2, are observed to disproportionate according to Eq. 4.2.

$$2[(\eta^2\text{-}O_2)Pd(IPr)_2] \longrightarrow Pd(IPr)_2 + (\eta^1\text{-}O_2)_2Pd(IPr)_2 \qquad (4.2)$$

The net reaction shown in Eq. 4.2 is assigned to the existence of an equilibrium between (η^2-O_2)Pd(IPr)$_2$ and free Pd(IPr)$_2$ + O_2, and trapping of O_2 by an intermediate (η^1-O_2)Pd(IPr)$_2$ complex to form *trans*-(η^1-O_2)$_2$Pd(IPr)$_2$. The reversible nature of O_2 binding suggests that a (η^1-O_2)Pd(IPr)$_2$ intermediate may in fact be accessible. Since binding of O_2 to form an η^2-O_2 may proceed through formation of an end-on adduct, it is logical to presume that it is the first step in dissociation of O_2 as well, and is in keeping with the principle of microscopic reversibility.[31] These qualitative observations made by NMR spectroscopy are in agreement with quantitative data obtained by stopped-flow kinetic studies performed at higher temperatures as described in the following section.

4.3.2. High Temperature Trapping of (η^1-O_2)Pd(IPr)$_2$ with O_2 to form (η^1-O_2)$_2$Pd(IPr)$_2$

Based on the findings from variable temperature NMR studies, additional stopped-flow experiments were performed at higher temperatures over a broad range (−40 °C to +25 °C) in an effort to probe the mechanism of formation of the unique (η^1-O_2)$_2$Pd(IPr)$_2$ adduct. Interestingly, at 0 °C, slow decay (10-20 minutes) of the absorbance band assigned to the starting Pd(IPr)$_2$ complex (λ = 478 nm) was observed and development of a new, broad spectral feature centered near λ = 444 nm was noted. Time-resolved spectra for reactions at 0 °C with varying initial concentrations of O_2 are shown in Figure 4.11. Of particular note in Figure 4.11 are the initial absorbance values recorded at λ = 478 nm which decrease as a function of $[O_2]_0$ (see also Figure 4A.4a).

This behavior has been attributed to the establishment of a rapid equilibrium between Pd(IPr)$_2$, which has a λ_{max} at this position, and the essentially colorless (η^2-O_2)Pd(IPr)$_2$ adduct. The rapidly established equilibrium is maintained throughout the course of the reaction, and we are now observing spectroscopic conversion to (η^1-O_2)$_2$Pd(IPr)$_2$ which is orange in color (as is the starting material) but has different absorbance characteristics. The appearance of isosbestic points that shift position depending upon $[O_2]$ reflect the changes in the (η^2-O_2)Pd(IPr)$_2$ / Pd(IPr)$_2$ ratio. Similar behavior was also noted with variable temperature spectra at a given O_2 concentration (see Figures 4A.3 and 4A.4b in Appendix 4). Furthermore, the intensity of the new broad absorbance band assigned to *trans*-(η^1-O_2)$_2$Pd(IPr)$_2$ becomes much more apparent upon increasing $[O_2]$ concentration, giving additional credibility for the pre-equilibrium assumption.

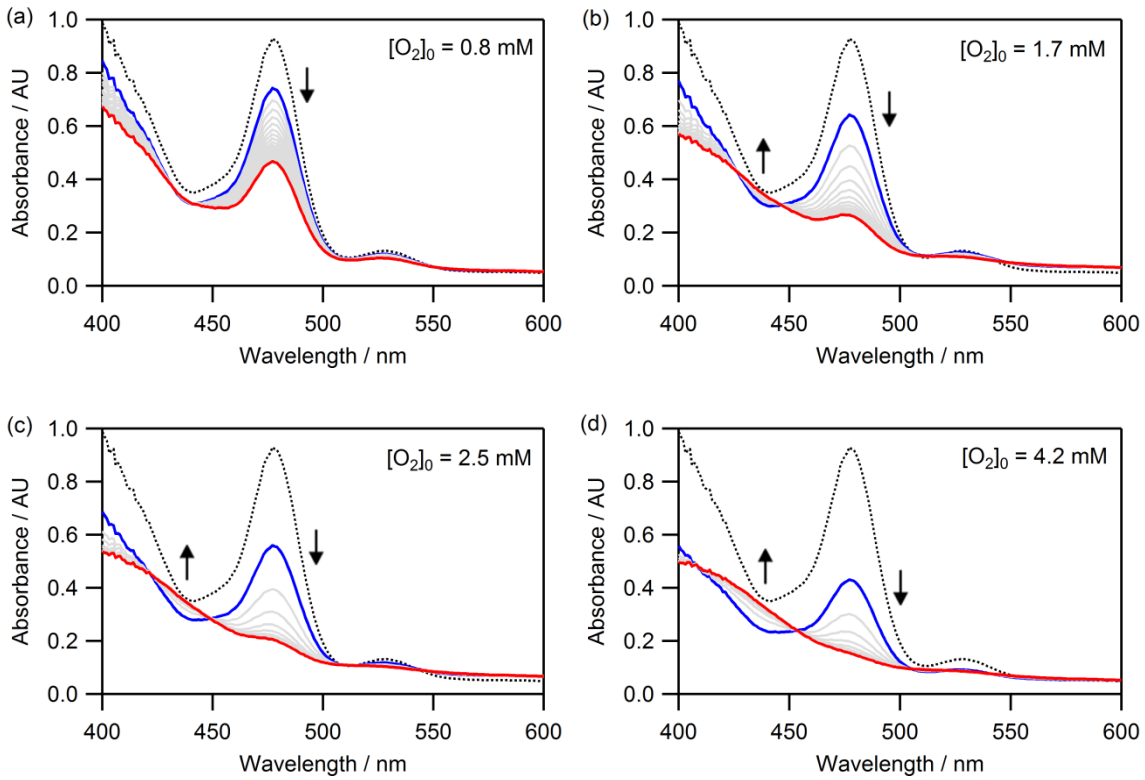

Figure 4.11. Time-resolved spectral changes for the reaction of $Pd(IPr)_2$ (0.25 mM) with varying $[O_2]_0$ at 0 °C: (a) $[O_2]_0$ = 0.8 mM (21 min reaction); (b) $[O_2]_0$ = 1.7 mM (21 min reaction); (c) $[O_2]_0$ = 2.5 mM (21 min reaction); (d) $[O_2]_0$ = 4.2 mM (10 min reaction). In all cases, the initial time = 0 s traces are shown in blue and final traces in red. A spectrum of the starting $Pd(IPr)_2$ complex at 0.25 mM (black dotted line) has been overlaid to emphasize the attenuation of the initial absorbance values recorded upon initiation of the reaction with O_2.

The equilibrium constant associated with the first O_2 binding step was derived at various temperatures (−20 °C to 20 °C) from the experimental data using the initial absorbance values noted upon reaction with O_2 at variable $[O_2]_0$. For example, non-linear least squares fitting of the plot of initial absorbance (A_0, at λ_{max} = 478 nm) versus $[O_2]$ at 20 °C to the expression given in Eq. 4.3 is shown in Figure 4.12 (the plots at additional temperatures are provided in Appendix 4, Figure 4A.5). Temperature dependent values of K_{eq} are provided in Table 4.3.

$$A_0\,(478\text{ nm}) = \frac{\varepsilon[\mathrm{Pd(IPr)_2}]_0}{(1 + K_{eq}[\mathrm{O_2}]_0)} \qquad (4.3)$$

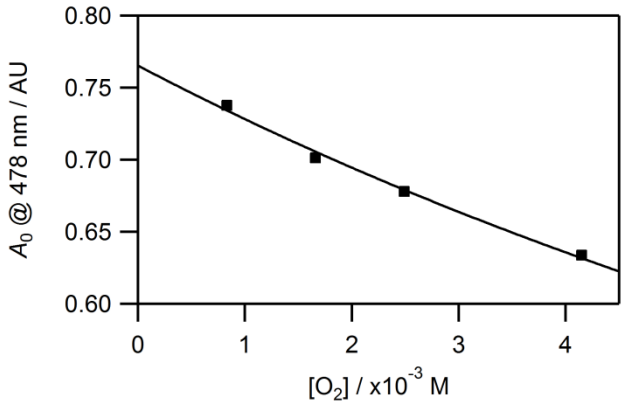

Figure 4.12. Plot of initial absorbance (λ = 478 nm) versus $[O_2]_0$ (markers) at 20 °C with non-linear fit to Eq. 4.3 (solid line). The derived value of K_{eq} at this temperature is 51 ± 3 M^{-1}.

A van't Hoff plot provided the thermodynamic parameters for O_2 binding to form (η^2-O_2)Pd(IPr)$_2$ (ΔH = −14 ± 1 kcal mol^{-1}; ΔS = −40 ± 3 cal mol^{-1} K^{-1}) as shown in Figure 4A.6. The experimentally derived values of ΔH and ΔS are in excellent agreement with those obtained from the kinetic model as described in Section 4.3.3.

Table 4.3. Temperature dependent equilibrium constants (K_{eq}) derived from fitting plots of initial absorbance (λ = 478 nm) versus $[O_2]_0$ to the expression in Eq. 4.3. $[Pd(IPr)_2]_0$ was fixed at 0.25 mM. At 20 °C only, the first data point (at $[O_2]$ = 0) was omitted.

T (°C)	K_{eq} (M^{-1})
+20	51 ± 3
+10	130 ± 10
0	230 ± 14
−10	850 ± 11
−20	2,270 ± 92

Owing to the slowness of the transformation observed at higher temperatures, reactions rates for formation of $(\eta^1\text{-}O_2)_2Pd(IPr)_2$ as a function of $[O_2]$ could only be readily measured over a temperature range of −20 °C to +20 °C. Interestingly, k_{obs} depends linearly on $[O_2]$ at −20 °C while the plots display curvature at $T \geq 0$ °C (Figure 4.13). This ultimately reveals a more complicated reaction order with respect to $[O_2]$. In this case, it is evident that the overall reaction rate is not dominated by a single elementary step in the temperature range of 20 °C $\leq T \geq$ 0 °C.

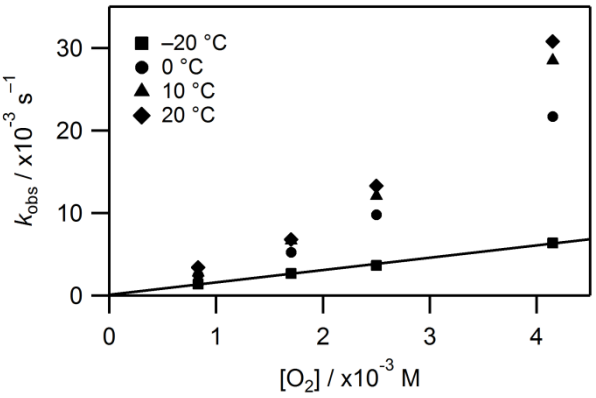

Figure 4.13. Plots of k_{obs} versus $[O_2]$ obtained over the temperature range of −20 to 20 °C. A linear fit is shown for the −20 °C plot, which yielded a second order rate constant (k_2) of 1.50 ± 0.06 M^{-1} s^{-1} (R^2 = 0.997).

From the spectrophotometric perspective, we are observing formation of *trans*-$(\eta^1\text{-}O_2)_2Pd(IPr)_2$ through the slow decay of the starting $Pd(IPr)_2$ complex at $T \geq 0$ °C (see Figure 4A.3). If we assume that $(\eta^2\text{-}O_2)Pd(IPr)_2$ contributes negligibly to the absorbance and that the $Pd(IPr)_2$ / $(\eta^2\text{-}O_2)Pd(IPr)_2$ pre-equilibrium is followed by rate limiting binding of the second O_2 molecule (Eq. 4.4), we can estimate the observed rate (k_{obs}) and K_{eq} as a function of $[O_2]$ according to Eq. 4.5 (derivation is provided in Appendix 4).

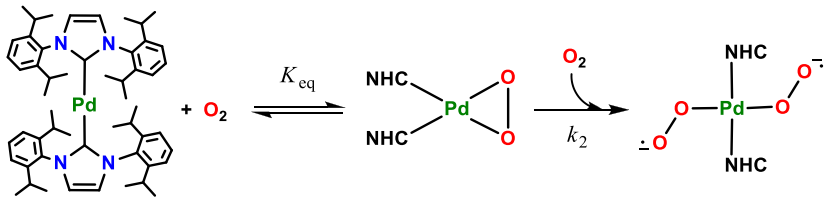

(4.4)

$$k_{obs} = \frac{k_2 K_{eq}[O_2]^2}{1 + K_{eq}[O_2]} \qquad (4.5)$$

Reasonable fits to Eq. 4.5 were obtained for the k_{obs} versus $[O_2]$ plots as shown in Figure 4A.7 and the derived value of K_{eq} and k_2 are given in Table 4.4. This was followed by full computer simulation of the time-resolved spectra using the ReactLab Kinetics program as outlined in the following section.

Table 4.4. Temperature dependent equilibrium constants (K_{eq}) and second order rate constants (k_2) obtained from fitting high T k_{obs} versus $[O_2]$ plots to Eq. 4.5.

T (°C)	K_{eq} (M^{-1})	k_2 (M^{-1} s^{-1})
+20	51[a]	43 ± 2
+10	207 ± 88	15 ± 4
0	303 ± 130	9.3 ± 1.9
−20	[b]	1.53 ± 0.03 (1.50 ± 0.06)[c]

[a] K_{eq} value was fixed. [b] An accurate value could not be obtained from the non-linear fit. [c] Value in parenthesis represents the slope of the linear plot of k_{obs} versus $[O_2]$ as shown in Figure 4.13.

4.3.3. Kinetic Modeling

Global modeling of the time-resolved spectra over a broad temperature range (−40 to +20 °C) to the mechanism provided in Eq. 4.4 was performed using the ReactLab Kinetics program in an effort to validate the experimental analyses described in the previous section as well as determine the rate of formation of *trans*-(η^1-O_2)$_2$Pd(IPr)$_2$ over

a broader temperature range. As discussed earlier, the first step of the reaction represents the equilibrium binding of the first O_2 to form the intermediate monooxygenated (η^2-O_2)Pd(IPr)$_2$ species; introduction of additional steps involving an (η^1-O_2)Pd(IPr)$_2$-(η^2-O_2)Pd(IPr)$_2$ interconversion were not included since the latter is essentially non-absorbing and the former is not detected spectroscopically (*vide infra*). The second step, governed by k_2, represents binding of the second O_2 molecule which leads to formation of the final *trans*-(η^1-O_2)$_2$Pd(IPr)$_2$ complex. The calculated equilibrium and rate constants are given in Table 4.5 and are in good agreement with estimates obtained directly from the experimental analyses.

Table 4.5. Modeled values of rate and equilibrium constants obtained from the kinetic model over a range of temperatures (−40 °C to 20 °C) with $[O_2]_0$ = 4.15 mM using ReactLab.[a,b] An average of two data sets is reported with standard deviations in all cases except at −30 and −40 °C, where only one data set is available. In those cases, the predicted standard deviation in k_2 was taken directly from the model and the error in K_{eq} is estimated at ± 30 %.

T (°C)	K_{eq} (M^{-1})	k_2 (M^{-1} s^{-1})
20	46 ± 1	50.5 ± 0.5
10	107 ± 2	25.9 ± 0.5
0[c]	202 ± 15	13 ± 1
−20	2,475 ± 85	1.59 ± 0.02
−30	7,730 ± 2,300	0.773 ± 0.001
−40	44,700 ± 13,400	0.295 ± 0.001

[a] The initial concentration of Pd(IPr)$_2$ was allowed to float; final calculated values ranged between 2.2 and 2.5 mM. [b] A known spectrum of (η^2-O_2)Pd(IPr)$_2$ obtained at −85 °C was incorporated at all temperatures. [c] The absorbance spectrum of the starting Pd(IPr)$_2$ complex was calculated by ReactLab to account for baseline shift; at all remaining temperatures, a known spectrum was used.

The calculated spectra and concentration profiles for the modeled reaction at 20 °C are shown below in Figure 4.14. Additional data obtained from the kinetic model at all remaining temperatures is provided in Appendix 4.

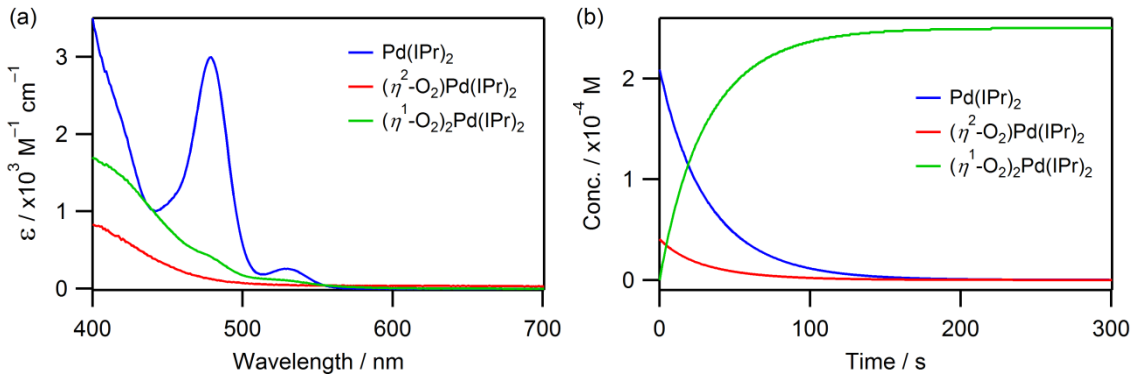

Figure 4.14. (a) Calculated spectra of colored components obtained from modeling the $Pd(IPr)_2$-O_2 system at 20 °C. (b) Concentration profiles for colored components. $[Pd(IPr)_2]_0$ = 0.25 mM and $[O_2]_0$ = 4.15 mM. See Appendix 4 for data at additional temperatures.

The modeled values of K_{eq} and k_2 were used to derive the thermodynamic (ΔH, ΔS) and activation parameters ($\Delta H^{\ddagger}$, $\Delta S^{\ddagger}$), respectively, associated with the two-step reaction as shown in Figure 4.15.

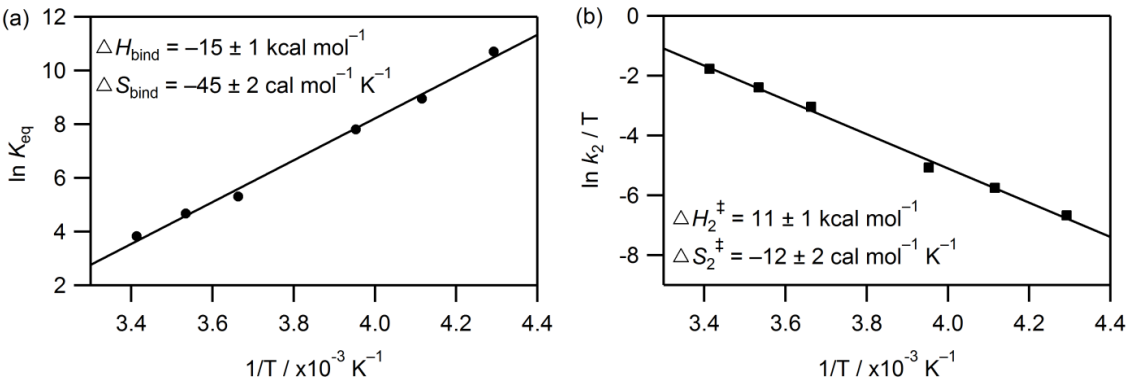

Figure 4.15. (a) van't Hoff plot constructed from the values of K_{eq} obtained from the kinetic model for equilibrium binding of O_2 to form $(\eta^2\text{-}O_2)Pd(IPr)_2$ with derived thermodynamic parameters. (b) Eyring plot for formation of *trans*-$(\eta^1\text{-}O_2)_2Pd(IPr)_2$ from the monooxygenated adduct (k_2 step) with derived activation parameters.

A plausible mechanism for stepwise O_2 binding that is consistent with the observed changes noted over the entire temperature range studied (−85 to 20 °C) is shown in Figure 4.16. This is proposed to involve, as originally delineated by Stahl,[15,32] initial formation of a reactive intermediate η^1-O_2 complex (complex I). Complex I serves as a branching point that can undergo O_2 loss to regenerate $Pd(IPr)_2$, rearrange to form the expected diamagnetic η^2-O_2 complex at low *T*, or, at elevated *T*, can add a second O_2 in the rate limiting step to form paramagnetic $(\eta^1\text{-}O_2)_2Pd(IPr)_2$. For $Pd(IMes)_2$, the k_2 step is not observed and thus corresponds to only the top row of the mechanism depicted below.

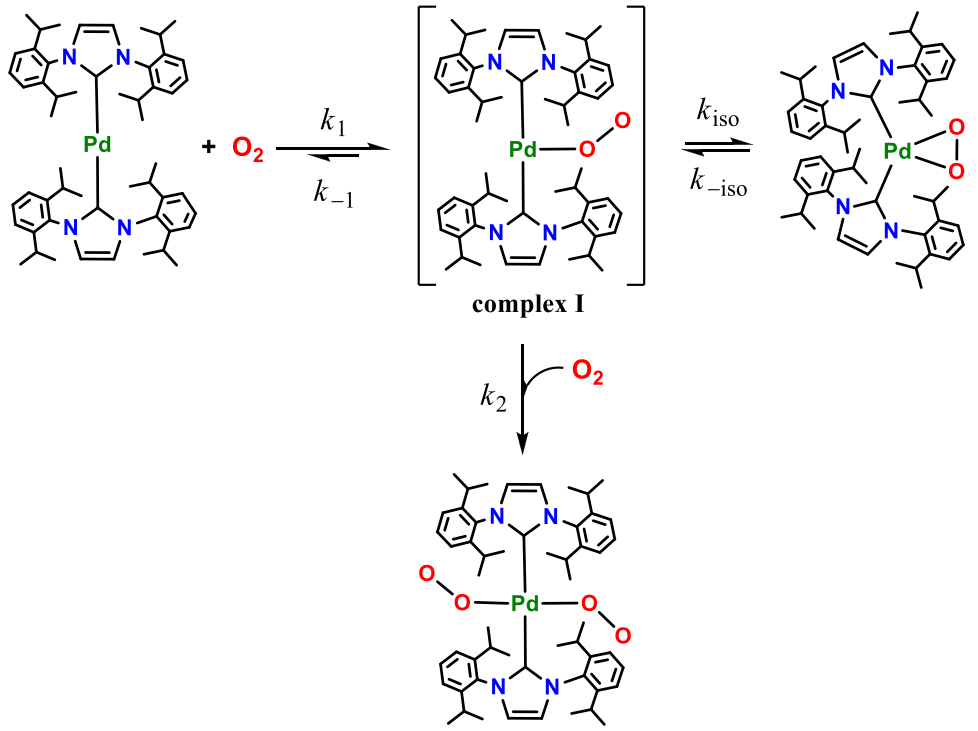

Figure 4.16. Proposed mechanism of formation of *cis*-$(\eta^2\text{-}O_2)Pd(IPr)_2$ and *trans*-$(\eta^1\text{-}O_2)_2Pd(IPr)_2$ from $Pd(IPr)_2$ and O_2.

The product distribution in Figure 4.16 is determined by the relative magnitudes of k_{iso}, k_{-iso}, and k_2 for $Pd(IPr)_2$. At very low temperatures (≈ −85 °C), entropic effects contribute negligibly to ΔG; k_{-iso} is essentially suppressed and $(\eta^2\text{-}O_2)Pd(IPr)_2$ is formed exclusively as the thermodynamically favored product. As temperature increases (≈ −70 °C and higher), entropy plays a more pronounced role and k_{-iso} increases;[a] more $(\eta^1\text{-}O_2)Pd(IPr)_2$ is present and can bind an additional molecule of O_2 to form the final product, $(\eta^1\text{-}O_2)_2Pd(IPr)_2$.

Also, the relative magnitudes of k_{iso} appear to depend critically on the specific ligand used (e.g., IMes versus IPr). It is possible that the rearrangement of $(\eta^1\text{-}O_2)Pd(IMes)_2$ (k_{iso}) is much faster than for $(\eta^1\text{-}O_2)Pd(IPr)_2$, or that k_{-iso} is much smaller and dissociation of $(\eta^2\text{-}O_2)Pd(IMes)_2$ back to $(\eta^1\text{-}O_2)Pd(IMes)_2$ is thermodynamically disfavored. An additional possibility is that binding of a second O_2 molecule (k_2) represents an inaccessible pathway for $Pd(IMes)_2$, though this seems unlikely since it is less sterically hindered than the $Pd(IPr)_2$ system. The more likely situation is that $(\eta^2\text{-}O_2)Pd(IPr)_2$ is destabilized, and the isomerization rates (k_{iso}, k_{-iso}) ultimately become critical in determining the fate of the $(\eta^1\text{-}O_2)Pd(NHC)_2$ intermediates.

The different reactivities of $(\eta^2\text{-}O_2)Pd(IPr)_2$ and $(\eta^2\text{-}O_2)Pd(IMes)_2$ towards H_2O also help to illustrate these points: $(\eta^2\text{-}O_2)Pd(IPr)_2$ reacts with H_2O at −78 °C to quantitatively produce the novel hydroxo-hydroperoxo complex, *trans*-$(OOH)(OH)Pd(IPr)_2$, as shown in Figure 4.17; the reaction must be performed at low T because the $(\eta^2\text{-}O_2)Pd(IPr)_2$ adduct is unstable at temperatures above −40 °C. In contrast,

[a] k_{-1} also increases with increasing temperature and therefore the relative magnitudes of k_{-1} and k_{-iso} will also contribute to how much $(\eta^1\text{-}O_2)Pd(IPr)_2$ builds up. In this particular case, it is likely that $k_{-1} >> k_{-iso}$ which explains the lack of accumulation of this intermediate and the slow decay of $Pd(IPr)_2$ observed at $T \geq$ 0 °C (see Figure 4A.3).

(η^2-O_2)Pd(IMes)$_2$ remains completely unreactive towards H_2O, even for extended periods at room temperature. The experimental observation suggests that the rate of isomerization (k_{iso}) may be retarded for the (η^1-O_2)Pd(IPr)$_2$ adduct, which allows for trapping of H_2O or an additional O_2 molecule.

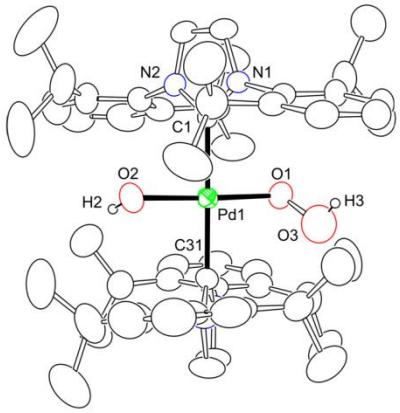

Figure 4.17. X-ray structure of *trans*-[Pd(IPr)$_2$(OOH)(OH)]. Selected distances (Å) and angles (°): Pd1–O1 = 2.009(3), Pd1–O2 = 2.009(3), O1–O3 = 1.465(6), Pd1–C1 = 2.051(3), Pd1–C31 = 2.050(3), O2–Pd1–O1 = 177.64(13), C1–Pd1–C31 = 179.30(13), Pd1–O1–O3 = 111.1(3).

Computational studies[2,15] on O_2 binding to [Pd(NHC)$_2$] systems (NHC = IMe, IMes, IPr) and Pd(IPr)(PPh_3) predict that the most stable η^1-O_2 structures exhibit a "T-shaped" conformation with a single O_2 bound end-on as superoxide. The optimized space filling structures shown in Figure 4.18 are oriented in such a way as to show the maximum possible amount of free space available for O_2 to move around. It appears clear that the aperture available for O_2 binding and subsequent isomerization increases on going from the (IPr)$_2$ (**Ia)** to (IMes)$_2$ **Ib** to (IPr, PPh_3) **Ic**, ligand sets, and is in line with the mechanistic considerations (and observed reactivities) discussed above.

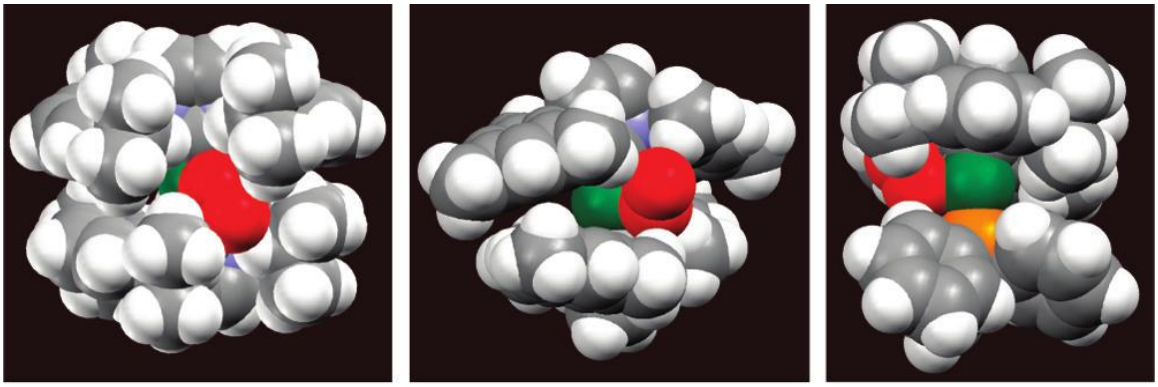

Figure 4.18. Space-filling models of the computed most stable forms of the T-shaped end-on adducts of [(η^1-O_2)Pd(IPr)$_2$] (**Ia**), [(η^1-O_2)Pd(IMes)$_2$] (**Ib**), and [(η^1-O_2)Pd(IPr)(PPh_3)] (**Ic**). Atomic dimensions are the atomic van der Waals radii. Pd, green; O, red; N, blue; C, gray; H, white; P, orange.

4.4. Conclusion

This study evolved out of simple measurements of the enthalpies of O_2 binding to Pd(L)(L') (L = NHC, L' = NHC or PR_3) complexes in an effort to determine the factors influencing the Pd-O_2 bond strength as a function of L and L'. The thermodynamic data reported in Table 4.1 reveals that ΔH for O_2 binding ranges from −28 kcal mol^{-1} for (η^2-O_2)Pd(IMes)$_2$ to −24 kcal mol^{-1} for (η^1-O_2)$_2$Pd(IPr)$_2$. The reaction between Pd(L)(L') (L = NHC, L' = IMes or PR_3) and O_2 is more exothermic than that found for Vaska's complex, Ir(Cl)(CO)(PPh_3)$_2$, in which ΔH = −17.1 kcal mol^{-1} and ΔS = −37 cal mol^{-1} K^{-1}.[29] The more exothermic nature of O_2 binding to the Pd(0) complexes versus the Ir(I) complex (≈ 7 - 11 kcal mol^{-1}) readily accounts for the reversible nature of O_2 binding to Vaska's complex as compared to the irreversible binding observed for the Pd(L)(L') complexes.

A major surprise beyond the calorimetric data was the orange color and paramagnetic NMR spectrum observed for the reaction of O_2 with $Pd(IPr)_2$ (at ambient *T*), which was ultimately shown to be due to formation of the novel *trans*-(η^1-O_2)$_2$Pd(IPr)$_2$ complex. From an energetic standpoint, this result seemed unusual. How can a highly stable complex which also binds two moles of O_2 irreversibly have such a low value of ΔH of −12 kcal mol^{-1} (= −24/2 mol O_2)? If the unfavorable entropy of binding corresponds similarly to that of Vaska's complex, then for two moles of O_2 one would expect ΔS = −74 cal mol^{-1} K^{-1} for formation of *trans*-(η^1-O_2)$_2$Pd(IPr)$_2$, which at 300 K would lead to a near zero value for ΔG. Furthermore, why did the seemingly small change in ligand set from IPr to IMes cause such an apparently large difference in observed reactivity?

These observations (and unanswered questions) prompted a more detailed study of the reaction mechanism. The biggest surprise occurred in low temperature (−85 °C to −70 °C) stopped-flow experiments, where expected formation of the orange *trans*-(η^1-O_2)$_2$Pd(IPr)$_2$ complex was not observed. Instead, rapid decay across the entire spectral window occurred, yielding a nearly colorless solution reminiscent of the behavior of *cis*-(η^2-O_2)Pd(IMes)$_2$. Low temperature NMR studies confirmed that the product gave sharp lines in the NMR and computational results allowed formulation of this complex as being *cis*-(η^2-O_2)Pd(IPr)$_2$.[1] In addition, the binding of the first O_2 molecule to form *cis*-(η^2-O_2)Pd(IPr)$_2$ is a reversible process. The rate of binding of O_2 to Pd(IMes)$_2$ was too fast to measure by the standard stopped-flow technique. We were, however, able to measure the rate of O_2 binding to Pd(IPr)(P(*p*-tolyl)$_3$),[2] which yielded a very low activation enthalpy of 2.2 ± 0.3 kcal mol^{-1}. We conclude that O_2 binding Pd(IMes)$_2$ occurs with an $\Delta H^{\ddagger} \leq 2.2$

kcal mol^{-1} since the reaction is even more rapid. η^1-O_2 intermediates were not observed in these reactions.

An intermediate η^1-O_2 adduct of $Pd(IPr)_2$ was also not observed in low temperature reactions, however, the rapid binding was measurable and yielded activation parameters of $\Delta H_1^{\ddagger} = 4.4 \pm 0.7$ kcal mol^{-1} and $\Delta S_1^{\ddagger} = -13 \pm 1$ cal mol^{-1} K^{-1}. In contrast to *cis*-(η^2-O_2)$Pd(IMes)_2$, which is stable even above room temperature for extended periods of time, *cis*-(η^2-O_2)$Pd(IPr)_2$ is unstable above ≈ −40 °C. Stopped-flow kinetic studies provide strong evidence that over the temperature range of −30 to +20 °C, there is a rapid on-off equilibrium between $Pd(IPr)_2$ and *cis*-(η^2-O_2)$Pd(IPr)_2$ for which $\Delta H = -14 \pm 1$ kcal mol^{-1} and $\Delta S = -42 \pm 2$ cal mol^{-1} K^{-1}. Thus, relative to *cis*-$Pd(IMes)_2$(η^2-O_2) which has an enthalpy of binding of −28 ± 2 kcal mol^{-1}, switching ligands to IPr cuts this value in half to −14 kcal/mol.[1]

At −20 °C, the formation of *trans*-(η^1-O_2)$_2Pd(IPr)_2$ is readily followed, and at this specific temperature, the kinetics follows the simple rate law shown in Eq. 4.6.

$$rate = k_2[(\eta^2\text{-}O_2)Pd(IPr)_2][O_2] \qquad (4.6)$$

As temperature increases, the formation of (η^2-O_2)$Pd(IPr)_2$ becomes progressively disfavored and contributions from dissociation become evident from analysis of the kinetic data. Kinetic modeling allowed for the isolation of the second order rate (k_2) constants associated with the binding of an additional O_2 molecule across a broad temperature range (see mechanism in Figure 4.16), which yielded activation parameters of $\Delta H_2^{\ddagger} = 11 \pm 1$ kcal mol^{-1} and $\Delta S_2^{\ddagger} = -13 \pm 1$ cal mol^{-1} K^{-1}. Addition of the second O_2

is clearly governed by enthalpic factors, since the entropy of activation is identical to that determined for the initial O_2 binding step at low temperatures. Although spectroscopic detection of the $(\eta^1\text{-}O_2)Pd(IPr)_2$ intermediate was not successful, calculations suggest that binding of O_2 in a sterically hindered environment would occur through one and not both of the oxygen atoms and its presence as a steady-state intermediate in the facile on/off binding of O_2 at low temperatures is reasonable.[22] This conclusion is also supported by the observed reactivity of the $(\eta^2\text{-}O_2)PdL_2$ (L = IMes, IPr) adducts towards H_2O.

In summary, we have conducted a detailed mechanistic study on the formation of the unique *trans*-$(\eta^1\text{-}O_2)_2Pd(IPr)_2$ complex. This work reveals the importance of how fine tuning of a ligand structure can alter reactivity patterns with O_2 and provides additional motivation to continue both experimental and computational study of O_2 binding in these and related systems.

4.5. References

(1) *This chapter is reproduced in part with permission from*: Cai, X.; Palluccio, T. D.; Majumdar, S.; Fortman, G. C.; Tomson, N.; Wieghardt, K.; Cazin, C. S. J.; Lhermitte, C.; Prabhakar, R.; Nolan, S. P.; Rybak-Akimova, E. V.; Temprado, M.; Hoff, C. D. The Mechanism of Reaction of O_2 with $Pd(IPr)_2$: Low Temperature Formation of (η^2-O_2)$Pd(IPr)_2$ and Trapping of (η^1-O_2)$Pd(IPr)_2$ with O_2 to form (η^1-O_2)$_2Pd(IPr)_2$ and with H_2O for form $Pd(IPr)_2(O_2H)(OH)$. *Manuscript in preparation.*

(2) *This chapter is also reproduced in part with permission from*: Cai, X.; Majumdar, S.; Fortman, G. C.; Cazin, C. S. J.; Slawin, A. M. Z.; Lhermitte, C.; Prabhakar, R.; Germain, M. E.; Palluccio, T.; Nolan, S. P.; Rybak-Akimova, E. V.; Temprado, M.; Captain, B.; Hoff, C. D. Oxygen Binding to [Pd(L)(L')] (L= NHC, L' = NHC or PR_3, NHC = *N*-Heterocyclic Carbene). Synthesis and Structure of a Paramagnetic *trans*-[$Pd(NHC)_2$(η^1-O_2)$_2$] Complex. *J. Am. Chem. Soc.*, **2011**, *133*(5), 1290. Copyright 2011 American Chemical Society.

(3) Vaska, L. *Acc. Chem. Res.*, **1976**, *9*, 175.

(4) Rybak-Akimova, E. V. In *Physical Inorganic Chemistry: Reactions, Processes, and Applications*; Bakac, A., Ed.; Wiley: Hoboken, NJ, 2010; pp 109−188.

(5) Vaska, L. *Science*, **1963**, *140*, 809.

(6) Nolte, M. J.; Singleton, E.; Laing, M. *J. Am. Chem. Soc.*, **1975**, *97*, 6396.

(7) Lebel, H.; Ladjel, C.; Bélanger-Gariépy, F.; Schaper, F., *J. Organomet. Chem.*, **2008**, *693*, 2645.

(8) Valentine, J. S. *Chem. Rev.*, **1973,** *73*, 235.

(9) Unno, M.; Chen, H.; Kusama, S.; Shaik, S.; Ikeda-Saito, M. *J. Am. Chem. Soc.*, **2007**, *129*, 13394.

(10) Lippard, S. J.; Berg, J. M. *Principles of Bioinorganic Chemistry*; University Science Books: Mill Valley, CA, 1994.

(11) Würtele, C.; Gaoutchenova, E.; Harms, K.; Holthausen, M. C.; Sundermeyer, J.; Schindler, S. *Angew. Chem. Int. Ed.*, **2006**, *45*, 3867.

(12) Maiti, D.; Lee, D. H.; Gaoutchenova, K.; Würtele, C.; Holthausen, M. C.; Narducci Sarjeant, A. A.; Sundermeyer, J.; Schindler, S.; Karlin, K. D. *Angew. Chem. Int. Ed.*, **2008**, *47*, 82.

(13) Cramer, C. J.; Tolman, W. B. *Acc. Chem. Res.*, **2007**, *40*, 601.

(14) Ashley, D. C.; Brinkley, D. W.; Roth, J. P. *Inorg. Chem.*, **2010**, *49*, 3661.

(15) Popp, B. V.; Wendlandt, J. E.; Landis, C. R.; Stahl, S. S. *Angew. Chem. Int. Ed.*, **2007**, *46*, 601.

(16) Cozzolino, A. F.; Tofan, D.; Cummins, C. C.; Temprado, M.; Palluccio, T. D.; Rybak-Akimova, E. V.; Majumdar, S.; Cai, X.; Captain, B.; Hoff, C. D. *J. Am. Chem. Soc.*, **2012,** *134*, 18249.

(17) (a) Sheldon, R. A.; Arends, I.; Hanfeld, U. *Green Chemistry and Catalysis*; Wiley-VCH: Weinheim, Germany, 2007; Chapter 4, pp 18-23. (b) van Leeuwen, P. V. N. M. *Homogeneous Catalysis: Understanding the Art*; Kluwer: Dordrecht, The Netherlands, 2004; Chapter 15. (c) Stahl, S. S. *Science*, **2005**, *309*, 1824.

(18) (a) Stahl, S. S. *Angew. Chem. Int. Ed.*, **2004**, *43*, 3400. (b) Stahl, S. S.; Rogers, M. M. *Top. Organomet. Chem.*, **2007**, *21*, 21. (c) Díez-González, S.; Marion, N.; Nolan, S. P. *Chem. Rev.*, **2009**, *109*, 3612.

(19) Fantasia, S.; Nolan, S. P. *Chem. Eur. J.*, **2008**, *14*, 6987.

(20) For one example of kinetic investigation of the involvement of [Pd(PPh3)2(η2-O2)] in homocoupling of boronic acids, see: Adamo, C.; Amatore, C.; Ciofini, I.; Jutand, A.; Lakmini, H. *J. Am. Chem. Soc.*, **2006**, *128*, 6829.

(21) (a) Konnick, M. M.; Guzei, I. A.; Stahl, S. S. *J. Am. Chem. Soc.*, **2004**, *126*, 10212. (b) Yamashita, M.; Goto, K.; Kawashima, T. *J. Am. Chem. Soc.*, **2005,** *127*, 7294. Additional LPd(η^2-O_2) complexes (L = bidentate chelating ligand) have been structurally characterized: (c) Stahl, S. S.; Thorman, J. L.; Nelson, R. C.; Kozee, M. A. *J. Am. Chem. Soc.*, **2001**, *123*, 7188. (d) Clegg, W.; Eastham, G. R.; Elsegood, M. R. J.; Heaton, B. T.; Iggo, J. A.; Tooze, R. P.; Whyman, R.; Zacchini, S. *J. Chem. Soc., Dalton Trans.*, **2002**, 3300.

(22) Cai, X. Thermodynamic, Kinetic and Mechanistic Investigations of Binding and Activation of Molecular Oxygen and Mesityl Nitrile Oxide, Ph.D. Thesis, University of Miami, 2013.

(23) Bohm, V. P. W.; Gstöttmayr, C. W. K.; Weskamp, T.; Herrmann, W. A., *J. Organomet. Chem.*, **2000**, *595*, 186.

(24) Battino, R.; Rettich, T. R.; Tominaga, T. *J. Phys. Chem. Ref. Data*, **1983**, *12*, 163.

(25) Huacuja, R.; Graham, D. J.; Fafard, C. M.; Chen, C. H.; Foxman, B. M.; Herbert, D. E.; Alliger, G.; Thomas, C. M.; Ozerov, O. V. *J. Am. Chem. Soc.*, **2011**, *133*(11), 3820.

(26) (a) Talsi, E. P.; Babenko, V. P.; Likholobov, V. A.; Nekipelov, V. M.; Chinakov, V. D. *J. Chem. Soc., Chem. Commun.*, **1985**, 1768. (b) Talsi, E. P.; Babenko, V. P.; Shubin, A. A.; Chinakov, V. D.; Nekipelov, V. M.; Zamaraev, K. I. *Inorg. Chem.*, **1987**, *26*, 3871. (c) Fiallo, M. M. L.; Garnier-Suillerot, A. *Inorg. Chem.*, **1990**, *29*, 893.

(27) Fortman, G. C.; Scott, N. M.; Linden, A.; Stevens, E. D.; Dorta, R.; Nolan, S. P. *Chem. Commun.*, **2010**, *46*, 1050.

(28) For NHC ligand steric parameters, see: (a) Clavier, H.; Nolan, S. P. *Chem. Commun.*, **2010**, *46*, 841. (b) de Frémont, P.; Marion, N.; Nolan, S. P. *Coord. Chem.*

Rev., **2009**, *253*, 862. (c) Kelly, R. A., III; Clavier, H.; Guidice, S.; Scott, N. M.; Stevens, E. D.; Bordner, J.; Samardjiev, I.; Hoff, C. D.; Cavallo, L.; Nolan, S. P. *Organometallics*, **2008**, *27*, 202.

(29) Vaska, L. *Acc. Chem. Res.*, **1968**, *1*, 335.

(30) (a) Rybak-Akimova, E. V.; Marek, K.; Masarwa, M.; Busch, D. H. *Inorg. Chim. Acta*, **1998**, *270*, 151. (b) Fry, H. C.; Scaltrito, D. V.; Karlin, K. D.; Meyer, G. J. *J. Am. Chem. Soc.*, **2003**, *125*, 11866.

(31) Tolman, R. C. *Proc. Natl. Acad. Sci.*, **1925**, *11*, 436.

(32) Popp, B. V.; Stahl, S. S. *J. Am. Chem. Soc.*, **2007**, *129*, 4410.

APPENDIX 4

The Mechanism of Reaction of O_2 with $Pd(IPr)_2$: Low Temperature Formation of $(\eta^2\text{-}O_2)Pd(IPr)_2$ and Trapping of $(\eta^1\text{-}O_2)Pd(IPr)_2$ with O_2 to Form *trans*-$(\eta^1\text{-}O_2)_2Pd(IPr)_2$

4.3.1. Low Temperature Formation of $(\eta^2\text{-}O_2)Pd(IPr)_2$

Table 4A.1. Temperature dependent pseudo-first order (k_{1obs} or k_{obs}) and second-order (k_1) rate constants for O_2 binding to $Pd(IPr)_2$ (0.25 mM) at low *T*, obtained from fitting decay traces (λ = 473 nm, decay) to a double exponential (at −85 °C only) or a single exponential equation (all remaining temperatures).

−85 °C	$[O_2]$ (M)	k_{1obs} (s^{-1})	k_1 ($\times 10^4$ M^{-1} s^{-1})
	1.7	97.2 ± 4.2	4.36 ± 0.18
	2.5	138 ± 9	
	3.3	169 ± 13	
	4.15	206 ± 15	
−80 °C	$[O_2]$ (M)	k_{obs} (s^{-1})	k_1 ($\times 10^3$ M^{-1} s^{-1})
	1.7	145 ± 12	6.08 ± 0.14
	2.5	193 ± 12	
	3.3	246 ± 20	
	4.15	293 ± 38	
−75 °C	$[O_2]$ (M)	k_{obs} (s^{-1})	k_1 ($\times 10^3$ M^{-1} s^{-1})
	1.7	206 ± 5	8.46 ± 0.05
	2.5	273 ± 4	
	3.3	342 ± 8	
	4.15	413 ± 8	
−70 °C	$[O_2]$ (M)	k_{obs} (s^{-1})	k_1 ($\times 10^3$ M^{-1} s^{-1})
	1.7	241 ± 3	11.2 ± 0.7
	2.5	353 ± 3	
	3.3	437 ± 6	
	4.15	518 ± 2	

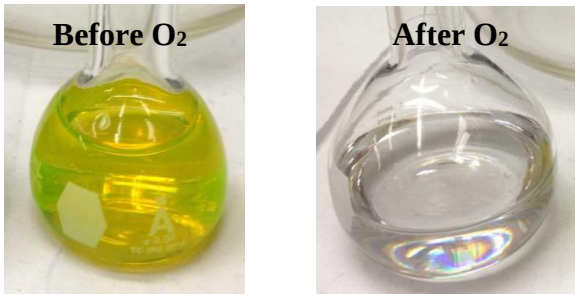

Figure 4A.1. Comparison of toluene solutions of $Pd(IMes)_2$ (1 mM) before (left) and immediately after (right) exposure to O_2.

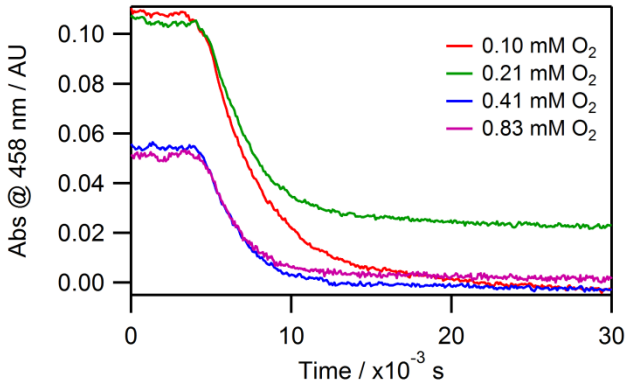

Figure 4A.2. Kinetic traces at λ = 458 nm as a function of $[O_2]_0$ obtained from the stopped-flow reaction of $Pd(IMes)_2$ with O_2 at −80 °C.

Table 4A.2. Pseudo-first order (k_{obs}) rate constants for O_2 binding to $Pd(IMes)_2$ (0.1 mM) at −80 °C. Kinetic traces were fit to a single exponential equation, $y = -A*\exp(-k_{obs}t) + C$ or $y = -A*\exp(-k_{obs}t) + Mx + C$. The average value taken from multiple datasets is reported with the standard deviation. Since the reaction is so rapid, it is not possible to obtain an accurate reaction order with respect to $[O_2]$; instead, an estimate for the presumed second order rate (k_1) constant was made from the stoichiometric reaction as shown below.

−80 °C	$[O_2]$ (M)	k_{obs} (s^{-1})	k_1 (M^{-1} s^{-1})
	0.10	267 ± 15	$= k_{obs}/[O_2] \approx 3 \times 10^6$
	0.21	338 ± 28	
	0.41	418 ± 13	
	0.83	475 ± 37	

4.3.2. High Temperature Kinetics: Trapping of of (η^1-O_2)$Pd(IPr)_2$ with O_2 to form (η^1-O_2)$_2Pd(IPr)_2$

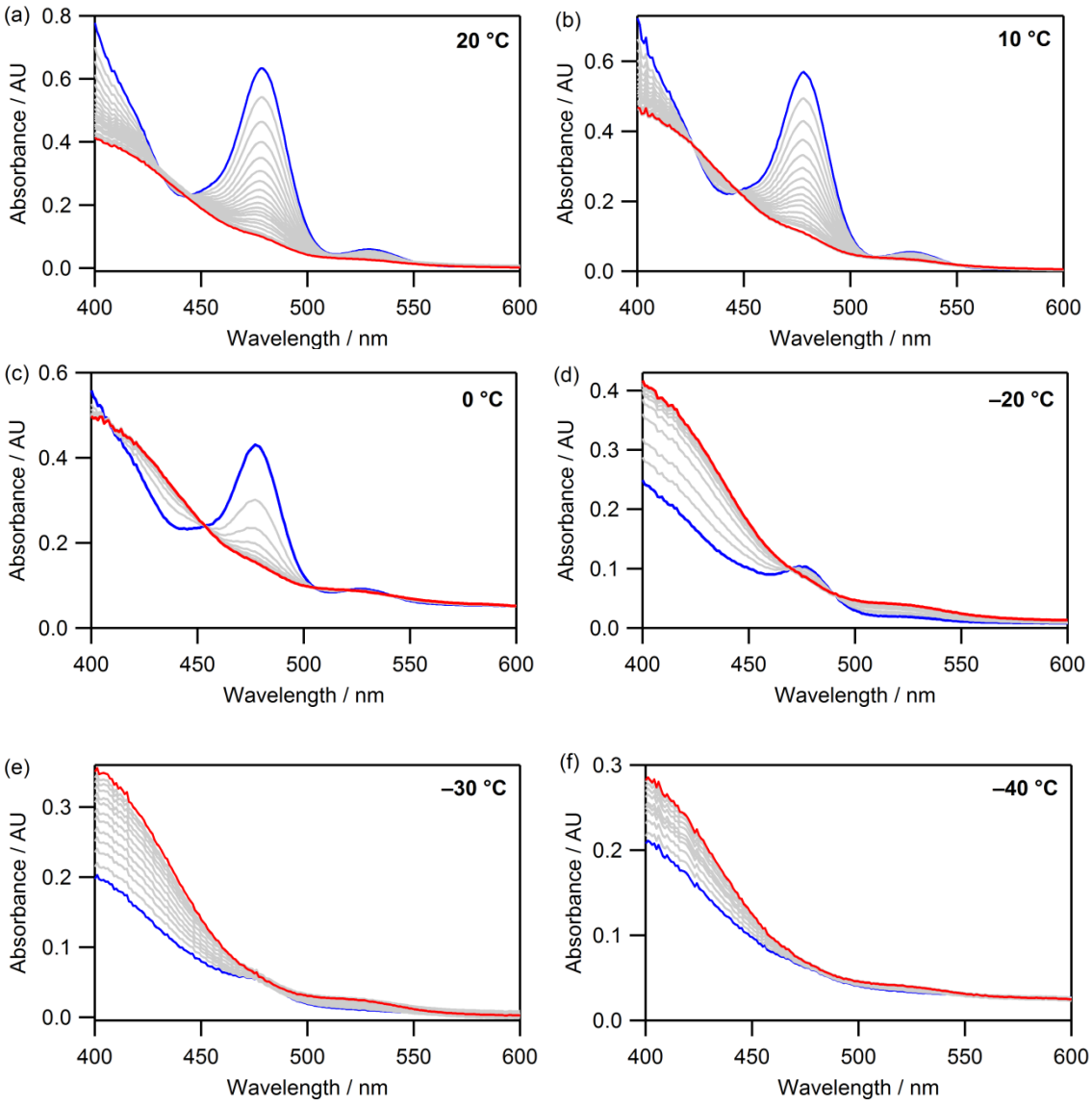

Figure 4A.3. Time-resolved spectral changes for the reaction of $Pd(IPr)_2$ (0.25 mM) with [O_2] (4.15 mM) at various temperatures: (a) 20 °C (630 s); (b) 10 °C (625 s); (c) 0 °C (600 s); (d) −20 °C (1005 s); (e) −30 °C (1200 s); (f) −40 °C (1200 s). In all cases, the initial time = 0 s traces are shown in blue and final traces in red. Selected traces are shown for clarity.

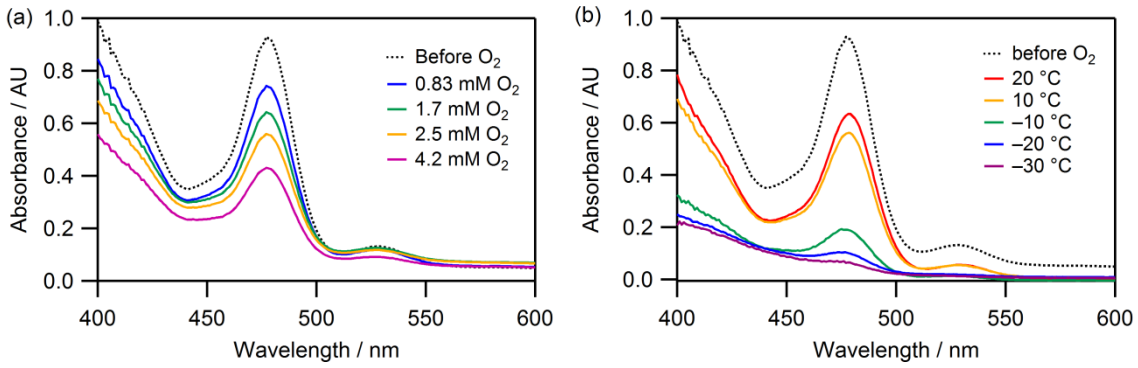

Figure 4A.4. (a) Overlay of initial time = 0 s spectra acquired for reactions of $Pd(IPr)_2$ with varying $[O_2]$ at 0 °C. (b) Overlay of initial time = 0 s spectra acquired for reactions of $Pd(IPr)_2$ with 4.15 mM O_2 at various temperatures.

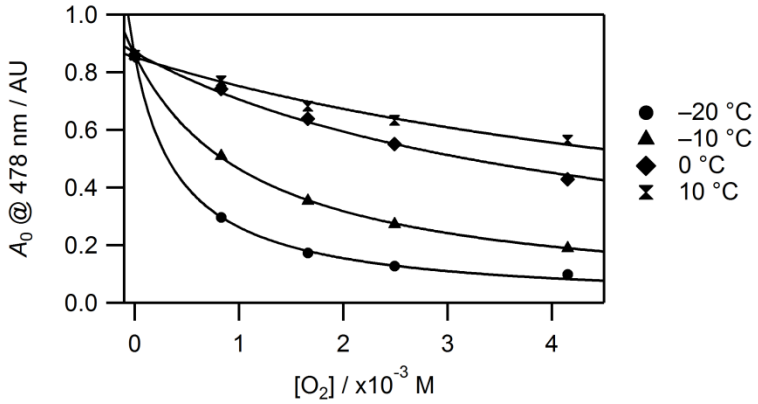

Figure 4A.5. Plots of initial absorbance (A_0 at λ = 478 nm) versus $[O_2]_0$ (markers) at various temperatures with non-linear fits to Eq. 4.3 (solid lines) from which K_{eq} values were derived.

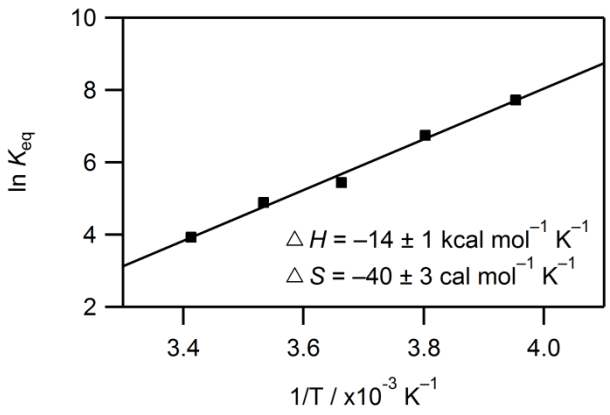

Figure 4A.6. van't Hoff plot for O_2 binding to $Pd(IPr)_2$ to form $(\eta^2\text{-}O_2)Pd(IPr)_2$ using experimentally derived values of K_{eq} (T range = −20 to 20 °C) with derived thermodynamic parameters.

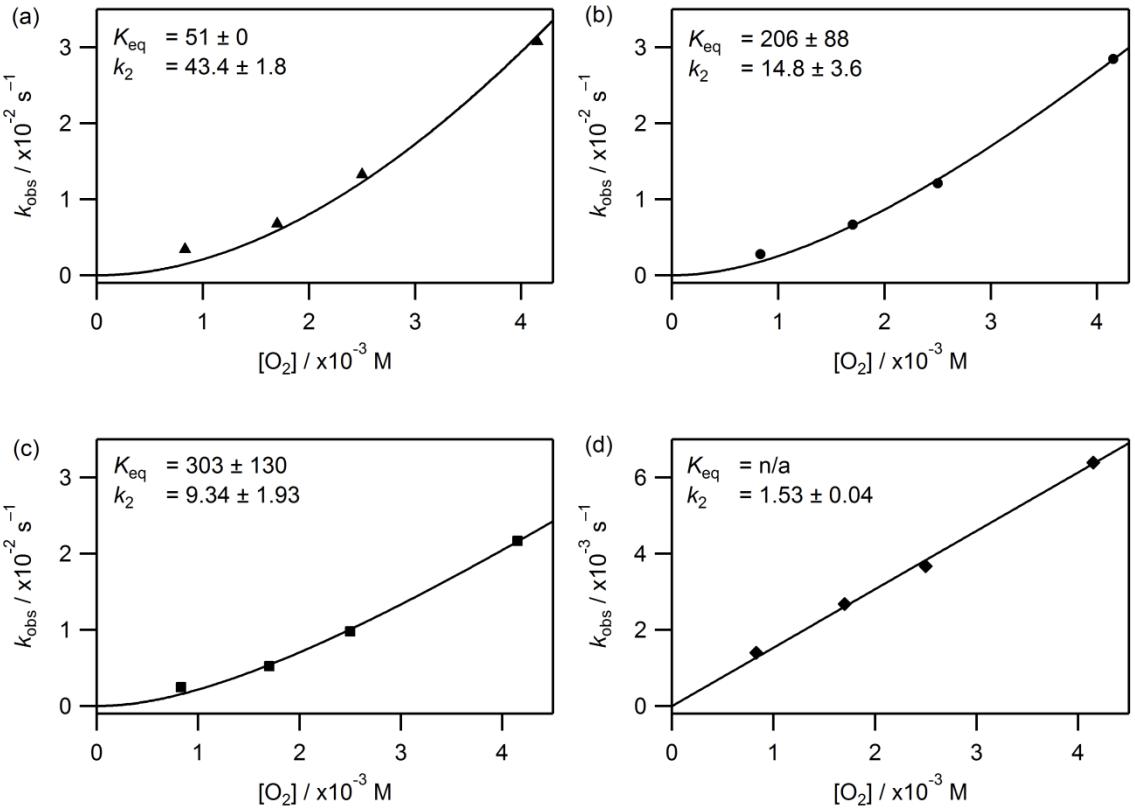

Figure 4A.7. Plots of k_{obs} versus $[O_2]$ at various temperatures (markers) with fits to Eq. 4.5 (lines). (a) 20 °C, (b) 10 °C, (c) 0 °C, (d) −20 °C.

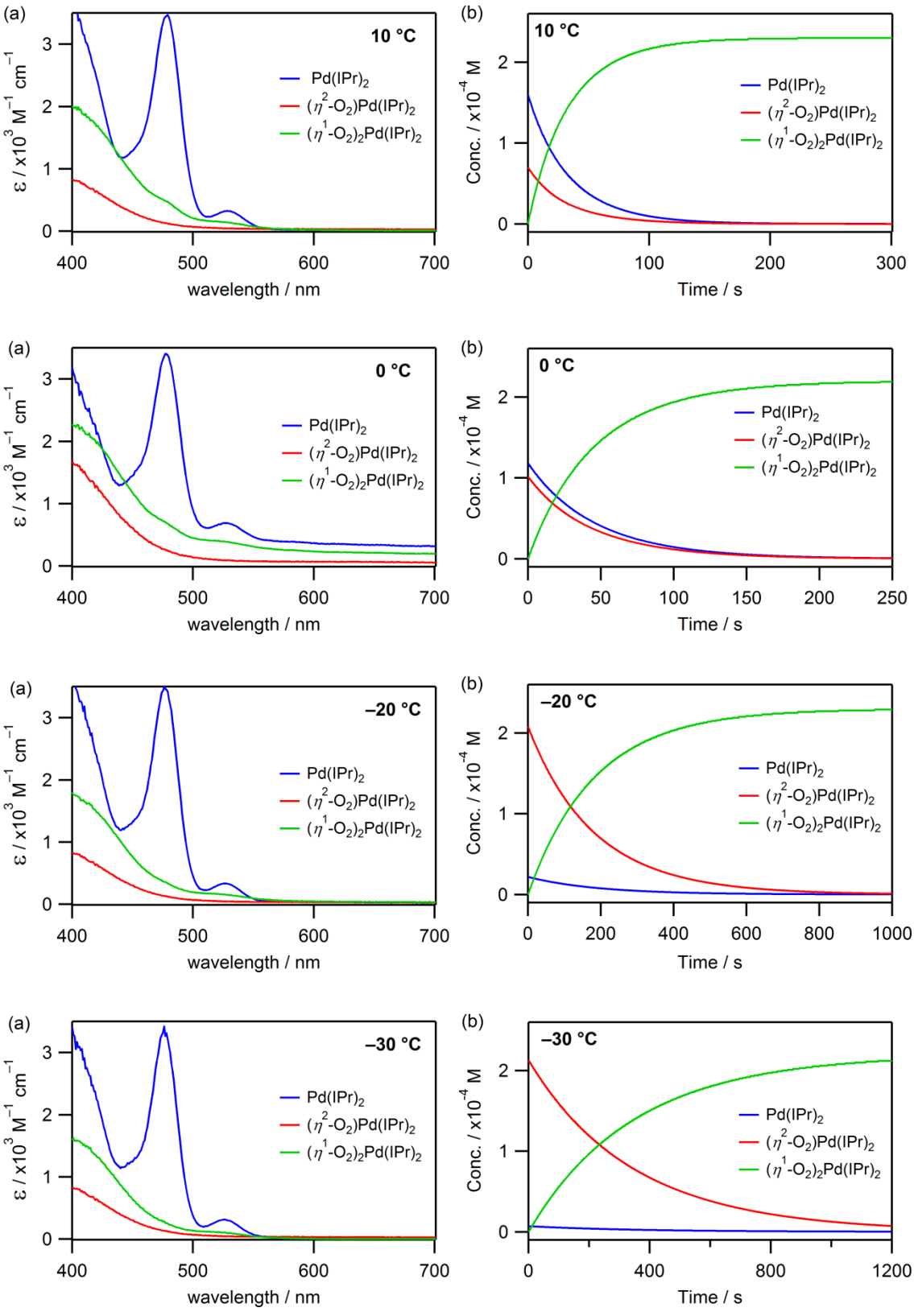
(a)
10 °C
Pd(IPr)2
(η2-O2)Pd(IPr)2
(η1-O2)2Pd(IPr)2
ε / x10^3 M^-1 cm^-1
wavelength / nm
(b)
10 °C
Conc. / x10^-4 M
Time / s
(a)
0 °C
(b)
0 °C
(a)
–20 °C
(b)
–20 °C
(a)
–30 °C
(b)
–30 °C

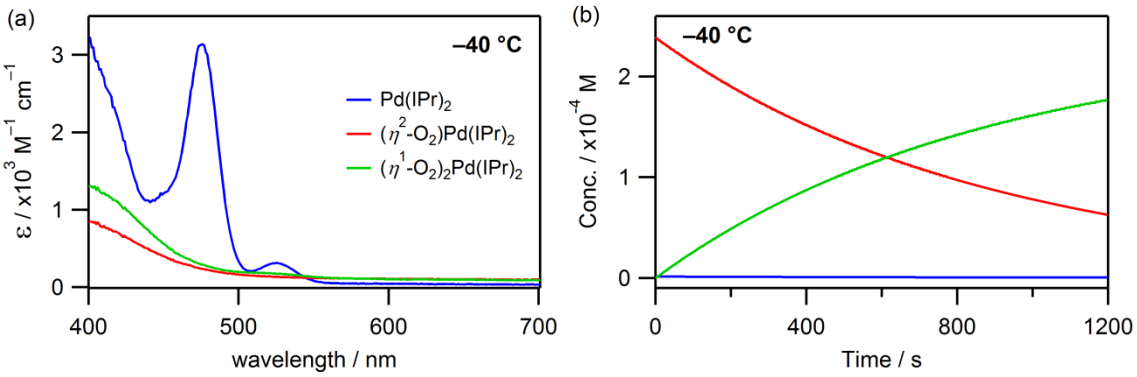

Figure 4A.8. (a) Calculated spectra of colored components obtained from the kinetic model at the remaining temperatures of 10 °C, 0 °C, −20 °C, −30 °C, and −40 °C with $[Pd(IPr)_2]_0$ = 0.22 to 0.25 mM and $[O_2]_0$ = 4.15 mM. A known spectrum for $Pd(IPr)_2$ was incorporated in all cases except for 0 °C due to difficulties with baseline shifts. A known spectrum of $(\eta^2\text{-}O_2)Pd(IPr)_2$ was incorporated in all cases. The spectrum of $(\eta^1\text{-}O_2)_2Pd(IPr)_2$ was calculated by the fitting program in all cases. (b) Concentration profiles for colored components.

Derivation of Eq. 4.5 for analysis of high temperature $[O_2]$ dependency plots:

Assumption 1: The $(\eta^2\text{-}O_2)Pd(IPr)_2$ absorbance is so weak that it does not contribute to the measurement; the total concentration of Pd containing species can be expressed as follows:

$$[Pd(I\,Pr)_2]_0 = [Pd(I\,Pr)_2] + [(\eta^2 - O_2)Pd(I\,Pr)_2] + [(\eta^1 - O_2)_2\,Pd(I\,Pr)_2] \quad (4A.1)$$

Taken in derivative form, and since $d[Pd(IPr)_2]_0 / dt = 0$, we know that:

$$\frac{d[Pd(I\,Pr)_2]_0}{dt} = 0 = \frac{d[Pd(I\,Pr)_2]}{dt} + \frac{d[(\eta^2 - O_2)Pd(I\,Pr)_2]}{dt} + \frac{d[(\eta^1 - O_2)_2\,Pd(I\,Pr)_2]}{dt} \quad (4A.2)$$

Rearranging to express in terms of product formation yields:

$$\frac{d[(\eta^1 - O_2)_2\,Pd(I\,Pr)_2]}{dt} = -\left(\frac{d[Pd(I\,Pr)_2]}{dt} + \frac{d[(\eta^2 - O_2)Pd(I\,Pr)_2]}{dt}\right) \quad (4A.3)$$

Assumption 2: The binding equilibrium is fast relative to all other observed steps; at all times we can assume the following:

$$K_{eq}[Pd(I\,\mathrm{Pr})_2][O_2] = [(\eta^2 - O_2)Pd(I\,\mathrm{Pr})_2] \quad (4A.4)$$

Incorporating Eq. 4A.4 into Eq. 4A.3 yields:

$$\frac{d[(\eta^1 - O_2)_2 Pd(I\,\mathrm{Pr})_2]}{dt} = -\frac{d[Pd(I\,\mathrm{Pr})_2]}{dt}(1 + K_{eq}[O_2]) \quad (4A.5)$$

Assumption 3: The rate law corresponds to a rapid pre-equilibrium initial binding step which is followed by a rate determining second step:

$$\frac{d[(\eta^1 - O_2)_2 Pd(I\,\mathrm{Pr})_2]}{dt} = -\frac{d[Pd(I\,\mathrm{Pr})_2]}{dt}(1 + K_{eq}[O_2]) = K_{eq}k_2[Pd(I\,\mathrm{Pr})_2][O_2]^2 \quad (4A.6)$$

Rearranging the above expression in terms of $Pd(IPr)_2$, since we are directly monitoring its decay:

$$-\frac{d[Pd(I\,\mathrm{Pr})_2]}{dt} = \frac{K_{eq}k_2[Pd(I\,\mathrm{Pr})_2][O_2]^2}{(1 + K_{eq}[O_2])} \quad (4A.7)$$

Upon integration, of Eq. 4A.7, first order decay of $Pd(IPr)_2$ is observed under pseudo-first order conditions (excess O_2), and k_{obs} for this process will simply be:

$$k_{obs} = \frac{K_{eq}k_2[Pd(I\,\mathrm{Pr})_2][O_2]^2}{1 + K_{eq}[O_2]} \quad (4A.8)$$

CHAPTER 5

H_2O_2 Activation by Biomimetic Non-Heme Ferrous Complexes Supported by Aminopyridine Macrocycles Bearing a Functionalized Pendant Arm

5.1. Introduction

Iron-containing metalloenzymes play a crucial role in biological systems where they are involved in a wide variety of notoriously challenging oxidation and oxygenation reactions, including selective mono- and dihydroxylation of unactivated hydrocarbons, alkene epoxidations, processing of nucleic acids, desaturation of fatty acids, antibiotic biosynthesis, and metabolite detoxification.[1] These remarkable systems bind and activate O_2 to generate highly reactive and transient iron-oxygen intermediates that are responsible for the efficient and selective oxidative transformations. For example, heme monooxygenases such as the cytochromes P450 (P450s) utilize one molecule of molecular oxygen, two reduction equivalents, and two protons to generate a high-valent oxoiron(IV) heme cation radical species called Compound I (Cpd I), which is the active oxidant that reacts with substrates (Figure 5.1).[2] Due to its high reactivity, Cpd I was only recently characterized by spectroscopic methods.[3]

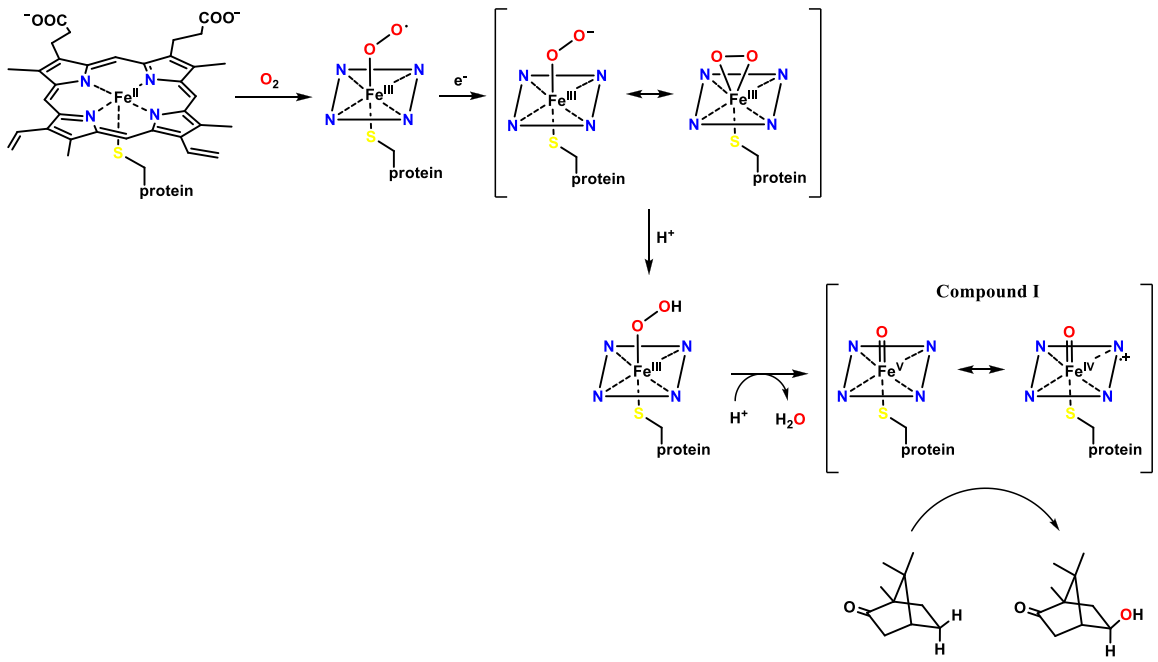

Figure 5.1. Accepted mechanism of O_2 activation by cytochrome $P450_{cam}$. Isomeric forms of the Fe(III) peroxo and high valent oxo intermediates are shown for instruction purposes; in the case of peroxo intermediates, however, all forms have been implicated from computational studies as well as experimental studies with mutant forms of the protein and model compounds. In wildtype $P450_{cam}$, spectroscopic evidence suggests that the η^1-peroxo is rapidly protonated at the distal oxygen atom to form the hydroperoxo intermediate.

High valent oxoiron(IV, V) species are often invoked as active oxidizing intermediates in the catalytic cycles of numerous non-heme iron enzymes that have been subject to extensive spectroscopic characterizations.[4] In selected cases, the (hydro)peroxoiron(III) complexes that form en route to higher valent species have also been implicated as reactive intermediates. A notable example includes the glycopeptide antibiotic bleomycin (BLM), a chemotherapeutic agent that binds iron *in vivo* and promotes oxidative DNA degradation.[5] The unique redox reactivity of iron BLM in many respects resembles oxygen and peroxide activation with heme proteins (Figure 5.2). Reaction with O_2 generates activated FeBLM, which is a low-spin ferric hydroperoxo

intermediate that is capable of abstracting hydrogen atoms from DNA bases.[6] Activated forms of FeBLM are also known to promote catalytic hydroxylations and epoxidations of small molecules,[7] which may rely on higher valent oxidizing intermediates that form from the reaction with O_2 (Figure 5.2). This notion of multiple intermediates has long been invoked in both heme and non-heme systems.[2c] For example, methane monooxygenase is thought to promote olefin epoxidation via a peroxo intermediate, while the high-valent $Fe^{IV}Fe^{IV}$ diamond core intermediate affects C−H hydroxylation.[8] It is therefore of much importance to establish the reactivity profiles of individual intermediates in model systems in the effort to design selective catalysts.[9]

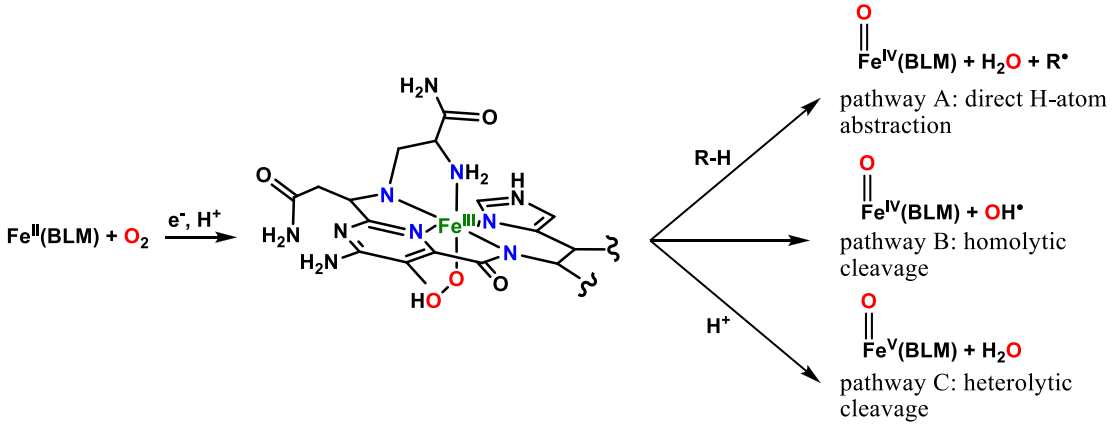

Figure 5.2. Accepted mechanism of O_2 activation by activated bleomycin. The low-spin ferric hydroperoxo intermediate (proposed structure) is thought to be responsible for H-atom abstraction from DNA sugar residues as depicted in pathway A. Image adapted from ref 6a.

Biomimetic systems are often constructed to aid in the clarification of enzymatic mechanisms[10] and to advance the current standing of catalytically active model complexes.[1] In this regard, synthetically accessible iron complexes that can activate oxygen or hydrogen peroxide are of particular interest in "green" oxidation chemistry.[11]

Non-heme iron model complexes often take advantage of a combination of amine and pyridine donors, usually provided by open-chain polydentate ligands. However, such ligands often do not fix all donor atoms in a well-defined geometry about the metal center, and as a result, the exact coordination environment in active oxidants remains unclear in many cases.[12] Macrocyclic ligands are attractive alternatives for their ability to establish well-defined coordination spheres with the added benefit of producing thermodynamically and kinetically stable metal complexes that are more likely to withstand the harsh oxidizing conditions that accompany the reactions of interest. Moreover, macrocycles can be further functionalized by covalently attaching pendant arms- a design that allows for systematic investigations of the role of axial donors in redox properties of iron complexes.[13] It is well known that O_2 binding and reactivity in heme-based systems depends strongly on the nature of the axially coordinated ligand. Detailed theoretical studies show a complex range of behavior in spin state, structure, and reaction energetics all dependent upon the nature of the specific axial donor.[14] Such factors are also relevant in non-heme systems,[15] and our biomimetic approach offers a valuable opportunity to explore such effects in more detail.

Our group has focused on the use of 14-membered pyridine azamacrocyclic ligands (PyMACs) (Figure 5.3, top row) as platforms suitable for coordination of several first row transition metal ions, including copper, nickel, and iron.[12,16,17] These simple systems, which resemble the coordination geometry of the active site of iron bleomycin, serve as rigid scaffolds that offer exquisite control over the equatorial coordination environment of the redox center, and structural modifications involving addition of a pendant arm that can serve as an additional ligand and/or an intramolecular proton source

in reactions with H_2O_2 have allowed for the comparative study of the role of axial donors on the structure and reactivity of these biomimetic systems.

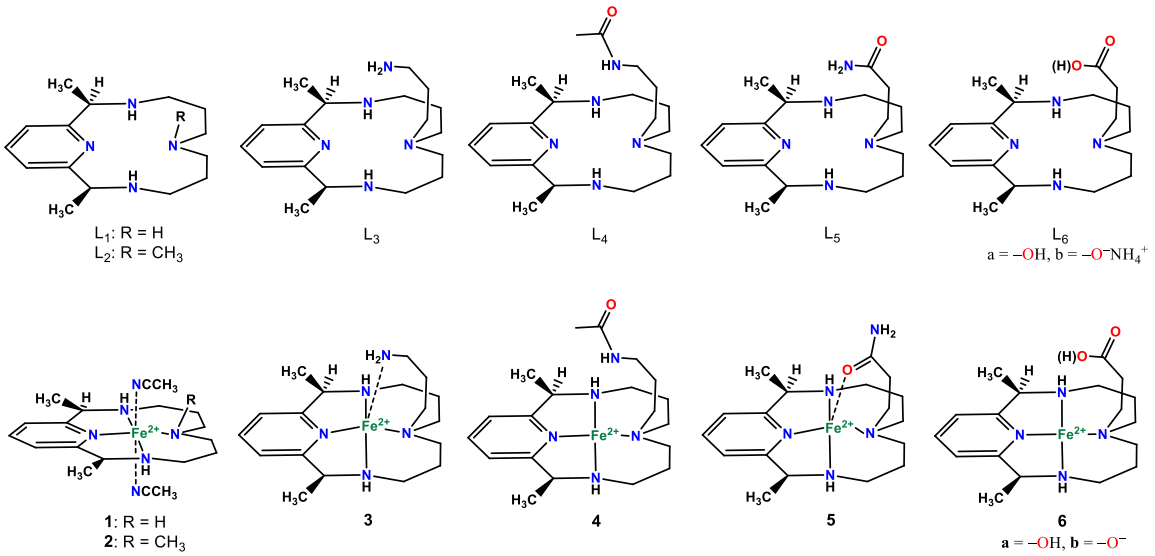

Figure 5.3. *Top row*: Structures of PyMAC ligands used in our work. *Bottom row*: Ferrous complexes supported by PyMAC ligands. Structurally characterized complexes **1** and **2** are six-coordinate with labile solvent molecules occupying the axial positions. Complexes **3**-**5** are also structurally characterized.

Ferrous complexes supported by tetradentate, unfunctionalized PyMACs L_1 and L_2 (Figure 5.3, bottom row) have been shown to be catalytically active in green alkene epoxidations with hydrogen peroxide under mild conditions.[12,17,18] Addition of an aminopropyl arm to the square-planar FeN_4 scaffold (complex **3**) revealed enhanced catalytic activity that was regulated by the acid-induced dissociation of the pendant amino group[12] as shown in Figure 5.4. In addition, coordination of the pendant amino group in **3** leads to a change in spin state at the metal center; five-coordinate **3** contains high-spin Fe(II) while complexes with tetradentate PyMACs (**1** and **2**) are octahedral and low-spin. Additional modification of the pendant amino group via acylation of L_3 leads to

further improvement in the catalytic activity of the corresponding iron complex (**4**) as well.[18] This work ultimately reveals that modifications of the pendant group (changing functional group and/or chain length) affect the structure and function of these biomimetic complexes, and is reminiscent of what is observed in heme systems.

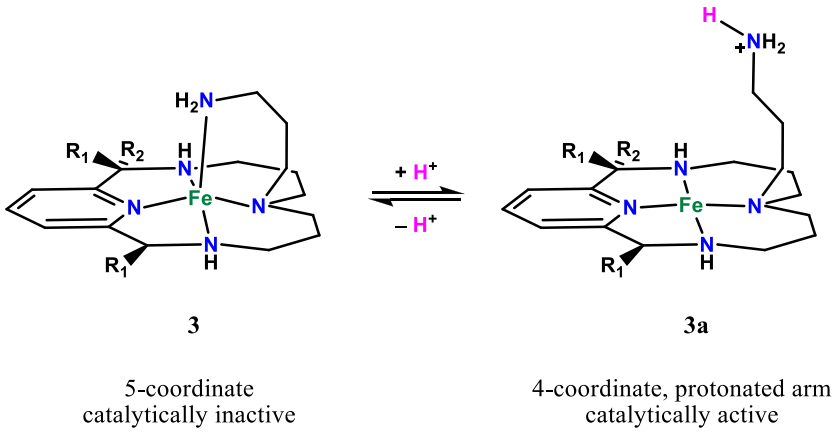

Figure 5.4. Reversible protonation of the pendant amine group regulates catalytic activity towards olefin epoxidation. $R_1 = CH_3$; $R_2 = H$. Figure adapted from ref 12.

Our interest in understanding the exact role of PyMAC ligand structure on catalytic reactivity has continued and more recent work[16c] revealed that selective mono-functionalization of intact macrocycle L_1 was possible at the N_3 position and novel PyMACs containing an amide (L_5) or carboxylic acid (L_{6a}) were successfully prepared and characterized (Figure 5.3). Interestingly, peroxidase-like activity was noted for the corresponding Ni(II) PyMAC complexes, which promoted catalytic $1e^-$ oxidation of 2,2'-azino-bis(3-ethylbenzthiazoline-6-sulphonic acid) (ABTS) with vastly different rates that depended on the identity of the functional group in the pendant arm.

We have extended this work to now include the preparation, characterization, and catalytic reactivity of novel iron(II) PyMAC complexes **5** and **6**, which is presented herein. These new systems show enhanced catalytic activity in olefin epoxidation reactions, allowing for a 10-fold decrease in catalyst loadings. Preliminary insight into the reaction mechanism and identity of catalytically competent intermediates of H_2O_2 activation and oxygen atom transfer reactions is provided and compared to that of the earlier derivatives.

5.2. Experimental Methods

General Considerations. All air-sensitive materials were manipulated in an MBraun glove box filled with ultra high purity argon (Airgas). Anhydrous acetonitrile, diethyl ether, and methanol were purchased from commercial vendors and dried on an Innovative Technologies PureSolv 400 solvent purification system. All other solvents were purchased and used without further purification. Cyclooctene and 1-decene were passed through a short column of activated alumina, degassed, and stored in the glove box prior to use. ^{1}H NMR spectra were obtained using a Bruker Avance 300 MHz or a Bruker Avance III 500 MHz spectrometer. Chemical shifts are reported in ppm (δ) and referenced against residual protio-solvent peaks or TMS. Electrospray ionization (ESI) mass spectra were acquired on a Finigan LTQ mass spectrometer in the positive ion detection mode. Gas chromatography experiments were performed on a Hewlett-Packard 5890 Series II instrument equipped with an Agilent DB-5 column (30 m length, 0.32 mm i.d., 0.25 μm film thickness) and a flame ionization detector. Infrared spectra were

recorded on a Nicolet Magna 760 FTIR instrument as KBr pellets. Elemental analyses were carried out by the University of Illinois Microanalysis Laboratory (Urbana, IL).

Electrochemical Measurements. Cyclic voltammetry experiments were performed under an argon atmosphere using a CH Instruments model 830 electrochemical analyzer. A three-electrode cell consisting of a glassy carbon working electrode (3 mm diameter) and platinum wires for the counter and pseudo-reference electrodes was used. Voltammograms for **5** (2.9 mM), **6a** (2.9 mM), and **6b** (2 mM) were acquired in dry CH_3CN using 0.1 M tetrabutylammonium hexafluorophosphate ($N(C_4H_9)_4PF_6$) as supporting electrolyte. In some experiments, small amounts of triflic acid or triethylamine were added (0-3 eq.). Ferrocene (Fc) was used as an internal standard and a 100 mV s^{-1} scan rate was used.

Measurement of Solution Effective Magnetic Moments. The spin states of complexes **5**, **6a**, and **6b** were determined using Evans method[19a] at room temperature. In the glove box, CD_3CN solutions of complex **5** or **6a** (1 mL of 3.6 mM) or **6b** (1 mL of 10 mM) were transferred to an NMR tube fitted with a septa-lined screw cap. A sealed capillary containing pure CD_3CN was also inserted into the tube and the sample was capped and removed from the glove box. ^1H NMR spectra were recorded and the shift of the CD_3CN signal in the presence of complex was compared to that of the pure CD_3CN signal. In some cases, pure triflic acid (HOTf, 1-5 eq.) was injected into the solution and the NMR reacquired. The effective magnetic moment (μ_{eff}, BM) was calculated from $\mu_{eff}^2 = 8\chi_g M_w T$,[20] where χ_g ($cm^3\ g^{-1}$) is the mass susceptibility derived from $\chi_g = 3\delta\nu/4\pi\nu_o C M_w +$

χ_o.[19b,c] $\delta\nu$ is the shift in frequency (Hz) from the value found for the pure solvent, C is the concentration of the complex (mol cm^{-3}), M_w is the molecular weight of the complex (g mol^{-1}), ν_o is the operating frequency of the NMR spectrometer (Hz), and χ_o is the mass susceptibility of the pure solvent (-0.682×10^{-6} cm^3 g^{-1} for acetonitrile). The $4\pi/3$ shape factor is for a cylindrical sample in a superconducting magnet. The number of unpaired electrons per molecule, *n*, can then be easily derived from the magnetic moment using $\mu^2 = g^2S(S + 1)$, where S is the electronic spin and *g* the Landé factor. This can be further simplified into $n(n + 2)$ for $g = 2$.[20]

Catalytic Epoxidation Reactions. Acetonitrile solutions containing **5** or **6a** (1.45 μmol or 0.145 μmol for 5 or 0.5 mole percent Fe, respectively), additives (1-5 equivalents (10-50 μL) of triflic or acetic acid solutions) and substrate (40 μL of a 0.73 M solution of cyclooctene or 100 μL of a 0.29 M solution of 1-decene) premixed with nitrobenzene (internal standard, 0.0012 mmol) were combined under an inert atmosphere (final volume without additives was maintained at 1.04 mL in all cases). Reactions were initiated with the addition of H_2O_2 (30 μL of a 1.45 M solution, added at once) and were run at ambient temperature for 5 min. Aliquots (50 μL) taken before the addition of H_2O_2 and after 5 min reaction were immediately diluted into 1 mL of diethyl ether, filtered, and analyzed by GC. All quantitative data represents an average of at least three experiments with acceptable standard deviations ($\leq$ 10 %). Epoxide yields were determined using nitrobenzene as internal standard.

Crystallographic Details. X-ray intensity data were acquired at low temperature (100 K) using a Bruker X8 Kappa DUO four-circle diffractometer equipped with a Bruker APEX2 CCD detector with Mo Kα radiation (λ = 0.71073 Å). The frames were integrated with the Bruker SAINT software package[21] using a narrow-frame integration algorithm. A semi-empirical absorption correction was applied to the diffraction data using SADABS.[22] All structures were solved by direct methods using SHELXS and refined against F^2 on all data by full-matrix least squares with SHELXL-97 or SHELXL-2014.[23] All non-hydrogen atoms were refined anisotropically and all hydrogen atoms bound to carbon were included at geometrically calculated positions and refined using a riding model.[24] The isotropic displacement parameters of all hydrogen atoms were fixed to 1.2 times the U_{eq} value of the atoms they are linked to (1.5 times U_{eq} for methyl groups). Additional crystallographic and refinement parameters are provided in Table 5.1. The author acknowledges Drs. Peter Mueller and Mike Takase (MIT, Cambridge, MA) for their help with acquisition of crystallographic data and structure refinement.

Complex **5** crystallized in the triclinic *P*−1 space group with one molecule (Fe^{2+} complexed to neutral L_5 plus two triflate anions) in the asymmetric unit. The entire ligand was found to be disordered over two positions (65:35). Hydrogen positions on all nitrogen atoms of the macrocycle were observed in the difference Fourier map, however, because of the disorder of the N atoms, refinement with only distance restraints was unstable and thus the hydrogens were added using a riding model. In addition, one of the two triflate counterions was modeled as a two component positional disorder (58:42).

[$FeLCO_2CH_3(Cl)$](OTf) crystallized in the triclinic *P*−1 space group with one molecule in the asymmetric unit. Several independent two component positional

disorders were modeled, including three carbon atoms of the macrocyclic ring (75:25), the $-C_3O_2$ moiety of the pendant arm (63:37), and the triflate counterion (74:26). Additional crystallographic and refinement parameters are provided in Table 5.1 and Appendix 5.

Stopped-Flow Kinetics. Acetonitrile solutions of **6a**, **2**, H_2O_2 (30 wt. % in H_2O), isopropyl 2-iodoxybenzoate (^{i}Pr-IBX), cyclooctene, and acetic acid (AcOH, glacial) were prepared in an MBraun glove box filled with ultra high purity argon (Airgas) and loaded in Hamilton gastight syringes. Time-resolved UV-visible spectra were acquired over a range of temperatures (–40 to 10 °C) using a Hi-Tech Scientific SF-61DX2 Multi-mixing CryoStopped-Flow system (TgK Scientific Ltd.) equipped with a tungsten halogen light source and a J&M TIDAS diode array detector. The instrument was equipped with stainless steel plumbing lined with PEEK tubing and a 1.00 cm^3 quartz mixing cell submerged in an ethanol cooling bath. The temperature in the mixing cell was maintained to ± 0.1 °C using a CAL 3200 automatic temperature controller. Data acquisition was performed using TIDAS-DAQ and Kinetic Studio software programs and mixing times were 2-3 ms. All flow lines were washed extensively with argon-saturated anhydrous acetonitrile prior to charging the drive syringes with reactant solutions. Experiments were typically performed in a single-mixing mode of the instrument with a 1:1 (v/v) mixing ratio. The reactivity of oxoiron(IV) intermediate **6a**−O was also assessed in double-mixing mode, where **6a** and ^{i}Pr-IBX (0.5 eq.) were mixed and aged until maximum accumulation of **6a**−O was reached followed by addition of substrate (cyclooctene) in the second mixing phase. Data analysis was performed using Kinetic Studio (TgK Scientific)

and IGOR Pro 5.0 (Wavemetrics, Inc.) software programs. All concentrations are reported after mixing in the stopped-flow cell.

Mössbauer Spectroscopy. Zero-field Mössbauer spectra were collected at 90 K on samples immobilized in Paratone-N with a constant acceleration spectrometer (SEE Co., Minneapolis, MN).Solid samples of **6a** and frozen CH_3CN solutions of reaction samples (**6a** + ^{i}Pr-IBX) were studied as described below. All samples were prepared in a glove box under N_2 atmosphere. A number of separate samples of the starting complex, intermediate, and decomposition products were prepared and measured to confirm reproducibility. In general, 100 mg of solid material was used per run (without ^{57}Fe enrichment). For studying reaction intermediates, 100 mg of solid **6a** was combined with 1 eq. of solid isopropyl 2-iodoxybenzoate (^{i}Pr-IBX, 47 mg) in a pre-cooled nylon sample holder at −35 °C. The solids were dissolved in minimal CH_3CN (also pre-cooled to −35 °C), aged for approximately 40 s, and quickly frozen in liquid nitrogen. Isomer shifts are given relative to α–Fe metal at 298 K. Data was analyzed using an in-house package written by E. R. King in Igor Pro (Wavemetrics). γ refers to the full-width-at-half-maximum. The author acknowledges Dr. Ted Betley and Raul Hernandez Sanchez (Harvard University, Cambridge, MA) for their assistance with acquisition of all Mössbauer spectra. Additional Mössbauer spectra of oxidation products of **6a** are provided in Appendix 5.

Synthetic Procedures. $Fe(OTf)_2{\cdot}2CH_3CN$ (OTf = $CF_3SO_3^-$) was prepared from $FeCl_2$ and $CF_3SO_3SiMe_3$ in CH_3CN following an unpublished procedure provided by Dr.

Miquel Costas and Prof. Lawrence Que, Jr. Isopropyl 2-iodoxybenzoate (^{i}Pr-IBX) was prepared according to the published procedure.[25] Free ligands L_1-L_5[16,17,26] and ferrous complexes of L_1-L_4[12,17,18] were prepared as described elsewhere. The synthesis of L_{6a} has been reported previously[16c] but has been described here in more detail below. ESI-MS, NMR, and IR spectra for ligands L_{6a} and L_{6b} and complexes **5**, **6a**, and **6b** are provided in Appendix 5.

Synthesis of L_{6a}. To a stirring solution of L_1 (502 mg, 1.91 mmol) in 15 mL H_2O was added dropwise ethyl acrylate (181 mg, 1.81 mmol) diluted in several milliliters of H_2O. The reaction was refluxed with stirring for 24 hours under N_2. Excess NH_4OH (2 mL) was added and unreacted L_1 was extracted with several portions of either $CHCl_3$ or CH_2Cl_2. The aqueous layer was evaporated to dryness, yielding a pale yellow oil that solidified within several days and was used as is (379 mg, 59 %). ESI-MS (+): *m/z* = 669.09 ($\{(L_{6a})_2 + H^+\}^+$, 48 %); 357.36 ($\{L_{6a} + Na^+\}^+$, 21 %); 335.36 ($\{L_{6a} + H^+\}^+$, 100 %). IR (KBr): 3417 (s, br), 3029 (m), 2971 (m), 2792 (m), 2416 (w, br), 1592 (s), 1573 (s), 1460 (s), 1383 (s), 1084 (m). A representative ^{1}H NMR is shown in Figure 5A.1.

Synthesis of L_{6b}. Ligand L_{6b} was prepared as described for L_{6a} except that after evaporation of the aqueous layer, the oily product was treated with a small amount of absolute ethanol. The resulting fine white precipitate was isolated on a fritted filter in approximately 30 % yield and was washed with a small amount of diethyl ether. The ^{1}H NMR spectrum (500 MHz, D_2O) is shown in Figure 5A.4. The ESI-MS spectrum of L_{6b} is identical to that of L_{6a}. ESI-MS (+): *m/z* = 669.00 ($\{(L_{6a})_2 + H^+\}^+$, 4 %}; 357.27 ($\{L_{6a}$ +

$Na^+\}^+$, 9 %); 335.27 ($\{L_{6a} + H^+\}^+$, 100 %). IR (KBr): 3476 (s), 3421 (s), 3010 (m), 2982 (m), 2835 (m), 2788 (m), 2353 (m, br), 1600 (m), 1554 (s), 1461 (s), 1407 (s), 1305 (s), 1274 (m), 1084 (m).

Synthesis of $[FeL_5](OTf)_2$ (5). To a stirring solution of L_5 (100 mg, 0.3 mmol) in ethanol (≈ 3 mL) was added dropwise $Fe(OTf)_2 \cdot 2CH_3CN$ (131 mg, 0.3 mmol) in acetonitrile (≈ 3 mL). The reaction mixture immediately turned green and gradually changed to brownish-yellow over the course of addition. After stirring overnight at room temperature, the solution was filtered and added dropwise to a large volume (≈ 100 mL) of diethyl ether. The following day the product was isolated as a light brown powder (170 mg, 82 %). Crystals of **5** suitable for diffraction analysis were grown in several days at room temperature from a dilute CH_2Cl_2 solution layered with diethyl ether in an NMR tube. ESI-MS (+): *m/z* = 538.09 ($\{FeL_5(OTf)\}^+$, 80 %); 194.55 ($\{FeL_5\}^{2+}$, 100 %). Anal. Calcd. for $C_{20}H_{31}F_6FeN_5O_7S_2$: C 34.94 %, H 4.55 %, N 10.19 %, Fe 8.12 %; found: C 34.17 %, H 4.4 %, N 9.68 %, Fe 7.76 %. IR (KBr): 3429 (br), 3254, 3216, 2924 (w), 1666, 1581 (m), 1254, 1165, 1029, 641 (s). μ_{eff} = 5.6 BM (Evans method).

Synthesis of $[FeL_{6a}](OTf)_2$ (6a). To a stirring solution of L_{6a} (94 mg, 0.281 mmol) in ethanol (≈ 11 ml) was added dropwise a solution of $Fe(OTf)_2 \cdot 2CH_3CN$ (123 mg, 0.281 mmol) in CH_3CN (≈ 3 ml). The reaction mixture immediately became bright yellow and was allowed to stir overnight at room temperature. The solvent was then removed under vacuum to afford the product as a yellowish powder (0.157 g, 81 %). Alternatively, the solution can be concentrated and added to a large volume of diethyl ether, which affords

the product as a white powder. Either method yields the same ESI-MS and IR. ESI-MS (+): *m/z* = 539.00 ({$FeL_{6a}(OTf)$}$^+$, 2 %); 389.27 ({FeL_{6a}− H}$^+$, 100 %). IR (KBr): 3441 (br), 2974-2866 (w), 1608 (m), 1432 (m), 1281 (vs), 1254 (vs), 1164 (m), 1028 (s), 640 (s). Anal. Calcd. for $C_{20}H_{30}F_6FeN_4O_8S_2$: C 34.89 %, H 4.39 %, N 8.14 %; found: C 34.25 %, H 4.06 %, N 7.74 %. μ_{eff} = 4.3 BM (Evans method).

Synthesis of [FeL_{6b}](OTf) (6b). L_{6b} (93 mg, 0.28 mmol) was slurried in 10 mL EtOH (CH_3CN also works). Upon dropwise addition of $Fe(OTf)_2 \cdot 2CH_3CN$ (122 mg, 0.28 mmol in ≈ 5 mL CH_3CN), the solution cleared up and turned bright yellow. After stirring overnight at room temperature, the solvent was fully evaporated to afford the product as an off-white powder (155 mg, 78-81 %). The ESI-MS and IR spectra of **6b** are essentially identical to that of **6a**. ESI-MS (+): *m/z* = 538.91 ({$FeL_{6a}(OTf)$}$^+$, 3 %); 425.09 ({$FeL_{6a}(Cl)$}$^+$, 29 %); 389.27 ({FeL_{6a}− H]}$^+$, 100 %). IR (KBr): 3447 (s, br), 3045-2870 (w), 1609 (m), 1445 (m), 1279 (vs), 1250 (vs), 1169 (s), 1030 (vs), 640 (s). μ_{eff} = 5.2 BM (Evans method).

5.3. Results and Discussion

5.3.1. Ligand Synthesis

Functionalized PyMAC ligands L_5 and L_{6a} can be prepared in good yield in several steps starting from the Ni(II)-templated Schiff base condensation of 2,6-diacetylpyridine with 3,3'-diaminodipropylamine. Reduction of the metallated Schiff base with $NaBH_4$ proceeds smoothly, and fractional crystallization affords the red *meso*-

diastereomer in 50 % yield. The free tetradentate PyMAC L_1 is then easily obtained upon treatment with excess NaCN as outlined in Figure 5.5. For L_2 and L_3, *N*,*N*-bis(3-aminopropyl)methylamine and tris(3-aminopropyl)amine can be used in place of 3,3'-diaminodipropylamine, respectively.

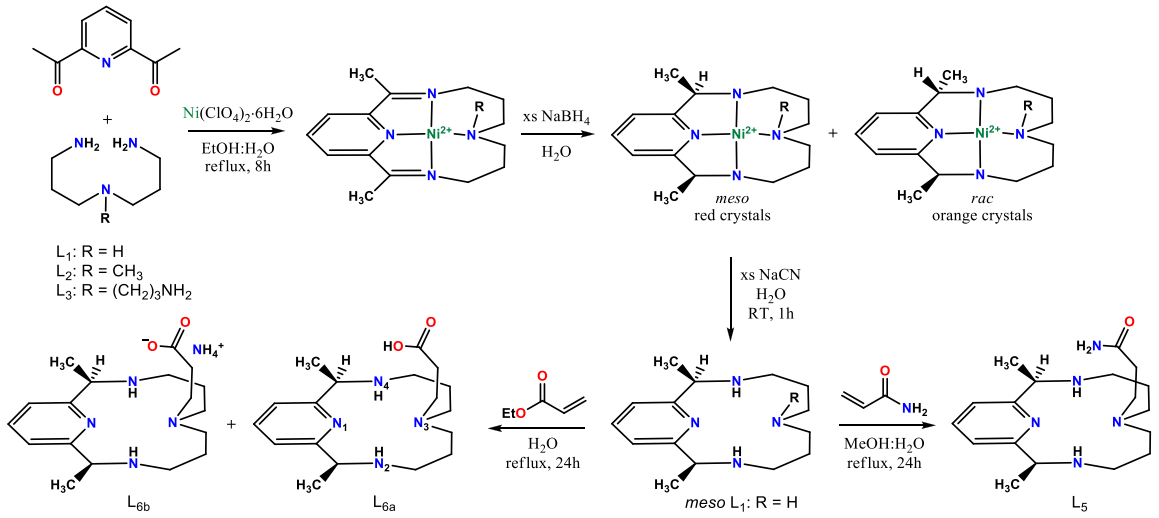

Figure 5.5. Synthetic route to functionalized PyMAC ligands.

L_1 serves as a suitable Michael donor for regioselective functionalization at N_3 using acrylamide or acrylic acid as Michael acceptors (ethyl acrylate also works in place of acrylic acid as shown in Figure 5.5). The regioselective alkylation at N_3, as opposed to alkylation at nitrogen atoms closer to the pyridine ring (denoted N_2 and N_4 in Figure 5.5), is likely due to steric hindrance provided by the methyl groups adjacent to pyridine, which renders N_2 and N_4 less accessible for nucleophilic attack.[16c]

The reaction of L_1 with acrylamide in CH_3OH:H_2O (1:1) solution yields monoalkylated L_5 as the major product, along with a small amount of dialkylated product as judged from electrospray ionization mass spectra (ESI-MS) of the reaction solutions.

The desired monoalkylated product can be isolated via fractional crystallization of the $Ni(ClO_4)_2$ complex as described previously.[16c]

The reaction of L_1 with ethyl acrylate in H_2O also leads to formation of the desired monoalkylated product L_{6a}, which can be isolated after extraction of unreacted L_1 from basified (NH_4OH) reaction solutions with $CHCl_3$. This simple work up allows for unreacted L_1 to be recovered and reused as well. After evaporation of the aqueous layer, the product L_{6a} is obtained in reasonable purity as a pale yellow oil that solidifies within days and can be manipulated as a powder. In most cases, this product was used as is for metallation with Fe(II). However, upon following the previously published purification procedure for L_{6a}, which called for dissolution of the ligand in minimal ethanol and precipitation via addition of diethyl ether, a solid could not be obtained. Instead, addition of minimal ethanol led directly to precipitation of a fine white powder (herein referred to as L_{6b}) that was collected and analyzed. The overlaid ^1H NMR spectra of L_{6a}, L_{6b}, and the leftover oily material after isolation of L_{6b} is shown in Figure 5.6.

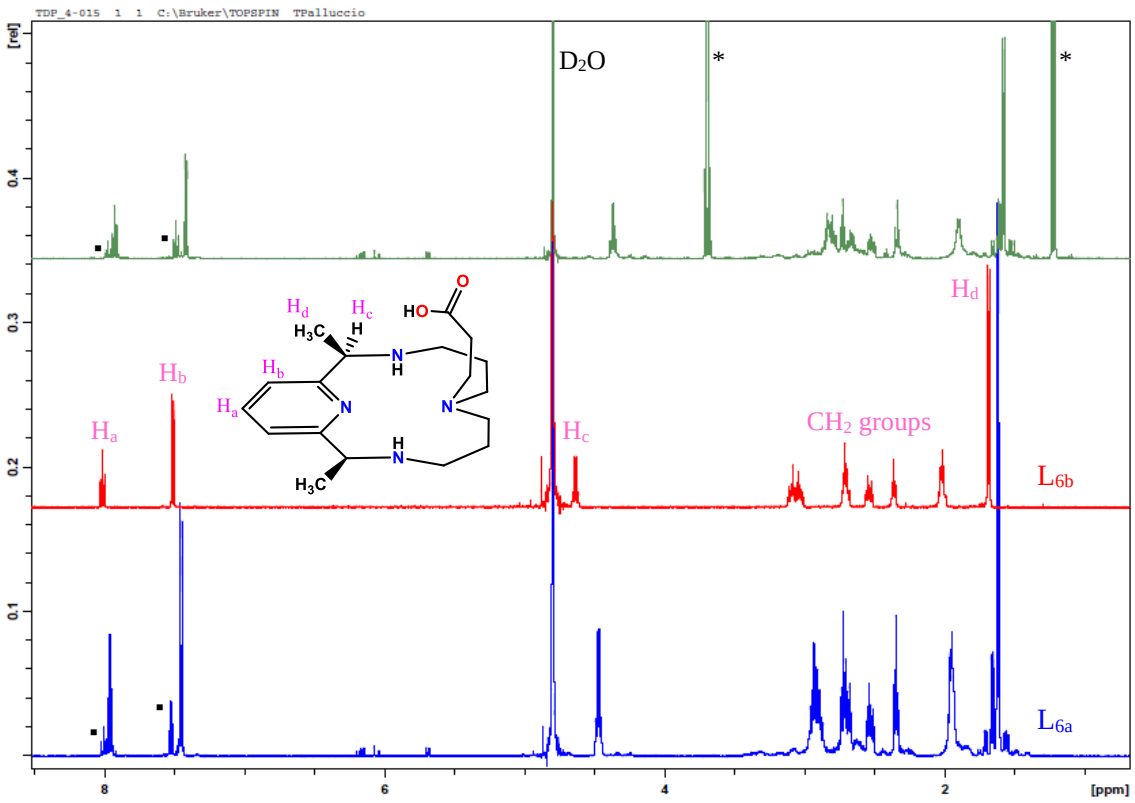

Figure 5.6. Overlay of 500 MHz ^{1}H NMR spectra of L_{6a} and L_{6b} in D_2O. The blue spectrum represents the initial L_{6a} product; the red spectrum is of the isolated white ppt L_{6b} from treatment of L_{6a} with minimal EtOH; the green spectrum represents the leftover oily-ish semisolid from EtOH filtrate (asterisks denote peaks from ethanol and squares denote peaks from *rac*-diastereomers of L_6). Individual spectra with integrated signals are provided in Appendix 5.

The ^{1}H NMR spectrum of L_{6a} is in line with the expected product as described previously.[16c] The ^{1}H NMR spectrum of L_{6b} simply looks like ultra pure L_{6a}, though subtle shifts of signals were noted; the spectrum is, however, consistent with expected symmetrical structure of the *meso*-monoalkylated macrocycle. The leftover material still contains desired product, along with minor amounts of dialkylated ligand. In all cases, ESI-MS yield identical +1 ions that correspond to the desired product (*m/z* = 335.36 for $\{L_{6a} + H^+\}$ and 669.27 for $\{[L_{6a}]_2 + H^+\}$); the deprotonated −1 ion (expected *m/z* = 333.23 for $\{L_{6a} - H^+\}$) was never detected. We suspect that L_{6a} and L_{6b} differ only in

protonation state, and to test this hypothesis, ^{13}C NMR spectra were acquired for L_{6b} in the absence and presence of varying amounts of $HClO_4$ as shown in Figure 5.7. Addition of acid led to a noticeable upfield shift of the signal corresponding to the carbonyl carbon atom (from δ = 181.39 ppm in the absence of additional acid to δ = 173.65 ppm with 3 eq. of $HClO_4$ added), which is consistent with protonation of the carboxylate anion.[27]

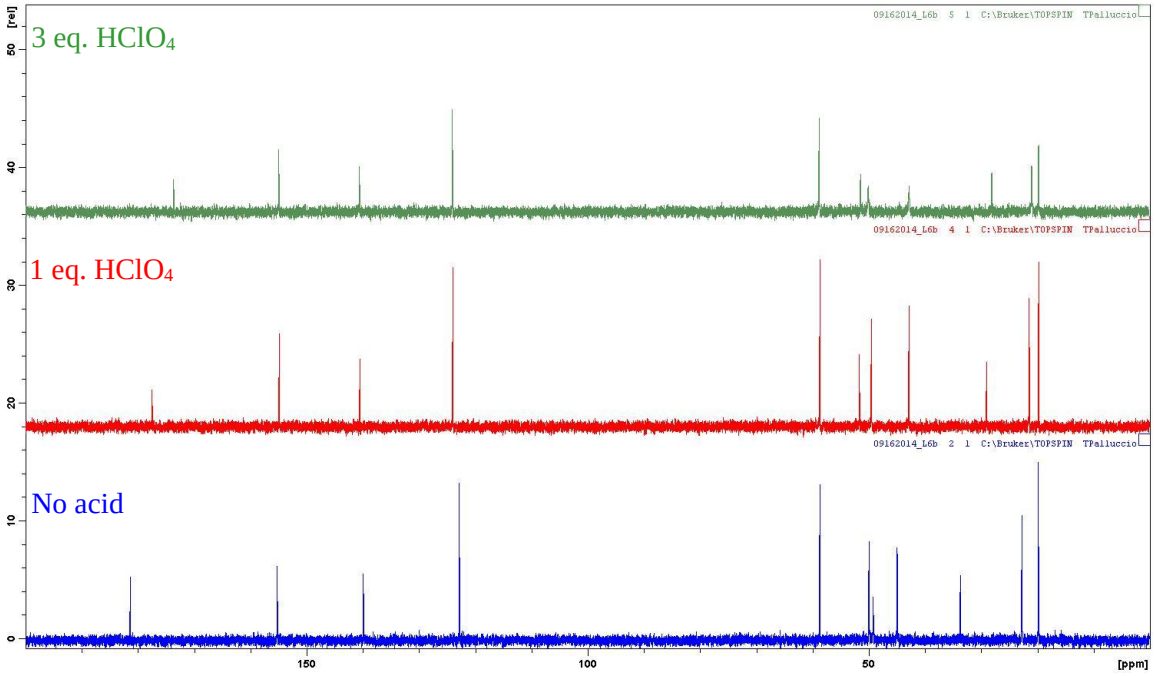

Figure 5.7. Overlay of 500 MHz ^{13}C NMR spectra of L_{6b} in D_2O in the absence (blue spectrum) and presence (red and green spectra) of varying amounts of $HClO_4$.

Additional evidence is provided in the FT-IR spectra for L_{6a} and L_{6b} (Figure 5.8). Although their spectra are quite comparable, some unique features support our assignment. L_{6a} clearly displays peaks attributable to O−H (broad stretch 3417 cm^{-1}) that is absent in L_{6b}. The C=O asymmetric stretching bands for both L_{6a} and L_{6b} are observed at relatively low energies (near 1600 cm^{-1}), which is consistent with the presence of

carboxylate salt. L_{6b} exhibits peaks that are in general much sharper, with more pronounced asymmetric and symmetric CO_2^- stretching bands at 1553 cm^{-1} and 1407 cm^{-1}, respectively. The relative differences in the C=O signal intensities ca. 1600 cm^{-1} may also reflect the relative differences in amount of carboxylic acid versus carboxylate in the samples. Also, the broad feature noted near 2350 cm^{-1} is consistent with the NH_4^+ ion which is more pronounced for L_{6b} as compared with L_{6a}. The complete absence of carboxylic acid in L_{6b}, however, cannot be ruled out from this data alone and it is likely that samples L_{6a} and L_{6b} differ only in the relative amounts of protonated *vs*. deprotonated ligand. This is supported by Mössbauer analysis of complexes **6a** and **6b** as discussed later.

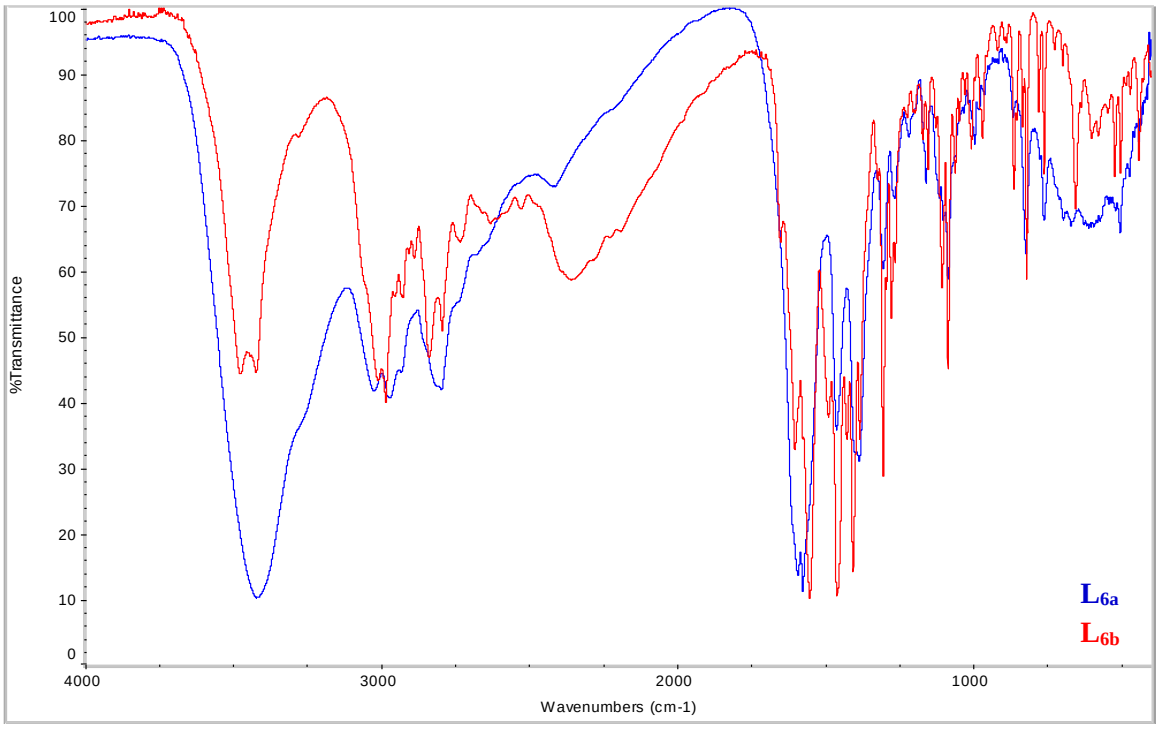

Figure 5.8. Overlay of FT-IR spectra for L_{6a} (blue) and L_{6b} (red). Individual spectra with peak assignments are provided in Appendix 5.

5.3.2. Synthesis and Structures of Complexes 5 and 6

The ferrous complexes are easily prepared in good yields as evidenced by the immediate color changes noted upon mixing equimolar amounts of $Fe(OTf)_2 \cdot 2CH_3CN$ and ligand in acetonitrile or acetonitrile/alcohol solutions at room temperature. ESI-MS and IR spectra are provided in Appendix 5. Complex **5** was structurally characterized as shown in Figure 5.9. The asymmetric unit contains the mononuclear FeL_5 unit and two triflate counterions. Like **3**, complex **5** is five-coordinate with a high-spin iron(II) center in a distorted square-pyramidal geometry (avg. Fe−N bond length of 2.143(9) Å, avg. N−Fe−N and N−Fe−O angles of 97.1(5)° and 107.0(4)°, respectively). In this case, the pendant carbonyl oxygen atom serves as the axial donor with a rather short bond length of 1.941(6) Å. Whole molecule disorder of the PyMAC ligand was observed, and despite the fact that all hydrogens bound to nitrogen atoms were directly detected, refinement with only distance restraints on N−H bonds was unstable and thus the hydrogens were added using a riding model. The presence of two triflate counterions also rules out the existence of a deprotonated pendant amide nitrogen atom. The metal center is displaced from the macrocyclic plane by 0.718(8) Å, which compares with 0.641(3) Å observed in the structure of **3**.[12] The displacement of iron towards the coordinated pendant group prevents coordination of a sixth ligand in the *trans* position. Crystallographic and refinement details are provided in Table 5.1.

Table 5.1. Structural and refinement parameters for $[FeLCONH_2](OTf)_2$ (**5**) and $[FeLCO_2CH_3(Cl)](OTf)$.

	$[FeLCONH_2](OTf)_2$ (5)	**$[FeLCO_2CH_3(Cl)](OTf)$**
Identification code (MIT)	X11062	X11185
Empirical formula	$C_{20}H_{31}F_6FeN_5O_7S_2$	$C_{20}H_{32}ClF_3FeN_4O_5S$
Formula weight	687.47	588.85
Temperature (K)	100(2)	100(2)
Wavelength (Å)	0.71073	0.71073
Crystal system	Triclinic	Triclinic
Space group	*P*−1	*P*−1
Unit cell dimensions		
a (Å)	8.7658(7)	8.9293(7)
b (Å)	9.8522(7)	9.1265(7)
c (Å)	17.1350(13)	17.5957(14)
α (°)	95.601(2)	103.7160(10)
β (°)	101.296(2)	92.220(2)
γ (°)	97.369(2)	113.4030(10)
Volume ($Å^3$)	1427.66(19)	1264.15(17)
Z	2	2
ρ_{calc} (Mg m^{-3})	1.599	1.547
Absorption coefficient (mm^{-1})	0.762	0.846
F(000)	708	612
Crystal size (mm^3)	0.35 × 0.25 × 0.25	0.40 × 0.10 ×0.07
Theta range for data collection	1.22 to 30.32 °	1.205 to 30.031 °
Index ranges	$-12 \le h \le 12$ $-13 \le k \le 13$ $-23 \le l \le 24$	$-12 \le h \le 12$ $-12 \le k \le 12$ $-24 \le l \le 24$
Reflections collected	61819	56213
Independent reflections	8550 [R(int) = 0.0237]	7392 [R(int) = 0.0283]
Completeness to theta max	99.9 %	99.9 % (theta = 25.242 °)
Absorption correction	Semi-empirical from equivalents	Semi-empirical from equivalents
Refinement method	Full-matrix least-squares on F^2	Full-matrix least-squares on F^2
Data / restraints / parameters	8550 / 1373 / 664	7392 / 1101 / 459
Goodness-of-fit on F^2	1.050	1.045
Final R indices [I>2sigma(I)]	R_1 = 0.0369, wR_2 = 0.0976	R_1 = 0.0410, wR_2 = 0.1086
R indices (all data)	R_1 = 0.0406, wR_2 = 0.1002	R_1 = 0.0455, wR_2 = 0.1121
Largest diff. peak and hole (e $Å^{-3}$)	0.597 and −0.674	1.414 and −0.425

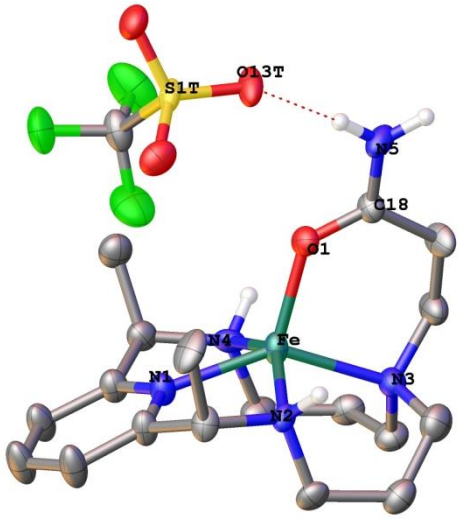

Figure 5.9. Thermal ellipsoid plot of **5** shown at the 50 % probability level. Hydrogen atoms bonded to carbon, disordered ligand atoms, and disordered counterions have been omitted for clarity. Only one triflate ion is shown to highlight hydrogen bonding pattern. Selected bond distances (Å) and angles (°): Fe−N1 = 2.063(4), Fe−N2 = 2.1925(17), Fe−N3 = 2.144(6), Fe−N4 = 2.172(6), Fe−O1 = 1.990(4), C18−N5 = 1.330(7), C18−O1 = 1.258(6), N1−Fe−N2 = 76.99(12), N1−Fe−N3 =143.4(3), N2−Fe−N3 = 91.92(16), N3−Fe−N4 = 95.3(2), N4−Fe−N1 = 77.9(2), N1−Fe−O1 = 120.3(3), N2−Fe−O1 = 102.27(15), N3−Fe−O1 = 96.0(2), N4−Fe−O1 = 109.4(2).

Attempts to isolate crystals of pure **6** (from reactions of Fe(II) salts with either L_{6a} or L_{6b}) have been unsuccessful thus far, although crystals suitable for diffraction studies were obtained after several months from a sample (prepared using L_{6a} and $Fe(OTf)_2 \cdot 2CH_3CN$) via vapor diffusion of diethyl ether into an acetonitrile/methanol solution of the complex. The structural data (Figure 5.10) revealed unexpected coordination of a chloride ion. Furthermore, the carboxylic acid pendant arm was found to convert to the methyl ester and the PyMAC ligand is the chiral stereoisomer of the macrocycle (a small amount of the *rac*-diastereomer is always present in samples but does not affect the chemistry).[12] The fact that it took a while for the sample to crystallize was a hint that minor impurities in the mixture actually helped crystallization over time.

($Fe(OTf)_2$ is made from $FeCl_2$, so chloride impurities are not surprising). Additionally, prolonged periods in methanol clearly lead to esterification of the pendant arm.

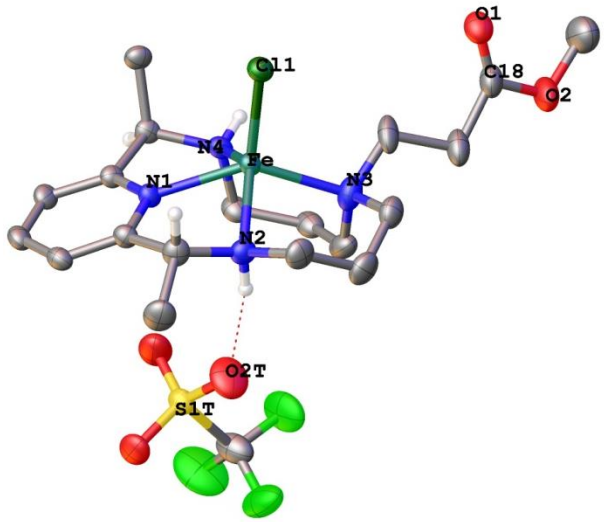

Figure 5.10. Thermal ellipsoid plot of $[FeLCO_2CH_3(Cl)](OTf)$ shown at the 50 % probability level. Selected hydrogen atoms, disordered ligand atoms, and disordered triflate ion have been omitted for clarity. Selected bond distances (Å) and angles (°): Fe−N1 = 2.1062(15), Fe−N2 = 2.1935(16), Fe−N3 = 2.1677(18), Fe−N4 = 2.2043(15), Fe−Cl1 = 2.2756(5), C18−O1 = 1.18(3), C18−O2 = 1.357(18), N1−Fe−N2 = 74.23(6), N1−Fe−N3 = 141.60(7), N2−Fe−N3 = 90.60(7), N3−Fe−N4 = 91.26(6), N4−Fe−N1 = 75.05(6), N1−Fe−Cl1 = 111.15(4), N2−Fe−Cl1 = 110.12(5), N3−Fe−Cl1 = 107.17(6), N4−Fe−Cl1 = 114.92(4).

The nickel(II) complex of L_{6a} reported previously by us[16c] forms a four-coordinate square planar structure with the pendant carboxylic acid located far from the metal center, which is in line with other metal complexes supported by azamacrocycles bearing an acetic or propionic acid pendant arm which show that the protonated arm does not bind with the metal center whereas the deprotonated form does.[28] Interestingly, the complex forms centrosymmetric head-to-tail dimers in the solid state, in which the carbonyl oxygen atom ($O_{carbonyl}$) of one molecule weakly interacts with the Ni(II) center of a neighboring molecule ($Ni\cdots O_{carbonyl}$ distance = 3.04 Å). This feature was previously

noted for $CuL_4(ClO_4)_2$[16b] ($Cu\cdots O_{carbonyl}$ distance = 2.60 Å) as well as ferrous complex **4** ($Fe\cdots O_{carbonyl}$ distance = 2.139(2) Å).[18] In addition, structural data for $CuL_{6a}(ClO_4)_2\cdot H_2O$ was recently obtained and is presented in Chapter 6. This complex also contains the neutral carboxylic acid ligand that does not coordinate to the Cu(II) center. The same head-to-tail dimeric structure is observed, with a $Cu\cdots O_{carbonyl}$ distance of 2.732(3) Å that is similar to that reported for $CuL_4(ClO_4)_2$. The carboxylic acid proton is involved in a hydrogen bond with a lattice water molecule.

Despite the difficulties in obtaining structural data for **6a** and/or **6b**, ESI-MS spectra reveal the existence of a single peak at *m/z* = 389.27 which corresponds to the deprotonated singly charged $\{FeL_{6a} - H^+\}$ ion. In fact, the FT-IR spectra of **6a** and **6b** are also indistinguishable, lending additional credence to the notion that the only difference is in the relative amounts of carboxylic acid versus carboxylate in L_{6a} and L_{6b}, respectively. The overlaid FT-IR spectra for **6a** and **6b** are shown in Figure 5.11. ESI-MS are provided in Appendix 5.

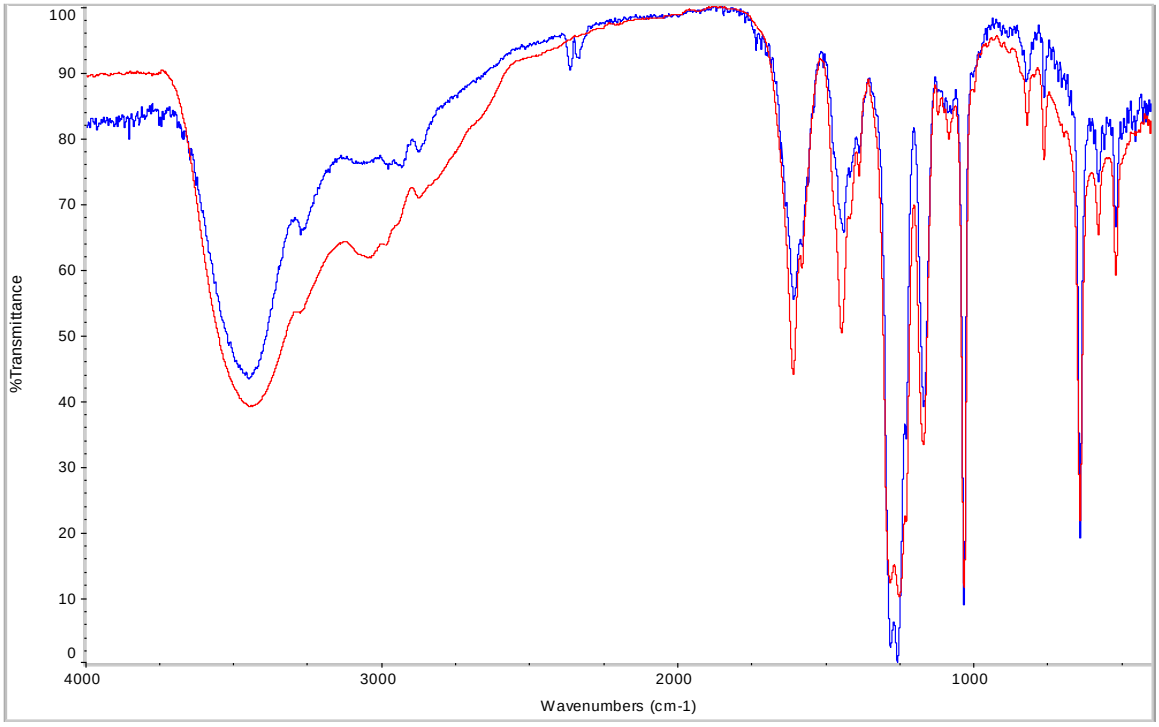

Figure 5.11. Overlay of FT-IR spectra for **6a** (blue) and **6b** (red). Individual FT-IR spectra with peak labels are provided in Appendix 5.

The following sections detail our physical studies of the novel Fe PyMAC complexes.

5.3.3. Characterization

5.3.3.1. Pendant Arm Protonation Equilibria

Similar to **3**, the UV-visible spectrum of complex **6a** in acetonitrile is essentially featureless in the visible region (a broad, weak feature is located at λ_{max} = 538 nm with ε ≈ 10 L mol^{-1} cm^{-1}) and contains two UV bands: another broad band near λ_{max} ≈ 355 nm (ε ≈ 330 L mol^{-1} cm^{-1}) and one very intense band under λ = 300 nm that corresponds to the pyridine π-π* transition.[12] Incremental addition (0.25 to 1.5 eq. per **6a**) of non-

coordinating triflic acid (HOTf) to solutions of **6a** resulted in a substantial increase in intensity of the broad absorbance band in the near UV region ($\lambda_{max} \approx 367$ nm, final $\varepsilon_{367nm} \approx 1430$ L mol^{-1} cm^{-1}, with shoulder at 389 nm, $\varepsilon_{389nm} \approx 1200$ L mol^{-1} cm^{-1}) as well as a small increase in absorbance in the visible region at $\lambda_{max} = 538$ nm (final $\varepsilon \approx 60$ L mol^{-1} cm^{-1}) as shown in Figure 5.12. The absorbance changes level off when an excess of HOTf (> 1 eq.) is added.

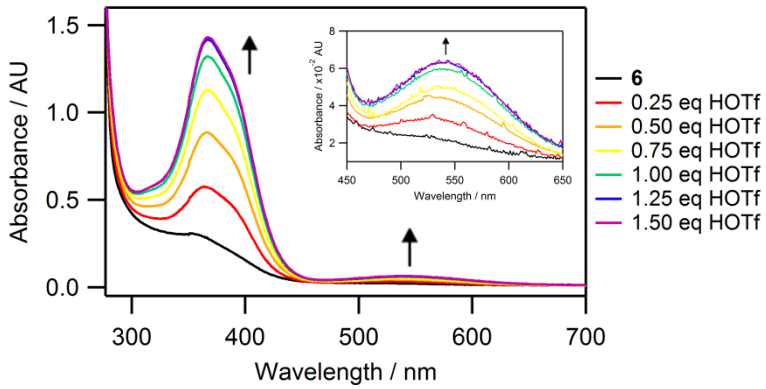

Figure 5.12. UV-visible spectra acquired upon incremental addition of HOTf (0.25 to 1.5 eq.) to complex **6a** (1 mM) in MeCN at 25 °C. Inset highlights the small increase in intensity of the visible band located at ≈ 538 nm.

Back titration using tetramethyl ammonium hydroxide (Me_4NOH) leads to the reversal of spectral changes noted upon addition of HOTf as shown in Figure 5.13, ending with a final spectrum that is very similar to that of the starting material. These results ultimately demonstrate the reversibility of this process and lend credence to the possibility of pendant arm coordination upon deprotonation.[12]

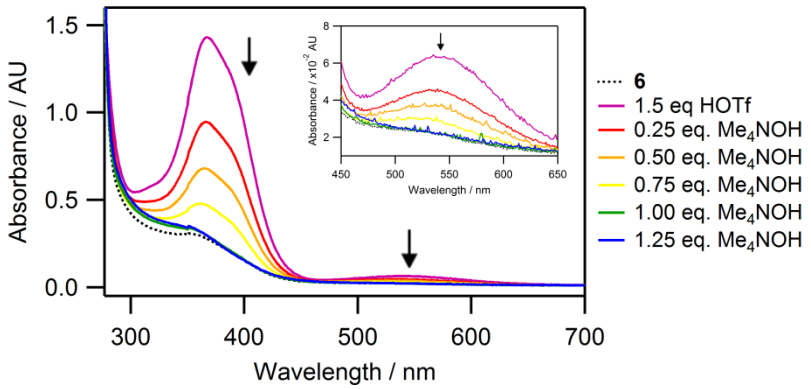

Figure 5.13. UV-visible spectra acquired upon incremental addition of Me_4NOH (0.25 to 1.25 eq.) to complex **6a** (1 mM) in MeCN at 25 °C. Inset highlights the decay in intensity of the visible band located at ≈ 538 nm.

The UV-visible spectra of complexes **1** and **2** (6-coordinate complexes in acetonitrile solution) contain weak absorbencies in visible region: λ_{max} = 526 nm for **1** (ε ≈ 120 L mol^{-1} cm^{-1})[12] and λ_{max} = 540 nm for **2** (ε ≈ 105 L mol^{-1} cm^{-1}) in addition to intense transitions near 400 nm. The electronic spectrum of five-coordinate **3** lacks these features; however, upon addition of HOTf, features at λ_{max} = 545 nm (ε ≈ 80 L mol^{-1} cm^{-1}) and λ_{max} = 367 nm (387 nm shoulder) (ε ≈ 2,090(1,465) L mol^{-1} cm^{-1}) grow in, indicating that protonation of the aminopropyl pendant arm leads to its dissociation from the metal center which may allow solvent to bind in axial positions. The high similarity between the UV-visible spectra of **6a** and that of **1**, **2**, and protonated **3** confirms that the macrocyclic complex **6a** remains intact in the presence of acid. Furthermore, the similarities also suggest similar coordination environments and spin states for the iron(II) center. The spectral changes noted upon addition of HOTf to **6a** are typical of high- to low-spin transformations,[29] a change that has been previously demonstrated for high-spin complex **3**, where addition of acid led to suppression of the effective magnetic moment.[12]

Investigation of the solution spin-state(s) of novel PyMAC complexes **5** and **6a** (in the absence and presence of HOTf) are discussed in the following section.

5.3.3.2. Solution Magnetic Properties

The magnetic susceptibilities of complexes **5** and **6** were investigated via Evans method in acetonitrile solution. For **6a** and **6b**, the experiments were performed both in the absence and presence of HOTf in an effort to understand the effects of acid addition on the spin state of the ferrous center in PyMAC complexes containing an acidic pendant donor.

The room temperature effective magnetic moment determined for **5** (μ_{eff} = 5.6 BM) is in reasonable agreement with published values for similar high-spin Fe(II) PyMAC complexes (Table 5.2)[12,30] and indicates that the solid state high-spin configuration is preserved upon dissolving in acetonitrile (Figure 5A.13).

Interestingly, complex **6a** was found to possess a magnetic moment (μ_{eff} = 4.4 BM) that is smaller than expected for a high-spin configuration. A similar observation was noted for **3** in the presence of 1-2 eq. HOTf, which yielded a μ_{eff} intermediate between the expected values for low- and high-spin configurations.[12] It has been hypothesized that coordination of two CH_3CN molecules to the metal center is hindered upon dissociation of the pendant arm due to steric effects, and thus precludes formation of the pure low-spin octahedral complex **3** with two axially bound solvent molecules.

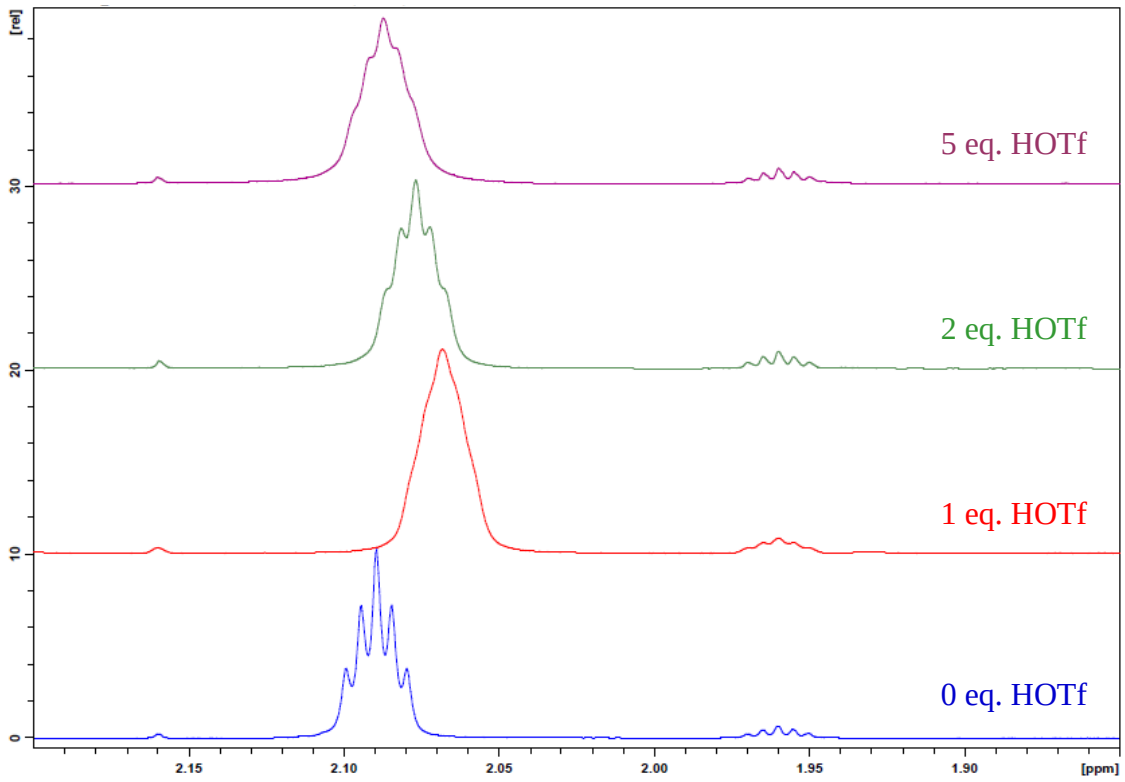

Figure 5.14. 500 MHz ^{1}H NMR shifts of CD_3CN noted for complex **6a** (3.6 mM) in the absence and presence of HOTf (1, 2 or 5 eq.). The center peak of the CD_3CN signals were used in calculations, with the pure solvent referenced at δ = 1.960 ppm.

In contrast to complex **3**, however, the magnetic moment of **6a** was found to be essentially unaffected by addition of up to 5 eq. HOTf as shown in Figure 5.14. We speculate that **6a** contains mostly neutral carboxylic acid ligand, so it is not surprising that addition of more HOTf does not lead to further changes in the effective magnetic moment. This is, however, in contradiction to the observed changes noted in the UV-visible spectra of **6a** discussed in the previous section, and additional work is in progress to reconcile these findings. We speculate that the spin equilibrium observed for **6a** in solution may be attributed to the competition between coordination of the carbonyl group from the pendant arm (yielding the high-spin form of the complex) and coordination of

one or two axial acetonitrile molecules in the arm-off form of the complex, similar to that noted for complex **4**.[18] The "dimeric" nature of both **4** and $CuL_{6a}(ClO_4)_2$ in the solid state, where the pendant carbonyl oxygen of one molecule interacts with the metal center of a neighboring molecule, would also be expected for **6a**.

Complex **6b**, which has been presumed thus far to contain mainly deprotonated carboxylate PyMAC, yields a μ_{eff} = 5.2 BM and is in line with a high-spin configuration (Figure 5A.14). Upon addition of HOTf, we expected to observe a decrease in μ_{eff} that would be in line with that observed for **6a**, however, the data revealed barely any effect from added acid (see Table 5.2 and Figure 5A.15).

Table 5.2. ^{1}H NMR shifts of CD_3CN and effective magnetic moments for Fe(II) PyMAC complexes obtained using Evans method.

Complex	Additive	$\delta\nu$ (Hz)	μ (BM)	Spin state	Ref
5[a]	none	106.5	5.6	hs	this work
6a[a]	none	65.0	4.4	hs-ls equilibrium	this work
	1 eq. HOTf	54.0	4.0	hs-ls equilibrium	this work
	2 eq. HOTf	58.5	4.1	hs-ls equilibrium	this work
	5 eq. HOTf	63.5	4.3	hs-ls equilibrium	this work
6b[a]	none	249.1	5.2	hs	this work
	1 eq. HOTf	236.6	5.0	hs	this work
	2 eq. HOTf	247.1	5.2	hs	this work
	5 eq. HOTf	255.1	5.2	hs	this work
3[a]	none	147.9	5.15	hs	12
	1-2 eq. HOTf	55.1	3.03	hs-ls equilibrium	12
[Fe(L$_1$)Cl]Cl[b]	none	---	5.20	hs	30
[Fe(L$_1$)Br]Br[b]	none	---	5.11	hs	30
[Fe(L$_1$)I]I[b]	none	---	5.05	hs	30
		Low-spin Fe(II) PyMACS			
[Fe(L$_1$)(NCS)$_2$][b]	none	---	0.8	ls	31
2	none	0	0	ls	17
4	none	0	0	ls	18

[a] Obtained at room temperature using Evans method in CD_3CN (3.6 mM **5** and **6a**; 10 mM **6b** and **3**; 1 mM **2** and **4**). [b] Obtained at room temperature using the Faraday technique (≈ 1 mM in MeOH).

5.3.3.3. Electrochemistry

The electrochemical behavior of complexes **5**, **6a**, and **6b** were investigated using cyclic voltammetry. The cyclic voltammogram of **5** in the absence of additives (Figure 5.15) clearly shows a reversible wave that is assigned to the $\mathbf{5}^{3+}/\mathbf{5}^{2+}$ couple. The measured redox potential ($E_{1/2}$ = 0.34V versus Fc, ΔE_p = 0.125 V) is similar to those noted for other pentadentate aminopyridine ferrous complexes[29c,32] and is somewhat lower than that observed for related PyMAC complexes reported previously,[12,17] which are in the range of 0.4 to 0.6 V. This may be due to a slight stabilization of the +3 oxidation state imparted by coordination of the pendant carbonyl oxygen. Incremental addition of HOTf to solutions of **5** followed by CV scans did not result in notable changes of the redox potential. Addition of more than 2 eq. HOTf leads to disappearance of the signal, which likely arises from loss of iron upon protonation of multiple macrocyclic N-donors (Figure 5A.16).

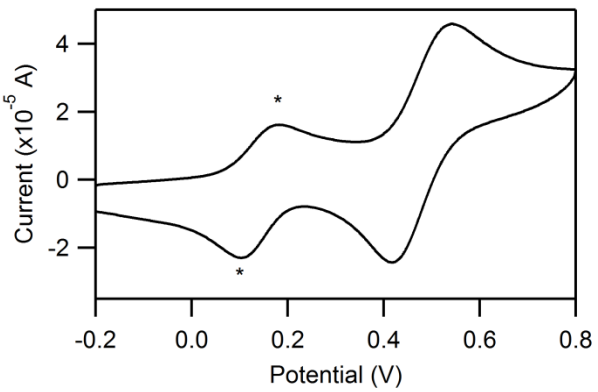

Figure 5.15. Cyclic voltammogram of **5** (2.9 mM) in CH_3CN. Asterisks denote the Fc^+/Fc^0 couple.

In contrast to **5**, complex **6a** appears to be irreversibly oxidized (ca. 0.4 V) in the absence of additives as shown in Figure 5.16a. Upon closer examination, the cathodic

scan appears to show two weak but separate features that overlap with the internal standard, which is somewhat reminiscent of the behavior noted for **3** and may be due to equilibrium protonation of the pendant carboxylic acid in neutral solution,[12] which is in keeping with the studies noted from UV-visible spectrophotometric titrations discussed earlier in Section 5.3.3.1. Increasing the scan rate did not lead to reversibility.

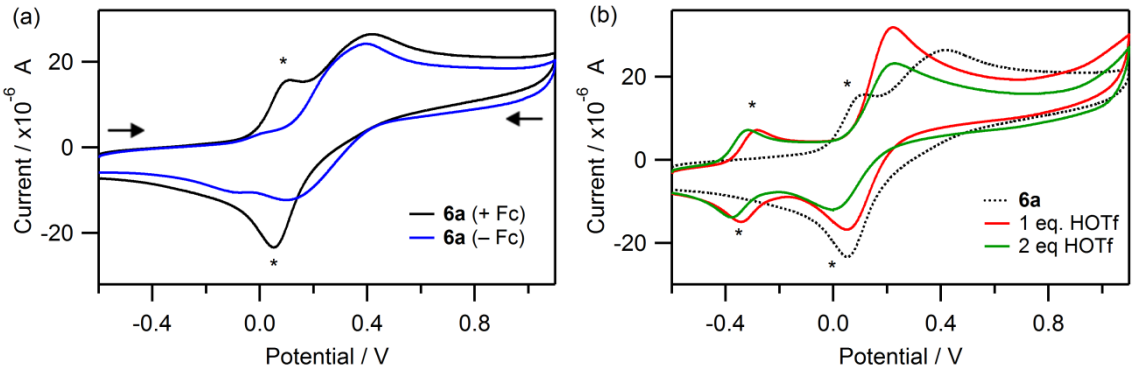

Figure 5.16. (a) Overlay of cyclic voltammograms of **6a** (2.9 mM) in CH_3CN in the absence (blue) or presence (black) of ferrocene. Asterisks denote the Fc^+/Fc^0 couple. In the absence of ferrocene, two weak cathodic features were noted during the reverse scan. (b) Overlay of cyclic voltammograms of **6a** upon addition of 1 or 2 eq. HOTf.

Addition of one equivalent of HOTf to **6a** (Figure 5.16b) leads to production of a single reversible couple with a redox potential of $E_{1/2}$ = 0.45 V vs. Fc (ΔE_p = 0.173 V).This is a rather dramatic shift towards more positive potential (as compared with **5**), indicating that fully protonated **6a** is more easily reduced than **5**. In addition, an Fe(III) complex of fully protonated L_6 is expected to be more easily reduced than the corresponding carboxylate complex and the electrochemical data is in keeping with this notion. Addition of NEt_3 to acidified solutions of **5** or **6a** does not regenerate the starting material; experiments using Me_4NOH in place of NEt_3 should be performed to determine

if the selection of base is critical for reversibility. All electrochemical data for Fe PyMAC complexes are compiled in Table 5.3 below.

Table 5.3. Redox potentials of FePyMAC complexes referenced against the ferrocenium/ferrocene couple in CH_3CN.

Complex	Additive	$E_{1/2}$ (V)[a]	ΔE_p (V)	$\lvert i_{pa}/i_{pc} \rvert$	Reversibility[b]	Ref
1	none	0.40	0.110	---	R	12
	1 eq. HOTf	0.40	0.120	---	R	12
2	none	0.49	0.055	---	R	17
3[c]	none	0.58, 0.56	0.26, 0.54	---	QR, QR	12
	1 eq. HOTf	0.51	0.14	---	R	12
4	none	0.50	0.037	---	R	18
5	none	0.34	0.125	1.37	R	This work
	1 eq. HOTf	0.33	0.117	1.85	R	This work
	2 eq. HOTf	0.36	0.150	2.30	R	This work
6a	none	---	---	---	IR	This work
	1 eq. HOTf	0.45	0.173	1.60	R	This work
	2 eq. HOTf	0.46	0.226	1.76	QR	This work

[a]Reported $E_{1/2}$ values are referenced against the Fc^+/Fc^0 couple. [b]R = reversible; QR = quasi-reversible; IR = irreversible. [c] Complex **3** displays two waves.

5.3.4. Catalytic Epoxidation of Olefins

Catalytic epoxidation of cyclooctene and 1-decene with complexes **2**, **5**, and **6a** using hydrogen peroxide as terminal oxidant was examined in the presence and in the absence of different acids (HOTf and AcOH) in an effort to compare the relative effectiveness of several structurally related complexes in the catalytic formation of epoxides from activated and unactivated olefins under mild conditions. We also sought to compare the reactions of **6a** with those of unfunctionalized complex **2** with added AcOH to test the effectiveness of the appended carboxylic acid versus free AcOH. *cis*-Cyclooctene is a commonly used substrate for catalyst screening in epoxidations with

H_2O_2 in the presence of non-heme iron catalysts.[33] Terminal olefins, such as 1-decene, are more challenging substrates that only undergo epoxidation in the presence of highly reactive catalysts.[34] Tables 5.4 and 5.5 show epoxide yields and turnover numbers after 5 min of reaction at room temperature with PyMAC complexes **1**-**6a** as catalysts.

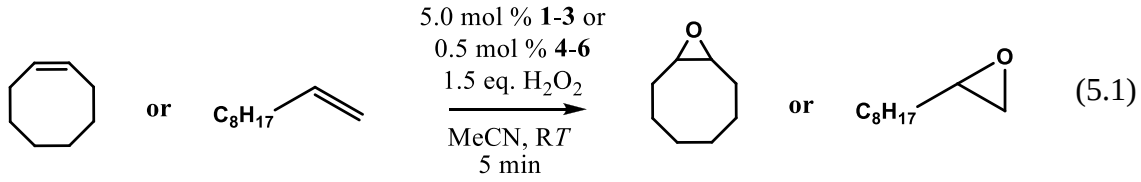

(5.1)

Table 5.4. Epoxide yields, conversion, TON, and selectivities from catalytic epoxidation reactions of cyclooctene with H_2O_2.

Catalyst[a]	Additive	Yield (%)[b]	Conv. (%)[c]	TON[d]	Sel. (%)[e]	Ref
1	none	32	43	6	74	12
	1 eq. HOTf	46	54	9	85	12
	5 eq. HOTf	67	73	13	92	12
2	none	24(36)	45(42)	5(8)	54(85)	This work(18)
	1 eq. HOTf	46(52)	67	10(9)	69	This work(18)
	5 eq. HOTf	40	---	7	---	18
	1 eq. AcOH	21	40	5	52	This work
	2 eq. AcOH	20	39	4	52	This work
	5 eq. AcOH	19	40	4	48	This work
3	none	9	16	1.8	56	12
	1 eq. HOTf	39	51	7.8	76	12
	2 eq. HOTf	70	76	14	92	12
	5 eq. HOTf	86	89	17.2	97	12
4	none	9.1	13	19	69	This work
	1 eq. HOTf	20	28	41	72	This work
	2 eq. HOTf	29	35	59	81	This work
	5 eq. HOTf	34	44	70	78	This work
5	none	< 1	4	< 1	----	This work
	1 eq. HOTf	28	40	59	70	This work
	2 eq. HOTf	47	67	98	70	This work
	5 eq. HOTf	55	74	111	75	This work
	2 eq. AcOH	< 1	----	< 1	----	This work

Catalyst[a]	Additive	Yield (%)[b]	Conv. (%)[c]	TON[d]	Sel. (%)[e]	Ref
6a	none	22	29	47	76	This work
	1 eq. HOTf	68	90	149	75	This work
	2 eq. HOTf	75	100	164	75	This work
	5 eq. HOTf	71	100	148	71	This work
	2 eq. AcOH	22	28	46	79	This work

[a] For 0.5 mol % catalyst loading, the final Fe:olefin:H_2O_2 ratio was 1:200:300; for 5 mol % loading it was 1:20:30. [b] Yield = mol cyclooctene oxide/mol cyclooctene × 100. [c] Conversion = 1 − (end mol cyclooctene/initial mol cyclooctene) × 100. [d] Turnover number (TON) = mol epoxide formed/mol catalyst. [e] Selectivity = GC yield/conversion × 100. All values are within ±10 %.

The data in Table 5.4 clearly shows a marked improvement in catalytic activity for complexes **5** and **6a** (especially when HOTf is present) as compared to all other Fe(II) PyMAC analogues. Complex **5** is inactive on its own, however, addition of up to 5 eq. HOTf results in increased reactivity that is comparable to **6a**. It is also clear from the catalytic reactions that addition of AcOH to complex **2** does not lead to the same level of reactivity as observed for complex **6a**, which contains the appended carboxylic acid.

Table 5.5. Epoxide yields, conversion, TON, and selectivities from catalytic epoxidation reactions of 1-decene with H_2O_2.

Catalyst[a]	Additive	Yield (%)[b]	Conv. (%)[c]	TON[d]	Sel. (%)[e]	Ref
1	none	20(33)	33(44)	4(8)	61(75)	12(17)
	5 eq. HOTf	26	56	5	47	12
2	none	18	22	4	81	17
	1 eq. HOTf	42	---	7	---	18
	5 eq. HOTf	28	---	5	---	18
3	none	7(4)	19(14)	1.4(0.8)	37(29)	12(17)
	5 eq. HOTf	64	81	13	79	12
4[f]	none	71	---	16	---	18
	1 eq. HOTf	77	---	16	---	18
5	none	< 1	6	< 1	n/a	This work
	1 eq. HOTf	13	22	26	56	This work
	2 eq. HOTf	22	34	44	64	This work
	5 eq. HOTf	36	55	71	65	This work

Catalyst[a]	Additive	Yield (%)[b]	Conv. (%)[c]	TON[d]	Sel. (%)[e]	Ref
6a	none	24	34	51	70	This work
	1 eq. HOTf	57	70	118	81	This work
	2 eq. HOTf	7	95	156	78	This work
	5 eq. HOTf	77	100	150	77	This work

[a] For 0.5 mol % catalyst loading, the final Fe:olefin:H_2O_2 ratio was 1:200:300; for 5 mol % loading it was 1:20:30. [b] Yield = mol cyclooctene oxide/mol cyclooctene × 100. [c] Conversion = 1−(end mol cyclooctene/initial mol cyclooctene) × 100. [d] Turnover number (TON) = mol epoxide formed/mol catalyst. [e] Selectivity = GC yield/conversion × 100. [f] 5 mol % catalyst loading for complex **4** used in 1-decene epoxidations. All values are within ±10 %.

The new complexes are also good catalysts for the epoxidation of 1-decene. Remarkably, complex **6a** afforded 51 turnovers in the absence of acid and over 150 turnovers with 2 eq. HOTf present. Similar to what was observed for cyclooctene, complex **5** becomes a competent catalyst only upon addition of HOTf, achieving up to 71 turnovers with modest selectivity. Moreover, the epoxidation of 1-decene serves to show the relatively large differences in reactivity between complexes **5** and **6a**. The data ultimately reveals that addition of a pendant arm containing an acidic functionality vastly improves catalytic reactivity.

Furthermore, efficient epoxidation was observed only when peroxides were used as the terminal oxidants (H_2O_2 as discussed above and *t*-BuOOH, which behaved similarly to H_2O_2). When ^{i}Pr-IBX was employed, epoxidation of cyclooctene was not observed in the presence of **5** or **6a** using our typical reaction conditions (5 min at RT). This is typical feature of FePyMAC complexes,[18] where ^{i}Pr-IBX promotes much slower epoxidations with modest turnover numbers. The fairly high selectivity for epoxides argues against the sole involvement of radical-type pathways contributing to the observed reactivity and may hint at the involvement of iron peroxide derived oxidants. As

discussed in the following section, we set out to identify catalytically competent metal-based intermediates using stopped-flow methodology.

5.3.5. Stopped-Flow Kinetics

Preliminary kinetic studies were undertaken for the most active catalyst, **6a**, as described below.

5.3.5.1. Formation of Oxoiron(IV) Intermediates

(a) Reactions with Hydrogen Peroxide. In an attempt to understand the origins of the enhanced catalytic epoxidation reactions observed for the system containing **6a** and H_2O_2, stopped-flow experiments with spectrophotometric detection were utilized in an effort to identify transient high valent iron-oxo intermediates that may form in such reactions. Time-resolved UV-visible spectra from reactions of **6a** (3 mM) with excess H_2O_2 (30 mM) at −35 °C led to an increase in absorbance across the entire spectral window, with production of a relatively distinct, low-intensity near-IR band indicative of an Fe(IV) oxo intermediate[2c,35] ($\lambda_{max} \approx 700$ nm) as shown in Figure 5.17a. Maximum accumulation of the oxoiron(IV) absorbance band is achieved within 5 s under these conditions and is followed by its decay. The kinetic traces reveal a sigmoidal shape that depends on [H_2O_2] (Figure 5.17b) which is consistent with an autocatalytic mechanism.

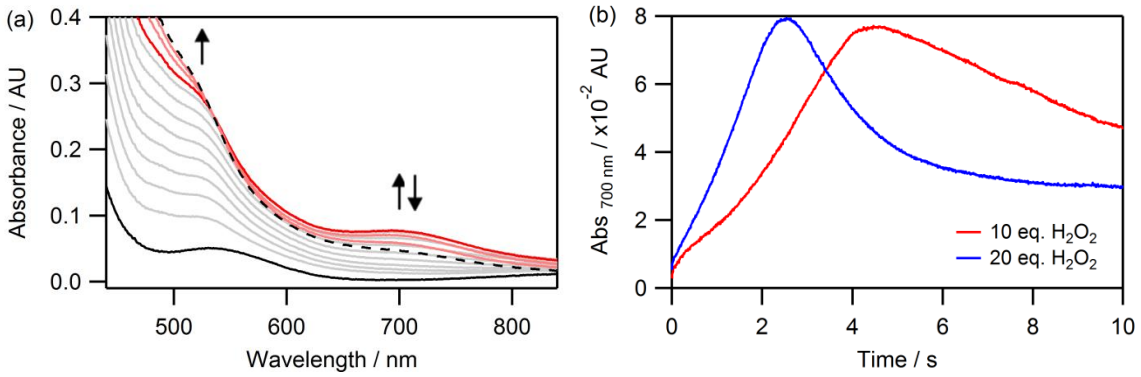

Figure 5.17. (a) Time-resolved spectral changes observed for the reaction between **6a** (3 mM) with 10 eq. H_2O_2 (30 mM) at −35 °C in MeCN, acquired over 10 s. Selected traces are shown for clarity. Maximum accumulation at λ_{max} = 700 nm occurs within the first 5 s of reaction at this temperature (accumulation traces shown in gray), followed by its decay (red traces). Initial spectrum is shown in black (solid line) and final 10 s spectrum is shown in black (dashed line). (b) Overlay of kinetic traces at λ = 700 nm for two different [H_2O_2].

While Fe(III) hydroperoxy intermediates frequently absorb in the λ =500-600 nm range,[36] our previous studies with unfunctionalized complex **2** showed that the Fe(II) complex with partially oxidized ligand (containing one or two C=N bonds adjacent to the pyridine ring) also display absorption bands near λ = 500-550 nm.[17] It is clear from these reactions that formation of oxoiron(IV) is not a clean process though it is present in the catalytically relevant system. Similar complications were also noted in reactions of **6a** with ^{t}BuOOH (see Figure 5A.17) and thus were not investigated further. Additional information regarding the reactivity of the putative oxoiron(IV) intermediate generated from reactions with H_2O_2 is provided in Section 5.3.5.2.

(b) Reactions with Isopropyl-2-Benzoate (^{i}Pr-IBX). In search of an oxidant that would cleanly generate the desired high-valent intermediate, we selected ^{i}Pr-IBX (isopropyl 2-

iodoxybenzoate) as terminal oxidant, similar to our previous studies with complexes **2** and **3**.[13,17] We initially screened for formation of an oxoiron(IV) intermediate at low temperatures (−40 and −20 °C) using 1.5 mM **6a** and varying concentrations of ^{i}Pr-IBX (1.5 - 18 mM). In contrast to other Fe PyMAC systems, rapid decay of a broad absorbance band near λ = 535 nm was noted to precede accumulation of the putative oxoiron(IV) intermediate, which shows a maximum absorption at λ ≈ 709 nm at −40 °C (Figure 5.18). The initial spectrum observed upon mixing is different from starting **6a** (see Figure 5A.18) and only becomes apparent in the presence of excess ^{i}Pr-IBX. It is possible that this process represents decay of a rapidly formed oxidant-bound iron adduct, however, attempts to interpret the kinetic behavior by extracting observed rate constants from fitting kinetic traces to exponential equations have been unsuccessful thus far. Ultimately, the kinetics of oxoiron(IV) formation is at least a two-step process, similar to what was observed for other Fe PyMAC complexes noted previously.[13,17]

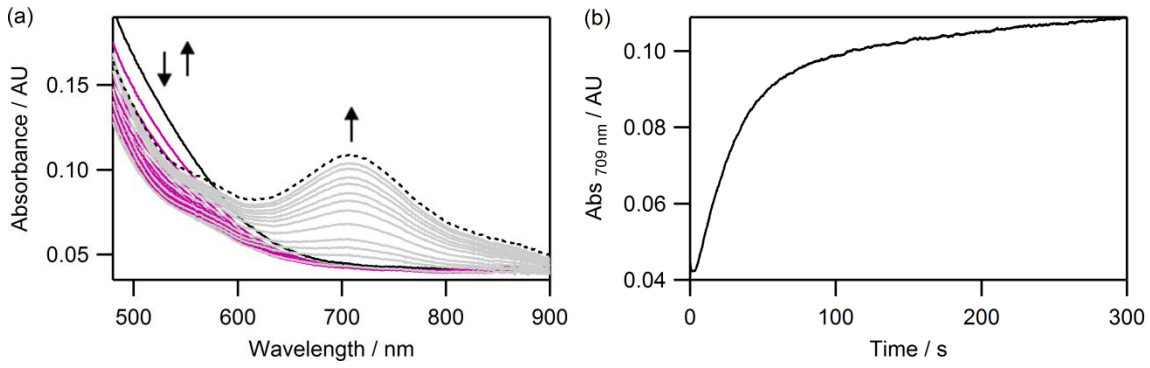

Figure 5.18. (a) Time-resolved spectral changes accompanying the reaction between **6a** (1.5 mM) and 12 eq. ^{i}Pr-IBX (18 mM) at −40 °C acquired over 300 s. Accumulation of the oxoiron(IV) intermediate (gray traces) is superimposed over the initial rapid decay (purple traces). The initial spectrum is shown as a solid black line and the final spectrum as a dashed black line. (b) Kinetic trace at λ = 709 nm.

At −20 °C, the rapid decay event proceeding formation of the oxoiron(IV) intermediate is again observed, though it occurs too fast to measure accurately at this temperature (see Figure 5A.19 for an example of the time-resolved spectra). Attempts to analyze the rate of formation of the oxoiron(IV) intermediate was undertaken by fitting kinetic traces at λ = 709 nm to a biexponential equation, $y = -A_1\exp(-k_{1obs}t) - A_2\exp(-k_{2obs}t) + C$. Only the initial formation phase governed by k_{1obs} was followed since k_{2obs} appeared to be random and irreproducible. Somewhat surprisingly, the analysis revealed no dependence of the observed rate constant on the oxidant concentration (Figure 5.19b). This observation is quite different from that noted for oxoiron(IV) formation with complexes **2** and **3** using ^{i}Pr-IBX, where a marked acceleration of the formation rate was noted upon addition of ≥ 6 eq. ^{i}Pr-IBX and suggested that coordination of a second oxidant molecule facilitated intermediate formation.[13,17] The data suggests either a rate-limiting dissociation of coordinated pendant arm from the metal center, or, alternatively, the reaction occurring with ^{i}Pr-IBX has already taken place in the very initial rapid stage of the reaction (characterized by decay in the λ = 500 - 600 nm range in the time-resolved spectra).

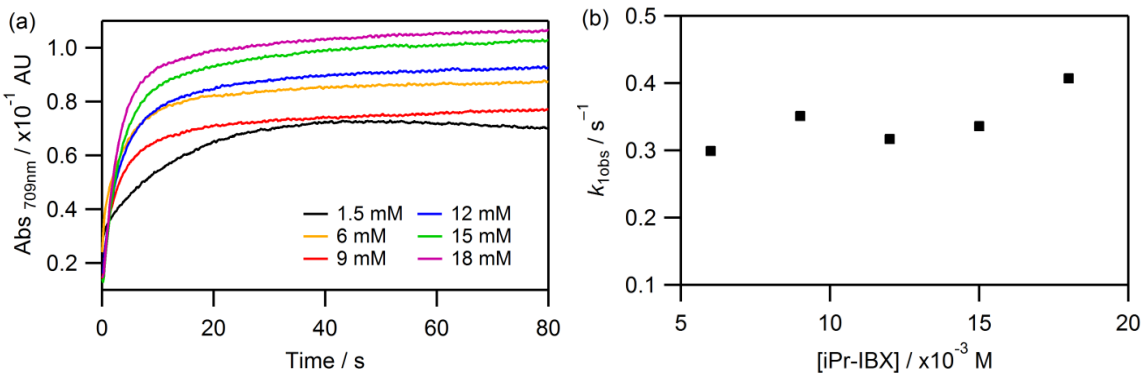

Figure 5.19. (a) Overlay of kinetic traces at λ = 709 nm as a function of [^{i}Pr-IBX] at −20 °C. (b) Plot of k_{obs} versus [^{i}Pr-IBX] for reactions performed at −20 °C with [**6a**]$_0$ = 1.5 mM and [^{i}Pr-IBX]$_0$ = 6 mM to 18 mM. k_{1obs} values were obtained from fitting formation traces at λ = 709 nm to a biexponential equation.

At higher temperature (+10 °C), the rapid decay that was noted previously is no longer observed, presumably since it occurs rapidly upon mixing at elevated temperature; the initial spectrum observed upon mixing at 10 °C is similar to that noted at lower temperatures as just discussed. Only growth in absorbance across the entire spectral window was noted, with the prominent near-IR absorbance band assigned to the oxoiron(IV) species accumulating within 4 s under stoichiometric conditions ([**6a**] = [^{i}Pr-IBX] = 3 mM). This is followed by slower self-decay of the intermediate over the course of the stopped-flow reactions as shown in Figure 5A.20.

In summary, we clearly observe formation of the oxoiron(IV) intermediate from reactions of **6a** with different oxidants (H_2O_2 and ^{i}Pr-IBX). It accumulates rapidly at low temperatures through a complicated multi-step process that remains under investigation. Despite these complications, we were able to assess the reactivity of the intermediate species via multi-mixing stopped-flow experiments with cyclooctene as described in the following section.

5.3.5.2. Reactivity of Oxoiron(IV) Intermediates towards Cyclooctene

The reactivity of the oxoiron(IV) intermediate generated from reactions of **6a** with H_2O_2 was initially assessed using single-mixing stopped-flow at −15 °C. Solutions of **6a** containing cyclooctene were reacted with 10 eq. H_2O_2 in an effort to determine if the intermediate's rate of formation and/or decay were affected by the presence of substrate. Indeed, changes in both the rate of formation and decay were noted in reactions containing cyclooctene as shown in Figure 5.20 below.

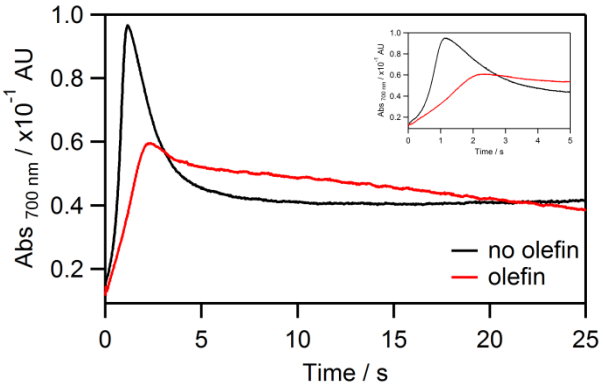

Figure 5.20. Overlay of kinetic traces at λ = 700 nm obtained from reactions of **6a** (3 mM) in the absence (black) or presence (red) of cyclooctene (18 eq., 54 mM) with 10 eq. H_2O_2 (30 mM) acquired over 25 s at −15 °C. Inset shows reaction over 5 s.

Subsequent double-mixing stopped-flow experiments were also conducted at −15 °C, whereby the intermediate was pre-generated in single-mixing mode and aged for 0.5 s (to reach maximum accumulation of its absorbance band at λ = 700 nm). The decay in absorbance of the oxoiron(IV) intermediate was then monitored upon double-mixing solvent (to assess self-decay) or various concentrations of cyclooctene into solutions of the pre-generated intermediate as shown in Figure 5.21a.

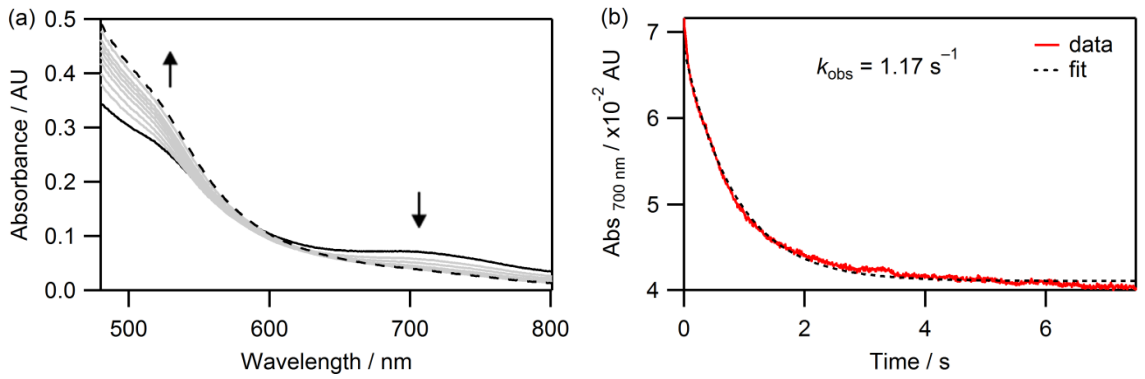

Figure 5.21. (a) Time-resolved spectral changes observed upon addition of cyclooctene (30 mM, 10 eq.) to pre-generated **6a**–O acquired at −15 °C over 7.5 s with [**6a**]$_0$ = 3 mM. The intermediate was generated using 30 mM H_2O_2 (10 eq.) and aged for 0.5 s prior to addition of cyclooctene. (b) Kinetic trace at λ = 700 nm with single exponential fit. Initial spectrum (solid black line) and final spectrum (dashed line).

Decay of the oxoiron(IV) band at λ = 700 nm is complete within 8 s at −15 °C and in the beginning stage of the reaction (first 1.5 s), an isosbestic point was observed near λ = 550 nm. As the reaction progresses further, however, the isosbestic point disappears, signaling production of additional colored side products.

Analysis of kinetic traces (λ = 700 nm) revealed that the rate of decay of the oxoiron(IV) intermediate was affected only subtly by the presence of olefin; the observed rate constant (k_{obs}) for self-decay was approximately 2x smaller than that found for the decay in the presence of 10 eq. cyclooctene (average k_{obs} = 0.71 s^{-1} for self-decay and 1.55 s^{-1} in reactions with 10 eq. cyclooctene, see Table 5A.1).Surprisingly, however, k_{obs} values were not affected by changes in [cyclooctene] (Figure 5.22).

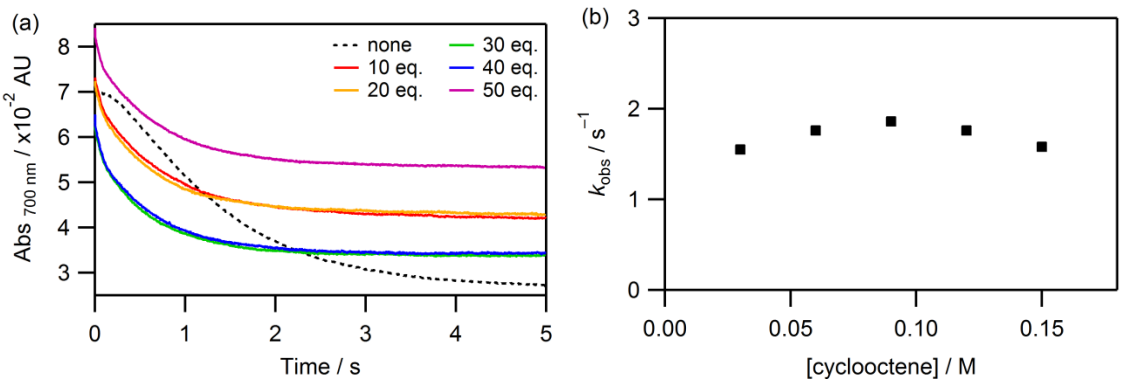

Figure 5.22. (a) Overlay of decay traces at λ = 700 nm for double-mixing reactions with solvent (CH_3CN) or varying amounts of cyclooctene (10 - 50 eq.) at −15 °C with $[\mathbf{6a}]_0$ = 3 mM. $[\mathbf{6a}]_0$ = was pregenerated as described in Figure 5.21 with $[\mathbf{6a}]_0$ = 6 mM. (b) Plot of the observed rate constant versus [cyclooctene] highlighting a zero order dependence. Observed rate constants were obtained from single exponential fits of the decay traces.

Self-decay is characterized by a rather shallow decay in absorbance (λ = 700 nm), whereas a rapid decay may be seen in the very initial stages of reactions in the presence of cyclooctene (immeasurable under the conditions tested), followed by a second decay phase comprising the bulk of the kinetic trace (what has been quantified, see Table 5A.1). In addition, the absorbance change is greater for self-decay than for reactions in the presence of cyclooctene. The data hints at the existence of a precursor intermediate that can either decay into the oxoiron(IV) species or react with olefin to form epoxide. Additional experiments involving the addition of acid and/or base are planned to determine if the reactivity towards olefin can be controlled based on the protonation/coordination state of the pendant arm. We also believe that stopped-flow investigation of complex **5** could aid in clarifying the nature of observed intermediates in this related system.

We subsequently explored the reactivity of the oxoiron(IV) intermediate generated from reactions of **6a** with ^{i}Pr-IBX using single-mixing stopped-flow

experiments as discussed above, and in this case, neither the formation nor decay rates of **6a**−O were affected by cyclooctene as shown below in Figure 5.23. To verify these results, the reactions were repeated under identical conditions using complex **2**, whose oxoiron(IV) intermediate is active towards cyclooctene, and as expected, the rate of decay of **2**−O was notably accelerated when the olefin was present (Figure 5A.21). Previous work showed that the decay of **2**−O was dependent on [cyclooctene] and the reaction was shown to obey a simple rate law: *rate* = *k*[**2**−O][cyclooctene].[17]

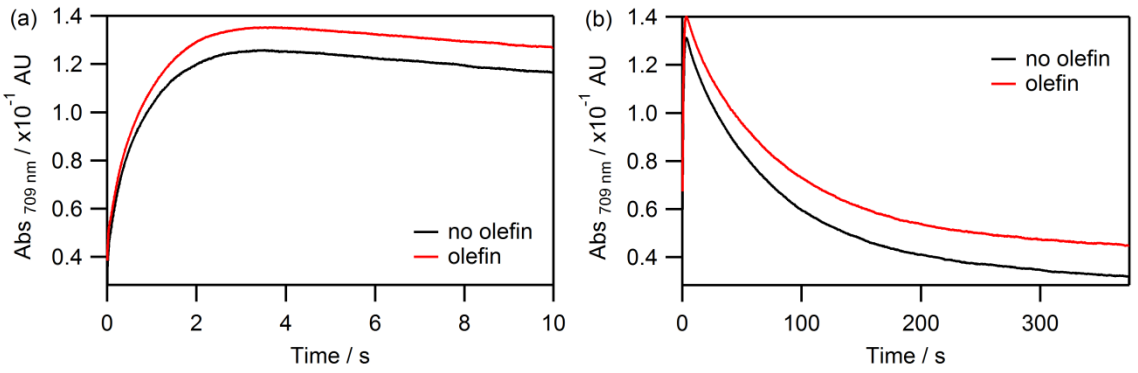

Figure 5.23. Overlay of kinetic traces at λ = 709 nm obtained from reactions of **6a** (3 mM) in the absence (black) or presence (red) of cyclooctene (100 eq., 300 mM) with 1 eq. ^{i}Pr-IBX (3 mM) at 10 °C highlighting the (a) rates of formation (10 s) and (b) rates of decay (375 s) of the oxoiron(IV) intermediate in the absence and presence of cyclooctene. k_{obs} values are unaffected by cyclooctene.

In summary, it is not readily apparent from the kinetic data that the oxoiron(IV) intermediate of **6a** is the active species in epoxidation of cyclooctene, or at least, oxygen atom transfer from this intermediate to cyclooctene is not the rate limiting step in the epoxidation reaction. Additional work is in progress to better understand the role of the oxoiron(IV) intermediate in these catalytic reactions.

5.3.5.3. Comparison of Oxoiron(IV) Intermediates: 6a *vs*. (2 + Acetic Acid)

An important question we were able to address is if the reactivity of **6a** could be matched by simply adding acetic acid to reactions of unfunctionalized complex **2**. Addition of 1 eq. AcOH to acetonitrile solutions of complex **2** does not lead to any observable color changes; time-resolved spectra for reactions of acidified **2** with ^{i}Pr-IBX reveal that AcOH has no affect on the rate of formation of the oxoiron(IV) intermediate (Figure 5A.22). On the other hand, AcOH drastically increases the rate of self-decay of **2**−O and leads to formation of **2** containing oxidized forms of the ligand as shown in Figure 5.24.

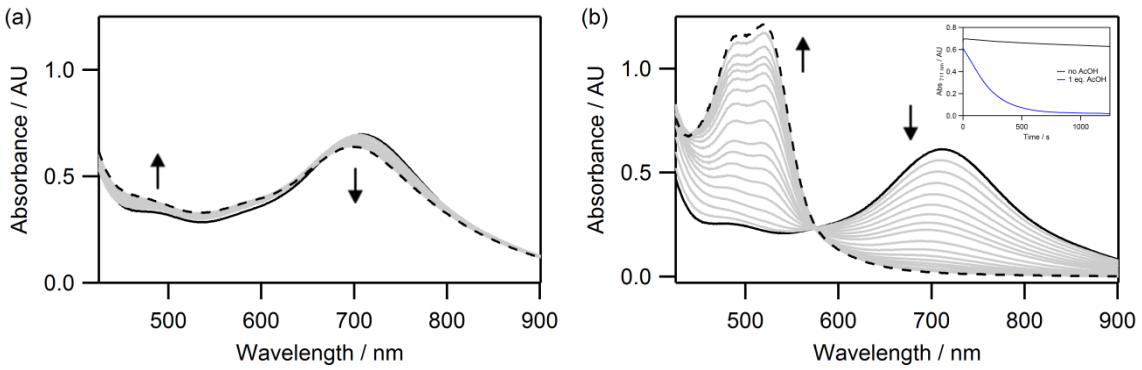

Figure 5.24. Time-resolved spectral changes highlighting self-decay of **2**−O at 10 °C (a) in the absence of AcOH and (b) presence of 1 eq. AcOH acquired over 1250 s from reactions of **2** (2 mM) with 1 eq. ^{i}Pr-IBX (2 mM). Selected traces are shown for clarity. Initial spectrum is shown as a solid black line and final spectrum as a dashed black line. Inset shows overlay of kinetic traces at λ = 711 nm for **2**−O decay in the absence (black) and presence (blue) of AcOH.

Reactions of acidified **2** were also performed in the presence of cyclooctene. The rate of decay of **2**−O is only mildly enhanced by added cyclooctene in these reactions as shown in Figure 5A.23 and suggests that AcOH is not effective for enhancement of the reactivity of **2**−O towards olefins. For example, the observed rate of decay of **2**−O (in the

absence of acid) is accelerated by a factor of two when cyclooctene is present; when AcOH is introduced, the observed rate is accelerated by only 1.3 times when cyclooctene is present. These results are in good agreement with those obtained from catalytic experiments discussed earlier in Section 5.3.4, where 1 eq. AcOH had little to no effect on the reactivity towards cyclooctene.

5.3.6. Mössbauer Spectroscopy

Zero field Mössbauer spectra were acquired on solid samples of **6a** and **6b**, and as shown in Figure 5.25, both samples are composed of two distinct quadrupole doublets with isomer shifts in the expected range for ferrous complexes with rather large quadrupole splittings. For **6a**, the major component (57 % of total Fe) has δ = 1.01 mm s^{-1} and $|\Delta E_q|$ = 3.48 mm s^{-1}; the minor component, which makes up the remaining 43 %, has δ = 1.26 mm s^{-1} and $|\Delta E_q|$ = 2.72 mm s^{-1}. The Mössbauer parameters for the major component of **6a** are quite similar to those of high-spin $[Fe(Me_6cyclam)(CH_3CO_2)_2]$[37] ($\delta$ = 1.07 mm s^{-1} and $|\Delta E_q|$ = 4.07 mm s^{-1}, Table 5.6) and vastly different from low-spin **2** (δ = 0.50(2) mm s^{-1} and $|\Delta E_q|$ = 0.78(2) mm s^{-1}).[17] Previous studies dating back to 1970 have shown that five-coordinate high-spin ferrous complexes of azamacrocyclic ligands exhibit unique Mössbauer spectra with unusually large quadrupole splittings[30] and isomer shifts that are typically greater than 0.9 mm s^{-1}.[37] The results for **6a** are in line with these observations. Interestingly, **6b** appears to be composed of the same material as **6a**, however, the relative amounts of each component are reversed. In other words, **6b** is enriched in what was the minor component of **6a**.

Collectively, the data suggest that the two distinct forms of complex **6** differ only in one or more of the following: (a) protonation state of the ligand pendant arm; (b) coordination state of the pendant arm to the metal center (which is influenced by protonation state). Although we typically see changes in spin state that are associated with pendant arm coordination, the Mössbauer data suggests that both components are high-spin complexes. At this point, we believe that the $\delta \approx 1.0$ mm s^{-1} component represents the protonated (carboxylic acid) form of the complex while the $\delta \approx 1.3$ mm s^{-1} component represents the deprotonated (carboxylate) form of the complex. Additional experiments are in progress to fully resolve these interesting findings.

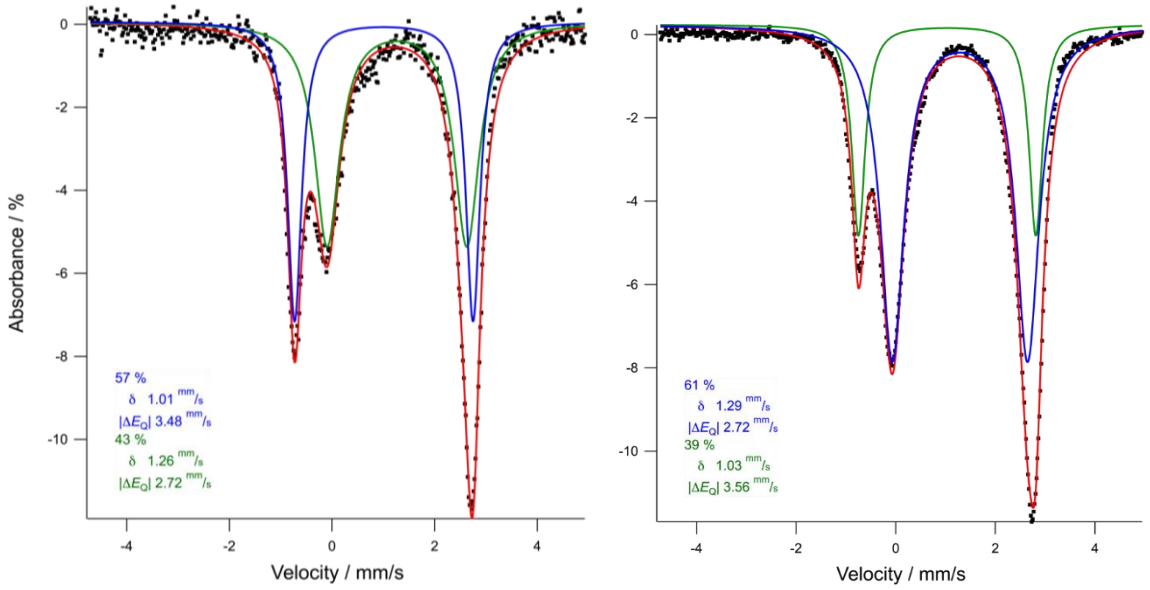

Figure 5.25. Zero field Mössbauer spectra of solid samples of **6a** (left) and **6b** (right) acquired at 90 K with derived parameters.

Despite the complexities associated with starting complexes **6a** and **6b**, a Mössbauer spectrum was obtained on a sample taken from the reaction between **6a** and 1

eq. ^{i}Pr-IBX in CH_3CN in an effort to probe the nature of the oxoiron(IV) intermediate that is observed in stopped-flow experiments. The resulting spectrum (Figure 5.26) confirms the existence of two Fe-containing species in the mixture.

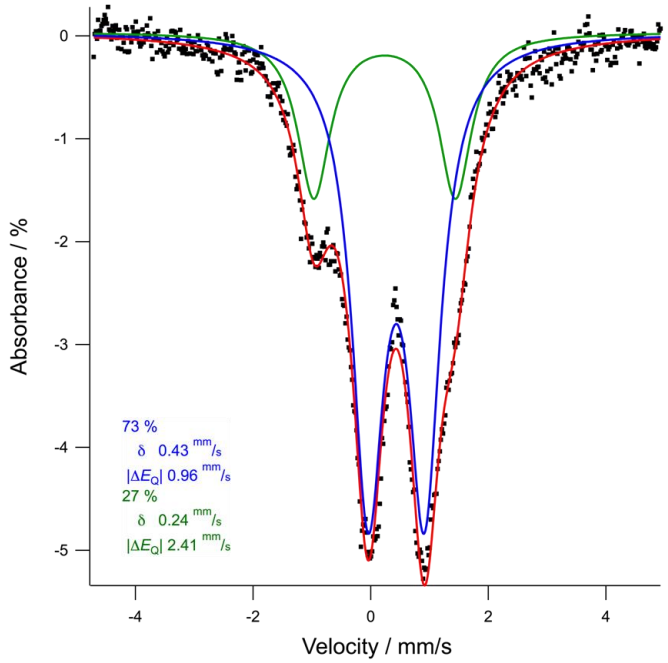

Figure 5.26. Zero field Mössbauer spectrum of the reaction between **6a** and ^{i}Pr-IBX (1 eq.) acquired at 90 K as a frozen CH_3CN solution with derived parameters. The reaction was performed at −35 °C, aged for 40 s, and frozen in liquid N_2 prior to analysis.

The majority of the sample, representing 73 % of the spectral area, displays a quadrupole doublet with δ = 0.43 mm s^{-1} and $|\Delta E_q|$ = 0.96 mm s^{-1} and is suspected to be a decomposition product. FePyMAC oxoiron(IV) complexes have been observed to decay into Fe(II) species with oxidized forms of the PyMAC ligand,[17] although this typically leads to a slight decrease in isomer shift with a concomitant increase in quadrupole splitting as compared to the parent Fe(II) PyMAC complex.[17,37] The Mössbauer parameters are actually in good agreement with low-spin μ-oxo bridged

diferric species,[37] although further studies are required to confidently identify this component. Additional Mössbauer studies regarding complex **6a** (and attempts to chemically oxidize it) are provided in Appendix 5.

The remaining 27 % corresponds to a quadrupole doublet with δ = 0.24 mm s^{-1} and $|\Delta E_q|$ = 2.41 mm s^{-1}. Although this isomer shift is rather high compared with most characterized synthetic Fe(IV) oxo systems reported in the literature (see Table 5.6), it is not unprecedented and is more consistent with formulation as a high-spin oxoiron(IV) species. It would be of much interest to pursue this further since synthetic high-spin oxoiron(IV) complexes are quite rare, despite the fact that they are postulated as the active oxidizing intermediates in several non-heme iron enzymes.[38] The fairly large quadrupole splitting associated with the putative oxoiron(IV) intermediates of FePyMAC complexes **2** and **6a** may be a general feature of the substantial electronic asymmetry in these complexes.

Table 5.6. Comparison of spin states and Mössbauer parameters for selected biomimetic Fe(II) and oxoiron(IV) complexes reported in the literature.[a]

Iron(II) Complexes	Spin state	δ (mm s^{-1})	$\|\Delta E_q\|$ (mm s^{-1})	Ref
6a	S = 2	1.01 (57 %)	3.47	This work
	S = 2	1.26 (43 %)	2.72	
6b	S = 2	1.03 (39 %)	3.56	This work
	S = 2	1.29 (61 %)	2.72	
$Fe(OTf)_2 \cdot 2CH_3CN$	-----	1.28	1.76	This work
$[FeL_1(Cl)]Cl$	S = 2	1.11	3.72	30
$[Fe(Me_6cyclam)(CH_3CO_2)_2]$	S = 2	1.07	4.07	37
$[Fe(TAAB)(CH_3CN)_2](ClO_4)_2$	S = 0	0.47	0.82	37
$[FeL_2(NCCH_3)_2](OTf)_2$ (**2**)	S = 0	0.50	0.78	17

Oxoiron(IV) Complexes				
6a−O	S = ?	0.24	2.41	This work
TauD	S = 2	0.31	−0.88	38a
$[Fe^{IV}(O)(H_2O)_5]^{2+}$	S = 2	0.38	−0.33	39
$[Fe^{IV}(O)(TMG_3tren)]^{2+}$	S = 2	0.09	−0.29	40
$[Fe(O)(TMC)(NCCH_3)]^{2+}$	S = 1	0.17	1.23	42
$[Fe^{IV}(O)(cyclam\text{-}Ac)]^{+}$	S = 1	0.01	1.37	41
$[Fe(O)(TMC\text{-}py)]^{2+}$	S = 1	0.18	1.08	42
$[Fe(O)(TMCS)]^{2+}$	S = 1	0.19	0.22	35
$[Fe(O)(N4Py)]^{2+}$	S = 1	−0.04	0.93	42
$[Fe(O)(TPA)(NCCH_3)]^{2+}$	S = 1	0.01	0.93	42
$[Fe(O)(TPA)(O_2CCF_3)]^{2+}$	S = 1	0.02	0.92	42
$[Fe(O)(BnTPEN)]^{2+}$	S = 1	0.01	0.87	35
2−O	S = 1	0.03	2.00	17

[a] See Appendix 5, Figure 5A.24 for depiction of structures.

5.4. Conclusion

In summary, we have prepared and characterized two novel Fe PyMAC catalysts that add to our family of structurally related complexes that differ in the identity of the axial donor, and have confirmed that this leads to dramatic differences in reactivity. We have found that complexes **5** and **6a** are superior epoxidation catalysts displaying some of the largest olefin TONs among related model complexes reported in the literature.[43] Distinct changes in the mechanism of oxidant activation are also observed, and work is still in progress to fully understand the nature of the active intermediate(s) in all FePyMAC systems.

With several members now included in the family of FePyMACs, we are able to observe some useful trends. For example, complex **5** is quite similar to **3** in that strong axial ligation and large displacements of iron from the macrocyclic plane shut down catalysis. Addition of external non-coordinating acids effectively remedies this situation,

and the presence of a nearby functional group that can potentially form hydrogen bonds with incoming oxidant molecules (i.e., peroxides) and/or participate in intramolecular proton transfers that facilitate peroxide O−O bond cleavage could easily explain the enhancement in reactivity over tetradentate PyMACs. This, however, does not fully explain the observed differences in reactivity noted for FePyMACs bearing pendant arms with similar hydrogen bonding properties (complexes **3**($+H^+$), **4**, **5**($+H^+$), **6a**), so other factors must be considered. The pendant arm can also modulate the spin state of the starting complexes,[12,18] and to some extent, Fe^{3+}/Fe^{2+} redox potentials. We note that the most active catalysts in the absence of additives, namely **6a** and **4**, contain non- or weakly coordinating groups in the pendant arm, have ionizable protons, and display spin equilibria in acetonitrile solutions.

It has also become clear that the carboxylic acid functionality is unique. The protonation state of the pendant arm in **6**, as well its role in oxoiron(IV) generation and reactivity still needs to be sorted out, but it is expected to be of significance. The role(s) of carboxylic acid in such reactions is well documented in the literature, where it is proposed to facilitate peroxide O−O bond heterolysis to generate active Fe(V) oxo intermediates in biomimetic non-heme systems with *cis*-labile sites,[34,43b] including the prominent Fe(BPMEN) and Fe(TPA) complexes. The addition of acetic acid to these reactions has been shown to lead to enhanced selectivity for epoxide products. Although our FePyMAC ligand topology is different, the carboxylic proton of **6a** perhaps offers the same effect as coordinated AcOH does for complexes containing *cis*-labile sites. Another possibility includes the *in situ* formation of peracetic acid,[44] which may explain the enhanced activity noted for **6a**.

On the other hand, we find that addition of non-coordinating strong acids like HOTf also improve reactivity for all FePyMAC complexes, even **6a**, which implies that the role of acid in these systems is complex; it does not only serve as a proton source for pendant arm protonation (and dissociation) as was observed for complex **3**. Additional acid promoted one-electron pathways lead to efficient olefin oxidation, but it is coupled with oxidation of the macrocyclic ligands.[13,18]

Stopped-flow experiments with **6a** reveal a complicated mechanisms of oxidant activation. Reactions with H_2O_2 hint at the involvement of radicals, though the observed selectivities in epoxidation reactions argue against them being the predominant active species. Although an oxoiron(IV) intermediate is detected spectrophotometrically, it forms alongside multiple other unidentified components which makes its reactivity difficult to assess for the catalytically relevant system. However, preliminary attempts suggest that this intermediate is, in fact, not the active species and may instead be a decay product that is generated upon reaction of the active species with substrate.

By using isopropyl 2-iodoxybenzoate as the terminal oxidant, an oxoiron(IV) intermediate of **6a** can be observed to form in a relatively clean reaction, allowing us to kinetically investigate the reactivity of this species towards cyclooctene. This intermediate, however, does not seem to react with substrate, which is in contrast to our previous studies with related complexes **2** and **3**. However, this is consistent with the observations noted in reactions with hydrogen peroxide, and ultimately suggests that a different intermediate that is generated in reactions of **6a** with oxidants can react with olefins and/or decompose into an oxoiron(IV) intermediate. Additional experiments are

planned to gain insight into the nature of the active oxidizing species in reactions with complex **6**.

Mössbauer studies have confirmed thus far that solid samples of complex **6** contains two distinct high-spin ferrous components, which are presumed to differ only in protonation state of the pendant carboxylic group (and possibly coordination number at the metal center). An intriguing finding from this work is the possibility that a high-spin oxoiron(IV) intermediate is generated from reactions of **6a** with ^{i}Pr-IBX; if this is confirmed, it would be of interest to understand why such an intermediate does not appear to be active towards substrate oxygenation, since $S = 2$ oxoiron(IV) species are predicted to be more reactive than their low-spin, $S = 1$ counterparts.[45] On the other hand, it appears that this difference in spin states for biomimetic non-heme iron oxo complexes does not lead to significant changes in reactivity for reasons that are not yet well understood.[46]

Additional experimental and computational studies are in progress towards the goal of obtaining a complete understanding of oxidant activation and OAT reactions in the FePyMAC systems.

5.5. References

(1) (a) Kovaleva, E. G.; Lipscomb, J. D. *Nat. Chem. Biol.*, **2008**, *4*, 186. (b) Hohenberger, J.; Ray, K.; Meyer, K. *Nat. Commun.*, **2012**, *3*, 720.

(2) (a) Denisov, I. G.; Makris, T. M.; Sligar, S. G.; Schlichting, I. *Chem. Rev.*, **2005**, *105*, 2253. (b) Watanabe, Y.; Nakajima, H.; Ueno, T. *Acc. Chem. Res.*, **2007**, *40*, 554. (c) Nam, W. *Acc. Chem. Res.*, **2007**, *40*, 522.

(3) Rittle, J.; Green, M. T. *Science*, **2010**, *330*, 933.

(4) Krebs, C.; Fujimori, D. G.; Walsh, C. T.; Bollinger, J. M. *Acc. Chem. Res.*, **2007**, *40*, 484.

(5) Burger, R. M. Nature of Activated Bleomycin. *Struct. Bond.*, **2000**, *97*, 287.

(6) (a) Decker, A.; Chow, M. S.; Kemsley, J. N.; Lehnert, N.; Solomon, E. I. *J. Am. Chem. Soc.*, **2006**, *128*, 4719. (b) Chow, M. S.; Liu, L. V.; Solomon, E. I. *Proc. Natl. Acad. Sci.*, **2008**, *105*, 13241.

(7) (a) Murugesan, N.; Hecht, S. M. *J. Am. Chem. Soc.*, **1985**, *107*, 493. (b) Hecht, S. M. *Acc. Chem. Res.*, **1986**, *19*, 383. (c) Heimbrook, D. C.; Carr, S. A.; Mentzer, M. A.; Long, E. C.; Hecht, S. M. *Inorg. Chem.*, **1987**, *26*, 3835.

(8) Valentine, A. M.; Stahl, S. S.; Lippard, S. J. *J. Am. Chem. Soc.*, **1999**, *121*, 3876.

(9) Kryatov, S. V.; Rybak-Akimova, E. V.; Schindler, S. *Chem. Rev.*, **2005**, *105*, 2175.

(10) Shan, X.; Que, Jr., L. *J. Inorg. Biochem.*, **2006**, *100*, 421.

(11) (a) White, M. C.; Doyle, A. G.; Jacobsen, E. N. *J. Am. Chem. Soc.*, **2001**, *123*, 7194. (b) Ryu, J. Y.; Kim, J.; Costas, M.; Chen, K.; Nam, W.; Que, L., Jr. *Chem. Commun.*, **2002**, *12*, 1288.

(12) Taktak, S.; Ye, W.; Herrera, A. M.; Rybak-Akimova, E. V. *Inorg. Chem.*, **2007**, *46*, 2929.

(13) Latifi, R.; Palluccio, T. D.; Ye, W.; Rybak-Akimova, E. V.; Quesne, M. G.; deVisser, S. P. Effect of Appended Aminopropyl Functionality in Aminopyridine Macrocyclic Iron(IV) Oxo Systems. *Manuscript in Preparation*.

(14) Liao, M.; Huang, M.; Watts, J. D. *J. Phys. Chem. A*, **2010**, *114*, 9554.

(15) de Visser, S. P.; Latifi, R.; Tahsini, L.; Wonwoo Nam, W. *Chem. Asian J.*, **2011**, *6*, 493.

(16) (a) Karn, J. L.; Busch, D. H. *Inorg.Chem.*, **1969**, *8*, 1149. (b) Herrera, A. M.; Staples, R. J.; Kryatov, S. V.; Nazarenko, A. Y.; Rybak-Akimova, E. V. *Dalton Trans.*, **2003**, 846. (c) Organo, V. G.; Filatov, A. S.; Quartararo, J. S.; Friedman, Z. M.; Rybak-Akimova, E. V. *Inorg. Chem.*, **2009**, *48*, 8456.

(17) Ye, W.; Ho, D. M.; Friedle, S.; Palluccio, T. D.; Rybak-Akimova, E. V. *Inorg.Chem.*, **2012**, *51*, 5006.

(18) Ye, W. Iron(II) Aminopyridine Macrocycles in Catalytic Oxidations: Structures, Reactivity, and Mechanistic Studies of Reactive Intermediates. Ph.D. Thesis, Tufts University, 2011.

(19) (a) Evans, D. F. *J. Chem. Soc.*, **1959**, 2003. (b) Sur, S. K. *J. Magn. Reson.*, **1989**, *82*, 169. (c) Piguet, C. *J. Chem. Educ.*, **1997**, *74*, 815.

(20) Girerd, J. J.; Journaux, Y. In *Physical Methods in Bioinorganic Chemistry*; Que, Jr., L., Ed.; University Science Books: Sausalito, CA, 2000; pp. 321-374.

(21) SAINT, Version 7.46A; Bruker AXS, Inc.: Madison, WI, 2001.

(22) SADABS; Bruker AXS, Inc.: Madison, WI, 2001.

(23) (a) Sheldrick, G. M. SHELXTL, Bruker AXS, Inc.: Madison, WI. (b) Sheldrick, G. M. *Acta Crystallogr. A64*, **2008**, *64*, 112.

(24) Müller, P.; Herbst-Irmer, R.; Spek, A. L.; Schneider, T. R.; Sawaya, M. R. *Crystal Structure Refinement: A Crystallographer's Guide to SHELXL*. IUCr Texts on Crystallography; Oxford University Press: Oxford, 2006.

(25) Zhdankin, V. V.; Koposov, A. Y.; Litvinov, D. N.; Ferguson, M. J.; McDonald, R.; Luu, T.; Tykwinski, R. R. *J. Org. Chem.*, **2005**, *70*, 6484.

(26) Rusnak, L.; Jordan, R. B. *Inorg. Chem.*, **1971**, *10*, 2199.

(27) Silverstein, R. M.; Webster, F. X.; Kiemle, D. J. *Spectrometric Identification of Organic Compounds*, 7th Ed.; John Wilet & Sons, Inc.: Hoboken, 2005.

(28) Kaden, T. A. *Pure Appl. Chem.*, **1993**, *65*, 1477.

(29) (a) Spiccia, L.; Fallon, G. D.; Grannas, M. J.; Nichols, P. J.; Tiekink, E. R. T. *Inorg. Chim. Acta*, **1998**, *279*, 192. (b) Mialane, P.; Nivorojkine, A.; Pratviel, G.; Azema, L.; Slany, M.; Godde, F.; Simaan, A.; Banse, F.; Kargar-Grisel, T.; Bouchoux, G.; Sainton, J.; Horner, O.; Guilhem, J.; Tchertanova, L.; Meunier, B.; Girerd, J. J. *Inorg. Chem.*, **1999**, *38*, 1085. (c) Goldsmith, C. R.; Jonas, R. T.; Cole, A. P.; Stack, T. D. P. *Inorg.Chem.*, **2002**, *41*, 4642.

(30) Merrell, P. H.; Goedken, V. L.; Busch, D. H. *J. Am. Chem. Soc.*, **1970**, *92*, 7590.

(31) Riley, D. P.; Merrell, P. H.; Stone, J. A.; Busch, D. H. *Inorg. Chem.*, **1975**, *14*, 490.

(32) Balland, V.; Banse, F.; Anxolabehere-Mallart, E.; Ghiladi, M.; Mattioli, T. A.; Philouze, C.; Blondin, G.; Girerd, J. J. *Inorg. Chem.*, **2003**, *42*, 2470.

(33) Lane, B. S.; Burgess, K. *Chem. Rev.*, **2003**, *103*, 2457.

(34) White, M. C.; Doyle, A. G.; Jacobsen, E. N. *J. Am. Chem. Soc.*, **2001**, *123*, 7194.

(35) Que, L., Jr. *Acc. Chem. Res.*, **2007**, *40*, 493.

(36) (a) Jensen, M. P.; Lange, S. J.; Mehn, M. P.; Que, E. L.; Que, L., Jr. *J. Am. Chem. Soc.*, **2003**, *125*, 2113. (b) Zang, Y.; Kim, J.; Dong, Y. H.; Wilkinson, E. C.; Appelman, E. H.; Que, L., Jr. *J. Am. Chem. Soc.*, **1997**, *119*, 4197. (c) Kim, J.;

Zang, Y.; Costas, M.; Harrison, R. G.; Wilkinson, E. C.; Que, L., Jr. *J. Biol. Inorg. Chem.*, **2001**, *6*, 275. (d) Wada, A.; Ogo, S.; Watanabe, Y.; Mukai, M.; Kitagawa, T.; Jitsukawa, K.; Masuda, H.; Einaga, H. *Inorg. Chem.*, **1999**, *38*, 3592. (e) Ogihara, T.; Hikichi, S.; Akita, M.; Uchida, T.; Kitagawa, T.; Moro-oka, Y. *Inorg. Chim. Acta*, **2000**, *297*, 162. (f) Gosiewska, S.; Permentier, H. P.; Bruins, A. P.; van Koten, G.; Gebbink, R. J. M. *Dalton Trans.*, **2007**, *31*, 3365. (g) Jensen, M. P.; Costas, M.; Ho, R. Y. N.; Kaizer, J.; Payeras, A. M. I.; Münck, E.; Que, L., Jr.; Rohde, J. U.; Stubna, A. *J. Am. Chem. Soc.*, **2005**, *127*, 10512. (h) Bukowski, M. R.; Halfen, H. L.; van den Berg, T. A.; Halfen, J. A.; Que, L., Jr. *Angew. Chem., Int. Ed.*, **2005**, *44*, 584.

(37) Dabrowiak, J. C.; Merrell, P. H.; Stone, J. A.; Busch, D. H. *J. Am. Chem. Soc.*, **1973**, *95*, 6613.

(38) (a) Price, J. C.; Barr, E. W.; Tirupati, B.; Bollinger, Jr., J. M.; Krebs, C. *Biochemistry*, **2003**, *42*, 7497. (b) Hoffart, L. M.; Barr, E. W.; Guyer, R. B.; Bollinger, Jr., J. M.; Krebs, C. *Proc. Natl. Acad. Sci. USA*, **2006**, *103*, 14738. (c) Eser, B. E.; Barr, E. W.; Frantom, P. A.; Saleh, L.; Bollinger, Jr., J. M.; Krebs, C.; Fitzpatrick, P. F. *J. Am. Chem. Soc.*, **2007**, *129*, 11334. (d) Galonic, D. P. Barr, E. W.; Walsh, C. T.; Bollinger, Jr., J. M.; Krebs, C. *Nat. Chem. Biol.*, **2006**, *3*, 113.

(39) Pestovsky, O.; Stoian, S.; Bominaar, E. L.; Shan, X.; Münck, E.; Que, Jr., L. Bakac, A. *Angew. Chem. Int. Ed.*, **2005**, *44*, 6871.

(40) England, J.; Martinho, M.; Farquhar, E. R.; Frisch, J. R.; Bominaar, E. L.; Münck, E.; Que, Jr., L. *Angew. Chem. Int. Ed.*, **2009**, *48*, 3622.

(41) Grapperhaus, C. A.; Mienert, B.; Bill, E.; Weyhermüller, T.; Wieghardt, K. *Inorg. Chem.*, **2000**, *39*, 5306.

(42) McDonald, A. R.; Guo, Y.; Vu, V. V.; Bominaar, E. L.; Münck, E.; Que, Jr., L. *Chem. Sci.*, **2012**, *3*, 1680 and references therein.

(43) (a) Oldenurg, P. D.; Que, Jr., L. *Catal. Today*, **2006**, *117*, 15. (b) Mas-Ballesté, R.; Que, Jr., L. *J. Am. Chem. Soc.*, **2007**, *129*, 15964.

(44) (a) Fujita, M.; Que, Jr., L., *Adv. Synth. Cat.*, **2004**, *346*, 190. (b) Dubois, G.; Murphy, A.; Stack, T. D. P. *Org. Lett.*, **2003**, *5*, 2469.

(45) Janardanan, D.; Wang, Y.; Schyman, P.; Que, Jr., L.; Shaik, S. *Angew. Chem. Int. Ed.*, **2010**, *49*, 3342.

(46) Nam, W.; Lee, Y. M.; Fukuzumi, S.; *Acc. Chem. Res.*, **2014**, *47*, 1146.

APPENDIX 5

H_2O_2 Activation by Biomimetic Non-Heme Ferrous Complexes Supported by Aminopyridine Macrocycles Bearing a Functionalized Pendant Arm

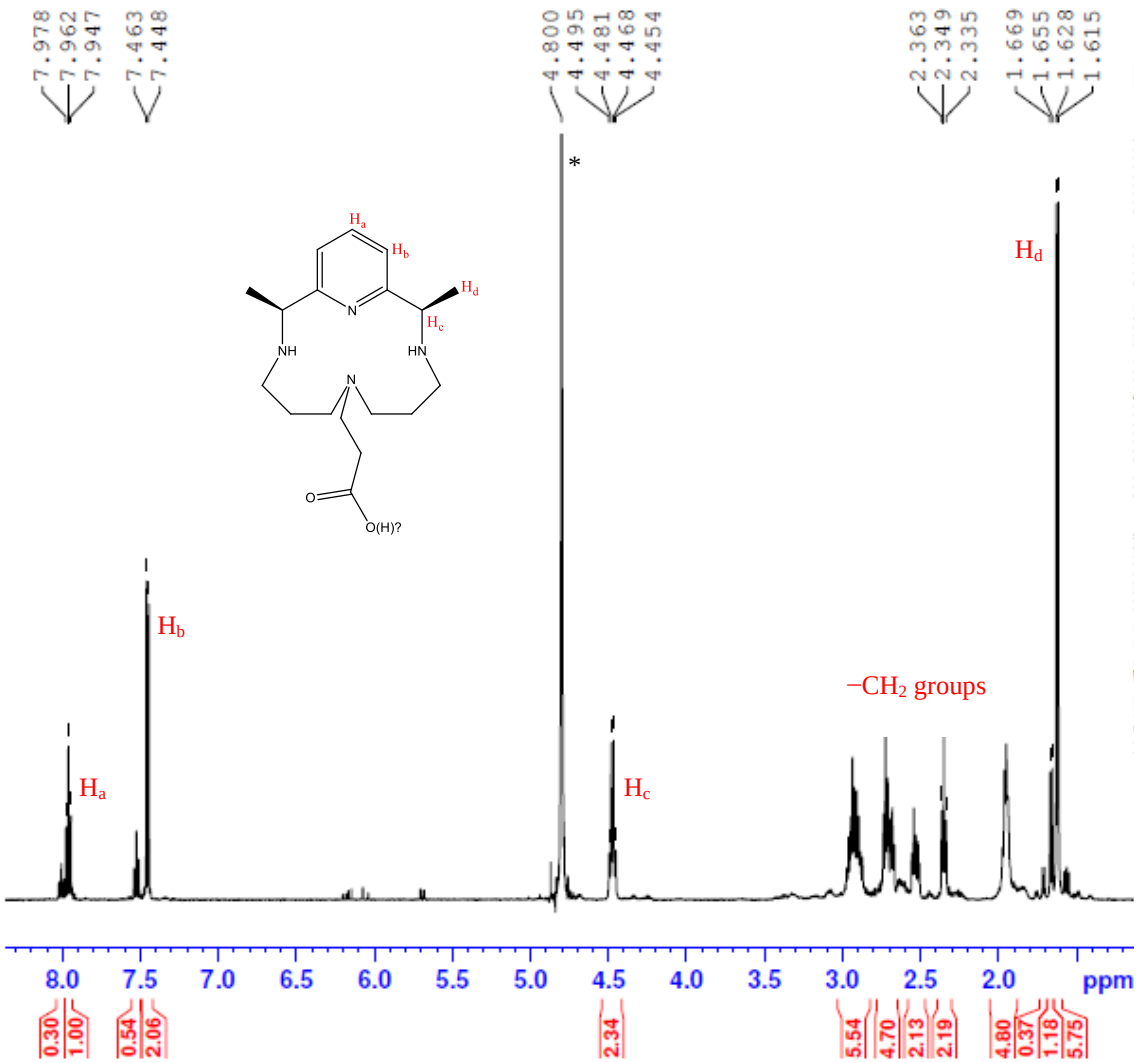

Figure 5A.1. 500 MHz ^{1}H NMR spectrum of L_{6a} in D_2O. Asterisk denotes solvent peak.

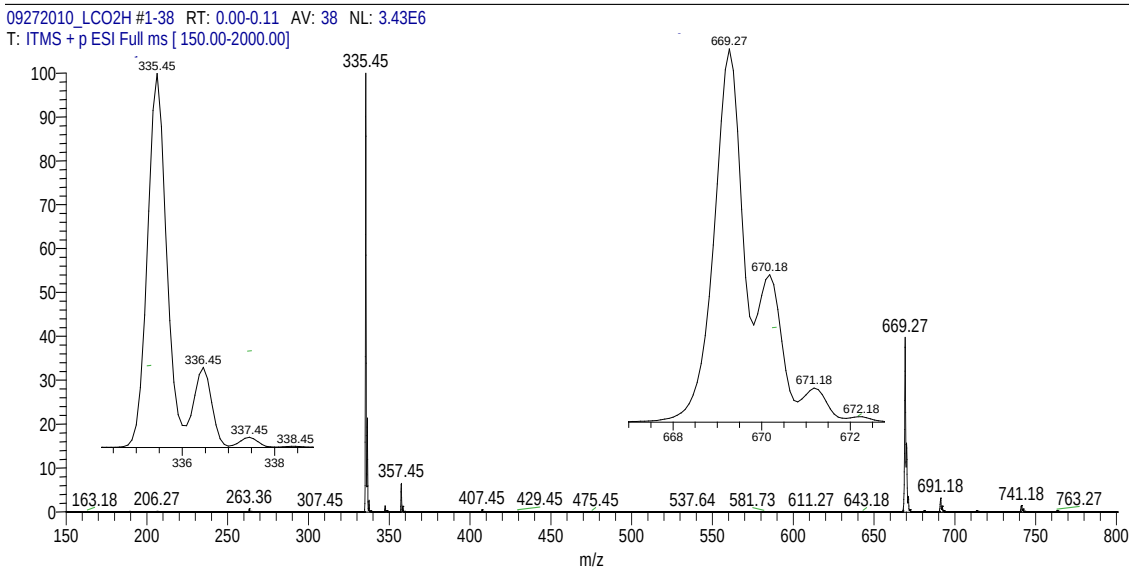

Figure 5A.2. ESI-MS (+) of L_{6a} in MeOH:H_2O (1:1). The ESI-MS is identical to that of L_{6b}. *m/z* = 669.09 ({$(L_{6a})_2$ + H^+}$^+$, 48 %); 357.36 ({L_{6a} + Na^+}$^+$, 21 %); 335.36 ({L_{6a} + H^+}$^+$, 100 %).

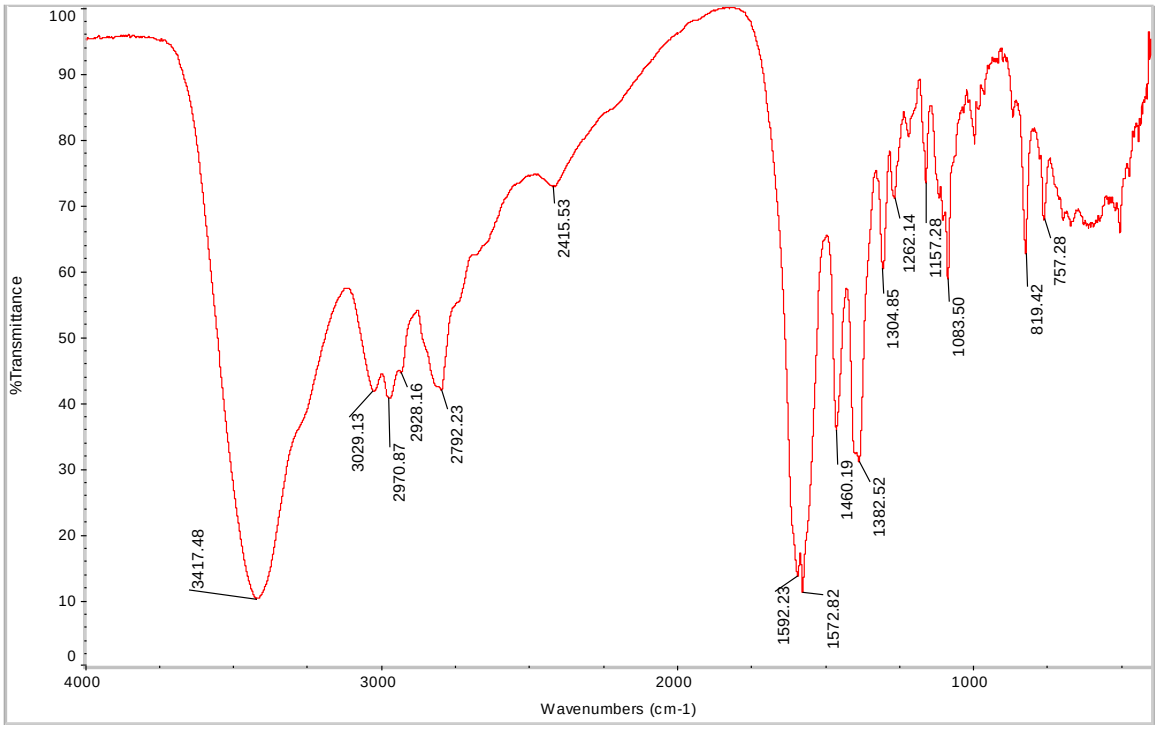

Figure 5A.3. FT-IR spectrum of L_{6a}.

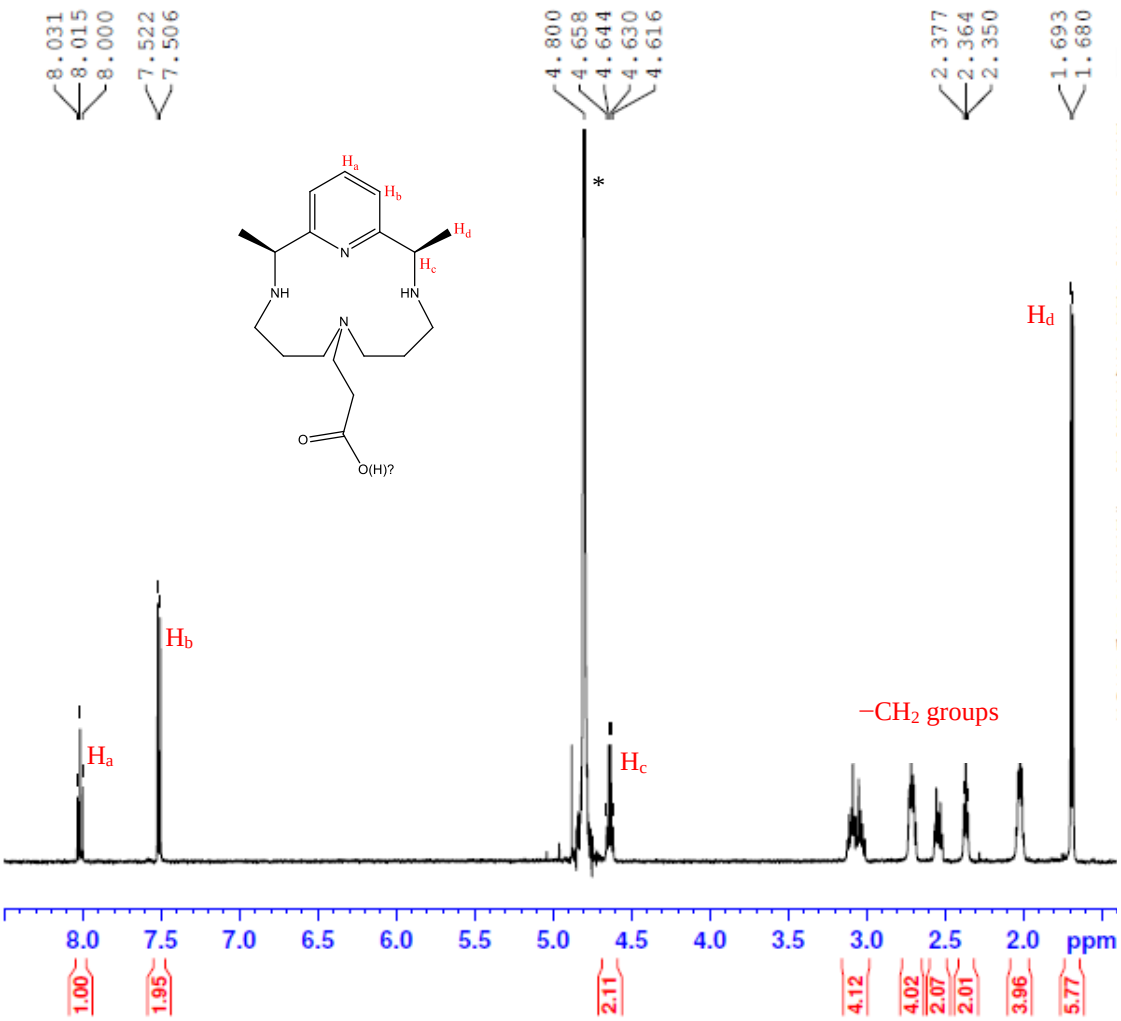

Figure 5A.4. 500 MHz ^{1}H NMR spectrum of L_{6b} in D_2O. Asterisk denotes solvent peak.

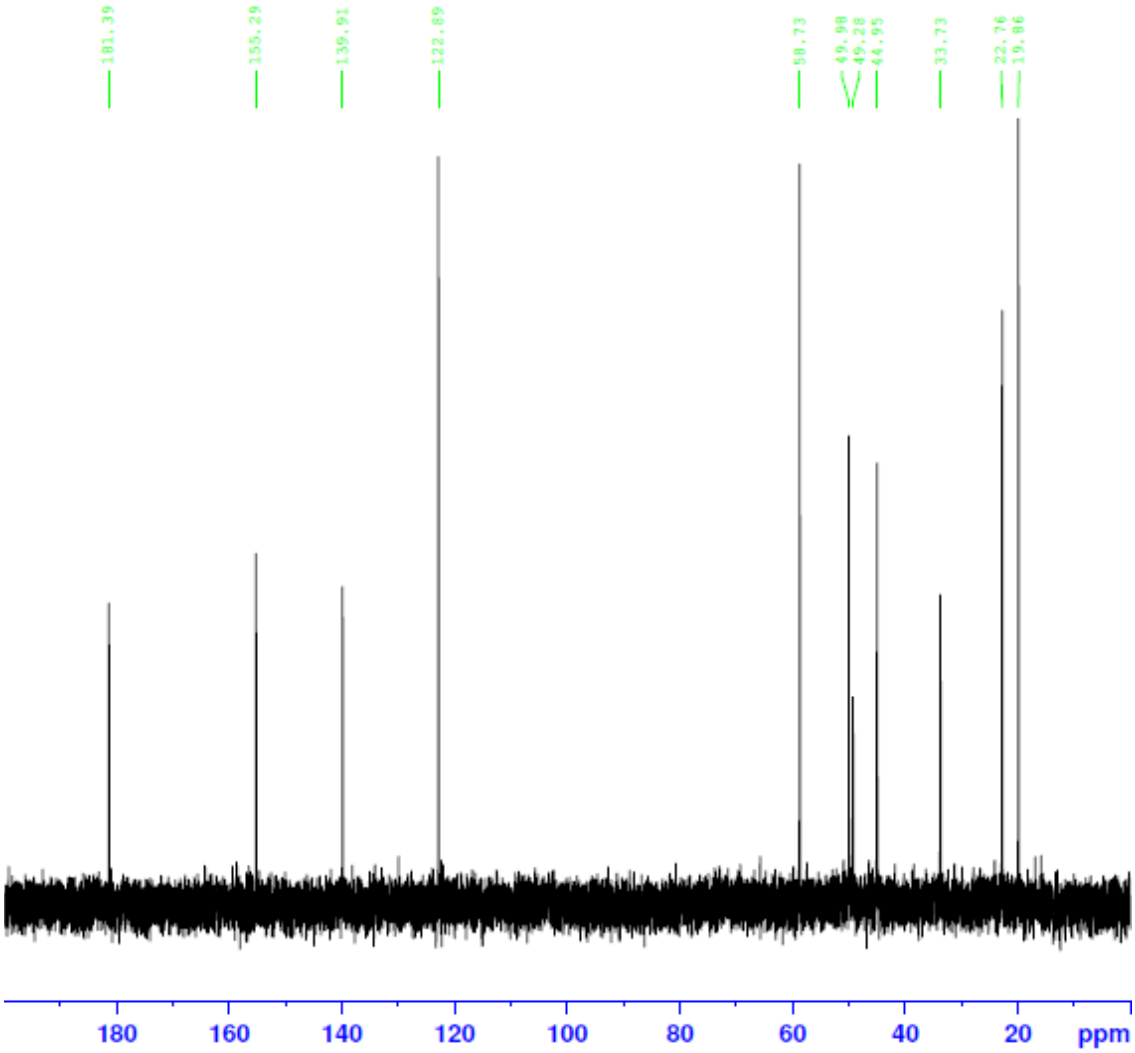

Figure 5A.5. 500 MHz ^{13}C NMR spectrum of L_{6b} in D_2O.

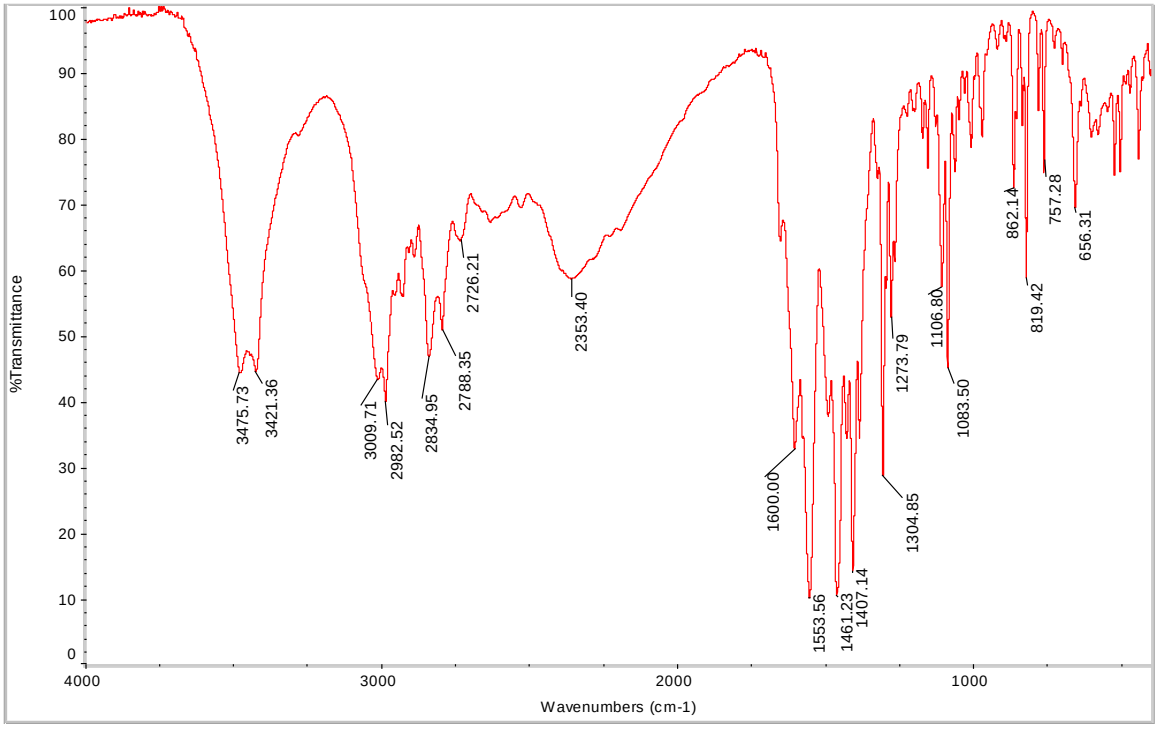

Figure 5A.6. FT-IR spectrum of L_{6b}.

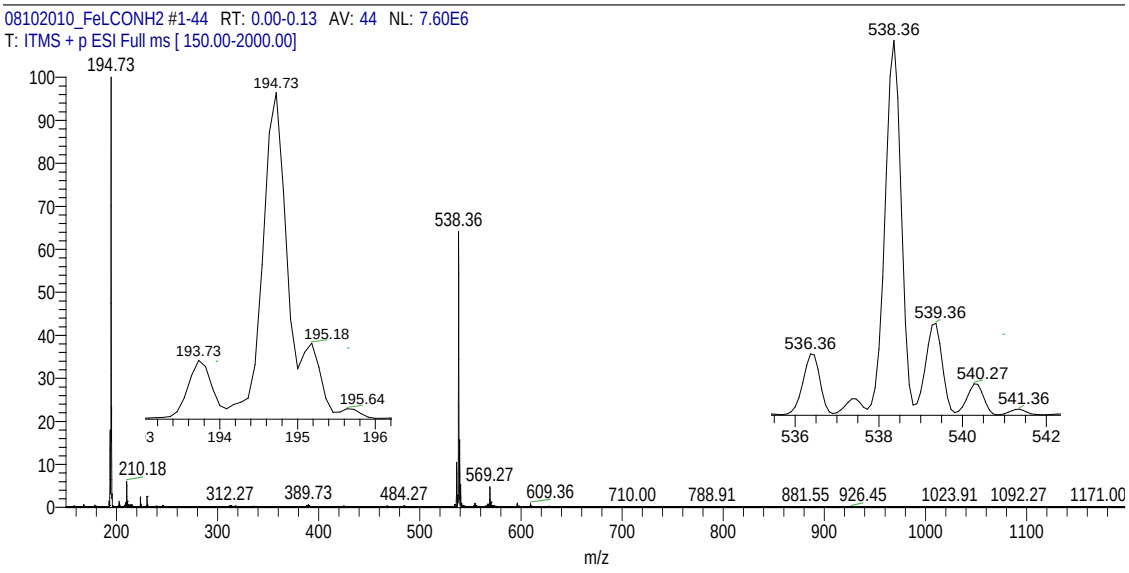

Figure 5A.7. ESI-MS (+) of **5** in CH_3CN; *m/z* = 538.09 ($\{FeL_5(OTf)\}^+$, 80 %); 194.55 ($\{FeL_5\}^{2+}$, 100 %).

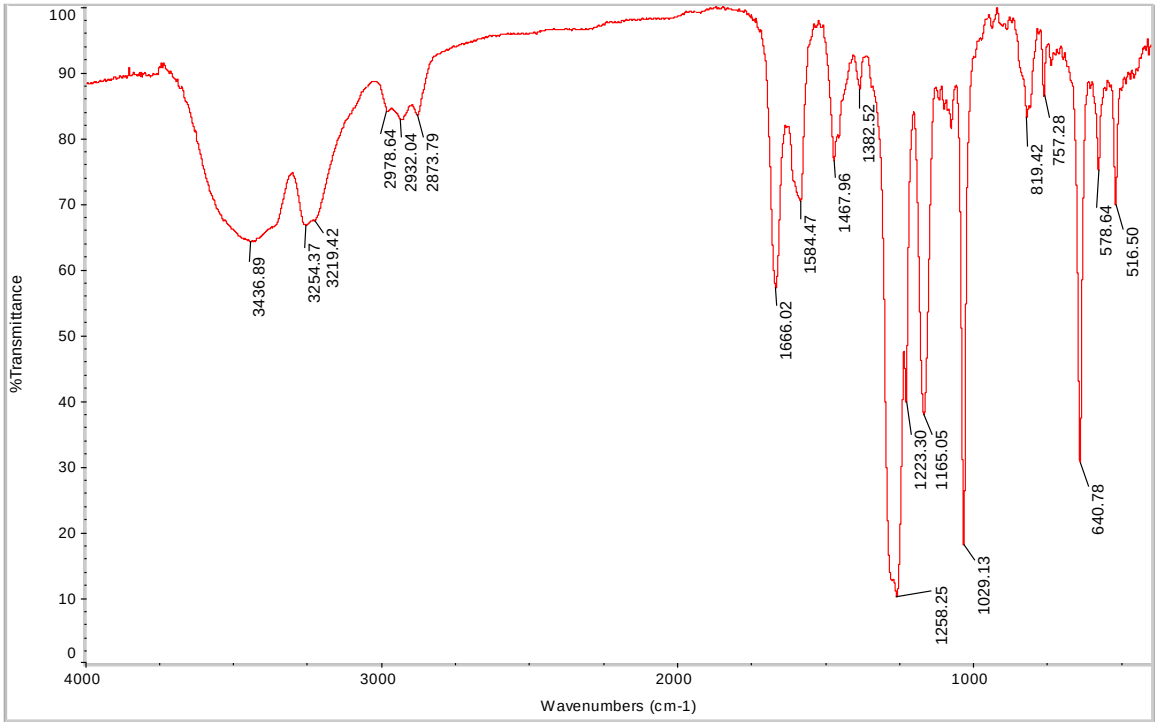

Figure 5A.8. FT-IR spectrum of **5**.

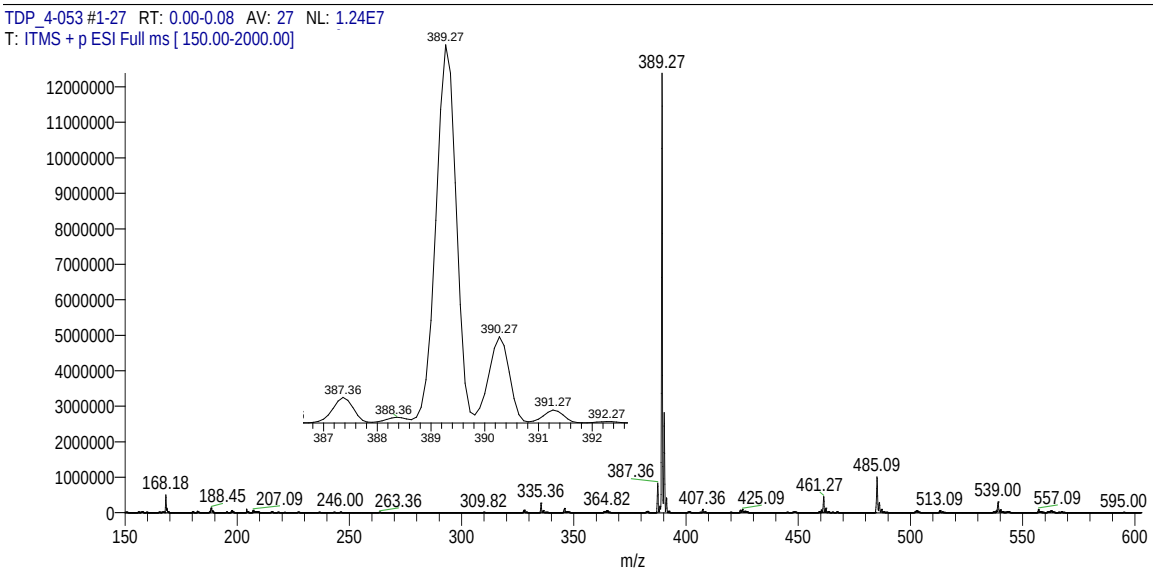

Figure 5A.9. ESI-MS (+) of **6a** in CH_3CN; *m/z* = 389.27 ($\{FeL_{6a} - H\}^+$, 100 %).

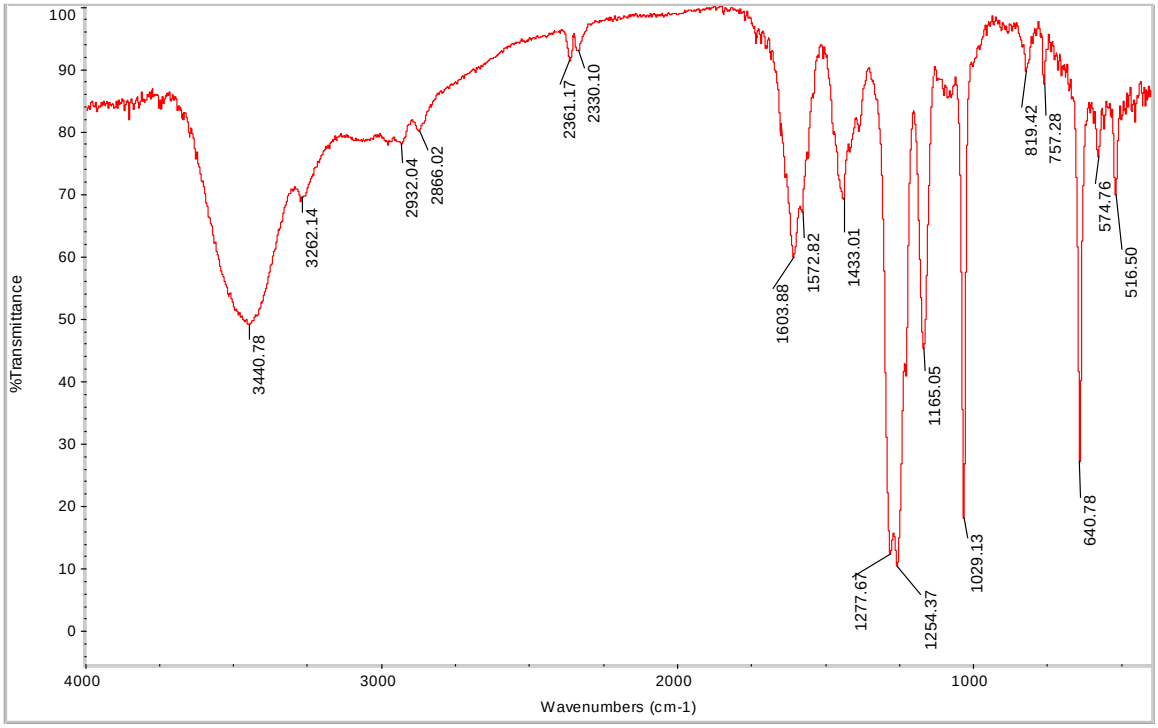

Figure 5A.10. FT-IR spectrum of **6a**. The bands near 2300 cm^{-1} are from incomplete purging of atmospheric CO_2.

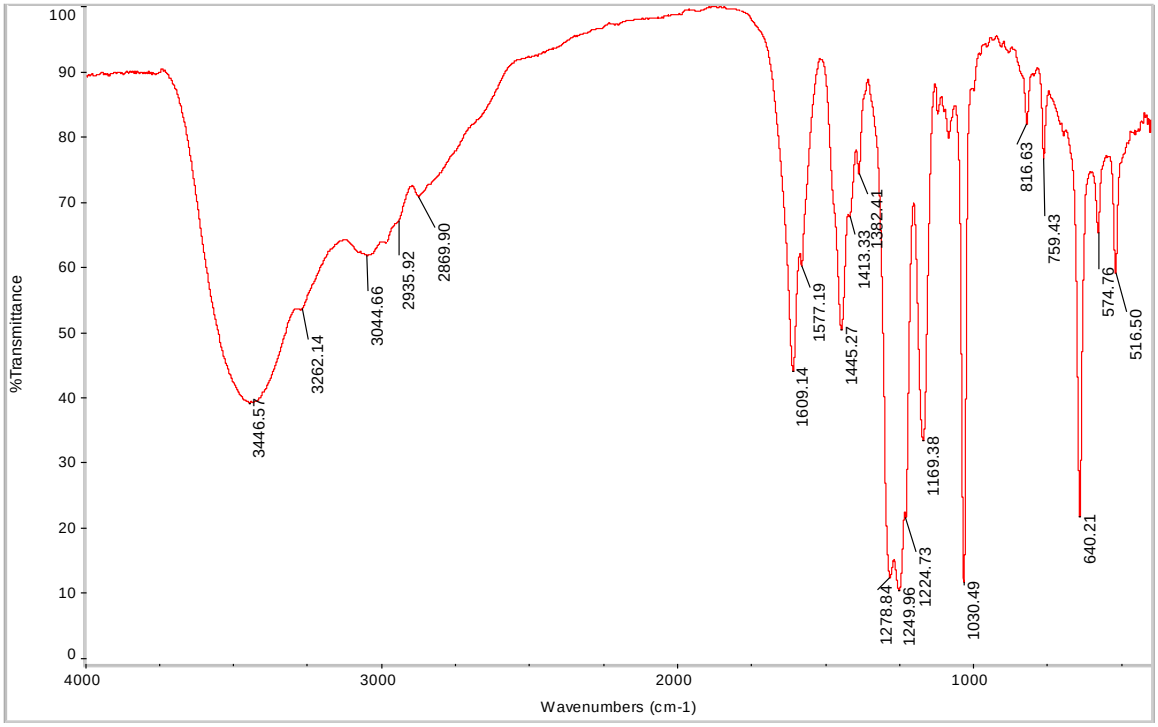

Figure 5A.11. FT-IR spectrum of **6b**.

5.3.3. Characterization

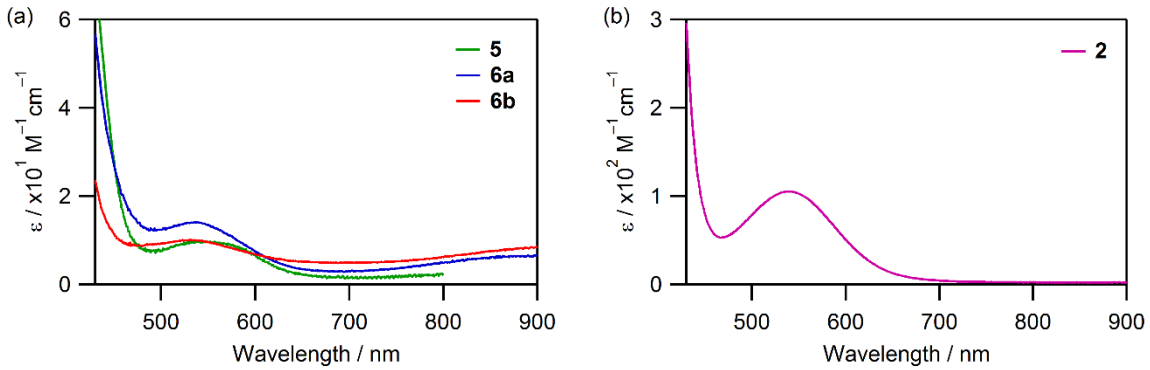

Figure 5A.12. (a) Overlay of UV-visible spectra of **5** (approx.1 mM), **6a** (3 mM), and **6b** (6 mM) in MeCN at −20 °C (**6a**, **6b**) or ambient temperature (**5**). For comparison, a UV-visible spectrum of **2** (3 mM) at +10 °C is shown in (b).

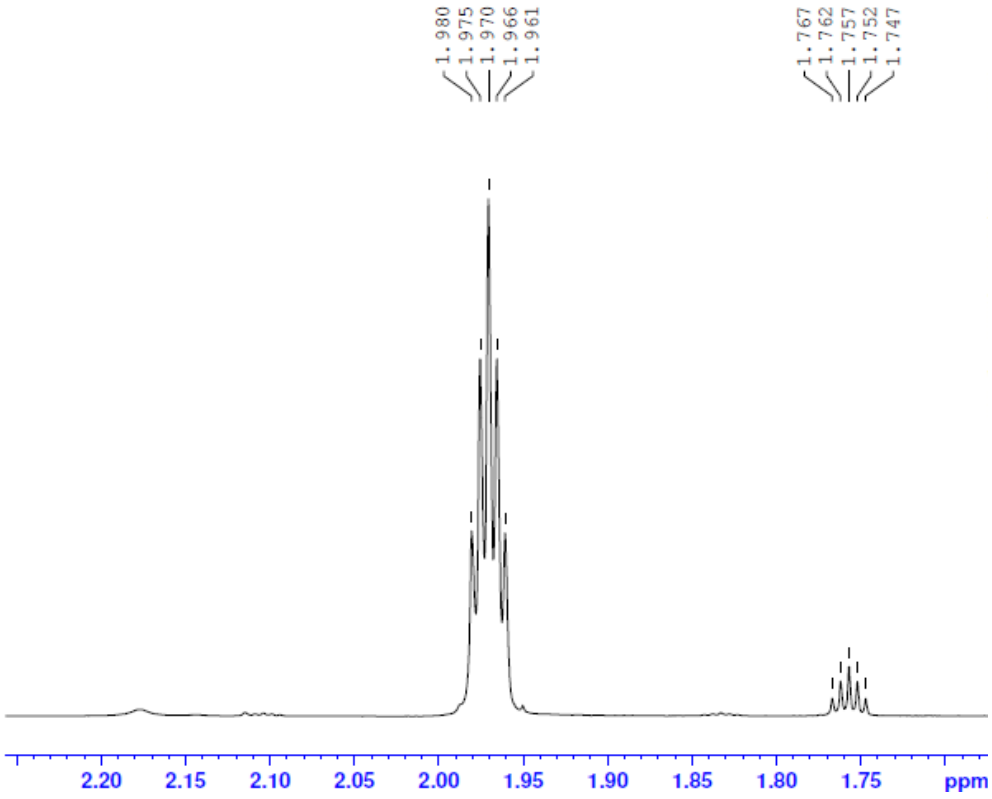

Figure 5A.13. ^{1}H NMR of CD_3CN shifts (Evans method) in the presence of complex **5** (3.6 mM). Signals at δ = 1.970 and 1.757 ppm were used to calculate μ_{eff}.

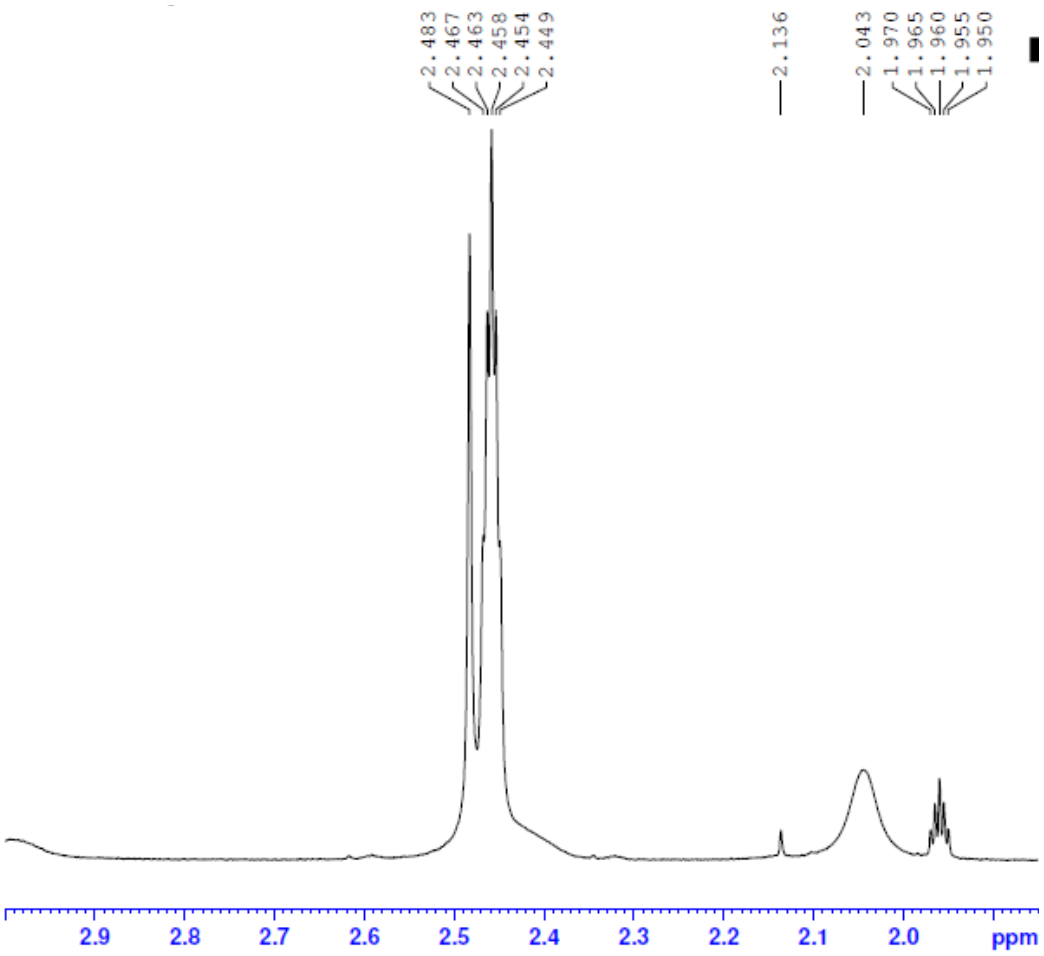

Figure 5A.14. 500 MHz ^{1}H NMR shifts of CD_3CN noted for complex **6b** (10 mM) in the absence HOTf. The center peak of the CD_3CN signals were used in calculations, with the pure solvent referenced at δ = 1.960 ppm. Some free ligand is present in the mixture but does not interfere with the measurement.

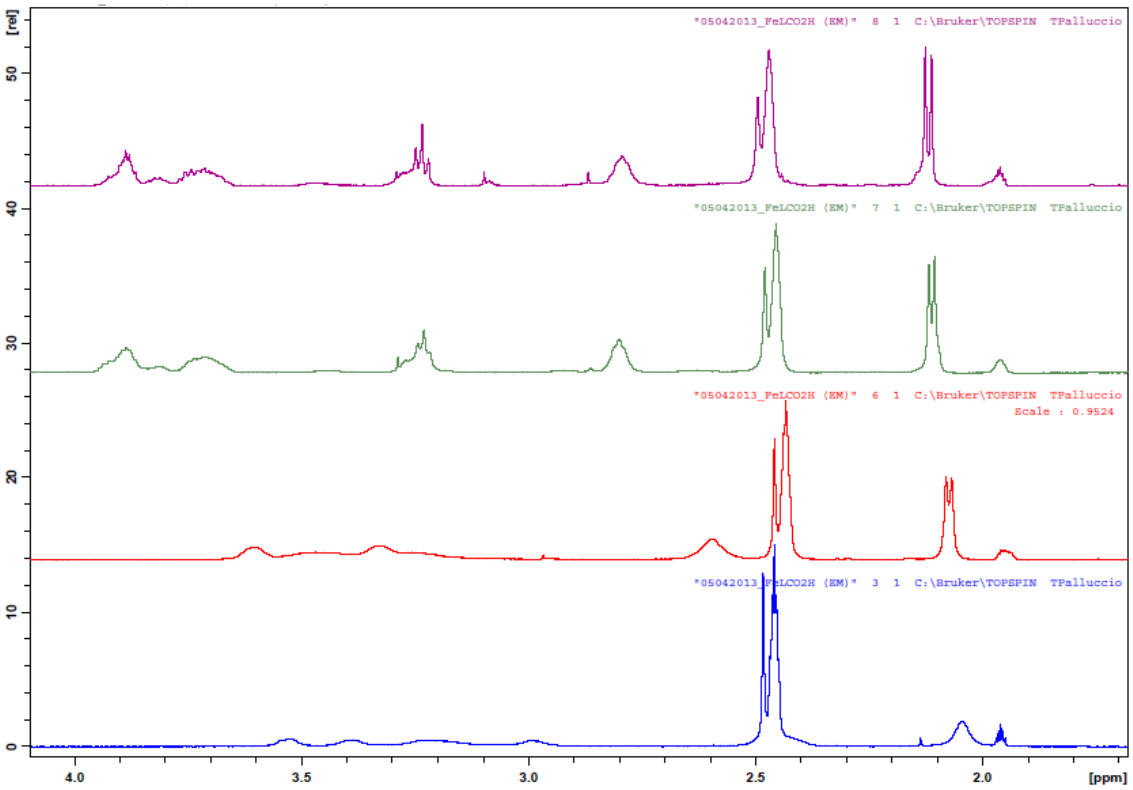

Figure 5A.15. 500 MHz ^{1}H NMR shifts of CD_3CN noted for **6b** (10 mM) in the absence and presence of HOTf. No acid, blue spectrum; 1 eq. HOTf, red; 2 eq. HOTf, green; 5 eq. HOTf, purple. The center peak of the CD_3CN signals were used in calculations, with the pure solvent referenced at δ = 1.960 ppm. Some free ligand is present in the mixture but does not interfere with the measurement.

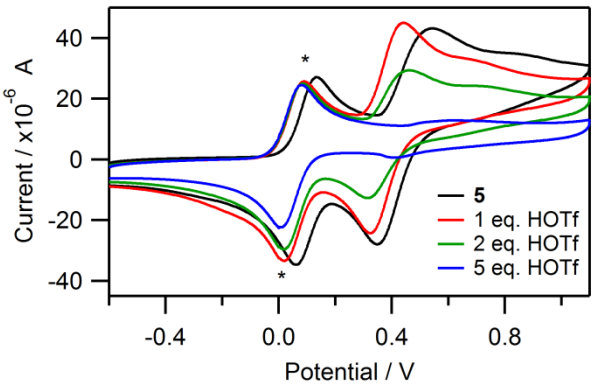

Figure 5A.16. Overlay of cyclic voltammograms for **5** in the absence and presence of HOTf (1, 2, or 5 eq.). Asterisks denote the Fc^{+}/Fc^{0} couple.

5.3.5. Stopped-Flow Kinetics

5.3.5.1. Formation of Oxoiron(IV) Intermediates

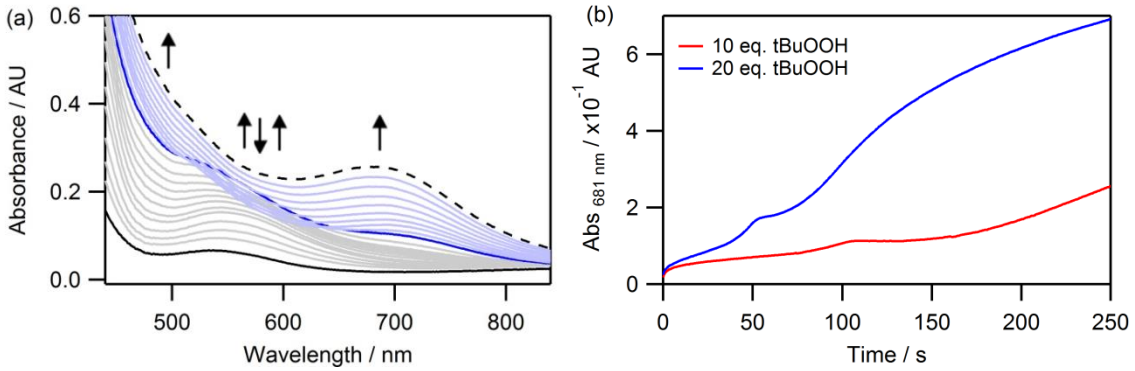

Figure 5A.17. (a) Time-resolved spectral changes observed for the reaction between **6a** (3 mM) with 10 eq. ^{t}BuOOH (30 mM) at −35 °C in MeCN, acquired over 250 s. Selected traces are shown for clarity. The first stage of the reaction is characterized by growth in absorbance across the entire spectral window (gray traces), with a broad band ($\lambda_{max} \approx 550$ nm) reaching maximum accumulation within 100 s (dark blue trace). This is followed by production of a prominent band centered near $\lambda = 681$ nm (light blue traces). The initial and final spectra are shown as solid black and dashed black lines, respectively. (b) Overlay of kinetic traces at $\lambda = 681$ nm as a function of [^{t}BuOOH].

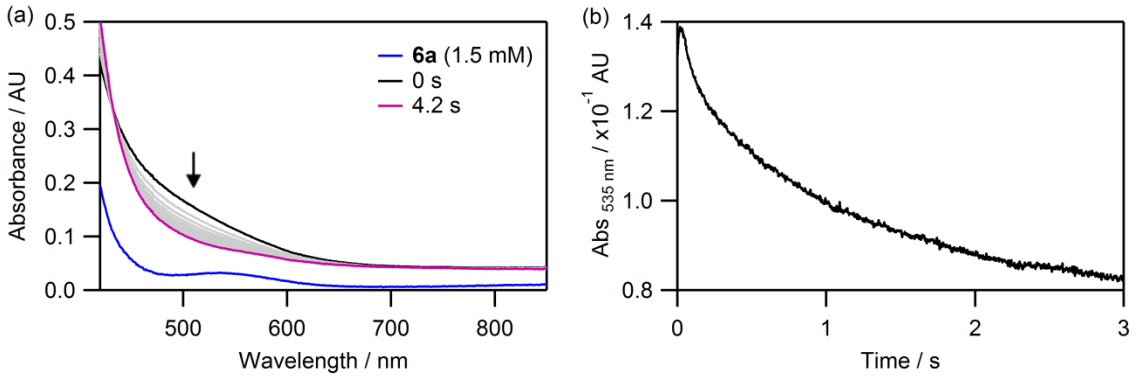

Figure 5A.18. (a) Time-resolved spectral changes accompanying the reaction between **6a** (1.5 mM) and 12 eq. ^{i}Pr-IBX (18 mM) at −40 °C highlighting the first 4.2 s of reaction, where initial rapid decay in absorbance is observed. Initial spectrum is shown in black and 4.2 s spectrum in purple. For comparison, the spectrum of **6a** is shown in blue. (b) Kinetic trace at $\lambda = 535$ nm.

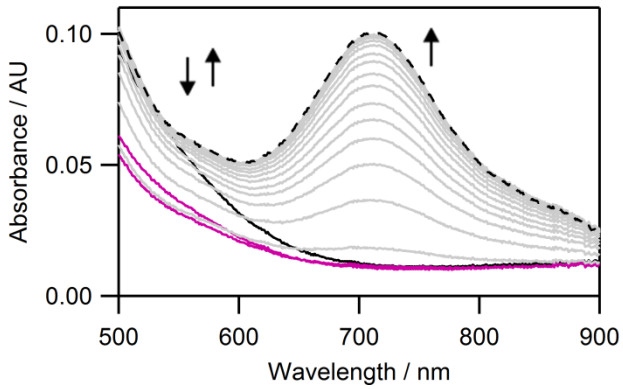

Figure 5A.19. Time-resolved spectral changes observed for the reaction between **6a** (1.5 mM) and 12 eq. ^{i}Pr-IBX (18 mM) at −20 °C in MeCN acquired over 150 s. Selected traces are shown for clarity. The initial spectrum is shown as a solid black line. Rapid decay is observed within the first 300 ms of reaction (purple traces) and is followed by an increase in absorbance with formation of the oxoiron(IV) intermediate ($\lambda_{max} \approx 709$ nm) whose accumulation is shown in gray. The final spectrum is shown as a dashed black line.

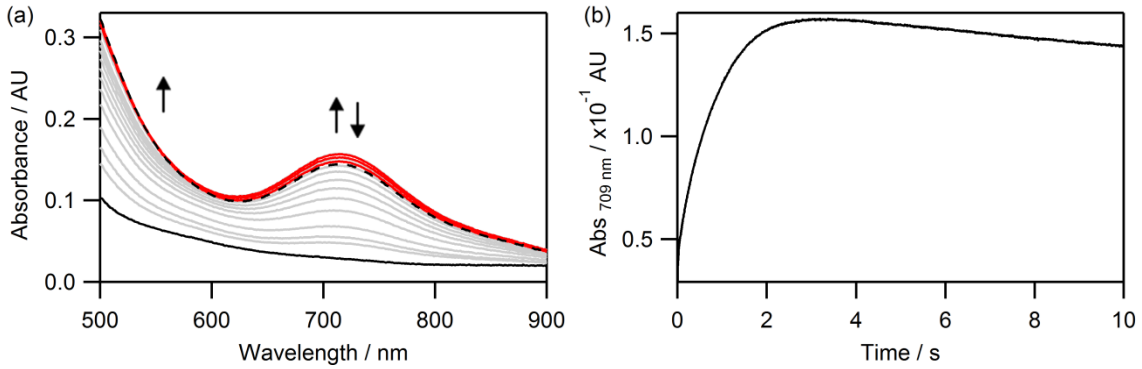

Figure 5A.20. (a) Time-resolved spectral changes observed for the reaction between **6a** (3 mM) and 1 eq. ^{i}Pr-IBX (3 mM) at 10 °C in MeCN acquired over 10 s. Selected traces are shown for clarity. The initial spectrum is shown as a solid black line and gray traces denote accumulation of the oxoiron(IV) intermediate. This is followed by slow self-decay (red traces) ultimately ending with the dashed black trace. (b) Kinetic trace at λ = 709 nm.

5.3.5.2. Reactivity of Oxoiron(IV) Intermediates towards Cyclooctene

Table 5A.1. Observed rate constants obtained from single exponential fitting of decay traces (λ = 700 nm) from double-mixing reactions of **6a**−O with varying [cyclooctene] at −15 °C using H_2O_2 (10 eq.) as terminal oxidant. $[\mathbf{6a}]_0$ = 3 mM. An average of at least three measurements is reported with standard deviations.

Eq. cyclooctene	[cyclooctene] (M)	k_{obs} (s^{-1})
0	none	0.713 ± 0.024
10	0.03	1.55 ± 0.13
20	0.06	1.76 ± 0.08
30	0.09	1.86 ± 0.09
40	0.12	1.76 ± 0.16
50	0.15	1.6 ± 0.1

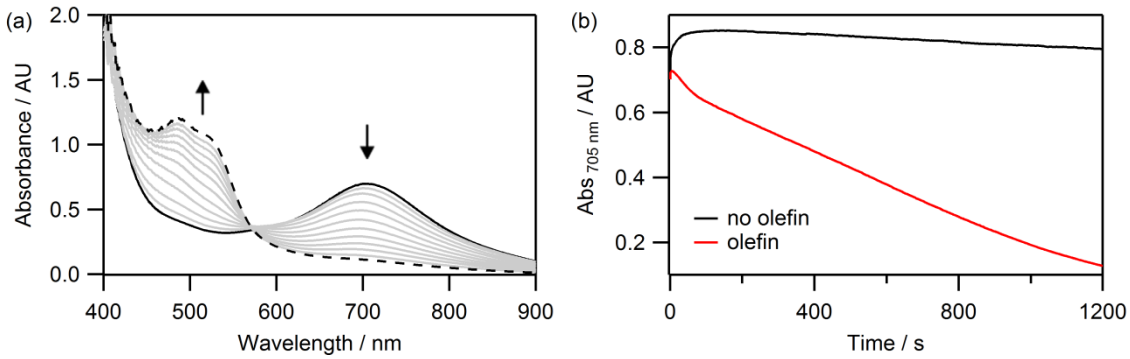

Figure 5A.21. (a) Time-resolved spectral changes observed upon reaction of **2** (3 mM, in the presence of 300 mM cyclooctene) with 1 eq. ^{i}Pr-IBX (3 mM) at 10 °C acquired over 1200 s. (b) Overlay of decay traces at λ = 705 nm in the absence (black) and presence (red) of 300 mM cyclooctene.

5.3.5.3. Comparison of Oxoiron(IV) Intermediates: 6a *vs.* (2 + Acetic Acid)

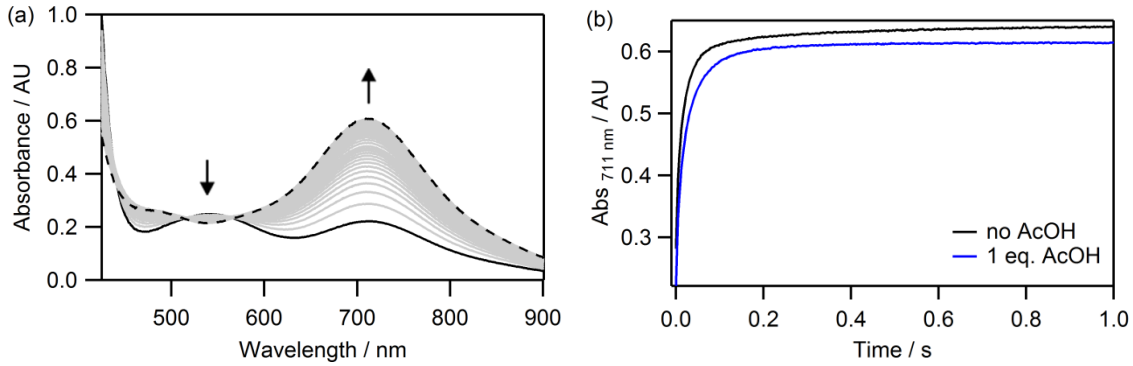

Figure 5A.22. (a) Time-resolved spectral changes accompanying the reaction between **2** (2 mM, containing 1 eq. AcOH) and 1 eq. ^{i}Pr-IBX (2 mM) at 10 °C acquired over 2.5 s. The spectral changes noted are identical to those in the absence of AcOH (refer to ref 17). (b) Overlay of kinetic traces at λ = 711 nm (zoomed in to first 1 s of reaction) highlighting no change in the formation rate of **2**−O but a slight decrease in its yield based upon the decrease in final absorbance value.

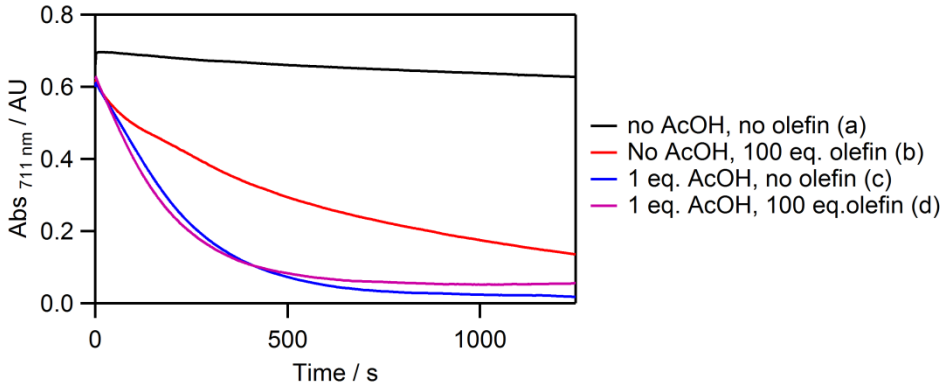

Figure 5A.23. Overlay of decay traces for **2**−O at 10 °C under various conditions: (a) Self-decay (no additives included), k_{obs} = 0.00086 ± 0.00003 s^{-1}; (b) Decay in the presence of 200 mM cyclooctene (100 eq.), k_{obs} = 0.00167 ± 0.00006 s^{-1}; (c) Decay in the presence of 2 mM AcOH (1 eq.), k_{obs} = 0.00449 ± 0.00012 s^{-1}; (d) Decay in the presence of 2 mM AcOH and 200 mM cyclooctene, k_{obs} = 0.00575 ± 0.00008 s^{-1}. Reactions were performed in single-mixing mode using $[\mathbf{2}]_0$ = 2 mM. Observed rate constants were obtained from single exponential fits.

5.3.6. Mössbauer Spectroscopy

Fe(II) Complexes

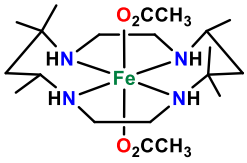

[Fe^{II}(Me_6cyclam)(CH_3CO_2)$_2$]

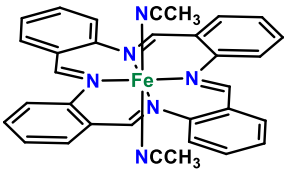

[Fe^{II}(TAAB)($NCCH_3$)$_2$]

Fe(IV) Complexes

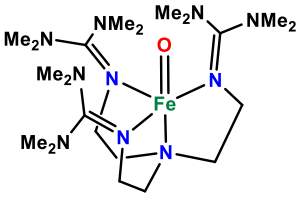

[Fe^{IV}(O)(TMG_3tren)]

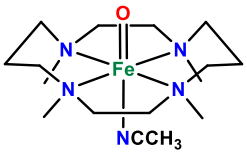

[Fe^{IV}(O)(TMC)($NCCH_3$)]

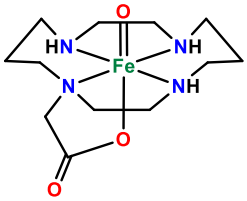

[Fe^{IV}(O)(cyclam-Ac)]

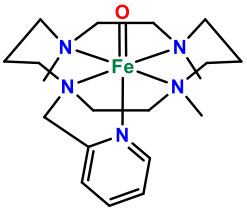

[Fe^{IV}(O)(TMC-py)]

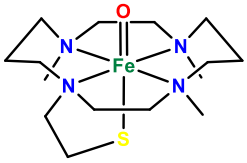

[Fe^{IV}(O)(TMCS)]

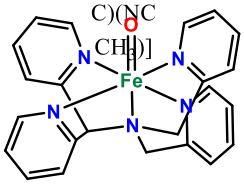

[Fe^{IV}(O)(N4Py)]

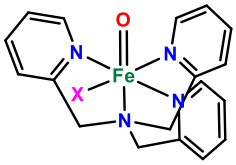

[Fe^{IV}(O)(TPA)(X)]
X = $NCCH_3$, O_2CCF_3

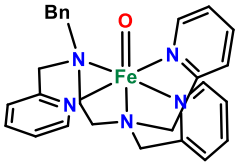

[Fe^{IV}(O)(BnTPEN)]

Figure 5A.24. Structures of complexes reported in Chapter 5, Table 5.6.

As stated in the Experimental Methods section in Chapter 5, a number of separate samples of the starting complex, intermediate, and decomposition products were prepared and measured to confirm reproducibility. In this regard, several attempts to isolate Fe(III) species of L_{6a} were attempted. All attempts to synthesize the ferric complexes directly from Fe(III) salts were unsuccessful, so chemical oxidations of **6a** were tried using

aminium salts (graciously supplied by Raul Hernandez Sanchez of the Betley Group, Harvard University, and used without further purification) as described below.

(a) Chemical Oxidation of 6a by $NOPF_6$. To a stirring solution of **6a** (58 mg, 0.084 mmol) in ≈ 4 mL CH_3CN was added solid $NOPF_6$ (15 mg, 0.084 mmol). An immediate color change to dark red-orange was observed and the mixture became opaque within minutes. After stirring at room temperature overnight, the solvent was removed in vacuo and the reddish-purple residue was triturated with several milliliters of diethyl ether to afford a mauve colored powder (72 mg). The ESI-MS spectrum is shown in Figure 5A.25 and the IR spectrum in Figure 5A.26. Based on ESI-MS data, the product appears to be impure and shows evidence of ligand oxidation (as opposed to metal oxidation). A Mössbauer spectrum was acquired on this product as shown in Figure 5A.27.

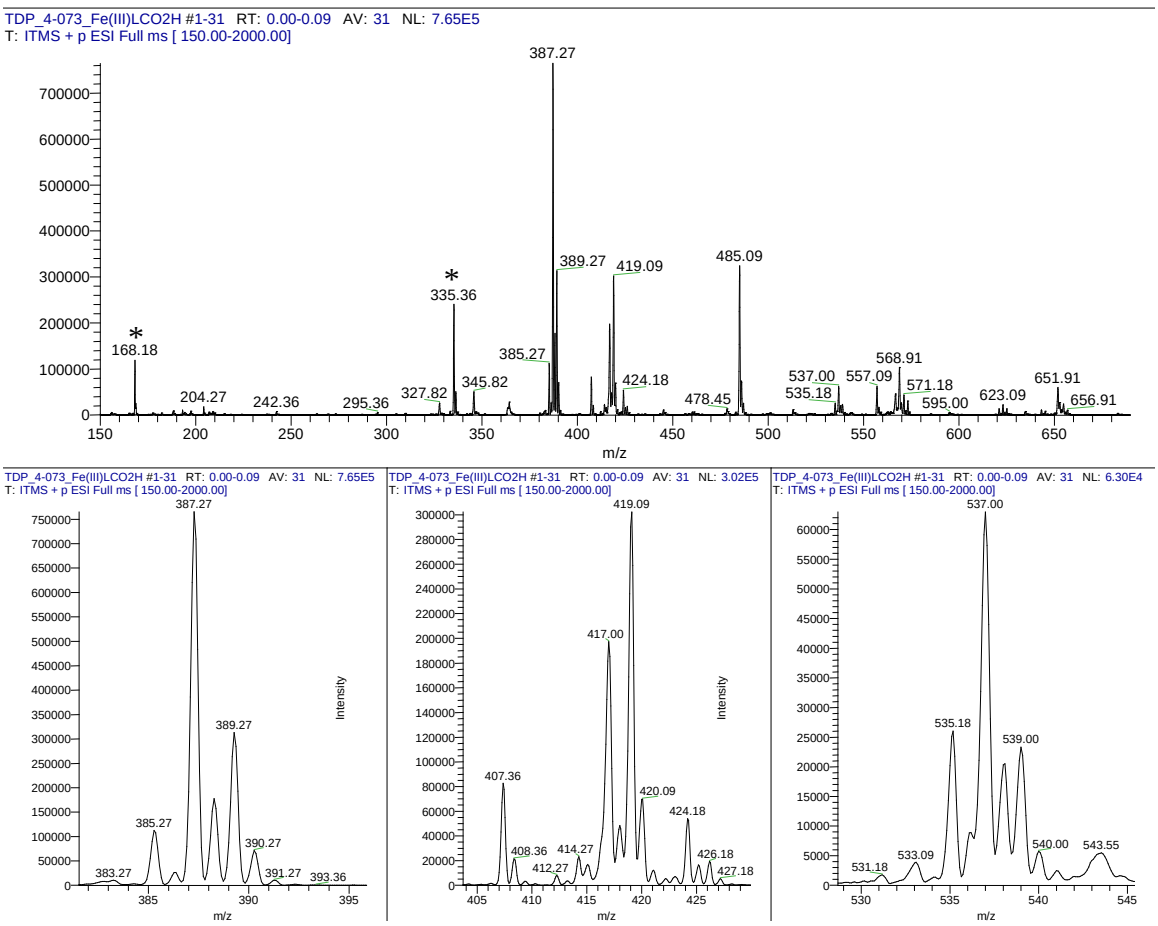

Figure 5A.25. *Top*: ESI-MS of the product from the reaction of **6a** with $NOPF_6$. Asterisks denote peaks due to free ligand L_{6a}. The signal with m/z = 485 is an unknown impurity (often observed in ESI-MS runs) and has an organic isotopic distribution. *Bottom*: Zoom in of major ions. Identifiable peaks are as follows: *m/z* = 387.27 ({(**6a** − 2H) − H^+}$^+$, 100 %) and 537.00 ({(**6a** − 2H)(OTf)}$^+$, 8 %).

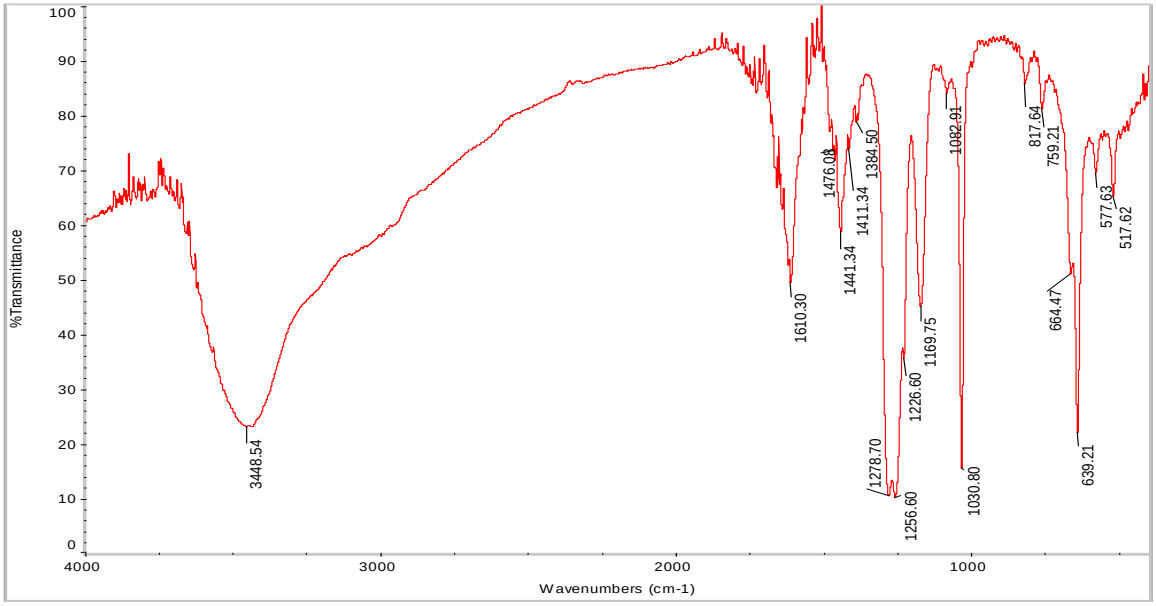

Figure 5A.26. FT-IR spectrum (KBr) of the oxidation product obtained from the reaction between **6a** and $NOPF_6$.

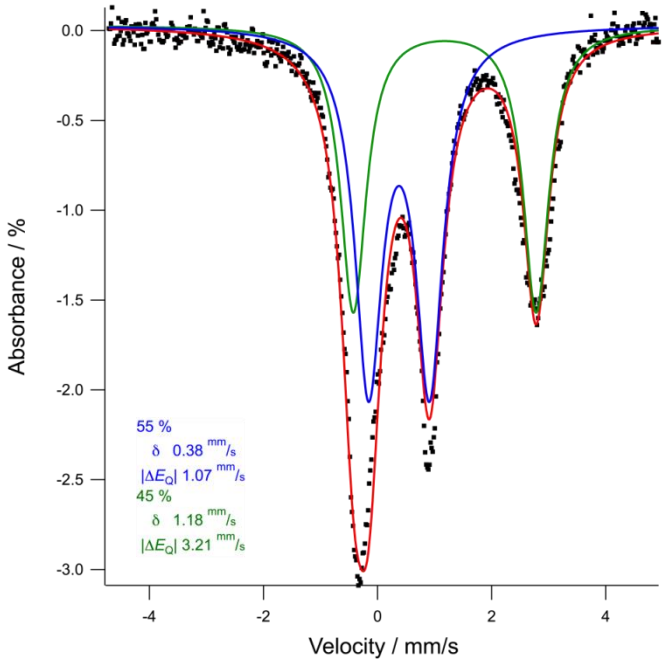

Figure 5A.27. Zero field Mössbauer spectrum of the oxidation product(s) obtained from the reaction of **6a** with $NOPF_6$ acquired as a frozen CH_3CN solution at 90 K with derived parameters.

(b) Chemical Oxidation by $(BrC_6H_4)_3NSbCl_6$. To a stirring solution of **6a** (72 mg, 0.10 mmol) in 3 mL CH_3CN was added solid $(BrC_6H_4)_3NSbCl_6$ (85 mg, 0.105 mmol). The golden orange solution became cloudy and more intense in color and within minutes took on the blackish-blue color of the aminium salt. Within an additional 10 mins the mixture was opaque brown. After stirring overnight at room temperature, the sample was filtered to remove a small amount of white precipitate. The red-orange filtrate was evaporated to dryness and the dark residue was triturated with toluene to acquire the product as a light brown powder (106 mg). The ESI-MS spectrum is shown in Figure 5A.28 and the IR spectrum in Figure 5A.29. A Mössbauer spectrum was acquired for the product (solid sample) as shown in Figure 5A.30. The major component (79 %) with δ = 0.34 mm s^{-1} is consistent with a high spin Fe(III) complex that may represents the desired product; the minor component (21 %) with δ = 0.93 mm s^{-1} and $|\Delta E_q|$ = 3.65 mm s^{-1} is consistent with an Fe(II) complex supported by an oxidized PyMAC ligand.

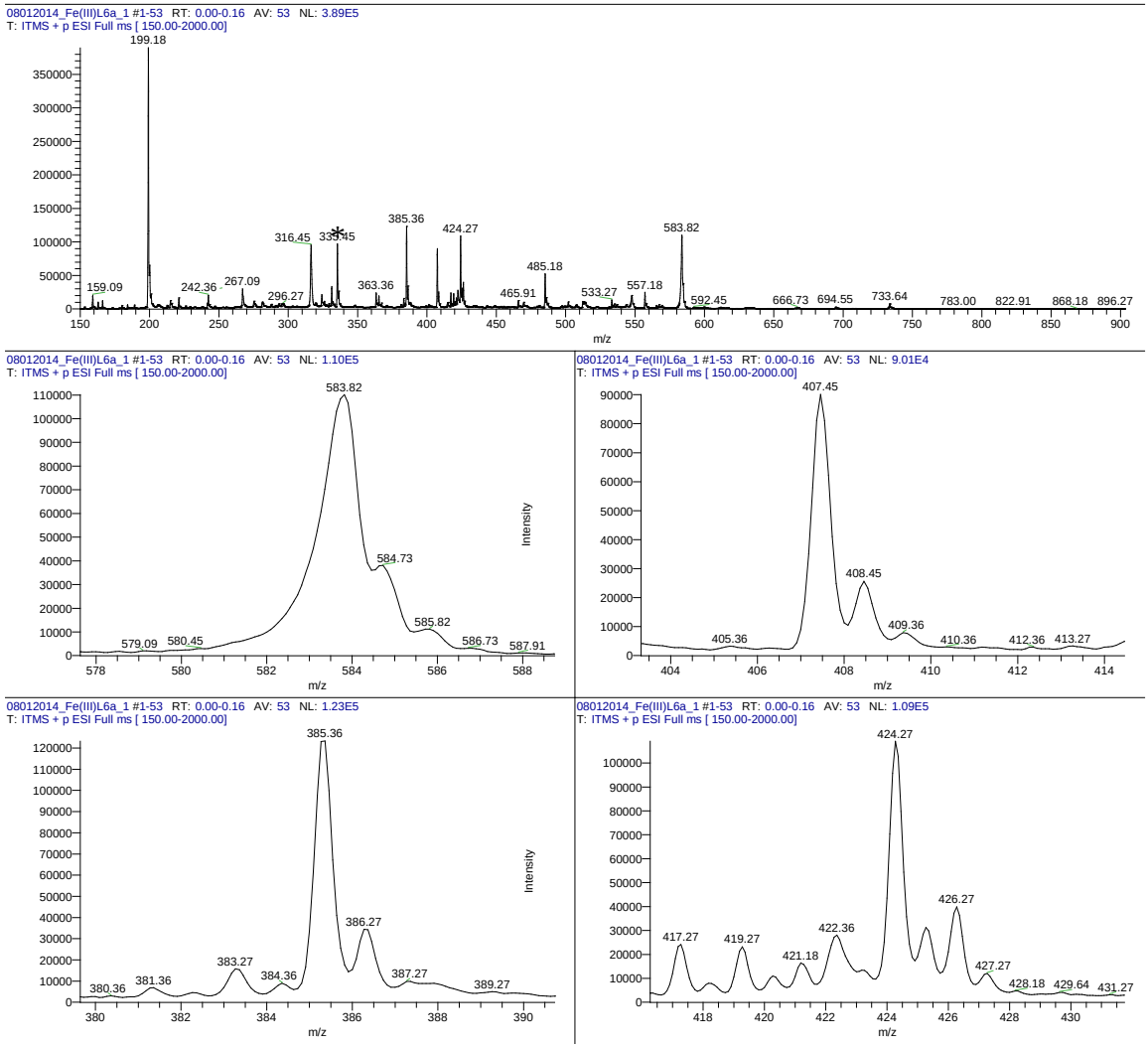

Figure 5A.28. *Top*: ESI-MS of the product from the reaction of **6a** with $(BrC_6H_4)_3NSbCl_6$. Asterisks denote peaks due to free ligand L_{6a}. The signal with *m/z* = 485 is an unknown impurity (often observed in ESI-MS runs) and has an organic isotopic distribution. The base peak at *m/z* = 199 is from background. *Bottom*: Zoom in of major ions. Identifiable peaks are as follows: *m/z* = 385.36 ({(**6a** − 4H) − H^+}$^+$, 32 %); 424.27 ({($Fe^{III}L_{6a}Cl$) − H^+}$^+$, 28 %); 407.45 ({(dialkylated L_{6a} + H^+)}$^+$, 23 %).

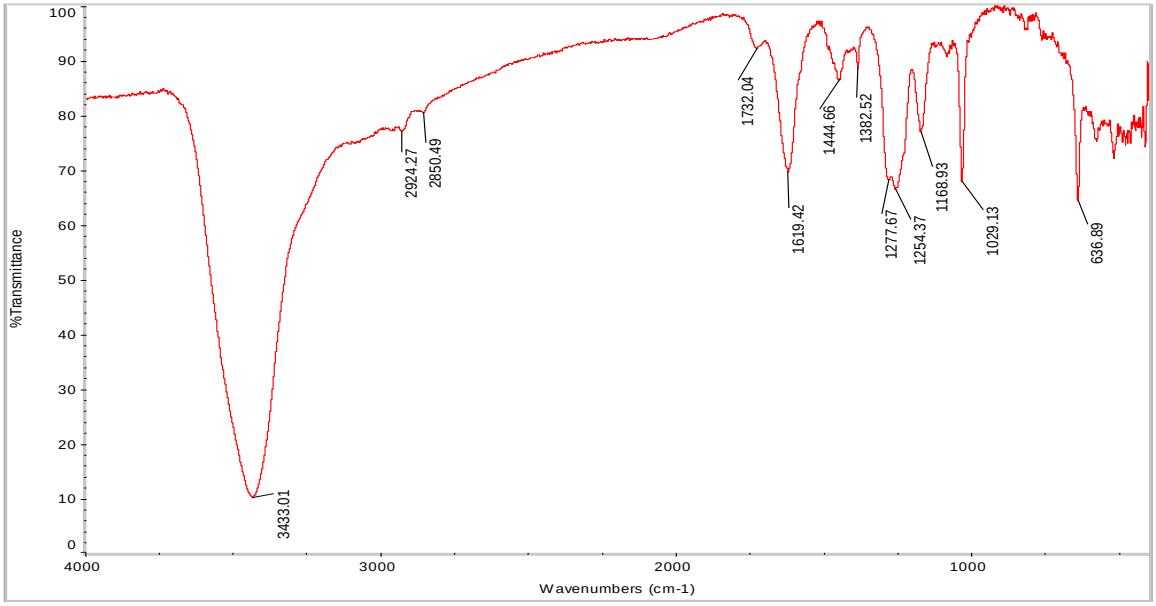

Figure 5A.29. FT-IR spectrum (KBr) of the oxidation product obtained from the reaction between **6a** and $(BrC_6H_4)_3NSbCl_6$.

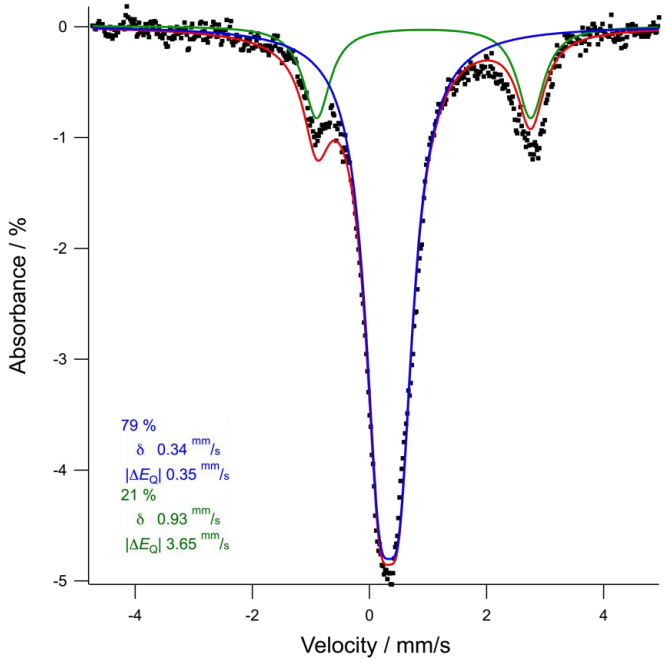

Figure 5A.30. Zero field Mössbauer spectrum of the oxidation product(s) obtained from the reaction of **6a** with $(BrC_6H_4)_3NSbCl_6$ acquired as a solid at 90 K with derived parameters.

Crystallographic Data for $[FeLCONH_2](CF_3SO_3)_2$ (5)

Table 5A.2. Atomic coordinates ($\times 10^4$) and equivalent isotropic displacement parameters ($Å^2 \times 10^3$) for **5**. U_{eq} is defined as one third of the trace of the orthogonalized U^{ij} tensor.

	x	y	z	U_{eq}
Fe(1)	9180(1)	1753(1)	2736(1)	25(1)
N(1)	9665(8)	80(8)	2056(3)	25(1)
C(1)	8864(5)	-247(7)	1301(3)	29(1)
C(2)	9282(4)	-1222(4)	777(2)	37(1)
C(3)	10564(4)	-1859(4)	1072(3)	44(1)
C(4)	11393(5)	-1490(4)	1856(2)	40(1)
C(5)	10904(4)	-512(3)	2348(2)	28(1)
C(6)	11635(3)	-64(3)	3213(2)	26(1)
C(7)	10831(4)	-986(3)	3737(2)	40(1)
N(2)	11442(2)	1382(2)	3423(1)	18(1)
C(8)	12629(4)	2349(4)	3161(2)	28(1)
C(9)	12725(9)	3833(7)	3520(8)	33(1)
C(10)	11273(3)	4309(3)	3709(2)	37(1)
N(3)	9798(7)	3942(6)	3056(4)	26(1)
C(11)	10065(3)	4662(3)	2362(2)	32(1)
C(12)	8785(12)	4399(8)	1617(4)	30(1)
C(13)	8629(10)	2930(7)	1187(5)	31(1)
C(16)	8467(4)	4413(3)	3361(2)	35(1)
C(17)	7763(6)	3870(6)	3971(3)	33(1)
C(18)	7394(13)	2353(7)	3991(7)	24(1)
N(5)	6667(13)	1913(12)	4552(6)	30(2)
O(1)	7775(5)	1477(7)	3508(3)	26(1)
N(4)	7766(8)	1870(7)	1559(4)	26(1)
C(14)	7426(5)	479(6)	1078(4)	29(1)
C(15)	5982(6)	-376(7)	1256(5)	36(1)
N(1A)	9510(15)	135(15)	1896(6)	32(2)
C(1A)	8460(12)	-222(12)	1208(6)	37(2)
C(2A)	8606(13)	-1294(9)	649(5)	62(2)
C(3A)	9903(13)	-1937(10)	819(6)	67(2)
C(4A)	11015(12)	-1589(8)	1505(7)	58(2)
C(5A)	10785(9)	-498(8)	2029(5)	46(2)
C(6A)	11930(8)	114(7)	2754(5)	62(2)
C(7A)	11579(11)	-575(10)	3458(5)	70(2)
N(2A)	11780(7)	1620(6)	2844(4)	59(2)
C(8A)	12835(10)	2432(8)	3472(5)	44(2)
C(9A)	12617(18)	3940(14)	3512(14)	31(2)
C(10A)	11305(4)	4511(4)	3002(2)	18(1)
N(3A)	9647(11)	3967(10)	3007(6)	21(2)

C(11A)	8589(4)	4651(4)	2413(2)	20(1)
C(12A)	8620(20)	4343(15)	1547(6)	27(2)
C(13A)	8320(20)	2864(14)	1177(9)	34(2)
C(16A)	9330(5)	4346(3)	3822(2)	18(1)
C(17A)	8136(9)	3759(9)	4129(5)	23(1)
C(18A)	7590(20)	2220(12)	4036(13)	26(2)
N(5A)	6480(20)	1790(20)	4420(11)	27(2)
O(1A)	8145(10)	1434(13)	3587(6)	26(2)
N(4A)	7517(13)	1895(11)	1606(6)	20(2)
C(14A)	7072(11)	516(12)	1126(8)	36(2)
C(15A)	5682(14)	-234(15)	1401(10)	58(3)
O(11T)	1991(8)	2777(7)	5389(5)	36(1)
O(12T)	4762(10)	3464(12)	5420(6)	35(1)
O(13T)	3704(17)	1064(9)	5260(7)	37(1)
S(1T)	3565(6)	2451(3)	5570(2)	25(1)
C(1T)	3964(11)	2458(9)	6657(4)	35(1)
F(11T)	2786(11)	1797(8)	6926(5)	57(1)
F(12T)	5249(14)	1940(11)	6953(4)	66(2)
F(13T)	4105(12)	3728(10)	7027(4)	45(2)
O(11U)	2253(17)	2868(16)	5449(9)	62(3)
O(12U)	5010(20)	3388(19)	5473(10)	55(3)
O(13U)	3820(30)	1003(14)	5394(11)	53(3)
S(1U)	3753(11)	2423(5)	5626(4)	40(1)
C(1U)	4244(15)	2612(13)	6706(6)	39(2)
F(11U)	3320(20)	1649(10)	6944(6)	61(2)
F(12U)	5734(14)	2372(16)	6876(7)	65(3)
F(13U)	4235(15)	3878(13)	7026(7)	41(2)
O(21T)	4862(2)	3345(2)	1976(1)	38(1)
O(22T)	4496(2)	2592(2)	554(1)	50(1)
O(23T)	2226(2)	2622(2)	1175(1)	44(1)
S(2T)	3838(1)	3175(1)	1194(1)	35(1)
C(2T)	3713(2)	4945(2)	984(1)	43(1)
F(21T)	3095(2)	5636(1)	1528(1)	50(1)
F(22T)	5114(2)	5642(2)	989(1)	60(1)
F(23T)	2791(2)	4955(2)	270(1)	67(1)

Table 5A.3. Bond lengths (Å) and angles (°) for **5**.

Fe(1)-O(1A)	1.892(9)
Fe(1)-O(1)	1.990(4)
Fe(1)-N(1)	2.063(4)
Fe(1)-N(1A)	2.129(8)
Fe(1)-N(3)	2.144(6)
Fe(1)-N(3A)	2.154(9)
Fe(1)-N(4)	2.172(6)
Fe(1)-N(2)	2.1925(17)
Fe(1)-N(4A)	2.212(9)
Fe(1)-N(2A)	2.272(6)
N(1)-C(5)	1.333(4)
N(1)-C(1)	1.334(5)
C(1)-C(2)	1.384(5)
C(1)-C(14)	1.530(5)
C(2)-C(3)	1.390(4)
C(2)-H(2)	0.9500
C(3)-C(4)	1.385(4)
C(3)-H(3)	0.9500
C(4)-C(5)	1.382(4)
C(4)-H(4)	0.9500
C(5)-C(6)	1.493(4)
C(6)-N(2)	1.474(3)
C(6)-C(7)	1.539(4)
C(6)-H(6)	1.0000
C(7)-H(7A)	0.9800
C(7)-H(7B)	0.9800
C(7)-H(7C)	0.9800
N(2)-C(8)	1.484(4)
N(2)-H(2A)	0.9300
C(8)-C(9)	1.515(7)
C(8)-H(8A)	0.9900
C(8)-H(8B)	0.9900
C(9)-C(10)	1.492(9)
C(9)-H(9A)	0.9900
C(9)-H(9B)	0.9900
C(10)-N(3)	1.513(6)
C(10)-H(10A)	0.9900
C(10)-H(10B)	0.9900
N(3)-C(16)	1.477(6)
N(3)-C(11)	1.485(6)
C(11)-C(12)	1.502(7)
C(11)-H(11A)	0.9900
C(11)-H(11B)	0.9900

C(12)-C(13)	1.535(7)
C(12)-H(12A)	0.9900
C(12)-H(12B)	0.9900
C(13)-N(4)	1.478(6)
C(13)-H(13A)	0.9900
C(13)-H(13B)	0.9900
C(16)-C(17)	1.427(5)
C(16)-H(16A)	0.9900
C(16)-H(16B)	0.9900
C(17)-C(18)	1.494(6)
C(17)-H(17A)	0.9900
C(17)-H(17B)	0.9900
C(18)-O(1)	1.258(6)
C(18)-N(5)	1.330(7)
N(5)-H(5A)	0.8800
N(5)-H(5B)	0.8800
N(4)-C(14)	1.492(6)
N(4)-H(4A)	0.9300
C(14)-C(15)	1.528(6)
C(14)-H(14)	1.0000
C(15)-H(15A)	0.9800
C(15)-H(15B)	0.9800
C(15)-H(15C)	0.9800
N(1A)-C(1A)	1.331(9)
N(1A)-C(5A)	1.341(9)
C(1A)-C(2A)	1.391(9)
C(1A)-C(14A)	1.486(10)
C(2A)-C(3A)	1.367(10)
C(2A)-H(2A1)	0.9500
C(3A)-C(4A)	1.355(11)
C(3A)-H(3A)	0.9500
C(4A)-C(5A)	1.393(9)
C(4A)-H(4A1)	0.9500
C(5A)-C(6A)	1.458(9)
C(6A)-N(2A)	1.502(7)
C(6A)-C(7A)	1.504(11)
C(6A)-H(6A)	1.0000
C(7A)-H(7A1)	0.9800
C(7A)-H(7A2)	0.9800
C(7A)-H(7A3)	0.9800
N(2A)-C(8A)	1.381(8)
N(2A)-H(2A2)	0.9300
C(8A)-C(9A)	1.518(11)
C(8A)-H(8A1)	0.9900

C(8A)-H(8A2)	0.9900
C(9A)-C(10A)	1.508(12)
C(9A)-H(9A1)	0.9900
C(9A)-H(9A2)	0.9900
C(10A)-N(3A)	1.486(9)
C(10A)-H(10C)	0.9900
C(10A)-H(10D)	0.9900
N(3A)-C(16A)	1.497(10)
N(3A)-C(11A)	1.508(10)
C(11A)-C(12A)	1.491(12)
C(11A)-H(11C)	0.9900
C(11A)-H(11D)	0.9900
C(12A)-C(13A)	1.500(12)
C(12A)-H(12C)	0.9900
C(12A)-H(12D)	0.9900
C(13A)-N(4A)	1.453(11)
C(13A)-H(13C)	0.9900
C(13A)-H(13D)	0.9900
C(16A)-C(17A)	1.352(8)
C(16A)-H(16C)	0.9900
C(16A)-H(16D)	0.9900
C(17A)-C(18A)	1.513(11)
C(17A)-H(17C)	0.9900
C(17A)-H(17D)	0.9900
C(18A)-O(1A)	1.249(11)
C(18A)-N(5A)	1.320(12)
N(5A)-H(5A1)	0.8800
N(5A)-H(5A2)	0.8800
N(4A)-C(14A)	1.481(10)
N(4A)-H(4A2)	0.9300
C(14A)-C(15A)	1.521(10)
C(14A)-H(14A)	1.0000
C(15A)-H(15D)	0.9800
C(15A)-H(15E)	0.9800
C(15A)-H(15F)	0.9800
O(11T)-S(1T)	1.438(6)
O(12T)-S(1T)	1.432(7)
O(13T)-S(1T)	1.445(6)
S(1T)-C(1T)	1.826(6)
C(1T)-F(13T)	1.326(7)
C(1T)-F(12T)	1.327(7)
C(1T)-F(11T)	1.332(7)
O(11U)-S(1U)	1.425(9)
O(12U)-S(1U)	1.443(10)

O(13U)-S(1U)	1.429(11)
S(1U)-C(1U)	1.802(10)
C(1U)-F(13U)	1.314(10)
C(1U)-F(11U)	1.317(9)
C(1U)-F(12U)	1.338(10)
O(21T)-S(2T)	1.4401(13)
O(22T)-S(2T)	1.4413(15)
O(23T)-S(2T)	1.4403(14)
S(2T)-C(2T)	1.827(2)
C(2T)-F(22T)	1.326(3)
C(2T)-F(23T)	1.330(2)
C(2T)-F(21T)	1.339(2)

O(1A)-Fe(1)-O(1)	9.5(4)
O(1A)-Fe(1)-N(1)	118.7(5)
O(1)-Fe(1)-N(1)	120.3(3)
O(1A)-Fe(1)-N(1A)	123.0(6)
O(1)-Fe(1)-N(1A)	123.3(6)
N(1)-Fe(1)-N(1A)	7.9(4)
O(1A)-Fe(1)-N(3)	96.3(4)
O(1)-Fe(1)-N(3)	96.0(2)
N(1)-Fe(1)-N(3)	143.4(3)
N(1A)-Fe(1)-N(3)	140.6(6)
O(1A)-Fe(1)-N(3A)	96.2(4)
O(1)-Fe(1)-N(3A)	95.2(3)
N(1)-Fe(1)-N(3A)	144.5(4)
N(1A)-Fe(1)-N(3A)	140.8(6)
N(3)-Fe(1)-N(3A)	4.0(4)
O(1A)-Fe(1)-N(4)	118.7(3)
O(1)-Fe(1)-N(4)	109.4(2)
N(1)-Fe(1)-N(4)	77.9(2)
N(1A)-Fe(1)-N(4)	70.1(3)
N(3)-Fe(1)-N(4)	95.3(2)
N(3A)-Fe(1)-N(4)	91.9(3)
O(1A)-Fe(1)-N(2)	92.8(3)
O(1)-Fe(1)-N(2)	102.27(15)
N(1)-Fe(1)-N(2)	76.99(12)
N(1A)-Fe(1)-N(2)	83.8(2)
N(3)-Fe(1)-N(2)	91.92(16)
N(3A)-Fe(1)-N(2)	95.9(3)
N(4)-Fe(1)-N(2)	146.56(19)
O(1A)-Fe(1)-N(4A)	112.4(4)
O(1)-Fe(1)-N(4A)	103.0(4)
N(1)-Fe(1)-N(4A)	82.2(3)

N(1A)-Fe(1)-N(4A)	74.5(4)
N(3)-Fe(1)-N(4A)	94.8(3)
N(3A)-Fe(1)-N(4A)	91.2(4)
N(4)-Fe(1)-N(4A)	6.5(5)
N(2)-Fe(1)-N(4A)	153.0(3)
O(1A)-Fe(1)-N(2A)	121.9(3)
O(1)-Fe(1)-N(2A)	131.4(2)
N(1)-Fe(1)-N(2A)	65.0(2)
N(1A)-Fe(1)-N(2A)	69.2(4)
N(3)-Fe(1)-N(2A)	88.4(2)
N(3A)-Fe(1)-N(2A)	91.8(3)
N(4)-Fe(1)-N(2A)	118.4(3)
N(2)-Fe(1)-N(2A)	29.14(18)
N(4A)-Fe(1)-N(2A)	124.9(4)
C(5)-N(1)-C(1)	122.0(4)
C(5)-N(1)-Fe(1)	118.8(3)
C(1)-N(1)-Fe(1)	118.5(3)
N(1)-C(1)-C(2)	121.5(3)
N(1)-C(1)-C(14)	115.2(4)
C(2)-C(1)-C(14)	123.3(4)
C(1)-C(2)-C(3)	117.3(3)
C(1)-C(2)-H(2)	121.4
C(3)-C(2)-H(2)	121.4
C(4)-C(3)-C(2)	120.3(3)
C(4)-C(3)-H(3)	119.9
C(2)-C(3)-H(3)	119.9
C(5)-C(4)-C(3)	119.3(3)
C(5)-C(4)-H(4)	120.3
C(3)-C(4)-H(4)	120.3
N(1)-C(5)-C(4)	119.6(3)
N(1)-C(5)-C(6)	115.3(3)
C(4)-C(5)-C(6)	125.2(3)
N(2)-C(6)-C(5)	109.3(2)
N(2)-C(6)-C(7)	109.5(2)
C(5)-C(6)-C(7)	109.8(2)
N(2)-C(6)-H(6)	109.4
C(5)-C(6)-H(6)	109.4
C(7)-C(6)-H(6)	109.4
C(6)-N(2)-C(8)	111.3(2)
C(6)-N(2)-Fe(1)	109.05(13)
C(8)-N(2)-Fe(1)	104.30(15)
C(6)-N(2)-H(2A)	110.7
C(8)-N(2)-H(2A)	110.7
Fe(1)-N(2)-H(2A)	110.7

N(2)-C(8)-C(9)	113.3(6)
N(2)-C(8)-H(8A)	108.9
C(9)-C(8)-H(8A)	108.9
N(2)-C(8)-H(8B)	108.9
C(9)-C(8)-H(8B)	108.9
H(8A)-C(8)-H(8B)	107.7
C(10)-C(9)-C(8)	118.7(6)
C(10)-C(9)-H(9A)	107.6
C(8)-C(9)-H(9A)	107.6
C(10)-C(9)-H(9B)	107.6
C(8)-C(9)-H(9B)	107.6
H(9A)-C(9)-H(9B)	107.1
C(9)-C(10)-N(3)	116.2(5)
C(9)-C(10)-H(10A)	108.2
N(3)-C(10)-H(10A)	108.2
C(9)-C(10)-H(10B)	108.2
N(3)-C(10)-H(10B)	108.2
H(10A)-C(10)-H(10B)	107.4
C(16)-N(3)-C(11)	110.0(4)
C(16)-N(3)-C(10)	108.9(4)
C(11)-N(3)-C(10)	107.8(4)
C(16)-N(3)-Fe(1)	106.1(3)
C(11)-N(3)-Fe(1)	112.3(3)
C(10)-N(3)-Fe(1)	111.7(3)
N(3)-C(11)-C(12)	117.7(5)
N(3)-C(11)-H(11A)	107.9
C(12)-C(11)-H(11A)	107.9
N(3)-C(11)-H(11B)	107.9
C(12)-C(11)-H(11B)	107.9
H(11A)-C(11)-H(11B)	107.2
C(11)-C(12)-C(13)	111.9(6)
C(11)-C(12)-H(12A)	109.2
C(13)-C(12)-H(12A)	109.2
C(11)-C(12)-H(12B)	109.2
C(13)-C(12)-H(12B)	109.2
H(12A)-C(12)-H(12B)	107.9
N(4)-C(13)-C(12)	113.7(6)
N(4)-C(13)-H(13A)	108.8
C(12)-C(13)-H(13A)	108.8
N(4)-C(13)-H(13B)	108.8
C(12)-C(13)-H(13B)	108.8
H(13A)-C(13)-H(13B)	107.7
C(17)-C(16)-N(3)	126.6(3)
C(17)-C(16)-H(16A)	105.7

N(3)-C(16)-H(16A)	105.7
C(17)-C(16)-H(16B)	105.7
N(3)-C(16)-H(16B)	105.7
H(16A)-C(16)-H(16B)	106.1
C(16)-C(17)-C(18)	121.7(5)
C(16)-C(17)-H(17A)	106.9
C(18)-C(17)-H(17A)	106.9
C(16)-C(17)-H(17B)	106.9
C(18)-C(17)-H(17B)	106.9
H(17A)-C(17)-H(17B)	106.7
O(1)-C(18)-N(5)	118.8(7)
O(1)-C(18)-C(17)	122.5(6)
N(5)-C(18)-C(17)	118.7(7)
C(18)-N(5)-H(5A)	120.0
C(18)-N(5)-H(5B)	120.0
H(5A)-N(5)-H(5B)	120.0
C(18)-O(1)-Fe(1)	129.5(5)
C(13)-N(4)-C(14)	113.4(5)
C(13)-N(4)-Fe(1)	107.8(4)
C(14)-N(4)-Fe(1)	109.5(4)
C(13)-N(4)-H(4A)	108.7
C(14)-N(4)-H(4A)	108.7
Fe(1)-N(4)-H(4A)	108.7
N(4)-C(14)-C(15)	110.8(5)
N(4)-C(14)-C(1)	107.9(4)
C(15)-C(14)-C(1)	109.6(4)
N(4)-C(14)-H(14)	109.5
C(15)-C(14)-H(14)	109.5
C(1)-C(14)-H(14)	109.5
C(1A)-N(1A)-C(5A)	119.1(7)
C(1A)-N(1A)-Fe(1)	119.4(6)
C(5A)-N(1A)-Fe(1)	121.5(6)
N(1A)-C(1A)-C(2A)	121.4(8)
N(1A)-C(1A)-C(14A)	114.9(7)
C(2A)-C(1A)-C(14A)	123.4(8)
C(3A)-C(2A)-C(1A)	117.5(8)
C(3A)-C(2A)-H(2A1)	121.3
C(1A)-C(2A)-H(2A1)	121.3
C(4A)-C(3A)-C(2A)	123.0(7)
C(4A)-C(3A)-H(3A)	118.5
C(2A)-C(3A)-H(3A)	118.5
C(3A)-C(4A)-C(5A)	115.8(7)
C(3A)-C(4A)-H(4A1)	122.1
C(5A)-C(4A)-H(4A1)	122.1

N(1A)-C(5A)-C(4A)	123.0(8)
N(1A)-C(5A)-C(6A)	113.2(6)
C(4A)-C(5A)-C(6A)	123.7(7)
C(5A)-C(6A)-N(2A)	105.5(6)
C(5A)-C(6A)-C(7A)	109.7(7)
N(2A)-C(6A)-C(7A)	112.3(7)
C(5A)-C(6A)-H(6A)	109.7
N(2A)-C(6A)-H(6A)	109.7
C(7A)-C(6A)-H(6A)	109.7
C(6A)-C(7A)-H(7A1)	109.5
C(6A)-C(7A)-H(7A2)	109.5
H(7A1)-C(7A)-H(7A2)	109.5
C(6A)-C(7A)-H(7A3)	109.5
H(7A1)-C(7A)-H(7A3)	109.5
H(7A2)-C(7A)-H(7A3)	109.5
C(8A)-N(2A)-C(6A)	115.7(6)
C(8A)-N(2A)-Fe(1)	117.9(5)
C(6A)-N(2A)-Fe(1)	106.9(4)
C(8A)-N(2A)-H(2A2)	105.0
C(6A)-N(2A)-H(2A2)	105.0
Fe(1)-N(2A)-H(2A2)	105.0
N(2A)-C(8A)-C(9A)	112.3(8)
N(2A)-C(8A)-H(8A1)	109.1
C(9A)-C(8A)-H(8A1)	109.1
N(2A)-C(8A)-H(8A2)	109.1
C(9A)-C(8A)-H(8A2)	109.1
H(8A1)-C(8A)-H(8A2)	107.9
C(10A)-C(9A)-C(8A)	125.7(11)
C(10A)-C(9A)-H(9A1)	105.9
C(8A)-C(9A)-H(9A1)	105.9
C(10A)-C(9A)-H(9A2)	105.9
C(8A)-C(9A)-H(9A2)	105.9
H(9A1)-C(9A)-H(9A2)	106.2
N(3A)-C(10A)-C(9A)	119.2(9)
N(3A)-C(10A)-H(10C)	107.5
C(9A)-C(10A)-H(10C)	107.5
N(3A)-C(10A)-H(10D)	107.5
C(9A)-C(10A)-H(10D)	107.5
H(10C)-C(10A)-H(10D)	107.0
C(10A)-N(3A)-C(16A)	109.4(6)
C(10A)-N(3A)-C(11A)	108.1(6)
C(16A)-N(3A)-C(11A)	108.0(6)
C(10A)-N(3A)-Fe(1)	111.5(5)
C(16A)-N(3A)-Fe(1)	108.2(5)

C(11A)-N(3A)-Fe(1)	111.6(5)
C(12A)-C(11A)-N(3A)	117.7(8)
C(12A)-C(11A)-H(11C)	107.9
N(3A)-C(11A)-H(11C)	107.9
C(12A)-C(11A)-H(11D)	107.9
N(3A)-C(11A)-H(11D)	107.9
H(11C)-C(11A)-H(11D)	107.2
C(11A)-C(12A)-C(13A)	118.5(11)
C(11A)-C(12A)-H(12C)	107.7
C(13A)-C(12A)-H(12C)	107.7
C(11A)-C(12A)-H(12D)	107.7
C(13A)-C(12A)-H(12D)	107.7
H(12C)-C(12A)-H(12D)	107.1
N(4A)-C(13A)-C(12A)	115.7(11)
N(4A)-C(13A)-H(13C)	108.4
C(12A)-C(13A)-H(13C)	108.4
N(4A)-C(13A)-H(13D)	108.4
C(12A)-C(13A)-H(13D)	108.4
H(13C)-C(13A)-H(13D)	107.4
C(17A)-C(16A)-N(3A)	126.8(6)
C(17A)-C(16A)-H(16C)	105.6
N(3A)-C(16A)-H(16C)	105.6
C(17A)-C(16A)-H(16D)	105.6
N(3A)-C(16A)-H(16D)	105.6
H(16C)-C(16A)-H(16D)	106.1
C(16A)-C(17A)-C(18A)	124.0(8)
C(16A)-C(17A)-H(17C)	106.3
C(18A)-C(17A)-H(17C)	106.3
C(16A)-C(17A)-H(17D)	106.3
C(18A)-C(17A)-H(17D)	106.3
H(17C)-C(17A)-H(17D)	106.4
O(1A)-C(18A)-N(5A)	123.7(13)
O(1A)-C(18A)-C(17A)	119.3(11)
N(5A)-C(18A)-C(17A)	117.0(12)
C(18A)-N(5A)-H(5A1)	120.0
C(18A)-N(5A)-H(5A2)	120.0
H(5A1)-N(5A)-H(5A2)	120.0
C(18A)-O(1A)-Fe(1)	132.1(10)
C(13A)-N(4A)-C(14A)	110.7(10)
C(13A)-N(4A)-Fe(1)	107.1(8)
C(14A)-N(4A)-Fe(1)	109.5(7)
C(13A)-N(4A)-H(4A2)	109.8
C(14A)-N(4A)-H(4A2)	109.8
Fe(1)-N(4A)-H(4A2)	109.8

N(4A)-C(14A)-C(1A)	109.7(8)
N(4A)-C(14A)-C(15A)	107.7(10)
C(1A)-C(14A)-C(15A)	113.9(9)
N(4A)-C(14A)-H(14A)	108.5
C(1A)-C(14A)-H(14A)	108.5
C(15A)-C(14A)-H(14A)	108.5
C(14A)-C(15A)-H(15D)	109.5
C(14A)-C(15A)-H(15E)	109.5
H(15D)-C(15A)-H(15E)	109.5
C(14A)-C(15A)-H(15F)	109.5
H(15D)-C(15A)-H(15F)	109.5
H(15E)-C(15A)-H(15F)	109.5
O(12T)-S(1T)-O(11T)	115.3(5)
O(12T)-S(1T)-O(13T)	112.7(8)
O(11T)-S(1T)-O(13T)	114.1(7)
O(12T)-S(1T)-C(1T)	105.4(5)
O(11T)-S(1T)-C(1T)	103.3(4)
O(13T)-S(1T)-C(1T)	104.4(5)
F(13T)-C(1T)-F(12T)	107.6(7)
F(13T)-C(1T)-F(11T)	102.2(8)
F(12T)-C(1T)-F(11T)	106.9(5)
F(13T)-C(1T)-S(1T)	110.8(5)
F(12T)-C(1T)-S(1T)	114.5(5)
F(11T)-C(1T)-S(1T)	113.9(6)
O(11U)-S(1U)-O(13U)	117.4(12)
O(11U)-S(1U)-O(12U)	113.4(9)
O(13U)-S(1U)-O(12U)	115.2(13)
O(11U)-S(1U)-C(1U)	103.8(7)
O(13U)-S(1U)-C(1U)	103.9(8)
O(12U)-S(1U)-C(1U)	100.1(8)
F(13U)-C(1U)-F(11U)	115.1(13)
F(13U)-C(1U)-F(12U)	107.1(10)
F(11U)-C(1U)-F(12U)	110.1(9)
F(13U)-C(1U)-S(1U)	112.2(8)
F(11U)-C(1U)-S(1U)	107.8(8)
F(12U)-C(1U)-S(1U)	103.9(9)
O(21T)-S(2T)-O(23T)	114.53(8)
O(21T)-S(2T)-O(22T)	114.49(9)
O(23T)-S(2T)-O(22T)	115.42(10)
O(21T)-S(2T)-C(2T)	103.53(9)
O(23T)-S(2T)-C(2T)	102.91(9)
O(22T)-S(2T)-C(2T)	103.71(9)
F(22T)-C(2T)-F(23T)	108.10(17)
F(22T)-C(2T)-F(21T)	107.55(19)

F(23T)-C(2T)-F(21T)	107.18(15)
F(22T)-C(2T)-S(2T)	111.92(13)
F(23T)-C(2T)-S(2T)	110.55(17)
F(21T)-C(2T)-S(2T)	111.35(13)

Table 5A.4. Anisotropic displacement parameters ($Å^2 \times 10^3$) for **5**. The anisotropic displacement factor exponent takes the form: $-2\pi^2[h^2 a^{*2} U^{11} + ... + 2 h k a^* b^* U^{12}]$.

	U^{11}	U^{22}	U^{33}	U^{23}	U^{13}	U^{32}
Fe(1)	29(1)	20(1)	24(1)	1(1)	0(1)	7(1)
N(1)	27(2)	24(1)	24(2)	1(1)	0(1)	8(1)
C(1)	27(2)	30(1)	27(2)	-1(1)	-1(1)	9(1)
C(2)	31(1)	45(2)	30(1)	-12(1)	-3(1)	13(1)
C(3)	37(2)	49(2)	41(2)	-16(2)	-3(1)	23(2)
C(4)	36(2)	40(2)	37(2)	-12(1)	-8(1)	20(1)
C(5)	28(1)	26(1)	26(1)	-2(1)	-4(1)	11(1)
C(6)	33(1)	21(1)	22(1)	7(1)	-4(1)	10(1)
C(7)	60(2)	20(1)	36(1)	15(1)	-2(1)	-3(1)
N(2)	25(1)	15(1)	12(1)	5(1)	-1(1)	2(1)
C(8)	18(1)	29(1)	35(2)	8(1)	-1(1)	2(1)
C(9)	33(2)	28(2)	34(3)	9(2)	-2(2)	-1(2)
C(10)	42(1)	34(1)	31(1)	3(1)	1(1)	2(1)
N(3)	32(2)	22(2)	26(2)	5(2)	8(1)	4(1)
C(11)	34(1)	31(1)	32(1)	10(1)	9(1)	2(1)
C(12)	25(3)	30(2)	37(2)	12(2)	3(2)	9(2)
C(13)	30(3)	36(2)	25(2)	11(1)	8(2)	-4(2)
C(16)	46(1)	23(1)	41(1)	5(1)	20(1)	8(1)
C(17)	48(2)	18(1)	42(3)	15(1)	19(2)	16(2)
C(18)	30(2)	20(2)	24(2)	7(2)	5(2)	9(1)
N(5)	39(3)	25(2)	23(3)	4(2)	4(3)	-7(2)
O(1)	29(2)	19(1)	31(2)	6(1)	7(2)	6(1)
N(4)	17(2)	32(1)	32(2)	7(1)	8(1)	8(1)
C(14)	25(2)	33(1)	27(2)	1(1)	2(1)	5(1)
C(15)	28(2)	37(2)	39(2)	2(1)	0(2)	5(1)
N(1A)	29(3)	27(3)	41(5)	4(3)	9(3)	10(2)
C(1A)	54(4)	32(3)	22(3)	-2(2)	8(3)	4(3)
C(2A)	95(6)	46(4)	44(4)	-7(3)	15(4)	15(4)
C(3A)	97(6)	52(4)	59(4)	-4(3)	33(4)	22(4)
C(4A)	60(5)	43(4)	78(6)	-7(4)	31(4)	21(4)
C(5A)	41(3)	34(3)	63(4)	-2(3)	9(3)	9(2)
C(6A)	47(3)	48(3)	81(4)	-8(3)	-7(3)	23(3)
C(7A)	75(6)	61(5)	61(4)	-11(3)	-21(4)	25(5)

	U^{11}	U^{22}	U^{33}	U^{23}	U^{13}	U^{32}
N(2A)	49(3)	45(2)	74(4)	-6(2)	-7(3)	17(2)
C(8A)	32(3)	38(3)	58(5)	6(3)	2(3)	8(2)
C(9A)	34(4)	29(3)	29(5)	10(3)	-2(3)	6(3)
C(10A)	18(1)	16(2)	20(2)	9(1)	3(1)	-1(1)
N(3A)	23(2)	19(3)	20(2)	7(2)	3(2)	2(2)
C(11A)	21(2)	18(2)	24(2)	12(1)	4(1)	9(1)
C(12A)	18(3)	37(3)	22(3)	15(2)	-5(2)	0(2)
C(13A)	29(5)	44(3)	24(3)	1(2)	7(3)	-11(3)
C(16A)	25(2)	9(1)	19(2)	2(1)	5(1)	2(1)
C(17A)	41(3)	16(2)	17(2)	8(2)	11(2)	11(2)
C(18A)	33(5)	14(3)	27(3)	10(2)	-2(3)	2(3)
N(5A)	35(4)	24(4)	18(5)	0(3)	-1(4)	-5(3)
O(1A)	31(4)	19(2)	27(2)	4(2)	-4(2)	11(3)
N(4A)	10(3)	30(2)	21(2)	7(2)	5(2)	2(2)
C(14A)	40(4)	40(3)	23(3)	4(2)	-4(3)	0(3)
C(15A)	39(5)	50(6)	75(9)	25(6)	-4(4)	-17(4)
O(11T)	32(2)	38(2)	33(2)	10(1)	-3(1)	1(1)
O(12T)	42(2)	22(2)	40(2)	2(2)	9(2)	-1(1)
O(13T)	67(3)	17(2)	30(3)	3(2)	18(2)	2(2)
S(1T)	39(1)	13(1)	20(1)	2(1)	2(1)	1(1)
C(1T)	50(3)	30(3)	26(2)	3(2)	1(2)	19(2)
F(11T)	82(3)	55(2)	48(2)	22(1)	33(2)	17(2)
F(12T)	78(3)	83(4)	53(2)	21(2)	12(2)	58(3)
F(13T)	65(4)	37(2)	30(2)	-8(2)	3(2)	15(2)
O(11U)	52(4)	89(6)	49(4)	14(4)	7(3)	28(4)
O(12U)	67(6)	29(3)	75(6)	-1(4)	39(5)	-6(4)
O(13U)	92(6)	23(2)	46(6)	10(3)	22(5)	4(2)
S(1U)	46(2)	32(1)	49(2)	18(1)	18(1)	11(1)
C(1U)	41(3)	30(3)	45(3)	9(2)	3(2)	9(3)
F(11U)	104(6)	41(3)	39(2)	18(2)	20(4)	-1(3)
F(12U)	59(4)	84(6)	54(3)	0(3)	-5(3)	49(4)
F(13U)	40(3)	33(2)	55(4)	4(2)	18(3)	14(2)
O(21T)	29(1)	48(1)	38(1)	14(1)	1(1)	8(1)
O(22T)	48(1)	66(1)	45(1)	9(1)	20(1)	29(1)
O(23T)	26(1)	67(1)	37(1)	3(1)	4(1)	8(1)
S(2T)	27(1)	50(1)	33(1)	10(1)	8(1)	16(1)
C(2T)	45(1)	60(1)	37(1)	21(1)	18(1)	28(1)
F(21T)	55(1)	58(1)	48(1)	15(1)	22(1)	31(1)
F(22T)	60(1)	61(1)	77(1)	36(1)	37(1)	24(1)
F(23T)	80(1)	94(1)	39(1)	29(1)	10(1)	48(1)

Table 5A.5. Hydrogen coordinates ($\times 10^4$) and isotropic displacement parameters ($Å^2 \times 10^3$) for **5**.

	x	y	z	U_{eq}
H(2)	8717	-1447	237	45
H(3)	10872	-2551	735	53
H(4)	12288	-1905	2053	48
H(6)	12781	-142	3310	31
H(7A)	11307	-683	4304	61
H(7B)	10968	-1946	3601	61
H(7C)	9706	-917	3639	61
H(2A)	11497	1574	3971	22
H(8A)	12366	2294	2569	34
H(8B)	13674	2057	3315	34
H(9A)	13540	3995	4023	39
H(9B)	13104	4433	3146	39
H(10A)	11486	5325	3843	45
H(10B)	11064	3915	4194	45
H(11A)	11038	4408	2214	38
H(11B)	10266	5667	2542	38
H(12A)	9016	5072	1247	36
H(12B)	7772	4540	1762	36
H(13A)	8077	2904	622	37
H(13B)	9695	2700	1185	37
H(16A)	8795	5411	3545	42
H(16B)	7600	4342	2885	42
H(17A)	6766	4249	3952	39
H(17B)	8463	4262	4492	39
H(5A)	6462	1023	4581	36
H(5B)	6392	2511	4894	36
H(4A)	6819	2148	1623	31
H(14)	7239	584	493	35
H(15A)	6159	-467	1830	53
H(15B)	5799	-1293	946	53
H(15C)	5060	85	1106	53
H(2A1)	7835	-1569	167	74
H(3A)	10030	-2660	439	80
H(4A1)	11897	-2060	1621	69
H(6A)	13015	-1	2685	74
H(7A1)	10553	-394	3553	106
H(7A2)	12396	-209	3937	106
H(7A3)	11560	-1573	3344	106
H(2A2)	12026	1937	2384	71
H(8A1)	13920	2350	3410	52

	x	y	z	U_{eq}
H(8A2)	12701	2091	3983	52
H(9A1)	12573	4233	4075	38
H(9A2)	13607	4445	3424	38
H(10C)	11462	5520	3165	22
H(10D)	11435	4371	2440	22
H(11C)	7494	4391	2474	24
H(11D)	8865	5662	2564	24
H(12C)	9663	4754	1472	32
H(12D)	7828	4829	1238	32
H(13C)	7680	2805	627	41
H(13D)	9339	2572	1132	41
H(16C)	10306	4265	4207	21
H(16D)	9248	5342	3858	21
H(17C)	7204	4182	3910	27
H(17D)	8412	4071	4713	27
H(5A1)	6101	912	4367	33
H(5A2)	6132	2393	4730	33
H(4A2)	6623	2217	1720	24
H(14A)	6727	642	550	44
H(15D)	5964	-270	1980	87
H(15E)	5408	-1175	1119	87
H(15F)	4778	259	1281	87

Table 5A.6. Hydrogen bonds for **5** (Å and °).

D-H...A	d(D-H)	d(H...A)	d(D...A)	DHA Angle
N(2)-H(2A)...O(11T)#1	0.93	2.53	3.430(10)	163.4
N(5)-H(5A)...O(13T)#2	0.88	2.09	2.965(15)	172.0
N(5)-H(5B)...O(12T)	0.88	2.10	2.919(17)	154.2
N(4)-H(4A)...O(21T)	0.93	2.34	3.250(7)	165.2
N(4)-H(4A)...O(22T)	0.93	2.57	3.243(6)	129.4
N(2A)-H(2A2)...O(23T)#1	0.93	2.27	3.194(8)	171.2
N(5A)-H(5A1)...O(13U)#2	0.88	1.98	2.79(3)	153.3
N(5A)-H(5A2)...O(12U)	0.88	2.01	2.88(3)	167.2
N(4A)-H(4A2)...O(21T)	0.93	2.10	3.019(12)	168.3
N(4A)-H(4A2)...O(22T)	0.93	2.54	3.094(10)	118.2

Symmetry transformations used to generate equivalent atoms: #1: *x*+1, *y*, *z*; #2: −*x*+1, −*y*, −*z*+1.

Crystallographic Data for $[FeLCO_2CH_3(Cl)](CF_3SO_3)$

Table 5A.7. Atomic coordinates ($\times 10^4$) and equivalent isotropic displacement parameters ($Å^2 \times 10^3$) for $[FeLCO_2CH_3(Cl)](CF_3SO_3)$. U_{eq} is defined as one third of the trace of the orthogonalized U^{ij} tensor.

	x	y	z	U_{eq}
Cl(1)	2893(1)	8540(1)	4268(1)	29(1)
Fe(1)	3536(1)	6885(1)	3276(1)	21(1)
N(1)	3420(2)	7722(2)	2229(1)	38(1)
C(1)	4735(4)	9464(4)	2355(2)	37(1)
C(2)	6487(4)	9690(4)	2551(2)	41(1)
C(1A)	5250(10)	8905(11)	2125(5)	33(2)
C(2A)	5991(11)	10123(10)	2940(5)	36(2)
C(3)	7009(3)	9570(3)	3376(1)	36(1)
N(2)	6224(2)	7780(2)	3348(1)	28(1)
C(4)	6855(2)	7385(2)	4030(1)	31(1)
C(14)	8662(3)	7690(3)	4082(2)	44(1)
C(5)	5702(2)	5600(2)	3990(1)	25(1)
N(3)	4136(2)	5165(2)	3684(1)	22(1)
C(6)	6138(2)	4479(2)	4251(1)	28(1)
C(7)	4919(2)	2906(2)	4191(1)	29(1)
C(8)	3307(2)	2466(2)	3859(1)	27(1)
C(9)	2958(2)	3640(2)	3605(1)	22(1)
C(10)	1264(2)	3363(2)	3238(1)	24(1)
C(15)	275(2)	3798(2)	3874(1)	29(1)
N(4)	1497(2)	4448(2)	2700(1)	23(1)
C(11)	1915(3)	3733(3)	1931(1)	32(1)
C(12)	2038(3)	4746(3)	1344(1)	35(1)
C(13)	3491(3)	6454(3)	1543(1)	38(1)
C(16)	1936(10)	8048(15)	2146(7)	42(2)
C(17)	1601(10)	8511(13)	1395(5)	44(2)
C(18)	46(15)	8850(20)	1418(5)	40(2)
O(1)	-510(12)	9254(12)	1990(4)	42(1)
O(2)	-422(12)	8914(14)	690(5)	53(2)
C(19)	-1930(30)	9190(40)	611(16)	65(2)
C(16A)	1748(16)	7750(30)	2130(11)	38(3)
C(17A)	1320(20)	8020(20)	1324(9)	46(2)
C(18A)	160(30)	8850(40)	1351(9)	48(3)
O(1A)	-100(20)	9549(19)	1946(8)	55(3)
O(2A)	-720(20)	8410(20)	622(8)	58(3)
C(19A)	-1830(50)	9230(70)	570(30)	65(2)
O(1T)	1905(8)	6509(11)	-2025(5)	44(1)
O(2T)	2873(8)	4381(5)	-2049(3)	64(1)
O(3T)	4836(5)	7177(8)	-1931(4)	63(1)

	x	y	z	U_{eq}
S(1T)	3219(4)	6109(4)	-1814(2)	30(1)
C(1T)	3408(6)	6544(7)	-745(3)	50(1)
F(1T)	3854(7)	8150(6)	-395(3)	94(2)
F(2T)	1987(5)	5695(9)	-510(2)	73(1)
F(3T)	4553(7)	6167(8)	-440(4)	71(2)
O(1U)	2110(20)	6720(30)	-1914(15)	44(3)
O(2U)	3470(20)	4835(16)	-2183(8)	60(3)
O(3U)	5009(14)	7726(14)	-1579(11)	63(3)
S(1U)	3449(10)	6320(11)	-1724(5)	30(1)
C(1U)	3102(16)	5964(18)	-777(7)	51(3)
F(1U)	3070(20)	7350(20)	-313(6)	94(4)
F(2U)	1656(11)	4780(18)	-805(9)	60(3)
F(3U)	4280(20)	5620(30)	-507(11)	74(4)

Table 5A.8. Bond lengths (Å) and angles (°) for [FeLCO_2CH_3(Cl)](CF_3SO_3).

Cl(1)-Fe(1)	2.2756(5)
Fe(1)-N(3)	2.1062(15)
Fe(1)-N(1)	2.1677(18)
Fe(1)-N(2)	2.1935(16)
Fe(1)-N(4)	2.2043(15)
N(1)-C(16)	1.478(6)
N(1)-C(13)	1.485(3)
N(1)-C(16A)	1.509(7)
N(1)-C(1)	1.512(3)
N(1)-C(1A)	1.607(8)
C(1)-C(2)	1.509(5)
C(1)-H(1A)	0.9900
C(1)-H(1B)	0.9900
C(2)-C(3)	1.549(4)
C(2)-H(2A)	0.9900
C(2)-H(2B)	0.9900
C(1A)-C(2A)	1.521(11)
C(1A)-H(1A1)	0.9900
C(1A)-H(1A2)	0.9900
C(2A)-C(3)	1.471(9)
C(2A)-H(2A1)	0.9900
C(2A)-H(2A2)	0.9900
C(3)-N(2)	1.488(2)
C(3)-H(3A)	0.9900
C(3)-H(3B)	0.9900

C(3)-H(3C)	0.9900
C(3)-H(3D)	0.9900
N(2)-C(4)	1.483(3)
N(2)-H(2N)	0.876(17)
C(4)-C(14)	1.520(3)
C(4)-C(5)	1.525(3)
C(4)-H(4)	1.0000
C(14)-H(14A)	0.9800
C(14)-H(14B)	0.9800
C(14)-H(14C)	0.9800
C(5)-N(3)	1.343(2)
C(5)-C(6)	1.391(3)
N(3)-C(9)	1.341(2)
C(6)-C(7)	1.391(3)
C(6)-H(6)	0.9500
C(7)-C(8)	1.392(3)
C(7)-H(7)	0.9500
C(8)-C(9)	1.388(2)
C(8)-H(8)	0.9500
C(9)-C(10)	1.521(2)
C(10)-N(4)	1.489(2)
C(10)-C(15)	1.529(3)
C(10)-H(10)	1.0000
C(15)-H(15A)	0.9800
C(15)-H(15B)	0.9800
C(15)-H(15C)	0.9800
N(4)-C(11)	1.487(2)
N(4)-H(4N)	0.852(16)
C(11)-C(12)	1.521(3)
C(11)-H(11A)	0.9900
C(11)-H(11B)	0.9900
C(12)-C(13)	1.528(3)
C(12)-H(12A)	0.9900
C(12)-H(12B)	0.9900
C(13)-H(13A)	0.9900
C(13)-H(13B)	0.9900
C(16)-C(17)	1.532(8)
C(16)-H(16A)	0.9900
C(16)-H(16B)	0.9900
C(17)-C(18)	1.536(8)
C(17)-H(17A)	0.9900
C(17)-H(17B)	0.9900
C(18)-O(1)	1.185(7)
C(18)-O(2)	1.356(8)

O(2)-C(19)	1.473(10)
C(19)-H(19A)	0.9800
C(19)-H(19B)	0.9800
C(19)-H(19C)	0.9800
C(16A)-C(17A)	1.553(12)
C(16A)-H(16C)	0.9900
C(16A)-H(16D)	0.9900
C(17A)-C(18A)	1.498(12)
C(17A)-H(17C)	0.9900
C(17A)-H(17D)	0.9900
C(18A)-O(1A)	1.177(12)
C(18A)-O(2A)	1.362(13)
O(2A)-C(19A)	1.477(15)
C(19A)-H(19D)	0.9800
C(19A)-H(19E)	0.9800
C(19A)-H(19F)	0.9800
O(1T)-S(1T)	1.421(4)
O(2T)-S(1T)	1.430(4)
O(3T)-S(1T)	1.441(4)
S(1T)-C(1T)	1.815(5)
C(1T)-F(3T)	1.332(5)
C(1T)-F(1T)	1.332(5)
C(1T)-F(2T)	1.339(5)
O(1U)-S(1U)	1.433(12)
O(2U)-S(1U)	1.412(10)
O(3U)-S(1U)	1.431(10)
S(1U)-C(1U)	1.788(11)
C(1U)-F(2U)	1.303(11)
C(1U)-F(3U)	1.311(12)
C(1U)-F(1U)	1.347(12)

N(3)-Fe(1)-N(1)	141.60(7)
N(3)-Fe(1)-N(2)	74.23(6)
N(1)-Fe(1)-N(2)	90.60(7)
N(3)-Fe(1)-N(4)	75.05(6)
N(1)-Fe(1)-N(4)	91.26(6)
N(2)-Fe(1)-N(4)	132.05(6)
N(3)-Fe(1)-Cl(1)	111.15(4)
N(1)-Fe(1)-Cl(1)	107.17(6)
N(2)-Fe(1)-Cl(1)	110.12(5)
N(4)-Fe(1)-Cl(1)	114.92(4)
C(16)-N(1)-C(13)	113.7(5)
C(13)-N(1)-C(16A)	108.6(8)
C(16)-N(1)-C(1)	99.2(5)

C(13)-N(1)-C(1)	115.4(2)
C(13)-N(1)-C(1A)	86.8(4)
C(16A)-N(1)-C(1A)	134.7(8)
C(16)-N(1)-Fe(1)	110.3(4)
C(13)-N(1)-Fe(1)	107.71(13)
C(16A)-N(1)-Fe(1)	105.8(7)
C(1)-N(1)-Fe(1)	110.23(15)
C(1A)-N(1)-Fe(1)	109.5(3)
C(2)-C(1)-N(1)	115.6(2)
C(2)-C(1)-H(1A)	108.4
N(1)-C(1)-H(1A)	108.4
C(2)-C(1)-H(1B)	108.4
N(1)-C(1)-H(1B)	108.4
H(1A)-C(1)-H(1B)	107.4
C(1)-C(2)-C(3)	117.5(3)
C(1)-C(2)-H(2A)	107.9
C(3)-C(2)-H(2A)	107.9
C(1)-C(2)-H(2B)	107.9
C(3)-C(2)-H(2B)	107.9
H(2A)-C(2)-H(2B)	107.2
C(2A)-C(1A)-N(1)	104.4(6)
C(2A)-C(1A)-H(1A1)	110.9
N(1)-C(1A)-H(1A1)	110.9
C(2A)-C(1A)-H(1A2)	110.9
N(1)-C(1A)-H(1A2)	110.9
H(1A1)-C(1A)-H(1A2)	108.9
C(3)-C(2A)-C(1A)	110.2(7)
C(3)-C(2A)-H(2A1)	109.6
C(1A)-C(2A)-H(2A1)	109.6
C(3)-C(2A)-H(2A2)	109.6
C(1A)-C(2A)-H(2A2)	109.6
H(2A1)-C(2A)-H(2A2)	108.1
C(2A)-C(3)-N(2)	114.7(4)
N(2)-C(3)-C(2)	106.48(19)
N(2)-C(3)-H(3A)	110.4
C(2)-C(3)-H(3A)	110.4
N(2)-C(3)-H(3B)	110.4
C(2)-C(3)-H(3B)	110.4
H(3A)-C(3)-H(3B)	108.6
C(2A)-C(3)-H(3C)	108.6
N(2)-C(3)-H(3C)	108.6
C(2A)-C(3)-H(3D)	108.6
N(2)-C(3)-H(3D)	108.6
H(3C)-C(3)-H(3D)	107.6

C(4)-N(2)-C(3)	113.92(16)
C(4)-N(2)-Fe(1)	108.59(11)
C(3)-N(2)-Fe(1)	111.04(13)
C(4)-N(2)-H(2N)	106.3(17)
C(3)-N(2)-H(2N)	106.5(17)
Fe(1)-N(2)-H(2N)	110.3(18)
N(2)-C(4)-C(14)	114.67(18)
N(2)-C(4)-C(5)	106.61(15)
C(14)-C(4)-C(5)	113.24(18)
N(2)-C(4)-H(4)	107.3
C(14)-C(4)-H(4)	107.3
C(5)-C(4)-H(4)	107.3
C(4)-C(14)-H(14A)	109.5
C(4)-C(14)-H(14B)	109.5
H(14A)-C(14)-H(14B)	109.5
C(4)-C(14)-H(14C)	109.5
H(14A)-C(14)-H(14C)	109.5
H(14B)-C(14)-H(14C)	109.5
N(3)-C(5)-C(6)	120.47(16)
N(3)-C(5)-C(4)	113.51(16)
C(6)-C(5)-C(4)	126.01(16)
C(9)-N(3)-C(5)	121.41(15)
C(9)-N(3)-Fe(1)	119.27(12)
C(5)-N(3)-Fe(1)	119.27(12)
C(7)-C(6)-C(5)	118.67(17)
C(7)-C(6)-H(6)	120.7
C(5)-C(6)-H(6)	120.7
C(6)-C(7)-C(8)	120.10(17)
C(6)-C(7)-H(7)	120.0
C(8)-C(7)-H(7)	120.0
C(9)-C(8)-C(7)	118.29(17)
C(9)-C(8)-H(8)	120.9
C(7)-C(8)-H(8)	120.9
N(3)-C(9)-C(8)	121.04(16)
N(3)-C(9)-C(10)	114.12(15)
C(8)-C(9)-C(10)	124.83(16)
N(4)-C(10)-C(9)	108.23(14)
N(4)-C(10)-C(15)	109.32(15)
C(9)-C(10)-C(15)	110.96(15)
N(4)-C(10)-H(10)	109.4
C(9)-C(10)-H(10)	109.4
C(15)-C(10)-H(10)	109.4
C(10)-C(15)-H(15A)	109.5
C(10)-C(15)-H(15B)	109.5

H(15A)-C(15)-H(15B)	109.5
C(10)-C(15)-H(15C)	109.5
H(15A)-C(15)-H(15C)	109.5
H(15B)-C(15)-H(15C)	109.5
C(11)-N(4)-C(10)	111.60(14)
C(11)-N(4)-Fe(1)	108.69(12)
C(10)-N(4)-Fe(1)	108.50(10)
C(11)-N(4)-H(4N)	103.7(17)
C(10)-N(4)-H(4N)	105.8(17)
Fe(1)-N(4)-H(4N)	118.6(17)
N(4)-C(11)-C(12)	112.99(16)
N(4)-C(11)-H(11A)	109.0
C(12)-C(11)-H(11A)	109.0
N(4)-C(11)-H(11B)	109.0
C(12)-C(11)-H(11B)	109.0
H(11A)-C(11)-H(11B)	107.8
C(11)-C(12)-C(13)	116.41(18)
C(11)-C(12)-H(12A)	108.2
C(13)-C(12)-H(12A)	108.2
C(11)-C(12)-H(12B)	108.2
C(13)-C(12)-H(12B)	108.2
H(12A)-C(12)-H(12B)	107.3
N(1)-C(13)-C(12)	115.73(17)
N(1)-C(13)-H(13A)	108.3
C(12)-C(13)-H(13A)	108.3
N(1)-C(13)-H(13B)	108.3
C(12)-C(13)-H(13B)	108.3
H(13A)-C(13)-H(13B)	107.4
N(1)-C(16)-C(17)	116.6(7)
N(1)-C(16)-H(16A)	108.1
C(17)-C(16)-H(16A)	108.1
N(1)-C(16)-H(16B)	108.1
C(17)-C(16)-H(16B)	108.1
H(16A)-C(16)-H(16B)	107.3
C(16)-C(17)-C(18)	109.4(6)
C(16)-C(17)-H(17A)	109.8
C(18)-C(17)-H(17A)	109.8
C(16)-C(17)-H(17B)	109.8
C(18)-C(17)-H(17B)	109.8
H(17A)-C(17)-H(17B)	108.3
O(1)-C(18)-O(2)	123.8(7)
O(1)-C(18)-C(17)	126.7(7)
O(2)-C(18)-C(17)	108.3(7)
C(18)-O(2)-C(19)	114.9(12)

O(2)-C(19)-H(19A)	109.5
O(2)-C(19)-H(19B)	109.5
H(19A)-C(19)-H(19B)	109.5
O(2)-C(19)-H(19C)	109.5
H(19A)-C(19)-H(19C)	109.5
H(19B)-C(19)-H(19C)	109.5
N(1)-C(16A)-C(17A)	112.8(10)
N(1)-C(16A)-H(16C)	109.0
C(17A)-C(16A)-H(16C)	109.0
N(1)-C(16A)-H(16D)	109.0
C(17A)-C(16A)-H(16D)	109.0
H(16C)-C(16A)-H(16D)	107.8
C(18A)-C(17A)-C(16A)	113.3(11)
C(18A)-C(17A)-H(17C)	108.9
C(16A)-C(17A)-H(17C)	108.9
C(18A)-C(17A)-H(17D)	108.9
C(16A)-C(17A)-H(17D)	108.9
H(17C)-C(17A)-H(17D)	107.7
O(1A)-C(18A)-O(2A)	125.8(14)
O(1A)-C(18A)-C(17A)	123.0(13)
O(2A)-C(18A)-C(17A)	110.2(12)
C(18A)-O(2A)-C(19A)	114.9(18)
O(2A)-C(19A)-H(19D)	109.5
O(2A)-C(19A)-H(19E)	109.5
H(19D)-C(19A)-H(19E)	109.5
O(2A)-C(19A)-H(19F)	109.5
H(19D)-C(19A)-H(19F)	109.5
H(19E)-C(19A)-H(19F)	109.5
O(1T)-S(1T)-O(2T)	115.5(4)
O(1T)-S(1T)-O(3T)	116.1(4)
O(2T)-S(1T)-O(3T)	113.9(3)
O(1T)-S(1T)-C(1T)	104.1(4)
O(2T)-S(1T)-C(1T)	101.9(3)
O(3T)-S(1T)-C(1T)	102.6(3)
F(3T)-C(1T)-F(1T)	105.6(4)
F(3T)-C(1T)-F(2T)	107.1(5)
F(1T)-C(1T)-F(2T)	107.3(4)
F(3T)-C(1T)-S(1T)	112.7(4)
F(1T)-C(1T)-S(1T)	111.9(4)
F(2T)-C(1T)-S(1T)	111.8(3)
O(2U)-S(1U)-O(3U)	113.5(9)
O(2U)-S(1U)-O(1U)	118.8(12)
O(3U)-S(1U)-O(1U)	111.9(12)
O(2U)-S(1U)-C(1U)	104.0(8)

O(3U)-S(1U)-C(1U)	104.9(8)
O(1U)-S(1U)-C(1U)	101.5(11)
F(2U)-C(1U)-F(3U)	110.7(12)
F(2U)-C(1U)-F(1U)	105.4(10)
F(3U)-C(1U)-F(1U)	113.0(13)
F(2U)-C(1U)-S(1U)	112.1(9)
F(3U)-C(1U)-S(1U)	109.1(11)
F(1U)-C(1U)-S(1U)	106.5(9)

Table 5A.9. Anisotropic displacement parameters ($Å^2 \times 10^3$) for $[FeLCO_2CH_3(Cl)](CF_3SO_3)$. The anisotropic displacement factor exponent takes the form: $-2\pi^2[h^2 a^{*2} U^{11} + ... + 2 h k a^* b^* U^{12}]$.

	U^{11}	U^{22}	U^{33}	U^{23}	U^{13}	U^{12}
Cl(1)	32(1)	24(1)	32(1)	5(1)	7(1)	13(1)
Fe(1)	20(1)	17(1)	25(1)	5(1)	2(1)	7(1)
N(1)	39(1)	34(1)	35(1)	16(1)	-1(1)	7(1)
C(1)	47(2)	27(1)	37(1)	14(1)	7(1)	13(1)
C(2)	38(2)	34(1)	44(2)	18(1)	9(1)	3(1)
C(1A)	36(3)	34(3)	35(3)	19(3)	13(3)	15(3)
C(2A)	37(4)	28(3)	43(4)	14(3)	14(3)	11(3)
C(3)	31(1)	26(1)	45(1)	13(1)	6(1)	2(1)
N(2)	24(1)	25(1)	31(1)	8(1)	4(1)	6(1)
C(4)	23(1)	29(1)	35(1)	8(1)	-1(1)	4(1)
C(14)	22(1)	52(1)	53(1)	19(1)	2(1)	9(1)
C(5)	21(1)	25(1)	26(1)	5(1)	2(1)	9(1)
N(3)	20(1)	19(1)	26(1)	5(1)	1(1)	7(1)
C(6)	27(1)	32(1)	27(1)	5(1)	3(1)	17(1)
C(7)	37(1)	28(1)	28(1)	7(1)	7(1)	21(1)
C(8)	33(1)	19(1)	30(1)	5(1)	7(1)	13(1)
C(9)	24(1)	17(1)	24(1)	3(1)	4(1)	8(1)
C(10)	21(1)	18(1)	29(1)	3(1)	1(1)	5(1)
C(15)	22(1)	27(1)	35(1)	9(1)	7(1)	7(1)
N(4)	20(1)	22(1)	26(1)	2(1)	1(1)	9(1)
C(11)	40(1)	32(1)	26(1)	2(1)	3(1)	20(1)
C(12)	45(1)	43(1)	23(1)	4(1)	4(1)	28(1)
C(13)	34(1)	60(1)	34(1)	22(1)	11(1)	25(1)
C(16)	71(3)	27(3)	32(2)	10(2)	-1(2)	25(2)
C(17)	69(3)	38(3)	35(2)	15(3)	3(2)	29(3)
C(18)	52(3)	37(3)	39(2)	18(2)	6(2)	22(2)
O(1)	54(3)	38(3)	36(2)	7(2)	4(2)	24(3)
O(2)	76(3)	68(4)	41(2)	28(2)	14(2)	49(3)
C(19)	63(3)	89(3)	60(3)	35(2)	11(3)	42(2)

	U^{11}	U^{22}	U^{33}	U^{23}	U^{13}	U^{12}
C(16A)	60(4)	36(6)	31(4)	8(3)	5(3)	35(4)
C(17A)	78(5)	39(5)	39(4)	11(4)	3(3)	41(4)
C(18A)	75(6)	32(5)	47(4)	11(4)	5(4)	33(4)
O(1A)	64(7)	25(4)	63(4)	-2(3)	9(4)	15(4)
O(2A)	75(5)	56(6)	53(4)	8(3)	-6(3)	45(5)
C(19A)	63(3)	89(3)	60(3)	35(2)	11(3)	42(2)
O(1T)	27(2)	65(3)	49(2)	25(2)	0(1)	23(2)
O(2T)	94(3)	38(2)	54(2)	-5(1)	4(2)	34(2)
O(3T)	37(2)	84(3)	92(3)	52(3)	22(2)	32(2)
S(1T)	29(1)	34(1)	28(1)	6(1)	1(1)	17(1)
C(1T)	50(2)	67(3)	36(2)	0(2)	-4(2)	36(2)
F(1T)	111(3)	75(2)	71(2)	-37(2)	-22(2)	49(2)
F(2T)	59(2)	134(4)	45(2)	42(2)	19(1)	50(2)
F(3T)	69(3)	110(4)	45(2)	13(2)	-15(2)	55(3)
O(1U)	41(6)	51(6)	54(8)	33(6)	15(5)	22(5)
O(2U)	87(8)	55(5)	50(5)	7(4)	17(5)	46(5)
O(3U)	47(4)	47(5)	99(9)	31(5)	24(5)	17(3)
S(1U)	29(1)	34(1)	28(1)	6(1)	1(1)	17(1)
C(1U)	48(4)	83(6)	28(4)	26(4)	11(3)	26(4)
F(1U)	119(9)	110(7)	42(4)	-4(5)	26(5)	51(6)
F(2U)	43(3)	87(6)	68(6)	53(5)	17(4)	25(4)
F(3U)	51(5)	133(11)	63(8)	63(8)	11(4)	43(6)

Table 5A.10. Hydrogen coordinates ($\times 10^4$) and isotropic displacement parameters ($Å^2 \times 10^3$) for $[FeLCO_2CH_3(Cl)](CF_3SO_3)$.

	x	y	z	U_{eq}
H(1A)	4649	9813	1870	44
H(1B)	4500	10219	2790	44
H(2A)	7235	10791	2499	49
H(2B)	6672	8844	2146	49
H(1A1)	5900	8254	1961	39
H(1A2)	5210	9496	1725	39
H(2A1)	6678	11239	2883	43
H(2A2)	5096	10201	3239	43
H(3A)	8225	10006	3492	44
H(3B)	6627	10222	3792	44
H(3C)	7281	10237	3936	44
H(3D)	8058	9800	3157	44
H(2N)	6480(30)	7250(30)	2926(12)	34
H(4)	6733	8117	4522	37

	x	y	z	U_{eq}
H(14A)	8826	6985	3608	66
H(14B)	8985	7422	4552	66
H(14C)	9341	8859	4120	66
H(6)	7246	4782	4466	33
H(7)	5187	2131	4377	34
H(8)	2467	1390	3809	33
H(10)	650	2175	2926	29
H(15A)	858	4973	4167	44
H(15B)	151	3110	4240	44
H(15C)	-817	3589	3625	44
H(4N)	550(20)	4410(30)	2576(14)	28
H(11A)	1059	2590	1696	39
H(11B)	2981	3663	2026	39
H(12A)	1005	4900	1293	42
H(12B)	2103	4090	821	42
H(13A)	4518	6317	1648	46
H(13B)	3564	6882	1072	46
H(16A)	2033	8961	2608	50
H(16B)	964	7045	2166	50
H(17A)	1442	7591	923	53
H(17B)	2556	9514	1360	53
H(19A)	-2178	9220	69	97
H(19B)	-2856	8280	728	97
H(19C)	-1767	10245	982	97
H(16C)	1724	8659	2563	45
H(16D)	896	6693	2175	45
H(17C)	2352	8705	1156	56
H(17D)	813	6928	922	56
H(19D)	-2417	8842	26	97
H(19E)	-2636	8956	934	97
H(19F)	-1186	10434	708	97

CHAPTER 6

Unpublished X-Ray Structural Data[1]

6.1. Experimental Methods

General Considerations. $FeCl_2$ and $Cu(ClO_4)_2 \cdot 6H_2O$ were obtained from commercially available sources and used without further purification. Anhydrous acetonitrile, diethyl ether, and methanol were purchased from commercial vendors and dried on an Innovative Technologies PureSolv 400 solvent purification system. Solvents used in bench top syntheses (e.g., copper(II) complexes) were purchased and used without further purification. Ligands L_2,[2] L_4,[3] and L_5[4] were prepared as described previously. The synthesis of L_{6a} is described in Chapter 5. Air-sensitive materials were manipulated in an MBraun glove box filled with ultra high purity argon (Airgas). Electrospray ionization (ESI) mass spectra were acquired on a Finigan LTQ mass spectrometer in the positive ion detection mode. Elemental analyses were carried out by the University of Illinois Microanalysis Laboratory (Urbana, IL).

Crystallographic Details. X-ray data for $[CuL_4](ClO_4)_2 \cdot CH_3CN \cdot H_2O$ (Section 6.3) and $[FeL_2(Cl)]Cl$ (Section 6.6) were graciously obtained from Dr. Alexander Filatov (University at Albany, SUNY, Albany, NY). The mother liquor was decanted from vials containing crystalline material and samples were coated in Paratone-N prior to shipment. Intensity data were measured on a Bruker SMART APEX CCD X-ray diffractometer

system equipped with a Mo-target X-ray tube (λ = 0.71073 Å). The frames were integrated with the Bruker SAINT software package[5] using a narrow-frame integration algorithm. The data were corrected for absorption effects using the empirical method (SADABS).[6] The structures were solved by direct methods and refined using the Bruker SHELXTL (Version 6.14) software package.[7] Only CIF files were provided for structures completed at SUNY Albany so further analysis of the refinements is not possible.

Single crystals of $[CuL_5](ClO_4)_2 \cdot H_2O$ and $[CuL_{6a}](ClO_4)_2 \cdot H_2O$ (Sections 6.4 and 6.5, respectively) were coated in Paratone-N and mounted on MiTeGen loops. X-ray intensity data were acquired at 100 K on a Bruker D8 Quest diffractometer equipped with Mo Kα radiation (λ = 0.71073 Å) and a Photon 100 CMOS detector. The frames were integrated with the Bruker SAINT software package[5] using a narrow-frame algorithm. The data were corrected for absorption effects using the empirical method (SADABS).[6] $[CuL_5](ClO_4)_2 \cdot H_2O$ was solved by direct methods and refined against F^2 on all data by full-matrix least squares using the SHELXTL software package.[7] $[CuL_{6a}](ClO_4)_2 \cdot H_2O$ was solved via the charge-flipping algorithm (CFA) and refined against F^2 on all data by full-matrix least squares using the SHELXL program embedded in Olex 2 (Version 1.2.6).[8]

All non-hydrogen atoms were refined anisotropically and all hydrogen atoms bound to carbon were included at geometrically calculated positions and refined using a riding model.[9] The isotropic displacement parameters of all hydrogen atoms were fixed to 1.2 times the U_{eq} value of the atoms they are linked to (1.5 times U_{eq} for methyl groups). Unless otherwise noted, all hydrogen atoms bound to electronegative elements (N, O) were found in the difference Fourier map and isotropic displacement parameters were

fixed to either 1.2 (N−H) or 1.5 (O−H) times the U_{eq} value of the atoms they are linked to.

For $[CuL_5](ClO_4)_2 \cdot H_2O$, similarity restratints (SADI) on 1,2- and 1,3-distances were applied to the two perchlorate ions in the asymmetric unit. All hydrogen atoms bound to nitrogen and oxygen were easily found from the difference Fourier map. N−H and O−H distances were restrained using the DFIX command (0.88 Å for N−H; 0.84 Å for O−H distances). The H−H distance of the lattice water molecule was also restrained with the use of the DANG command (1.39 Å). The finalized structure reveals a less than optimal H−O−H angle for the water molecule (100 °) and one of these hydrogen atoms clashes with the nearby amide hydrogen atom (H_{water}−H_{amide} = 1.28 Å). Attempts to disorder selected atoms of the pendant amide and lattice water molecule did not improve the model.

For $[CuL_{6a}](ClO_4)_2 \cdot H_2O$, O−H (1,2-) and H−H (1,3-) distance restraints were applied to the lattice water molecule using the DFIX command. DFIX restraints on amine N−H distances were disagreeable and thus were not applied. The acidic carboxylic acid hydrogen atom (H2O) was included in a calculated position using the HFIX 147 command. Similarity restratints (SADI) on 1,2- and 1,3-distances were applied to the two perchlorate ions in the asymmetric unit. No disorders were incorporated into the model.

6.2. Synthetic Procedures

Synthesis of $[CuL_4](ClO_4)_2 \cdot CH_3CN \cdot H_2O$. The synthesis involved dropwise addition of an acetonitrile solution (≈ 2 mL) of $Cu(ClO_4) \cdot 6H_2O$ (20 mg, 0.055 mmol) into an

equimolar amount of L_4 (20 mg, 0.055 mmol) in CH_3CN (2-3 mL) on the bench top at ambient temperature. Upon mixing, the color immediately became intense violet. The mixture was allowed to stir for several minutes, filtered, and prepared for crystallization. Since we were mainly concerned with obtaining structural data, the yield of product was not calculated. ESI-MS (+): *m/z* = 523.36 ($\{CuL_4(ClO_4)\}^+$, 40 %); 362.45 ($\{L_4 + H^+\}^+$, 100 %); 212.18 ($\{CuL_4\}^{2+}$, 24 %). Crystals of marginal quality were grown in several days at room temperature (after several attempts) by slow vapor diffusion of diethyl ether into dilute acetonitrile solutions of the complex. Crystallographic data for $[CuL_4](ClO_4)_2 \cdot CH_3CN \cdot H_2O$ is presented in Section 6.3.

Synthesis of $[CuL_5](ClO_4)_2 \cdot H_2O$. A solution of $Cu(ClO_4)_2 \cdot 6H_2O$ (56 mg, 0.15 mmol) in 1 mL CH_3OH was added dropwise to a stirring solution of L_5 (50 mg, 0.15 mmol) in 2 mL CH_3OH. Upon addition, the solution became intense blue-violet in color and blue precipitate was visible. The precipitate was collected, washed with cold CH_3OH, and used for subsequent crystallization attempts. The reaction can also be carried out using CH_3CN (or mixtures of CH_3CN and CH_3OH; L_5 is not very soluble in CH_3CN) to afford the same product, although it does not readily precipitate from these solutions. In this case, the blue powder was isolated via dropwise addition of solutions to a large volume (≈ 100 mL) of diethyl ether. ESI-MS (+): *m/z* = 495.09 ($\{CuL_5(ClO_4)\}^+$, 48 %); 198.09 ($\{CuL_5\}^{2+}$, 100 %). Violet crystals suitable for diffraction studies were obtained by slow evaporation of a CH_3CN solution of complex in the refrigerator. Crystallographic data for $[CuL_5](ClO_4)_2 \cdot H_2O$ is provided in Section 6.4.

Synthesis of $[CuL_{6a}](ClO_4)_2 \cdot H_2O$. The same procedures were followed as outlined in the synthesis of $[CuL_5](ClO_4)_2 \cdot H_2O$ above and identical observations were noted. ESI-MS (+): *m/z* = 496.18 ($\{CuL_{6a}(ClO_4)\}^+$, 16 %); 396.27 ($\{(CuL_{6a} - H^+\}^+$, 100 %); 198.73 ($\{CuL_{6a}\}^{2+}$, 10 %).Violet crystals suitable for diffraction studies were obtained after two weeks from slow vapor diffusion of methyl *tert*-butyl ether (MTBE) into a CH_3CN solution of complex at ambient temperature. Crystallographic data for $[CuL_{6a}](ClO_4)_2 \cdot H_2O$ is given in Section 6.5.

Synthesis of $[FeL_2(Cl)]Cl$. In the glove box, a methanolic solution of $FeCl_2$ (51 mg, 0.402 mmol in ≈ 3 mL) was added dropwise to a stirring solution of L_2 (117 mg, 0.424 mmol) in CH_3OH (2-3 mL). After several minutes of stirring, the yellow solution was filtered and prepared for crystallization. Crystals suitable for diffraction studies were obtained by slow vapor diffusion of diethyl ether into the methanolic solution of complex. ESI-MS (+): *m/z* = 367.36 ($\{FeL_2Cl\}^+$, 100 %). Anal. Calcd. for $C_{18}H_{28}Cl_2FeN_4$: C 47.66 %, H 7.00 %, N 13.90 %, Fe 13.85 %; found: C 47.83 %, H 7.05 %, N 13.63 %, Fe 13.99 %. Crystallographic data for $[FeL_2(Cl)]Cl$ is presented in Section 6.6.

6.3. Crystallographic Information for $[CuL_4](ClO_4)_2 \cdot CH_3CN \cdot H_2O$

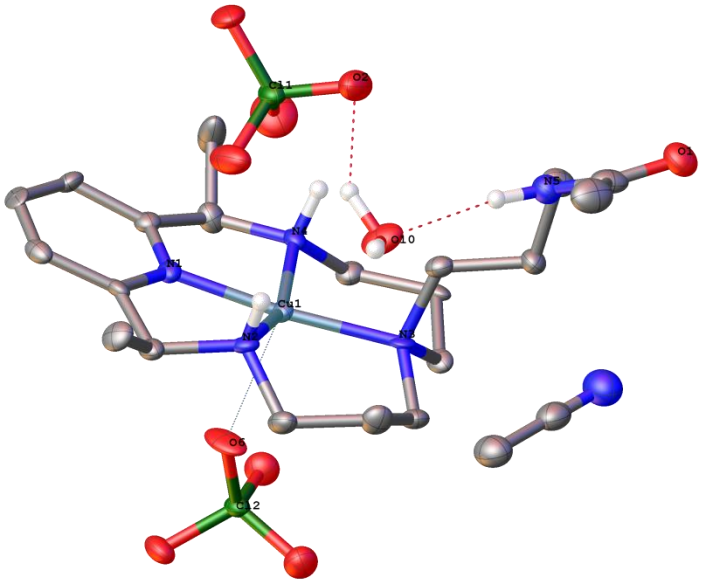

Figure 6.1. Thermal ellipsoid plot of $[CuL_4](ClO_4)_2 \cdot CH_3CN \cdot H_2O$ shown at the 50 % probability level. Carbon-bound hydrogen atoms are omitted for clarity. Selected distances (Å) and angles (°): Cu1−N1 = 1.908(6), Cu1−N2 = 2.021(6), Cu1−N3 = 2.001(6), Cu1−N4 = 2.025(6), Cu1−O6 = 2.394(6), N1−Cu1−N2 = 82.7(3), N1−Cu1−N4 = 81.8(3), N2−Cu1−N3 = 97.7(3), N3−Cu1−N4 = 96.2(2), N1−Cu1−N3 = 174.2(2), N2−Cu1−N4 = 158.2(2), O6−Cu1−N1 = 85.7(2), O6−Cu1−N2 = 87.8(2), O6−Cu1−N3 = 100.1(2), O6−Cu1−N4 = 106.2(2).

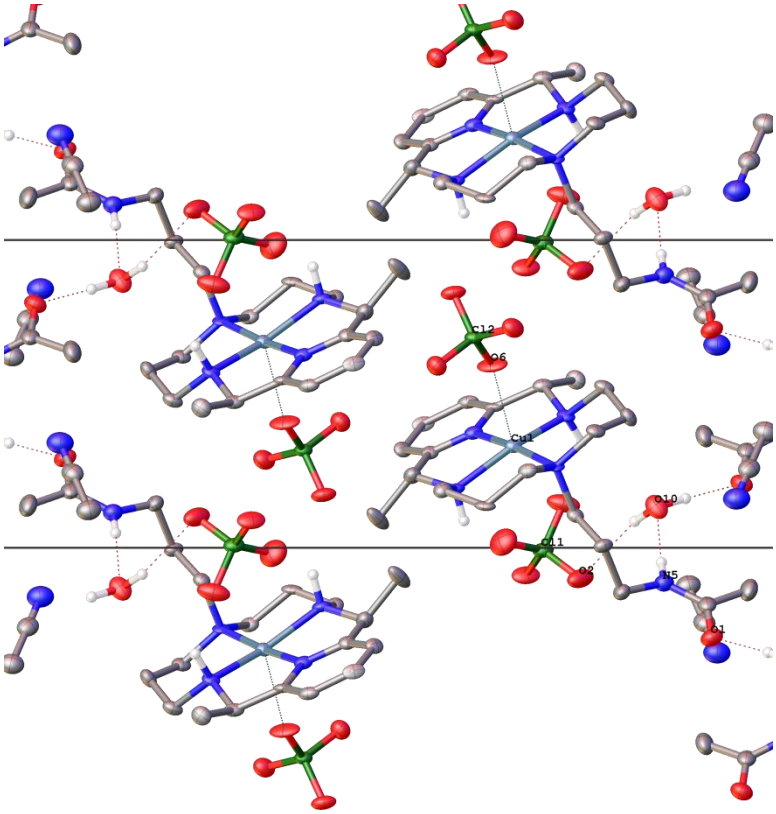

Figure 6.2. Packing diagram for $[CuL_4](ClO_4)_2 \cdot CH_3CN \cdot H_2O$ projected along the *c* axis. Selected distances (Å) and angles (°): Cu1−O6 = 2.393(6), N5−O10 = 2.924(9), N5−H5···O10 = 171.8(5), O1−O10 = 2.657(10), O10−H1O···O1 = 170(9), O10−O2 = 2.931(10), O10−H2O···O2 = 138(7).

Table 6.1. Crystallographic and refinement parameters for $[CuL_4](ClO_4)_2 \cdot CH_3CN \cdot H_2O$.

Identification code	str1285_Taryn (data collection by A. Filatov)	
Empirical Formula	C22 H40 Cl2 Cu N6 O10	
Formula weight	683.04	
Temperature (K)	100(2)	
Wavelength (Å)	0.71073	
Crystal system	Monoclinic	
Space group	$P2_1/n$ (no. 14)	
Unit cell dimensions:	a = 8.4431(9) Å	α = 90.00°
	b = 37.017(4) Å	β = 94.604(2)°
	c = 9.1372(10) Å	γ = 90.00°
Volume (Å^3)	2846.5(5)	
Z	4	
ρ_{calc} (g cm^{-1})	1.594	
Absorption coefficient (mm^{-1})	1.020	
F(000)	1428	

Crystal size (mm^3)	0.24 × 0.18 × 0.02
Crystal color	purple
Crystal morphology	plate
Theta range for data collection (deg)	2.20 to 28.34
Index ranges	$-11 \leq h \leq 11$ $-45 \leq k \leq 47$ $-12 \leq l \leq 12$
Reflections collected	23901
Independent reflections	6575 [R(int) = 0.0768]
Completeness to θ = 25 ° (%)	99.9
Absorption correction	Semi-empirical from equivalents
Max. and min. transmission	0.9799 and 0.7919
Refinement method	Full-matrix least squares on F^2
Data / restraints / parameters	6575 / 2 / 380
Goodness-of-fit on F^2	1.091
Final R indices [I>2sigma(I)]	R_1 = 0.1140, wR_2 = 0.2362
R indices (all data)	R_1 = 0.1360, wR_2 = 0.2470
Largest diff. peak and hole (e $Å^{-3}$)	2.282 and −0.941

Table 6.2. Atomic coordinates (× 10^4) and equivalent isotropic displacement parameters ($Å^2$ × 10^3) for $[CuL_4](ClO_4)_2 \cdot CH_3CN \cdot H_2O$. U_{eq} is defined as one third of the trace of the orthogonalized U^{ij} tensor.

	x	y	z	U_{eq}
Cu(1)	8304(1)	922(1)	2641(1)	17(1)
N(1)	8735(7)	629(2)	4345(7)	18(1)
N(2)	9284(7)	1312(2)	3971(7)	18(1)
N(3)	7633(7)	1236(2)	920(7)	17(1)
N(4)	6911(7)	495(2)	2010(6)	17(1)
N(5)	3854(8)	2037(2)	1682(8)	26(2)
N(6)	1592(11)	2427(3)	5133(10)	45(2)
Cl(1)	4919(2)	1142(1)	5399(2)	24(1)
Cl(2)	11832(2)	630(1)	905(2)	18(1)
O(1)	2084(7)	2390(2)	380(7)	35(2)
O(2)	4001(8)	1418(2)	4634(8)	47(2)
O(3)	5183(10)	850(2)	4441(9)	54(2)
O(4)	6441(8)	1293(2)	5927(7)	48(2)
O(5)	4106(7)	1015(2)	6612(7)	38(2)
O(6)	10935(7)	767(2)	2062(7)	40(2)
O(7)	12143(7)	919(2)	-67(7)	36(2)
O(8)	10913(7)	356(2)	117(7)	32(1)
O(9)	13284(7)	479(2)	1548(7)	31(1)

	x	y	z	U_{eq}
O(10)	1325(8)	3018(2)	9104(7)	36(2)
C(1)	9022(9)	257(2)	6924(8)	22(2)
C(2)	9731(9)	589(2)	6840(8)	21(2)
C(3)	9562(8)	779(2)	5525(8)	18(2)
C(4)	10270(9)	1141(2)	5230(8)	21(2)
C(5)	10456(10)	1383(2)	6573(8)	25(2)
C(6)	10213(9)	1595(2)	3259(9)	23(2)
C(7)	9243(10)	1774(2)	1997(9)	26(2)
C(8)	8793(9)	1531(2)	700(9)	22(2)
C(9)	7499(9)	1028(2)	-470(8)	20(2)
C(10)	6360(8)	713(2)	-536(8)	21(2)
C(11)	6872(9)	397(2)	431(8)	21(2)
C(12)	7345(10)	176(2)	2954(9)	24(2)
C(13)	5947(12)	-79(3)	3082(11)	39(2)
C(14)	8092(9)	306(2)	4406(8)	18(2)
C(15)	8192(9)	105(2)	5711(8)	22(2)
C(16)	6057(9)	1380(2)	1291(8)	20(2)
C(17)	5063(9)	1587(2)	130(9)	22(2)
C(18)	3561(10)	1724(2)	752(10)	26(2)
C(19)	3152(10)	2353(2)	1392(10)	29(2)
C(20)	3629(12)	2663(3)	2354(12)	39(2)
C(21)	2569(11)	2335(3)	5999(10)	33(2)
C(22)	3775(11)	2215(3)	7082(11)	38(2)

Table 6.3. Bond lengths (Å) and angles (°) for $[CuL_4](ClO_4)_2 \cdot CH_3CN \cdot H_2O$.

Cu(1)-N(1)	1.908(6)
Cu(1)-N(3)	2.001(6)
Cu(1)-N(2)	2.021(6)
Cu(1)-N(4)	2.025(6)
Cu(1)-O(6)	2.394(6)
N(1)-C(14)	1.316(10)
N(1)-C(3)	1.355(9)
N(2)-C(6)	1.492(9)
N(2)-C(4)	1.503(10)
N(2)-H(2)	0.9300
N(3)-C(9)	1.480(9)
N(3)-C(8)	1.491(9)
N(3)-C(16)	1.499(9)
N(4)-C(11)	1.486(9)
N(4)-C(12)	1.491(10)

N(4)-H(4)	0.9300
N(5)-C(19)	1.329(11)
N(5)-C(18)	1.445(11)
N(5)-H(5)	0.8800
N(6)-C(21)	1.148(13)
Cl(1)-O(3)	1.420(7)
Cl(1)-O(5)	1.430(6)
Cl(1)-O(2)	1.430(7)
Cl(1)-O(4)	1.449(7)
Cl(2)-O(7)	1.430(6)
Cl(2)-O(9)	1.430(6)
Cl(2)-O(8)	1.436(6)
Cl(2)-O(6)	1.441(6)
O(1)-C(19)	1.246(11)
C(1)-C(2)	1.371(11)
C(1)-C(15)	1.382(11)
C(1)-H(1)	0.9500
C(2)-C(3)	1.390(11)
C(2)-H(2A)	0.9500
C(3)-C(4)	1.503(11)
C(4)-C(5)	1.518(10)
C(4)-H(4A)	1.0000
C(5)-H(5A)	0.9800
C(5)-H(5B)	0.9800
C(5)-H(5C)	0.9800
C(6)-C(7)	1.511(11)
C(6)-H(6A)	0.9900
C(6)-H(6B)	0.9900
C(7)-C(8)	1.512(11)
C(7)-H(7A)	0.9900
C(7)-H(7B)	0.9900
C(8)-H(8A)	0.9900
C(8)-H(8B)	0.9900
C(9)-C(10)	1.511(11)
C(9)-H(9A)	0.9900
C(9)-H(9B)	0.9900
C(10)-C(11)	1.508(11)
C(10)-H(10A)	0.9900
C(10)-H(10B)	0.9900
C(11)-H(11A)	0.9900
C(11)-H(11B)	0.9900
C(12)-C(14)	1.502(11)
C(12)-C(13)	1.523(11)
C(12)-H(12)	1.0000

C(13)-H(13A)	0.9800
C(13)-H(13B)	0.9800
C(13)-H(13C)	0.9800
C(14)-C(15)	1.401(10)
C(15)-H(15)	0.9500
C(16)-C(17)	1.508(10)
C(16)-H(16A)	0.9900
C(16)-H(16B)	0.9900
C(17)-C(18)	1.518(11)
C(17)-H(17A)	0.9900
C(17)-H(17B)	0.9900
C(18)-H(18A)	0.9900
C(18)-H(18B)	0.9900
C(19)-C(20)	1.480(13)
C(20)-H(20A)	0.9800
C(20)-H(20B)	0.9800
C(20)-H(20C)	0.9800
C(21)-C(22)	1.433(13)
C(22)-H(22A)	0.9800
C(22)-H(22B)	0.9800
C(22)-H(22C)	0.9800

N(1)-Cu(1)-N(3)	174.2(2)
N(1)-Cu(1)-N(2)	82.7(3)
N(3)-Cu(1)-N(2)	97.7(3)
N(1)-Cu(1)-N(4)	81.8(3)
N(3)-Cu(1)-N(4)	96.2(2)
N(2)-Cu(1)-N(4)	158.2(2)
N(1)-Cu(1)-O(6)	85.7(2)
N(3)-Cu(1)-O(6)	100.1(2)
N(2)-Cu(1)-O(6)	87.8(2)
N(4)-Cu(1)-O(6)	106.2(2)
C(14)-N(1)-C(3)	121.7(7)
C(14)-N(1)-Cu(1)	119.9(5)
C(3)-N(1)-Cu(1)	118.0(5)
C(6)-N(2)-C(4)	110.5(6)
C(6)-N(2)-Cu(1)	116.4(5)
C(4)-N(2)-Cu(1)	109.6(5)
C(6)-N(2)-H(2)	106.6
C(4)-N(2)-H(2)	106.6
Cu(1)-N(2)-H(2)	106.6
C(9)-N(3)-C(8)	105.7(6)
C(9)-N(3)-C(16)	111.8(6)
C(8)-N(3)-C(16)	111.9(6)

C(9)-N(3)-Cu(1)	111.7(5)
C(8)-N(3)-Cu(1)	112.6(5)
C(16)-N(3)-Cu(1)	103.3(4)
C(11)-N(4)-C(12)	110.6(6)
C(11)-N(4)-Cu(1)	115.8(5)
C(12)-N(4)-Cu(1)	110.1(4)
C(11)-N(4)-H(4)	106.6
C(12)-N(4)-H(4)	106.6
Cu(1)-N(4)-H(4)	106.6
C(19)-N(5)-C(18)	122.4(8)
C(19)-N(5)-H(5)	118.8
C(18)-N(5)-H(5)	118.8
O(3)-Cl(1)-O(5)	109.7(5)
O(3)-Cl(1)-O(2)	110.4(5)
O(5)-Cl(1)-O(2)	109.8(4)
O(3)-Cl(1)-O(4)	108.7(5)
O(5)-Cl(1)-O(4)	109.7(4)
O(2)-Cl(1)-O(4)	108.6(5)
O(7)-Cl(2)-O(9)	110.8(4)
O(7)-Cl(2)-O(8)	109.7(4)
O(9)-Cl(2)-O(8)	109.9(4)
O(7)-Cl(2)-O(6)	109.0(4)
O(9)-Cl(2)-O(6)	108.6(4)
O(8)-Cl(2)-O(6)	108.8(4)
Cl(2)-O(6)-Cu(1)	142.9(4)
H(1O)-O(10)-H(2O)	107(10)
C(2)-C(1)-C(15)	120.9(7)
C(2)-C(1)-H(1)	119.6
C(15)-C(1)-H(1)	119.6
C(1)-C(2)-C(3)	119.2(7)
C(1)-C(2)-H(2A)	120.4
C(3)-C(2)-H(2A)	120.4
N(1)-C(3)-C(2)	119.4(7)
N(1)-C(3)-C(4)	114.2(6)
C(2)-C(3)-C(4)	126.4(7)
N(2)-C(4)-C(3)	108.0(6)
N(2)-C(4)-C(5)	112.7(7)
C(3)-C(4)-C(5)	113.5(6)
N(2)-C(4)-H(4A)	107.5
C(3)-C(4)-H(4A)	107.5
C(5)-C(4)-H(4A)	107.5
C(4)-C(5)-H(5A)	109.5
C(4)-C(5)-H(5B)	109.5
H(5A)-C(5)-H(5B)	109.5

C(4)-C(5)-H(5C)	109.5
H(5A)-C(5)-H(5C)	109.5
H(5B)-C(5)-H(5C)	109.5
N(2)-C(6)-C(7)	111.6(6)
N(2)-C(6)-H(6A)	109.3
C(7)-C(6)-H(6A)	109.3
N(2)-C(6)-H(6B)	109.3
C(7)-C(6)-H(6B)	109.3
H(6A)-C(6)-H(6B)	108.0
C(6)-C(7)-C(8)	115.2(7)
C(6)-C(7)-H(7A)	108.5
C(8)-C(7)-H(7A)	108.5
C(6)-C(7)-H(7B)	108.5
C(8)-C(7)-H(7B)	108.5
H(7A)-C(7)-H(7B)	107.5
N(3)-C(8)-C(7)	117.1(6)
N(3)-C(8)-H(8A)	108.0
C(7)-C(8)-H(8A)	108.0
N(3)-C(8)-H(8B)	108.0
C(7)-C(8)-H(8B)	108.0
H(8A)-C(8)-H(8B)	107.3
N(3)-C(9)-C(10)	116.1(6)
N(3)-C(9)-H(9A)	108.3
C(10)-C(9)-H(9A)	108.3
N(3)-C(9)-H(9B)	108.3
C(10)-C(9)-H(9B)	108.3
H(9A)-C(9)-H(9B)	107.4
C(11)-C(10)-C(9)	115.1(6)
C(11)-C(10)-H(10A)	108.5
C(9)-C(10)-H(10A)	108.5
C(11)-C(10)-H(10B)	108.5
C(9)-C(10)-H(10B)	108.5
H(10A)-C(10)-H(10B)	107.5
N(4)-C(11)-C(10)	111.2(6)
N(4)-C(11)-H(11A)	109.4
C(10)-C(11)-H(11A)	109.4
N(4)-C(11)-H(11B)	109.4
C(10)-C(11)-H(11B)	109.4
H(11A)-C(11)-H(11B)	108.0
N(4)-C(12)-C(14)	108.9(6)
N(4)-C(12)-C(13)	112.3(7)
C(14)-C(12)-C(13)	113.8(7)
N(4)-C(12)-H(12)	107.2
C(14)-C(12)-H(12)	107.2

C(13)-C(12)-H(12)	107.2
C(12)-C(13)-H(13A)	109.5
C(12)-C(13)-H(13B)	109.5
H(13A)-C(13)-H(13B)	109.5
C(12)-C(13)-H(13C)	109.5
H(13A)-C(13)-H(13C)	109.5
H(13B)-C(13)-H(13C)	109.5
N(1)-C(14)-C(15)	121.3(7)
N(1)-C(14)-C(12)	113.5(7)
C(15)-C(14)-C(12)	125.1(7)
C(1)-C(15)-C(14)	117.4(7)
C(1)-C(15)-H(15)	121.3
C(14)-C(15)-H(15)	121.3
N(3)-C(16)-C(17)	118.5(6)
N(3)-C(16)-H(16A)	107.7
C(17)-C(16)-H(16A)	107.7
N(3)-C(16)-H(16B)	107.7
C(17)-C(16)-H(16B)	107.7
H(16A)-C(16)-H(16B)	107.1
C(16)-C(17)-C(18)	109.9(7)
C(16)-C(17)-H(17A)	109.7
C(18)-C(17)-H(17A)	109.7
C(16)-C(17)-H(17B)	109.7
C(18)-C(17)-H(17B)	109.7
H(17A)-C(17)-H(17B)	108.2
N(5)-C(18)-C(17)	112.3(7)
N(5)-C(18)-H(18A)	109.1
C(17)-C(18)-H(18A)	109.1
N(5)-C(18)-H(18B)	109.1
C(17)-C(18)-H(18B)	109.5
H(18A)-C(18)-H(18B)	109.5
O(1)-C(19)-N(5)	109.5
O(1)-C(19)-C(20)	109.5
N(5)-C(19)-C(20)	109.5
C(19)-C(20)-H(20A)	179.0(11)
C(19)-C(20)-H(20B)	109.5
H(20A)-C(20)-H(20B)	109.5
C(19)-C(20)-H(20C)	109.5
H(20A)-C(20)-H(20C)	109.5
H(20B)-C(20)-H(20C)	109.5
N(6)-C(21)-C(22)	117.9(8)
C(21)-C(22)-H(22A)	120.1(8)
C(21)-C(22)-H(22B)	121.9(8)
H(22A)-C(22)-H(22B)	107.9

C(21)-C(22)-H(22C)	109.1
H(22A)-C(22)-H(22C)	109.5
H(22B)-C(22)-H(22C)	109.5

Table 6.4. Anisotropic displacement parameters ($Å^2 \times 10^3$) for $[CuL_4](ClO_4)_2 \cdot CH_3CN \cdot H_2O$. The anisotropic displacement factor exponent takes the form: $-2\pi^2[h^2 a^{*2} U^{11} + ... + 2 h k a^* b^* U^{12}]$.

	U^{11}	U^{22}	U^{33}	U^{23}	U^{13}	U^{12}
Cu(1)	15(1)	24(1)	13(1)	1(1)	4(1)	-1(1)
N(1)	15(3)	28(4)	13(3)	1(2)	4(2)	3(3)
N(2)	13(3)	27(4)	15(3)	-1(2)	7(2)	-4(2)
N(3)	8(3)	27(3)	18(3)	0(2)	8(2)	0(2)
N(4)	10(3)	29(3)	14(3)	0(2)	2(2)	3(2)
N(5)	23(4)	31(4)	25(4)	1(3)	2(3)	1(3)
N(6)	37(5)	59(6)	39(5)	1(4)	5(4)	-1(4)
Cl(1)	18(1)	36(1)	18(1)	2(1)	6(1)	2(1)
Cl(2)	13(1)	28(1)	15(1)	0(1)	3(1)	0(1)
O(1)	26(3)	40(4)	39(4)	1(3)	2(3)	7(3)
O(2)	29(4)	56(5)	57(5)	29(4)	11(3)	8(3)
O(3)	59(5)	59(5)	46(4)	-16(4)	11(4)	11(4)
O(4)	27(4)	88(6)	28(4)	-1(4)	3(3)	-13(4)
O(5)	25(3)	64(5)	26(3)	13(3)	13(3)	1(3)
O(6)	17(3)	75(5)	29(3)	-16(3)	11(3)	8(3)
O(7)	31(3)	38(4)	39(4)	10(3)	2(3)	-5(3)
O(8)	31(3)	32(3)	33(3)	-2(3)	1(3)	-4(3)
O(9)	16(3)	51(4)	27(3)	2(3)	1(2)	6(3)
O(10)	46(4)	41(4)	23(3)	6(3)	14(3)	10(3)
C(1)	19(4)	41(5)	6(3)	5(3)	7(3)	4(3)
C(2)	14(3)	36(5)	13(3)	-6(3)	2(3)	3(3)
C(3)	7(3)	32(4)	14(3)	-3(3)	1(3)	1(3)
C(4)	15(3)	34(4)	14(3)	1(3)	4(3)	1(3)
C(5)	30(4)	32(5)	13(4)	-5(3)	4(3)	-3(3)
C(6)	17(4)	33(4)	19(4)	1(3)	2(3)	-7(3)
C(7)	27(4)	22(4)	28(4)	1(3)	1(3)	-9(3)
C(8)	15(4)	30(4)	22(4)	4(3)	6(3)	-3(3)
C(9)	18(4)	30(4)	12(3)	-4(3)	4(3)	3(3)
C(10)	8(3)	37(5)	17(4)	-5(3)	4(3)	-2(3)
C(11)	20(4)	26(4)	18(4)	0(3)	7(3)	2(3)
C(12)	22(4)	25(4)	26(4)	0(3)	-2(3)	2(3)
C(13)	38(5)	40(5)	37(5)	18(4)	-16(4)	-22(4)
C(14)	15(3)	25(4)	16(4)	0(3)	6(3)	1(3)
C(15)	20(4)	26(4)	19(4)	7(3)	8(3)	-2(3)

	U^{11}	U^{22}	U^{33}	U^{23}	U^{13}	U^{12}
C(16)	18(4)	24(4)	18(4)	0(3)	6(3)	-3(3)
C(17)	16(4)	30(4)	21(4)	4(3)	2(3)	4(3)
C(18)	21(4)	24(4)	35(5)	-1(3)	5(3)	3(3)
C(19)	21(4)	29(5)	38(5)	-2(4)	13(4)	0(3)
C(20)	40(6)	27(5)	52(6)	-1(4)	16(5)	6(4)
C(21)	30(5)	39(5)	33(5)	-6(4)	12(4)	-3(4)
C(22)	33(5)	50(6)	32(5)	2(4)	7(4)	3(4)

Table 6.5. Hydrogen coordinates ($\times 10^4$) and isotropic displacement parameters ($Å^2 \times 10^3$) for $[CuL_4](ClO_4)_2 \cdot CH_3CN \cdot H_2O$.

	x	y	z	U_{eq}
H(1)	9102	129	7829	26
H(2)	8448	1429	4374	22
H(4)	5878	558	2191	21
H(5)	4521	2017	2469	32
H(1O)	1600(130)	2805(18)	9670(110)	54
H(2O)	860(120)	3180(20)	9750(100)	54
H(2A)	10331	687	7669	25
H(4A)	11355	1099	4899	25
H(5A)	10819	1623	6288	37
H(5B)	11238	1278	7301	37
H(5C)	9431	1406	6998	37
H(6A)	11174	1485	2892	28
H(6B)	10564	1781	3996	28
H(7A)	9853	1981	1653	31
H(7B)	8257	1870	2366	31
H(8A)	8349	1684	-122	26
H(8B)	9778	1419	388	26
H(9A)	8567	936	-650	24
H(9B)	7166	1196	-1280	24
H(10A)	5317	799	-254	25
H(10B)	6209	627	-1564	25
H(11A)	6125	193	228	26
H(11B)	7942	316	199	26
H(12)	8177	38	2468	29
H(13A)	5157	38	3655	59
H(13B)	6321	-302	3575	59
H(13C)	5462	-136	2099	59
H(15)	7709	-126	5760	26
H(16A)	6247	1540	2156	24

	x	y	z	U_{eq}
H(16B)	5414	1174	1596	24
H(17A)	4779	1428	-722	27
H(17B)	5681	1794	-212	27
H(18A)	2772	1788	-67	32
H(18B)	3104	1529	1328	32
H(20A)	4070	2854	1769	59
H(20B)	4433	2584	3120	59
H(20C)	2698	2755	2810	59
H(22A)	3522	2298	8054	57
H(22B)	4805	2314	6858	57
H(22C)	3824	1950	7075	57

6.4. Crystallographic Information for $[CuL_5](ClO_4)_2 \cdot H_2O$

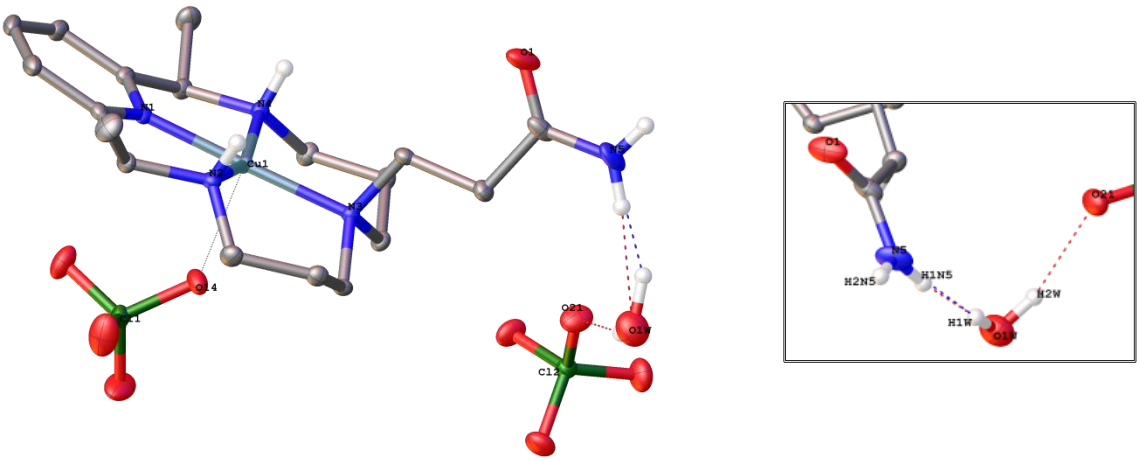

Figure 6.3. Thermal ellipsoid plot of $[CuL_5](ClO_4)_2 \cdot H_2O$ shown at the 50 % probability level. Carbon-bound hydrogen atoms are omitted for clarity. Selected distances (Å) and angles (°): Cu1−N1 = 1.9307(14), Cu1−N2 = 2.0423(14), Cu1−N3 = 2.0111(14), Cu1−N4 = 2.0385(14), Cu1−O14 = 2.4782(12), N1−Cu1−N2 = 82.64(6), N1−Cu1−N4 = 82.27(6), N2−Cu1−N3 = 96.30(5), N3−Cu1−N4 = 98.45(5), N1−Cu1−N3 = 178.34(6), N2−Cu1−N4 = 159.83(6). Inset shows different perspective of the water molecule.

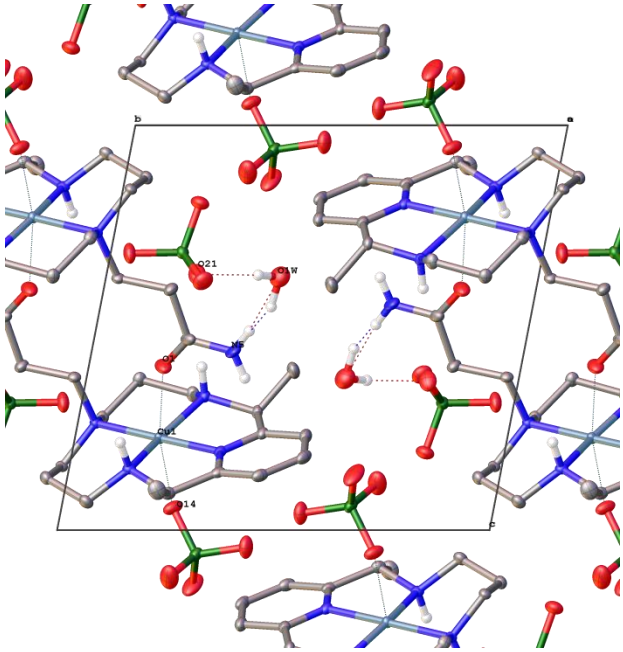

Figure 6.4. Packing diagram for $[CuL_5](ClO_4)_2 \cdot H_2O$ projected along the *a* axis. Selected distances (Å) and angles (°): Cu1−O1 = 2.8275(14), Cu1−O14 = 2.4782(12), N5−O1W = 2.996(3), N5−H1N5···O1W = 173.2, O1W−H1W···N5 = 154.3, O21−O1W = 2.838(2) O1W−H2W···O21 = 164.3.

Table 6.6. Crystallographic and refinement parameters for $[CuL_5](ClO_4)_2 \cdot H_2O$.

Identification code	040714 (completed in house)
Empirical Formula	C18 H33 Cl2 Cu N5 O10
Formula weight	613.93
Temperature (K)	100(2)
Wavelength (Å)	0.71073
Crystal system	Triclinic
Space group	*P*−1 (no. 2)
Unit cell dimensions	
a (Å)	9.2474(6)
b (Å)	11.8945(9)
c (Å)	12.0058(9)
α (deg)	76.628(2)
β (deg)	68.8140(19)
γ (deg)	81.052(2)
Volume ($Å^3$)	1194.15(15)
Z	2
ρ_{calc} (g cm^{-1})	1.707
Absorption coefficient (mm^{-1})	1.204

F(000)	638
Crystal size (mm^3)	0.37 × 0.27 × 0.22
Crystal color	blue
Crystal morphology	block
Theta range for data collection (deg)	2.70 to 27.10
Index ranges	$-11 \leq h \leq 11$
	$-15 \leq k \leq 15$
	$-15 \leq l \leq 15$
Reflections collected	39534
Independent reflections	5251 [R(int) = 0.0186]
Completeness to θ = 25.242 ° (%)	99.9 %
Absorption correction	Semi-empirical from equivalents
Max. and min. transmission	0.7780 and 0.6640
Refinement method	Full-matrix least squares on F^2
Data / restraints / parameters	5251 / 101 / 345
Goodness-of-fit on F^2	1.091
Final R indices [I>2sigma(I)]	R_1 = 0.0269, wR_2 = 0.0670
R indices (all data)	R_1 = 0.0286, wR_2 = 0.0679
Largest diff. peak and hole (e $Å^{-3}$)	0.577 and −0.325

Table 6.7. Atomic coordinates and equivalent isotropic displacement parameters ($Å^2$) for $[CuL_5](ClO_4)_2 \cdot H_2O$. U_{eq} is defined as one third of the trace of the orthogonalized U^{ij} tensor.

	x	y	z	U_{eq}
Cu1	0.22184(2)	0.19565(2)	0.22736(2)	0.01006(6)
N1	0.10770(16)	0.34228(12)	0.19381(12)	0.0119(3)
C1	0.12293(19)	0.43094(14)	0.23925(15)	0.0137(3)
C2	0.0270(2)	0.53271(15)	0.23212(16)	0.0178(3)
C3	0.9137(2)	0.53792(16)	0.18024(16)	0.0194(4)
C4	0.8986(2)	0.44450(16)	0.13515(15)	0.0176(3)
C5	0.00040(19)	0.34636(15)	0.14239(15)	0.0138(3)
C6	0.00647(19)	0.24028(15)	0.09092(15)	0.0146(3)
N2	0.08796(16)	0.13944(12)	0.15129(12)	0.0119(3)
C7	0.1617(2)	0.05423(15)	0.07023(15)	0.0159(3)
C8	0.2452(2)	0.95117(14)	0.12906(15)	0.0145(3)
C9	0.37960(19)	0.98209(14)	0.15756(14)	0.0124(3)
N3	0.33485(15)	0.04077(12)	0.26468(12)	0.0104(3)
C10	0.48633(19)	0.05423(14)	0.27776(15)	0.0129(3)
C11	0.4762(2)	0.12346(14)	0.37233(16)	0.0146(3)
C12	0.4419(2)	0.25312(15)	0.33598(16)	0.0152(3)
N4	0.28234(16)	0.28165(12)	0.33045(13)	0.0118(3)
C13	0.2526(2)	0.40985(14)	0.29168(15)	0.0140(3)

	x	y	z	U_{eq}
C14	0.2221(2)	0.47488(16)	0.39458(17)	0.0209(4)
C15	0.8470(2)	0.21299(17)	0.09902(19)	0.0229(4)
C16	0.22985(19)	0.97114(14)	0.37790(14)	0.0131(3)
C17	0.2905(2)	0.84463(15)	0.40512(15)	0.0167(3)
C18	0.1954(2)	0.78197(16)	0.52897(16)	0.0198(4)
O1	0.07789(18)	0.82795(12)	0.59530(13)	0.0307(3)
N5	0.2523(2)	0.67284(15)	0.55861(15)	0.0270(4)
Cl1	0.46685(5)	0.33185(3)	0.93961(4)	0.01655(9)
O11	0.3856(2)	0.28056(14)	0.88395(16)	0.0388(4)
O12	0.62633(18)	0.33820(14)	0.86422(15)	0.0408(4)
O13	0.39383(17)	0.44433(12)	0.95806(14)	0.0279(3)
O14	0.45905(16)	0.25772(12)	0.05551(12)	0.0236(3)
Cl2	0.85333(5)	0.83452(3)	0.31389(4)	0.01419(9)
O21	0.70074(16)	0.79065(12)	0.36837(14)	0.0270(3)
O22	0.94891(17)	0.77422(13)	0.38440(13)	0.0280(3)
O23	0.92230(17)	0.81602(12)	0.19154(12)	0.0249(3)
O24	0.83780(16)	0.95636(11)	0.31598(13)	0.0252(3)
O1W	0.5492(2)	0.59816(14)	0.37457(15)	0.0363(4)

Table 6.8. Bond lengths (Å) and angles (°) for $[CuL_5](ClO_4)_2 \cdot H_2O$.

Cu1-N1	1.9307(14)
Cu1-N2	2.0423(14)
Cu1-N3	2.0111(14)
Cu1-N4	2.0385(14)
N1-C5	1.335(2)
N1-C1	1.341(2)
C1-C2	1.390(2)
C1-C13	1.509(2)
C2-C3	1.386(3)
C2-H2	0.95
C3-C4	1.389(3)
C3-H3	0.95
C4-C5	1.388(2)
C4-H4	0.95
C5-C6	1.513(2)
C6-N2	1.498(2)
C6-C15	1.523(2)
C6-H6	1.0
N2-C7	1.483(2)
N2-H2N	0.870(15)

C7-C8	1.515(2)
C7-H7A	0.99
C7-H7B	0.99
C8-C9	1.519(2)
C8-H8A	0.99
C8-H8B	0.99
C9-N3	1.501(2)
C9-H9A	0.99
C9-H9B	0.99
N3-C16	1.501(2)
N3-C10	1.501(2)
C10-C11	1.519(2)
C10-H10A	0.99
C10-H10B	0.99
C11-C12	1.519(2)
C11-H11A	0.99
C11-H11B	0.99
C12-N4	1.484(2)
C12-H12A	0.99
C12-H12B	0.99
N4-C13	1.500(2)
N4-H4N	0.866(15)
C13-C14	1.525(2)
C13-H13	1.0
C14-H14A	0.98
C14-H14B	0.98
C14-H14C	0.98
C15-H15A	0.98
C15-H15B	0.98
C15-H15C	0.98
C16-C17	1.526(2)
C16-H16A	0.99
C16-H16B	0.99
C17-C18	1.512(2)
C17-H17A	0.99
C17-H17B	0.99
C18-O1	1.227(2)
C18-N5	1.341(3)
N5-H1N5	0.873(17)
N5-H2N5	0.826(16)
Cl1-O11	1.4416(15)
Cl1-O12	1.4277(15)
Cl1-O13	1.4293(14)
Cl1-O14	1.4486(13)

Cl2-O21	1.4475(14)
Cl2-O22	1.4405(14)
Cl2-O23	1.4288(13)
Cl2-O24	1.4390(13)
O1W-H1W	0.920(17)
O1W-H2W	0.879(17)

N1-Cu1-N3	178.34(6)
N1-Cu1-N4	82.27(6)
N3-Cu1-N4	98.45(5)
N1-Cu1-N2	82.64(6)
N3-Cu1-N2	96.30(5)
N4-Cu1-N2	159.83(6)
C5-N1-C1	122.39(15)
C5-N1-Cu1	118.50(11)
C1-N1-Cu1	118.35(11)
N1-C1-C2	120.23(16)
N1-C1-C13	114.20(14)
C2-C1-C13	125.53(16)
C3-C2-C1	118.12(17)
C3-C2-H2	120.9
C1-C2-H2	120.9
C2-C3-C4	120.70(16)
C2-C3-H3	119.6
C4-C3-H3	119.6
C5-C4-C3	118.40(16)
C5-C4-H4	120.8
C3-C4-H4	120.8
N1-C5-C4	120.14(16)
N1-C5-C6	114.63(14)
C4-C5-C6	125.18(16)
N2-C6-C5	109.48(13)
N2-C6-C15	112.03(14)
C5-C6-C15	113.05(14)
N2-C6-H6	107.3
C5-C6-H6	107.3
C15-C6-H6	107.3
C7-N2-C6	110.87(13)
C7-N2-Cu1	117.99(10)
C6-N2-Cu1	110.51(10)
C7-N2-H2N	109.0(14)
C6-N2-H2N	106.9(14)
Cu1-N2-H2N	100.6(14)
N2-C7-C8	112.01(13)

N2-C7-H7A	109.2
C8-C7-H7A	109.2
N2-C7-H7B	109.2
C8-C7-H7B	109.2
H7A-C7-H7B	107.9
C7-C8-C9	113.94(14)
C7-C8-H8A	108.8
C9-C8-H8A	108.8
C7-C8-H8B	108.8
C9-C8-H8B	108.8
H8A-C8-H8B	107.7
N3-C9-C8	115.60(13)
N3-C9-H9A	108.4
C8-C9-H9A	108.4
N3-C9-H9B	108.4
C8-C9-H9B	108.4
H9A-C9-H9B	107.4
C16-N3-C10	111.64(12)
C16-N3-C9	111.85(12)
C10-N3-C9	104.82(12)
C16-N3-Cu1	108.44(10)
C10-N3-Cu1	111.37(10)
C9-N3-Cu1	108.68(10)
N3-C10-C11	115.93(13)
N3-C10-H10A	108.3
C11-C10-H10A	108.3
N3-C10-H10B	108.3
C11-C10-H10B	108.3
H10A-C10-H10B	107.4
C12-C11-C10	114.26(14)
C12-C11-H11A	108.7
C10-C11-H11A	108.7
C12-C11-H11B	108.7
C10-C11-H11B	108.7
H11A-C11-H11B	107.6
N4-C12-C11	111.64(13)
N4-C12-H12A	109.3
C11-C12-H12A	109.3
N4-C12-H12B	109.3
C11-C12-H12B	109.3
H12A-C12-H12B	108.0
C12-N4-C13	110.62(13)
C12-N4-Cu1	116.68(10)
C13-N4-Cu1	109.65(10)

C12-N4-H4N	108.2(14)
C13-N4-H4N	107.3(14)
Cu1-N4-H4N	103.8(14)
N4-C13-C1	108.68(13)
N4-C13-C14	112.06(14)
C1-C13-C14	113.35(14)
N4-C13-H13	107.5
C1-C13-H13	107.5
C14-C13-H13	107.5
C13-C14-H14A	109.5
C13-C14-H14B	109.5
H14A-C14-H14B	109.5
C13-C14-H14C	109.5
H14A-C14-H14C	109.5
H14B-C14-H14C	109.5
C6-C15-H15A	109.5
C6-C15-H15B	109.5
H15A-C15-H15B	109.5
C6-C15-H15C	109.5
H15A-C15-H15C	109.5
H15B-C15-H15C	109.5
N3-C16-C17	113.86(13)
N3-C16-H16A	108.8
C17-C16-H16A	108.8
N3-C16-H16B	108.8
C17-C16-H16B	108.8
H16A-C16-H16B	107.7
C18-C17-C16	112.39(15)
C18-C17-H17A	109.1
C16-C17-H17A	109.1
C18-C17-H17B	109.1
C16-C17-H17B	109.1
H17A-C17-H17B	107.9
O1-C18-N5	123.86(17)
O1-C18-C17	122.51(17)
N5-C18-C17	113.62(16)
C18-N5-H1N5	119.8(17)
C18-N5-H2N5	117.4(18)
H1N5-N5-H2N5	123.(2)
O12-Cl1-O13	111.07(9)
O12-Cl1-O11	109.67(12)
O13-Cl1-O11	109.39(9)
O12-Cl1-O14	108.65(9)
O13-Cl1-O14	109.91(9)

O11-Cl1-O14	108.09(9)
O23-Cl2-O24	110.21(9)
O23-Cl2-O22	109.79(9)
O24-Cl2-O22	109.33(9)
O23-Cl2-O21	109.94(9)
O24-Cl2-O21	108.88(8)
O22-Cl2-O21	108.66(9)
H1W-O1W-H2W	101.(2)

Table 6.9. Anisotropic displacement parameters ($Å^2$) for $[CuL_5](ClO_4)_2 \cdot H_2O$. The anisotropic displacement factor exponent takes the form: $-2\pi^2[h^2\, a^{*2}\, U^{11} + ... + 2\, h\, k\, a^*\, b^*\, U^{12}]$.

	U^{11}	U^{22}	U^{33}	U^{23}	U^{13}	U^{12}
Cu1	0.00995(10)	0.00956(10)	0.01121(10)	-0.00260(7)	-0.00449(7)	0.00085(7)
N1	0.0098(6)	0.0120(6)	0.0112(6)	0.0000(5)	-0.0016(5)	-0.0008(5)
C1	0.0136(8)	0.0115(7)	0.0123(7)	-0.0005(6)	-0.0011(6)	-0.0012(6)
C2	0.0189(9)	0.0122(8)	0.0176(8)	-0.0019(6)	-0.0024(7)	0.0019(6)
C3	0.0166(8)	0.0167(8)	0.0164(8)	0.0023(7)	-0.0015(7)	0.0055(7)
C4	0.0137(8)	0.0210(9)	0.0137(8)	0.0013(7)	-0.0039(6)	0.0028(7)
C5	0.0114(7)	0.0162(8)	0.0098(7)	0.0012(6)	-0.0013(6)	-0.0007(6)
C6	0.0128(8)	0.0177(8)	0.0129(8)	-0.0016(6)	-0.0059(6)	0.0013(6)
N2	0.0100(6)	0.0146(7)	0.0098(6)	-0.0021(5)	-0.0021(5)	-0.0006(5)
C7	0.0179(8)	0.0180(8)	0.0143(8)	-0.0063(6)	-0.0069(7)	-0.0001(7)
C8	0.0163(8)	0.0135(8)	0.0146(8)	-0.0047(6)	-0.0049(6)	-0.0018(6)
C9	0.0130(8)	0.0126(7)	0.0100(7)	-0.0032(6)	-0.0017(6)	-0.0003(6)
N3	0.0098(6)	0.0110(6)	0.0100(6)	-0.0027(5)	-0.0024(5)	-0.0007(5)
C10	0.0094(7)	0.0134(8)	0.0155(8)	-0.0020(6)	-0.0045(6)	0.0001(6)
C11	0.0140(8)	0.0146(8)	0.0175(8)	-0.0026(6)	-0.0088(6)	0.0003(6)
C12	0.0141(8)	0.0145(8)	0.0200(8)	-0.0048(6)	-0.0086(7)	-0.0007(6)
N4	0.0116(7)	0.0107(6)	0.0122(7)	-0.0013(5)	-0.0035(5)	-0.0013(5)
C13	0.0151(8)	0.0097(7)	0.0158(8)	-0.0022(6)	-0.0036(6)	-0.0016(6)
C14	0.0276(10)	0.0151(8)	0.0227(9)	-0.0079(7)	-0.0100(8)	0.0007(7)
C15	0.0162(9)	0.0274(10)	0.0304(10)	-0.0083(8)	-0.0137(8)	0.0013(7)
C16	0.0123(7)	0.0151(8)	0.0097(7)	-0.0021(6)	-0.0009(6)	-0.0021(6)
C17	0.0175(8)	0.0150(8)	0.0136(8)	0.0010(6)	-0.0025(7)	-0.0020(6)
C18	0.0291(10)	0.0191(9)	0.0115(8)	-0.0026(7)	-0.0036(7)	-0.0112(7)
O1	0.0390(9)	0.0233(7)	0.0178(7)	-0.0055(5)	0.0084(6)	-0.0100(6)
N5	0.0440(11)	0.0174(8)	0.0137(8)	0.0033(6)	-0.0032(7)	-0.0108(7)
Cl1	0.0170(2)	0.01337(19)	0.01618(19)	0.00125(15)	-0.00485(15)	-0.00017(15)
O11	0.0582(11)	0.0291(8)	0.0459(10)	-0.0105(7)	-0.0370(9)	0.0003(7)
O12	0.0251(8)	0.0299(8)	0.0392(9)	0.0090(7)	0.0122(7)	-0.0011(6)
O13	0.0278(7)	0.0163(7)	0.0427(9)	-0.0066(6)	-0.0176(7)	0.0051(5)

	U^{11}	U^{22}	U^{33}	U^{23}	U^{13}	U^{12}
O14	0.0199(7)	0.0271(7)	0.0164(6)	0.0051(5)	-0.0044(5)	0.0010(5)
Cl2	0.01494(19)	0.01339(19)	0.01406(19)	-0.00325(14)	-0.00443(15)	-0.00080(14)
O21	0.0184(7)	0.0245(7)	0.0344(8)	-0.0065(6)	-0.0020(6)	-0.0067(5)
O22	0.0311(8)	0.0298(8)	0.0264(7)	0.0012(6)	-0.0184(6)	-0.0006(6)
O23	0.0319(8)	0.0280(7)	0.0146(6)	-0.0073(5)	-0.0052(6)	-0.0038(6)
O24	0.0254(7)	0.0137(6)	0.0344(8)	-0.0083(6)	-0.0054(6)	-0.0015(5)
O1W	0.0414(10)	0.0319(9)	0.0348(9)	-0.0023(7)	-0.0112(7)	-0.0105(7)

Table 6.10. Hydrogen coordinates and isotropic displacement parameters ($Å^2$) for $[CuL_5](ClO_4)_2 \cdot H_2O$.

	x	y	z	U_{eq}
H2	0.0387	0.5969	0.2619	0.021
H3	-0.1542	0.6061	0.1755	0.023
H4	-0.1795	0.4477	0.1002	0.021
H6	0.0711	0.2568	0.0027	0.017
H2N	0.017(2)	0.1067(17)	0.2163(16)	0.014
H7A	0.2370	0.0928	-0.0062	0.019
H7B	0.0808	0.0267	0.0493	0.019
H8A	0.2852	-0.1056	0.0741	0.017
H8B	0.1693	-0.0868	0.2055	0.017
H9A	0.4453	-0.0899	0.1724	0.015
H9B	0.4440	0.0335	0.0849	0.015
H10A	0.5558	0.0920	0.1978	0.015
H10B	0.5358	-0.0240	0.2985	0.015
H11A	0.3936	0.0944	0.4492	0.018
H11B	0.5759	0.1097	0.3883	0.018
H12A	0.4537	0.2931	0.3956	0.018
H12B	0.5183	0.2818	0.2554	0.018
H4N	0.217(2)	0.2617(18)	0.4030(15)	0.014
H13	0.3487	0.4382	0.2248	0.017
H14A	0.1281	0.4491	0.4617	0.031
H14B	0.2075	0.5583	0.3647	0.031
H14C	0.3110	0.4590	0.4235	0.031
H15A	-0.1428	0.1414	0.0687	0.034
H15B	-0.1965	0.2769	0.0496	0.034
H15C	-0.2224	0.2031	0.1840	0.034
H16A	0.1266	-0.0261	0.3696	0.016
H16B	0.2156	0.0075	0.4478	0.016
H17A	0.2886	-0.1955	0.3420	0.02
H17B	0.3999	-0.1587	0.4011	0.02

	x	y	z	U_{eq}
H1N5	0.337(2)	-0.355(2)	0.508(2)	0.032
H2N5	0.203(3)	-0.366(2)	0.6244(17)	0.032
H1W	0.473(3)	-0.395(3)	0.448(2)	0.055
H2W	0.612(3)	-0.351(2)	0.370(3)	0.055

Table 6.11. Hydrogen bond distances (Å) and angles (°) for $[CuL_5](ClO_4)_2 \cdot H_2O$.

	Donor-H	Acceptor-H	Donor-Acceptor	DHA Angle
C4-H4...O13	0.95	2.42	3.272(2)	148.9
C6-H6...O23	1.0	2.65	3.418(2)	133.9
N2-H2N...O1	0.870(15)	2.379(19)	2.9575(19)	124.3(17)
N2-H2N...O24	0.870(15)	2.426(17)	3.2051(19)	149.3(18)
C7-H7A...O11	0.99	2.63	3.484(3)	145.0
C8-H8B...Cl2	0.99	2.94	3.7823(17)	143.5
C9-H9A...O11	0.99	2.62	3.543(2)	154.3
C9-H9B...O14	0.99	2.63	3.321(2)	127.2
C10-H10A...O14	0.99	2.57	3.217(2)	123.0
C10-H10B...O21	0.99	2.63	3.604(2)	168.3
C11-H11A...O21	0.99	2.66	3.268(2)	120.1
N4-H4N...O22	0.866(15)	2.433(16)	3.291(2)	171.3(19)
C13-H13...O12	1.0	2.64	3.267(2)	120.8
C17-H17B...O21	0.99	2.66	3.628(2)	167.1
N5-H1N5...O1W	0.873(17)	2.127(17)	2.996(3)	173.(2)
O1W-H1W...N5	0.920(17)	2.14(2)	2.996(3)	154.(3)
O1W-H2W...O21	0.879(17)	1.983(19)	2.838(2)	164.(3)

6.5. Crystallographic Information for $[CuL_{6a}](ClO_4)_2 \cdot H_2O$

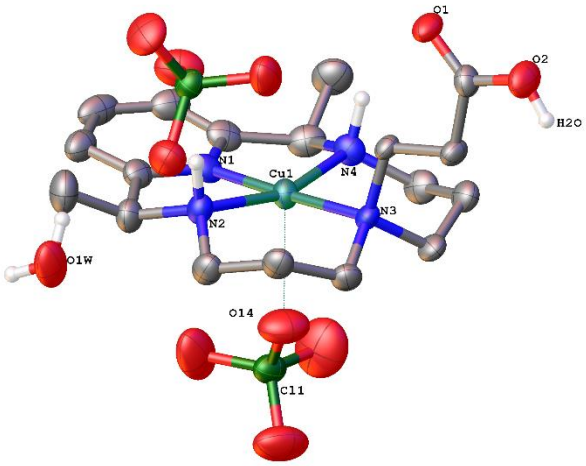

Figure 6.5. Thermal ellipsoid plot of $[CuL_{6a}](ClO_4)_2 \cdot H_2O$ shown at the 50 % probability level. Hydrogen atoms on carbon have been omitted for clarity. Selected distances (Å) and angles (°): Cu1−N1 = 1.922(4), Cu1−N2 = 2.035(4), Cu1−N3 = 2.020(4), Cu1−N4 = 2.035(4), Cu1−O14 = 2.481(4), N1−Cu1−N2 = 82.28(16), N1−Cu1−N3 = 177.92(15), N1−Cu1−N4 = 83.03(16), N2−Cu1−N4 = 160.89(16), N3−Cu1−N2 = 97.73(15), N3−Cu1−N4 = 96.52(15).

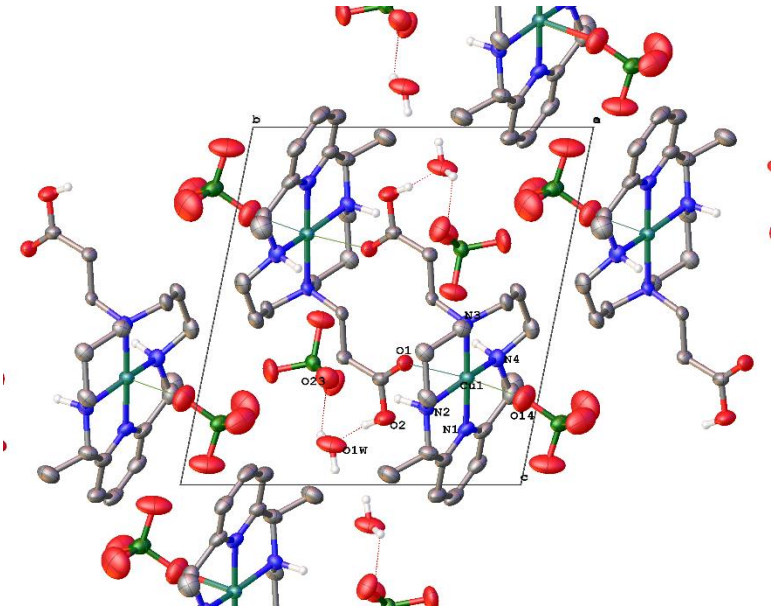

Figure 6.6. Packing diagram for $[CuL_{6a}](ClO_4)_2 \cdot H_2O$ projected along the *a* axis. Selected distances (Å) and angles (°): Cu1−O1 = 2.732(3), Cu1−O14 = 2.481(4), O2−O1W = 2.664(6), O2−H2···O1W = 168.3.

Table 6.12. Crystallographic and refinement parameters for $[CuL_{6a}](ClO_4)_2 \cdot H_2O$.

Identification code	053013 (completed in house)
Empirical Formula	C18 H32 Cl2 Cu N4 O11
Formula weight	614.91
Temperature (K)	100(2)
Wavelength (Å)	0.71076
Crystal system	Triclinic
Space group	*P*−1 (no. 2)
Unit cell dimensions:	
a (Å)	9.3242(7)
b (Å)	11.9724(10)
c (Å)	12.0303(10)
α (deg)	76.208(3)
β (deg)	81.430(3)
γ (deg)	68.254(2)
Volume ($Å^3$)	1208.70(17)
Z	2
ρ_{calc} ($g\ cm^{-1}$)	1.690
Absorption coefficient (mm^{-1})	1.191
F(000)	638
Crystal size (mm^3)	0.25 × 0.20 × 0.18
Crystal color	purple
Crystal morphology	block
Theta range for data collection (deg)	2.678 to 26.370
Index ranges	$-11 \le h \le 11$
	$-14 \le k \le 14$
	$-15 \le l \le 15$
Reflections collected	33366
Independent reflections	4931 [R(int) = 0.0462]
Completeness to θ = 25.243 ° (%)	99.8
Absorption correction	Semi-empirical from equivalents
Max. and min. transmission	0.8140 and 0.7550
Refinement method	Full-matrix least squares on F^2
Data / restraints / parameters	4931 / 97 / 334
Goodness-of-fit on F^2	1.052
Final R indices [I>2sigma(I)]	R_1 = 0.0637, wR_2 = 0.1621
R indices (all data)	R_1 = 0.0841, wR_2 = 0.1747
Largest diff. peak and hole (e $Å^{-3}$)	2.075 and −0.699

Table 6.13. Atomic coordinates (× 10^4) and equivalent isotropic displacement parameters (Å^2 × 10^3) for $[CuL_{6a}](ClO_4)_2 \cdot H_2O$. U_{eq} is defined as one third of the trace of the orthogonalized U^{ij} tensor.

	x	y	z	U_{eq}
Cu1	2124.8(6)	2220.3(5)	7011.4(4)	27.31(19)
N1	964(4)	1940(3)	8445(3)	30.3(8)
N2	2750(4)	3249(4)	7841(3)	29.9(8)
N3	3277(4)	2569(3)	5485(3)	25.2(8)
N4	814(5)	1454(4)	6459(3)	33.2(9)
C1	-103(6)	1428(5)	8489(4)	37.0(11)
C2	-1145(6)	1400(5)	9432(5)	42.0(13)
C3	-1026(6)	1896(5)	10332(5)	48.4(15)
C4	110(6)	2397(5)	10288(4)	41.8(12)
C5	1085(6)	2418(4)	9307(4)	33.5(10)
C6	2416(6)	2899(5)	9113(4)	38.4(11)
C7	4342(6)	3264(5)	7581(4)	37.3(11)
C8	4711(6)	3615(5)	6301(4)	35.7(11)
C9	4798(5)	2664(5)	5634(4)	33.5(10)
C10	3716(6)	1503(4)	4900(4)	33(1)
C11	2376(6)	1231(5)	4619(4)	35.9(11)
C12	1587(6)	631(5)	5627(5)	40.9(12)
C13	35(6)	842(5)	7454(5)	41.4(12)
C14	-1499(7)	848(6)	7189(6)	52.9(15)
C15	2131(8)	3936(6)	9713(5)	53.0(15)
C16	2244(5)	3719(4)	4795(3)	24.1(9)
C17	2855(5)	4049(4)	3564(4)	29.5(10)
C18	1776(6)	5248(4)	2955(4)	31.1(10)
O1	595(4)	5865(3)	3406(3)	39.2(8)
O2	2200(5)	5614(4)	1869(3)	47.9(10)
Cl1	4787.7(14)	-789.8(12)	8284.3(10)	38.6(3)
O11	6413(5)	-1380(5)	8219(5)	83.6(16)
O12	4168(6)	-652(6)	9425(4)	85.9(17)
O13	4087(8)	-1433(6)	7814(6)	100.0(19)
O14	4466(5)	416(4)	7587(4)	70.5(13)
Cl2	1609.9(13)	6837.4(10)	6591.7(9)	30.7(3)
O21	844(5)	8032(3)	6818(4)	56.2(11)
O22	1742(5)	6862(5)	5387(3)	59.6(12)
O23	3119(4)	6319(4)	7014(4)	54.9(10)
O24	712(5)	6093(4)	7146(4)	56.8(11)
O1W	5039(5)	5800(5)	8871(3)	62.8(13)

Table 6.14. Bond lengths (Å) and angles (°) for $[CuL_{6a}](ClO_4)_2 \cdot H_2O$.

Cu1-N1	1.922(4)
Cu1-N2	2.035(4)
Cu1-N3	2.020(4)
Cu1-N4	2.035(4)
N1-C1	1.337(6)
N1-C5	1.335(6)
N2-C6	1.504(6)
N2-C7	1.478(6)
N3-C9	1.504(6)
N3-C10	1.499(6)
N3-C16	1.491(5)
N4-C12	1.490(6)
N4-C13	1.487(6)
C1-C2	1.382(7)
C1-C13	1.536(8)
C2-C3	1.388(8)
C3-C4	1.387(8)
C4-C5	1.380(7)
C5-C6	1.518(7)
C6-C15	1.503(7)
C7-C8	1.519(7)
C8-C9	1.514(7)
C10-C11	1.504(7)
C11-C12	1.496(7)
C13-C14	1.509(7)
C16-C17	1.520(6)
C17-C18	1.503(6)
C18-O1	1.210(6)
C18-O2	1.324(6)
Cl1-O11	1.414(4)
Cl1-O12	1.430(4)
Cl1-O13	1.425(5)
Cl1-O14	1.433(4)
Cl2-O21	1.415(4)
Cl2-O22	1.430(4)
Cl2-O23	1.428(4)
Cl2-O24	1.429(4)
N1-Cu1-N2	82.28(16)
N1-Cu1-N3	177.92(15)
N1-Cu1-N4	83.03(16)
N3-Cu1-N2	97.73(15)
N3-Cu1-N4	96.52(15)

N4-Cu1-N2	160.89(16)
C1-N1-Cu1	118.4(3)
C5-N1-Cu1	119.0(3)
C5-N1-C1	121.9(4)
C6-N2-Cu1	109.8(3)
C7-N2-Cu1	116.9(3)
C7-N2-C6	110.8(4)
C9-N3-Cu1	111.5(3)
C10-N3-Cu1	109.7(3)
C10-N3-C9	104.3(3)
C16-N3-Cu1	107.6(2)
C16-N3-C9	112.0(3)
C16-N3-C10	111.8(3)
C12-N4-Cu1	117.0(3)
C13-N4-Cu1	110.3(3)
C13-N4-C12	111.1(4)
N1-C1-C2	120.5(5)
N1-C1-C13	113.6(4)
C2-C1-C13	125.8(5)
C1-C2-C3	118.0(5)
C4-C3-C2	121.0(5)
C5-C4-C3	117.7(5)
N1-C5-C4	120.9(5)
N1-C5-C6	113.7(4)
C4-C5-C6	125.3(5)
N3-C10-C11	115.0(4)
C12-C11-C10	114.7(4)
N4-C12-C11	112.0(4)
N4-C13-C1	108.9(4)
N4-C13-C14	113.0(5)
C14-C13-C1	112.6(5)
N3-C16-C17	114.9(3)
C18-C17-C16	111.0(4)
O1-C18-C17	123.5(4)
O1-C18-O2	120.7(4)
O2-C18-C17	115.7(4)
O11-Cl1-O12	112.5(3)
O11-Cl1-O13	109.5(4)
O11-Cl1-O14	107.0(3)
O12-Cl1-O14	107.5(3)
O13-Cl1-O12	111.9(4)
O13-Cl1-O14	108.2(4)
O21-Cl2-O22	110.7(3)
O21-Cl2-O23	110.5(3)

O21-Cl2-O24	108.4(3)
O23-Cl2-O22	109.2(2)
O23-Cl2-O24	109.7(3)
O24-Cl2-O22	108.2(3)

Table 6.15. Anisotropic displacement parameters ($Å^2 \times 10^3$) for $[CuL_{6a}](ClO_4)_2 \cdot H_2O$. The anisotropic displacement factor exponent takes the form: $-2\pi^2[h^2 a^{*2} U^{11} + ... + 2 h k a^* b^* U^{12}]$.

	U^{11}	U^{22}	U^{33}	U^{23}	U^{13}	U^{12}
Cu1	33.1(3)	27.8(3)	23.7(3)	-5.3(2)	-0.7(2)	-14.0(2)
N1	33(2)	30(2)	27(2)	3.9(16)	-6.4(16)	-12.8(17)
N2	31(2)	33(2)	28(2)	-11.1(16)	0.9(16)	-12.5(17)
N3	24.8(19)	24.3(18)	24.9(18)	-9.6(15)	1.1(14)	-5.2(15)
N4	34(2)	33(2)	37(2)	-5.9(17)	-5.3(17)	-17.2(18)
C1	39(3)	33(3)	33(3)	9(2)	-4(2)	-15(2)
C2	36(3)	36(3)	43(3)	8(2)	2(2)	-12(2)
C3	41(3)	41(3)	39(3)	10(2)	11(2)	-3(2)
C4	42(3)	41(3)	29(3)	-2(2)	3(2)	-5(2)
C5	35(3)	34(3)	25(2)	1.1(19)	-3.4(19)	-8(2)
C6	41(3)	47(3)	26(2)	-10(2)	1(2)	-14(2)
C7	29(3)	48(3)	41(3)	-19(2)	-1(2)	-16(2)
C8	27(2)	44(3)	42(3)	-14(2)	-1(2)	-16(2)
C9	23(2)	41(3)	35(3)	-10(2)	-0.1(19)	-9(2)
C10	33(3)	26(2)	37(3)	-14.1(19)	-4(2)	-0.9(19)
C11	38(3)	34(3)	38(3)	-17(2)	-3(2)	-9(2)
C12	43(3)	35(3)	53(3)	-16(2)	-6(2)	-16(2)
C13	38(3)	32(3)	54(3)	-5(2)	-2(2)	-15(2)
C14	39(3)	60(4)	67(4)	-18(3)	0(3)	-24(3)
C15	66(4)	63(4)	38(3)	-22(3)	3(3)	-28(3)
C16	24(2)	21(2)	24(2)	-8.0(17)	2.9(17)	-3.5(17)
C17	27(2)	30(2)	26(2)	-6.9(18)	3.9(18)	-5.1(19)
C18	40(3)	32(2)	22(2)	-4.6(19)	-1.2(19)	-14(2)
O1	40(2)	31.1(18)	31.1(18)	-5.9(14)	0.4(15)	3.3(15)
O2	55(2)	46(2)	27.8(18)	-1.0(16)	5.7(16)	-8.8(18)
Cl1	31.4(6)	43.2(7)	32.6(6)	-1.9(5)	1.3(5)	-8.0(5)
O11	41(3)	97(4)	84(4)	4(3)	3(2)	-8(3)
O12	68(3)	152(5)	43(3)	-19(3)	15(2)	-52(3)
O13	109(5)	106(5)	120(5)	-41(4)	3(4)	-69(4)
O14	54(3)	53(3)	82(3)	4(2)	-8(2)	-3(2)
Cl2	31.2(6)	29.7(6)	33.5(6)	-10.0(5)	1.3(4)	-12.4(5)
O21	71(3)	33(2)	70(3)	-21.8(19)	-4(2)	-17(2)

	U^{11}	U^{22}	U^{33}	U^{23}	U^{13}	U^{12}
O22	49(2)	93(3)	37(2)	-20(2)	4.1(18)	-23(2)
O23	45(2)	66(3)	56(3)	-19(2)	-7.2(19)	-17(2)
O24	48(2)	45(2)	78(3)	4(2)	-5(2)	-25.4(19)
O1W	54(3)	110(4)	34(2)	-20(2)	13.7(18)	-43(3)

Table 6.16. Hydrogen coordinates (Å × 10^4) and isotropic displacement parameters (Å^2 × 10^3) for $[CuL_{6a}](ClO_4)_2 \cdot H_2O$.

	x	y	z	U_{eq}
H2N	2045	4115	7600	36
H4N	-33	2154	6048	40
H2	-1919	1053	9464	50
H3	-1734	1893	10987	58
H4	213	2715	10913	50
H6	3349	2209	9427	46
H7A	5084	2441	7882	45
H7B	4470	3857	7973	45
H8A	3907	4401	5991	43
H8B	5715	3748	6179	43
H9A	5303	2854	4864	40
H9B	5472	1853	6027	40
H10A	4382	763	5398	40
H10B	4339	1666	4179	40
H11A	1605	2009	4255	43
H11B	2753	691	4050	43
H12A	806	398	5355	49
H12B	2359	-129	6020	49
H13	727	-35	7654	50
H14A	-1355	484	6514	79
H14B	-2227	1694	7035	79
H14C	-1913	369	7847	79
H15A	3025	4207	9554	80
H15B	1976	3656	10542	80
H15C	1205	4621	9435	80
H16A	2069	4406	5182	29
H16B	1230	3634	4785	29
H17A	3887	4109	3560	35
H17B	2974	3392	3152	35
H2O	3029	5085	1678	72
H1W	4980(80)	5540(70)	9579(14)	94
H2W	4160(40)	6170(70)	8620(50)	94

Table 6.17. Hydrogen bond distances (Å) and angles (°) for $[CuL_{6a}](ClO_4)_2 \cdot H_2O$.

D-H···A	Donor-H	Acceptor-H	Donor-Acceptor	DHA Angle
N2-H2N···O24	1.00	2.20	3.198(6)	172.7
N4-H4N···O1[a]	1.00	2.46	3.019(5)	114.9
N4-H4N···O22[a]	1.00	2.32	3.250(6)	154.9
C2-H2···O12[b]	0.95	2.45	3.281(7)	145.6
C9-H9B···O14	0.99	2.55	3.202(7)	123.4
C10-H10A···O14	0.99	2.57	3.260(7)	126.4
C10-H10B···O13[c]	0.99	2.64	3.587(8)	161.3
C16-H16B···O1[a]	0.99	2.60	3.126(5)	113.3
C17-H17A···O23[d]	0.99	2.66	3.593(6)	157.5
O2-H2O···O1W[d]	0.84	1.84	2.664(6)	168.3
O1W-H1W···O1W[e]	0.834(10)	2.16(3)	2.935(9)	155(8)
O1W-H2W···O23	0.836(10)	2.23(5)	2.879(6)	135(7)

Symmetry transformations used to generate equivalent atoms: [a] $-x, 1-y, 1-z$; [b] $-x, -y, 2-z$; [c] $1-x, -y, -z$; [d] $1-x, 1-y, 1-z$; [e] $1-x, 1-y, 2-z$.

6.6. Crystallographic Information for [Fe(L_2)Cl]Cl

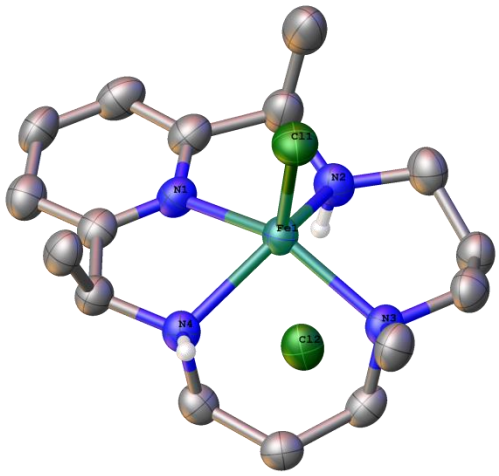

Figure 6.7. Thermal ellipsoid plot of [FeL_2(Cl)]Cl shown at the 50 % probability level. Carbon-bound hydrogen atoms are omitted for clarity. Selected distances (Å) and angles (°): Fe1−N1 = 2.115(4), Fe1−N2 = 2.197(5), Fe1−N3 = 2.158(4), Fe1−N4 = 2.174(5), Fe1−Cl1 = 2.2837(16), N1−Fe1−N2 = 72.38(18), N1−Fe1−N4 = 75.06(18), N2−Fe1−N3 = 91.84(18), N3−Fe1−N4 = 94.05(17), N1−Fe1−N3 = 144.90(17), Cl1−Fe1−N1 = 110.21(14), Cl1−Fe1−N2 = 113.30(14), Cl1−Fe1−N3 = 104.80(13), Cl1−Fe1−N4 = 112.42(12).

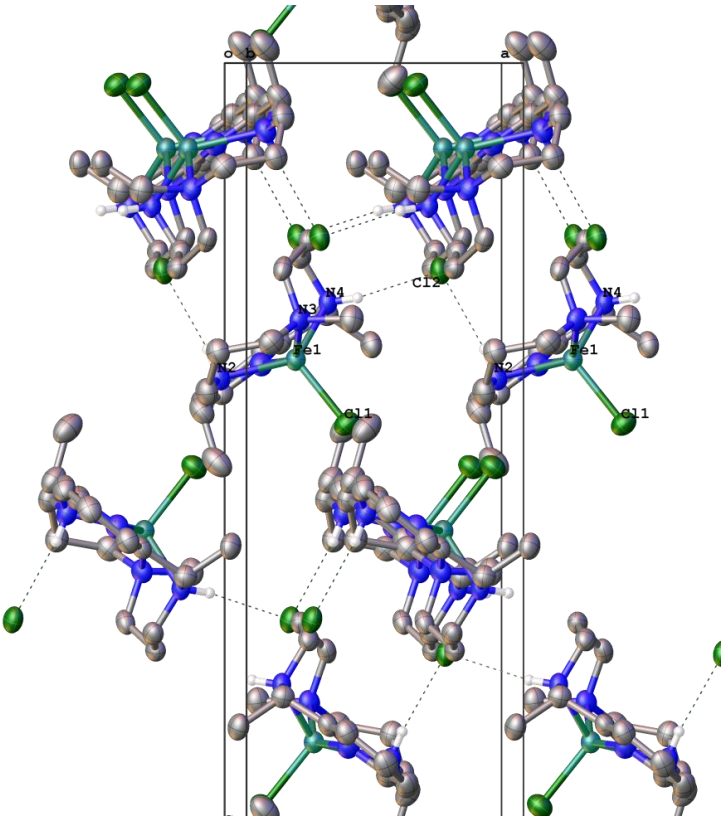

Figure 6.8. Packing diagram for [FeL$_2$(Cl)]Cl projected along the *b* axis. Selected distances (Å) and angles (°): Cl2−N2 = 3.365(5), Cl2−N4 = 3.304(4), N2−H2···Cl2 = 171(5), N4−H4···Cl2 = 169(5).

Table 6.18. Crystallographic and refinement parameters for [FeL$_2$(Cl)]Cl.

Identification code	080309 (data collection by A. Filatov)
Empirical Formula	C16 H28 Cl2 Fe N4
Formula weight	403.17
Temperature (K)	173(2)
Wavelength (Å)	0.71073
Crystal system	Orthorhombic
Space group	$P2_12_12_1$ (no. 19)
Unit cell dimensions:	
a (Å)	7.6668(11)
b (Å)	11.6122(16)
c (Å)	21.157(3)
α (deg)	90.00
β (deg)	90.00
γ (deg)	90.00
Volume (Å^3)	1883.6(5)

Z	4
ρ_{calc} (g cm^{-1})	1.422
Absorption coefficient (mm^{-1})	1.089
F(000)	848
Crystal size (mm^3)	0.18 × 0.16 × 0.10
Crystal color	yellow
Crystal morphology	block
Theta range for data collection (deg)	1.93 to 28.10
Index ranges	$-10 \leq h \leq 10$ $-15 \leq k \leq 15$ $-26 \leq l \leq 27$
Reflections collected	15021
Independent reflections	4302 [R(int) = 0.0436]
Completeness to θ = 26 ° (%)	100
Absorption correction	Semi-empirical from equivalents
Max. and min. transmission	0.8989 and 0.8282
Refinement method	Full-matrix least squares on F^2
Data / restraints / parameters	4302 / 2 / 218
Goodness-of-fit on F^2	1.027
Final R indices [I>2sigma(I)]	R_1 = 0.0627, wR_2 = 0.1350
R indices (all data)	R_1 = 0.0763, wR_2 = 0.1419
Largest diff. peak and hole (e Å^{-3})	0.091 and −0.291

Table 6.19. Atomic coordinates (× 10^4) and equivalent isotropic displacement parameters (Å^2 × 10^3) for [FeL$_2$(Cl)]Cl. U_{eq} is defined as one third of the trace of the orthogonalized U^{ij} tensor.

	x	y	z	U_{eq}
Fe(1)	7862(1)	10412(1)	1121(1)	36(1)
N(1)	8981(6)	8751(4)	1060(2)	43(1)
N(2)	10633(6)	10626(4)	884(2)	45(1)
N(3)	7828(6)	12006(4)	1646(2)	40(1)
N(4)	6620(5)	9427(4)	1870(2)	38(1)
Cl(1)	6043(2)	10725(1)	284(1)	52(1)
Cl(2)	2623(2)	181(1)	2280(1)	47(1)
C(1)	8173(7)	7852(5)	1339(3)	40(1)
C(2)	8761(8)	6736(5)	1246(3)	48(1)
C(3)	10155(8)	6570(5)	836(3)	49(1)
C(4)	11001(8)	7494(5)	558(3)	53(2)
C(5)	10388(8)	8601(5)	689(3)	47(1)
C(6)	11194(8)	9704(5)	451(3)	52(1)
C(7)	10666(10)	9935(6)	-220(3)	68(2)
C(8)	11180(8)	11790(5)	699(3)	51(2)

	x	y	z	U_{eq}
C(9)	10842(8)	12651(5)	1227(3)	48(1)
C(10)	8937(8)	12930(5)	1350(3)	49(1)
C(11)	6001(8)	12459(5)	1653(3)	50(2)
C(12)	8435(7)	11801(5)	2312(3)	41(1)
C(13)	7422(7)	10894(4)	2680(2)	41(1)
C(14)	7611(6)	9644(5)	2460(2)	41(1)
C(15)	6565(7)	8182(5)	1714(3)	43(1)
C(16)	4940(7)	7929(5)	1318(3)	47(1)

Table 6.20. Bond lengths (Å) and angles (°) for $[FeL_2(Cl)]Cl$.

Fe(1)-N(1)	2.115(4)
Fe(1)-N(3)	2.158(4)
Fe(1)-N(4)	2.174(5)
Fe(1)-N(2)	2.197(5)
Fe(1)-Cl(1)	2.2837(16)
N(1)-C(5)	1.346(8)
N(1)-C(1)	1.350(7)
N(2)-C(8)	1.468(7)
N(2)-C(6)	1.473(7)
N(2)-H(2)	0.88(2)
N(3)-C(11)	1.497(7)
N(3)-C(12)	1.503(7)
N(3)-C(10)	1.505(7)
N(4)-C(15)	1.483(7)
N(4)-C(14)	1.483(7)
N(4)-H(4)	0.87(2)
C(1)-C(2)	1.385(8)
C(1)-C(15)	1.515(8)
C(2)-C(3)	1.389(9)
C(2)-H(2A)	0.9500
C(3)-C(4)	1.385(9)
C(3)-H(3)	0.9500
C(4)-C(5)	1.396(8)
C(4)-H(4A)	0.9500
C(5)-C(6)	1.508(8)
C(6)-C(7)	1.502(10)
C(6)-H(6)	1.0000
C(7)-H(7A)	0.9800
C(7)-H(7B)	0.9800
C(7)-H(7C)	0.9800

C(8)-C(9)	1.522(8)
C(8)-H(8A)	0.9900
C(8)-H(8B)	0.9900
C(9)-C(10)	1.519(8)
C(9)-H(9A)	0.9900
C(9)-H(9B)	0.9900
C(10)-H(10A)	0.9900
C(10)-H(10B)	0.9900
C(11)-H(11A)	0.9800
C(11)-H(11B)	0.9800
C(11)-H(11C)	0.9800
C(12)-C(13)	1.522(7)
C(12)-H(12A)	0.9900
C(12)-H(12B)	0.9900
C(13)-C(14)	1.531(7)
C(13)-H(13A)	0.9900
C(13)-H(13B)	0.9900
C(14)-H(14A)	0.9900
C(14)-H(14B)	0.9900
C(15)-C(16)	1.530(8)
C(15)-H(15)	1.0000
C(16)-H(16A)	0.9800
C(16)-H(16B)	0.9800
C(16)-H(16C)	0.9800

N(1)-Fe(1)-N(3)	144.90(17)
N(1)-Fe(1)-N(4)	75.06(18)
N(3)-Fe(1)-N(4)	94.05(17)
N(1)-Fe(1)-N(2)	72.38(18)
N(3)-Fe(1)-N(2)	91.84(18)
N(4)-Fe(1)-N(2)	130.51(17)
N(1)-Fe(1)-Cl(1)	110.21(14)
N(3)-Fe(1)-Cl(1)	104.80(13)
N(4)-Fe(1)-Cl(1)	112.42(12)
N(2)-Fe(1)-Cl(1)	113.30(14)
C(5)-N(1)-C(1)	121.5(5)
C(5)-N(1)-Fe(1)	118.6(4)
C(1)-N(1)-Fe(1)	119.5(4)
C(8)-N(2)-C(6)	114.8(5)
C(8)-N(2)-Fe(1)	116.2(4)
C(6)-N(2)-Fe(1)	110.0(4)
C(8)-N(2)-H(2)	111(4)
C(6)-N(2)-H(2)	106(4)
Fe(1)-N(2)-H(2)	97(4)

C(11)-N(3)-C(12)	109.6(4)
C(11)-N(3)-C(10)	106.4(4)
C(12)-N(3)-C(10	109.1(4)
C(11)-N(3)-Fe(1)	108.5(3)
C(12)-N(3)-Fe(1)	110.1(3)
C(10)-N(3)-Fe(1)	113.0(3)
C(15)-N(4)-C(14)	111.5(4)
C(15)-N(4)-Fe(1)	111.3(3)
C(14)-N(4)-Fe(1)	107.4(3)
C(15)-N(4)-H(4)	110(4)
C(14)-N(4)-H(4)	107(4)
Fe(1)-N(4)-H(4)	109(4)
N(1)-C(1)-C(2)	120.8(5)
N(1)-C(1)-C(15)	114.0(5)
C(2)-C(1)-C(15)	125.2(5)
C(1)-C(2)-C(3)	117.9(6)
C(1)-C(2)-H(2A)	121.0
C(3)-C(2)-H(2A)	121.0
C(4)-C(3)-C(2)	121.2(5)
C(4)-C(3)-H(3)	119.4
C(2)-C(3)-H(3)	119.4
C(3)-C(4)-C(5)	118.1(6)
C(3)-C(4)-H(4A)	121.0
C(5)-C(4)-H(4A)	121.0
N(1)-C(5)-C(4)	120.3(6)
N(1)-C(5)-C(6)	114.4(5)
C(4)-C(5)-C(6)	125.3(5)
N(2)-C(6)-C(7)	112.3(5)
N(2)-C(6)-C(5)	106.9(4)
C(7)-C(6)-C(5)	110.9(5)
N(2)-C(6)-H(6)	108.9
C(7)-C(6)-H(6)	108.9
C(5)-C(6)-H(6)	108.9
C(6)-C(7)-H(7A)	109.5
C(6)-C(7)-H(7B)	109.5
H(7A)-C(7)-H(7B)	109.5
C(6)-C(7)-H(7C)	109.5
H(7A)-C(7)-H(7C)	109.5
H(7B)-C(7)-H(7C)	109.5
N(2)-C(8)-C(9)	111.1(5)
N(2)-C(8)-H(8A)	109.4
C(9)-C(8)-H(8A)	109.4
N(2)-C(8)-H(8B)	109.4
C(9)-C(8)-H(8B)	109.4

H(8A)-C(8)-H(8B)	108.0
C(10)-C(9)-C(8)	115.5(5)
C(10)-C(9)-H(9A)	108.4
C(8)-C(9)-H(9A)	108.4
C(10)-C(9)-H(9B)	108.4
C(8)-C(9)-H(9B)	108.4
H(9A)-C(9)-H(9B)	107.5
N(3)-C(10)-C(9)	117.5(5)
N(3)-C(10)-H(10A)	107.9
C(9)-C(10)-H(10A)	107.9
N(3)-C(10)-H(10B)	107.9
C(9)-C(10)-H(10B)	107.9
H(10A)-C(10)-H(10B)	107.2
N(3)-C(11)-H(11A)	109.5
N(3)-C(11)-H(11B)	109.5
H(11A)-C(11)-H(11B)	109.5
N(3)-C(11)-H(11C)	109.5
H(11A)-C(11)-H(11C)	109.5
H(11B)-C(11)-H(11C)	109.5
N(3)-C(12)-C(13)	115.5(4)
N(3)-C(12)-H(12A)	108.4
C(13)-C(12)-H(12A)	108.4
N(3)-C(12)-H(12B)	108.4
C(13)-C(12)-H(12B)	108.4
H(12A)-C(12)-H(12B)	107.5
C(12)-C(13)-C(14)	116.9(4)
C(12)-C(13)-H(13A)	108.1
C(14)-C(13)-H(13A)	108.1
C(12)-C(13)-H(13B)	108.1
C(14)-C(13)-H(13B)	108.1
H(13A)-C(13)-H(13B)	107.3
N(4)-C(14)-C(13)	111.6(4)
N(4)-C(14)-H(14A)	109.1(5)
C(13)-C(14)-H(14A)	109.9(5)
N(4)-C(14)-H(14B)	109.4(4)
C(13)-C(14)-H(14B)	108.0
H(14A)-C(14)-H(14B)	109.3
N(4)-C(15)-C(1)	109.3
N(4)-C(15)-C(16)	109.3
C(1)-C(15)-C(16)	109.3
N(4)-C(15)-H(15)	109.5
C(1)-C(15)-H(15)	109.5
C(16)-C(15)-H(15)	109.5
C(15)-C(16)-H(16A)	109.5

C(15)-C(16)-H(16B)	109.5
H(16A)-C(16)-H(16B)	109.5
C(15)-C(16)-H(16C)	109.5
H(16A)-C(16)-H(16C)	109.5
H(16B)-C(16)-H(16C)	109.5

Table 6.21. Anisotropic displacement parameters ($Å^2 \times 10^3$) for $[FeL_2Cl]Cl$. The anisotropic displacement factor exponent takes the form: $-2\pi^2[h^2 a^{*2} U^{11} + ... + 2 h k a^* b^* U^{12}]$.

	U^{11}	U^{22}	U^{33}	U^{23}	U^{13}	U^{12}
Fe1	33(1)	34(1)	41(1)	0(1)	-0(3)	-0(3)
N1	42(2)	40(2)	47(3)	-7(2)	1(2)	1(2)
N2	38(2)	45(3)	51(3)	1(2)	6(2)	0(2)
N3	37(2)	36(2)	46(2)	1(2)	-4(2)	7(2)
N4	29(2)	38(2)	46(2)	1(2)	1(2)	2(2)
Cl1	53(1)	57(1)	47(1)	1(1)	-10(1)	-1(1)
Cl2	34(1)	47(1)	59(1)	3(1)	6(1)	5(1)
C1	35(3)	41(3)	43(3)	-3(2)	-8(2)	1(2)
C2	46(3)	41(3)	56(4)	-1(3)	-6(3)	3(2)
C3	50(3)	36(3)	62(4)	-12(3)	-6(3)	6(2)
C4	43(3)	58(4)	58(4)	-18(3)	3(3)	6(3)
C5	44(3)	48(3)	50(3)	-10(3)	0(3)	0(3)
C6	51(3)	45(3)	60(4)	-6(3)	15(3)	-4(3)
C7	73(4)	56(4)	74(5)	-9(3)	25(4)	-12(3)
C8	42(3)	48(3)	61(4)	4(3)	4(3)	-6(3)
C9	46(3)	40(3)	57(4)	-1(3)	3(3)	-4(2)
C10	54(3)	38(3)	53(3)	3(3)	-4(3)	3(3)
C11	47(3)	38(3)	65(4)	-5(3)	-2(3)	4(3)
C12	31(3)	42(3)	51(3)	-11(3)	-6(2)	3(2)
C13	34(3)	47(3)	41(3)	-2(2)	-1(2)	4(2)
C14	36(3)	43(3)	44(3)	6(2)	-1(2)	5(2)
C15	46(3)	38(3)	44(3)	-2(2)	0(2)	1(2)
C16	38(3)	43(3)	60(4)	-6(3)	4(3)	-7(2)

Table 6.22. Hydrogen coordinates ($\times 10^4$) and isotropic displacement parameters ($Å^2 \times 10^3$) for $[FeL_2(Cl)]Cl$.

	x	y	z	U_{eq}
H2	11050(70)	10450(50)	1257(15)	54
H4	5570(40)	9690(50)	1930(30)	45
H2A	8228	6104	1456	58
H3	10534	5809	746	59
H4A	11971	7378	286	63
H6	12493	9633	472	62
H7A	9410	10086	-238	101
H7B	10942	9263	-482	101
H7C	11302	10607	-379	101
H8A	10533	12028	316	61
H8B	12439	11785	595	61
H9A	11358	12346	1622	57
H9B	11459	13376	1124	57
H10A	8891	13616	1627	58
H10B	8396	13147	942	58
H11A	5945	13147	1920	75
H11B	5215	11869	1821	75
H11C	5646	12658	1221	75
H12A	8367	12538	2546	49
H12B	9677	11568	2299	49
H13A	6170	11100	2664	49
H13B	7789	10936	3128	49
H14A	8859	9472	2388	49
H14B	7182	9123	2796	49
H15	6523	7722	2114	51
H16A	3894	8132	1561	71
H16B	4907	7108	1211	71
H16C	4976	8386	929	71

6.7. References

(1) Crystallographic information files (CIFs) and additional files are available on the Tufts University research drive: \\rstore1.tufts.ad.edu\as-rsch-rybakgroup$

(2) Ye, W.; Ho, D. M.; Friedle, S.; Palluccio, T. D.; Rybak-Akimova, E. V. *Inorg. Chem.* **2012**, *51*, 5006.

(3) Herrera, A. M.; Staples, R. J.; Kryatov, S. V.; Nazarenko, A. Y.; Rybak-Akimova, E. V. *Dalton Trans.* **2003**, 846.

(4) Organo, V. G.; Filatov, A. S.; Quartararo, J. S.; Friedman, Z. M.; Rybak-Akimova, E. V. *Inorg. Chem.* **2009**, *48*, 8456.

(5) SAINT, Version 6.02; Bruker AXS, Inc.: Madison, WI, 2001.

(6) SADABS; Bruker AXS, Inc.: Madison, WI, 2001.

(7) (a) Sheldrick, G. M. SHELXTL, Version 6.14; Bruker AXS, Inc.: Madison, WI. (b) Sheldrick, G. M. *Acta Crystallogr. A64*, **2008**, *64*, 112.

(8) Dolomanov, O. V.; Bourhis, L. J.; Gildea, R. J.; Howard, J. A. K.; Puschmann, H., OLEX2: A complete structure solution, refinement and analysis program (2009). *J. Appl. Cryst. 42*, 339.

(9) Müller, P.; Herbst-Irmer, R.; Spek, A. L.; Schneider, T. R.; Sawaya, M. R. *Crystal Structure Refinement: A Crystallographer's Guide to SHELXL*. IUCr Texts on Crystallography; Oxford University Press: Oxford, 2006.